به نام خدا

# مرکز دانلود رایگان
# مهندسی متالورژی و مواد

---

www.Iran-mavad.com

Tie Jun Cui
David R. Smith
Ruopeng Liu
*Editors*

# Metamaterials

## Theory, Design, and Applications

Springer

# Metamaterials

Tie Jun Cui · David R. Smith · Ruopeng Liu
Editors

# Metamaterials

## Theory, Design, and Applications

Springer

*Editors*
Tie Jun Cui
Department of Radio Engineering
Southeast University
2 Si-Pai Lou
210096 Nanjing
People's Republic of China
tjcui@seu.edu.cn

Ruopeng Liu
Department of Electrical &
Computer Engineering
Duke University
130 Hudson Hall
Durham NC 27706
USA
ruopeng.liu@duke.edu

David R. Smith
Department of Electrical &
Computer Engineering
Duke University
P.O.Box 90291
Durham NC 27708
USA
davidrsmith@ee.duke.edu

ISBN 978-1-4419-0572-7 e-ISBN 978-1-4419-0573-4
DOI 10.1007/978-1-4419-0573-4
Springer New York Dordrecht Heidelberg London

Library of Congress Control Number: 2009937582

*To the exciting, fast growing, and fully challenging area — Metamaterials.*

# Preface

Metamaterial, first known as left-handed material (LHM) or negative refractive index material (NIM), has attracted attention in the scientific communities over the past 10 years. The concept of metamaterial has a much broader scope than that of LHM or NIM. Due in large part to metamaterials, the classical subject of electromagnetism and optics have experienced a number of new discoveries and advances in research. First proposed by Veselago theoretically in 1968 for a material whose electric permittivity and magnetic permeability are simultaneously negative, LHM possesses many new features such as negative refraction, backward wave propagation, reversed Doppler shift, and backward Cerenkov radiation. Research in LHM was stagnant for more than 30 years due to the lack of experimental verification. The first revolution dealing with LHM occurred in 1996 when Sir Pendry discovered the wire medium whose permittivity is negative, followed by the discovery of negative permeability by Sir Pendry et al. in 1999 and LHM by Smith et al. in 2001. Inspired by the experimental realization, LHM – also called negative refractive index material – has attracted growing attention in both theoretical exploration and experimental study. However, LHM has the unavoidable disadvantage of big loss and narrow bandwidth, and such disadvantages restrict the applications of LHM. Hence scientists seek other features of metamaterial beyond negative refraction.

The second revolution in metamaterials came in 2005 when the gradient refraction index medium was realized to bend electromagnetic waves, which was discovered by Smith et al. In 2006 the optical transformation was proposed to make invisible cloaks to control the propagation of electromagnetic waves using metamaterials was discovered by Pendry et al. Metamaterial has a much broader definition than LHM, which does not require the negative permittivity and/or negative permeability, and hence opens a completely new area. The soul of metamaterial is the ability to control electromagnetic waves. After the experimental realization of invisible cloaks in the microwave regime, an even larger explosion of interest has occurred in metamaterials and optical transformation. This resulted in many scientific papers and popular science articles being published in journals and magazines.

As a summary of these scientific papers, up to date nine books on metamaterials have been published since 2003. Below is a glance at such published books:

- S. Zouhdi, A. Sihvola, and M. Arsalane, *Advances in Electromagnetics of Complex Media and Metamaterials*, Springer, 2003.
- S. Tretyakov, *Analytical Modeling in Applied Electromagnetics*, Artech House, 2003.
- G. V. Eleftheriades and K. G Balmain, *Negative-Refraction Metamaterials: Fundamental Principles and Applications*, Wiley-IEEE Press, 2005.
- C. Caloz and T. Itoh, *Electromagnetic Metamaterials: Transmission Line Theory and Microwave Applications*, Wiley-IEEE Press, 2006.
- N. Engheta and R. W. Ziolkowski, *Metamaterials: Physics and Engineering Explorations*, Wiley-IEEE Press, 2006.
- Sir J. B. Pendry, *Fundamentals and Applications of Negative Refraction in Metamaterials*, Princeton University Press, 2007.
- R. Marques, F. Martin, and M. Sorolla, *Metamaterials with Negative Parameters*, Wiley, 2007.
- S. A. Ramakrishna and T. M. Grzegorczyk, *Physics and Applications of Negative Refractive Index Materials*, SPIE and CRC Press, 2009.
- B. A. Munk, *Metamaterials: Critique and Alternatives*, Wiley, 2009.

These books are all valuable contributions to metamaterials. However, such books have mainly focused on LHM, negative refraction, photonic band-gap structures, and numerical methods. Only the books published in 2009 mentioned a few discussions on invisible cloaks. The main purpose of this book is to address the recent progress in metamaterials. We will introduce the optical transformation theory, revealing invisible cloaks, concentrators, beam bending, and new type antennas. We will present a general effective medium theory on artificial metamaterials composed of periodic structures. We also propose a rapid design method for inhomogeneous metamaterials, which makes it easier to design cloaks. Finally, we present broadband and low-loss non-resonant metamaterials, along with optical metamaterials.

Chapter 1 by Tie Jun Cui, David R. Smith and Ruopeng Liu, discusses the broad concepts of metamaterials and briefly reviews recent progress in the field. Chapter 2 by Wei Xiang Jiang and Tie Jun Cui presents the concepts and principles of optical transformation and discusses optical transformation devices, such as electromagnetic cloaks, concentrators, wave bending and antennas. Chapter 3 by Ruopeng Liu, Tie Jun Cui, and David R. Smith builds a general effective medium theory for artificial metamaterials composed of periodic structures. The theory provides effective permittivity and permeability in the system level by considering mutual coupling and spatial dispersion. Chapter 4 by Jessie Yao Chin, Ruopeng Liu, Tie Jun Cui and David R. Smith describes a rapid design method for complicated inhomogeneous metamaterials based on the general effective medium theory and the optimal-searching approach. Chapter 5 by Ruopeng Liu, Qiang Cheng, Tie Jun Cui and David R. Smith presents broadband and low-loss metamaterials using non-resonant structures, including the unit-cell design, the physical principle, and the effective medium theory. In Chapter 6, Ruopeng Liu, Jessie Y. Chin, Chunlin Ji, Tie Jun Cui, and David R. Smith show the design of electromagnetic cloaks using metamaterials, the 2D measurement system, and the measurement results of electromagnetic cloaks.

Chapter 7 by Christos Argyropoulos, Yan Zhao, Efthymios Kallos, and Yang Hao provides the full-wave simulations of electromagnetic cloaks using the radially dependent dispersive FDTD method to reveal the physics of the cloaks. In Chapter 8 Yijun Feng analyzes image focusing, rotation and lateral shift, as well as image magnification with sub-wavelength resolutions through differently designed structures of compensated anisotropic metamaterials. Chapter 9 by Xunya Jiang, Zheng Liu, Zixian Liang, Peijun Yao, Xulin Lin and Huanyang Chen investigates the dynamical performance of metamaterial systems, including the causality limit, the dynamical process, the correlation (coherence) study in metamaterial and extending the cloaking frequency range. In Chapter 10, Xueqin Huang, Shiyi Xiao, Lei Zhou, Weijia Wen, C. T. Chan and Ping Sheng show that a metallic plate with sub-wavelength fractal-shaped slits supports surface plasmon polaritons with the plasmon frequency tuned efficiently by the geometry of the fractal structure. The chapter also derives effective medium models to describe tunable plasmonic metamaterials. Chapter 11 by H. Liu, Y. M. Liu, T. Li, S. M. Wang, S. N. Zhu and X. Zhang reveals the recent developments in magnetic plasmonics arising from the coupling effect in metamaterials. Chapter 12 by Jun Xu, Anil Kumar, Pratik Chaturvedi, Keng H. Hsu and Nicholas X. Fang presents the development of plasmonic optical antennas for light concentration and near-field enhancement. In Chapter 13, Le-Wei Li, Ya-Nan Li and Li Hu investigate the applications of metamaterials in the microwave and RF components using wideband and low-loss metamaterials, and introduce some fast numerical methods to simulate metamaterials. Chapter 14 by Qiang Cheng, Xin Mi Yang, Tie Jun Cui, Ruopeng Liu and David R. Smith presents the applications of metamaterials in the design of new microwave components, antennas, and experiments. Finally in Chapter 15, Xin Hu and Sailing He propose a left-handed transmission line of low pass and study its applications.

We hope that the contents presented in this book will reflect new avenues of research on metamaterials and give appropriate guidance to scientists, engineers, and graduate students in this exciting area, and also generate novel microwave/optical devices and structures.

Southeast University, China, May, 2009 *Tie Jun Cui*
Duke University, USA, May, 2009 *David R. Smith*
Duke University, USA, May, 2009 *Ruopeng Liu*

# Acknowledgments

This book gathers the latest research results on metamaterials from several groups (in the order which appears in the book): Southeast University, China (TJC); Duke University, USA (DRS); Queen Mary, University of London, UK (Yang Hao); Nanjing University, China (Yijun Feng); Institute of Microsystem and Information Technology, China (Xunya Jiang); Fudan University, China (Lei Zhou); Nanjing University, China (Hui Liu); University of Illinois at Urbana-Champaign, USA (Nick Fang); National University of Singapore, Singapore (Le-Wei Li); and Zhejiang University, China (Sailing He). We would like to acknowledge all contributors in the above groups for their great contributions.

We specifically thank Mr. Wei Xiang Jiang, a graduate student at Southeast University, China, who took a lot of time in re-editing all chapters of the book and converting Word files into the LaTex format for some chapters. We also appreciate Dr. Jessie Yao Chin, Dr. Qiang Cheng, Dr. Zhong Lei Mei, and graduate students Xin Mi Yang, Hui Feng Ma, Xi Chen, Ning Ning Wan, Quan Hui Sun, Ben Geng Cai, and Xiao Peng Shen at Southeast University for their help in editing the book.

Finally, we would like to address a special thanks to Mr. Steven Elliot, the Senior Editor at Springer US, who provided good suggestions for the proposal of the book and had great patience in us completing the book.

TJC acknowledges support from the National Science Foundation of China (Major Project) under Grant Nos. 60990320 and 60990324, the Natural Science Foundation of Jiangsu Province under Grant No. BK2008031, the National Basic Research Program (973) of China under Grant No. 2004CB719802, the National Science Foundation of China under Grant Nos. 60871016, 60671015, and 60621002, and the 111 Project under Grant No. 111-2-05.

Nanjing, China — *Tie Jun Cui*
Durham, NC, USA — *David R. Smith*
Durham, NC, USA — *Ruopeng Liu*

# Contents

# List of Contributors

Christos Argyropoulos
Department of Electronic Engineering, Queen Mary, University of London, Mile End Road, London, E1 4NS, United Kingdom, e-mail: christos.a@elec.qmul.ac.uk

C. T. Chan
Department of Physics, Hong Kong University of Science and Technology, ClearWater Bay, Kowlong, Hong Kong, China, e-mail: phchan@ust.hk

Pratik Chaturvedi
Department of Mechanical Science and Engineering, University of Illinois at Urbana-Champaign, Urbana, IL, USA, e-mail: pchatur2@illinois.edu

Huanyang Chen
Department of Physics, Hong Kong University of Science and Technology, ClearWater Bay, Kowlong, Hong Kong, China and Department of Physics, Suzhou University, Suzhou 215006, China, e-mail: kenyou@ust.hk

Qiang Cheng
State Key Laboratory of Millimeter Waves, Department of Radio Engineering, Southeast University, Nanjing 210096, P. R. China, e-mail: qiangcheng@emfield.org

Jessie Y. Chin,
State Key Laboratory of Millimeter Waves, Department of Radio Engineering, Southeast University, Nanjing 210096, P. R. China, e-mail: jychin@seu.edu.cn

Tie Jun Cui
State Key Laboratory of Millimeter Waves, Department of Radio Engineering, Southeast University, Nanjing 210096, P. R. China, e-mail: tjcui@seu.edu.cn

Nicholas X. Fang
Department of Mechanical Science and Engineering, University of Illinois at Urbana-Champaign, Urbana, IL, USA e-mail: nicfang@illinois.edu

Yijun Feng
Department of Electronic Science and Engineering, Nanjing University, Nanjing, 210093, China, e-mail: yjfeng@nju.edu.cn

Yang Hao
Department of Electronic Engineering, Queen Mary, University of London, Mile End Road, London, E1 4NS, United Kingdom, e-mail: yang.hao@elec.qmul.ac.uk

Sailing He
Division of Electromagnetic Engineering, School of Electrical Engineering, Royal Institute of Technology, S-100 44 Stockholm, Sweden and Center for Optical and Electromagnetic Research, Zhejiang University, Hangzhou, 310058, China, e-mail: sailing@kth.se

Keng H. Hsu
Department of Mechanical Science and Engineering, University of Illinois at Urbana-Champaign, e-mail: khsu5@uiuc.edu

Li Hu
Department of Electrical and Computer Engineering, National University of Singapore, 10 Kent Ridge Crescent, Singapore 119260, e-mail: g0600165@nus.edu.sg

Xin Hu
Center for Optical and Electromagnetic Research, Zhejiang University, Hangzhou, 310058, China, e-mail: xinhu@kth.se

Xueqin Huang
Surface Physics Laboratory (State Key Laboratory) and Physics Department, Fudan University, Shanghai 200433, P. R. China, e-mail: xqhuang@fudan.edu.cn

Chunlin Ji
Department of Statistical Science, Duke University, Durham, NC 27708, USA, e-mail: chunlin.ji@duke.edu

Wei Xiang Jiang
State Key Laboratory of Millimeter Waves, Department of Radio Engineering, Southeast University, Nanjing 210096, P. R. China, e-mail: wxjiang@emfield.org

Xunya Jiang
National Key-Lab of the Functional Material, Institute of Microsystem and Information Technology, CAS, Shanghai 200050, Peoples Republic of China, e-mail: xyjiang@mail.sim.ac.cn

Efthymios Kallos
Department of Electronic Engineering, Queen Mary, University of London, Mile End Road, London, E1 4NS, United Kingdom, e-mail: themos.kallos@elec.qmul.ac.uk

Anil Kumar
Department of Mechanical Science and Engineering, University of Illinois at Urbana-Champaign, e-mail: anilku2@illinois.edu

Le-Wei Li
Department of Electrical and Computer Engineering, National University of Singapore, 10 Kent Ridge Crescent, Singapore 119260, e-mail: lwli@nus.edu.sg

T. Li
Department of Physics, Nanjing University, Nanjing 210093, Peoples Republic of China, e-mail: taoli@nju.edu.cn

Ya-Nan Li
Department of Electrical and Computer Engineering, National University of Singapore, 10 Kent Ridge Crescent, Singapore 119260, e-mail: bennyhappy@gmail.com

Zixian Liang
National Key-Lab of the Functional Material, Institute of Microsystem and Information Technology, CAS, Shanghai 200050, Peoples Republic of China, e-mail: zxliang@mail.sim.ac.cn

Xulin Lin
National Key-Lab of the Functional Material, Institute of Microsystem and Information Technology, CAS, Shanghai 200050, Peoples Republic of China, e-mail: xllin@mail.sim.ac.cn

H. Liu
Department of Physics, Nanjing University, Nanjing 210093, Peoples Republic of China, e-mail: liuhui@nju.edu.cn

Ruopeng Liu
Center for Metamaterials and Integrated Plasmonics, Department of Electrical and Computer Engineering, Duke University, Box 90291, Durham, North Carolina 27708, USA, e-mail: ruopeng.liu@duke.edu

Y. M. Liu
Nanoscale Science and Engineering Center, University of California, 5130 Etcheverry Hall, Berkeley, California 94720-1740, USA, e-mail: ymliu@berkeley.edu

Zheng Liu
National Key-Lab of the Functional Material, Institute of Microsystem and Information Technology, CAS, Shanghai 200050, Peoples Republic of China, e-mail: liuzheng@mail.sim.ac.cn

Hui Feng Ma
State Key Laboratory of Millimeter Waves, Department of Radio Engineering, Southeast University, Nanjing 210096, Peoples Republic of China, e-mail: hfma@emfield.org

Ping Sheng
Department of Physics, Hong Kong University of Science and Technology, ClearWater Bay, Kowlong, Hong Kong, China, e-mail: sheng@ust.hk

David R. Smith
Center for Metamaterials and Integrated Plasmonics, Department of Electrical and Computer Engineering, Duke University, Box 90291, Durham, North Carolina 27708, USA, e-mail: drsmith@duke.edu

S. M. Wang
Department of Physics, Nanjing University, Nanjing 210093, Peoples Republic of China, e-mail: smwang@nju.edu.cn

Weijia Wen
Department of Physics, Hong Kong University of Science and Technology, ClearWater Bay, Kowlong, Hong Kong, China, e-mail: phwen@ust.hk

Shiyi Xiao
Surface Physics Laboratory (State Key Laboratory) and Physics Department, Fudan University, Shanghai 200433, P. R. China, e-mail: xsy@fudan.edu.cn

Jun Xu
Department of Mechanical Science and Engineering, University of Illinois at Urbana-Champaign, e-mail: jebxu@illinois.edu

Xin Mi Yang
State Key Laboratory of Millimeter Waves, Department of Radio Engineering, Southeast University, Nanjing 210096, People Republic of China, e-mail: xmyang@emfield.org

Peijun Yao
National Key-Lab of the Functional Material, Institute of Microsystem and Information Technology, CAS, Shanghai 200050, Peoples Republic of China, e-mail: pjyao@mail.sim.ac.cn

X. Zhang
Nanoscale Science and Engineering Center, University of California, 5130 Etcheverry Hall, Berkeley, California 94720-1740, USA and Materials Sciences Division, Lawrence Berkeley National Laboratory, 1 Cycletron Road, Berkeley, CA 94720, USA, e-mail: xiang@berkeley.edu

Yan Zhao
Department of Electronic Engineering, Queen Mary, University of London, Mile End Road, London, E1 4NS, United Kingdom, e-mail: yan.zhao@elec.qmul.ac.uk

Lei Zhou
Surface Physics Laboratory (State Key Laboratory) and Physics Department, Fudan University, Shanghai 200433, P. R. China, e-mail: phzhou@fudan.edu.cn

S. N. Zhu
Department of Physics, Nanjing University, Nanjing 210093, Peoples Republic of China, e-mail: snzhu@nju.edu.cn

# Chapter 1
# Introduction to Metamaterials

Tie Jun Cui, Ruopeng Liu and David R. Smith

**Abstract** There have been increasing interests in metamaterials in the past 10 years in the scientific communities. However, metamaterials are sometimes regarded as left-handed materials or negative refractive index materials by a lot of people including researchers. In fact, the rapid development in this exciting area has shown that metamaterials are far beyond left-handed materials. In this chapter, we will clarify what metamaterial is and report the recent progress on metamaterials. We also summarize the important issues for the development and future of metamaterials, including the optical transformation, effective medium theory for periodic structures, broadband and low-loss metamaterials, rapid design of metamaterials, and potential applications. The impact of computational electromagnetics on metamaterials is briefly discussed.

**Key words:** Metamaterials, left-handed materials, negative refraction, optical transformation, invisible cloaks, general effective medium theory, spatial dispersion, rapid design of metamaterials, non-resonant metamaterials, broadband metamaterials, applications of metamaterials, computational electromagnetics.

## 1.1 What Is Metamaterial?

The term of metamaterial was synthesized by Rodger M. Walser, University of Texas at Austin, in 1999, which was originally defined as "Macroscopic composites having a synthetic, three-dimensional, periodic cellular architecture designed to produce an optimized combination, not available in nature, of two or more responses

Tie Jun Cui*
State Key Laboratory of Millimeter Waves, Department of Radio Engineering, Southeast University, Nanjing 210096, P. R. China. *email: tjcui@seu.edu.cn
Ruopeng Liu and David R. Smith
Department of Electrical and Computer Engineering, Duke University, Box 90291, Durham, North Carolina 27708, USA.

T.J. Cui et al. (eds.), *Metamaterials*, DOI 10.1007/978-1-4419-0573-4_1,

to specific excitation" [52, 53]. Based on *Wikipedia*, the metamaterial is defined as "a material which gains its properties from its structure rather than directly from its composition" [53].

The above definitions reflect certain natures of metamaterial, but not all. Actually, **a metamaterial is a macroscopic composite of periodic or non-periodic structure, whose function is due to both the cellular architecture and the chemical composition.** If the metamaterial is regarded as an effective medium, there is an additional requirement that the cellular size is smaller than or equal to the sub-wavelength.[1] In this book, the metamaterials are required to have sub-wavelength for the unit cell so that they can be described using the effective medium theory. Figure 1.1 shows two typical metamaterial structures in the microwave regime, in which Fig. 1.1(a) is a periodic structure that is equivalent to a homogeneous medium and Fig. 1.1(b) is a non-periodic structure that is equivalent to an inhomogeneous (gradient) medium. The microwave metamaterials are fabricated with printed circuit boards (PCB) by making different metal architectures on PCB. The properties of such metamaterials are mainly due to the cellular architecture, and also dependent

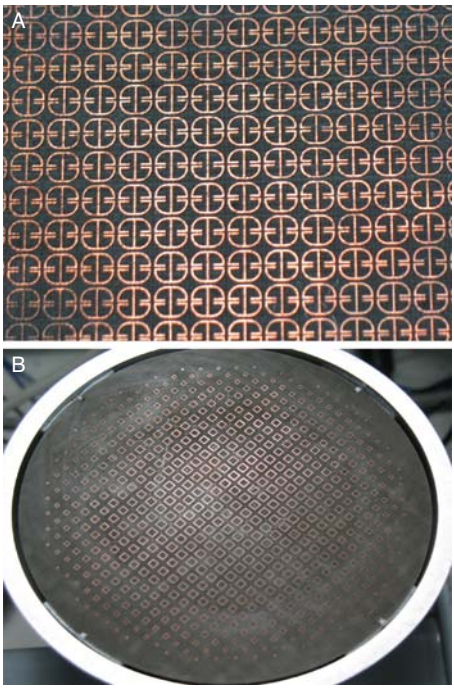


**Fig. 1.1** Two typical metamaterial structures in the microwave regime. (**a**) A periodic structure, which is equivalent to a homogeneous medium (*above*). (**b**) A non-periodic structure, which is equivalent to an inhomogeneous (gradient) medium (*below*).

[1] Sometimes the photonic bandgap structure is also regarded as metamaterial whose cellular size is larger than sub-wavelength.

on the PCB substrates, which can be FR4, F4B, and Rodges. The dependence of metamaterial properties on the cellular architecture provides great flexibility to control metamaterials. One can create new materials which are unavailable in nature but can be realized in practice using metamaterial structures. This is the biggest advantage of metamaterials.

Usually, the material properties are characterized by an electric permittivity ($\varepsilon$) and a magnetic permeability ($\mu$). The thinnest material in nature is free space or air, whose permittivity is $\varepsilon_0$ and permeability is $\mu_0$. The relative permittivity and permeability of a material are defined as $\varepsilon_r = \varepsilon/\varepsilon_0$ and $\mu_r = \mu/\mu_0$, respectively, which define another important material parameter, the refractive index, as $n = \sqrt{\varepsilon_r \mu_r}$. In nature, most materials have the permeability $\mu_0$ and permittivity larger than $\varepsilon_0$. The metamaterial opens a door to realize all possible material properties by designing different cellular architectures and using different substrate materials. Figure 1.2 illustrates all possible properties of isotropic and lossless materials in the $\varepsilon$–$\mu$ domain. In Fig. 1.2, the first quadrant ($\varepsilon > 0$ and $\mu > 0$) represents right-handed materials (RHM), which support the forward propagating waves. From the Maxwell's equations, the electric field **E**, the magnetic field **H**, and the wave vector **k** form a right-handed system. The second quadrant ($\varepsilon < 0$ and $\mu > 0$) denotes electric plasma, which support evanescent waves. The third quadrant ($\varepsilon < 0$ and $\mu < 0$) is the well-known left-handed materials (LHM), which was proposed by Veselago in 1968 [51], supporting the backward propagating waves. In LHM, the electric field **E**, the magnetic field **H**, and the wave vector **k** form a left-handed system. The fourth quadrant ($\varepsilon > 0$ and $\mu < 0$) represents magnetic plasma, which supports evanescent waves.

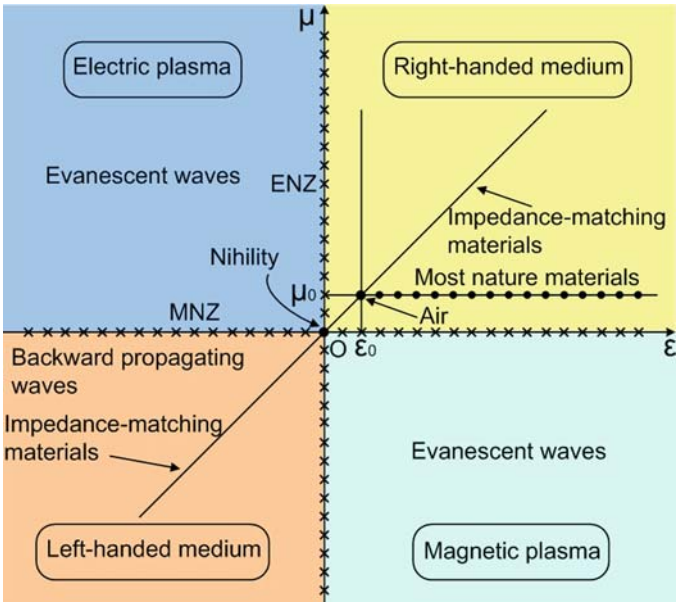


**Fig. 1.2** All possible properties of isotropic materials in the $\varepsilon$–$\mu$ domain.

In Fig. 1.2, most natural materials only occur at certain discrete points on the line $\mu = \mu_0$ and $\varepsilon \geq \varepsilon_0$, and seldom natural electric plasma and magnetic plasma occur in very small parts in the second and fourth quadrants. Most of material properties have to be realized using metamaterials, even for RHM. In a long period, metamaterials, LHM, negative-refractive index materials (NIM), double negative materials (DNG), and backward-wave materials have been regarded as the same terms. However, they actually represent different meanings. Metamaterials have much broader scope than LHM, as shown in Fig. 1.2. In the $\varepsilon$–$\mu$ domain, there are several special lines and points indicating special material properties. For example, the point $\mu = -\mu_0$ and $\varepsilon = -\varepsilon_0$ represents an anti-air in the LHM region, which will produce a perfect lens; the point $\mu = 0$ and $\varepsilon = 0$ represents a nihility, which can yield a perfect tunneling effect; the line $\mu = \varepsilon$ in both RHM and LHM regions represents impedance-matching materials, which have perfect impedance matching with air, resulting no reflections. Also, the vicinity of $\mu = 0$ is called as $\mu$-near zero (MNZ) material, and the vicinity of $\varepsilon = 0$ is called as $\varepsilon$-near zero (ENZ) material, which has special properties.

Actually, metamaterials have much more features beyond those shown in Fig. 1.2. Metamaterials can be designed as weakly and highly anisotropic, depending on different requirements. The flexibility to design various material properties together with the optical transformation makes it possible to control electromagnetic waves at will using metamaterials.

## 1.2 From Left-Handed Material to Invisible Cloak: A Brief History

Metamaterials were first known as LHM or NIM. Although the concept of LHM was proposed by Veselago in 1968 [51], the negative refraction and backward-wave media had been discovered theoretically much earlier [50, 32, 31, 44]. The earliest publication on negative refraction was in lecture notes of Prof. Mandelshtam from Moscow University [32]. Then the Sommerfeld radiation condition in backward-wave media was studied by Malyuzhinets in 1951 [31], who showed that the phase velocity of waves pointed from infinity to the source. Furthermore in 1957, Sivukhin investigated materials with negative parameters and noticed the backward-wave property [44]. Except the theoretical study, backward-wave structures had been developed for the design of microwave tubes in 1960s [19, 1, 42], and the negative refraction was discovered even in periodical media [41]. A significant progress was made by Veselago in 1968,[2] who proposed a systematic analysis of electromagnetic behaviors in materials with negative permittivity and permeability, and named the term of LHM [51]. Besides the negative refraction and backward-wave propagation, Veselago also showed some new features like reversed Doppler shift and backward Cerenkov radiation in LHM.

However, due to the non-existence in nature and lack of experimental verification, LHM had not attracted attention over 30 years in the scientific community.

[2] The Russian version was published in 1967.

The first revolution on LHM or metamaterials occurred in 1996, when Pendry et al. realized the artificially electric plasma using the wire medium whose permittivity is negative [36]. Then Pendry and his coworkers discovered the artificially magnetic plasma whose permeability is negative in 1999 [35]. In this work, the well-known split-ring resonators (SRR) are used to achieve the magnetic response. The first artificial LHM was made by Smith et al. in 2001 using the combination of wires and SRRs [40]. In this famous experiment, the negative refraction phenomenon was verified. Inspired by the experimental realization, LHM has attracted growing attention in both theoretical exploration and experimental study [45, 34, 46, 3, 17, 12, 13], including the exciting discovery of perfect lens and super lens [34]. However, LHM has unavoidable disadvantages of big loss and narrow bandwidth, and such disadvantages restrict the applications of LHM.

In the meantime, an alternative representation of LHM was presented by three groups (Eleftheriades, Oliner, and Caloz-Itoh), almost simultaneously in June 2002, using the transmission-line (TL) approach [20, 33, 4, 21, 5, 6]. It is well known that a conventional TL is composed of distributed series inductance ($L$) and shunt capacitance ($C$), which can be shown equivalent to a one-dimensional (1D) RHM. As a dual model of the conventional TL, a new TL consisting of series capacitance and shunt inductance will support backward waves and hence can represent LHM. In the realization of left-handed (LH) TL, the distributed components have been used. Since the series capacitance is always accompanied by an inductance and the shunt inductance is accompanied by a capacitance, a general composite right-left-handed (CRLH) TL model has been proposed to represent RHM and LHM [6]. Based on the CRLH structures, a lot of microwave components and antennas have been proposed [6].

Despite the good properties, LHM suffers from the large loss and narrow bandwidth. Hence scientists seek other features of metamaterial beyond the negative refraction. Then the second revolution on metamaterial came in 2005 when the gradient refractive index medium was realized to bend electromagnetic waves [47], and in 2006 when the optical transformation was proposed to make invisible cloaks and to control the propagation of electromagnetic waves using metamaterials [37, 25]. From then on, metamaterials have a much broader meaning than LHM, which do not require the negative permittivity and/or negative permeability, and hence open a completely new area. After the experimental realization of invisible cloak in the microwave regime [39, 28], a large explosion of interest has been paid to metamaterials and the optical transformation, and many scientific papers have been published in journals, which are not cited here.

## 1.3 Optical Transformation and Control of Electromagnetic Waves

Metamaterials have great advantage to realize the required material parameters, including those unavailable in nature, by adjusting the cellular architecture and its chemical composition. However, there remain two questions: What is the requirement for the metamaterial parameters? How to choose the metamaterial parameters?

In some cases, we can get the solutions easily using the known theory and geometrical optics, such as the perfect/super lens [34] and gradient refractive index lens [47]. In general cases to control electromagnetic waves, it is not so easy before the appearance of the optical transformation.

The optical transformation [37], or the transformation optics, is one of the most important methods in the development of metamaterials, which is going to have further impact on the future metamaterials. Based on the principle of form invariance in Maxwell's equations, the optical transformation is derived rigorously in closed forms. The optical transformation builds up a bridge between the device functions and material properties. For example, if one wants to make a spherical invisible cloak which can hide the objects inside, one can obtain the material parameters using the optical transformation as [37]

$$\varepsilon_r = \mu_r = \frac{b}{b-a}\frac{(r-a)^2}{r^2}, \tag{1.1}$$

$$\varepsilon_\theta = \mu_\theta = \frac{b}{b-a}, \tag{1.2}$$

$$\varepsilon_\phi = \mu_\phi = \frac{b}{b-a}, \tag{1.3}$$

in which $a \leq r \leq b$, and $a$ and $b$ are radii of the inner and outer spherical surfaces of the cloak, respectively. Apparently, the spherical cloak is required to be biaxially anisotropic in the spherical coordinate system, and the three components of the permittivity and permeability have to satisfy Eqs. (1.1)–(1.3). From these equations, we also notice that the cloak is made of impedance-matching materials to eliminate any reflections.

Hence, the optical transformation enables the direct manipulation of electromagnetic waves and offers a powerful tool to design novel and complicated devices. Besides the invisible cloak, the optical transformation has also been used to generate electromagnetic concentrators which can focus electromagnetic waves into a small enclosed region [38, 22]; electromagnetic field and polarization rotators which can rotate electromagnetic fields [7]; wave-shape transformers which can transform cylindrical waves to plane waves to make high-gain antennas [23, 26]; electromagnetic-wave bending structures to bend the waves to desired directions [24, 18]; and other optical transformation devices. Chapter 2 gives more detailed discussions on this topic.

## 1.4 Homogenization of Artificial Particles and Effective Medium Theory

### *1.4.1 General Description*

The optical transformation sets up a bridge between the device functions and material parameters. In order to realize the device functions, however, there is another

gap between the material parameters and the realistic metamaterial structures. As we mentioned earlier, metamaterials are composed of periodic or non-periodic structures with sub-wavelength unit cells. Now we must ask two questions: Is a periodic structure with sub-wavelength unit cell equivalent to a homogenous effective medium? How to determine the effective medium parameters once the periodic structure is known? The solutions to such questions are key points for the homogenization of artificial particles and effective medium theory.

In periodically structured metamaterials, the artificial inclusions with sub-wavelength size replace the atoms and molecules of conventional materials. Since the scale of these inclusions is much smaller than the wavelength, a homogenized description in the macroscope is valid [48]. In the homogenization of the periodically structured metamaterials, the macroscopic electromagnetic fields are determined by averaging the local fields. The detailed definition of the averaged fields can be found in Refs. [48] and [27]. From the averaged fields, the averaged permittivity and permeability are further defined [48, 27]. The above field-averaging method can be applied to homogenize any periodic structures with arbitrarily shaped sub-wavelength unit cells.

However, the averaged permittivity and permeability only represent the particle responses, or local properties, and hence cannot be used as the effective material parameters of the effective medium. In fact, the averaged permittivity and permeability are similar to the constitutive parameters in the Drude–Lorentz medium models [43], which are derived in the static and quasi-static limits. Apparently, the Drude–Lorentz medium models are inaccurate in microwave and higher frequencies. A scattering (S) parameter retrieval method has been shown an accurate approach to obtain the effective constitutive parameters [49]. This is a numerical- or an experimental-based approach, in which the S parameters (reflection and transmission coefficients) of the periodic structure are used to derive the effective permittivity and permeability. Figure 1.3 shows the constitutive parameters (permeability) of a periodic structure whose inclusion is SRR, obtained from the Drude–Lorentz model and the S-parameter retrieval.

From Fig. 1.3, there exists a significant difference of the permeability between the two methods. Although the S-parameter retrieval method can provide accurate material parameters, it is numerically or experimentally oriented and hence is difficult to be used in the design of metamaterials. The Drude–Lorentz medium models have simply closed-form expressions, but are inaccurate since only the particle responses are involved. The mutual coupling among different unit cells, or the spatial dispersion, is not considered. In order to set up a relationship between the particle responses and the macroscopical system behaviors for artificial metamaterials composed of periodic structures, a general theory of effective media has been proposed [27]. Based on the general theory, the effective permittivity and permeability were derived using the discrete Maxwell's equations in the macroscale, which have closed forms [27]. The excellent agreements between theoretical predictions and S-parameter retrieval results indicate the accuracy of the general theory. For details refer to Chapter 3.

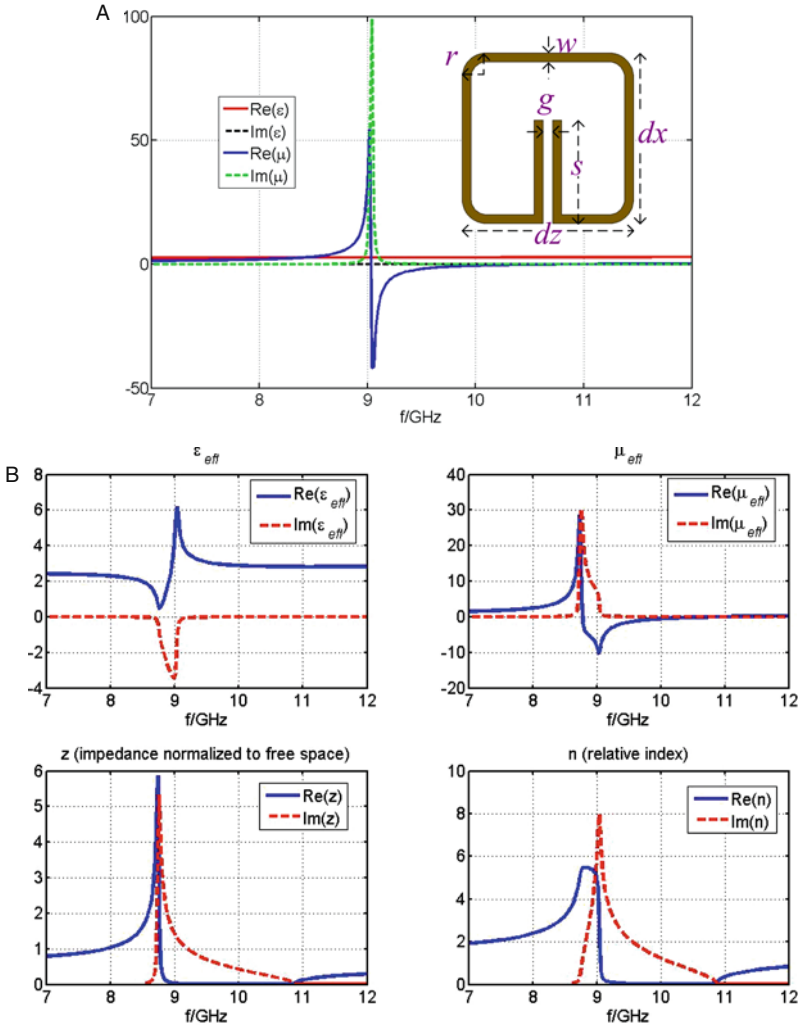


**Fig. 1.3** The constitutive parameters (permeability) of a periodic structure whose inclusion is SRR. (**a**) From the Drude–Lorentz model under the static and quasi-static limits (*above*). (**b**) From the S-parameter retrieval under full-wave simulations (*below*).

## *1.4.2 A TL-Metamaterial Example*

In order to show the role of spatial dispersion in the effective medium parameters, we consider a simple 1D TL metamaterial [11], as shown in Fig. 1.4(a). This is an infinite 1D periodic structure with series impedance $Z_s$ and shunt admittance $Y_p$, with the period of $p$. The unit cell of the periodic structure is chosen as a symmetrical T form, as illustrated in Fig. 1.4(b). The general forms of $Z_s$ and $Y_p$ are written as

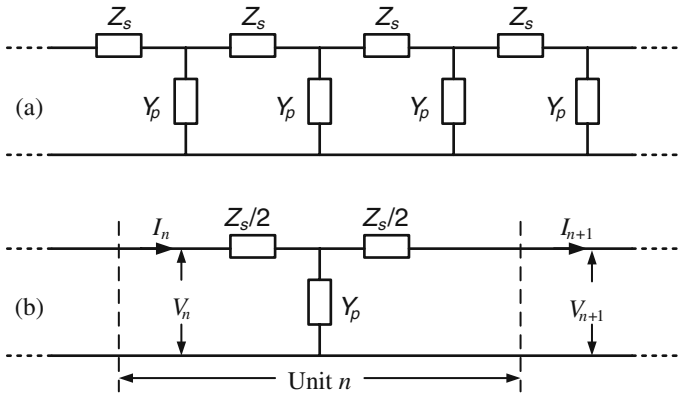


**Fig. 1.4** (**a**) A general 1D periodic structure of series impedance and shunt admittance. (**b**) The T-type unit cell of the periodic structure.

$Z_s = -i\omega L_s - 1/(i\omega C_s)$ and $Y_p = -i\omega C_p - 1/(i\omega L_p)$, in which $L_s$ and $C_s$ are series inductance and capacitance, and $L_p$ and $C_p$ are shunt inductance and capacitance. According to Eqs. (3.23a) and (3.23b) in Ref. [6], the particle-based permittivity and permeability are expressed as

$$\mu = \mu(\omega) = \frac{1}{p}[L_s - 1/(\omega^2 C_s)], \tag{1.4}$$

$$\varepsilon = \varepsilon(\omega) = \frac{1}{p}[C_p - 1/(\omega^2 L_p)]. \tag{1.5}$$

Apparently, the spatial dispersion was not considered in the above expressions.

To involve the spatial dispersion in the effective medium parameters, one starts from the Bloch theorem and circuit theory. After simple derivation, one obtains the dispersion equation as [11]

$$\sin^2(\theta/2) = ZY/4, \tag{1.6}$$

and the wave impedance as

$$Z_0 = V_n/I_n = \frac{1}{2}Z/\tan(\theta/2), \tag{1.7}$$

in which $\theta = kp$, and $Z = \omega L_s - 1/(\omega C_s)$ and $Y = \omega C_p - 1/(\omega L_p)$ are real numbers. They can be either positive or negative. Next we discuss the dispersion equation with different values of $Z$ and $Y$.

If $0 \le ZY \le 4$, then $\theta$ will be a real number: $\theta = \pm 2\arcsin(\sqrt{ZY}/2)$, and hence the TL metamaterial supports propagating modes. When $Z$ and $Y$ are both positive, $\theta$ is positive, corresponding a forward propagating mode; when $Z$ and $Y$ are both negative, $\theta$ is negative, representing a backward propagating mode. If $ZY < 0$, then $\theta$ is a pure imaginary number: $\theta = \pm i2\text{arcsinh}(\sqrt{-ZY}/2)$, which corresponds to

pure plasma modes. When "−" is taken, it denotes an active metamaterial; when "+" is taken, it represents a passive metamaterial, which is considered here. If $ZY > 4$, then $\theta$ is a complex number: $\theta = \theta_R + i\theta_I = \pm\pi + i2\text{arccosh}(\sqrt{ZY}/2)$. Hence the TL metamaterial supports resonant crystal bandgap modes.

From above discussions, $ZY = 0$ and $ZY = 4$ define boundaries of such three kinds of modes. When $ZY = 0$, one obtains two critical frequencies

$$\omega_1 = \min\{\omega_s,\ \omega_p\},\quad \omega_2 = \max\{\omega_s,\ \omega_p\}, \tag{1.8}$$

in which $\omega_s = 1/\sqrt{L_sC_s}$ and $\omega_p = 1/\sqrt{L_pC_p}$ are resonant frequencies of the series and shunt branches, respectively. When $ZY = 4$, one gets the other two critical frequencies

$$\omega_3 = \sqrt{\omega_c^2 - \omega_d^2},\quad \omega_4 = \sqrt{\omega_c^2 + \omega_d^2}, \tag{1.9}$$

in which $\omega_c^2 = 2/(L_sC_p) + (\omega_s^2 + \omega_p^2)/2$ and $\omega_d^4 = \omega_c^4 - \omega_s^2\omega_p^2$. The four critical frequencies satisfy $\omega_3 < \omega_1 < \omega_2 < \omega_4$. Hence the whole frequency regime is divided into five regions by the four critical frequencies, as shown in Fig. 1.5.

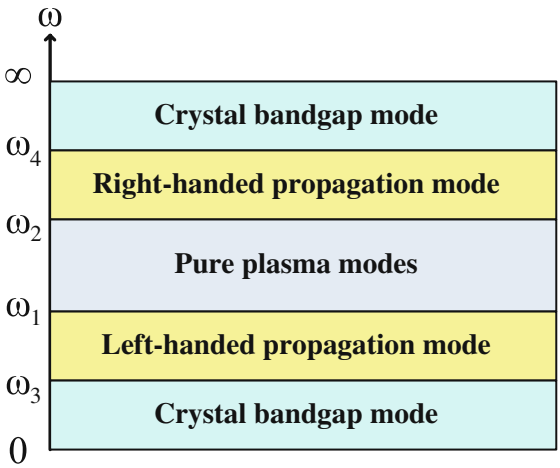


**Fig. 1.5** Different wave modes of the general periodic structure.

In regions $\omega_3 < \omega < \omega_1$ and $\omega_2 < \omega < \omega_4$, we have $0 < ZY < 4$. Hence such two regions support the propagating modes: $k = \theta_p/p$. In the first region, both $Z$ and $Y$ are negative, and hence $\theta_p = -2\arcsin(\sqrt{ZY}/2)$, corresponding to the backward propagating mode. In the second region, both $Z$ and $Y$ are positive, and hence $\theta_p = 2\arcsin(\sqrt{ZY}/2)$, corresponding to the forward propagating mode. In such two regions, the wave impedance $Z_0 = Z/[2\tan(\theta_p/2)]$ is always real and positive. Then the effective permittivity $\varepsilon_{\text{eff}}$ and permeability $\mu_{\text{eff}}$ of the TL metamaterial are easily derived from the wavenumber and wave impedance as

$$\mu_{\text{eff}} = L_{\text{eff}}\theta_p/\tan(\theta_p/2), \qquad \varepsilon_{\text{eff}} = C_{\text{eff}}\theta_p\tan(\theta_p/2). \tag{1.10}$$

Here, $L_{\text{eff}} = Z/(2\omega p)$ and $C_{\text{eff}} = 2/(Z\omega p)$ are effective inductance and capacitance, which can be either positive and negative. Apparently, the general circuit periodic structure is equivalent to an LHM in the frequency region $\omega_3 < \omega < \omega_1$, where both $\varepsilon_{\text{eff}}$ and $\mu_{\text{eff}}$ are negative and is equivalent to an RHM in the frequency region $\omega_2 < \omega < \omega_4$, where both $\varepsilon_{\text{eff}}$ and $\mu_{\text{eff}}$ are positive.

In the region $\omega_1 < \omega < \omega_2$, we have $ZY < 0$, corresponding to pure plasma modes: $k = i\theta_I/p$. Here, $\theta_I = 2\ln(\sqrt{-ZY/4} + \sqrt{-ZY/4+1})$. In this case, the wave impedance is a pure imaginary number: $Z_0 = -iZ/[2\tanh(\theta_I/2)]$. Hence one easily derives $\varepsilon_{\text{eff}}$ and $\mu_{\text{eff}}$ as

$$\mu_{\text{eff}} = L_{\text{eff}}\theta_I/\tanh(\theta_I/2), \qquad \varepsilon_{\text{eff}} = -C_{\text{eff}}\theta_I\tanh(\theta_I/2). \tag{1.11}$$

When $Z > 0$, then $\mu_{\text{eff}} > 0$ and $\varepsilon_{\text{eff}} < 0$, representing an electric plasma; when $Z < 0$, then $\mu_{\text{eff}} < 0$ and $\varepsilon_{\text{eff}} > 0$, denoting a magnetic plasma.

In regions $0 < \omega < \omega_3$ and $\omega > \omega_4$, we have $ZY > 4$. Hence such two regions support the resonant crystal bandgap modes: $k = (\pi + i\theta_I)/p$, in which $\theta_I = 2\ln(\sqrt{ZY/4} + \sqrt{ZY/4-1})$. The wave impedance is also a pure imaginary number: $Z_0 = -iZ\tanh(\theta_I/2)/2$. One easily obtains $\varepsilon_{\text{eff}}$ and $\mu_{\text{eff}}$ as

$$\mu_{\text{eff}} = L_{\text{eff}}(\theta_I - i\pi)\tanh(\theta_I/2), \qquad \varepsilon_{\text{eff}} = C_{\text{eff}}(-\theta_I + i\pi)/\tanh(\theta_I/2). \tag{1.12}$$

Hence the general circuit periodic structure behaves like a crystal bandgap metamaterial in such two regions. When $Z > 0$, then $\text{Re}\{\mu_{\text{eff}}\} > 0$ and $\text{Re}\{\varepsilon_{\text{eff}}\} < 0$, and the metamaterial is electric–plasma type; when $Z < 0$, it is magnetic–plasma type. From Eq. (1.12), one of imaginary parts of the permittivity and permeability is positive (positive loss) and the other is negative (*negative loss*). They appear always in conjugate forms, representing the lossless nature of the original circuit structure.

In order to validate the proposed medium model for the TL metamaterial, we choose the circuit parameters arbitrarily as $L_s = 20$ nH, $L_p = 5$ nH, $C_s = 2.5$ pF, and $C_p = 2$ pF. Then we get the four critical frequencies as $f_1 = 0.71$ GHz, $f_2 = 1.59$ GHz, $f_3 = 0.49$ GHz, and $f_4 = 2.31$ GHz. In such a situation, the wavenumber and wave impedance versus frequencies are illustrated in Fig. 1.6. From the dispersion curve shown in Fig. 1.6(a), we clearly observe the crystal bandgap mode, backward propagating mode, pure plasma mode, forward propagating mode, and another crystal bandgap mode, which are exactly the same as predicted. We get similar conclusions to the wave impedance.

The effective permittivity and permeability of the TL metamaterial are demonstrated in Fig. 1.7(a) and (b), respectively. From Fig. 1.7, we observe the magnetic–plasma-type crystal bandgap metamaterial, LHM, the pure electric plasma, RHM, and the electric–plasma-type crystal bandgap metamaterial, which are exactly coincident to the earlier predictions. From Fig. 1.7, we also notice the conjugate imaginary parts of permittivity and permeability in the crystal bandgap regimes. Such a phenomenon has not been discovered in the earlier circuit-medium models [6].

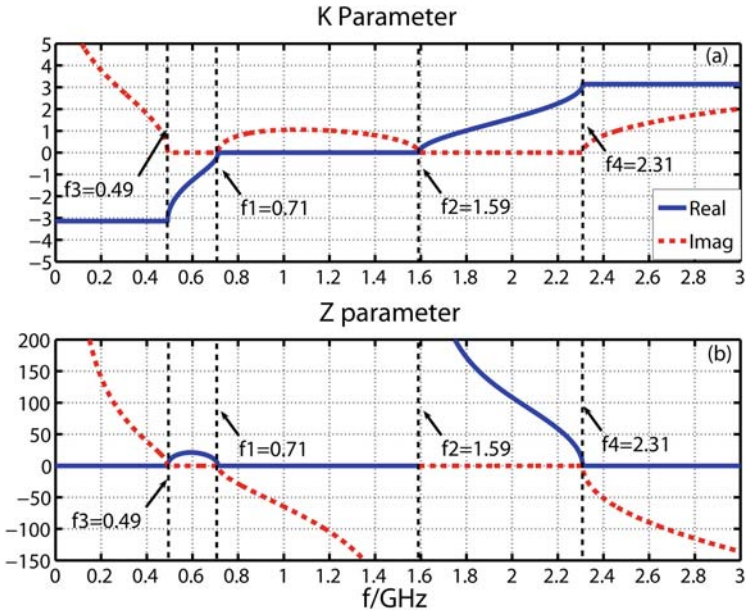


**Fig. 1.6** (**a**) The dispersion curve of the general periodic structure. (**b**) The wave impedance of the general periodic structure.

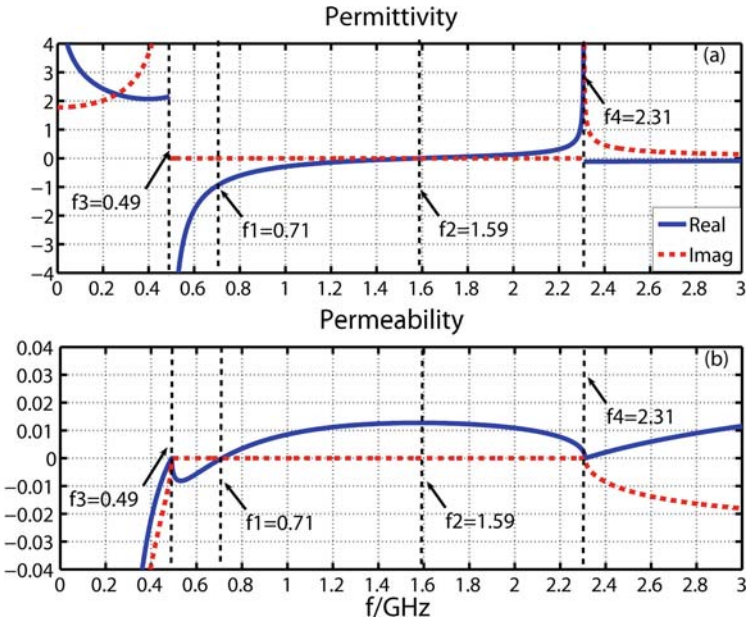


**Fig. 1.7** The effective medium parameters of the general periodic structure. (**a**) Permittivity. (**b**) Permeability.

Now we verify the correctness and accuracy of the proposed equivalent medium models. To do so, we have computed the transmission coefficients ($S_{21}$ parameters) of a 10-cell TL metamaterial in the whole frequency band. Three methods have been applied: (1) circuit simulations using the agilent advanced design system (ADS); (2) and (3) effective medium models using the proposed formulas and those in Ref. [6]. In the effective medium models, the transmission coefficient is calculated analytically based on the electromagnetic wave theory. Figure 1.8 illustrates the comparison of computational results from the three methods. We clearly observe that the theoretical predictions using the proposed effective medium parameters have perfect agreements with the circuit simulation results in the whole frequency band. However, the theoretical predictions using Eqs. (1.4) and (1.5) [6] are only accurate in the pure plasma, LHM and RHM regions. In the crystal bandgap metamaterial regions, Eqs. (1.4) and (1.5) become invalid. Even in the pure plasma, LHM and RHM regions, the proposed medium parameters are much more accurate [11].

From the above TL example, we clearly see the role of spatial dispersion (or mutual coupling of unit cells) in the effective medium model. If only the particle response is considered, the model is less accurate or even invalid at all in certain cases. Hence the general effective medium theory provides an accurate and efficient link between the periodic structures and effective medium models by considering the spatial dispersion.

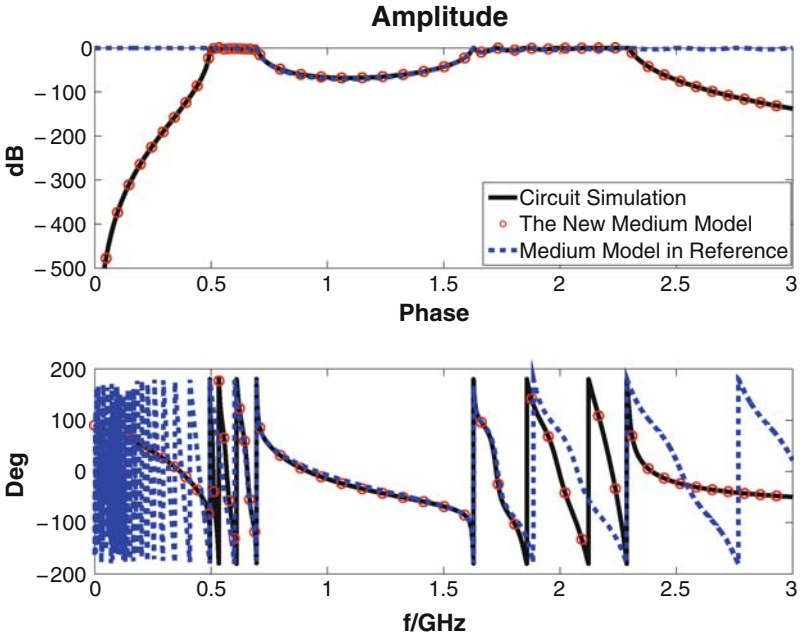


**Fig. 1.8** The transmission coefficients of a 10-cell periodic structure computed by circuit simulations and effective medium models. (**a**) Amplitude. (**b**) Phase.

## 1.5 Rapid Design of Metamaterials

The homogenization of artificial particles and effective medium theory provide an efficiently analytical way to determine the effective medium parameters once the periodic structure is known. This is in fact a *forward scattering problem*. In experiments and applications of metamaterials, however, the *inverse scattering problem* is more important. Recall the earlier discussions, the metamaterial device functions produce the requirement to material parameters via the optical transformation. Hence one should determine the metamaterial structures once the material parameters are known. This procedure is called as the design of metamaterials.

The design of metamaterials is an essential path between theory and practice. The traditional method to design metamaterials is based on large amount of full-wave electromagnetic simulations and S-parameter retrievals, in which the numerical simulations are repeated to optimize the constitutive parameters for a single metamaterial particle. Hence it is very time consuming even for a simple gradient refractive index lens. When the desired metamaterial devices are complicated, the overall number of designed metamaterial particles with different parameters will be very large. For example, the invisible cloaks in the microwave regime contain tens of thousands of different particles [39, 28]. Then it will take a few weeks or months to make the overall optimization of material parameters.

The effective medium theory [27, 11] provides an easier and faster way to design metamaterials due to the analytical relation between the effective material parameters and the averaged material parameters (particle responses), which can avoid the large amount of numerical simulations. An automated and rapid method for metamaterial design has been proposed, which is able to design metamaterials with both accuracy and efficiency. The detailed algorithm will be presented in Chapter 4, and a few examples are given to demonstrate the speed and validity of the method. The accuracy of the design is also proved by experimental results.

## 1.6 Resonant and Non-resonant Metamaterials

In the rapid design of metamaterials, more specifically, the particle design, it is important to choose the types of particles. Generally, metamaterials are classified into two classes: resonant and non-resonant metamaterials. Both resonant and nonresonant metamaterials have their own advantages and disadvantages. Figure 1.3(b) shows the material properties of a typical resonant metamaterial composed of SRR, as illustrated in the inset of Fig. 1.3(a). From Fig. 1.3(b), one clearly observes that both the permittivity and the permeability have a large dynamic range near the resonant frequency. When the frequency changes a little bit, $\varepsilon$ and $\mu$ vary a lot. In the other word, when the size of SRR particle has a small change, the resonant frequency has a small shift, which results in significant change of $\varepsilon$ and $\mu$. Hence one can realize large dynamic-range material parameters using the resonant particle. This is the advantage of resonant metamaterials. However, one also notices from

Fig. 1.3(b) that $\varepsilon$ and $\mu$ have a narrow bandwidth and a large loss near the resonant frequency, which are disadvantages of resonant metamaterials.

In fact, non-resonant metamaterials have also resonant frequencies, but they are much higher. Figure 1.9 demonstrates the constitutive parameters of a typical non-resonant metamaterial composed of I-shaped inclusion (see the inset of Fig. 1.9). It is clear that both $\varepsilon$ and $\mu$ vary slowly with respect to the frequency and have very small loss. Hence the broad bandwidth and low loss are the big advantages of the non-resonant metamaterial. On the other hand, when the size of I-shaped particle has a small change, $\varepsilon$ and $\mu$ have also small change. Hence one can only realize small dynamic-range material parameters using the non-resonant particle, which is the disadvantage of non-resonant metamaterial.

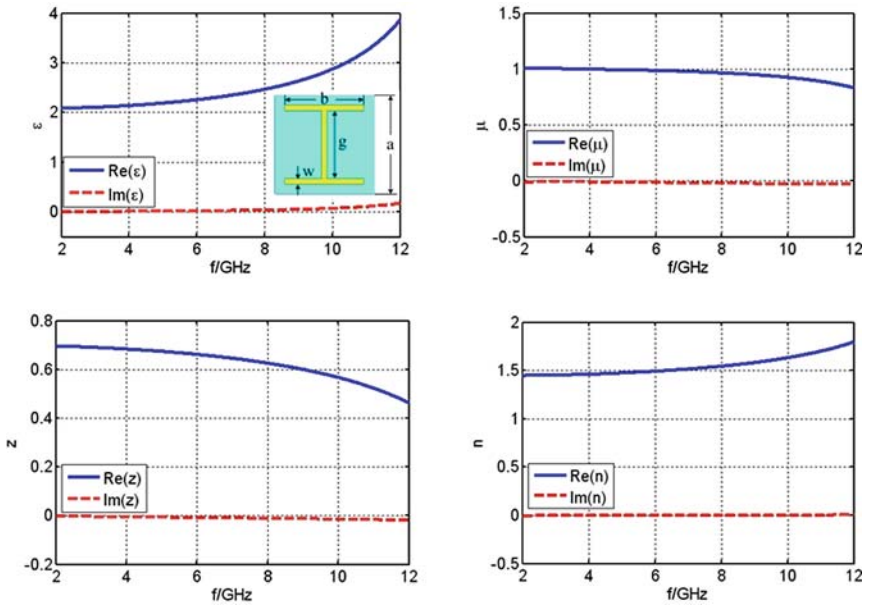


**Fig. 1.9** The effective constitutive parameters of a non-resonant metamaterial whose inclusion is I-shaped.

In the actual design of metamaterials, the choice of particle types depends on the device functions. For example, in the design of simplified circularly invisible cloak [39], large dynamic-range material parameters are required. Hence the resonant metamaterials had to be used [39]. The cloak has a narrow bandwidth, and the invisible effect is not perfect due to the loss. On the other hand, in the design of ground invisible cloak (or invisible carpet) [28], small dynamic-range material parameters are desired, and hence the non-resonant metamaterials had been chosen. The ground cloak has a broad bandwidth and small loss, and the invisible effect is perfect [28]. Chapter 5 gives detailed discussions on non-resonant metamaterials.

## 1.7 Applications of Metamaterials

Due to the exciting and unusual features, metamaterials have found and are finding a lot of applications or potential applications. For LHM, the most attractive feature is superlens [34], which can be widely used in the super-resolution medical imaging, optical imaging, and nondestructive detections. The first superlens in the microwave regime was realized in 2004 [16], which demonstrated resolution three times better than the diffraction limit. Later, Fang et al. proposed the first optical superlens using thin silver film [15], which breaks the diffraction limit and produces super-resolution images. The big obstacle of superlens in applications is the loss. In the meantime, the LHTL or CRLH structures have been widely used in the microwave and antenna applications [6].

For general metamaterials, the cloaking devices have attracted more and more attention. The successful demonstrations of invisible cloaks experimentally in the microwave regime [39, 28] make it possible to realize cloaking devices in the future. In fact, the waveguided or planar metamaterials which are composed of complimentary structures like CSRR [14] have been used to design microwave components like filters, power dividers, and phase shifters [2]. Recently, narrowband and broadband polarizers have been realized using three-dimensional (3D) anisotropic metamaterials [9, 10]. The gradient refractive index metamaterials are also utilized to produce beam-bending lens and beam-focusing lenses. Based on such properties, high-gain and broadband gradient planar lens antennas [29] and Luneberg-like lens antennas [30] have been proposed and realized. We expect that more and more applications will be found in the near future with the rapid development of metamaterials.

## 1.8 Computational Electromagnetics: A New Aspect of Metamaterials

Computational electromagnetics (CEM) has been studied extensively in the past 30 years [8]. CEM and metamaterials seem to be in different subjects, but they are closely related. As discussed earlier, all numerical simulations on metamaterial particles and S-parameter retrievals are dependent on CEM, such as the finite element method (FEM) and the finite-difference time-domain (FDTD) method, and the corresponding commercial software like CST Microwave Studio and ANSOFT HFSS. In the optical transformation, CEM is used to simulate the field distributions inside and outside the metamaterial devices. The FEM-based commercial software, the COMSOL Multiphysics, has been widely adopted.

However, the current CEM methods and commercial software are insufficient to support metamaterial study. For example, COMSOL can only handle two-dimensional (2D) optical transformation problems and limited small 3D problems. When the metamaterial devices are 3D and have large sizes, COMSOL cannot work due to the huge memory requirement and very long computational time. Hence

it is very necessary to develop new CEM methods to solve large, inhomogeneous, and anisotropic 3D problems. Another example is more important. Currently, full-wave numerical simulations are only performed to metamaterial particles, which are greatly helpful in the metamaterial design. However, it is extremely difficult to simulate the metamaterial system using CEM methods due to the huge memory requirement. The only way to study the system-level metamaterial devices (such as invisible cloaks) is experiment.

It is no doubt that the experiment is the most essential approach for the scientific research. Sometimes, however, it has unavoidable limitations. For example, in the 2D experiments of invisible cloaks, the probe is placed in the gap between the cloaks and the upper metal plate of 2D waveguide [39, 28]. Hence, what one measured are only near fields instead of the internal fields. It is impossible to measure the internal fields inside the cloaks. If one can develop an efficient CEM method, which can simulate accurately the internal fields of a real-structured metamaterial system, then one can analyze the real physics inside the system. This will be a great support to metamaterials. This is also a challenging problem for CEM.

**Acknowledgments** This work was supported in part by a major project of the National Science Foundation of China under Grant Nos. 60990320 and 60990324, the Natural Science Foundation of Jiangsu Province under Grant No. BK2008031, the National Basic Research Program (973) of China under Grant No. 2004CB719802, the National Science Foundation of China under Grant Nos. 60871016, 60671015, and 60621002, and in part by the 111 Project under Grant No. 111-2-05.

## References

1. Altman, J.L.: Microwave circuits. Van Nostrand Reinhold, Princeton, NJ, 304 (1964)
2. Baena, J.D., Bonache, J., Martin, F., et al.: Equivalent-circuit models for split- ring resonators and complementary split-ring resonators coupled to planar transmission lines. IEEE Trans. Micro. Theo. Tech. **53**, 1451–1461 (2005)
3. Baena, J.D., Marques, R., Medina, F., Martel, J.: Artificial magnetic metamaterial design by using spiral resonators. Phys. Rev. B **69**, 014402 (2004)
4. Caloz, C., Itoh, T.: Application of the transmission line theory of left-handed (LH) materials to the realization of a microstrip LH transmission line. IEEE-AP-S Digest **2**, 412–415, San Antonio, TX (2002)
5. Caloz, C., Itoh, T.: Transmission line approach of left-handed (LH) structures and microstrip realization of a low-loss broadband LH filter. IEEE Trans. Antennas Propagat. **52**, 1159–1166 (2004)
6. Caloz, C., Itoh, T.: Electromagnetic Metamaterials: Transmission Line Theory and Microwave Applications. Wiley-IEEE Press (2006)
7. Chen, H., Chan, C.T.: Transformation media that rotate electromagnetic fields. Appl. Phys. Lett. **90**, 241105 (2007)
8. Chew, W.C., Jin, J.-M., Michielssen, E., Song, J.-M.: Fast and efficient algorithms in computational electromagnetics. Artech House Publishers, Boston (2001)
9. Chin, J.Y., Lu, M., Cui, T.J.: Metamaterial polarizers by electric-field-coupled resonators. Appl. Phys. Lett. **93**, 251903 (2008)
10. Chin, J.Y., Gollub, J.G., Mock, J.J., Liu, R., Harrison, C., Smith, D.R., Cui, T.J.: An efficient broadband metamaterial wave retarder. Opt. Express **17**, 7640–7647 (2009)

11. Cui, T.J., Ma, H.F., Liu, R., Zhao, B., Cheng, Q., Chin, J.Y.: A symmetrical circuit model describing all kinds of circuit metamaterials. Progr. Electromagn. Res. B **5**, 63–76 (2008)
12. Cui, T.J., Kong, J.A.: Time-domain electromagnetic energy in a frequency-dispersive left-handed medium. Phys. Rev. B **70**, 205106 (2004)
13. Cui, T.J., Cheng, Q., Lu, W.B., Jiang, Q., Kong, J.A.: Localization of electromagnetic energy using a left-handed medium slab. Phys. Rev. B **71**, 045114 (2005)
14. Falcone, F., Lopetegi, T., Laso, M.A.G., et al.: Babinet principle applied to metasurface and metamaterial design. Phys. Rev. Lett. **93**, 197401 (2004)
15. Fang, N., et al.: Sub-diffraction-limited optical imaging with a silver superlens. Science **308**, 53 (2005)
16. Grbic, A., Eleftheriadesm, G.V.: Overcoming the diffraction limit with a planar left-handed transmission-line lens. Phys. Rev. Lett. **92**, 117403 (2004)
17. Huangfu, J., Ran, L.X., Chen, H.S., Zhang, X.M., Chen, K.S., Grzegorczyk, T.M., Kong, J.A.: Experimental confirmation of negative refractive index of a metamaterial composed of Omega-like metallic patterns. App. Phys. Lett. **84**, 1537–1539 (2004)
18. Huangfu, J., Xi, S., Kong, F., Zhang, J., Chen, H., Wang, D., Wu, B.-I., Ran, L., Kong, J.A.: Application of coordinate transformation in bent waveguides. J. Appl. Phys. **104**, 014502 (2008)
19. Hutter, R.G.E.: Beam and wave electronics in microwave tubes. Van Nostrand Reinhold, Princeton, NJ, 220–230 (1960)
20. Iyer, A.K., Eleftheriades, G.V.: Negative refractive index metamaterials supporting 2-D waves. IEEE-MTT-S **2**, 412–415, Seattle, WA (2002)
21. Iyer, A.K., Kremer, P.C., Eleftheriades, G.V.: Experimental and theoretical verification of focusing in a large, periodically loaded transmission line negative refractive index metamaterial. Opt. Express **11**, 696–708 (2003)
22. Jiang, W.X., Cui, T.J., Cheng, Q., Chin, J.Y., Yang, X.M., Liu, R., Smith, D.R.: Design of arbitrarily shaped concentrators based on conformally optical transformation of nonuniform rational B-spline surfaces. Appl. Phys. Lett. **92**, 264101 (2008)
23. Jiang, W.X., Cui, T.J., Ma, H.F., Zhou, X.Y., Cheng, Q.: Cylindrical-to-plane-wave conversion via embedded optical transformation. Appl. Phys. Lett. **92**, 261903 (2008)
24. Jiang, W.X., Cui, T.J., Zhou, X.Y., Yang, X.M., Cheng, Q.: Arbitrary bending of electromagnetic waves using realizable inhomogeneous and anisotropic materials. Phys. Rev. E **78**, 066607 (2008)
25. Leonhardt, U.: Optical conformal mapping. Science **312**, 1777–1780 (2006)
26. Lin, L., Wang, W., Cui, J., Du, C., Luo, X.: Design of electromagnetic refractor and phase transformer using coordinate transformation theory. Opt. Express **16**, 6815 (2008)
27. Liu, R., Cui, T.J., Huang, D., Zhao, B., Smith, D.R.: Description and explanation of electromagnetic behaviors in artificial metamaterials based on effective medium theory. Phys. Rev. E **76**, 026606 (2007)
28. Liu, R., Ji, C., Mock, J.J., Chin, J.Y., Cui, T.J., Smith, D.R.: Broadband ground-plane cloak. Science **323**, 366 (2009)
29. Ma, H.F., Chen, X., Yang, X.M., Cui, T.J.: High-gain beam scanning antennas realized by gradient index metamaterials. Phys. Rev. E (to be published) (2009)
30. Ma, H.F., Chen, X., Yang, X.M., Xu, H.S., Cheng, Q., Cui, T.J.: A broadband metamaterial cylindrical lens antenna. Chin. Sci. Bull. (to be published) (2009)
31. Malyuzhinets, G.D.: A note on the radiation principle. Zhurnal Technicheskoi Fiziki **21**, 940–942 (1951) (in Russian)
32. Mandlshtam, L.: Group velocity in a crystal lattice. Zhurnal Eksperimentalnoii Teoreticheskoi Fiziki **15**, 476–478 (1945) (in Russian. English translation in Sov. Phys. ZETF)
33. Oliner, A.A.: A periodic-structure negative-refractive-index medium without resonant elements. IEEE-AP-S Digest, San Antonio, TX, p. 41 (2002)
34. Pendry, J.B.: Negative refraction makes a perfect lens. Phys. Rev. Lett. **85**, 3966 (2000)
35. Pendry, J.B., Holden, A.J., Robbins, D.J., Stewart, W.J.: Magnetism from conductors and enhanced nonlinear phenomena. IEEE Trans. Micro. Theory Tech. **47**, 2075–2084 (1999)

36. Pendry, J.B., Holden, A.J., Stewart, W.J., Youngs, I.: Extremely low frequency plasmons in metallic mesostructures. Phys. Rev. Lett. **76**, 4773–4776 (1996)
37. Pendry, J.B., Schurig, D., Smith, D.R.: Controlling electromagnetic fields. Science **312**, 1780–1782 (2006)
38. Rahm, M., Schurig, D., Roberts, D.A., Cummer, S.A., Smith, D.R., Pendry, J.B.: Design of electromagnetic cloaks and concentrators using form-invariant coordinate transformations of Maxwell's equations. Photo. Nano. Fund. Appl. **6**, 87 (2008).
39. Schurig, D., Mock, J.J., Justice, B.J., et al.: Metamaterial electromagnetic cloak at microwave frequencies. Science **314**, 977–980 (2006)
40. Shelby, R.A., Smith, D.R., Schultz, S.: Experimental verification of a negative index of refraction. Science **292**, 77–79 (2001)
41. Silin, R.A.: Waveguiding properties of two-dimensional periodical slow-wave systems. Voprosy Radioelektroniki. Elektronika **4**, 11–33 (1959) (in Russian)
42. Silin, R.A., Sazonov, V.P.: Slow-wave structures. Moscow, Soviet Radio (1966) (in Russian)
43. Simovski, C.R., Belov, P.A., He, S.: Backward wave region and negative material parameters of a structure formed by lattices of wires and split-ring resonators. IEEE Trans. Antennas Propagat. **51**, 2582 (2003)
44. Sivukhin, D.V.: The energy of electromagnetic waves in dispersive media. Opt. Spektrosk. **3**, 308–312 (1957)
45. Smith, D.R., Padilla, W.J., Vier, D.C., Nemat-Nasser, S.C., Schultz, S.: Composite medium with simultaneously negative permeability and permittivity. Phys. Rev. Lett. **84**, 4184 (2000)
46. Smith, D.R., Schurig, D., Rosenbluth, M., Schultz, S., Ramakrishna, S.A., Pendry, J.B.: Limitations on subdiffraction imaging with a negative refractive index slab. App. Phys. Lett. **82**, 1506 (2003)
47. Smith, D.R., Mock, J.J., Starr, A.F., Schurig, D.: Gradient index metamaterials. Phys. Rev. E **71**, 036609 (2005)
48. Smith, D.R., Pendry, J.B.: Homogenization of metamaterials by field averaging. J. Opt. Soc. Amer. B **23**, 391 (2006)
49. Smith, D.R., Vier, D.C., Koschny, T., Soukoulis, C.M.: Electromagnetic parameter retrieval from inhomogeneous metamaterials. Phys. Rev. E **71**, 036617 (2005)
50. Tretyakov, S.A.: Research on negative refraction and backward-wave media: A historical perspective. Negative refraction: revisiting electromagnetics from microwaves to optics, EPFL Latsis Symposium, Lausanne (2005)
51. Veselago, V.G.: The electrodynamics of substances with simultaneously negative values of ? and $\mu$. Sov. Phys. Usp. **10**, 509 (1968)
52. Weiglhofer, W.S., Lakhtakia, A.: Introduction to complex mediums for optics and electromagnetics. SPIE Press, Bellingham, WA, USA (2003)
53. http://en.wikipedia.org/wiki/Metamaterial

# Chapter 2
# Optical Transformation Theory

Wei Xiang Jiang and Tie Jun Cui

**Abstract** In the past few years, a rapid progress has been achieved in the subject of optical transformation, which is based on the property of form invariance in Maxwell's equations. The optical transformation, also termed as transformation optics, allows artificial metamaterials to be tailor-made according to practical needs and desires. In this chapter, we introduce the general theory of optical transformation and discuss the recent development on the optical transformation devices, such as invisibility cloaks, beam bends and splitters, wave-shape transformers, EM concentrators, rotators, antennas. The methodology of optical transformation can also be applied when the sources are included in the transformed space. Such a technique is expected to have further impact on the real-life applications.

**Key words:** Optical transformation, anisotropic and inhomogeneous metamaterials, transformation medium, invisibility cloaks, concentrator, field rotator, polarization rotator, wave-shape transformer, wave bending, beam modulator, lens antenna.

## 2.1 Introduction

In 2006, Pendry et al. proposed the mathematical description of optical transformation [69] as a design strategy to manipulate electromagnetic (EM) waves with inhomogeneous and anisotropic medium. Negative refraction, perfect lens, and invisibility cloak are special applications of transformation optics in which the material of a device implements a coordinate transformation for EM fields

Wei Xiang Jiang and Tie Jun Cui*
State Key Laboratory of Millimeter Waves, Department of Radio Engineering, Southeast University, Nanjing 210096, P. R. China. *e-mail: tjcui@seu.edu.cn

T.J. Cui et al. (eds.), *Metamaterials*, DOI 10.1007/978-1-4419-0573-4_2,

[42, 43]. The electric permittivity and magnetic permeability of the medium could be derived from the methodology of optical transformation [69, 77]. Alternatively, an optical conformal mapping method was used to design a medium that generates perfect invisibility in the ray-tracing limit [40, 41]. The invisibility cloaks were analyzed in detail using geometric ray-tracing method [77] and verified numerically by full-wave simulations [13] and experimentally by a two-dimensional (2D) near-field mapping configuration at the microwave frequency [76]. Inspired by the theoretical and experimental results, more researches had been conducted for cylindrical and spherical cloaks up to now [1, 2, 7, 9, 21, 75, 91, 92, 101, 107]. Due to the possibilities of the transformation medium to control EM fields, different devices with novel functionalities have been constructed besides the invisibility cloaks, such as EM rotators [4, 6], EM concentrators [73, 24], and planar focusing antennas [32, 52, 64, 65, 78].

The development of modern metamaterial technology endows materials with versatile and very complex properties, for example, the independent control of the permittivity and permeability with both positive and negative values, anisotropic parameters, and designed gradient index [51, 79]. However, it was not quite clear how to design novel EM devices with such versatile media until the appearance of transformation optics. The technique of optical transformation provides an intuitive and direct method to design in the enlarged material parameter space. We imagine a fictitious space with some geometrical character that enacts a desired electromagnetic phenomenon, and the transformation method yields the material property that facilitates the behavior. For example, to design an invisibility cloak, one imagines a space with a hole. Then one constructs the coordinate transformation of the space with this hole, i.e., the cloaked region. Using such a methodology one can then calculate a set of material properties that will implement the invisibility in the physical space.

The organization of the chapter is as follows: in Section 2.2, we begin with the concept of transformation media and give a brief proof of the property of metric invariance of Maxwell's equations. In Section 2.3, we discuss some examples of transformation devices, such as invisibility devices, EM concentrators, field rotators, wave-shape transformers, wave bends, and some other novel transformation devices. Section 2.4 is the summary.

## 2.2 Optical Transformation Medium

Media that perform coordinate transformations are known as transformation media. The transformation media exhibit two interesting properties. First, the optical path in the transformation media is exactly the same as that in the virtual space [43]. Second, the transformation media are reflectionless if the outer boundary before and after a coordinate transformation is unchanged. Furthermore, it was found by heuristical means that EM media designed by finite embedded coordinate transformation

can be reflectionless if a topological condition is satisfied, i.e., the metric of the transformation space in the direction normal and parallel to the interface between the transformation medium and the surrounding medium is continuous on the boundary [71]. In this section, we will give a brief proof of the form invariance of Maxwell's equations under coordinate transformations, which is the basic of optical transformation. We here restrict our discussions to transformations that are time invariant [42, 43, 62, 77], that is to say, the media implement purely spatial coordinate transformations of electromagnetic fields. We start from Maxwell's equations in the original space

$$\bigtriangledown \times \mathbf{E} + \mathrm{i}\omega\mu \cdot \mathbf{H} = \mathbf{0}, \tag{2.1}$$

$$\bigtriangledown \times \mathbf{H} - \mathrm{i}\omega\varepsilon \cdot \mathbf{E} = \mathbf{0}, \tag{2.2}$$

where both $\varepsilon$ and $\mu$ may depend on position. Suppose that the coordinate transformation between the virtual space and the physical space is

$$\mathbf{x}' = \mathbf{x}'(\mathbf{x}). \tag{2.3}$$

Can such a transformation give the equivalent relations? The answer is "yes." Maxwell's equations in the new coordinate system become

$$\bigtriangledown' \times \mathbf{E}' + \mathrm{i}\omega\mu' \cdot \mathbf{H}' = \mathbf{0}, \tag{2.4}$$

$$\bigtriangledown' \times \mathbf{H}' - \mathrm{i}\omega\varepsilon' \cdot \mathbf{E}' = \mathbf{0}, \tag{2.5}$$

with

$$\mathbf{E}'(\mathbf{x}') = (\Lambda^T)^{-1}\mathbf{E}(\mathbf{x}); \quad \mathbf{H}'(\mathbf{x}') = (\Lambda^T)^{-1}\mathbf{H}(\mathbf{x}), \tag{2.6}$$

$$\mu'(\mathbf{x}') = \frac{\Lambda \cdot \mu(\mathbf{x}) \cdot \Lambda^T}{\det(\Lambda)}; \quad \varepsilon'(\mathbf{x}') = \frac{\Lambda \cdot \varepsilon(\mathbf{x}) \cdot \Lambda^T}{\det(\Lambda)}, \tag{2.7}$$

where the Jacobian transformation matrix is defined as

$$\Lambda_{ki} = \frac{\partial x'_k}{\partial x_i}; \ [\Lambda^{-1}]_{ij} = \frac{\partial x_i}{\partial x'_j}. \tag{2.8}$$

To observe the metric invariance of Maxwell's equations does hold, we consider that

$$-\mathrm{i}\omega\mu' \cdot \mathbf{H}' = \frac{-\mathrm{i}\omega\Lambda \cdot \mu \cdot \mathbf{H}}{\det(\Lambda)} = \frac{\Lambda \cdot (\nabla \times \mathbf{E})}{\det(\Lambda)}. \tag{2.9}$$

Then we need only to show the following equation:

$$\nabla' \times \mathbf{E}' = \frac{\Lambda \cdot (\nabla \times \mathbf{E})}{\det(\Lambda)}. \tag{2.10}$$

In index notation, the left-hand side of Eq. (2.10) can be written as

$$
\begin{aligned}
[\nabla' \times \mathbf{E}']_h &= \left[\nabla' \times \left(\Lambda^{-T} \cdot \mathbf{E}\right)\right]_h \\
&= e_{hlm} \frac{\partial}{\partial x'_l} \left( \frac{\partial x_k}{\partial x'_m} E_k \right) \\
&= e_{hlm} \frac{\partial^2 x_k}{\partial x'_l \partial x'_m} E_k + e_{hlm} \frac{\partial x_k}{\partial x'_m} \frac{\partial E_k}{\partial x'_l} \\
&= e_{hlm} \frac{\partial x_k}{\partial x'_m} \frac{\partial E_k}{\partial x'_l},
\end{aligned} \tag{2.11}
$$

in which $e_{hlm}$ is the Levi–Civita symbol. The first term in the middle equation evaluates to zero by swapping the dummy indices $l$ and $m$. The right-hand side of Eq. (2.10) reads

$$
\begin{aligned}
\frac{[\Lambda \cdot (\nabla \times \mathbf{E})]_h}{\det(\Lambda)} &= \frac{1}{\det(\Lambda)} \frac{\partial x'_h}{\partial x_j} e_{jmk} \frac{\partial E_k}{\partial x_m} \\
&= \frac{1}{\det(\Lambda)} \frac{\partial x'_h}{\partial x_j} e_{jmk} \frac{\partial x'_l}{\partial x_m} \frac{\partial E_k}{\partial x'_l}.
\end{aligned} \tag{2.12}
$$

This will agree with Eq. (2.11) if

$$
e_{hlm} \frac{\partial x_k}{\partial x'_m} \frac{\partial E_k}{\partial x'_l} = \frac{1}{\det(\Lambda)} \frac{\partial x'_h}{\partial x_j} e_{jmk} \frac{\partial x'_l}{\partial x_m} \frac{\partial E_k}{\partial x'_l}, \tag{2.13}
$$

or that

$$
\det(\Lambda) e_{hlm} \frac{\partial x_k}{\partial x'_m} = \frac{\partial x'_h}{\partial x_j} e_{jmk} \frac{\partial x'_l}{\partial x_m}. \tag{2.14}
$$

Multiply both sides by the non-singular matrix $\Lambda$, i.e., multiplying by $\partial x'_p / \partial x_k$ and summing over $k$, we get

$$
\det(\Lambda) e_{hlm} \frac{\partial x_k}{\partial x'_m} \frac{\partial x'_p}{\partial x_k} = \frac{\partial x'_h}{\partial x_j} e_{jmk} \frac{\partial x'_l}{\partial x_m} \frac{\partial x'_p}{\partial x_k} \tag{2.15}
$$

or

$$
\det(\Lambda) e_{hlm} \frac{\partial x'_p}{\partial x'_m} = \det(\Lambda) e_{hlm} \delta_{pm} = \det(\Lambda) e_{hlp} = \frac{\partial x'_h}{\partial x_j} e_{jmk} \frac{\partial x'_l}{\partial x_m} \frac{\partial x'_p}{\partial x_k}, \tag{2.16}
$$

where $\delta_{pm}$ is the Kronecker delta, the matrix elements of the unity matrix. Both sides of the above equation are completely antisymmetric with respect to $h$, $l$, and $p$. For example, to see the antisymmetry in $h$ and $l$, we can swap $h$ and $l$, at the same time swap the dummy indices $j$ and $m$, and notice the fact that $e_{mjk} = -e_{jmk}$. Hence it suffices to take $h = 1,\ l = 2,\ p = 3$, and we can write

$$
\det(\Lambda) = e_{jmk} \frac{\partial x'_1}{\partial x_j} \frac{\partial x'_2}{\partial x_m} \frac{\partial x'_3}{\partial x_k}. \tag{2.17}
$$

This equation is the well-known formula for the determinant of the Jacobian matrix. Hence Eq. (2.4) holds. We can follow the similar procedure to show that Eq. (2.2) also maintains its form with respect to coordinate transformations. In other words, Eq. (2.5) holds. The form invariance of Maxwell's equations under spatial transformations has been verified.

We remark that the transformation electric and magnetic fields are written in Eq. (2.6), and the constitutive parameter tensors of the medium in the transformed space are expressed in Eq. (2.7). Since some components of the permittivity and permeability of the required media are often less than 1, generally, the transformation devices are composed of inhomogeneous and anisotropic metamaterials.

For most practical devices, Eq. (2.7) are the primary tools for the transformation design method. If the host medium does not possess magnetoelectric coupling and the desired device moves or changes shape with speeds much less than that of light, the above discussions are valid. Media that facilitate space–time transformations have been discussed in [42, 43]. Equations (2.6) and (2.7) can be shown to be exactly equivalent to the results obtained by Ward and Pendry [87].

## 2.3 Transformation Devices

### *2.3.1 Invisibility Cloaks*

Invisibility cloaks have attracted much attention, thanks to their exciting property of invisibility of the shielded objects. Following the theory of optical transformation, a volume of free space can be transformed into a shell-type region, which can therefore render the object inside the shell invisible to the incident waves. Inspired by the early pioneering work [13, 69, 76], more intensive investigations on cylindrical and spherical cloaks have been conducted [1, 2, 7, 21, 101]. In order to reveal the nature of invisible cloaking, analytical methods based on Maxwell's equations have been used to provide more insights into the physical principles [9, 75].

In the earlier investigations, all parameter designs, numerical simulations, and theoretical analysis were devoted to circularly cylindrical or spherical cloaks, which were relatively easy to be designed, simulated, and analyzed. Theoretically, the circularly cylindrical or spherical cloaks can make any objects invisible. However, they are not efficient or convenient for long and thin objects. As a consequence, cylindrical cloaks with elliptical shapes were presented to design invisibility with generality [29, 35, 36, 58]. Consider an elliptical–cylindrical object with arbitrary axis ratio embedded in free space, which is covered by an invisibility cloak. The cross section of such a cloak is an elliptical shell with the inner and outer short semi-axes $a$ and $b$, respectively. The inner and outer ellipses have the same axis ratio $k$, which represents a horizontal elliptical cloak when $k > 1$, a vertical elliptical cloak when $k < 1$, and a circular cloak when $k = 1$ (see Fig. 2.1). The transformation for a cylindrical cloak is an identity along $z$-axis, hence we present the coordinate transformation

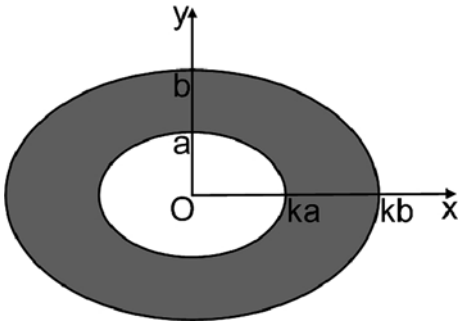


**Fig. 2.1** The cross section of an elliptical–cylindrical cloak with arbitrary axis ratio in the Cartesian coordinate system. The *grey region* is the cloaking layer.

in the *xoy* plane. Similar to the circularly cylindrical cloak, we can define a spatial transformation in the Cartesian coordinates

$$x' = \left(\frac{b-a}{b} + \frac{ka}{r_0}\right)x, \tag{2.18}$$

$$y' = \left(\frac{b-a}{b} + \frac{ka}{r_0}\right)y, \tag{2.19}$$

$$z' = z, \tag{2.20}$$

in which $r_0 = \sqrt{x^2 + k^2 y^2}$. From this transformation, we can easily compute the Jacobian transformation matrix as

$$\begin{aligned}\bar{\Lambda} &= \begin{pmatrix} \frac{\partial x'}{\partial x} & \frac{\partial x'}{\partial y} & \frac{\partial x'}{\partial z} \\ \frac{\partial y'}{\partial x} & \frac{\partial y'}{\partial y} & \frac{\partial y'}{\partial z} \\ \frac{\partial z'}{\partial x} & \frac{\partial z'}{\partial y} & \frac{\partial z'}{\partial z} \end{pmatrix} \\ &= \begin{pmatrix} \frac{r'}{r} - \frac{kax^2}{r_0^3} & -\frac{k^3 axy}{r_0^3} & 0 \\ -\frac{kaxy}{r_0^3} & \frac{r'}{r} - \frac{k^3 ay^2}{r_0^3} & 0 \\ 0 & 0 & 1 \end{pmatrix},\end{aligned} \tag{2.21}$$

which represents the derivative of the new coordinates with respect to the original coordinates as mentioned in Section 2.2, $r' = \sqrt{x'^2 + y'^2}$ and $r = \sqrt{x^2 + y^2}$ in Eq. (2.21). The determinant of the Jacobian matrix can be written in a closed-form expression:

$$\det(\bar{\Lambda}) = \frac{r'}{r}\left(\frac{r'}{r} - \frac{ka}{r_0}\right). \tag{2.22}$$

Based on Eqs. (2.7), (2.21), and (2.22), we easily obtain the relative permittivity and permeability tensors for the cloaking shell:

$$\bar{\varepsilon}_r' = \bar{\mu}_r' = \begin{pmatrix} \varepsilon_{xx} & \varepsilon_{xy} & 0 \\ \varepsilon_{yx} & \varepsilon_{yy} & 0 \\ 0 & 0 & \varepsilon_{zz} \end{pmatrix}, \tag{2.23}$$

in which

$$\varepsilon_{xx} = \frac{r_1}{r_1 - ka} + \frac{k^2a^2R^2 - 2kar_1^3}{(r_1 - ka)r_1^5}x^2, \tag{2.24}$$

$$\varepsilon_{xy} = \frac{k^2a^2R^2 - ka(1+k^2)r_1^3}{(r_1 - ka)r_1^5}xy = \varepsilon_{yx}, \tag{2.25}$$

$$\varepsilon_{yy} = \frac{r_1}{r_1 - ka} + \frac{k^2a^2R^2 - 2k^3ar_1^3}{(r_1 - ka)r_1^5}y^2, \tag{2.26}$$

$$\varepsilon_{zz} = \left(\frac{b}{b-a}\right)^2 \frac{r_1 - ka}{r_1}, \tag{2.27}$$

where $r_1 = \sqrt{x^2 + k^2y^2}$ and $R = \sqrt{x^2 + k^4y^2}$. We have dropped the primes for aesthetic reasons in these formulae and assumed that the original space is the free space.

When the axis ratio $k = 1$, the elliptical–cylindrical cloak reduces to a circular–cylindrical cloak. Therefore, the material parameters, Eqs. (2.24)–(2.27), are simplified as

$$\varepsilon_{xx} = \frac{r}{r-a} + \frac{a^2 - 2ar}{(r-a)r^3}x^2, \tag{2.28}$$

$$\varepsilon_{xy} = \frac{a^2 - 2ar}{(r-a)r^3}xy = \varepsilon_{yx}, \tag{2.29}$$

$$\varepsilon_{yy} = \frac{r}{r-a} + \frac{a^2 - 2ar}{(r-a)r^3}y^2, \tag{2.30}$$

$$\varepsilon_{zz} = (\frac{b}{b-a})^2 \frac{r-a}{r}, \tag{2.31}$$

which are exactly the same as Eq. (29) in [77].

Equations (2.24–2.27) give full design parameters for the permittivity and permeability tensors in elliptical–cylindrical cloaking layer. Comparing with the circular–cylindrical cloaks discussed in [77], the elliptical cloaks have two advantages. First, larger ranges of shape selections are provided. Second, they have fewer singularities in the cloaking region. As shown in Eqs. (2.28–2.31), the permittivity and permeability components $\varepsilon_{xx}$, $\varepsilon_{xy}$, $\varepsilon_{yx}$, and $\varepsilon_{yy}$ tend to infinity, while $\varepsilon_{zz}$ tends to zero along the circle $r = a$ for the circular–cylindrical invisibility cloak. That is to say, singular material parameters are distributed on the whole circle ($r = a$), which are difficult to be fabricated in real applications. For the elliptical–cylindrical cloaking, however,

the material parameters are singular at only two points ($r_1 = ka$): the adjoint points of inner ellipse with the $x$-axis, as shown in Eqs. (2.24)–(2.27). Hence the material parameters in elliptical cloak are much easier to achieve.

Figure 2.2 shows the comparison of the propagation of a transverse-magnetic (TM) polarized plane wave in the free space with and without perfectly elliptical–cylindrical cloak. Distributions of magnetic fields and the power flow lines in the virtual space and the physical space are illustrated. In the cloaking shell, the power flow lines propagate smoothly around the cloaked region and the wave fronts are warped smoothly in the predicted way. Outside the cloak, the plane waves are nearly unchanged as if there were no objects in the free space. Hence the invisible cloaking performance is well verified.

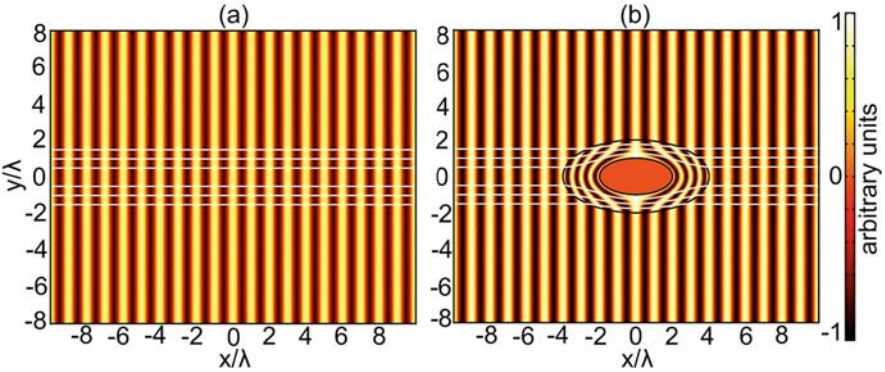


**Fig. 2.2** (**a**) Virtual space. The figure shows the propagation of a plane wave in the free space. (**b**) Physical space. The cloaking layer makes the EM waves propagate around the cloaked region and return to their original propagation directions without distorting the waves outside the perfect cloak.

Similar to the invisibility cloak, constitutive tensors for EM masking of arbitrarily convex conducting objects has been given in [80]. Such a masking shell can be regarded as a partial cloaking layer. When the maximum and minimum radii of the object equals, i.e., the object is a sphere, the masking is exactly an invisible cloak. Invisibility cloaks for diversified-shaped objects were reported including square cloak [6, 11, 20, 23, 25, 46, 53, 56, 57, 63, 73, 95, 97, 98]. Next, a general method, which can be used to design arbitrarily shaped transformation devices, will be discussed: the nonuniform rational B-spline (NURBS) [70].

As one of the parametric curve representations, NURBS is a very popular geometrical tool. It is feasible to split an arbitrary curve into a sequence of B*é*zier curves. By introducing NURBS to describe the geometric modeling of any objects, analytical formulas of the permittivity and permeability for the arbitrarily shaped transformation devices can be expressed [23, 24]. Furthermore, the usage of NURBS will expand the generality of the transformation optics and could make a very general tool to interface with commercial software packages such as 3D STUDIOMAX and MAYA. Therefore, the transformation optical design is possible to

become industrialization. Figure 2.3 demonstrates the full-wave simulation results of a perfect heart-shaped cloak when the plane waves are incident from two different directions [23]. Both the inner and the outer boundaries of the cloak are represented by NURBS. In both cases, the power flow lines inside the cloak layer propagate smoothly around the heart-shaped object, making it invisible to the observers. It is even true when the incident waves impinge on the concave area of the cloak, as shown in Fig. 2.3(b).

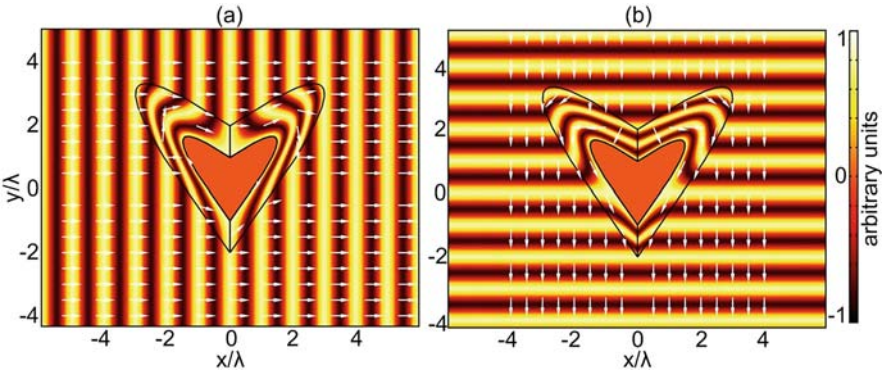


**Fig. 2.3** The magnetic field distributions and power flow lines for the perfect invisible cloak of a heart-shaped PEC object with different incident directions. (**a**) The TM-polarized plane waves propagate from the *left* to the *right*. (**b**) The TM-polarized plane waves propagate from the *top* to the *bottom*.

One challenge of the perfectly full-parameter cloak is that, on its inner boundary, some components of material parameters often require singular values, which makes the full-parameter cloak difficult to achieve even by using recent metamaterial techniques [76]. In view of the difficulty to realize the full-parameter cloak and the imperfection of reduced-parameter cloak, a recently published work has described a carpet cloak. By using this concept, one can cause any object wrapped under a conducting plane to seem to disappear [48]. The great advantage of the carpet cloak is that it relaxes singular value requirement for the material parameters. The experimental validations of the carpet cloak has been achieved with low-loss and broadband metamaterials at microwave frequencies [50] and at optical frequencies recently [16, 82]. A similar cloaking over a dielectric half-space using a singular cloak was proposed in [104]. More recently, the optical transformation of a curved, non-Euclidean space has been presented, which relaxes the needs of the material extreme properties and can yield invisibility in a broad band of the spectrum [45].

To avoid any singular values in the constitutive parameters, it was also demonstrated that an elliptical cloaking region can be crushed to a line segment using the coordinate transformation in the classical elliptical–cylindrical coordinate system [28], instead of being shrunk to a point. In this context, the relationship between classical elliptical–cylindrical coordinates $(\xi,\ \eta,\ z)$ and Cartesian coordinates $(x,\ y,\ z)$ is necessary. It is expressed as

$$x = p\cosh\xi\cos\eta, \quad y = p\sinh\xi\sin\eta, \quad z = z, \tag{2.32}$$

in which $p$ is the half focus of the ellipse. In the elliptical–cylindrical coordinate system, if we assume $p$ to be constant, then isolines for $\xi$ will be a series of elliptical–cylindrical shells with the same focus value.

Similar to the circular cloak design, a spatial transformation from the elliptical region $\xi \in [0, \xi_2]$ to the annular region $\xi' \in [\xi_1, \xi_2]$ can be described mathematically as

$$\xi' = \frac{\xi_2 - \xi_1}{\xi_2}\xi + \xi_1, \ \eta' = \eta, \ z' = z, \tag{2.33}$$

where $\xi_1$ and $\xi_2$ are coordinate parameters of the inner and outer boundaries of the elliptical cloak. We denote the lengths of major axes for inner and outer shells of the cloak as $a_1$ and $a_2$. The nonlinear relationship between coordinate parameters and the lengths of major axes can be written as $\xi_i = \ln\left(a_i/p + \sqrt{(a_i/p)^2 - 1}\right)$, $i = 1, 2$. We remark that the inner and outer ellipses have the same focus value $2p$. Hence the inner boundary will be crushed to the line segment $2p$ using the above-defined coordinate transformation.

Following the procedure stated in Section 2.2, one can derive the parameter tensors of the elliptical cloak. The relative electric permittivity and magnetic permeability are expressed as

$$\varepsilon'_{\xi'} = \mu'_{\xi'} = k, \tag{2.34}$$

$$\varepsilon'_{\eta'} = \mu'_{\eta'} = \frac{1}{k}, \tag{2.35}$$

$$\varepsilon'_{z'} = \mu'_{z'} = \frac{1}{k}\frac{\cosh^2\alpha - \cos^2\eta'}{\cosh^2\xi' - \cos^2\eta'}, \tag{2.36}$$

in which $\alpha = k(\xi' - \xi_1)$, $k = (\xi_2 - \xi_1)/\xi_2$, $\xi_1 \le \xi' \le \xi_2$, and $0 \le \eta' \le 2\pi$.

Equations (2.34)–(2.36) present full design parameters for the elliptical cloak in the classical elliptical–cylindrical coordinates. Clearly, the cloak is composed of inhomogeneous and uniaxially anisotropic metamaterials with finite parameters. For circularly cylindrical cloaks with full parameters, singular material parameters are distributed on the whole inner boundary [9, 75], which are difficult to achieve in the actual applications [76]. For elliptical cloaks which shrink the cloaked objects to a point, singular values still exist on the inner boundary of the cloaks [26, 35, 36]. The material parameters for the elliptical–cylindrical cloak here which crushes the cloaked object to the line segment $2p$, however, have no singularity. This makes it possible to realize the perfectly full-parameter cloak using man-made metamaterials.

When the focus of the ellipse becomes very small, the elliptical cloak approaches a circular cloak. In such a case, $\varepsilon_\xi$ becomes $\varepsilon_r$ and $\varepsilon_\eta$ becomes $\varepsilon_\phi$, indicating the radian and angular components of the permittivity. In order to compare with the ordinary circular cloak [13, 77], in the following simulation results, we choose

the shape of cloak as an exact circle while the material parameters are given by those of nearly circular cloak:

$$\varepsilon_r' = \mu_r' = k, \tag{2.37}$$

$$\varepsilon_\phi' = \mu_\phi' = \frac{1}{k}, \tag{2.38}$$

$$\varepsilon_z' = \mu_z' = \frac{\cosh^2\beta}{k\cosh^2\xi}, \tag{2.39}$$

in which $\beta = (\xi - \xi_1)/k$, $\xi = \ln\left(r/p + \sqrt{(r/p)^2 - 1}\right)$, $\xi_1 = \ln\left(R_1/p + \sqrt{(R_1/p)^2 - 1}\right)$, and $\xi_2 = \ln\left(R_2/p + \sqrt{(R_2/p)^2 - 1}\right)$.

The advantages of such invisibility cloak are that none of the parameters is singular and the changing range of all parameters is relatively small. When transverse magnetic (TM) polarized waves are incident on the cloak with different small values of $p$, the full-wave simulation results are illustrated in Fig. 2.4(a)–(c). From these

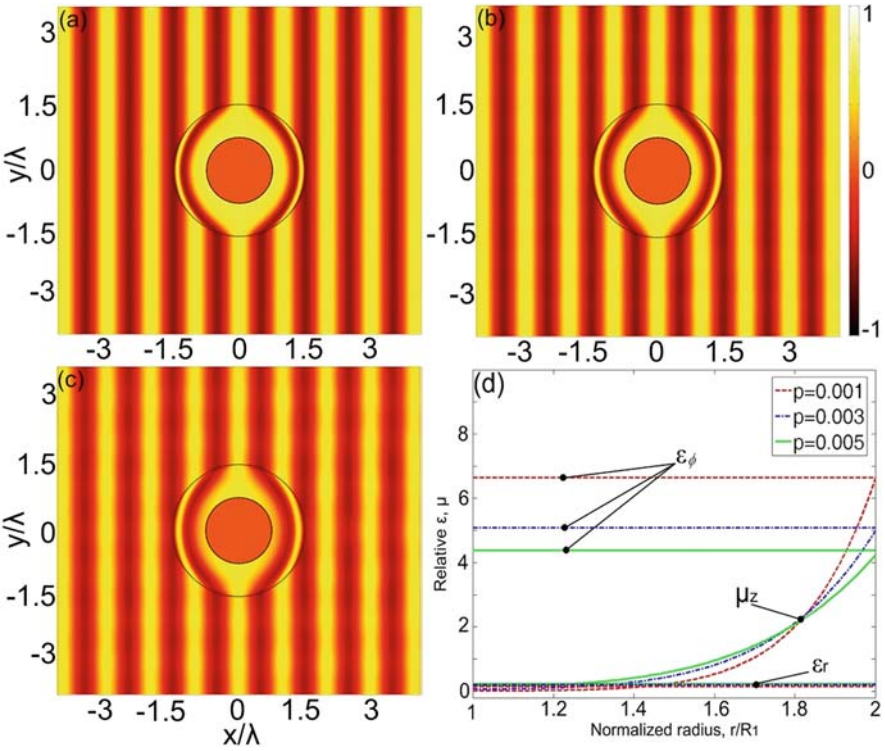


**Fig. 2.4** The distributions of magnetic fields inside circular cloaks with inner radius 0.025 m ($0.75\lambda_0$), and, outer radius 0.05 m ($1.5\lambda_0$). (**a**) The half focus p = 0.001 m, (**b**) the half focus p = 0.003 m, (**c**) the half focus p = 0.005 m, and (**d**) the distributions of $\mu_z$, $\varepsilon_\phi$, and $\varepsilon_r$ components in the cloaking region.

figures, one observes that the phase fronts are bent smoothly around the perfectly electric-conducting (PEC) object inside the cloak, and the fields are smoothly excluded from the interior region with tiny scattered fields. All material parameters for the above circular cloaks have relatively small ranges. Figure 2.4(d) illustrates the parameter distributions inside the approximate cloaks. Obviously, for each case, $\varepsilon_\phi$ and $\varepsilon_r$ are constants, and $\mu_z$ changes in a small range, all of which can be achieved using artificial metamaterials. From Fig. 2.4(a)–(c), it is clearly observed that the approximate cloak can achieve almost perfect cloaking performance because the cloaked object is crushed nearly to a point, which leads to a tiny scattering.

An approximate quantum cloaking was presented in [19], and some other designs of transformation functions and nonmagnetic cloaks were reported in [2, 3, 12, 17, 21, 30, 54, 90, 94]. We focused primarily on the electromagnetic invisibility cloaks and only mentioned cloaks of other waves [14, 105] without going into details. In the above discussions, the transformation medium is a metamaterial shell with its interior and exterior boundaries of similar shapes. In reality, however, the shielded object may have an arbitrary shape and the interior boundary of the metamaterial shell is preferred to be the same as the shape of the cloaked object. Meanwhile the shape of the exterior boundary has to fit the external environment. Hence the exterior shape of the metamaterial layer is not always the same as the interior shape. As a result, it is necessary to discuss cloaks with different inner and outer boundaries by following the method of optical transformation.

An invisible cloak with non-conformal interior and exterior boundaries using the transformation optical design [100] was proposed. As a practical case, consider the shape with square in the outer boundary and circle in the inner boundary. Other cloaks with more complicated and non-conformal interior and exterior boundary shapes can be achieved in a similar way [47]. Figure 2.5 illustrates the numerical

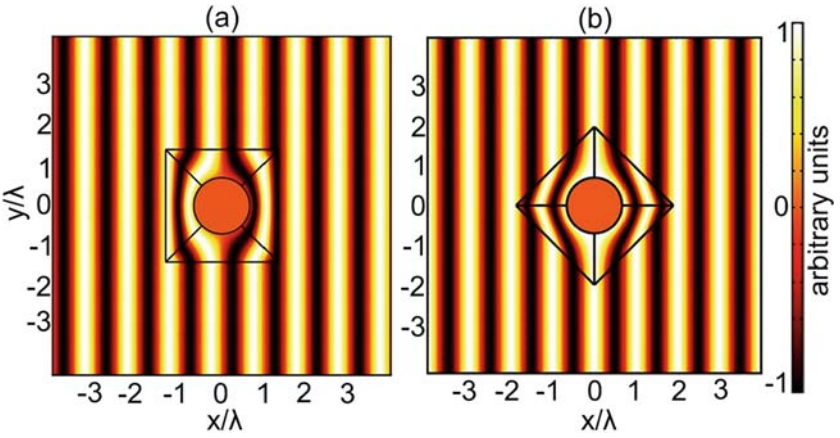


**Fig. 2.5** The distributions of magnetic fields for the non-conformal cloak with different inner and outer boundaries. The shielded object is a PEC cylinder. (**a**) The *square outline* of the cloak is parallel to the *x*-direction. (**b**) The *square outline* of the cloak is rotated by $\pi/4$ with respect to the *x*-direction.

results of the cloaks with square in the outer boundary and circle in the inner boundary. In Fig. 2.5(a), the phase fronts of incident waves are parallel to one border of the cloak. When the waves pass through the cloak, the cloaking effect is very obvious as expected, although the cloak boundary possesses sharp corners. From Fig. 2.5(a), the plane wave is almost unaltered, as if no scatterer were present. Inside the cloaking material, the phase fronts are bent smoothly around the target. The fields are smoothly excluded from the interior region with the minimal scattering in any directions. Figure 2.5(b) shows the magnetic field distributions when the cloak is rotated by an angle of 45°. In such a case, the cloaking effect is also clear, although the equal-phase faces of incident waves are not parallel to any sides of the cloak boundary. More invisible devices will be discussed in Section 2.3.6 after we introduce the concept of finite embedded optical transformation.

### 2.3.2 EM Concentrators

Electromagnetic concentrator is another transformation device which can concentrate EM waves into a small enclosed region. This concept was first proposed by Rahm et al. [73], and the reduced-parameter concentrator was studied in [84] for future practical implementation. Such a novel device may find its applications in the energy concentration. EM concentrators with arbitrary shapes were later presented using the coordinate transformation by using NURBS in representation of the geometrical boundary [24]. Based on the transformation optics, closed-form formulae for the arbitrarily shaped concentrators were obtained, and a square concentrator could be used to amplify plane waves.

In order to present the transformation design, we take a circularly cylindrical EM concentrator as example. Due to its cylindrical symmetry, it is convenient to define the transformation functions in the cylindrical coordinates $(r,\ \phi,\ z)$. A linear transformation for the optical design of the cylindrical concentrator is written as

$$r' = \begin{cases} k_1 r, & 0 \le r \le R_2, \\ k_2 r - k_3 R_3, & R_2 \le r \le R_3, \end{cases} \tag{2.40}$$

$$\phi' = \phi, \tag{2.41}$$

$$z' = z, \tag{2.42}$$

where the coefficients are $k_1 = R_1/R_2$, $k_2 = (R_3 - R_1)/(R_3 - R_2)$ and $k_3 = (R_2 - R_1)/(R_3 - R_2)$. The definitions of $R_1,\ R_2$, and $R_3$ are shown in Fig. 2.6. The above transformation implies that the cylindrical region with radius $R_2$ is compressed into a smaller region with radius $R_1$, while space between $R_2$ and $R_3$ is expanded to the space between $R_1$ and $R_3$. Clearly, the transformation is continuous to free space at $R_3$. According to Eq. (2.7), the relative material parameters in cylindrical coordinates can be calculated [73]. A rigorous analysis on circularly cylindrical concentrator has been discussed in [52].

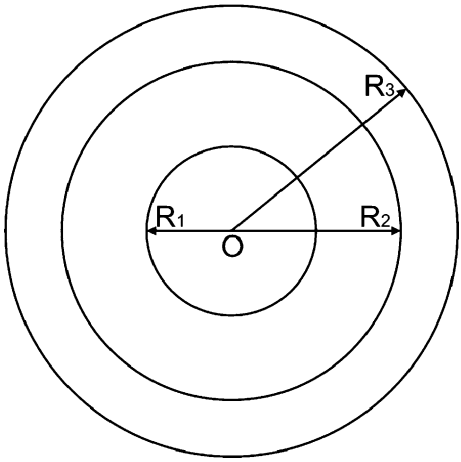


**Fig. 2.6** The cross section of a circularly cylindrical concentrator. The cylindrical region with radius $R_2$ is compressed into a smaller region with radius $R_1$, while space between $R_2$ and $R_3$ is expanded to the space between $R_1$ and $R_3$.

Figure 2.7 demonstrates the numerical results of a concentrator with heart shape, when the TE waves propagate from the left to the right. Both the inner and the outer boundaries of the concentrator are described by the NURBS curves [24]. The ratio among the principal radii of the three "hearts" is 1:6:10. The distributions of electric fields and power flow lines are shown in Fig. 2.7(a). It is obvious that the fraction of plane waves is completely focussed into the inner region within the concentrator material. There are no reflected waves outside the concentrator due to the inherent impedance matching in the method of optical transformation. Figure 2.7(b) illustrates the normalized power flow intensity distributions of the plane waves. The white arrows represent the directions of the power flows. Clearly, the energy intensities are strongly enhanced in the inner region of the concentrator.

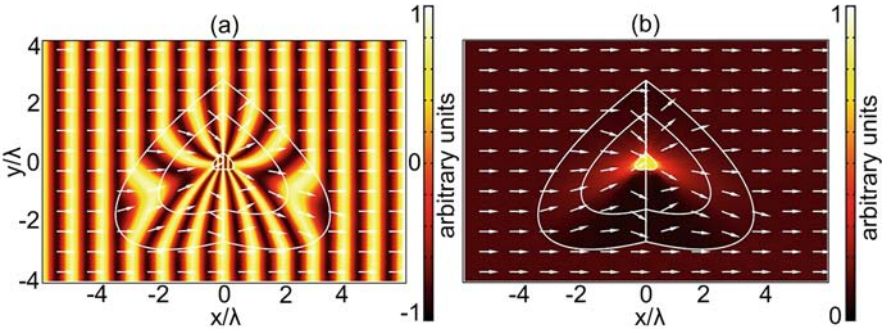


**Fig. 2.7** (**a**) The distributions of electric fields and power flow lines for a concentrator with *heart shape*. The incident plane waves propagate from the *left* to the *right*. (**b**) Power flow distributions for the concentrator with *heart shape*. Much stronger power flow enhancements can be observed in the inner region.

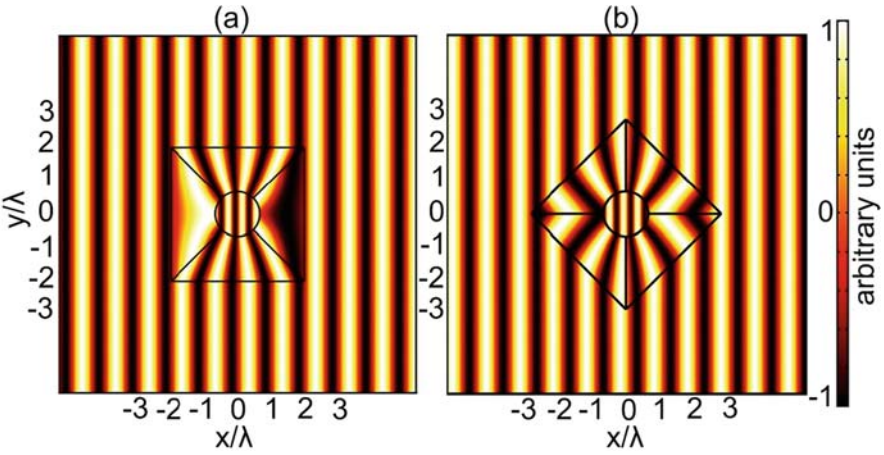


**Fig. 2.8** The distributions of electric fields for a non-conformal concentrator with different inner and outer boundaries. (**a**) The *square outline* of the concentrator is parallel to the $x$-axis. (**b**) The *square outline* of the concentrator is rotated by $\pi/4$ with respect to the $x$-axis.

Similar to the cloak with non-formal boundaries, one can also design microwave concentrator with different inner and outer boundaries [100]. Figure 2.8 demonstrates the simulated results of the electric field for concentrators with non-conformal inner and outer boundaries. TE-polarized plane waves are incident horizontally. It is obviously shown that the fields are concentrated in the small circular region in both cases, which leads to large strengthened intensities within the inner region. Hence, such a non-conformal concentrator is also a power flow enhancer.

### *2.3.3 EM-Field and Polarization Rotators*

Cylindrical rotation coating was first proposed by Chen and Chan [4]. It is one kind of two-dimensional transformation media which rotate electromagnetic fields. Hence it is also called "EM-field rotator." For the invisibility cloak, the mapping is from a point or a line to a circle, while for the concentrator, the mapping is from a circle to another circle. The EM-field rotator performs a rotation of wave fronts and the mapping can be defined as

$$r' = r, \quad z' = z, \quad \theta' = \theta \quad (\text{for } r > b), \tag{2.43}$$

$$r' = r, \quad z' = z, \quad \theta' = \theta + \theta_0 \quad (\text{for } r < a), \tag{2.44}$$

$$r' = r, \quad z' = z, \quad \theta' = \theta + f(r)\theta_0 \quad (\text{for } a < r < b). \tag{2.45}$$

The above transformation means that the wave front is an angle $\theta_0 > 0$ rotation at the inner cylinder ($r = a$) and the rotational angle is reduced to zero as the radius approaches $r = b$. $f(r)$ could be any continuous function of $r$ with $f(a) = 1$ and

$f(b) = 0$. When two observers inside and outside the rotation coating communicate with each other, the information will be rotated. The physical consequence of this kind of transformation media has been investigated in [5, 52]. An experimental realization of the rotation coating requires building blocks that have anisotropic dielectric functions [6].

It is very interesting that a similar transformation in 3D can describe another novel transformation devices. For example, a conical device which can be used to arbitrarily control the polarization of EM waves has been proposed in [55]. Consider a similar transformation in a spherical coordinate system

$$r' = r, \quad \theta' = \theta, \quad \phi' = \phi \quad (\text{for } \theta > \alpha), \tag{2.46}$$

$$r' = r, \quad \theta' = \theta, \quad \phi' = \phi + \phi_0 \quad (\text{for } \theta < \beta), \tag{2.47}$$

$$r' = r, \quad \theta' = \theta, \quad \phi' = \phi + f(\theta)\phi_0 \quad (\text{for } \beta < \theta < \alpha), \tag{2.48}$$

where $f(\theta)$ is also an arbitrary continuous function with $f(\alpha) = 0$ and $f(\beta) = 1$. It can be seen that the above mapping rotates at an angle $\phi_0$ for region $\theta < \beta$. A circularly cylindrical polarization rotator was proposed in [38]. These devices can arbitrarily control the polarization of EM waves getting through without any scattering [38, 55].

### *2.3.4 Wave-Shape Transformers*

An approach to convert cylindrical waves to plane waves in a short range using the optical transformation was proposed in Refs. [27, 49], which can be used either as a four-beam antenna or a compact range for near-field measurement of plane waves. Figure 2.9(a) illustrates the structure of a wave-shape transformer and electric field distributions inside and outside the transformer. When the cylindrical waves propagate through the conversion metamaterial layer, four beams of plane waves emerge in the surrounding medium, free space here. Hence, in a very short distance, the cylindrical waves emitted from a line source are converted to plane waves in four directions. Figure 2.9(b) shows normalized power flow intensity distributions for the EM wave transformer. Clearly, the scattering effect at four corners of the square is quite small. In another word, the transformer provides high-directivity radiation beams to four directions, hence it can be employed to design high-gain antenna or wave collimators [37].

Similarly, the transformation design method was employed to realize substrates that can modify the emission of an embedded source [103]. With proper transformation functions, the energy radiated by a source embedded in these space variant media will be concentrated in a narrow beam [34]. Hence, the technique of optical transformations is a powerful approach for good performance antenna designs [44, 102].

A more general situation that converts a wave front from an arbitrary shape to another arbitrary style has been considered in [60]. The authors proposed a general method of designing wave-shape transformers. By adopting this method, a

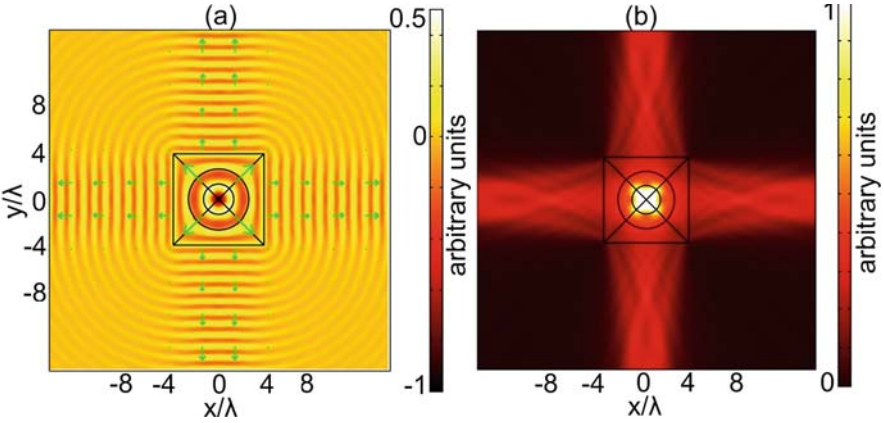


**Fig. 2.9** (**a**) The distributions of electric fields and power flow lines for the transformer from cylindrical waves to plane waves. (**b**) Power flow distributions for the cylindrical-to-plane-wave transformer.

wave-shape transformer that convert wave fronts with arbitrary shape and size to another arbitrary style can be constructed.

The basic idea comes from that waves which propagate perpendicular to the phase fronts in the free space. Hence, the wave shape and size of a non-plane wave will be changed momentarily. If a device can limit the propagation of a wave in one certain region and convert the wave shape to another style when the wave leaves, it is called wave-shape transformer. In topological interpretation, such a device causes the spatial deformation by mapping the points traced by the wave propagating in the virtual space (free space here) to the points within the physical space. Therefore, the electric permittivity and magnetic permeability for this device can be established by using the coordinate transformation theory.

One can also design a transformation device that keeps wave shape. Such a transformation device keeps the phase front without changing the shape and size when a wave propagates through it [61]. An interesting property of such media is that the power will be transmitted along a given direction, whatever the wave shape might be.

### *2.3.5 EM-Wave Bending*

Rahm et al. expanded the class of transformation of optical structures by introducing finite embedded coordinate transformations, which allow the field manipulations performed by a transformation medium to be transferred to the wave that exits the medium [71]. For example, they proposed a parallel beam shifter and a beam splitter. They are different from the known transformation optical designs, which are inherently reflectionless. The embedded optical transformation can also be used to bend EM waves to the desired directions inside a waveguide or in free space

without any reflections (or with tiny reflections) by designing proper inhomogeneous and anisotropic materials [15, 22, 30, 37, 72, 74].

One can employ the finite embedded optical transformation to realize the waveguide bends [30]. Define a mapping from the original space to the physical space as

$$x' = x\cos\frac{\theta y}{h}, \tag{2.49}$$

$$y' = x\sin\frac{\theta y}{h}, \tag{2.50}$$

$$z' = z, \tag{2.51}$$

in which $\theta$ is the radian of the bending angle and $h$ is an optional variable. When such a wave bender is filled inside metallic waveguide bends, the incident waves will be guided through the bends with very small reflections. The simulation results of the waveguide bends with different bending angles and different values of $h$ are shown in Fig. 2.10(a)–(d). TM-polarized plane waves are incident from the bottom with the working frequency of 8 GHz, for which the free-space wavelength

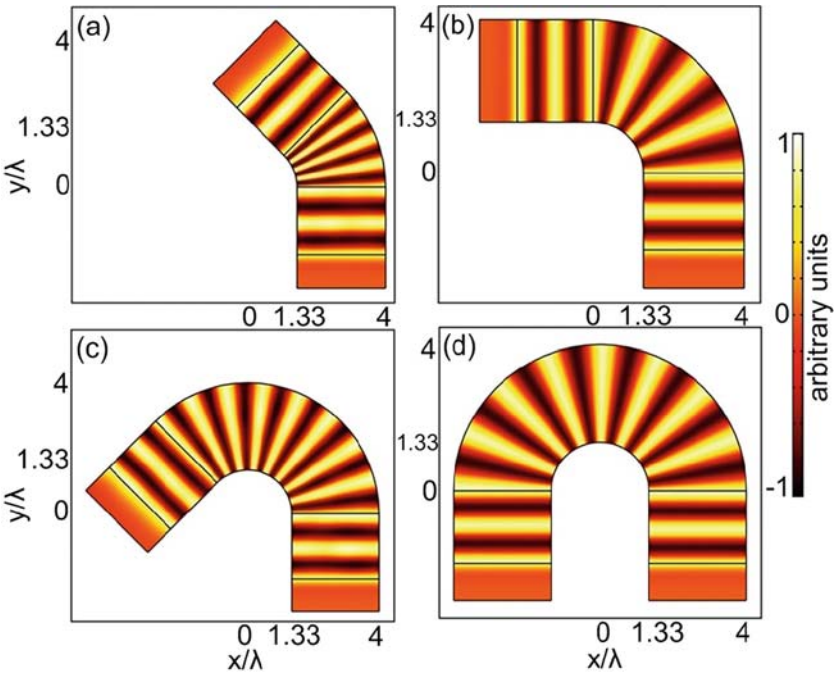


**Fig. 2.10** The distribution of magnetic fields ($z$ components) inside different *waveguide bends*. (**a**) $\theta = \pi/4$ and $h = 4\lambda_0$; (**b**) $\theta = \pi/2$ and $h = 4\lambda_0$; (**c**) $\theta = 3\pi/4$ and $h = 8\lambda_0$; and (**d**) $\theta = \pi$ and $h = 8\lambda_0$. $\lambda_0$ is the free-space wavelength.

is $\lambda_0 = 37.5$ mm. It is clear that incident waves travel through the waveguide bends smoothly and maintain their original field patterns without any distortions in all cases.

The arbitrary wave-bending structure with reduced EM parameters have been designed and analyzed using the optical transformation [30], which is composed of simple and realizable metamaterials. The reduced-parameter wave bender is uniaxial and hence easy to realize using artificial structures. When such wave bender is placed in the air, the incident waves will be bent to any designed directions. The layered wave benders also have good performance in the wave bending.

We have mentioned that the finite embedded approach does not inherently lead to reflectionless devices in contrast to optical elements designed by continuous coordinate transformations. However, reflections at the boundaries of these transformation elements can be completely avoided when they satisfy some certain conditions. It has been found by heuristical means that transformation media designed by finite embedded coordinate transformation can be reflectionless if the metric of the transformation medium in the direction normal and parallel to the interface between the transformation medium and the surrounding medium is continuous at the boundary [71].

### *2.3.6 More Invisibility Devices*

We will discuss more interesting invisibility devices proposed more recently. Greenleaf et al. presented a mathematical description of invisible tunnel, which allows EM wave propagation inside the tunnel, but it is invisible to the observers [18]. According to the embedded optical transformation approach mentioned in the above section, a class of invisible slab cloaks was proposed and analyzed in [99]. The designed slab cloaking structures could force the incident EM waves to propagate around the cloaked objects in the slabs without any distortions. The potential application of such slab cloaks is a type substrate for integrated circuits, which will protect the devices inside from the interference of EM waves but not disturb their EM properties. Figure 2.11(a) shows the distribution of magnetic fields and EM power flow lines (white arrows) when the TM Gaussian beam is normally incident to the slab. Although there are some sharp angles on the boundary of the cloaked object, the Gaussian beam outside the slab is almost unaltered. We can observe that the incident beam propagates around the cloaked prism smoothly and return to its original direction, as if no scatterers exist.

Similarly, a kind of one-directional perfect cloak composed of only homogeneously anisotropic materials was proposed in [88]. The idea is raised based on the fact that there will be no scattering when TM-polarized waves impinge onto an infinitesimal PEC surface, with the electric fields perpendicular to the surface. Therefore, we can define a transformation that maps a diamond space containing the infinitesimal PEC surface to the space with a diamond PEC inner boundary (see Fig. 2.11(b)). For this transformation, the topology of the space stays unchanged and

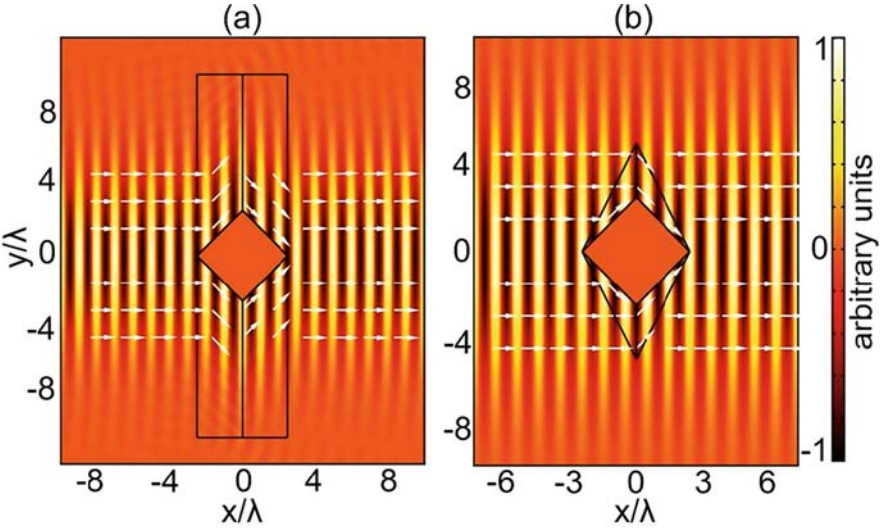


**Fig. 2.11** The distributions of magnetic fields and power flow lines for the one-directional perfect invisible cloaks when a TM Gaussian beam is normally incident. (**a**) The *slab cloak*. (**b**) The *diamond cloak*.

a perfect cloak for TM waves is obtained. The advantage of this kind of cloak is that the parameters are only homogeneously anisotropic, which will facilitate practical realizations. A similar layered one-dimensional cloak was discussed in [5].

Will the embedded objects inside the cloak impact on the perfect cloaking effect? The aforementioned examples did not consider this problem. The answer is that the perfect cloaking effect can be defeated by adding another kind of transformation media inside the cloak [8]. The authors showed that the invisible cloak cannot hide the enclosed domain if the inside domain has a shell of anti-cloak. The anti-cloak region is an anisotropic negative refractive shell which is impedance matched to the cloaking layer outside. The idea comes from that a negative refractive index medium "cancels" the space of a positive index medium that has the same impedance [68]. A heuristic way of understanding the operation of an anti-cloak is that it destroys the functionality of the inner part of the invisibility cloak and effectively shifts the enclosed region outward to make contact with the outer part of the cloaking layer which is not "canceled." This results in a finite cross section. Hence, if an object is covered by an outer layer made of a specific form of negative index anisotropic material, it will not be made entirely invisible by the invisibility cloak.

The previously mentioned invisible cloaks are all closed ones. As we discussed, closed cloaks have the continuous shell region in which the wave energy is guided smoothly so that the light is excluded from the shielded region without distortions. One disadvantage of closed cloaks is that they are not practical, especially for the moving objects. As we all know that the moving object must have at least one window through which both information and matter can be transmitted. However, the closed cloaks do not allow such windows. Ma et al. have proposed a kind of open cloaks that have one or more windows, hence a hidden object can exchange

information and matter with the outer environment [59]. Compared with closed cloaks, open cloaks are not perfect in performance, but they are more meaningful in applications.

More recently, a new recipe for an invisibility cloak has been proposed, which can hide an object that lies outside the invisible device itself [39]. The key idea behind this design is the concept of complementary media, which can be regarded as a special kind of transformation media and can optically "cancel" a certain volume of space at a certain frequency. This concept has various important implications, such as the perfect lens, the superscatterer, the cylindrical superlens, and the "anti-cloak" [8, 10, 66, 68, 93, 96].

Such an invisibility device embedded in a negative index shell can make an object that is external to the device invisible. The working principle is described in two steps. First, the object as well as the surrounding space is optically canceled by using a complementary media layer with an enclosed complementary "image" of the object. Then, the correct optical path in the canceled space is restored by a dielectric core material. As a consequence, the whole system is effectively equal to a piece of empty space fitted into the canceled space, and invisibility is realized.

### *2.3.7 Other Optical-Transformation Devices*

Besides the transformation elements mentioned above, the optical transformation method can also be used to design many other devices, such as high-performance antennas, EM-beam modulators, superscatterer, imaging devices, polarization splitters [26, 31, 38, 81, 85, 86, 89, 93, 96, 106]. As an example, we introduce a lens antenna realized by a finite embedded optical transformation [26], which could find important applications in wireless communications and other microwave engineering. Using the discrete embedded optical transformation, a layered high-directivity lens antenna has been designed. All layers of the lens antenna are composed of homogeneous and uniaxially anisotropic metamaterials, which are easy to manipulate. When the layered lens is embedded into a PEC horn, the lens antenna provides a high-directivity radiation beam [26]. The proposed method can also be used to realize the beam modulation [89].

While applying the method of discrete optical transformation, one divides the physical and virtual spaces into several layers in the same way [26]. For each layer, define a separate function which maps virtual space to physical space. Hence the device region, so-called physical space, is actually the staircase approximation of the trapezium obtained by stacking rectangles on top of each other. At this point, the larger the layer number is, the more accurate the transformation will be. We write out the medium parameters for $k$th layer of the discrete lens,

$$\varepsilon_{xx}^{k} = \mu_{xx}^{k} = \alpha_k, \tag{2.52}$$

$$\varepsilon_{yy}^{k} = \mu_{yy}^{k} = 1/\alpha_k, \tag{2.53}$$

$$\varepsilon_{zz}^{k} = \mu_{zz}^{k} = 1/\alpha_k, \tag{2.54}$$

where $\alpha_k = 1 + (k-0.5)(b-a)/(na)$ and $n$ is total number of the layers.

The above equations provide full expressions of the permittivity and permeability tensors in each layer of the lens. For practical reason, we concentrate on the TE wave incidence with the electric fields polarized along the $z$-axis. In such a case, only $\varepsilon_{zz}^k$, $\mu_{xx}^k$, and $\mu_{yy}^k$ are required in above equations. The dispersion relations keep unchanged if the products of $\mu_{xx}^k\varepsilon_{zz}^k$ and $\mu_{yy}^k\varepsilon_{zz}^k$ are the same as those in the above equations. Hence one advantageous choice is to select

$$\varepsilon_{zz}^k = 1, \tag{2.55}$$

$$\mu_{xx}^k = 1, \ \ \mu_{yy}^k = 1/\alpha_k^2. \tag{2.56}$$

In this set of parameters, only $\mu_{yy}^k$ is different in each layer of the lens antenna, which makes the whole structure very easy to realize. We remark that the reduced-parameter transformation media provide the same wave trajectory inside the lens antenna, and there will be no reflection for the normal incidence because of the wave-impedance matching at the inner boundaries. In the following simulation results, the layered lens antenna is composed of man-made materials defined in Eqs. (2.55) and (2.56).

As a comparison, we also consider the lens designed by continuous transformation method. In such a case, the constitutive tensors are expressed as

$$\bar{\varepsilon} = \bar{\mu} = \begin{pmatrix} \varepsilon_{xx} & \varepsilon_{xy} & 0 \\ \varepsilon_{yx} & \varepsilon_{yy} & 0 \\ 0 & 0 & \varepsilon_{zz}, \end{pmatrix}, \tag{2.57}$$

in which

$$\varepsilon_{xx} = \frac{La+(b-a)y}{La} + \frac{La(b-a)^2x^2}{(La+(b-a)y)^3}, \tag{2.58}$$

$$\varepsilon_{xy} = \frac{(b-a)x}{La+(b-a)y} = \varepsilon_{yx}, \tag{2.59}$$

$$\varepsilon_{yy} = \frac{La}{La+(b-a)y} = \varepsilon_{zz}. \tag{2.60}$$

Obviously, the lens is composed of inhomogeneous and strongly anisotropic materials, which are very complicated and much more difficult to fabricate in real applications.

To reveal the performance of the above-mentioned lens antennas, full-wave simulation results are illustrated in Fig. 2.12. The distributions of electric fields inside and outside the lens antenna designed by continuous optical transformation are shown in Fig. 2.12(a). Figure 2.12(b) demonstrates the electric field distributions of the layered lens antenna designed by discrete optical transformation, in which the size of PEC horn is the same as that in Fig. 2.12(a). However, fewer reflections are observed inside the lens antenna in Fig. 2.12(b). It is obvious that almost all EM powers are concentrated as a beam of plane waves in the front of the lens antennas.

For comparison with the conventional lens, we designed a horn antenna filled with a collimating lens, which is made of regular dielectric in accordance with the

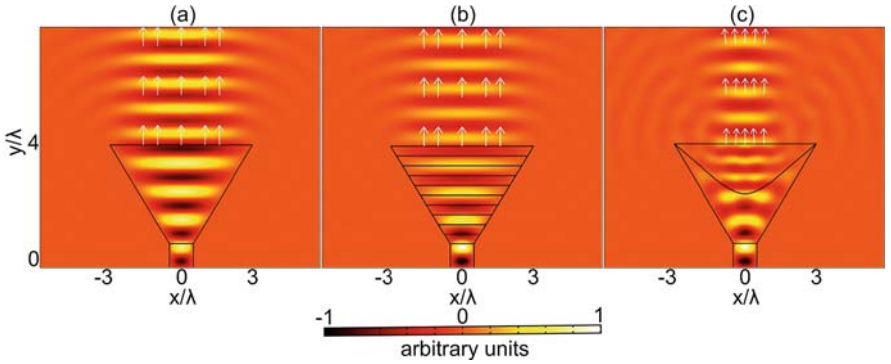


**Fig. 2.12** The distribution of normalized electric fields inside and outside the lens antennas, under the excitation of line-current sources. (**a**) The lens is designed by continuous optical transformation. (**b**) The lens is designed by discrete optical transformation. (**c**) The collimating lens is made of regular dielectric.

method in [33]. Figure 2.12(c) demonstrates the electric field distribution inside and outside the regular lens antenna, in which the size of the PEC horn is the same as that in transformation design lens antennas. Clearly, the transformation-optics lens antennas have much better performance than the conventional lens. The directivity of the transformation lens antennas is above 30 and the regular lens antenna is about 20.

In order to unify a range of EM "meta-phenomena," Leonhardt and Philbin pointed out that a perfect lens made by negative refraction [66, 83] could be interpreted as a result of a coordinate transformation [42]. For perfect lens, a single region in virtual EM space is mapped to multiple regions in physical space, hence EM space is multi-valued. An extension of this viewpoint for designing perfect lens with additional operation functions has been presented in [78].

A similar cylindrical lens was analyzed in [93], which can be considered as deployment of a spatial mapping in cylindrical coordinates. Compared with a slab lens, such a cylindrical lens has two advantages. First, the whole structure has a finite cross-sectional size. No structural truncation in cross section is necessary for its physical implementation. Second, it can form magnified or demagnified image. Compared with a perfect cylindrical lens proposed by Pendry [67], which is based on rolling up a perfect slab lens existing in the virtual EM space, the cylindrical lens [93] has all finite material parameters, and an appropriate design can leave the exterior region unaltered as free space. Therefore, such a device is much more favorable from both realization and application points of view.

## 2.4 Summary

In this chapter, we introduced the concept of optical transformation and discussed several categories of transformation optical devices that came forth in the past years. The optical transformation enables the direct manipulation of EM waves, and

therefore it offers a powerful tool for design of novel and complicated devices. Invisibility, previously thought purely in the realms of science fiction, now can be realized by metamaterials with the help of the theory discussed here. We believe that transformation optical design will prove to be a useful methodology. Together with advancing metamaterial technology, it should lead to the realization of devices that would be very difficult to fabricate any other way. The optical transformation is expected to have further impact on real-life applications.

**Acknowledgments** Our work was supported in part by a major project of the National Science Foundation of China under Grant Nos. 60990320 and 60990324, the Natural Science Foundation of Jiangsu Province under Grant No. BK2008031, the National Basic Research Program (973) of China under Grant No. 2004CB719802, the National Science Foundation of China under Grant Nos. 60871016, 60671016, 60901011, and 60621002, and in part by the 111 Project under Grant No. 111-2-05. WXJ acknowledges the support from Graduate Innovation Program of Jiangsu Province under No. CX08B_074Z and the Scientific Research Foundation of Graduate School of Southeast University under No. YBJJ0816.

## References

1. Cai, W., Chettiar, U.K., Kildishev, A.V., Shalaev, V.M.: Optical cloaking with metamaterials. Nat. Photon. **1**, 224 (2007)
2. Cai, W., Chettiar, U.K., Kildishev, A.V., Shalaev, V.M.: Nonmagnetic cloak with minimized scattering. Appl. Phys. Lett. **91**, 111105 (2007)
3. Cai, W., Chettiar, U.K., Kildishev, A.V., Shalaev, V.M.: Designs for optical cloaking with high-order transformations. Opt. Express **16**, 5444 (2008)
4. Chen, H., Chan, C.T.: Transformation media that rotate electromagnetic fields. Appl. Phys. Lett. **90**, 241105 (2007)
5. Chen, H., Chan, C.T.: Electromagnetic wave manipulation by layered systems using the transformation media concept. Phys. Rev. B **78**, 054204 (2008)
6. Chen, H., Hou, B., Chen, S., Ao, X., Wen, W., Chan, C.T.: Design and experimental realization of a broadband transformation media field rotator at microwave frequencies. Phys. Rev. Lett. **102**, 183903 (2009)
7. Chen, H., Liang, Z., Yao, P., Jiang, X., Ma, H., Chan, C.T.: Extending the bandwidth of electromagnetic cloaks. Phys. Rev. B **76**, 241104 (2007)
8. Chen, H., Luo, X., Ma, H.: The anti-cloak. Opt. Express **16**, 14603 (2008)
9. Chen, H., Wu, B.-I., Zhang, B., Kong, J.A.: Electromagnetic wave interactions with a metamaterial cloak. Phys. Rev. Lett. **99**, 063903 (2007)
10. Chen, H., Zhang, X., Luo, X., Ma, H., Chan, C.T.: Reshaping the perfect electrical conductor cylinder arbitrarily. New J. Phys. **10**, 113016 (2008)
11. Chen, T., Weng, C.-N.: Invisibility cloak with a twin cavity. Opt. Express **17**, 8614 (2009)
12. Cummer, S.A., Liu, R., Cui, T.J.: A rigorous and nonsingular two dimensional cloaking coordinate transformation. J. Appl. Phys. **105**, 056102 (2009)
13. Cummer, S.A., Popa, B.-I., Schurig, D., Smith, D.R., Pendry, J.B.: Full-wave simulations of electromagnetic cloaking structures. Phys. Rev. E **74**, 036621 (2006)
14. Cummer, S.A., Popa, B.-I., Schurig, D., Smith, D.R., Pendry, J.B., Rahm, M., Starr, A.: Scattering theory derivation of a 3D acoustic cloaking shell. Phys. Rev. Lett. **100**, 024301 (2008)
15. Donderici, B., Teixeira, F.L.: Metamaterial blueprints for reflectionless waveguide bends. IEEE Micro. Wirel. Comp. Lett. **18**, 233 (2008)

16. Gabrielli, L.H., Cardenas, J., Poitras, C.B., Lipson, M.: Cloaking at optical frequencies. arXiv: 0904.3508 (2009)
17. Gallina, I., Castaldi, G., Galdi, V.: A higher-order optical transformation for nonmagnetic cloaking. Micro Opt. Tech. Lett. **50**, 3186 (2008)
18. Greenleaf, A., Kurylev, Y., Lassas, M., Uhlmann, G.: Electromagnetic wormholes and virtual magnetic monopoles from metamaterials. Phys. Rev. Lett. **99**, 183901 (2007)
19. Greenleaf, A., Kurylev, Y., Lassas, M., Uhlmann, G.: Approximate quantum cloaking and almost-trapped states. Phys. Rev. Lett. **101**, 220404 (2008)
20. Hu, J., Zhou, X., Hu, G.: Design method for electromagnetic cloak with arbitrary shapes based on Laplace's equation. Opt. Express **17**, 1308 (2009)
21. Huang, Y., Feng, Y., Jiang, T.: Electromagnetic cloaking by layered structure of homogeneous isotropic materials. Opt. Express **15**, 11133 (2007)
22. Huangfu, J., Xi, S., Kong, F., Zhang, J., Chen, H., Wang, D., Wu, B.-I., Ran, L., Kong, J.A.: Application of coordinate transformation in bent waveguides. J. Appl. Phys. **104**, 014502 (2008)
23. Jiang, W.X., Chin, J.Y., Li, Z., Cheng, Q., Liu, R., Cui, T.J.: Analytical design of conformally invisible cloaks for arbitrarily shaped objects. Phys. Rev. E **77**, 066607 (2008)
24. Jiang, W.X., Cui, T.J., Cheng, Q., Chin, J.Y., Yang, X.M., Liu, R., Smith, D.R.: Design of arbitrarily shaped concentrators based on conformally optical transformation of nonuniform rational B-spline surfaces. Appl. Phys. Lett. **92**, 264101 (2008)
25. Jiang, W.X., Cui, T.J., Chin, J.Y., Cheng, Q., Yu, G.X., Yang, X.M., Liu, R.: Equal-thickness invisible cloaks for arbitrarily polygonal-cylindrical regions. Eur. Phys. J. Appl. Phys. **46**, 20702 (2009)
26. Jiang, W.X., Cui, T.J., Ma, H.F., Yang, X.M., Cheng, Q.: Layered high-gain lens antennas via discrete optical transformation. Appl. Phys. Lett. **93**, 221906 (2008)
27. Jiang, W.X., Cui, T.J., Ma, H.F., Zhou, X.Y., Cheng, Q.: Cylindrical-to-plane-wave conversion via embedded optical transformation. Appl. Phys. Lett. **92**, 261903 (2008)
28. Jiang, W.X., Cui, T.J., Yang, X.M., Cheng, Q., Liu, R., Smith, D.R.: Invisibility cloak without singularity. Appl. Phys. Lett. **93**, 194102 (2008)
29. Jiang, W.X., Cui, T.J., Yu, G.X., Lin, X.Q., Cheng, Q., Chin, J.Y.: Arbitrarily elliptical cylindrical invisible cloaking. J. Phys. D: Appl. Phys. 41, 085504 (2008)
30. Jiang, W.X., Cui, T.J., Zhou, X.Y., Yang, X.M., Cheng, Q.: Arbitrary bending of electromagnetic waves using realizable inhomogeneous and anisotropic materials. Phys. Rev. E **78**, 066607 (2008)
31. Kildishev, A.V., Shalaev, V.M.: Engineering space for light via transformation optics. Opt. Lett. **33**, 43 (2008)
32. Kong, F., Wu, B.-I., Kong, J.A., Huangfu, J., Xi, S., Chen, H.: Planar focusing antenna design by using coordinate transformation technology. Appl. Phys. Lett. **91**, 253509 (2007)
33. Kraus, J.D., Marhefka, R.J.: Antennas for all applications, 3rd edn. McGraw-Hill, New York (2002)
34. Kundtz, N., Roberts, D.A., Allen, J., Cummer, S., Smith, D.R.: Optical source transformations. Opt. Express **16**, 21215 (2008)
35. Kwon, D.-H., Werner, D.H.: Two-dimensional eccentric elliptic electromagnetic cloaks. Appl. Phys. Lett. **92**, 013505 (2008)
36. Kwon, D.-H., Werner, D.H.: Two-dimensional electromagnetic cloak having a uniform thickness for elliptic cylindrical regions. Appl. Phys. Lett. **92**, 113502 (2008)
37. Kwon, D.-H., Werner, D.H.: Transformation optical designs for wave collimators, flat lenses and right-angle bends. New J. Phys. **10**, 115023 (2008)
38. Kwon, D.-H., Werner, D.H.: Polarization splitter and polarization rotator designs based on transformation optics. Opt. Express **16**, 18731 (2008)
39. Lai, Y., Chen, H., Zhang, Z.-Q., Chan, C.T.: Complementary media invisibility cloak that cloaks objects at a distance outside the cloaking shell. Phys. Rev. Lett. **102**, 093901 (2009)
40. Leonhardt, U.: Optical conformal mapping. Science **312**, 1777 (2006)
41. Leonhardt, U.: Notes on conformal invisibility devices. New J. Phys. **8**, 118 (2006)

42. Leonhardt, U., Philbin, T.G.: General relativity in electrical engineering. New J. Phys. **8**, 247 (2006)
43. Leonhardt, U., Philbin, T.G.: Transformation optics and the geometry of light. arXiv: 0805.4778 (2008)
44. Leonhardt, U., Tyc, T.: Superantenna made of transformation media. New J. Phys. **10**, 115026 (2008)
45. Leonhardt, U., Tyc, T.: Broadband invisibility by non-Euclidean cloaking. Science **323**, 110 (2009)
46. Li, C., Li, F.: Two-dimensional electromagnetic cloaks with arbitrary geometries. Opt. Express **16**, 13414 (2008)
47. Li, C., Yao, K., Li, F.: Two-dimensional electromagnetic cloaks with non-conformal inner and outer boundaries. Opt. Express **16**, 19366 (2008)
48. Li, J., Pendry, J.B.: Hiding under the carpet: a new strategy for cloaking. Phys. Rev. Lett. **101**, 203901 (2008)
49. Lin, L., Wang, W., Cui, J., Du, C., Luo, X.: Design of electromagnetic refractor and phase transformer using coordinate transformation theory. Opt. Express **16**, 6815 (2008)
50. Liu, R., Ji, C., Mock, J.J., Chin, J.Y., Cui, T.J., Smith, D.R.: Broadband ground-plane cloak. Science **323**, 366 (2009)
51. Liu, R., Yang, X.M., Gollub, J.G., Mock, J.J., Cui, T.J., Smith, D.R.: Gradient index circuit by waveguided metamaterials. Appl. Phys. Lett. **94**, 073506 (2009)
52. Luo, Y., Chen, H., Zhang, J., Ran, L., Kong, J.: Design and analytical full-wave validation of the invisibility cloaks, concentrators, and field rotators created with a general class of transformations. Phys. Rev. B **77**, 125127 (2008)
53. Luo, Y., Zhang, J., Chen, H., Wu, B.-I.: Full-wave analysis of prolate spheroidal and hyperboloidal cloaks. J. Phys. D: Appl. Phys. **41**, 235101 (2008)
54. Luo, Y., Zhang, J., Chen, H., Xi, S., Wu, B.-I.: Cylindrical cloak with axial permittivity/permeability spatially invariant. Appl. Phys. Lett. **93**, 033504 (2008)
55. Luo, Y., Zhang, J., Wu, B.-I., Chen, H.: Interaction of an electromagnetic wave with a cone-shaped invisibility cloak and polarization rotator. Phys. Rev. B **78**, 125108 (2008)
56. Ma, H., Qu, S., Xu, Z., Wang, J.: Numerical method for designing approximate cloaks with arbitrary shapes. Phys. Rev. E **78**, 036608 (2008)
57. Ma, H., Qu, S., Xu, Z., Wang, J.: Approximation approach of designing practical cloaks with arbitrary shapes. Opt. Express **16**, 15449 (2008)
58. Ma, H., Qu, S., Xu, Z., Zhang, J., Chen, B., Wang, J.: Material parameter equation for elliptical cylindrical cloaks. Phys. Rev. A **77**, 013825 (2008)
59. Ma, H., Qu, S., Xu, Z., Wang, J.: The open cloak. Appl. Phys. Lett. **94**, 103501 (2009)
60. Ma, H., Qu, S., Xu, Z., Wang, J.: General method for designing wave shape transformers. Opt. Express **16**, 22072–22082 (2008)
61. Ma, H., Qu, S., Xu, Z., Wang, J.: Wave-shape-keeping media. Opt. Lett. **34**, 127–129 (2009)
62. Milton, G.W., Briane, M., Willis, J.: On cloaking for elasticity and physical equations with a transformation invariant form. New J. Phys. **8**, 248 (2006)
63. Nicolet, A., Zolla, F., Guenneau, S.: Electromagnetic analysis of cylindrical cloaks of an arbitrary cross section. Opt. Lett. **33**, 1584 (2008)
64. Ozgun, O., Kuzuoglu, M.: Electromagnetic metamorphosis: reshaping scatters via conformal anisotropic metamaterial coatings. Micro. Opt. Tech. Lett. **49**, 2386 (2007)
65. Ozgun, O., Kuzuoglu, M.: Utilization of anisotropic metamaterial Layers in waveguide miniaturization and transitions. IEEE Micro. Wirel. Comp. Lett. **17**, 754 (2007)
66. Pendry, J.B.: Negative refraction makes a perfect lens. Phys. Rev. Lett. **85**, 3966 (2000)
67. Pendry, J.B.: Perfect cylindrical lenses. Opt. Express **11**, 755 (2003)
68. Pendry, J.B., Ramakrishna, S.A.: Focusing light using negative refraction. J. Phys.: Con. Mat. **15**, 6345 (2003)
69. Pendry, J.B., Schurig, D., Smith, D.R.: Controlling electromagnetic fields. Science **312**, 1780 (2006)
70. Piegl, L., Tiller, W.: The NURBS book, 2nd ed. Springer-Verlag, New York (1996)

71. Rahm, M., Cummer, S.A., Schurig, D., Pendry, J.B., Smith, D.R.: Optical design of reflectionless complex media by finite embedded coordinate transformations. Phys. Rev. Lett. **100**, 063903 (2008)
72. Rahm, M., Roberts, D.A., Pendry, J.B., Smith, D.R.: Transformation-optical design of adaptive beam bends and beam expanders. Opt. Express **16**, 11555 (2008)
73. Rahm, M., Schurig, D., Roberts, D.A., Cummer, S.A., Smith, D.R., Pendry, J.B.: Design of electromagnetic cloaks and concentrators using form-invariant coordinate transformations of Maxwell's equations. Photo. Nano. Fund. Appl. **6**, 87 (2008)
74. Roberts, D.A., Rahm, M., Pendry, J.B., Smith, D.R.: Transformation-optical design of sharp waveguide bends and corners. Appl. Phys. Lett. **93**, 251111 (2008)
75. Ruan, Z., Yan, M., Neff, C.W., Qiu, M.: Ideal cylindrical cloak: perfect but sensitive to tiny perturbations. Phys. Rev. Lett. **99**, 113903 (2007)
76. Schurig, D., Mock, J.J., Justice, B.J., Cummer, S.A., Pendry, J.B., Starr, A.F., Smith, D.R.: Metamaterial electromagnetic cloak at microwave frequencies. Science **314**, 977 (2006)
77. Schurig, D., Pendry, J.B., Smith, D.R.: Calculation of material properties and ray tracing in transformation media. Opt. Express **14**, 9704 (2006)
78. Schurig, D., Pendry, J.B., Smith, D.R.: Transformation-designed optical elements. Opt. Express **15**, 14772 (2007)
79. Smith, D.R., Mock, J.J., Starr, A.F., Schurig, D.: Gradient index metamaterials. Phys. Rev. E **71**, 036609 (2005)
80. Teixeira, F.L.: Closed-form metamaterial blueprints for electromagnetic masking of arbitrarily shaped convex PEC objects. IEEE Ant. Wirel. Prop. Lett. **6**, 163 (2007)
81. Tsang, M., Psaltis, D.: Magnifying perfect lens and superlens design by coordinate transformation. Phys. Rev. B **77**, 035122 (2008)
82. Valentine, J., Li, J., Zentgraf, T., Bartal, G., Zhang, X.: An optical cloak made of dielectrics. Nat Materials, DOI: 10.1038/nmat2461 (2009)
83. Veselago, V.G.: The electrodynamics of substances with simultaneously negative values of $\varepsilon$ and $\mu$. Sov. Phys. Usp. **10**, 509 (1968)
84. Wang, W., Lin, L., Ma, J., Wang, C., Cui, J., Du, C.: Electromagnetic concentrators with reduced material parameters based on coordinate transformation. Opt. Express **16**, 11431 (2008)
85. Wang, W., Lin, L., Yang, X., Cui, J., Du, C., Luo, X.: Design of oblate cylindrical perfect lens using coordinate transformation. Opt. Express **16**, 8094 (2008)
86. Wang, W., Xing, H., Fang, L., Liu, Y., Ma, J., Lin, L., Wang, C., Luo, X.: Far-field imaging device: planar hyperlens with magnification using multi-layer metamaterial. Opt. Express **16**, 21142 (2008)
87. Ward, A.J., Pendry, J.B.: Refraction and geometry in Maxwell's equations. J. Mod. Opt. **43**, 773–793 (1996)
88. Xi, S., Chen, H., Wu, B.-I., Kong, J.A.: One-directional perfect cloak created with homogeneous material. IEEE Micro. Wirel. Comp. Lett. **19**, 131–133 (2009)
89. Xu, X., Feng, Y., Jiang, T.: Electromagnetic beam modulation through transformation optical structures. New J. Phys. **10**, 115027 (2008)
90. Xu, X., Feng, Y., Zhao, L., Jiang, T., Lu, C., Xu, Z.: Designing the coordinate transformation function for non-magnetic invisibility cloaking. J. Phys. D: Appl. Phys. **41**, 215504 (2008)
91. Yan, M., Ruan, Z., Qiu, M.: Scattering characteristics of simplified cylindrical invisibility cloaks. Opt. Express **15**, 17772 (2007)
92. Yan, M., Ruan, Z., Qiu, M.: Cylindrical invisibility cloak with simplified material parameters is inherently visible. Phys. Rev. Lett. **99**, 233901 (2007)
93. Yan, M., Yan, W., Qiu, M.: Cylindrical superlens by a coordinate transformation. Phys. Rev. B **78**, 125113 (2008)
94. Yan, W., Yan, M., Qiu, M.: Non-magnetic simplified cylindrical cloak with suppressed zeroth order Scattering. Appl. Phys. Lett. **93**, 021909 (2008)
95. Yan, W., Yan, M., Ruan, Z., Qiu, M.: Coordinate transformations make perfect invisibility cloaks with arbitrary shape. New J. Phys. **10**, 043040 (2008)

96. Yang, T., Chen, H., Luo, X., Ma, H.: Superscatterer: enhancement of scattering with complementary media. Opt. Express **16**, 18545 (2008)
97. You, Y., Kattawar, G.W., Yang, P.: Invisibility cloaks for toroids. Opt. Express **17**, 6591 (2009)
98. You, Y., Kattawar, G.W., Zhai, P.-W., Yang, P.: Invisibility cloaks for irregular particles using coordinate transformations. Opt. Express **16**, 6134 (2008)
99. Yu, G.X., Jiang, W.X., Cui, T.J.: Invisible slab cloaks via embedded optical transformation. Appl. Phys. Lett. **94**, 041904 (2009)
100. Yu, G.X., Jiang, W.X., Zhou, X.Y., Cui, T.J.: Non-rotationally invariant invisibility cloaks and concentrators of EM Waves. Eur. Phys. J. Appl. Phys. **44**, 181 (2008)
101. Zhang, B., Chen, H., Wu, B.-I., Luo, Y., Ran, L., Kong, J.A.: Response of a cylindrical invisibility cloak to electromagnetic waves. Phys. Rev. B **76**, 121101 (2007)
102. Zhang, J., Luo, Y., Chen, H., Wu, B.-I.: Manipulating the directivity of antennas with metamaterial. Opt. Express **16**, 10962 (2008)
103. Zhang, J., Luo, Y., Xi, S., Chen, H., Ran, L., Wu, B.-I., Kong, J.A.: Directive emission obtained by coordinate transformation. Prog. Electro. Res. **81**, 437 (2008)
104. Zhang, P., Jin, Y., He, S.: Cloaking an object on a dielectric half-space. Opt. Express **16**, 3161 (2008)
105. Zhang, S., Genov, D.A., Sun, C., Zhang, X.: Cloaking of matter waves. Phys. Rev. Lett. **100**, 123002 (2008)
106. Zhang, X., Chen, H., Luo, X., Ma, H.: Transformation media that turn a narrow slit into a large window. Opt. Express **16**, 11764 (2008)
107. Zolla, F., Guenneau, S., Nicolet, A., Pendry, J.B.: Electromagnetic analysis of cylindrical invisibility cloaks and the mirage effect. Opt. Lett. **32**, 1069 (2007)

# Chapter 3
# General Theory on Artificial Metamaterials

Ruopeng Liu, Tie Jun Cui and David R. Smith

**Abstract** In this chapter, we present a general theory of effective media to establish the relationship between the local field responses on metamaterial structure and the macroscopical behaviors for artificial metamaterials composed of periodic resonant structures. By treating the unit cell of the periodic structure as a particle, we average the local field to define the local average permittivity and permeability for different unit structures and derive a general form of discrete Maxwell's equations in macroscale. We obtain different wave modes in metamaterials including propagation mode, pure plasma mode, and resonant crystal bandgap mode. The distortion in the electromagnetic parameters has been well explained by the derived spatial dispersion model. Thus, the unfamiliar behaviors of metamaterials from the numerical S-parameter retrieval approach is further verified and described. The excellent agreements between the theoretical predictions and the numerical retrieval results indicate that the new defined model and method of analysis fit better to the physical structures and is thereafter a more advanced form of fitting formula for the effective electromagnetic parameters of metamaterials.

**Key words:** Effective medium theory, spatial dispersion, dispersion relationship, metamaterial structure, retrieval method, photonic crystal, magnetic resonance, electric resonance, negative index materials.

Ruopeng Liu, David R. Smith*
Center for Metamaterials and Integrated Plasmonics, Department of Electrical and Computer Engineering, Duke University, Durham, NC 27708, USA. *e-mail: drsmith@duke.edu

Tie Jun Cui+
State Key Laboratory of Millimeter Waves, Southeast University, Nanjing 210096, China.
+email: tjcui@seu.edu.cn

T.J. Cui et al. (eds.), *Metamaterials*, DOI 10.1007/978-1-4419-0573-4_3,

## 3.1 Local Field Response and Spatial Dispersion Effect on Metamaterials

Metamaterials are composed of subwavelength resonant structures and can respond to the electric and magnetic field as a homogenous material. In this section, we will discuss the field averaging technology [7, 6] and understand the local field response in such subwavelength metamaterial structure. As shown in Fig. 3.1, the split ring resonator (SRR) is a typical metamaterial structure with magnetic resonance [6]. To take SRR as an example of practical metamaterial structure, its equivalent circuit topology can be interpreted in Fig. 3.2. If an external magnetic field penetrates through SRR structure, it can excite the resonant current in this LC resonator and so a magnetic dipole moment can be generated. To define the effective permittivity and permeability to this type of subwavelength structure, one approach is to average the local filed flux and field intensity and relate the equivalent electromagnetic parameters to the ratio of such averaging flux and intensity. We hereby use this SRR structure shown in Fig. 3.2 as an example to show the approach of solving such local field response and thus obtain $\overline{\varepsilon}$ and $\overline{\mu}$. As there is no fundamental response to the electric field from SRR, we focus on the magnetic response here on the SRR structure.

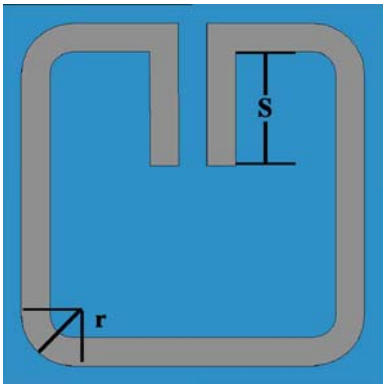


**Fig. 3.1** SRR unit cell structure.

In Fig. 3.2, $L$, $C$, and $R$ are the equivalent inductor, capacitor, and resistor. $S_0$ is the area of SRR unit cell while $V$ is the volume of a unit cell. The circuit resonance can be excited by magnetic flux across the area of SRR unit cell.

The analytical solution for the structure becomes difficult because of the interaction between the unit cell and the complex local field distribution. However, people have used the Drude-Lorentz resonance form to model ideal SRR particle response [7].

Recall that in Drude–Lorentz model, $F$,$\gamma$, and $f_0$ are the fitting parameters standing for oscillation factor, damping factor, and resonant frequency, respectively,

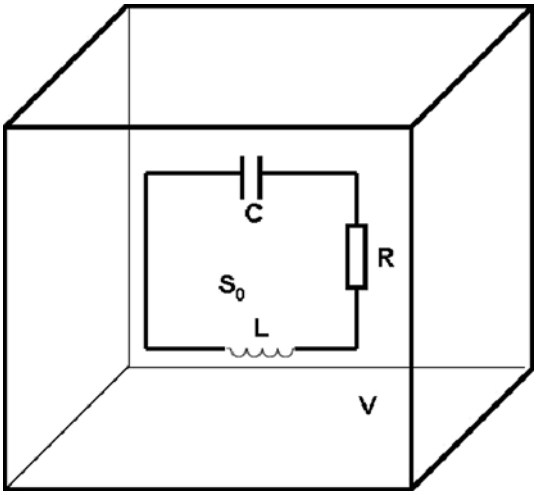


**Fig. 3.2** Circuit topology of SRR unit cell.

$$\overline{\mu} = \mu_0 \left(1 - \frac{F f^2}{f^2 - f_0^2 + i\gamma f}\right), \tag{3.1}$$

in which

$$F = \frac{\mu_0 S_0^2 / V}{L + \mu_0 S_0^2 / V}, \tag{3.2}$$

$$f_0 = \frac{1}{2\pi\sqrt{(L + \mu_0 S_0^2 / V)C}}, \tag{3.3}$$

$$\gamma = \frac{R}{2\pi(L + \mu_0 S_0^2 / V)}. \tag{3.4}$$

Figure 3.3 demonstrates the typical magnetic response from this theoretical solution that has a Drude–Lorentz resonant lineshape. On the other hand, the permittivity is expected to be a flat response with frequency as no fundamental electric resonance occurs.

Besides this field averaging solution, another approach called EM parameters retrieval process was developed recently [2]. Such retrieval process is based on the full wave simulation to the practical metamaterial structure. By assuming the wave propagation in a thin slab, the equivalent effective permittivity and permeability of a particular structure can be extracted and analyzed. Thus, we can achieve the typical response of a practical SRR structure via such full wave simulation analysis, shown in Fig. 3.4.

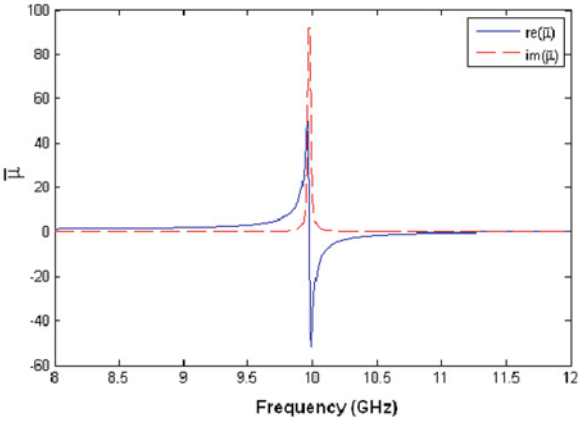


**Fig. 3.3** A typical Drude–Lorentz response to a magnetic resonator according to the theoretical calculation on the local field response.

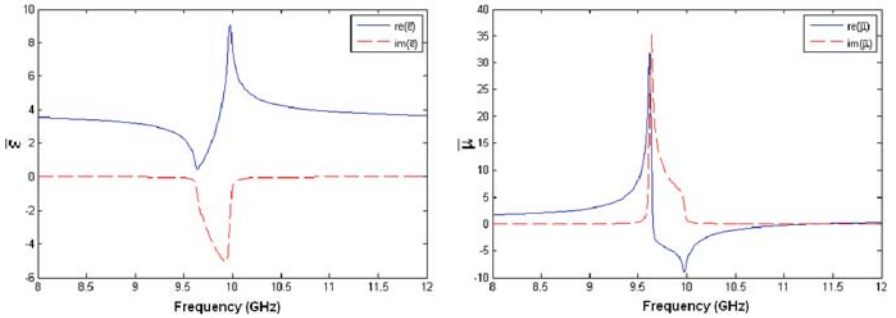


**Fig. 3.4** A typical effective permittivity and permeability extracted by the standard retrieval process.

Comparing Figs. 3.3 and 3.4, we can observe a significant discrepancy between the theoretical prediction and practical retrieval. An unexpected anti-resonance (electric resonance) occurs in the magnetic resonator and the magnetic resonance deviates from Drude–Lorentz resonant lineshape. Such difference is attributed by the assumption that the unit cell structure is infinitesimal in the theoretical derivation, whereas the metamaterial structure is of a finite size in reality so that it causes the permittivity and permeability to depend on both frequency and coordinate. We call it spatial dispersion effect on metamaterials. In the current metamaterial structures, the unit cell is approximately one-tenth of the wavelength in reality. In such a case, the spatial dispersion will strongly distort the local field response from Drude–Lorentz resonance to such unfamiliar responses [2, 15, 1, 17, 12, 10, 16, 4, 11, 5, 18, 8, 9, 13, 14, 3]. To address this gap, we establish the macroscopic behavior and local field response in the next section.

## 3.2 Spatial Dispersion Model on Artificial Metamaterials

To address the unfamiliar response caused by spatial dispersion effect, we are going to establish a spatial dispersion model to describe the artificial metamaterials. If we start with the integral form of Maxwell's equations and imagine averaging the fields over a unit cell, we arrive at a finite-difference form of Maxwell's equations in which the averaged electric fields are defined on the edges of one cubic lattice, while the averaged magnetic fields are defined on the edges of a second offset lattice [10]. To simplify the analysis, we assume a wave whose electric field is polarized in the $x$-direction and propagates along the $z$-axis (Fig. 3.5). The unit cell of the metamaterial is assumed to have a periodicity $p$. Under these conditions, one of the Maxwell's curl equations reduces to

$$\overline{E}_x[(n+1/2)p] - \overline{E}_x[(n-1/2)p] = i\omega\overline{\mu}p\overline{H}_y[np], \tag{3.5}$$

in which $n = 0, \pm 1, \ldots$, and the averaged electric field $\overline{E}_x$ and magnetic field $\overline{H}_y$ are defined by the line integrals

$$\overline{E}_x(z) = \frac{1}{p}\int_{-p/2}^{+p/2} E(x,0,z)dx, \tag{3.6}$$

$$\overline{H}_y(z) = \frac{1}{p}\int_{-p/2}^{+p/2} H(0,y,z)dy. \tag{3.7}$$

Under this form of averaging, the average permeability $\overline{\mu}$ has the form [10]

$$\overline{\mu} = \frac{1}{p^2\overline{H}_y(0)}\int_{-p/2}^{+p/2}\int_{-p/2}^{+p/2} \mu_a H(x,0,z)dxdz. \tag{3.8}$$

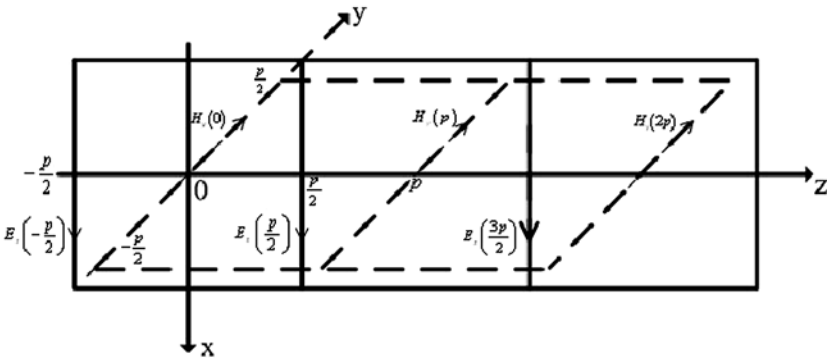


**Fig. 3.5** Metamaterial composed of periodic particles, where a plane wave is incident along the $z$-direction.

Similarly, the other Maxwell's curl equation in integral form can be simplified to

$$\overline{H}_y[(n+1)p] - \overline{H}_y[(np)] = i\omega\overline{\varepsilon}p\overline{E}_x[(n+1/2)p] \tag{3.9}$$

after introducing the average permittivity

$$\overline{\varepsilon} = \frac{1}{p^2\overline{E}_x(p/2)} \int_{-p/2}^{+p/2} \int_{-p/2}^{+p/2} \varepsilon_a E(0,y,z)dydz. \tag{3.10}$$

In Eqs. (3.8) and (3.10), $\varepsilon_a$ and $\mu_a$ are the permittivity and permeability of the background medium. Equations (3.7) and (3.9) together represent a discrete set of Maxwell's equations (DME).

In order that the DME represents an infinite periodic structure, we apply the Bloch boundary conditions: $\overline{E}_x[(n+1/2)p] = \overline{E}_x[p/2]e^{i(n\theta+\theta/2)}$ and $\overline{H}_y[(np)] = \overline{H}_y[0]e^{in\theta}$, in which $\theta$ is the phase advance across one cell. Substituting the boundary conditions into the DME, we obtain the dispersion equation

$$\sin(\theta/2) = S_d\omega p\sqrt{\overline{\mu}\overline{\varepsilon}}/2, \tag{3.11}$$

where $S_d = 1$ if the wave is propagating in a material where $\overline{\varepsilon}$ and $\overline{\mu}$ are both positive, and $S_d = -1$ if the wave is propagating in a material where $\overline{\varepsilon}$ and $\overline{\mu}$ are both negative. Equation (3.11) shows that the phase advance is related not only to the average constitutive parameters, but also to the periodicity $p$.

To obtain a complete description of wave propagation in a medium, it is also necessary to determine the wave impedance of the medium, which is defined as $\eta(z) = \overline{E}_x(z)/\overline{H}_y(z)$. Part of the difficulty in obtaining an analytic expression for the averaged impedance is that averaged electric and magnetic fields for the effective finite-difference Maxwell's equations are defined on the edges of lattices that are offset from each other, whereas the definition of impedance requires the ratio of electric and magnetic fields at the same point. We state without justification here that we can interpolate the field value on a point midway between two lattice edges by taking the linear average of fields located at the nearest neighbors [3].

Using the linear average, we arrive at two possible definitions of the impedance: one is obtained by averaging the magnetic field defined on two adjacent edges of the magnetic lattice, while the other is obtained by averaging the electric field defined on two adjacent edges of the electric lattice. The two averages lead to two different expressions for the impedance that can be summarized as

$$\eta = \sqrt{\overline{\mu}/\overline{\varepsilon}}(\cos\theta/2)^{S_b}. \tag{3.12}$$

$S_b = 1$ for unit cells that have predominantly electric response, while $S_b = -1$ for unit cells that have predominantly magnetic response. The ambiguity in the impedance expression is resolved by a rigorous derivation leading to an exact formula, which will be presented elsewhere. In the limit that the unit cell has a resonant electric or magnetic response, the general expression reduces to Eq. (3.12).

With the phase advance Eq. (3.11) and impedance Eq. (3.12), we can now obtain an analytic solution for the constitutive parameters of a metamaterial. Denoting the effective permittivity and permeability as $\varepsilon_{\text{eff}}$ and $\mu_{\text{eff}}$, then the phase shift $\theta$ and wave impedance $\eta$ can be expressed in terms of $\varepsilon_{\text{eff}}$ and $\mu_{\text{eff}}$ as $\theta = \omega p\sqrt{\mu_{\text{eff}}\varepsilon_{\text{eff}}}$ and $\eta = \sqrt{\mu_{\text{eff}}/\varepsilon_{\text{eff}}}$. Considering Eqs. (2.7) and (2.8), we obtain the general solution for the effective permittivity and permeability as [3]

$$\varepsilon_{\text{eff}} = \overline{\varepsilon} \cdot \frac{(\theta/2)}{\sin(\theta/2)}[\cos(\theta/2)]^{-S_b}, \tag{3.13}$$

$$\mu_{\text{eff}} = \overline{\mu} \cdot \frac{(\theta/2)}{\sin(\theta/2)}[\cos(\theta/2)]^{S_b}. \tag{3.14}$$

Equations (3.13) and (3.14) demonstrate the relationship between local field response and macroscopic equivalent electromagnetic parameters. As expected, the permittivity and permeability are not only frequency dependent but also phase advance (wave vector) dependent. If the periodicity of the unit cell goes to infinitesimal, we can achieve $\varepsilon_{\text{eff}} = \overline{\varepsilon}$ and $\mu_{\text{eff}} = \overline{\mu}$ and so the structure can be described by Drude–Lorentz model again.

## 3.3 Explanation of the Behavior on Metamaterial Structures

According to the general solution we achieved in the last section, we can analyze the wave propagation modes and explain the physical origin behind the retrieval curves.

When $0 < \overline{\mu\varepsilon} < 4/(\omega p)^2$, $\theta$ is real and thus the corresponding modes are propagating. The effective constitutive parameters predicted by Eqs. (3.13) and (3.15) provide useful insight. The wave impedance approaches zero for an electric resonator or infinity for a magnetic resonator when $\theta = \pi$ or $-\pi$. This behavior implies that when either $\overline{\varepsilon}$ or $\overline{\mu}$ takes large values, then $\overline{\mu}$ or $\overline{\varepsilon}$ will take accordingly small values. The medium as a whole in these cases can be viewed as a spatial resonator.

When the averaged permittivity and permeability satisfy $\overline{\mu\varepsilon} < 0$, only evanescent waves exist in the metamaterial based on Eq. (3.11). In such a case, Eqs. (3.13) and (3.14) represent purely evanescent modes with either electric or magnetic character, depending on the signs of $\overline{\mu}$ and $\overline{\varepsilon}$.

When $\overline{\mu\varepsilon} > 4/(\omega p)^2$, Eq. (3.11) shows that $\theta$ will be a complex number $\theta = S_d\pi + i\theta_I$, which corresponds to a resonant crystal bandgap mode. Here, $S_d$ is the dispersion sign defined earlier corresponding to left- or right-handed average parameters and $\theta_I = 2\ln(u + \sqrt{1+u^2})$. The resonant crystal bandgap results from the periodicity inherent to the metamaterial combined with large effective constitutive parameters associated with the resonant metamaterial elements. In this case, the effective permittivity and permeability are expressed as [3]

$$\varepsilon_{\text{eff}} = -S_b \cdot \overline{\varepsilon} \cdot \frac{\theta_I - i\pi}{\cosh(\theta_I/2)} [\sinh(\theta_I/2)]^{-S_b}, \tag{3.15}$$

$$\mu_{\text{eff}} = S_b \cdot \overline{\mu} \cdot \frac{\theta_I - i\pi}{\cosh(\theta_I/2)} [\sinh(\theta_I/2)]^{S_b}. \tag{3.16}$$

From Eqs. (3.15) and (3.16), we observe three important features. First, only evanescent waves are supported in the crystal bandgap regime. Second, the phase shifts by $\pm 180^\circ$ from one cell to an adjacent cell, where the sign depends on whether the averaged parameters are both positive or negative. Finally, the imaginary parts in the effective permittivity and permeability appear in conjugate forms. Hence one of the constitutive parameters will always acquire a negative imaginary part (i.e., *negative loss* assuming an $\exp(-i\omega t)$ time dependence). The negative loss compensates the positive loss in the other parameter to generate an overall lossless behavior [3].

## 3.4 Verification of the Spatial Dispersion Model

To validate the analytic theory, we consider a metamaterial formed from split ring resonators (SRRs), which possess a strong magnetic resonance [8]. Since the SRR is a magnetic-response structures, $S_b = -1$ must be chosen. Were we to analyze a structure with an electric resonance, such as the ELC introduced in [13], we would choose $S_b = 1$. From an analytic, quasistatic theory, the SRR structure shown in Fig. 3.6(a) possesses an averaged permeability in the absence of spatial dispersion of the form

$$\overline{\mu}_{\text{SRR}} = \mu_a \left[1 - F f^2/(f^2 - f_0^2 + i\gamma f)\right], \tag{3.17}$$

in which $f_0$ is the magnetic resonant frequency and $\gamma$ is the loss factor. The SRR usually does not exhibit a strongly dispersive permittivity, so we take for the averaged permittivity $\overline{\varepsilon}_{\text{SRR}} = \varepsilon_a \sin(v)/v$ as homogeneous model for background medium, in which $v = \omega p \sqrt{\varepsilon_a \mu_a}/2$.

Based on the ideal form, we calculate the effective permittivity and permeability using the analytic formulas above. Figure 3.6 compares the predicted parameters for the SRR structure with those from the numerical S-parameter retrieval. The S parameters are simulated using HFSS (Ansoft), a commercial, full-wave electromagnetic solver whose accuracy has been verified earlier [6, 2, 10]. In the simulations, a single unit cell is simulated along the $z$-direction, with periodic boundaries applied along the $x$- and $y$-directions. From Fig. 3.6, excellent agreement is found between the analytic theory and simulations.

The frequency regimes of various modes can easily be identified from the phase advance shown in Fig. 3.6(c). Below the frequency of 9.6 GHz, the wave is propagating. From 9.6 to 10 GHz, the phase advance reaches $180^\circ$ and hence the wave is in the resonant crystal bandgap regime. From 10 to 11.5 GHz, modes are

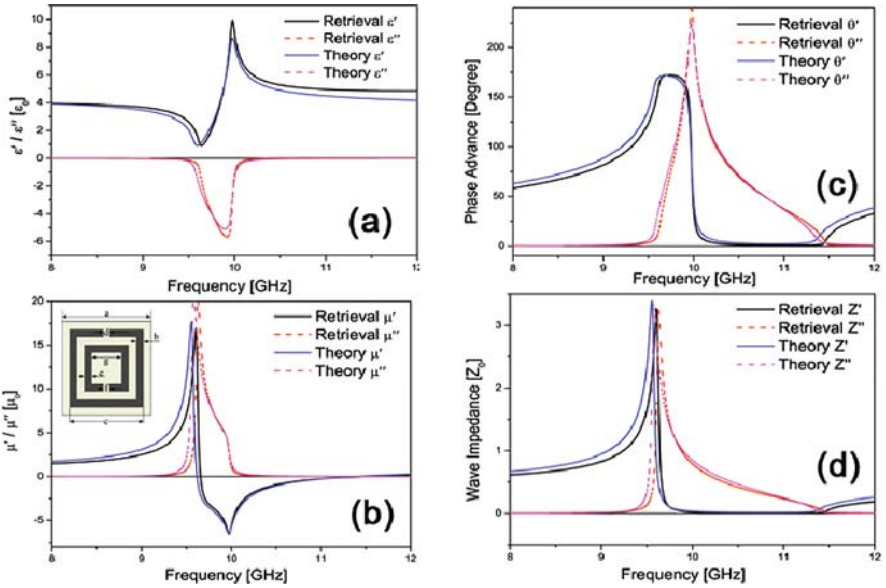


**Fig. 3.6** Comparison of theoretical prediction results and retrieval results from S parameters for the SRR structure. The parameters used for the theoretical calculation are chosen as $f_0 = 9.975$ GHz, $\varepsilon_a = 4.4\varepsilon_0$, $\mu_a = \mu_0$, $\gamma = 5 \times 10^7$, $p = 2.5$ mm, and $F = 0.23$. SRR structure is inserted in (**b**). The substrate is FR4 ($\varepsilon = 4.4 + 0.044i$) with a thickness of 0.25 mm. The dimensions are $a = 2.5$ mm, $c = 2.2$ mm, $g = 1.1$ mm, $b = e = 0.2$ mm, and $d = f = 0.22$ mm. Ref. [12].

evanescent. The resonant frequency of SRR occurs at 10 GHz. Above 11.5 GHz, all modes once again correspond to propagating.

The above analysis provides insight into the behavior of the effective constitutive parameters for the SRR metamaterial. For example, the large discontinuity in the permeability and corresponding damping of permittivity at 9.6 GHz occurs because $\theta = 180$ at this frequency, which is the transition frequency between propagating modes and resonant crystal modes. The wave impedance becomes very large at this frequency, as shown in Fig. 2.2(d). The critical frequency of the resonant crystal bandgap has previously been misidentified as the resonant frequency of the permeability, which actually occurs at 10 GHz.

Similarly, for the other type of particles, ELC resonator, which can provide electric resonance, shown in Fig. 3.7, can be calculated from the form

$$\overline{\varepsilon}_{\mathrm{ELC}} = \varepsilon_a \left[1 - F f^2/(f^2 - f_0^2 + i\gamma f)\right], \tag{3.18}$$

and $\overline{\mu}_{\mathrm{ELC}} = \mu_a \sin(v)/v$. Here, $f_0$ is the electric resonant frequency [3].

The relatively analytic formulas presented here provide an accurate description of electromagnetic metamaterials. Because the equations are closed form and relatively simple, the influence of spatial dispersion can be clearly identified and the anomalous form of the constitutive parameters understood. It has been a large step

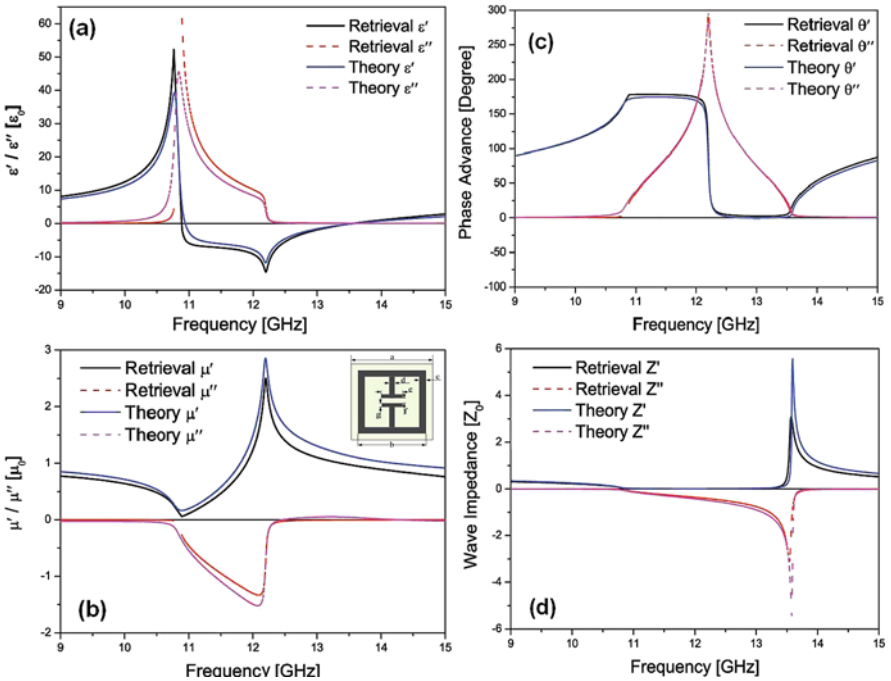


**Fig. 3.7** The ELC structure. Comparison of theoretical-prediction results and retrieval results from the S scattering parameters for the ELC structure. The parameters used in theoretical calculation are that $f_0 = 12.2$ GHz, $\varepsilon_a = 4.2\varepsilon_0$, $\mu_a = \mu_0$, $\gamma = 4 \cdot 10^7$, $p = 3.333$ mm, and $F = 0.19$. The substrate is FR4 ($\varepsilon = 4.4 + 0.001i$) whose thickness is 0.2026 mm. The dimension is that $a = 3.333$ mm, $b = 3$ mm, $c = d = g = f = 0.2$ mm, and $e = 1.4$ mm. Ref. [12].

toward a full characterization of metamaterials and will become a method to analyze and extract the local field response from numerical retrieval process. By achieving the fitting formulas to the structure response, a further rapid design approach can be generated in the following chapter.

## References

1. Chen, X., Grzegorczyk, T.M., Wu, B.-I., Pacheco, J., Jr., Kong, J.A.: Robust method to retrieve the constitutive effective parameters of metamaterials. Phys. Rev. E **70**, 016608 (2004)
2. Koschny, T., Markos, P., Smith, D.R., Soukoulis, C.M.: Resonant and antiresonant frequency dependence of the effective parameters of metamaterials. Phys. Rev. E **68**, 065602 (2003)
3. Liu, R., Cui, T.J., Huang, D., Zhao, B., Smith, D.R.: Description and explanation of electromagnetic behaviors in artificial metamaterials based on effective medium theory. Phys. Rev. E **76**, 026606 (2007)
4. Liu, R., Cui, T.J., Zhao, B., Lin, X.Q., Ma, H.F., Huang, D., Smith, D.R.: Resonant crystal band gap metamaterials in the microwave regime and their exotic amplification of evanescent waves. Appl. Phys. Lett. **90**, 091912 (2007)

5. Pendry, J.B.: Negative refraction makes a perfect lens. Phys. Rev. Lett. **85**, 3966 (2000)
6. Pendry, J.B., Holden, A.J., Robbins, D.J., Stewart, W.J.: Magnetism from conductors and enhanced nonlinear phenomena. IEEE Trans. Micro. Theory Tech. **47**, 2075 (1999)
7. Pendry, J.B., Holden, A.J., Stewart, W.J., Youngs, I.: Extremely low frequency plasmons in metallic mesostructures. Phys. Rev. Lett. **76**, 4773–4776 (1996)
8. Pendry, J.B., Schurig, D., Smith, D.R.: Controlling electromagnetic fields. Science **312**, 1780 (2006)
9. Schruig, D., Mock, J.J., Justice, B.J., Cummer, S.A., Pendry, J.B., Starr, A.F., Smith, D.R.: Metamaterial electromagnetic cloak at microwave frequencies. Science **314**, 977–980 (2006)
10. Schurig, D., Mock, J.J., Smith, D.R.: Electric-field-coupled resonators for negative permittivity metamaterials. Appl. Phys. Lett. **88**, 041109 (2006)
11. Shelby, R.A., Smith, D.R., Schultz, S.: Experimental verification of a negative index of refraction. Science **292**, 77 (2001)
12. Simovski, C.R., Belov, P.A., He, S.: Backward wave region and negative material parameters of a structure formed by lattices of wires and split-ring resonators. IEEE Trans. Ant. Prop. **51**, 2582 (2003)
13. Smith, D.R., Padilla, W.J., Vier, D.C., Nemat-Nasser, S.C., Schultz, S.: Composite medium with simultaneously negative permeability and permittivity. Phys. Rev. Lett. **84**, 4184 (2000)
14. Smith, D.R., Pendry, J.B.: Homogenization of metamaterials by field averaging. J Opt. Soc. Am. B **23**, 321 (2006)
15. Smith, D.R., Vier, D.C., Koschny, T., Soukoulis, C.M.: Electromagnetic parameter retrieval from inhomogeneous metamaterials. Phys. Rev. E **71**, 036617 (2005)
16. Starr, A.F., Rye, P.M., Smith, D.R., Nemat-Nasser, S.: Fabrication and characterization of a negative-refractive-index composite metamaterial. Phys. Rev. B **70**, 115113 (2004)
17. Varadan, V., Sheng, Z., Penumarthy, S., Puligalla, S.: Comparison of measurement and simulation of both amplitude and phase of reflected and transmitted fields in resonant Omega media. Micro. Opt. Tech. Lett. **48**, 1549 (2006)
18. Yen, T.J., Padilla, W.J., Fang, N., Vier, D.C., Smith, D.R., Pendry, J.B., Basov, D.N., Zhang, X.: Terahertz magnetic response from artificial materials. Science **303**, 1494–1496 (2004)

# Chapter 4
# Rapid Design for Metamaterials

Jessie Y. Chin, Ruopeng Liu, Tie Jun Cui and David R. Smith

**Abstract** Metamaterials are generally composed of sub-wavelength structures with designable geometries. The macroscopic properties of metamaterials are harnessed by engineering the geometric dimensions of the particles. During the past few years, designing metamaterials has become increasingly time-consuming due to the growing complexity of their electromagnetic properties and the complexity has been spurred by the arising interest in generating inhomogeneous and anisotropic metamaterials. Motivated by accelerating the design process for metamaterials with excellent accuracy, rapid design for metamaterials is introduced in this chapter. This method is based on full-wave simulation, S-parameter retrieval technique, and the effective medium theory for metamaterials. The rapid design algorithm for metamaterials is widely applicable to all particles with or without resonances from microwave to optical regime. Its efficiency is validated and demonstrated by a few examples.

**Key words:** Rapid design for metamaterials, system level design, particle level design, material parameters, geometric parameters, Lorentz parameters, modified permittivity, modified permeability, full-wave simulation, S-parameter retrieval, effective medium theory, Drude-Lorentz model, curve fitting.

Jessie Y. Chin and Tie Jun Cui*
State Key Laboratory of Millimeter Waves, Southeast University, Nanjing 210096, China.
*e-mail: jychin@seu.edu.cn and tjcui@seu.edu.cn

Ruopeng Liu and David R. Smith +
Center for Metamaterials and Integrated Plasmonics, Department of Electrical and Computer Engineering, Duke University, Durham, NC, 27708, USA.
+ email: ruopeng.liu@duke.edu and drsmith@duke.edu

T.J. Cui et al. (eds.), *Metamaterials*, DOI 10.1007/978-1-4419-0573-4_4,

## 4.1 Introduction

In the burgeoning research area of metamaterials, a good variety of artificially engineered sub-wavelength metamaterial particles have been proposed to generate the desired magnetic and/or electric responses to externally applied fields [30, 1, 2, 37, 29, 45, 39, 40, 14, 7, 24, 11]. The electric and magnetic responses are often characterized by constitutive parameters, permittivity and permeability, which can be tailored by altering the geometric dimensions of the metamaterial particles. Since metamaterials provide an easy and affordable approach to accurately controlling the spatial distribution of inhomogeneous materials, a great deal of recent research interest has involved novel phenomena associated with metamaterials with inhomogeneous constitutive parameters [41, 10, 32, 18, 44, 36, 22, 26]. More recently, the technique of optical transformation based on metamaterials [31, 21] has become a powerful tool to manipulate electromagnetic waves by metamaterials in various desired manners and has inspired many novel electromagnetic devices [36, 5, 15, 16, 35, 33, 34, 22, 20, 25]. However, optical transformation dramatically increases the complexity of metamaterials to be designed, because not only the constitutive parameters are, in many cases, spatially inhomogeneous [36, 15, 16, 35, 34, 22, 25] and anisotropic [36, 35], but the overall size of the metamaterials can be much larger [22, 25]. This has led to the obvious burden of metamaterial design.

One approach to design a metamaterial is by setting up analytical equivalent circuit models for the metamaterial particles [6, 13, 2, 3]. However, the analytical method can only be applied under limited classes of structures and is often unable to accurately predict the macroscopic behavior of metamaterials. Alternatively, metamaterials are more often designed by full-wave electromagnetic simulations, e.g., finite element method (FEM) and finite integration technique (FIT). Commercial software including FIT-based CST Microwave Studio and FEM solver of ANSOFT HFSS are widely used. ANSOFT has provided a specific technical document [48] to address the simulation of metamaterial-based microwave devices. The commonly adopted design method repeats simulations to optimize the constitutive parameters for a single metamaterial particle. To improve the efficiency of optimization, attempts have been made to incorporate density method [19], genetic algorithm (GA) [12, 8], and topology optimization [46, 47, 38] into metamaterial design.

In more complicated cases, simultaneous optimization of material parameters is necessary and the overall number of the designed metamaterial particles with different parameters can be fairly large. Metamaterials designed to realize optical transformation may contain from a few to tens of thousands of different particles [36, 25]. Designing such a material would be too time-consuming even with optimization techniques. This is because the full-wave simulations consume a considerably large amount of time and the optimization requires running multiple simulations.

In this chapter, we introduce an automated and rapid method for metamaterial design, which is capable of designing metamaterials with both accuracy and efficiency.

The detailed algorithm is explained and a few examples are given to demonstrate the speed and validity of the method. The accuracy of the design is also proved by experimental results.

## 4.2 The Algorithm of Rapid Design for Metamaterials

Metamaterials are composed of spatially discrete sub-wavelength unit cells, each of which is considered as a particle. The principle function of rapid design for metamaterials is to automatically and efficiently obtain the optimized geometric parameters for every metamaterial particle of a complicated metamaterial system with inhomogeneous (or homogeneous) material parameters to be designed.

### *4.2.1 Schematic Description of Rapid Design*

The schematic process of rapid design is illustrated by the flowchart in Fig. 4.1. It includes the following three essential steps.

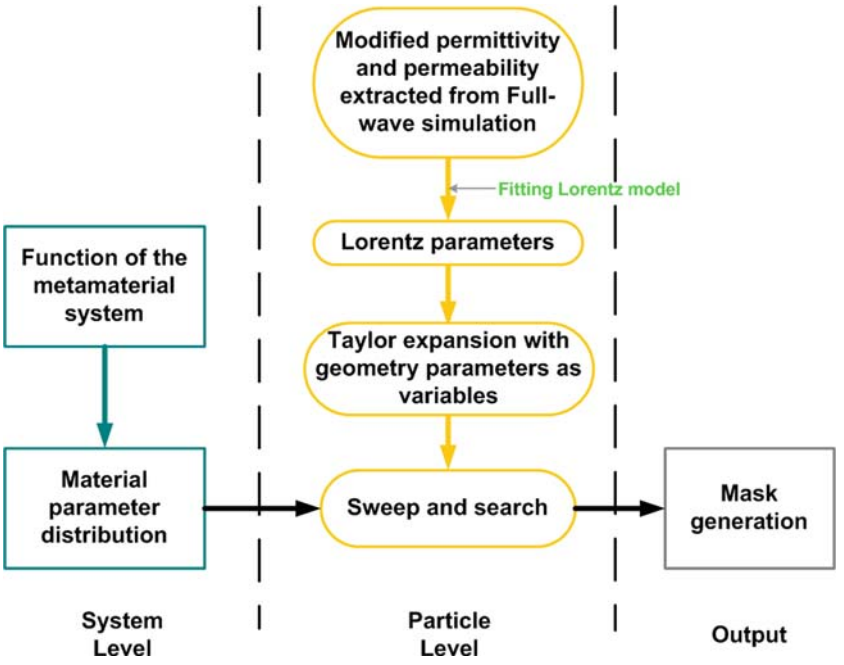


**Fig. 4.1** The flowchart of rapid design for metamaterials including three basic steps: the system level design, the particle level design, and mask generation.

#### 4.2.1.1 System Level Design

The system level design computes spatial distribution of the material parameters based on the desired function of the metamaterial. It applies optical transformation or geometric optics to compute the spatially varying permittivity, permeability, refractive index, etc. The computation can be analytical, and when the problem is too complicated to solve by analytical solutions it can be numerical as well [25].

#### 4.2.1.2 Particle Level Design

The particle level design outputs the optimized geometric parameters of the metamaterial particles for each set of material parameters. It has four sub-steps as follows.

In sub-step 1, a small number of metamaterial particles with different geometric parameter values are simulated as samples. From the simulated transmission $T$ and reflection coefficients $R$, the local field responses of the simulated particles defined as permittivity and permeability are then retrieved, which are in the form of Drude–Lorentz model when the metamaterial particles are resonant.

In sub-step 2, the curves of permittivity and permeability are fitted with a Drude–Lorentz model if the metamaterial particles are resonant and by Taylor expansion if they are non-resonant. Curve fitting by Drude–Lorentz model extracts the Lorentz model parameters defined in Section 4.2.2.2.

In sub-step 3, a mathematical relation between the Drude–Lorentz model and the geometric parameters of physical dimensions of the metamaterial particles is set up. Another fitting process is carried out to obtain the mathematical relation between the geometric parameters and the Drude–Lorentz parameters/the Taylor coefficients obtained in sub-step 2 by Taylor expansion.

In sub-step 4, by sweeping through the available geometric parameters, material parameters are calculated by the mathematical relation obtained in sub-step 3, in order to search for the geometric parameters which optimize the material parameters. The sweeping procedure takes into consideration the fabrication precision limit and the practical physical dimensions.

The particle level design is detailed in Section 4.2.2.

#### 4.2.1.3 Mask Generation

This step incorporates all the different metamaterial particles whose dimensions are determined by step (b) and generates integrated masks for fabrication.

### *4.2.2 Particle Level Design*

The particle level design aims at designing geometric dimensions of metamaterial particles to implement the material parameters determined by the system level

design. It is based on full-wave simulation and the S-parameter retrieval technique. The advantage of rapid design is that only a limited number of simulations need to be run, regardless of the number of particles with different material parameters.

#### 4.2.2.1 Extraction of Permittivity and Permeability

**(a) Drude–Lorentz Model**

Most metamaterials by far are composed of resonant particles, e.g., the split-ring resonator (SRR) [30], the electric-field-coupled resonator (ELC) [37, 29], and the complimentary SRR (CSRR) [11]. The resonances lead to responses to electric fields characterized by dispersive permittivity $\bar{\varepsilon}$ or responses to magnetic fields characterized by dispersive permeability $\bar{\mu}$. The dispersion is described by a Drude–Lorentz model, which can be obtained by averaging the local fields [42]. Meanwhile, the standard retrieval technique [43] provides an easier approach to retrieve the effective permittivity $\varepsilon_e$ and the effective permeability $\mu_e$ from simulated reflection and transmission coefficients. In our nomenclature, $\bar{\varepsilon}$ and $\bar{\mu}$ are termed the average permittivity and permeability while $\varepsilon_e$ and $\mu_e$ are termed the effective permittivity and permeability. As discussed in the previous chapter, the two sets of constitutive parameters obtained from microscopic and macroscopic prospectives do not quite agree with each other. This is because metamaterial particles are not infinitely small compared to the wavelength, which generates the effect of spatial dispersion. Yet they are viewed as the homogeneous materials by homogenization approximation [42]. The distortion between the two sets of constitutive parameters is bridged by the effective medium theory [23, 49, 50].

Take a SRR for instance, its permeability has a frequency dispersion described by the Drude–Lorentz model,

$$\bar{\mu} = \mu_0 \left(1 + \frac{F f^2}{f^2 - f_0^2 + i\gamma f}\right). \tag{4.1}$$

Fig. 4.2 compares its local permeability $\bar{\mu}$ to the retrieved permeability $\mu_e$. A disagreement between the two parameters can be observed. The effective permittivity $\varepsilon_e$ and the effective permeability $\mu_e$ are related to the refractive index by

$$n = \pm\sqrt{\mu_e \varepsilon_e}. \tag{4.2}$$

Meanwhile, the connection between the refractive index and the average permittivity $\bar{\varepsilon}$ and average permeability $\bar{\mu}$ is given by [42, 23]

$$\sin\left(\frac{nk_0 d}{2}\right) = \pm\frac{\omega d}{2}\sqrt{\bar{\mu}\bar{\varepsilon}}, \tag{4.3}$$

where $d$ is the dimension of the metamaterial unit cell in the direction of wave propagation. As can be found out from the two equations above, $\varepsilon_e$, $\mu_e$, and $\bar{\varepsilon}$, $\bar{\mu}$

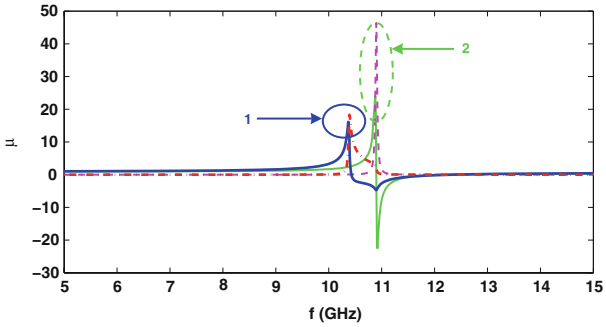


**Fig. 4.2** Comparison of effective permeability (marked 1) and average permeability (marked 2) of a SRR. The real parts are plotted by *solid lines* and the imaginary parts by *dash lines*.

should be different unless $d \to 0$, when the unit cell is infinitely small and Eq. (4.2) becomes equivalent to Eq. (4.3).

The wave impedance $\eta$ representing the ratio of electric and magnetic field intensity relates to the effective permittivity and permeability by

$$\eta = \sqrt{\frac{\mu_e}{\varepsilon_e}}, \tag{4.4}$$

and approximately relates to the average permittivity and permeability in a more complicated manner [23]. In the cases of pure electric resonances

$$\eta = \sqrt{\frac{\bar{\mu}}{\bar{\varepsilon}}} \cdot \cos\frac{\theta}{2}, \tag{4.5}$$

and for pure magnetic resonances

$$\eta = \sqrt{\frac{\bar{\mu}}{\bar{\varepsilon}}} \cdot \left(\cos\frac{\theta}{2}\right)^{(-1)}. \tag{4.6}$$

As refractive index and wave impedance are easily obtained from reflection and transmission coefficients by

$$\cos(nkd) = \frac{1}{2T}(1 - R^2 + T^2), \tag{4.7}$$

$$\eta = \sqrt{\frac{(1+R)^2 - T^2}{(1-R)^2 - T^2}}. \tag{4.8}$$

We are therefore able to achieve the frequency-dispersive constitutive parameters of electric or magnetic particles in the form of Drude–Lorentz model by full-wave electromagnetic simulation, the retrieval procedure, and Eqs. (4.3) and (4.5)–(4.6).

**(b) Modified permittivity and permeability for complex medium**

However, most resonant metamaterial particles behave in more complicated fashions than a pure electric, a pure magnetic resonance, or simultaneous electric and magnetic resonances. Even a typical magnetically resonant SRR exhibits an electric resonance at a frequency range higher than that of its fundamental magnetic resonance mode. This is because the induced electric currents distributed symmetrically over the ring at the electric resonant frequency, as shown in Fig. 4.3.

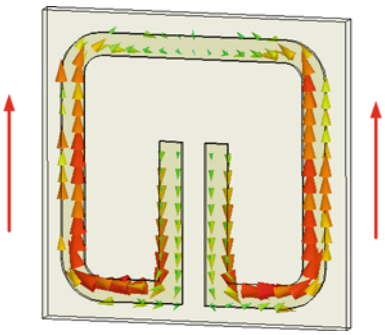

**Fig. 4.3** Current distribution of a SRR at its electrically resonant frequency.

As for metamaterials with electric and magnetic resonances that coexist at different frequencies, we are unable to apply Eqs. (4.5)–(4.6) to all the case. It is necessary to generalize the method to retrieve the dispersion curves of permittivity and permeability. We hence introduce another set of modified constitutive parameters $\varepsilon_m$ and $\mu_m$, which satisfy

$$\tan\frac{nk_0d}{2} = \pm\frac{\omega d}{2}\sqrt{\mu_m\varepsilon_m}, \tag{4.9}$$

$$\eta = \sqrt{\frac{\mu_m}{\varepsilon_m}}. \tag{4.10}$$

$\varepsilon_m$ and $\mu_m$ are approximated transformation of $\bar{\varepsilon}$ and $\bar{\mu}$ for the purpose of formula fitting. Particularly, when a particle is purely electrically resonant, $\mu_m = \bar{\mu}$, $\varepsilon_m = \bar{\varepsilon}\cdot\frac{1}{\cos^2(\theta/2)}$; when it is purely magnetically resonant, $\mu_m = \bar{\mu}\cdot\frac{1}{\cos^2(\theta/2)}$, $\varepsilon_m = \bar{\varepsilon}$; and when it has simultaneous electric and magnetic resonances, $\mu_m = \bar{\mu}\cdot\frac{1}{\cos(\theta/2)}$, $\varepsilon_m = \bar{\varepsilon}\cdot\frac{1}{\cos(\theta/2)}$. $\varepsilon_m$ and $\mu_m$ preserve the form of Drude–Lorentz model and are applicable to all the particles we have tested so far.

By using Eqs. (4.9) and (4.10), different orders of both electric and magnetic resonances are separated without ambiguity. Fig. 4.4 shows an example of a combined

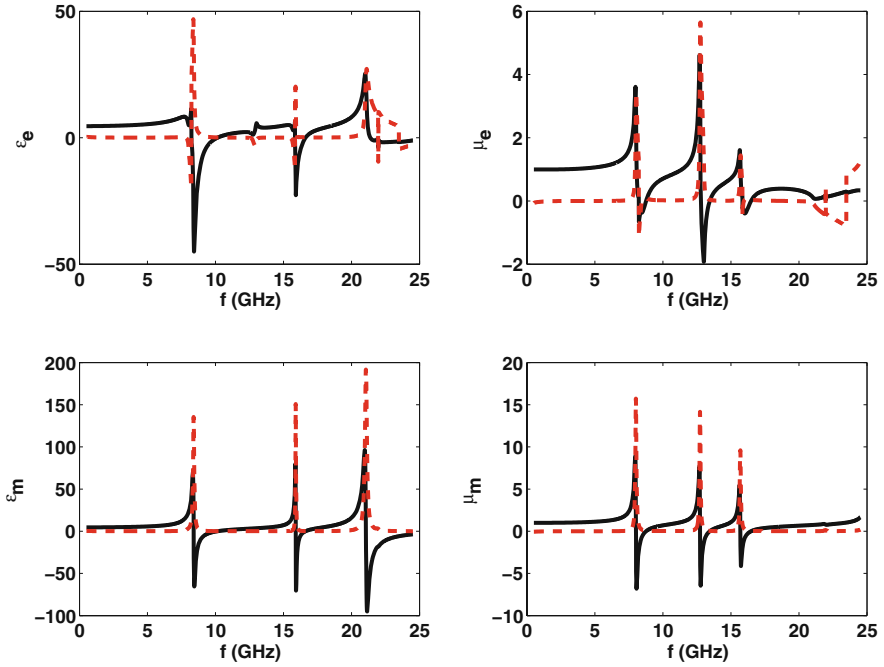


**Fig. 4.4** Comparison of effective constitutive parameters and modified constitutive parameters of a complex metamaterial particle composed of a SRR and an ELC. The real parts are plotted by *solid lines* and the imaginary parts by *dash lines*.

SRR and ELC particle [24]. The effective permittivity $\varepsilon_e$ and the effective permeability $\mu_e$ are shown to be chaotic due to multiple electric resonances accompanied by multiple magnetic resonances, so that it is difficult to determine the resonant properties of the complex particle. Yet the modified permittivity $\varepsilon_m$ and the modified permeability $\mu_m$, in the contrary, unambiguously indicate the three resonant frequencies at 8.4, 16, and 21 GHz and three magnetic resonant frequencies at 8, 12.75, and 15.5 GHz.

We note that the resonant frequencies of the modified permittivity and permeability are slightly different from those of $\bar{\varepsilon}$ and $\bar{\mu}$. However, in order to develop a sophisticated design method for metamaterials, our task is to calculate material parameters including refractive index, wave impedance, effective permittivity and permeability, reflection and transmission coefficients. The calculation can be accomplished by $\varepsilon_m$ and $\mu_m$ without $\bar{\varepsilon}$ and $\bar{\mu}$.

#### 4.2.2.2 Fitting Drude–Lorentz Model

Now that we have derived how to retrieve the frequency dispersive curves of modified permittivity and permeability, which provides values of $\varepsilon_m(f)$ and $\mu_m(f)$ at discrete frequency points densely distributed over the simulated frequency range, we next consider how to obtain their analytical expressions.

Typical metamaterial particles have permittivity or permeability of the Drude–Lorentzian resonance. We therefore discuss how to fit the curves of $\varepsilon_m(f)$ and $\mu_m(f)$ in the following form:

$$\mu_m(f) = \mu_0 \left(1 - \frac{F_u f^2}{f^2 - f_{0u}^2 + i\gamma_u f}\right), \tag{4.11}$$

$$\varepsilon_m(f) = \varepsilon_0 \left(1 - \frac{F_e f^2}{f^2 - f_{0e}^2 + i\gamma_e f}\right). \tag{4.12}$$

For $\mu_m$, we need to extract the values of the background permeability $\mu_0$, the magnetic resonant intensity $F_u$, the magnetic resonant frequency $f_{0u}$, and the damping factor of the resonance $\gamma_u$, and likewise for $\varepsilon_m$, the values of the background permittivity $\varepsilon_0$, the electric resonant intensity $F_e$, the electric resonant frequency $f_{0e}$, and the damping factor or the resonance $\gamma_e$. We name these coefficients Lorentz parameters.

Take Eq. (4.11), for example, to extract the Lorentz parameters $\mu_0$, $F_u$, $f_{0u}$, and $\gamma_u$. At the resonant frequency $f_{0u}$, the imaginary part of $\mu_m$ has the maximum value. Therefore, $f_{0u}$ can be obtained by determining the frequency where $\mu_m = max(imag(\mu_m(f)))$.

Picking up the frequency $f_{pu}$ higher than $f_{0u}$ where $\mu_m = min(real(\mu_m(f)))$, we will have

$$1 - \frac{F_u f_{pu}^2}{f_{pu}^2 - f_{0u}^2 + i\gamma_u f_{pu}} = 0 + i\delta, \tag{4.13}$$

where $\delta = imag(\mu_m(f_{pu}))$. Generally, the value of $\gamma_u$ is around the scale from $f_{pu}/1000$ to $f_{pu}/10$. Hence, Eq. (4.12) can be approximated by

$$1 - \frac{F_u f_{pu}^2}{f_{pu}^2 - f_{0u}^2} = 0. \tag{4.14}$$

And $F_u$ can be given by

$$F_u = 1 - \frac{f_{0u}^2}{f_{pu}^2}. \tag{4.15}$$

Submitting $f_{0u}$ and $F_u$ into Eq. (4.11), we now only need to decide the values of $\mu_0$ and $\gamma_u$. As we know, what we have from simulation and post-processing are a series of discrete frequencies $f$ corresponding to the values of $\mu_m$ at all of these frequencies. Assigning an initial value of $\mu_0$, we define

$$[f] = \begin{bmatrix} f_1 \\ f_2 \\ \cdots \\ f_m \end{bmatrix}, [f^2] = \begin{bmatrix} f_1^2 \\ f_2^2 \\ \cdots \\ f_m^2 \end{bmatrix}, [\mu_m] = \begin{bmatrix} \mu_m(f_1) \\ \mu_m(f_2) \\ \cdots \\ \mu_m(f_m) \end{bmatrix}, \tag{4.16}$$

where $f_{1,2,\ldots,m}$ are the series of discrete frequencies, such that

$$F_u\left[f^2\right] = \left(1 - \frac{[\mu_m]}{\mu_0}\right)\left(f_{0u}^2 - \left[f^2\right] + i\gamma_u[f]\right) \tag{4.17}$$

is an overdetermined equation to be solved and $\gamma_u$ can be achieved. For background material without magnetic polarizability, we are usually able to assume $\mu_0 = 1$.

In cases of $\mu_0 \neq 1$, submitting $\gamma_u$ back into Eq. (4.17) and solving the overdetermined equation again will give us an improved value of $\mu_0$. Iterating the calculations of $\mu_0$ and $\gamma_u$ alternatively until $\mu_0$ and $\gamma_u$ converge at stable values will give us the final solution. Consequently, we have obtained all the parameters for Eq. (4.10) and reconstructed the Drude–Lorentz model.

In terms of particles with more than one electric resonances and/or magnetic resonances, its dispersion property is described by the multiple-resonance Lorentz model [28]

$$\mu_m(f) = \mu_0\left(1 - \sum_{i=1}^{p} \frac{F_{iu}f^2}{f^2 - f_{0iu}^2 + i\gamma_{iu}f}\right), \tag{4.18}$$

where $p$ is the number of resonances. Without difficulty, resonant frequencies $f_{0iu}$ and zero-crossing frequencies $f_{piu}$ can be sequentially determined for each resonance.

Since any of the two resonances take place at two frequencies with a distinct difference, around the resonant frequency of the $i$th resonance, the items donated by the other resonances are relatively minor. Therefore, we can approximately assume that

$$\mu_m(f) = \mu_0\left(1 - \frac{F_{iu}f_{0iu}^2}{f_{0iu}^2 - f_{0iu}^2 + i\gamma_{iu}f_{0iu}}\right), \tag{4.19}$$

when $f_{0iu} \leq f \leq f_{piu}$. Conclusively, we are able to get $F_{iu}$ for every $i$ by solving

$$1 - \frac{F_{iu}f_{piu}^2}{f_{piu}^2 - f^20iu} = 0. \tag{4.20}$$

Similar to the case of single resonance, we assign an initial value to $\mu_0$ and define the discrete frequency series from $f_{0iu}$ to $f_{piu}$ to be $[f]$ and the correlated series of $\mu_m$ to be $[\mu_m]$ such that

$$F_{iu}\left[f^2\right] = \left(1 - \frac{[\mu_m]}{\mu_0}\right)\left(f_{0u}^2 - \left[f^2\right] + i\gamma_{iu}[f]\right), \tag{4.21}$$

$\gamma_{iu}$ $(i = 1, 2, \ldots, p)$ will be obtained. By substituting $F_{iu}$, $f_{0iu}$, and $\gamma_{iu}$ into Eq. (4.18), an updated $\mu_0$ will be achieved. Iterating this procedure several times, the values of $\mu_0$ and $\gamma_{iu}$ converge at stable values and all the Lorentz parameters of the multiple-resonance Lorentz model will be achieved. We note that the case of multiple-resonance Lorentz model is of special interest to design complex metamaterial particles, e.g., the wallpaper group metamaterials [4].

To validate the algorithm of extracting Lorentz parameters, we simulated a metamaterial particle with a SRR and an ELC, which has two electric resonances and one magnetic resonance between 1 and 16 GHz. By the retrieval routine based on Eqs. (4.7)–(4.10), modified permittivity and permeability are presented in Fig. 4.5(b). Afterward, by extracting the Lorentz parameters of the modified permittivity and permeability, the curves of $\varepsilon_m$ and $\mu_m$ were well reconstructed as shown in Fig. 4.5(a).

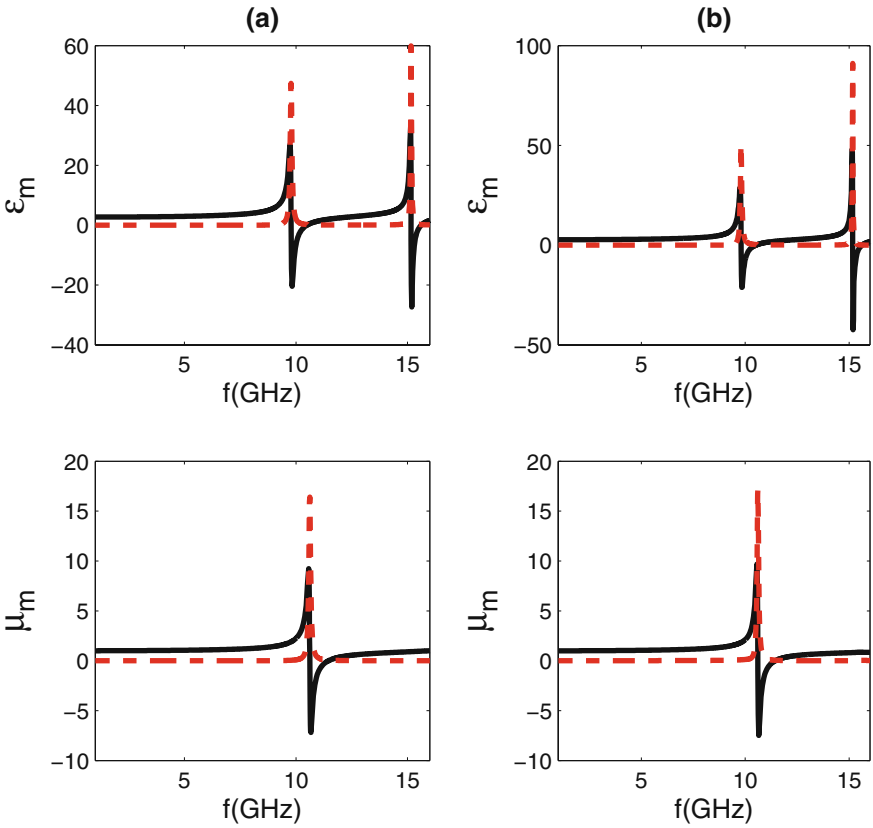


**Fig. 4.5** Comparison of reconstructed $\varepsilon_m$ of two resonances and $\mu_m$ of single resonance (a) with $\varepsilon_m$ and $\mu_m$ retrieved from HFSS simulation (b). Excellent agreement can be found between the two sets of material parameters. The real parts are plotted by *solid lines* and the imaginary parts by *dash lines*.

#### 4.2.2.3 Taylor Expansion of Lorentz Parameters

The next step is to set up the relation between geometric parameters and the Lorentz parameters. As an example, we consider the SRR shown in Fig. 4.6 with the arm

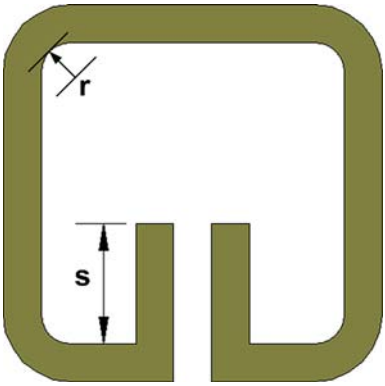


**Fig. 4.6** Topology of a SRR with $s$ as the length of the two arms and $r$ as the radius of the corners.

length $s$ as the adjustable geometric parameter and keep the other geometric parameters unchanged. By full-wave simulations we are able to obtain reflection and transmission coefficients of different $s$, and, by the method described above, $f_{0u}$, $F_u$, $\gamma_u$, and $\mu_0$ are calculated for each value of $s$. As the Lorentz parameters vary smoothly when $s$ increases, we choose to expand each of them into Taylor series as the function of $s$

$$f_{0u} = a_0 + a_1 s + a_2 s^2 + a_3 s^3 + \ldots, \tag{4.22}$$

$$F_u = b_0 + b_1 s + b_2 s^2 + b_3 s^3 + \ldots, \tag{4.23}$$

$$\gamma_u = c_0 + c_1 s + c_2 s^2 + c_3 s^3 + \ldots, \tag{4.24}$$

$$\mu_0 = d_0 + d_1 s + d_2 s^2 + d_3 s^3 + \ldots. \tag{4.25}$$

Usually, the variation of the parameters is not dramatic and the fitting by second- or third-order Taylor expansion will be accurate enough. However, the order can be increased in special cases.

Thereafter, it is enabled to rapidly calculate the modified permeability with any value of $s$ by Eqs. (4.21)–(4.24) and the related Taylor coefficients. If the SRR does not have any electric resonance in the frequency range and its modified permittivity is approximately non-dispersive, it can be regarded as $\varepsilon_m = \varepsilon_0$, where $\varepsilon_0$ is a constant and can be expanded into Taylor series as

$$\varepsilon_0 = e_0 + e_1 s + e_2 s^2 + e_3 s^3 + \ldots. \tag{4.26}$$

If both the radius of the corners $r$ and the arm length $s$ of the SRR are varying, $f_{0u}$, $F_u$, $\gamma_u$, $\mu_0$, and $\varepsilon_0$ should be expanded into bivariable Taylor series in the similar manner.

$$f_{0u} = a_0 + a_1 s + a_2 r + a_3 s^2 + a_4 r^2 + a_5 sr + a_6 s^3 + a_7 r^3 + a_8 s^2 r + a_9 s r^2 + \cdots, \tag{4.27}$$

$$F_u = b_0 + b_1 s + b_2 r + b_3 s^2 + b_4 r^2 + b_5 sr + b_6 s^3 + b_7 r^3 + b_8 s^2 r + b_9 s r^2 + \cdots, \tag{4.28}$$

$$\gamma_u = c_0 + c_1 s + c_2 r + c_3 s^2 + c_4 r^2 + c_5 sr + c_6 s^3 + c_7 r^3 + c_8 s^2 r + c_9 s r^2 + \cdots, \quad (4.29)$$

$$\mu_0 = d_0 + d_1 s + d_2 r + d_3 s^2 + d_4 r^2 + d_5 sr + d_6 s^3 + d_7 r^3 + d_8 s^2 r + d_9 s r^2 + \cdots, \quad (4.30)$$

$$\varepsilon_0 = e_0 + e_1 s + e_2 r + e_3 s^2 + e_4 r^2 + e_5 sr + e_6 s^3 + e_7 r^3 + e_8 s^2 r + e_9 s r^2 + \cdots. \quad (4.31)$$

Likewise, for multiple geometry variables, Taylor series of many variables will be employed.

If the modified permittivity is slightly dispersive, we expand $\varepsilon_0$ changing with $f$ by Taylor expansion

$$\varepsilon_0 = A_{0e} + A_{1e} f + A_{2e} f^2 + \cdots, \quad (4.32)$$

and the coefficients $A_{0e}$, $A_{1e}$, and $A_{2e}$ are to be expanded into Taylor series of the geometric variables.

With all the Taylor series coefficients, we are able to calculate the modified permittivity $\varepsilon_m$ and permeability $\mu_m$ and hence the effective material parameters by Eqs. (4.9), (4.10), (4.2), and (4.4) for any geometric parameters.

In order to test the soundness of the procedure, we simulated the SRR in Fig. 4.6 from 5 to 15 GHz with 16 different paired values of $s$ and $r$ and calculated the Taylor series coefficients of the extracted $f_{0u}$, $F_u$, $\gamma_u$, $\mu_0$, and $\varepsilon_0$. If we need to know the macroscopic material properties of the SRR when $s = 0.68$ mm and $r = 0.26$ mm, calculation is carried out based on Eqs. (4.26)–(4.31), (4.11), (4.9), and (4.10), which immediately gives $\varepsilon_m$, $\mu_m$, $n$, and $\eta$. Further calculation of $\varepsilon_e$ and $\mu_e$ is done according to

$$\varepsilon_e = n/\eta, \quad (4.33)$$

$$\mu_e = n\eta. \quad (4.34)$$

The results are shown in Fig. 4.7(a), with effective permittivity, effective permeability, wave impedance, and refractive index at any frequency from 5 to 15 GHz. Comparing to the direct simulation results shown in Fig. 4.7(b), accuracy of the procedure is demonstrated. The same algorithm can be applied to any other electric and/or magnetic resonant particles.

#### 4.2.2.4 Sweep and Search

Finally, we take into consideration the precision of fabrication and sweep the geometric parameters with steps decided by the minimum fabrication resolution.

In this step, it requires systematic considerations to select the geometric parameters corresponding to the most optimized material parameters. In some cases, effective permittivity and permeability are desired to be simultaneously optimized or permeability may need to be prioritized. In other cases, the accuracy of the refractive index is the most important factor while wave impedance should be kept matched

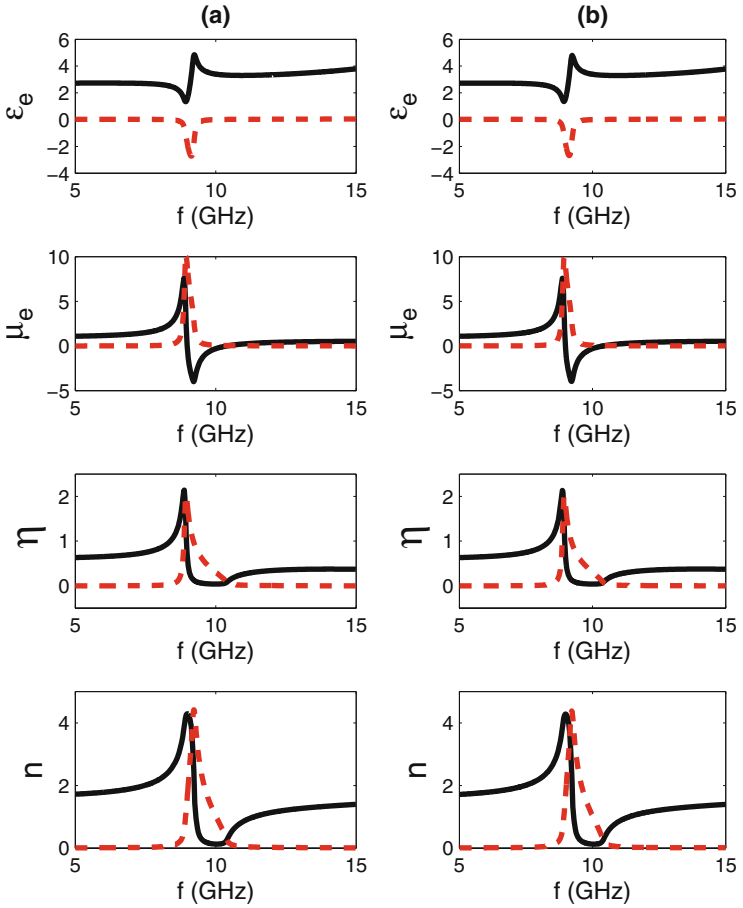


**Fig. 4.7** Real parts (*solid line*) and imaginary parts (*dash line*) of effective permittivity $\varepsilon_e$, effective permeability $\mu_e$, wave impedance $\eta$, and refractive index $n$ calculated by the rapid design (**a**) compared with those retrieved from HFSS simulation (**b**). Excellent agreement can be found between the two sets of material parameters.

to the background material. In most cases, metamaterials with good transmission properties are preferred, which indicates a minimum imaginary part of refractive index going with the other criteria.

#### 4.2.2.5 Additional Considerations

We note that

- The background permittivity $\varepsilon_0$ or permeability $\mu_0$ is often a little dispersive when there is another resonance at a frequency higher than the simulated frequency range. To address the error caused by the dispersion, we consider the

dispersive background permittivity and permeability in the same way as dealing with dispersive permittivity by Eq. (4.32).

- To guarantee the fitting accuracy over the entire domain of the geometric variables, the sampled values of geometric parameters to be simulated are preferred to be evenly distributed over the variable domain being simulated.

## 4.3 Examples

To further explain the rapid design algorithm and test its efficiency and robustness, a few metamaterial designs are shown below.

### *4.3.1 Gradient Index Lens by ELC*

A monotonically gradient index metamaterial lens is capable of steering an electromagnetic wave beam [41]. The two-dimensional lens steering the beam normally incident along $y$-axis to the right side is shown in Fig. 4.8. We discrete the lens by square blocks of unit cells with side length $d$ and used electric resonant metamaterial particles to implement such a lens. There are $p$ different unit cells with gradiently varying refractive indices along the $x$-axis and $q$ uniform unit cells along the $y$-axis. The refractive indices along the $x$-axis are $n_1, n_2, \ldots, n_p$ and $n_1 < n_2 < \cdots n_p$, so that the waves with normal incidence will pass through the lens along with an equal phase difference between each of two neighboring cells. The constant phase difference between neighboring cells $\Delta n$ is decided by the re-

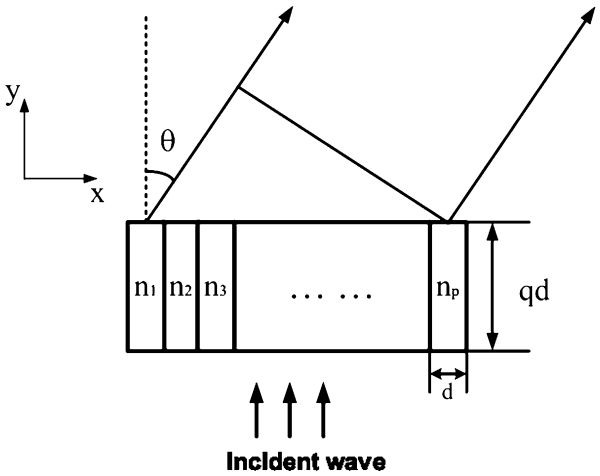


**Fig. 4.8** Configuration of a gradient-index lens which redirects the waves to an angle $\theta$ with respect to the incidence. There are $p$ layers along $x$-axis of different refractive index with $d$ as the thickness of each layer. The thickness of the lens in the direction of $y$-axis.

fraction angle $\theta$. By geometric optics, $\Delta n$ and $\theta$ are approximately related to each other by

$$q \cdot \Delta n = \sin\theta \tag{4.35}$$

when $\theta = 19.3^\circ$ and $q = 10$, we have $\Delta n = 0.033$. The calculation based on the function of the lens was coded as the first part of the design procedure – the system level design.

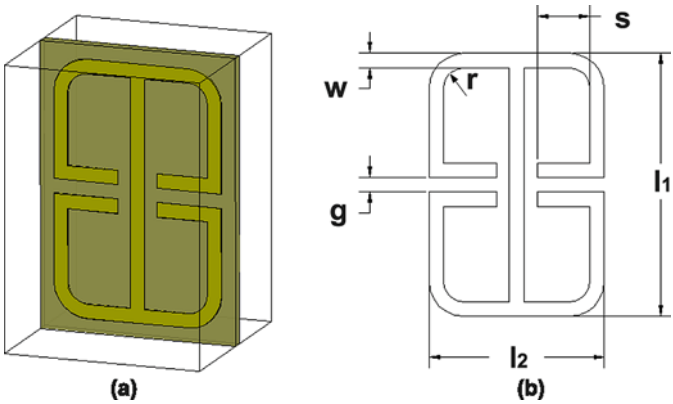


**Fig. 4.9** The metamaterial particle of ELC used to implement the gradient index lens (**a**) and its geometric.

Next we consider implementing the metamaterial lens by the ELC with two splits [29], as shown in Fig. 4.9(a). The geometric dimension of the ELC is illustrated in Fig. 4.9(b). There are 31 cells along the $x$-axis and 2 cells along the $y$-axis. The ELC particle is chosen to have an overall size of 3.5 mm × 3.5 mm × 5 mm, by 0.018 mm thick copper patterned on 0.2026 mm thick substrate with a permittivity of $3.84 + i0.02$. Some of the geometric parameters shown in Fig. 4.9(b) are fixed as $l_1 = 4.5$ mm, $l_2 = 3$ mm, $w = g = 0.25$ mm and two of them, $s$ and $r$, are variables. The working frequency of the lens is chosen to be 10 GHz.

Due to the geometric limit and the minimum size of gap by fabrication limit, $s$ ranges from 0 to 0.925 mm and $r$ from 0 to 1 mm. We sampled $4 \times 4$ sets of geometric parameters to simulate, with $s = 0$, 0.3, 0.6, 0.9 mm and $r = 0.05$, 0.35, 0.65, 0.95 mm, respectively. For each of the 16 samples, full-wave simulation was done by ANSOFT HFSS for the frequency range from 5 to 15 GHz and retrieval of modified permittivity and permeability was carried out based on Eqs. (4.7)–(4.10). For every ELC simulated, there is an electric resonance between 5 and 15 GHz. The permittivity curves were fitted with the Drude–Lorentz model and the Lorentz parameters, $F_e$, $f_{0e}$, $\gamma_e$, and $\varepsilon_0$, were extracted. The background permittivity $\varepsilon_0$ is a little dispersive since there is another electric resonance at a frequency higher than 15 GHz. The dispersion is addressed by Eq. (4.32). The permeability $\mu_m = \mu_0$ of

the ELCs are also dispersive due to a magnetic resonance at higher than 15 GHz. Hence, we applied Taylor series expansion to $\mu_0$ too, which gave

$$\mu_0 = A_{0u} + A_{1u} f + A_{2u} f^2 + \ldots \tag{4.36}$$

Conclusively, we expanded all the coefficients to third-order Taylor series with two variables, and all of the Taylor series were saved into a matrix $M$, which corresponds to

$$\begin{bmatrix} F_e \\ f_{0e} \\ \gamma_e \\ real(A_{0e}) \\ imag(A_{0e}) \\ real(A_{1e}) \\ imag(A_{1e}) \\ real(A_{2e}) \\ imag(A_{2e}) \\ real(A_{0u}) \\ imag(A_{0u}) \\ real(A_{1u}) \\ imag(A_{1u}) \\ real(A_{2u}) \\ imag(A_{2u}) \end{bmatrix} = M \begin{bmatrix} 1 \\ s \\ r \\ sr \\ s^2 \\ r^2 \\ s^2 r \\ sr^2 \\ s^3 \\ r^3. \end{bmatrix} \tag{4.37}$$

Next, we searched for the optimized geometry by sweeping $s$ and $r$ over the entire available range – $s$ from 0 to 0.925 mm and $r$ from 0 to 1 mm – with the fabrication resolution 0.005 mm as the sweeping step in order to select the most optimized material parameters. In terms of the gradient index lens design, the following factors had to be considered.

(a) The refractive indices of the 31 different ELCs must be gradient with a constant difference $\Delta n = 0.033$, which is the prioritized factor when selecting the optimized parameters.
(b) The wave impedances of the ELCs are preferred to be close to that of air ($\eta/\eta_0 = 1$). We selected the geometric parameter range with the best wave impedance matched at the center of the lens rather than at the edges, such that a maximum transmission of energy from a collimated incident beam is ensured.
(c) To reduce the undesired absorption of the metamaterial lens, we restricted the refractive indices with imaginary parts to be smaller than 0.2 and made sure the unit cells at the center of the lens had small imaginary parts of refractive indices less than 0.1.

Table 4.1 shows the designed results with the distribution of geometric parameters $s$ and $r$, and the material parameters $n$ and $\eta/\eta_0$. Here $j$ marks in sequence the unit cells along the $x$-axis. The searching step took less than 10 seconds. Simulation with the sampled geometric parameters by CST Microwave Studio cost about

**Table 4.1** Design results of a gradient-index metamaterial lens by ELCs

| $j$ | $s$ (mm) | $r$ (mm) | $n$ | $\eta/\eta_0$ |
|---|---|---|---|---|
| 1 | 0.460 | 0.185 | $0.453+i0.154$ | $2.043-i0.714$ |
| 2 | 0.470 | 0.250 | $0.486+i0.141$ | $1.957-i0.587$ |
| 3 | 0.470 | 0.165 | $0.520+i0.131$ | $1.862-i0.487$ |
| 4 | 0.480 | 0.220 | $0.553+i0.121$ | $1.775-i0.405$ |
| 5 | 0.490 | 0.270 | $0.586+i0.112$ | $1.691-i0.339$ |
| 6 | 0.495 | 0.240 | $0.620+i0.104$ | $1.608-i0.286$ |
| 7 | 0.505 | 0.280 | $0.652+i0.098$ | $1.535-i0.244$ |
| 8 | 0.520 | 0.380 | $0.686+i0.091$ | $1.465-i0.207$ |
| 9 | 0.525 | 0.330 | $0.720+i0.085$ | $1.397-i0.178$ |
| 10 | 0.535 | 0.345 | $0.753+i0.080$ | $1.337-i0.153$ |
| 11 | 0.545 | 0.355 | $0.786+i0.075$ | $1.281-i0.133$ |
| 12 | 0.560 | 0.420 | $0.820+i0.070$ | $1.228-i0.116$ |
| 13 | 0.575 | 0.475 | $0.853+i0.066$ | $1.178-i0.101$ |
| 14 | 0.595 | 0.575 | $0.887+i0.062$ | $1.133-i0.089$ |
| 15 | 0.600 | 0.495 | $0.920+i0.058$ | $1.090-i0.078$ |
| 16 | 0.605 | 0.400 | $0.953+i0.055$ | $1.051-i0.069$ |
| 17 | 0.625 | 0.480 | $0.986+i0.051$ | $1.013-i0.061$ |
| 18 | 0.635 | 0.460 | $1.013+i0.049$ | $0.984-i0.055$ |
| 19 | 0.655 | 0.515 | $1.047+i0.046$ | $0.950-i0.049$ |
| 20 | 0.670 | 0.505 | $1.080+i0.043$ | $0.918-i0.043$ |
| 21 | 0.690 | 0.535 | $1.113+i0.040$ | $0.888-i0.039$ |
| 22 | 0.705 | 0.500 | $1.147+i0.038$ | $0.860-i0.034$ |
| 23 | 0.725 | 0.505 | $1.180+i0.035$ | $0.833-i0.031$ |
| 24 | 0.750 | 0.545 | $1.214+i0.033$ | $0.807-i0.027$ |
| 25 | 0.775 | 0.570 | $1.247+i0.030$ | $0.783-i0.024$ |
| 26 | 0.805 | 0.615 | $1.280+i0.028$ | $0.760-i0.022$ |
| 27 | 0.830 | 0.605 | $1.313+i0.026$ | $0.738-i0.019$ |
| 28 | 0.875 | 0.705 | $1.347+i0.024$ | $0.717-i0.017$ |
| 29 | 0.910 | 0.715 | $1.380+i0.023$ | $0.697-i0.015$ |
| 30 | 0.930 | 0.635 | $1.413+i0.021$ | $0.677-i0.013$ |
| 31 | 0.980 | 0.680 | $1.447+i0.019$ | $0.659-i0.012$ |

4.5 hours. In contrast, conventional design methods for a metamaterial of 31 different unit cells and two geometric variables, with or without sophisticated optimization, may take a few weeks or even a few months.

The designed lens was fabricated by printed circuit board (PCB) lithography and measured in two-dimensional (2D) electric field mapping system [17] to characterize its performance. In order to reduce the edge effect, the two unit cells at the most outer sides were duplicated. Since the lens was to be placed in the 11 mm high planar waveguide of the 2D experimental system, the fabricated sample was 10 mm high, with two ELCs in the vertical direction. By measuring the spatial distribution of electric field amplitude and phase, we achieved the real part of electric field in and out of the metamaterial lens, as displayed in Fig. 4.10. Redirection of the incident wave beam can be observed. The refraction angle is approximately 19.5°, which proves excellent agreement with the designed angle. From the field intensity, it can be concluded that the reflection and absorption of the lens is neglectable.

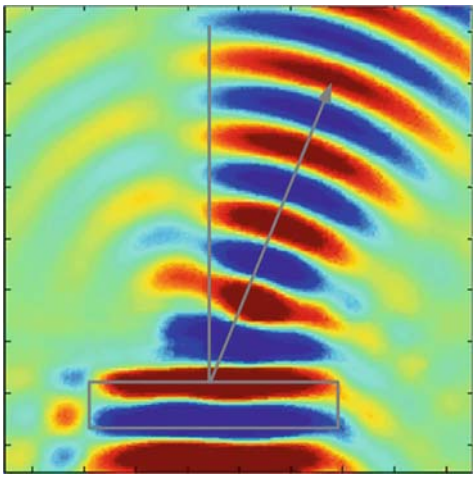

**Fig. 4.10** Measurement results of electric field distribution of the gradient-index ELC lens.

### *4.3.2 Gradient-Index Metamaterials Designed with Three Variables*

To further test the speed of the rapid design method, we apply the design procedure to design a gradient-index metamaterial with the metamaterial structure shown in Fig. 4.11(a), which has an ELC and an SRR combined in one unit cell. Three geometric variables are length of ELC arms *es*, length of the SRR arms *ss*, and the gap size of the SRR *gs*. Suppose the metamaterial needs 60 different unit cells with a constant grade $\Delta n = 0.033$. The simulations of $4 \times 4 \times 4$ particles with different geometric variable values took $10 \sim 20$ hours, and the searching step took less than 45 seconds. The results of the rapid design procedure is shown in Figs. 4.11(b) and 4.12. In Fig. 4.11(b) real and imaginary parts of refractive indices of the 60 designed unit cells are shown.

The time consumed by the rapid design algorithm increases when there are more geometric variables and more different particles to be designed. However, the time consumption of the algorithm is proportionally faster than the conventional method when the numbers of geometric variables and particles to be designed increase.

### *4.3.3 Reduced Parameter Invisible Cloak*

By the rapid design method, we now present the design of a reduced parameter cloak introduced in Ref. [36], with the same substrate of 0.381 mm thick Duroid 5870 and the same geometric dimensions of SRR. The geometric variables are the arm length *s* and the radius of the corners *r*. SRR with 16 different pairs of *s* and *r*

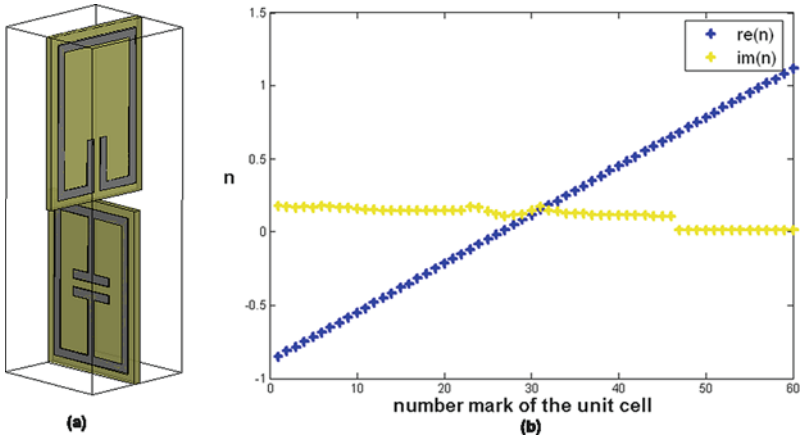


**Fig. 4.11** Topology of a combined SRR and ELC metamaterial particle used for the gradient index lens (**a**) and the designed gradient refractive indices $n$ of 60 different particles calculated by the rapid design method (**b**).

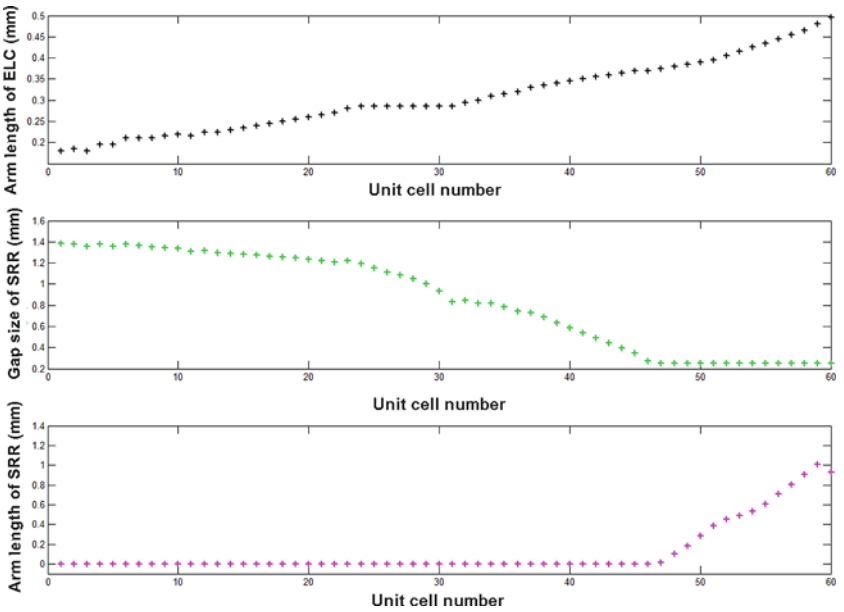


**Fig. 4.12** Designed results of the geometry parameters.

were simulated. By retrieving the modified permittivity and permeability and fitting the corresponding coefficients, the relationship was set up between the geometric parameters and the material parameters. Sweeping though the available values of $s$ and $r$, we searched for the desired values of effective permeability, with the effective permittivity as close as possible to the wanted values. The designed results of a cloak at 8.5 GHz is shown in Table 4.2, where $\varepsilon$ and $\mu$ are effective permittivity and

**Table 4.2** Design results of a reduced parameter invisible cloak

| $j$ | $s$ | $r$ | $\varepsilon$ | $\mu$ |
|---|---|---|---|---|
| 1 | 2.221 | 0.112 | $0.279 + i0.005$ | $3.423 + i0.003$ |
| 2 | 2.129 | 0.125 | $0.250 + i0.006$ | $3.423 + i0.003$ |
| 3 | 2.045 | 0.139 | $0.220 + i0.006$ | $3.423 + i0.002$ |
| 4 | 1.965 | 0.155 | $0.188 + i0.006$ | $3.423 + i0.002$ |
| 5 | 1.891 | 0.172 | $0.154 + i0.006$ | $3.423 + i0.002$ |
| 6 | 1.827 | 0.189 | $0.120 + i0.007$ | $3.423 + i0.002$ |
| 7 | 1.767 | 0.207 | $0.085 + i0.007$ | $3.423 + i0.001$ |
| 8 | 1.718 | 0.224 | $0.052 + i0.008$ | $3.423 + i0.001$ |
| 9 | 1.680 | 0.238 | $0.023 + i0.008$ | $3.423 + i0.001$ |
| 10 | 1.655 | 0.248 | $0.003 + i0.009$ | $3.423 + i0.001$ |

permeability obtained from the rapid design method and $j$ numbers the different layers of the cloak.

Comparing our designed geometric parameters with those in Ref. [36], there is a slight difference. To verify the designed results, the cloaked was fabricated according to the geometric parameters in Table 4.2. Field mapping results of electric field distribution are shown in Fig. 4.13, which demonstrates the performance of the designed cloak.

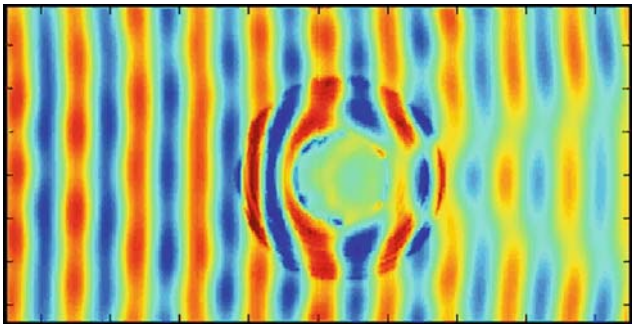

**Fig. 4.13** Experimental results of electric field distribution of the reduced parameter cloak.

In this example, we optimized the values of permittivity and permeability rather than the refractive index. The full-wave simulations of the 16 samples take 2–3 hours and the searching procedure for the 10 unit cells with two geometric variables takes less than 10 seconds.

### *4.3.4 Metamaterial Polarizer*

The rapid design for metamaterials can be applied to optimization requirements other than the material parameters. As an example, we consider the metamaterial polarizer by an ELC-constructed anisotropic metamaterial [9]. As analyzed in Ref.

[9], the requirement of a polarizer converting linear polarized waves to circular polarized waves is

$$|T_x| = |T_y|, \tag{4.38}$$

$$arg(T_x) - arg(T_y) = -\frac{3\pi}{2}, \tag{4.39}$$

where $T^x$ and $T^y$ are the transmission coefficients of the two wave modes with electric fields polarized along $x$- and $y$-directions, respectively. arg($T^x$) and arg($T^y$) are the phase advances of the two wave modes in the metamaterial. They can be calculated by

$$T^{x,y} = \frac{\exp(ik_{x,y}d) - r_{x,y}^2 \exp(ik_{x,y}d)}{1 - r_{x,y}^2 \exp(2ik_{x,y}d)}, \tag{4.40}$$

in which $k_{x,y} = n_{x,y}k_0$, $r_{x,y} = \frac{\eta_0 - \eta_{x,y}}{\eta_0 + \eta_{x,y}}$, and $d$ is the thickness of the metamaterial.

The three variables to be designed are the arm length $s$, the corner radius $r$ of the ELC and the thickness of the polarizer $d$. Here $d = 4\text{mm} \cdot h$ and $h = 1, 2, \ldots$ is the number of ELCs in the direction of the incident waves. We sampled 16 different pairs of $s$ and $r$ for simulations and each pair involved two simulations with orthogonal electric field polarization. Then we retrieved permittivity and permeability before expanding all the correlated coefficients into Taylor series. By searching through available values of $s$, $r$, and $h$, optimized transmission coefficients are achieved at 9.5 GHz with $s = 0.99$ mm, $r = 1.18$ mm, and $h = 2$. Maximum values of $|T_x| = |T_y|$ were selected to ensure a minimum reflection and small loss of the metamaterial. The searching step took less than 10 seconds and the simulations needed 4–10 hours. Experimental results presented in Ref. [9] proved the good performance of the designed metamaterial polarizer.

## 4.4 Summary

In this chapter, we introduced the rapid design for metamaterials which addresses the increasing burden of large-scale metamaterial design. It is widely applicable to various cases of metamaterial design with different metamaterial particles and, compared to the conventional methods, dramatically reduces the time consumed by metamaterial design. Detailed algorithm and considerations in the rapid design procedure have been addressed and several examples have been given to further explain the algorithm and demonstrate its efficiency. The rapid design method may be further extended to more complicated cases with magneto-electric responses. As it simplifies and accelerates the design of metamaterials, the rapid design for metamaterials is expected to boost the development of complex and inhomogeneous metamaterial systems.

**Acknowledgments** This work was supported in part by a major project of the National Science Foundation of China under Grant Nos. 60990320 and 60990324, the Natural Science Foundation

of Jiangsu Province under Grant No. BK2008031, the National Basic Research Program (973) of China under Grant No. 2004CB719802, the National Science Foundation of China under Grant Nos. 60871016, 60671015, 60901011, and 60621002, and in part by the 111 Project under Grant No. 111-2-05.

## References

1. Baena, J.D., Marques, R., Medina, F.: Artificial magnetic metamaterial design by using spiral resonators. Phys. Rev. B **69**, 014402 (2004)
2. Bilotti, F., Toscano, A., Vegni, L.: Design of spiral and multiple split-ring resonators for the realization of miniaturized metamaterial samples. IEEE Trans. Antennas Propag. **55**, 2258–2267 (2007)
3. Bilotti, F., Toscano, A., Vegni, L., Aydin, K., Alici, K.B., Ozbay, E.: Equivalent-circuit models for the design of metamaterials based on artificial magnetic inclusions. IEEE Trans. Micro. Theory Tech. **55**, 2865–2873 (2007)
4. Bingham, C.M., Tao, H., Liu, X., Averitt, R.D., Zhang, X., Padilla, W.J.: Planar wallpaper group metamaterials for novel terahertz applications. Opt. Express **16**, 18565–18575 (2008)
5. Chen, H., Chan, C.T.: Transformation media that rotate electromagnetic fields. Appl. Phys. Lett. **90**, 241105 (2007)
6. Chen, H., Ran, L., Huangfu, J., Grzegorczyk, T.M., Kong, J.A.: Equivalent circuit model for left-handed metamaterials. J. Appl. Phys. **100**, 024915 (2006)
7. Chen, H., Ran, L., Huangfu, J., Zhang, X., Chen, K., Grzegorczyk, T.M., Kong, J.A.: Negative refraction of a combined double S-shaped metamaterial. Appl. Phys. Lett. **86**, 151909 (2005)
8. Chen, P.Y., Chen, C.H., Wang, H., Tsai, J.H., Ni, W.X.: Synthesis design of artificial magnetic metamaterials using a genetic algorithm. Opt. Express **16**, 12806–12818 (2008)
9. Chin, J.Y., Lu, M., Cui, T.J.: Metamaterial polarizers by electric-field-coupled resonators. Appl. Phys. Lett. **93**, 251903 (2008)
10. Driscoll, T., Basov, D.N., Starr, A.F., Rye, P.M., Nemat-Nasser, S., Schurig, D., Smith, D.R.: Free-space microwave focusing by a negative-index gradient lens. Appl. Phys. Lett. **88**, 081101 (2006)
11. Falcone, F., Lopetegi, T., Laso, M.A.G., Baena, J.D., Bonache, J., Beruete, M., Marques, M., Martin, F., Sorolla, M.: Babinet principle applied to the design of metasurfaces and metamaterials. Phys. Rev. Lett. **93**, 197401 (2004)
12. Ge, Y., Esselle, K.P.: GA/FDTD technique for the design and optimisation of periodic metamaterials. IET Micro. Antennas Propag. **1**, 158–164 (2007)
13. Gil, I., Bonache, J., Garcia-Garcia, J., Martin, F.: Tunable metamaterial transmission lines based on varactor-loaded split-ring resonators. IEEE Trans. Micro. Theory Tech. **54**, 2665–2674 (2006)
14. Huangfu, J., Ran, R., Chen, H., Zhang, X.-M., Chen, K., Grzegorczyk, T.M., Kong, J.A.: Experimental confirmation of negative refractive index of a metamaterial composed of Ω-like metallic patterns. Appl. Phys. Lett. **84**, 091537–091539 (2004)
15. Jiang, W.X., Chin, J.Y., Li, Z., Cheng, Q., Liu, R., Cui, T.J.: Analytical design of conformally invisible cloaks for arbitrarily shaped objects. Phys. Rev. E **77**, 066607 (2008)
16. Jiang, W.X., Cui, T.J., Ma, H.F., Zhou, X.Y., Cheng, Q.: Cylindrical-to-plane-wave conversion via embedded optical transformation. Appl. Phys. Lett. **92**, 261903 (2008)
17. Justice, B.J., Mock, J.J., Guo, L., Degiron, A., Schurig, D., Smith, D.R.: Spatial mapping of the internal and external electromagnetic fields of negative index metamaterials. Opt. Express **14**, 8694–8705 (2008)
18. Justice, B.J., Nguyen, V.N., Yonak, S.H., Kim, J., Smith, D.R.: Electric-field-coupled metamaterials for microwave beam formation. IEEE AP-S Symposium, 2566–2569 (2007)
19. Kiziltas, G., Volakis, J.L., Kikuchi, N.: Metamaterial design via the density method. IEEE AP-S Symposium **1**, 748–751 (2002)

20. Kundtz, N., Roberts, D.A., Allen, J., Cummer, S., Smith, D.R.: Optical source transformations. Opt. Express **16**, 21215 **312** (5781), 1777 (2008)
21. Leonhadt, U.: Optical conformal mapping. Science –21222–1780 (2006)
22. Li, J., Pendry, J.B.: Hiding under the carpet: a new strategy for cloaking. Phys. Rev. Lett. **101**, 203901 (2008)
23. Liu, R., Cui, T.J., Huang, D., Zhao, B., Smith, D.R.: Description and explanation of electromagnetic behaviors in artificial metamaterials based on effective medium theory. Phys. Rev. E **76**, 026606 (2007)
24. Liu, R., Degiron, A., Mock, J.J., Smith, D.R.: Negative index material composed of electric and magnetic resonators. Appl. Phys. Lett. **90**, 263504 (2007)
25. Liu, R., Ji, C., Mock, J.J., Chin, J.Y., Cui, T.J., Smith, D.R.: Broadband ground-plane cloak. Science **323** (5912), 366–369 (2009)
26. Liu, R., Yang, X.M., Gollub, J.N., Mock, J.J., Cui, T.J., Smith, D.R.: Gradient index circuit by waveguided metamaterials. Appl. Phys. Lett. **94**, 073506 (2009)
27. Nguyen, V.N., Justice, B.J., Yonak, S.H., Smith, D.R.: Electrically coupled graded index metamaterial antenna technology: small antennas and novel metamaterials. International Workshop on iWAT 2008, 119–122 (2008)
28. Oughstun, K.E., Shen, S.: Velocity of energy transport for a time-harmonic field in a multiple resonance Lorentz medium. J. Opt. Soc. Am. B **5**, 2395–2398 (1988)
29. Padilla, W.J., Aronsson, M.T., Highstrete, C., Lee, M., Taylor, A.J., Averitt, R.D.: Electrically resonant terahertz metamaterials: theoretical and experimental investigations. Phys. Rev. B **75**, 041102 (2007)
30. Pendry, J.B., Holden, A.J., Robbins, D.J., Stewart, W.J.: Magnetism from conductors and enhanced non-linear phenomena. IEEE Trans. Micro. Theory Tech. **47**, 2075–2084 (1999)
31. Pendry, J.B., Schurig, D., Smith, D.R.: Controlling electromagnetic fields. Science **312** (5781), 1780–1782 (2006)
32. Pinchuk, A.O., Schatz, G.C.: Metamaterials with gradient negative index of refraction. J. Opt. Soc. Am. A **24**, A39–A44 (2007)
33. Rahm, M., Cummer, S.A., Schurig, D., Pendry, J.B., Smith, D.R.: Optical design of reflectionless complex media by finite embedded coordinate transformations. Phys. Rev. Lett. **100**, 063903 (2008)
34. Rahm, M., Roberts, D.A., Pendry, J.B., Smith, D.R.: Transformation-optical design of adaptive beam bends and beam expanders. Opt. Express **16**, 11555–11567 (2008)
35. Rahm, M., Schurig, D., Roberts, D.A., Cummer, S.A., Smith, D.R., Pendry, J.B.: Design of electromagnetic cloaks and concentrators using form-invariant coordinate transformations of Maxwell's equations. Photon. Nanostruct.: Fundam. Applic. **6**, 87–95 (2008)
36. Schurig, D., Mock, J.J., Justice, B.J., Cummer, S.A., Pendry, J.B., Starr, A.F., Smith, D.R.: Metamaterial electromagnetic cloak at microwave frequencies. Science **314** (5801), 977–980 (2006)
37. Schurig, D., Mock, J.J., Smith, D.R.: Electric-field-coupled resonators for negative permittivity metamaterials. Appl. Phys. Lett. **88**, 041109 (2006)
38. Sigmund, O.: Systematic design of metamaterials by topology optimization. Springer, Netherlands (2008)
39. Smith, D.R., Padilla, W.J., Vier, D.C., Nemat-Nasser, S.C., Schultz, S.: Composite medium with simultaneously negative permeability and permittivity. Phys. Rev. Lett. **84**, 4184–4187 (2000)
40. Shelby, R., Smith, D.R., Schultz, S.: Experimental verification of a negative index of refraction. Science **292**, 77–79 (2001)
41. Smith, D.R., Mock, J.J., Starr, A.F., Schurig, D.: Gradient index metamaterials. Phys. Rev. E **71**, 036617 (2005)
42. Smith, D.R., Pendry, J.B.: Homogenization of metamaterials by field averaging, J. Opt. Soc. Am. B **23**, 391–403 (2006)
43. Smith, D.R., Schultz, S., Markos, P., Soukoulis, C.M.: Determination of effective permittivity and permeability of metamaterials from reflection and transmission coefficients. Phys. Rev. B **65**, 195104 (2002)

44. Smolev, S., Brueck, S.R.J.: Graded index optical lens using inhomogeneous metamaterials. Conference on lasers and electro-optics/quantum electronics and laser science conference and photonic applications systems technologies, San Jose, May 4 (2008)
45. Tang, W.X., Zhao, H., Chin, J.Y., Cui, T.J.: A meander line resonator to realize negative index materials. IEEE Antennas and Propagation Society International Symposium, San Diego, July 5–11 (2008)
46. Tsuyoshi, N.: Metamaterials and automotive applications: topology optimization of electromagnetic materials. R&D Rev. Toyota CRDL **41**, 9–15 (2006)
47. Yoshinori, I., Tsuyoshi, N., Yasuhide, T., Koichi, H.: Metamaterials and automotive applications: design of optical devices based on topology optimization. R&D Rev. Toyota CRDL **41**, 26–31 (2006)
48. Left-handed metamaterial design guide using ANSOFT designer and HFSS. http://www.ansoft.com/metamaterial/
49. Simovski, C.R., Tretyakov S.A.: Local constitutive parameters of metamaterials from an effective-medium perspective. Physical Review B 75, 195111 (2007)
50. Simovski, C.R.: Bloch material parameters of magneto-dielectric metamaterials and the concept of Bloch lattices. Metamaterials 1, 62–80 (2007)

# Chapter 5
# Broadband and Low-Loss Non-Resonant Metamaterials

Ruopeng Liu, Qiang Cheng, Tie Jun Cui and David R. Smith

**Abstract** Loss and bandwidth have been major problems that limit the potential applications on metamaterials for a long time. To bring the ultimate opportunity to metamaterials, we analyze and discuss, in this chapter, another type of metamaterials that perform at low loss and broad bandwidth. Although the range of structures is limited to those having only electric response, with an electric permittivity always equal to or greater than unity, there are still numerous metamaterial design possibilities enabled by leveraging the non-resonant elements. For example, a gradient, impedance matching layer can be added that drastically reduces the return loss of the optical elements, making them essentially reflectionless and lossless. In microwave experiments, we demonstrate the broadband design concepts with a gradient-index lens and a beam-steering element, both of which are confirmed to operate over the entire X-band (roughly 8–12 GHz) frequency spectrum.

**Key words:** Metamaterials, broadband metamaterial, non-resonant element, artificial dielectric, gradient index optics, gradient index metamaterials, anti-reflection coating.

## 5.1 Analysis of the Metamaterial Structure

Artificial dielectric materials can be constructed by conducting scatter systems and have existed for a long time [12, 7, 5, 4, 16, 3, 2, 1, 15]. However, the design methodology of artificial dielectric materials was limited by the computational ability at

Ruopeng Liu, David R. Smith*
Center for Metamaterials and Integrated Plasmonics, Department of Electrical and Computer Engineering, Duke University, Durham, NC 27708, USA. * email: drsmith@duke.edu

Qiang Cheng, Tie Jun Cui+
State Key Laboratory of Millimeter Waves, Southeast University, Nanjing 210096, China. +
email: tjcui@seu.edu.cn

T.J. Cui et al. (eds.), *Metamaterials*, DOI 10.1007/978-1-4419-0573-4_5,

an early time, thus prohibiting the further development of such complex scattering systems. Recently the electromagnetic response of metamaterial elements can be precisely controlled so that they can be viewed as fundamental building blocks for a wide range of complex, electromagnetic media [17, 21]. To date, metamaterials have commonly been formed from resonant conducting circuits whose dimensions and spacing are much less than the wavelength of operation. By engineering the large dipolar response of these resonant elements, an unprecedented range of effective material responses can be realized, including artificial magnetism and large positive and negative values of the effective permittivity and permeability tensor elements [20, 14, 6, 23, 9]. Leveraging the flexibility inherent in these resonant elements, metamaterials have been used to implement structures that would have been otherwise difficult or impossible to achieve using conventional materials. Negative index materials, for example, sparked a surge of interest in metamaterials, since negative refractive index is not a material property available in nature. Still, as remarkable as negative index media are, they represented only the beginning of the possibilities available with artificially structured media. Inhomogeneous media, in which the material properties vary in a controlled manner throughout space, also can be used to develop optical components and are an extremely good match for implementation by metamaterials. Indeed, gradient index optical elements have already been demonstrated at microwave frequencies in numerous experiments. Moreover, since metamaterials allow unprecedented freedom to control the constitutive tensor elements independently, point-by-point throughout a region of space, metamaterials can be used as the technology to realize structures designed by the method of transformation optics [18]. The "invisibility" cloak, demonstrated at microwave frequencies in 2006, is an example of a metamaterial [19]. Although metamaterials have proven successful in the realization of unusual electromagnetic response, the structures demonstrated are often of only marginal utility in practical applications due to the large losses that are inherent to the resonant elements most typically used. The situation can be illustrated using the curves presented in Fig. 5.1, in which the effective constitutive parameters are shown in Fig. 5.1(a) and (b) for the metamaterial unit cell in the inset. According to the effective medium theory described in Ref. [13], the retrieved curves are significantly affected by spatial dispersion effect. To remove the spatial dispersion factor, we can apply the formulas in the theorem [13] and achieve that

$$\overline{\varepsilon} = \varepsilon \sin(\theta)/\theta, \tag{5.1}$$

$$\overline{\mu} = \mu \sin(\theta)/\theta, \tag{5.2}$$

in which $\theta = \omega p\sqrt{\varepsilon\mu}$ and $p$ is the periodicity of the unit cell.

Note that the unit cell possesses a resonance in the permittivity at a frequency near 42 GHz. In addition to the resonance in the permittivity, there is also structure in the magnetic permeability. These artifacts are phenomena related to spatial dispersion – an effect due to the finite size of the unit cell with respect to the wavelengths. As previously pointed out, the effects of spatial dispersion are simply described analytically, and can thus be removed to reveal a relatively uncomplicated

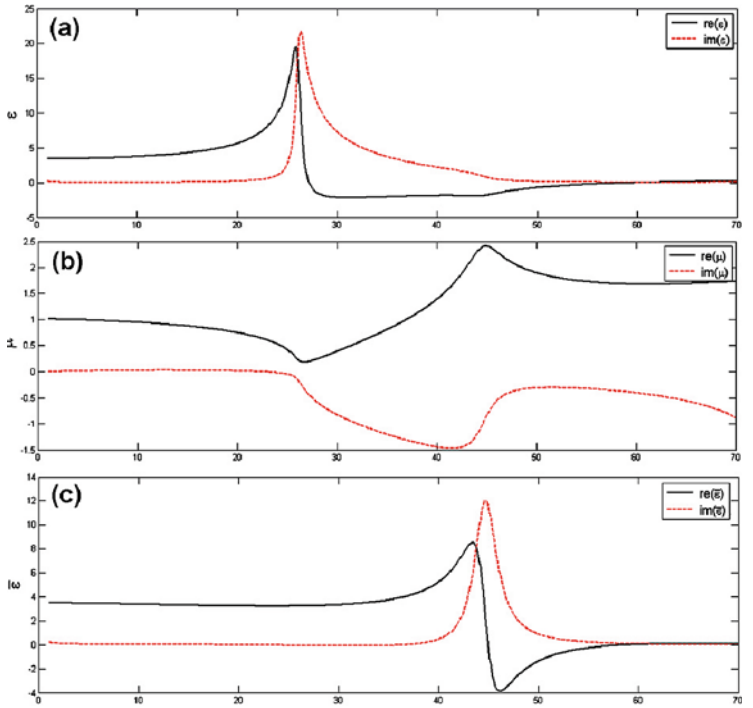


**Fig. 5.1** (**a**) Retrieved permittivity for a metamaterial composed of the repeated unit cell shown in the inset; (**b**) retrieved permeability for a metamaterial composed of the repeated unit cell shown in the inset. (**c**) The distortions and artifacts in the retrieved parameters are due to spatial dispersion, which can be removed to find the Drude–Lorentz-like resonance shown in the lower figure.

Drude–Lorentz-type oscillator characterized by only a few parameters. The observed resonance takes the form

$$\varepsilon(\omega) = 1 - \frac{\omega_p^2}{\omega^2 - \omega_0^2 + i\Gamma\omega} = \frac{\omega^2 - \omega_0^2 - \omega_p^2 - i\Gamma\omega}{\omega^2 - \omega_0^2 + i\Gamma\omega}, \tag{5.3}$$

where $\omega_p$ is the plasma frequency, $\omega_0$ is the resonance frequency, and $\Gamma$ is a damping factor. The frequency where $\varepsilon(\omega) = 0$ occurs at $\omega_L^2 = \omega_0^2 + \omega_p^2$.

As can be seen from either Eq. (5.3) or Fig. 5.1, the effective permittivity can achieve very large values, either positive or negative, near the resonance. Yet, these values are inherently accompanied by both dispersion and relatively large losses, especially for frequencies very close to the resonance frequency. Thus, although a very wide and interesting range of constitutive parameters can be accessed by working with metamaterial elements near the resonance, the advantage of these values is somewhat tempered by the inherent loss and dispersion. The strategy in utilizing metamaterials in this regime is to reduce the losses of the unit cell as much as

possible. If we examine the response of the electric metamaterial shown in Fig. 5.1 at very low frequencies, we find, in the zero frequency limit,

$$\varepsilon(\omega \longrightarrow 0) = 1 + \frac{\omega_p^2}{\omega_0^2} = \frac{\omega_L^2}{\omega_0^2}. \tag{5.4}$$

The equation is reminiscent of the Lyddane–Sachs–Teller relation that describes the contribution of the polariton resonance to the dielectric constant at zero frequency [11]. At frequencies far away from the resonance, we see that the permittivity approaches a constant that differs from unity by the square of the ratio of the plasma to the resonance frequencies. Although the values of the permittivity are necessarily positive and greater than unity, the permittivity is both dispersionless and lossless – a considerable advantage. Note that this property does not extend to magnetic metamaterial media, such as split-ring resonators, which are generally characterized by effective permeability of the form

$$\mu(\omega) = 1 - \frac{F\omega^2}{\omega^2 - \omega_0^2 + i\Gamma\omega}, \tag{5.5}$$

which approaches unity in the low-frequency limit. Because artificial magnetic effects are based on induction rather than polarization, artificial magnetic response must vanish at zero frequency. The effective constitutive parameters of metamaterials are not only complicated by spatial dispersion but also possess an infinite number of higher order resonances that should properly be represented as a sum over oscillators. It is thus expected that the simple analytical formulas presented above are only approximate. Still, we can investigate the general trend of the low-frequency permittivity as a function of the high-frequency resonance properties of the unit cell. By adjusting the dimension of the square closed ring in the unit cell, we can compare the retrieved zero-frequency permittivity with that predicted by Eq. (5.2). The simulations are carried out using HFSS (Ansoft), a commercial electromagnetic, finite-element solver that can determine the exact field distributions and scattering (S-) parameters for an arbitrary metamaterial structure. The permittivity and permeability can be retrieved from the S-parameters by a well-established algorithm. Table 5.1 demonstrates the comparison between such simulated extraction and theoretical prediction. We should notice that as the unit cell is combined with a dielectric

**Table 5.1** The predicted and actual zero-frequency permittivity values as a function of the unit cell dimension $a$.

| $a$ | $f_0$ | $f_L$ | Epredicted | Eactual |
|---|---|---|---|---|
| 1.70 | 44.0 | 59.0 | 3.416 | 3.425 |
| 1.55 | 54.0 | 64.0 | 2.670 | 2.720 |
| 1.40 | 64.0 | 71.0 | 2.338 | 2.315 |
| 1.20 | 77.4 | 79.2 | 1.989 | 1.885 |

substrate, Eq. (5.3) has been modified into $\varepsilon(\omega \longrightarrow 0) = \varepsilon_a(1 + \frac{\omega_p^2}{\omega_0^2}) = \varepsilon_a \frac{\omega_F^2}{\omega_0^2}$, in which $\varepsilon_a = 1.9$. The additional fitting parameter can represent the practical situation of the affect from substrate dielectric constant and the contribution to DC permittivity from high-order resonances. Though there is significant disagreement between the predicted and retrieved values of permittivity, the values are of similar order and clearly show a similar trend: the high-frequency resonance properties are strongly correlated to the zero-frequency polarizability. By modifying the high-frequency resonance properties of the element, the zero- and low-frequency permittivity can be adjusted to arbitrary values.

Because the closed-ring design shown in Fig. 5.2 can easily be tuned to provide a range of dielectric values, we utilize it as the base element to illustrate more complex gradient-index structures. Though its primary response is electric, the closed ring also possesses a weak, diamagnetic response that is induced when the incident magnetic field lies along the ring axis. The closed-ring medium therefore is characterized by a magnetic permeability that differs from unity, and which must be taken into account for a full description of the material properties. The presence of both electric and magnetic dipolar responses is generally useful in designing complex media, having been demonstrated in the metamaterial cloak. By changing the dimensions of the ring, it is possible to control the contribution of the magnetic response.

The permittivity can be accurately controlled by changing the geometry of the closed-ring. The electric response of the closed-ring structure is identical to the "cut-wire" structure previously studied, where it has been shown that the plasma and resonance frequencies are simply related to circuit parameters according to $\omega_p^2 \approx 1/L$ and $\omega_0^2 \approx 1/(LC)$. Here, $L$ is the inductance associated with the arms of the closed ring and $C$ is the capacitance associated with the gap between adjacent closed rings. For a fixed unit cell size, the inductance can be tuned either by changing the thickness $w$ of the conducting rings or their length $a$. The capacitance can be controlled primarily by changing the overall size of the ring.

Changing the resonance properties in turn changes the low-frequency permittivity value, as illustrated by the simulation results presented in Fig. 5.2. The closed-ring structure shown in Fig. 5.2(a) is assumed to be deposited on FR4 substrate, whose permittivity is 3.85+i0.02 and thickness is 0.2026 mm. The unit cell dimension is 2 mm, and the thickness of the deposited metal layer (assumed to be copper) is 0.018 mm. For this structure, a resonance occurs near 25 GHz with the permittivity nearly constant over a large frequency region (roughly DC to 15 GHz). Three different unit cells with ring dimensions of $a = 0.7$, 1.4, and 1.625 mm were also simulated to illustrate the effect on the material parameters. In Fig. 5.2(b), it is observed that the index value becomes larger as the ring dimension is increased, reflecting the larger polarizability of the larger rings.

The refractive index remains, for the most part, relatively flat as a function of frequency for frequencies well below the resonance. The index does exhibit a slight monotonic increase as a function of frequency, however, which is due to the higher frequency resonance. The impedance changes also exhibits some amount of frequency dispersion, due to the effects of spatial dispersion on the permittivity and

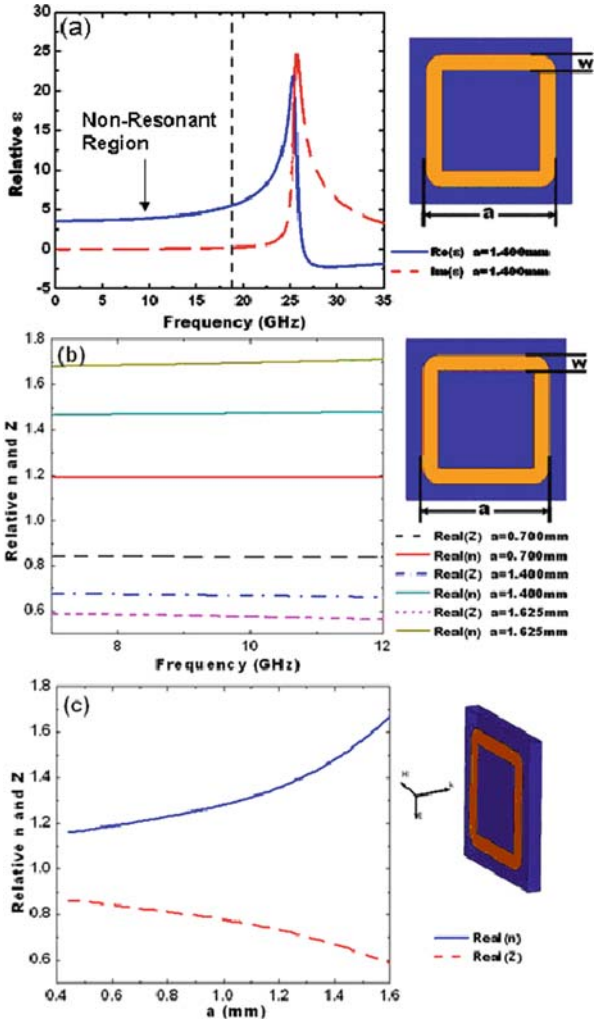


**Fig. 5.2** Retrieval results for the closed ring medium. In all cases the radius of curvature of the corners is 0.6 mm, and $w$ = 0.2 mm. (**a**) The extracted permittivity with $a$ =1.4 mm. (**b**) The extracted index and impedance for several values of $a$. The low-frequency region is shown. (**c**) The relationship between the dimension $a$ and the extracted refractive index and wave impedance.

permeability. The losses in this structure are found to be negligible, as a result of being far away from the resonance frequency. This result is especially striking, because the substrate is not the one optimized for RF circuits – in fact, the FR4 circuit board substrate assumed here is generally considered quite lossy.

As can be seen from the simulation results in Fig. 5.2, metamaterial structures based on the closed-ring element should be nearly non-dispersive and low loss, provided the resonances of the elements are sufficiently above the desired range

of operating frequencies. To illustrate the point, we make use of the closed-ring element to realize two gradient index devices: a gradient-index lens and a beam-steering lens. The use of resonant metamaterials to implement positive and negative gradient-index structures was introduced in [22] and subsequently applied in various contexts. The design approach is the first to determine the desired continuous index profile to accomplish the desired function (e.g., focusing or steering) and then to stepwise approximate the index profile using a discrete number of metamaterial elements. The elements can be designed by performing numerical simulations for a large number of variations of the geometrical parameters of the unit cell; once enough simulations have been run so that a reasonable interpolation can be formed of the permittivity as a function of the geometrical parameters, the metamaterial gradient-index structure can be laid out and fabricated. This basic approach has been followed in [8].

## 5.2 Demonstration of Broadband Inhomogeneous Metamaterials

Two gradient-index samples were designed to test the bandwidth of the non-resonant metamaterials. The color maps in Fig. 5.3 show the index distribution corresponding to the beam-steering layer (Fig. 5.3(a)) and the beam-focusing lens (Fig. 5.3(b)).

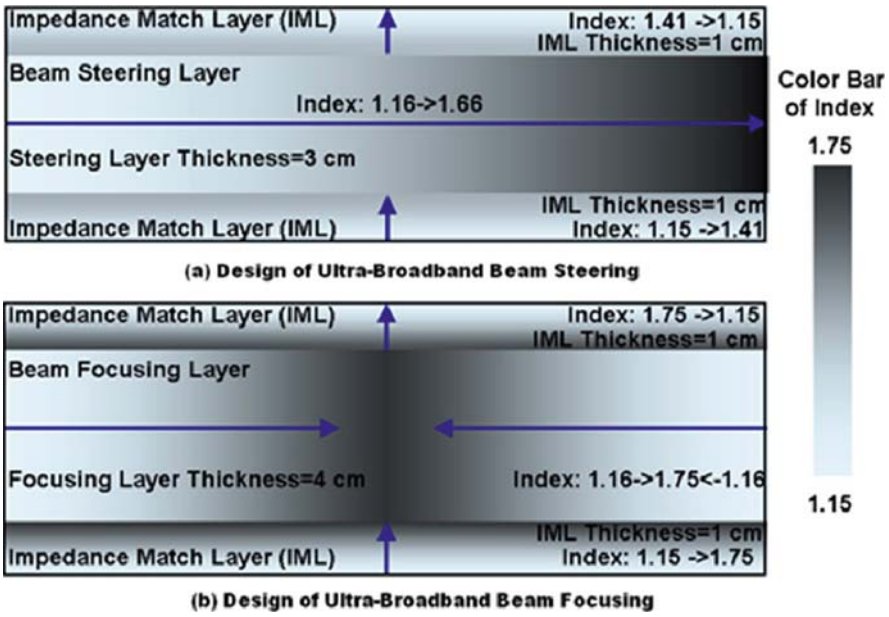


**Fig. 5.3** Refractive index distributions for the designed gradient-index structures. (**a**) A beam-steering element based on a linear index gradient. (**b**) A beam-focusing lens, based on a higher order polynomial index gradient. Note the presence in both designs of an impedance-matching layer (IML), provided to improve the insertion loss of the structures.

Although the gradient-index distributions provide the desired function of either focusing or steering a beam, a substantial mismatch exists between the predominantly high index structure and free space. This mismatch was managed in prior demonstrations by adjusting the properties of each metamaterial element such that the permittivity and permeability were essentially equal. This flexibility in design is an inherent advantage of resonant metamaterials, where the permeability response can be engineered on a nearly equal footing with the electric response. In contrast, that flexibility is not available for designs involving non-resonant elements, so we have instead made use of a gradient-index impedance matching layer (IML) to provide a match from free space to the lens, as well as a match from the exit of the lens back to free space.

The beam-steering layer is a slab with a linear index gradient in the direction transverse to the direction of wave propagation. The index values range from $n$ = 1.16 to 1.66, consistent with the range available from our designed set of closed-ring metamaterial elements. To improve the insertion loss and to minimize reflection, the IML is placed on both sides of the sample (input and output). The index values of the IML gradually change from unity (air) to $n$ = 1.41, the index value at the center of the beam-steering slab. This index value was chosen because most of the energy of the collimated beam passes through the center of the sample. To implement the actual beam-steering sample, we made use of the closed-ring unit cell shown in Fig. 5.2 and designed an array of unit cells having the distribution shown in Fig. 5.3(a).

The beam-focusing lens is a planar slab with the index distribution as represented in Fig. 5.3(b). The index distribution has the functional form of

$$\mathrm{Re}(n) \approx 4 \times 10^{-6}|x|^3 - 5 \times 10^{-4}|x|^2 - 6 \times 10^{-4}|x| + 1.75, \tag{5.6}$$

in which $x$ is the distance away from the center of the lens. Once again, an IML was used to match the sample to free space. In this case, the index profile in the IML was ramped linearly from $n$ = 1.15 to 1.75, the latter value selected to match the index at the center of the lens. The same unit cell design was utilized for the beam-focusing lens as for the beam-steering lens.

To confirm the properties of the gradient-index structures, we fabricated the two designed samples using copper-clad FR4 printed circuit board substrate shown in Fig. 5.4. Following a procedure previously described, sheets of the samples were fabricated by standard optical lithography, then cut into 1 cm tall strips that could be assembled together to form the gradient index slabs. To measure the sample, we placed them into a 2D mapping apparatus, which has been described in detail and mapped the near-field distribution [10].

Figure 5.5 shows the beam steering of the ultra-broadband metamaterial design, in which a large broadband is covered. The actual bandwidth starts from DC and goes up to approximately 14 GHz. From Fig. 5.5, it is obvious that beam steering occurs at all the four different frequencies from 7.38 to 11.72 GHz with an identical steering angle of 16.2°. The energy loss through propagation is extremely low and can barely be observed. Figure 5.6 shows the mapping result of the beam focusing sample. Broadband property is demonstrated again at four different frequencies with an exact focal distance of 35 mm and low loss.

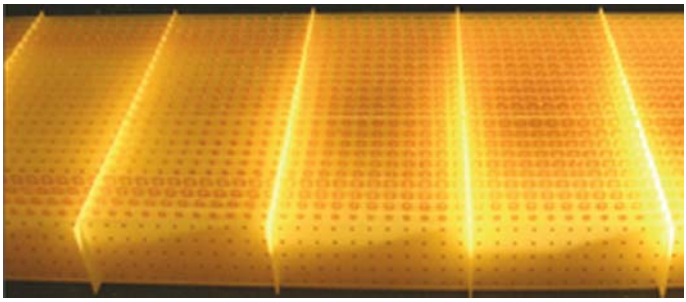

**Fig. 5.4** Fabricated sample in which the metamaterial structures vary with space coordinate.

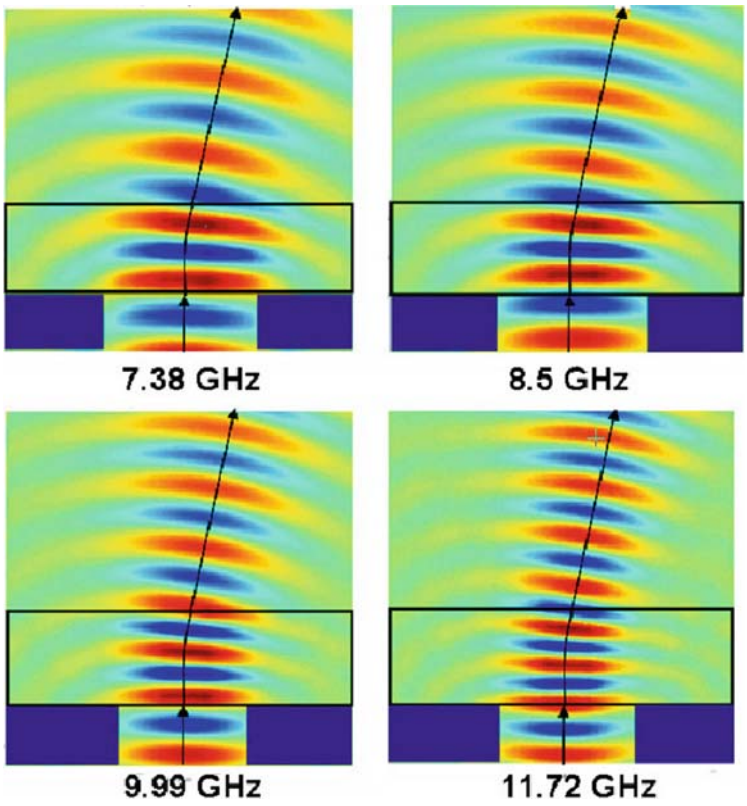


**Fig. 5.5** Field mapping measurements of the beam-steering lens. The lens has a linear gradient that causes the incoming beam to be deflected by an angle of 16.2°. The effect is broadband, as can be seen from the identical maps taken at four different frequencies that span the X-band range of the experimental apparatus.

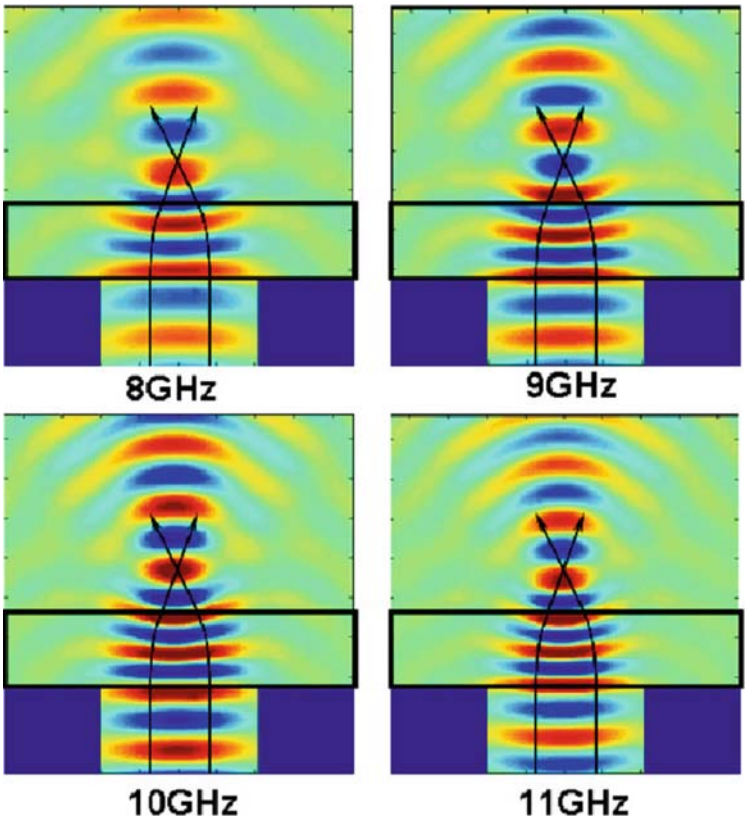


**Fig. 5.6** Field mapping measurements of the beam-focusing lens. The lens has a symmetric profile about the center (given in the text) that causes the incoming beam to be focused to a point. Once again, the function is broadband, as can be seen from the identical maps taken at four different frequencies that span the X-band range of the experimental apparatus.

In summary, we propose ultra-broadband metamaterials, based on which complex inhomogeneous material can be realized and accurately controlled. The configuration of ultra-broadband metamaterials and the design approach are validated by experiments. Due to their low loss, designable properties, and easy access to inhomogeneous material parameters, ultra-broadband metamaterials have been applied to design Luneberg cylindrical lens antennas (see Chapter 14) and will find wide applications in the future.

## References

1. Awai, I.: Artificial dielectric resonators for miniaturized filters. IEEE Micro. Magazine **9**, 55–64 (2008)
2. Awai, I., Kida, S., Mizue, O.: Very thin and flat lens antenna made of artificial dielectrics. 2007 Korea-Japan Microwave Conference, Okinawa, 177–180 (2007)

3. Awai, I., Kubo, H., Iribe, T., Wakamiya, D., Sanada, A.: An artificial dielectric material of huge permittivity with novel anisotropy and its application to a microwave BPF. IEEE MTTS **2**, 1085–1088 (2003)
4. Bahl, I., Gupta, K.: A leaky-wave antenna using an artificial dielectric medium. IEEE Trans. Ant. Prop. **22**, 119–122 (1974)
5. Brown, J., Jackson, W.: The relative permittivity of tetragonal arrays of perfectly conducting thin discs. Proc. IEE **102B**, 37–42 (1995)
6. Chen, X., Grzegorczyk, T.M., Wu, B.-I., Pacheco, J., Kong, J.A.: Robust method to retrieve the constitutive effective parameters of metamaterials. Phys. Rev. E **70**, 016608 (2004)
7. Corkum, R.W.: Isotropic artificial dielectric. Proc. IRE **40**, 574 (1952)
8. Driscoll, T., Basov, D.N., Starr, A.F., Rye, P.M., Nemat-Nasser, S., Schurig, D., Smith, D.R.: Free-space microwave focusing by a negative-index gradient lens. Appl. Phys. Lett. **88**, 081101 (2006)
9. He, S., Ruan, Z., Chen, L., Shen, J.: Focusing properties of a photonic crystal slab with negative refraction. Phys. Rev. B **70**, 115113 (2004)
10. Justice, B.J., Mock, J.J., Guo, L., Degiron, A., Schurig, D., Smith, D.R.: Spatial mapping of the internal and external electromagnetic fields of negative index metamaterials. Opt. Express **14**, 8694 (2006)
11. Kittel, C.: Solid state physics, 6th ed. John Wiley and Sons, New York, 275 (1986)
12. Kock, W.E.: Metallic delay lenses. Bell Syst. Tech. J. **27**, 58 (1948)
13. Liu, R., Cui, T.J., Huang, D., Zhao, B., Smith, D.R.: Description and explanation of electromagnetic behaviors in artificial metamaterials based on effective medium theory. Phys. Rev. E **76**, 026606 (2007)
14. Liu, R., Degiron, A., Mock, J.J., Smith, D.R.: Negative index material composed of electric and magnetic resonators. Appl. Phys. Lett. **90**, 263504 (2007)
15. Ma, Y., Rejaei, B., Zhuang, Y.: Artificial dielectric shields for integrated transmission lines. IEEE Micro. Wirel. Comp. Lett. **19**, 431–433 (2008)
16. Mukoh, Y., Nojima, T., Hasebe, N.: A reflector lens antenna consisting of an artificial dielectric. Electron. Commun. Jpn, Part 1 **82**, 44–52 (1999)
17. Pendry, J.B., Holden, A.J., Robbins, D.J., Stewart, W.J.: Magnetism from conductors and enhanced nonlinear phenomena. IEEE Trans. Micro. Theory Tech. **47**, 2075 (1999)
18. Pendry, J.B., Schurig, D., Smith, D.R.: Controlling electromagnetic fields. Science **312**, 1780 (2006)
19. Schurig, D., Mock, J.J., Justice, B.J., Cummer, S.A., Pendry, J.B., Starr, A.F., Smith, D.R.: Metamaterial electromagnetic cloak at microwave frequencies. Science **314**, 977–980 (2006)
20. Shelby, R., Smith, D.R., Schultz, S.: Experimental verification of a negative index of refraction. Science **292**, 77 (2001)
21. Smith, D.R., Padilla, W.J., Vier, D.C., Nemat-Nasser, S.C., Schultz, S.: Composite medium with simultaneously negative permeability and permittivity. Phys. Rev. Lett. **84**, 4184 (2000)
22. Smith, D.R., Rye, P.M., Mock, J.J., Vier, D.C., Starr, A.F.: Enhanced diffraction from a grating on the surface of a negative-index metamaterial. Phys. Rev. Lett. **93**, 137405 (2004)
23. Varadan, V., Sheng, Z., Penumarthy, S., Puligalla, S.: Comparison of measurement and simulation of both amplitude and phase of reflected and transmitted fields in resonant Omega media. Micro. Opt. Tech. Lett. **48**, 1549–1553 (2006)

# Chapter 6
# Experiment on Cloaking Devices

Ruopeng Liu, Jessie Y. Chin, Chunlin Ji, Tie Jun Cui and David R. Smith

**Abstract** In this chapter, we will discuss the approach of utilizing transformation optic approach and metamaterial technology to construct various cloaking devices in experiment. We take the advantage of rapid design approach to demonstrate the reduced cloaking device in free space. Then we discuss the next-generation cloaking device of broadband and low-loss feature. The experiment at microwave verifies the broadband complex cloaking design.

**Key words:** Transformation optics, metamaterial design, invisibility cloak, broadband metamaterials, rapid design for metamaterials, spatial dispersion, cloaking experiment.

## 6.1 Invisibility Cloak Design in Free Space

In Chapter 2, we discussed the transformation optics approach that enables a conceptual design on the invisibility cloak and also gave an example of a cloaking experiment in 2006 [6]. In this section, we will further discuss the details of such cloaking design and experiment and also illustrate a new set of cloaking design and experiment by applying the rapid design approach that has been discussed in Chapter 3.

The design on this particular cylindrical cloaking device employs the coordinate transform from a cylindrical volume to a shell excluding the object in the center. Assuming the inner radius is $a$ and outer radius is $b$, one can achieve the materials'

Ruopeng Liu[1], Jessie Y. Chin[2], Chunlin Ji[3], Tie Jun Cui[2*] and David R. Smith[1+]
[1]Center for Metamaterials and Integrated Plasmonics, Department of Electrical and Computer Engineering, Duke University, Durham, NC 27708, USA. [+]e-mail: drsmith@ee.duke.edu
[2]State Key Laboratory of Millimeter Waves, Southeast University, Nanjing 210096, China. [*]e-mail: tjcui@seu.edu.cn
[3]Department of Statistical Science, Duke University, Durham, NC 27708, USA

T.J. Cui et al. (eds.), *Metamaterials*, DOI 10.1007/978-1-4419-0573-4_6,

parameters by Eq. (6.1) and achieve that [6]

$$\begin{aligned}\mu_r &= \frac{r-a}{r},\\ \mu_\theta &= \frac{r}{r-a},\\ \varepsilon_z &= \left(\frac{b}{b-a}\right)^2 \frac{r}{r-a}\end{aligned} \tag{6.1}$$

for a TE polarization. However, such parameters are highly anisotropic and inhomogeneous and of singularity at the inner boundary $r = a$. Although the conceptual design provides the opportunity of a perfect invisibility, the practical implementation is limited by the finite response of metamaterials and complexity of 3D structure fabrication. To address this practical difficulty, Schurig et al. proposed a reduced design to the cylindrical cloaking device by relaxing the impedance requirement but remaining the refractive index to the materials. One can imagine a ray-tracing process to such reduced cloak. The remaining refractive index can allow the trajectory of wave propagation still rendering the object. Whereas the imperfect reflection and field distortion on transmission will unavoidably occur in reality. The reduced parameters design can then be achieved from Eq. (6.2) and be expressed by

$$\begin{aligned}\mu_r &= \left(\frac{r-a}{r}\right)^2,\\ \mu_\theta &= 1,\\ \varepsilon_z &= \left(\frac{b}{b-a}\right)^2.\end{aligned} \tag{6.2}$$

Although the first demonstration of cloaking experiment was far from perfect, the breakthrough on the concept and methodology has led this work to one of the most impact developments on metamaterials. To further study this experiment, we can find that such anisotropic and inhomogeneous media are implemented by a set of split ring resonators (SRRs). The change of geometry of SRR will allow the implementation of different local material properties. In the experiment in Fig. 6.1, 10 unique SRRs have been designed from inner layer to outer layer and to achieve $\mu_r = 0$–$0.278$. The traditional design process follows a loop that many full wave simulations have to be taken on various SRRs until the effective permittivity and permeability meet the requirement from transformation optics calculation at certain spatial point and certain frequency.

Therefore, in this cylindrical cloaking design, there are 10 unique structures. Approximately 10 iterations are needed to design a particular structure. One iteration will consume 5 min on the step of full wave simulations. Ideally a thousand minutes is requested to design a particular cloak at a particular frequency. This efficiency also challenges the metamaterial technology. To address this difficulty, we incorporate the rapid design approach described in Chapter 3. By employing the rapid design algorithm on metamaterial structure calculation, metamaterial response can be easily predicted and expressed in terms of analytical form based on the library built by pre-simulated data. Once the library of certain type of unit cell structure is built, it

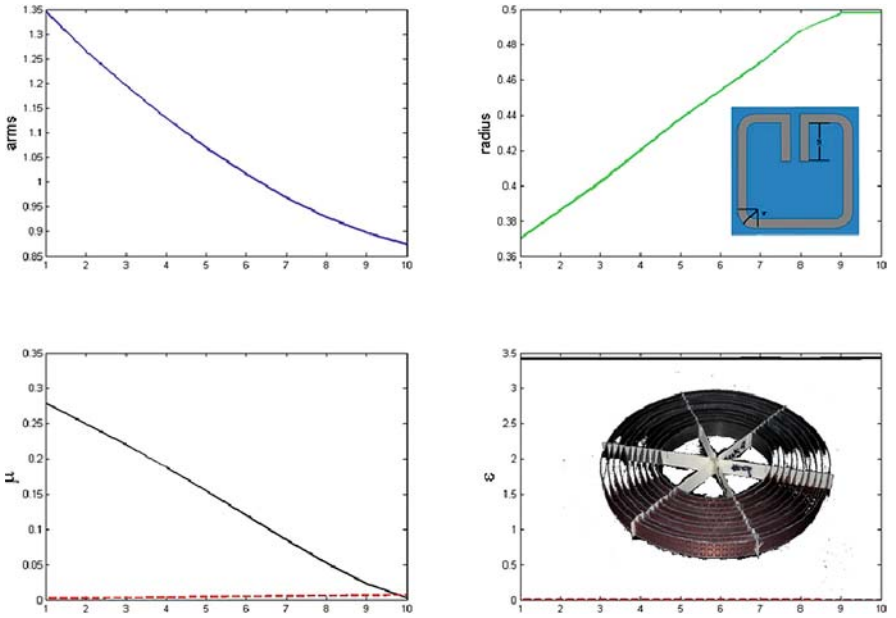


**Fig. 6.1** Rapid design for a reduced cloak, working at 10 GHz.

can be integrated together with the system-level design, experimental configuration, and fabrication requirement. The system-level design indicates the electromagnetic parameters requirement calculation. For example, transformation optics is a type of system-level design, from which required permittivity and permeability distributions for certain function can be calculated. The experimental configuration means the type of metamaterials, such as 1D transmission line metamaterials, 2D waveguided metamaterials, or 3D structural metamaterials. Different types of metamaterials have their special features for various applications, and thus appear different in the design system.

Applying the rapid design system, we can design the reduced cloak automatically and achieve the material's parameters and metamaterial structure geometry, for example, shown in Fig. 6.1. Based on the same design library, we designed and fabricated various different cloaks with different dimensions and operational frequencies. Figure 6.2 shows the fabricated cloaks by our sophisticated design system. The cloaks a, b & c are made on FR4substrate while the cloaks d & e are on Duroid5880 substrate withlower loss. Excluding the design library extraction (as we only did that once), all these different cloaking devices were designed in 10 s, comparing with a thousand minutes for a particular one in the past. Figure 6.3 shows the series of invisible cloak measurements. All the experiments are designed by the same structure library (Rogers Duroid5880 SRR unit cell) and measured within 0.1 GHz error around designed frequency from rapid design system, showing the accuracy of this rapid metamaterial design approach.

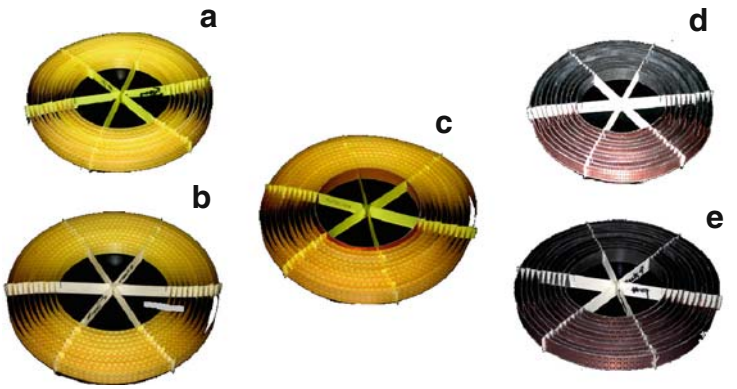


**Fig. 6.2** Fabricated invisible cloak by rapid design system.

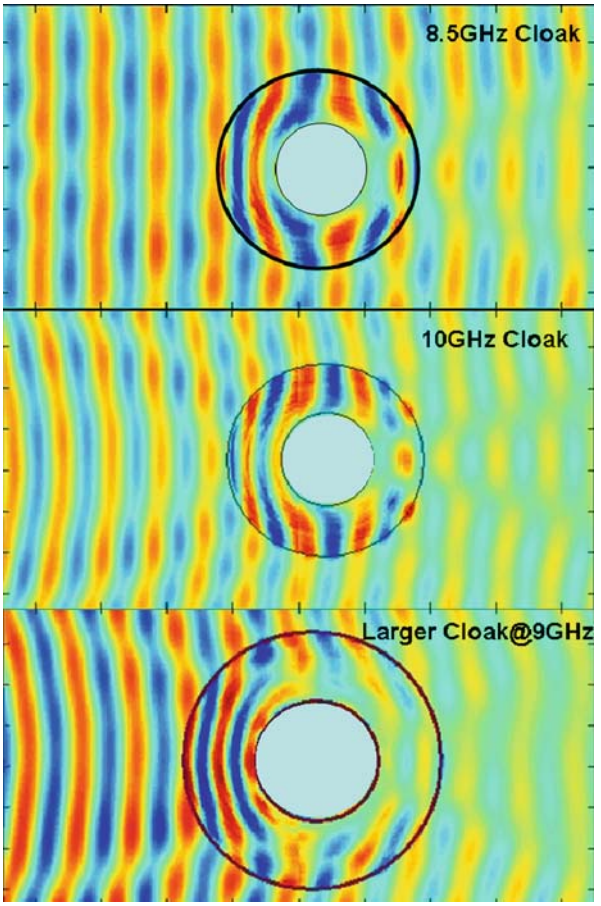


**Fig. 6.3** Invisible cloak measurement.

## 6.2 Transformation Optics Approach to Theoretical Design of Broadband Ground Plane Cloak

Transformation optics is a novel method for the design of complex electromagnetic media that offers new opportunities for the control of electromagnetic waves [5, 6]. Applying the transformation optical approach, a wide variety of devices can be designed with unique properties, including beam shifters, beam bends, beam splitters, focusing and collimating lenses, and structures that concentrate electromagnetic waves. However, one of the most compelling examples of the transformation optical technique has been the prescription for an invisibility cloak – a material that can be used to hide other objects from detection. The prospect of cloaking has proven a tantalizing prospect to the community, with numerous cloaking concepts currently being investigated.

The transformation optical approach is conceptually simple. One imagines warping space so as to control the trajectories of light in a desired manner. Light that flows in a straight line in the unwarped space instead follows a route in the warped space dictated by the details of the coordinate transformation that connects the two spaces. As what is now an iconic example of the transformation optical approach, an invisibility cloak can be conceptually constructed by poking a hole in space and compressing the space within a sphere to within a shell.

Although physically warping space is not an option, the coordinate transformation can be applied to Maxwells' equations. Because Maxwells' equations contain terms that define the properties of a material, the transformation can alternatively yield a specification for a medium in the form of spatially varying electric permittivity and magnetic permeability values. The resulting medium is highly complex, being anisotropic with spatial gradients in the tensor elements of the constitutive parameters. The prospect of realizing transformation optical structures then comes down to being able to find or construct the specified materials.

Though the specifications for transformation optical structures would generally be difficult to achieve using conventional materials, the prospects are much better for achieving them using artificially structured metamaterials. Over the past several years, metamaterials have been shown to possess a wide range of electromagnetic properties that would be difficult or even impossible to achieve with conventional materials. Moreover, the properties of metamaterials can be engineered with great precision over a broad range of frequencies and are well suited to implement the complex gradients required by transformation optical structures. In 2006, a cloak design was realized in a metamaterial sample, which demonstrated the cloaking mechanism over a narrowband of microwave frequencies.

The metamaterial cloak represented an approximation to the ideal cloak specification, arrived at by the transformation optical approach. In fact, the required constitutive parameters for the ideal cloaking structures are highly demanding even for metamaterials, generally requiring separate control over at least three of the constitutive parameters. An ideal metamaterial implementation of the cylindrical cloak has yet to be achieved. Also, given that some of the elements of the rela-

tive permittivity and permeability tensors must be between zero and unity, most cloak designs will need to be based on resonant elements. The use of these elements sets an inherent limit on the bandwidth over which the cloaking effect exists and leads to a greater dissipation of the waves as they propagate through the structure.

There are endless number of transformations that will arrive at a structure that will provide varying degrees of cloaking. The spherical and cylindrical cloaks considered in 2006 both have singular regions that necessitate rather extreme values for some of the constitutive tensor elements (elements that require values near zero or approach infinity, for example). However, if certain conditions are relaxed, it is possible to design structures that are practically much more achievable. In a recent theoretical study, Li and Pendry describe the design of a structure that can cloak objects placed on a conducting sheet. Though a more limited form of cloaking, the required constitutive parameters for this ground-plane cloak are much easier to achieve with the metamaterial techniques currently available.

To design the ground plane cloak, Li and Pendry first restrict the problem to a 2D plane of uniform dielectric value $\varepsilon_b$ with the electric field assumed polarized out of the plane (transverse electric polarization). In general, the transformation would lead to an anisotropic medium with values of $\varepsilon_z$, $\mu_x$, and $\mu_y$ that vary as a function of the spatial coordinate. Because there are infinite number of coordinate maps that will lead to the same cloaking behavior, Li and Pendry search for a map that minimizes the anisotropy in the permeability components. Defining an anisotropy factor as $\alpha = max(n_x/n_y, n_y/n_x)$, it is possible to find transformations for which $\alpha$ is near unity. For such transformations, the permeability can be simply set to unity and the permittivity varied. If the background dielectric in the original space is sufficiently greater than unity, then the values for the permittivity of the cloaking structure are always greater than unity; this feature allows the possibility of utilizing non-resonant metamaterial elements and thus making the cloak broadband.

Following the procedure outlined by Li and Pendry, we design a ground plane cloak that minimizes the anisotropy factor. Li and Pendry stated that the quasiconformal map [3], generated by minimizing the modified-Liao functional [2] upon slipping boundary condition, minimizes the anisotropy in the permeability components. Numerical mapping technique is then applied to achieve the Jacobian matrix $\Lambda$ of quasiconformal mapping from the physical system and virtual system, and then the required index distribution $n^2 = \frac{1}{\sqrt{|\Lambda^T \Lambda|}}$. In our final design, $\alpha = 1.04$, which we treat as negligible (that is, we assume $n_x = n_y = 1$). A color map indicating the transformed space and the associated refractive index distribution is shown in Fig. 6.4. (The final map is generated numerically by the optimization procedure, so there are no closed-form analytic expressions that define the transformation.) To simplify the design so that non-resonant metamaterial elements can be used, we assume the entire cloak is embedded in a background material with refractive index $n = 1.331$. Under these assumptions, the transformation leads to refractive index values for the ground plane cloak that range from $n = 1.08$ to 1.67. Note on the right and left sides of the cloak, the refractive index distribution is uniform, taking the value of the background material.

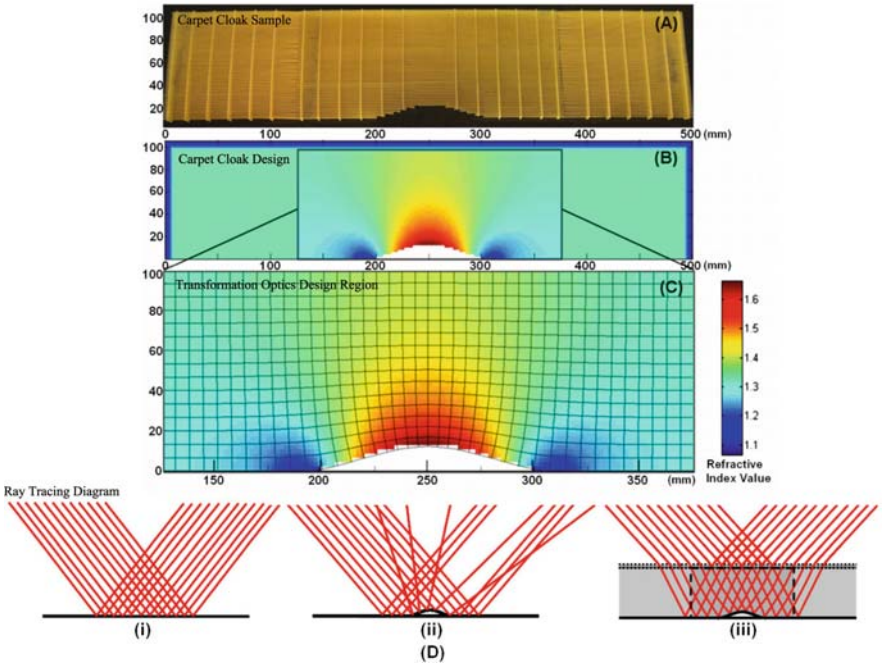


**Fig. 6.4** The transformation optics design for carpet cloak embedded with background materials and impedance matching layers. The *white part* is the object supposed to be hid and *meshing line* indicates the quasi-conformal mapping. The *color map* shows the designed refractive index distribution. From Ref. [4].

Because it is convenient to launch waves in free space, the homogeneous background material in which the cloak is embedded presents a complication, since incident waves from free space will encounter an impedance mismatch and scatter. To avoid this complication, we add an impedance matching layer (IML) around the structure, for which the index changes gradually and linearly from the index of air to the background dielectric. Although the entire configuration is not hidden from detection by the incident waves from free space, the embedded IML and cloak structure can render an object invisible inside the background medium and above the ground plane. Because of the index gradient coupled with the cloak, we expect no amplitude scattering and only a slight redirection of the wave reflected from the ground plane structure. The effect should be similar to observing a mirror through an extremely thin, glass plate; objects on top of the mirror remain hidden from detection.

Because the required index distribution for both the IML and the cloak always take values greater than unity, it is possible to utilize metamaterial elements far from resonance to implement the cloak. For example, a short wire has a very high frequency resonant permittivity of the form

$$\varepsilon(w) = 1 - w_p^2/(w^2 - w_0^2 + iw\gamma), \tag{6.3}$$

where $w_p$, $w_0$, and $\gamma$ can be related to the geometry of the wire and the size of the gap between wires. If the resonance of the wire is at very high frequency compared with the frequency range of use, then the permittivity reduces to the form of $\varepsilon(w) = 1 + w_p^2/w_0^2$, which can easily be tuned from unity to large positive and non-dispersive values. Non-resonant elements have been used to construct a variety of broadband and low-loss gradient index optical elements at microwave frequencies.

## 6.3 Metamaterial Structure Design to Implement Ground-Plane Cloak

To implement the transformation optical design for the ground plane cloak, we make use of the I-shaped particle shown in Fig. 6.5. Following a well-established retrieval process, the effective permittivity for a given element can be found. By varying the geometry, a range of refractive index values can be obtained as illustrated in the inset to Fig. 6.5, according to which a regression can be made to relate the refractive index value with geometry dimension $a$. The transformation optical design in Fig. 6.4 can thus be implemented by utilizing the metamaterial unit cell variations shown in Fig. 6.5. The assembled cloak, shown also in Fig. 6.1, contains more than 60,000 unit cells – roughly half of which are distinct – and is fabricated on copper-clad printed circuit board with FR4 substrate (the substrate thickness is 0.2026 mm with a dielectric constant of 3.85+i*0.02). The completed sample is 500 mm by 106 mm with a height of 10 mm, in which the center 250 mm by 96 mm corresponds to the transformed region. The shape of the object hidden within the ground plane cloak follows the curve $y = 12 * cos^2((x - 125)\pi/125)$ (units in mm), analogous to the perturbation considered by Li and Pendry.

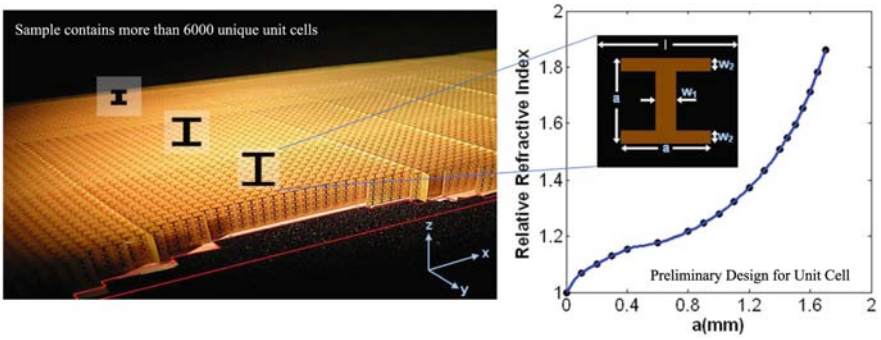


**Fig. 6.5** The unit cell design of the non-resonant element and fabricated sample according to the relationship between the geometry dimension and effective index. From Ref. [4].

To address the numerical burden associated with the design of such a large-scale metamaterial structure, we have automated several aspects of the design process,

enabling us to produce thousands of unique metamaterial elements rapidly that are consistent with the optimized transformation optical map. We define as system level the overall spatially varying constitutive parameters defined by the transformation optical procedure and define as particle level the design of the constituent elements that form the metamaterial implementation. The first step of the automated design process – the system-level design – employs numerical computation of the transformation optical mapping. The arbitrary shape of the cloaked perturbation can be modeled by a free curve regression. We then numerically computed the relationship at every spatial point between the original space and the transformed space by using a quasi-conformal mapping algorithm [2]. Once the mapping has been determined numerically, the transformation optics formula can then be used to calculate the permittivity and permeability tensors, in which a numerical derivative is taken. The conclusion of the first step, or the system-level design, results in the spatial distribution of the constitutive parameters.

The second step in the process is to design and calculate the physical dimensions and structure for each unit cell that forms the cloaking. This step is the particle-level design step. We note that Li and Pendry [3] suggested a transformation optical (system-level) design in which the permeability should remain unity everywhere and only the permittivity varies. Such a transformation would imply the particle-level design should be relatively straightforward, since only electric response would be necessary to control. However, metamaterial structures, even those based on non-resonant elements, always exhibit spatial dispersion (i.e., constitutive parameters that depend on the direction of wave propagation) due to the finite size of the unit cell relative to the wavelength. The impact of spatial dispersion is to introduce frequency dispersion into the constitutive parameters, which leads to a frequency-dependent magnetic response in addition to that of the frequency-dependent electric response, as shown in Fig. 6.6.

Thus, it is necessary to consider the spatial dispersion associated with each unit cell as part of the particle-level design process. We incorporate all of the details associated with the finite unit cell into the design procedure using a quasi-analytical method previously described [3]. The complete response of the metamaterial element, including the effects of spatial dispersion, can then be mathematically modeled by linear or nonlinear regression. Once we choose one or several physical dimensions of the unit cell as variables for a given unit cell topology, we can then build a mathematical model to express the dispersive constitutive parameters via sampling a small set of unit-cell structures whose properties are computed by full wave simulations. Once the library of a certain type of structure is built, a rapid searching algorithm, such as the sequential Monte Carlo, can be applied to determine the appropriate physical dimension of the structure that achieves the required refractive index and impedance.

In our design, the refractive index remains approximately constant with frequency but the impedance may vary as a function of frequency for different unit cell designs. In the final cloak, the unit cells on the periphery of the structure are designed to have an impedance that is non-dispersive, while the impedances of the unit cells within the cloaking region change continuously as a function of the spatial co-

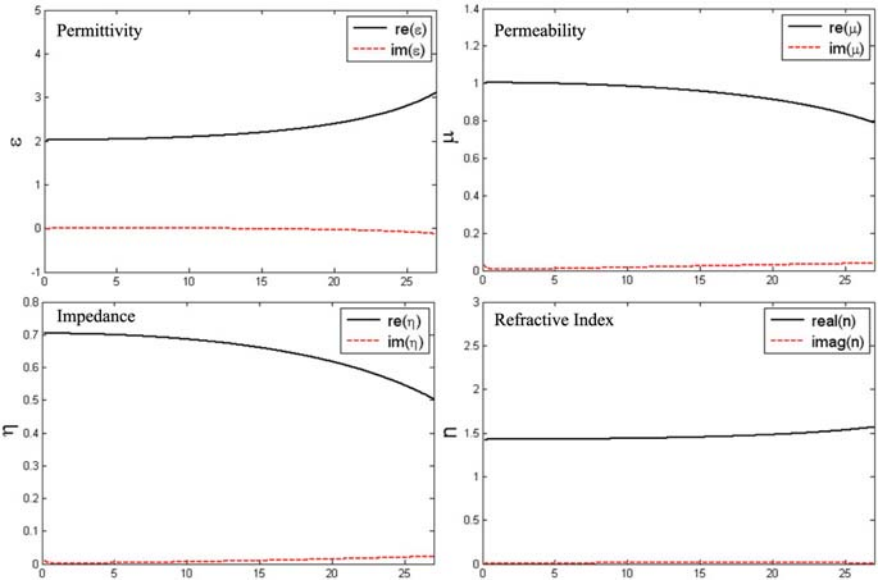


**Fig. 6.6** Effective permittivity, permeability, impedance, and refractive index of I-shaped unit cell with the dimension $a = 1.4$ mm. From Ref. [4].

ordinate at all operational frequencies. The waves thus neither reflect at the outside edge of the cloak nor inside the cloak due to the careful design of the outside edge unit cells and the gradually varying impedance. Integrating all of these constraints into the optimization algorithm, we arrive at a metamaterial element (as shown in Fig. 6.5) for which the refractive index value of the element can be directly related to its physical dimensions.

The final step of the process is to take each unit cell geometry determined in the particle-level design step and generate a large-scale mask of the entire layout for fabrication by printed circuit board (PCB) lithographic methods. The final mask, shown in Fig. 6.7, has more than 30,000 unit cells with more than 6,000 unique unit cells. The mask is generated by the same Matlab program that also performs the first two steps, so that the entire process – system- and particle-level designs, followed by layout and mask generation – is combined together. The Matlab program has calls to AutoCAD functions that draw all of the unit cells into the layout, producing the final mask [4].

## 6.4 Experimental Measurement Platform

Figure 6.8(a) shows a top view of the closed mapping apparatus with six coaxial cables running from a switch to six antenna positions. Microwave measurements are made by a vector network analyzer and the planar waveguide fields are launched by

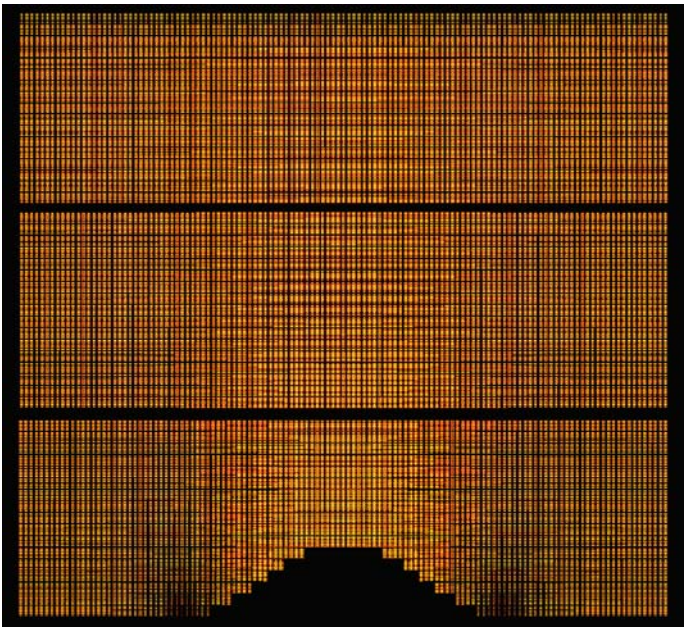

**Fig. 6.7** Ground-plane cloak mask (transformation region) generated by automatic design system. Not shown here are the cutting outlines, with slots for assembly, around which each strip (5 unit cells, 10 mm, in height) is cut out by circuit board prototype milling machine (LPRF). From Ref. [4].

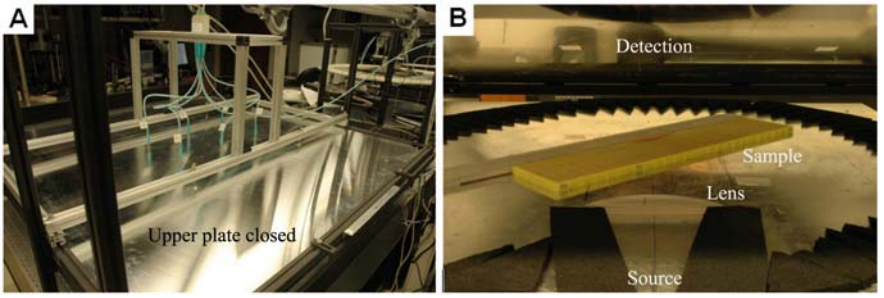


**Fig. 6.8** Ground-plane cloak mask (experimental apparatus for the ground-plane cloak measurement). The apparatus consists of two metal plates separated by 1 cm, which form a 2D planar waveguide region. From Ref. [4].

an X-band waveguide coupler toward a polycarbonate collimating lens, as shown in the open chamber view of Fig. 6.8(b), which creates the narrow beam seen in the measurements. This beam is reflected off of the ground plane at an angle of about 40° from the surface normal. By scanning the top plate (with detector antenna) relative to the bottom plate (and sample) with 181 × 181 1 mm steps, we can create

a field map of the microwave beam incident on the ground-plane cloak. Due to the large area required for characterizing the full incident and reflected beams, at each plate step we simultaneously measure the electric field from four distinct antenna positions using the switch. These four scan areas can then be patched together into one large field map using Matlab code to match up the phase and amplitude at the boundaries of each probe region.

Comparing the reflection from the ground plane, the ground plane with the perturbation and the ground plane with the cloaked perturbation (shown in Fig. 6.8(b)), we can demonstrate the cloaking effect. Broadband performance is confirmed from mapping the field incident upon the cloak for 13–16 GHz for this certain experiment. While we expect that the cloak would work for much lower and higher frequencies, we do not obtain clean measurements due to constraints of the experimental apparatus. The beam, formed by the finite width polycarbonate lens and used to illuminate the ground plane, is distorted by diffraction for frequencies $<13$ GHz and, at the other end of the spectrum, propagating fields become multimode within the planar waveguide for frequencies $>16$ GHz [4].

## 6.5 Field Measurement on the Ground-Plane Cloak

To verify the predicted behavior of the ground-plane cloak design, we make use of a phase-sensitive, near-field microwave scanning system to map the electric field distribution inside a planar waveguide. The planar waveguide restricts the wave polarization to transverse electric. The details of the apparatus have been described previously [1]. A large area field map of the scattering region, including the collimated incident and scattered beams, is shown in Fig. 6.9. The waves are launched into the chamber from a standard X-band coax-to-waveguide coupler and pass through a dielectric lens that produces a nearly collimated microwave beam. The beam is arbitrarily chosen to be incident on the ground plane at an angle of $40^\circ$ with respect to the normal. A flat ground plane produces a near-perfect reflection of the incident beam in Fig. 6.9(a), while the presence of the perturbation produces considerable scattering in Fig. 6.9(b) (note the presence of the strongly scattered secondary beam). By covering the space surrounding the perturbation with the metamaterial cloaking structure, however, the reflected beam is restored, as if the ground plane were flat in Fig. 6.9(c). The beam is slightly bent as it enters the cloaking region due to the refractive index change of the embedding material but is bent back upon exiting. The gradient index IML introduced into the design minimizes reflections at the boundaries of the cloaking region.

As the ground-plane cloak makes use of non-resonant elements, it is expected to exhibit a large frequency range of operation. The cloaking behavior was confirmed in our measurements from the range 13 to 16 GHz, though we expect the bandwidth

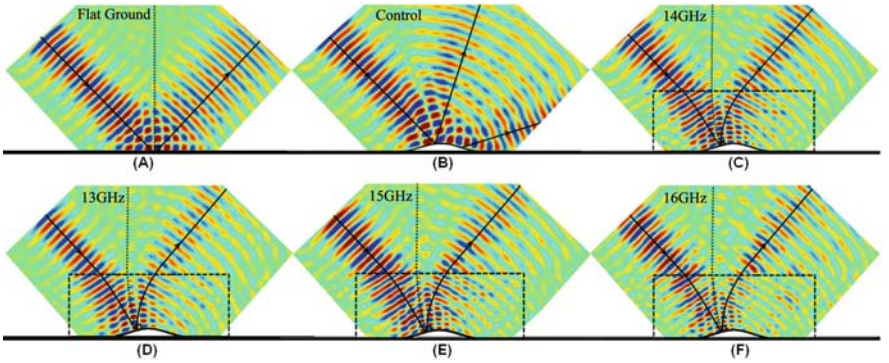


**Fig. 6.9** Measured field mapping (E-field) of the ground, perturbation, and ground-plane cloaked perturbation. The rays display the wave propagation direction and the *dash line* indicates the normal of the ground in the case of free space and that of the ground-plane cloak in the case of the transformed space. (**a**) A collimated beam incident on the ground plane at 14 GHz, (**b**) a collimated beam incident on the perturbation at 14 GHz (control), (**c**) a collimated beam incident on the ground-plane cloaked perturbation at 14 GHz, (**d**) a collimated beam incident on the ground-plane cloaked perturbation at 13 GHz, (**e**) a collimated beam incident on the ground-plane cloaked perturbation at 15 GHz, and (**f**) a collimated beam incident on the ground-plane cloaked perturbation at 16 GHz. From Ref. [4].

to actually stretch to very low frequencies (less than 1 GHz) which cannot be verified experimentally due to limitations of the measurement apparatus and the beam forming lens. We illustrate the broad bandwidth of the cloak with the field maps taken at 13 GHz in Fig. 6.9(d), 15 GHz in Fig. 6.9(e) and 16 GHz in Fig. 6.9(f), which shows similar cloaking behavior to the map taken at 14 GHz in Fig. 6.9(c). The collimated beam at 16 GHz has begun to deteriorate due to multimode propagation in our 2D measurement chamber, which is also observed in the flat ground plane control experiment at that frequency (not shown here). However, based on the predicted response of the broadband unit cells we expect this cloak to function up to approximately 18 GHz.

To further visualize the performance of the ground-plane cloak, we illuminated the sample from the side (90° from the surface normal) with a narrow collimated beam. As the ground-plane cloaked perturbation should also be cloaked with respect to an observer located on the ground, the wave, which should follow the metric as defined by the quasi-transformation map in Fig. 6.4, can be expected to detour around the perturbation and then return back to its original propagation direction. The field map for this case is shown in Fig. 6.10(b), which corresponds with the predicted transformation extremely well (a low-resolution representation of the transformation grid is overlaid on the experimental data). For comparison, Fig. 6.10(a) shows a map of the field strongly scattered from the perturbation in the absence of the cloak [4].

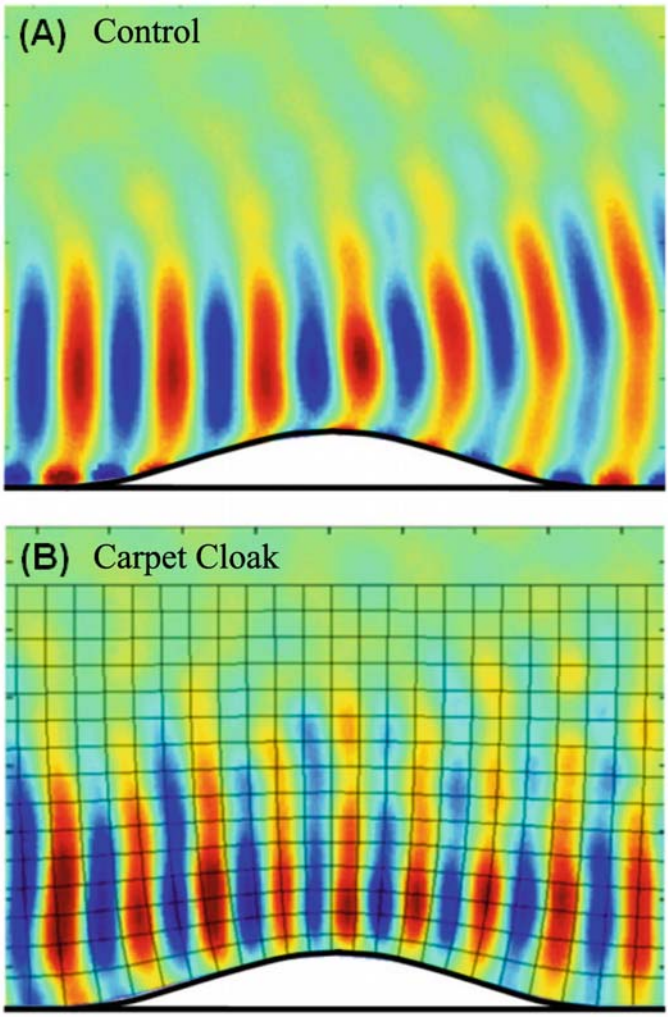


**Fig. 6.10** Two-dimensional field mapping (E-field) of the perturbation and ground-plane cloaked perturbation, illuminated by the waves from the left side (**a**) perturbation, (**b**) ground-plane cloaked perturbation. The grid pattern indicates the quasi-conformal mapping of the transformation optics material parameters. From Ref. [4].

## 6.6 Power and Standing Wave Measurement on the Ground-Plane Cloak

To study the cloaking effect in more detail, we conducted standing wave measurement and observe the intensity pattern within the transformed area on both control and cloaking cases. In either of them, the incident and the reflected waves produce a standing wave pattern that we use as a measure of the scattering produced by the

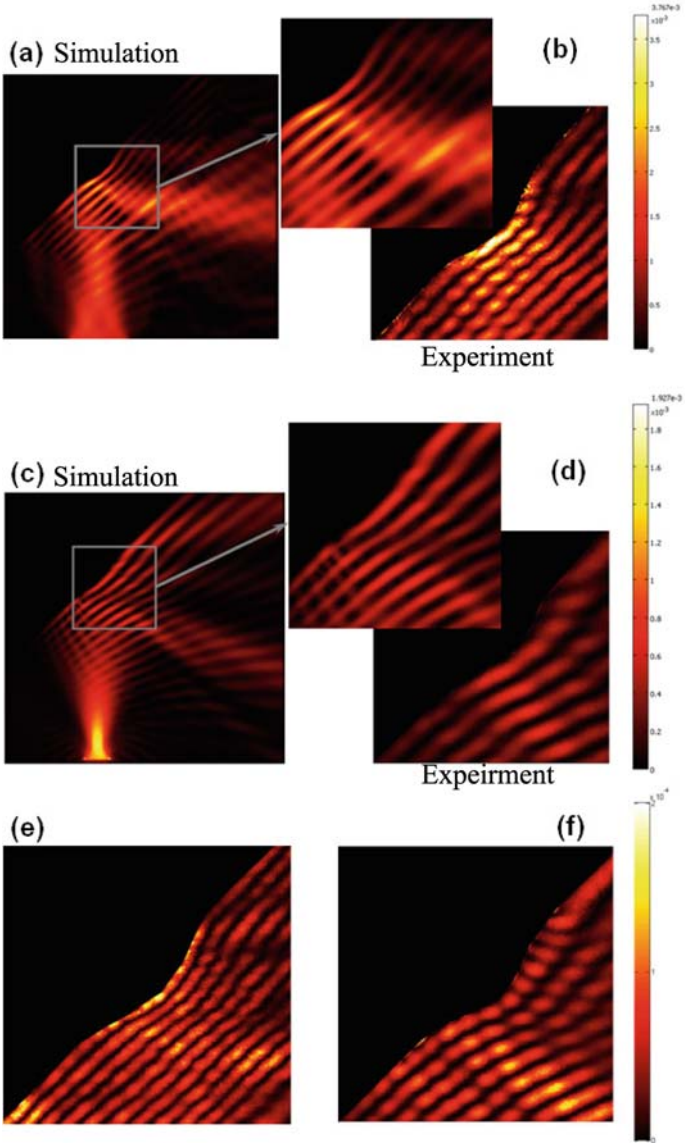


**Fig. 6.11** Power plot of the standing waves of the carpet cloak and control by simulation and experiment: (**a**) simulated power plot of only ground at 14 GHz; (**b**) simulated power plot of carpet cloak at 14GHz; (**c**) simulated control scatter at 14 GHz; (**d**) experimental power plot of only ground at 14 GHz; (**e**) experimental power plot of carpet cloak at 14 GHz; (**f**) experimental power plot of control scatter at 8 GH; and (**g**) experimental power plot of carpet cloak at 8 GHz. From Ref. [4].

perturbation on the ground plane. In the absence of the cloak, the ground plane is no longer flat, and the perturbation introduces a significant distortion into the standing wave pattern; in particular, the interference pattern is no longer parallel to the plane, as can be seen in Fig. 6.11(a). However, when the ground plane cloak is present, the perturbation is effectively removed from detection and the standing waves pattern is once again parallel with the ground, as shown in Fig. 6.11(b). Moreover, since the cloak makes use of elements far away from resonance, the metamaterial cloak can be seen to have a large bandwidth, at least over the range 8–14.8 GHz confirmed in our experiment. The bandwidth of cloak is anticipated to stretch from very low frequencies (less than 1 GHz) to around 17 GHz, where the first resonance of the metamaterial elements occurs. The broad bandwidth of the cloak is illustrated by the power maps taken at 8 GHz in Fig. 6.11(c) and (d), which show the identical behavior to the maps taken at 14 GHz [4].

## 6.7 Conclusion

The experiment on reduced cloak and broadband ground-plane cloak provided solid evidence of the controllability to electromagnetic waves by metamaterial technology and transformation optic approach. The complex media can be designed and constructed by metamaterials efficiently by using rapid design approach. The bandwidth and loss performance can be dramatically improved by taking use of non-resonant element metamaterials. Although the progress of cloaking device design is in the initial step, the underlying technology offers a unique approach to control electromagnetic wave propagation by complex media and will have great potential in various RF and optical applications in the future.

## References

1. Justice, B.J., Mock, J.J., Guo, L.H., Degiron, A., Schurig, D., Smith, D.R.: Spatial mapping of the internal and external electromagnetic fields of negative index metamaterials. Opt. Express **14**, 8694 (2006)
2. Knupp, P., Steinberg, S.: Fundamentals of grid generation. CRC Press, Boca Raton (1994)
3. Li, J., Pendry, J.B.: Hiding under the carpet: a new strategy for cloaking. Phys. Rev. Lett. **101**, 203901 (2008)
4. Liu, R., Ji, C., Mock, J.J., Chin, J.Y., Cui, T.J., Smith, D.R.: Broadband ground-plane cloak. Science **323**, 366 (2009)
5. Pendry, J.B., Schurig, D., Smith, D.R.: Controlling electromagnetic fields. Science **312**, 1780 (2006)
6. Schurig, D., Mock, J.J., Justice, B.J., Cummer, S.A., Pendry, J.B., Starr, A.F., Smith, D.R.: Metamaterial electromagnetic cloak at microwave frequencies. Science **314**, 977–980 (2006)

# Chapter 7
# Finite-Difference Time-Domain Modeling of Electromagnetic Cloaks

Christos Argyropoulos, Yan Zhao, Efthymios Kallos and Yang Hao

**Abstract** A radially dependent dispersive finite-difference time-domain (FDTD) method is proposed to simulate electromagnetic cloaking devices. The Drude dispersion model is applied to model the electromagnetic characteristics of the cloaking medium. Both lossless and lossy cloaking materials are examined and their operating bandwidth investigated. It is demonstrated that the perfect "invisibility" of electromagnetic cloaks is only available for lossless metamaterials and within an extremely narrow frequency band. Spherical cloaks are simulated and investigated with a parallel dispersive FDTD technique. Finally, ground-plane cloaking devices are examined and analyzed with non-orthogonal and orthogonal FDTD methods.

**Key words:** Metamaterials, cloaking, transformation electromagnetics, carpet cloaking, ground-plane cloaking, dispersion, FDTD, non-orthogonal FDTD, Drude model, bandwidth, absorber, dielectric materials, conformal mapping, cylindrical cloak, spherical cloak, invisibility cloak.

Christos Argyropoulos*
Department of Electronic Engineering, Queen Mary, University of London, London, E1 4NS, U.K.,
*e-mail: christos.a@elec.qmul.ac.uk

Yang Hao+
Department of Electronic Engineering, Queen Mary, University of London, London, E1 4NS, U.K.,
email: yang.hao@elec.qmul.ac.uk

Yan Zhao
Department of Electronic Engineering, Queen Mary, University of London, London, E1 4NS, U.K.,
email: yan.zhao@elec.qmul.ac.uk

Efthymios Kallos
Department of Electronic Engineering, Queen Mary, University of London, London, E1 4NS, U.K.,
email: themos.kallos@elec.qmul.ac.uk

T.J. Cui et al. (eds.), *Metamaterials*, DOI 10.1007/978-1-4419-0573-4_7,

## 7.1 Introduction

Cloaking devices have received unprecedented attention from the scientific community. Based on the form invariance of Maxwell's equations, linear coordinate transformations have been applied in order to manipulate the electromagnetic characteristics of the propagation medium [38, 31, 30]. These techniques are inspired from the theory of General Relativity and conformal mapping procedures. After the transformations, the medium produced is able to guide the electromagnetic waves around an object without any disturbances and reflections. This is equivalent to waves propagating through free space. Hence, the object placed inside the cloak becomes practically "invisible" to an external observer. The permittivity and permeability of such cloaking devices are in general anisotropic and dispersive, as first demonstrated by Pendry et al. [38].

The implementation of cloaks relies on metamaterials [51], which are artificially constructed materials with extraordinary electromagnetic properties that cannot be obtained in nature. In practice, it is easier to implement the cloaking device when some of the material parameters are spatially uniform. To solve this problem, approximate cloaks using reduced parameter sets were proposed in [15, 5, 53], operating at different polarizations. A simplified cloaking device was constructed and tested at microwave frequencies, with promising results [44]. Currently, there are efforts for an experimental verification of cloaking at optical frequencies. One of them uses silver nanowires with subwavelength dimensions embedded in a silica dielectric host [5]. Another approach uses a concentric structure made of a layered gold-dielectric material [47]. Finally, cloaks derived from a higher-order coordinate transformation [7] have been proposed for a future optical cloaking device [6].

Due to causality constraints, metamaterials are often frequency dispersive and, hence, have limited bandwidth. These limitations are thoroughly analyzed in [11] and [56]. Another drawback of metamaterials is their lossy nature [39]. To avoid using anisotropic elements, an alternative approach was proposed [23], constructing the cloaking shell from layers of homogeneous isotropic materials with subwavelength dimensions. However, it is difficult to realize this structure, due to the alternating values of permittivity required for different layers of the cloaking device. A different approach, which applied sensors and active sources near the surface of the cloaked object, has been described in [35] and can be functional in a broader bandwidth. Finally, wider bandwidth cloaking applications can be achieved, if the hard surface (meta-surface) concept [25, 26, 19] is employed to construct the cloaking device.

Apart from the traditional cylindrical and spherical cloaking structures, many interesting potential applications have been proposed, derived from different coordinate transformations. The technique was used for the construction of elliptic [28] and square [42] cloaks. Moreover, it has been applied to achieve cloaking in the acoustic frequency spectrum [16, 9]. Other proposed devices are carpet cloaking structures [32, 34], concave mirrors for all angles [55], super-absorbers [37], field concentrators [42], spherical [50] and cylindrical [54] superlens, flat near-field and far-field focusing lenses [46], reflectionless phase shifters and beam splitters [40],

field rotators [10], adaptive beam benders and expanders [41], and novel antenna designs [27, 24].

This chapter focuses on the simulation and characterization of cloaking devices. The lossless cloaking structure has been modeled analytically in [38, 31, 45]. A cylindrical wave expansion technique was used to simulate a lossless cylindrical cloak in [43]. An analytical method, based on the Mie scattering model, was proposed to exploit the lossy spherical [12] and cylindrical [57] cloaking structures. The commercial simulation package COMSOL Multiphysics$^{TM}$ has been widely used to model different cloaks and to compare theoretical predictions [15, 5, 7, 28, 42]. It uses the finite element method (FEM), a frequency-domain numerical method. However, such frequency-domain techniques can become inefficient if a wideband solution is desirable. The cloak has also been modeled analytically in the time-domain [52], using a time-dependent scattering theory. The cloaking structure was first simulated with the finite-difference time-domain (FDTD) method in [59]. Another FDTD cloaking model, employing the Lorentz dispersive model, is presented in [33]. Here, we present a radially-dependent dispersive FDTD method to model lossless and lossy cloaking devices and evaluate their bandwidth limitations. The auxiliary differential equation (ADE) method [17] is used, based on the Drude model, to produce the updating FDTD equations. This dispersive FDTD method is a more general approach to the previously proposed numerical technique [59] and has been expanded to model three-dimensional (3-D) spherical cloaks. Finally, the newly introduced isotropic ground-plane cloaks [32] are examined and analyzed using both conformal and the Yee's FDTD methods. The proposed numerical methods are able to fully exploit the cloaking phenomenon and the physical insight.

## 7.2 FDTD Modeling of Two-Dimensional Lossy Cylindrical Cloaks

### *7.2.1 Derivation of the Method*

The FDTD method is based on the temporal and spatial discretization of Faraday's and Ampere's Laws, which are

$$\nabla \times \boldsymbol{E} = -\frac{\partial \boldsymbol{B}}{\partial t}, \tag{7.1}$$

$$\nabla \times \boldsymbol{H} = \frac{\partial \boldsymbol{D}}{\partial t}, \tag{7.2}$$

where $\boldsymbol{E}$, $\boldsymbol{H}$, $\boldsymbol{D}$, and $\boldsymbol{B}$ are the electric field, magnetic field, electric flux density, and magnetic flux density components, respectively. Note that harmonic time dependence $\exp(j\omega t)$ of the field components is assumed throughout this chapter. For the dispersive FDTD method, the constitutive equations have also to be discretized; they are given by the following equations:

$$\boldsymbol{D} = \varepsilon \boldsymbol{E}, \tag{7.3}$$

$$\boldsymbol{B} = \mu \boldsymbol{H}, \tag{7.4}$$

where the permittivity $\varepsilon$ and permeability $\mu$ can have either scalar or tensor form. For the following cloaking structure modeling, the ADE FDTD technique was employed. Both Faraday's and Ampere's laws were discretized with the common procedure [48]; the conventional updating FDTD equations are

$$\boldsymbol{H}^{n+1} = \boldsymbol{H}^{n} - \left(\frac{\Delta t}{\mu}\right) \cdot \widetilde{\nabla} \times \boldsymbol{E}^{n+\frac{1}{2}}, \tag{7.5}$$

$$\boldsymbol{E}^{n+1} = \boldsymbol{E}^{n} + \left(\frac{\Delta t}{\varepsilon}\right) \cdot \widetilde{\nabla} \times \boldsymbol{H}^{n+\frac{1}{2}}, \tag{7.6}$$

where $\Delta t$ is the temporal discretization, $\widetilde{\nabla}$ is the discrete curl operator, and $n$ is the number of the current time step.

The full set of electromagnetic parameters of the cloaking structure, in cylindrical coordinates, is given by the following [15]:

$$\varepsilon_r(r) = \mu_r(r) = \frac{r - R_1}{r}, \quad \varepsilon_\phi(r) = \mu_\phi(r) = \frac{r}{r - R_1},$$
$$\varepsilon_z(r) = \mu_z(r) = \left(\frac{R_2}{R_2 - R_1}\right)^2 \frac{r - R_1}{r}, \tag{7.7}$$

where $R_1$ is the inner radius, $R_2$ the outer radius, and $r$ an arbitrary radius of the cloaking structure. The ranges of the cloaking parameters were derived from Eq. (7.7):

$$\varepsilon_r, \mu_r \in \left[0, \frac{(R_2 - R_1)}{R_2}\right], \quad \varepsilon_\phi, \mu_\phi \in \left[\frac{R_2}{(R_2 - R_1)}, \infty\right], \quad \varepsilon_z, \mu_z \in \left[0, \frac{R_2}{(R_2 - R_1)}\right].$$

It is observed that the values of $\varepsilon_r$ and $\mu_r$ are always less than 1 as $r$ varies between $R_1$ and $R_2$, the values of $\varepsilon_z$ and $\mu_z$ are less than 1 for some points of $r$, and the values of $\varepsilon_\phi$ and $\mu_\phi$ are always greater than 1, as with conventional materials. Thus, the conventional FDTD method cannot correctly simulate materials with the properties of $\varepsilon_r, \mu_r, \varepsilon_z, \mu_z$ and new dispersive FDTD techniques must be developed, as with FDTD simulation of left-handed metamaterials (LHMs) [60]. The material parameters were mapped with the well-known and widely used Drude dispersive material model, for example, the frequency-dependent permittivity can be written as

$$\hat{\varepsilon}_r = 1 - \frac{\omega_p^2}{\omega^2 - j\omega\gamma}, \tag{7.8}$$

where $\omega_p$ is the plasma frequency and $\gamma$ is the collision frequency, which characterizes the losses of the dispersive material. The plasma frequency $\omega_p$ was varied in order to simulate the material properties of the radially-dependent parameters,

as given in Eq. (7.7). The required lossy permittivity can also be presented in an alternative way by the formula $\hat{\varepsilon}_r = \varepsilon_r(1 - j\tan\delta)$, where $\varepsilon_r$ is radially dependent and $\tan\delta$ is the loss tangent of the cloaking material. Substituting this formula into Eq. (7.8) and simplifying gave the following analytical equations for the plasma and collision frequencies:

$$\omega_p^2 = (1 - \varepsilon_r)\omega^2 + \varepsilon_r \omega\gamma\tan\delta, \tag{7.9}$$

$$\gamma = \frac{\varepsilon_r \omega\tan\delta}{(1 - \varepsilon_r)}. \tag{7.10}$$

From Eqs. (7.9) and (7.10), it is obvious that both plasma and collision frequencies vary according to the radius of the cloaking device. Moreover, the plasma frequency is also dependent on the losses of the material represented by $\tan\delta$ and $\gamma$. The permeability can be described using the same Drude model, though, there have been some examples where the Lorentz model were applied.

The $\varepsilon_\phi$ parameter always has values greater than 1 and was simulated with the conventional lossy dielectric material model:

$$\hat{\varepsilon}_\phi = \varepsilon_\phi + \frac{\sigma}{j\omega}, \tag{7.11}$$

where the parameter $\varepsilon_\phi$ is dependent on the radius of the cloaking shell as in Eq. (7.7) and $\sigma$ is a measurement of the conductivity losses. The loss tangent for the lossy dielectric material is given by $\tan\delta = \sigma/\omega\varepsilon_\phi$. It is also radially dependent, because it is a function of the $\varepsilon_\phi$ parameter. The two-dimensional (2 D) transverse electric (TE) polarized incidence was used during simulations, without loss of generality, reducing the non-zero fields to three components $E_x, E_y$, and $H_z$. For TE wave polarization, only three parameters from the full set (7.7) are employed: $\varepsilon_r$, $\varepsilon_\phi$, and $\mu_z$.

The classical Cartesian FDTD grid was used in the modeling and the previously mentioned parameters were transformed from the cylindrical coordinates $(r, \phi, z)$ to the Cartesian ones $(x, y, z)$, as given below:

$$\begin{aligned}
\varepsilon_{xx} &= \hat{\varepsilon}_r \cos^2\phi + \hat{\varepsilon}_\phi \sin^2\phi, \\
\varepsilon_{xy} = \varepsilon_{yx} &= (\hat{\varepsilon}_r - \hat{\varepsilon}_\phi)\sin\phi\cos\phi, \\
\varepsilon_{yy} &= \hat{\varepsilon}_r \sin^2\phi + \hat{\varepsilon}_\phi \cos^2\phi.
\end{aligned} \tag{7.12}$$

Hence, the constitutive equation – Eq. (7.3) – is given in tensor form by

$$\begin{pmatrix} D_x \\ D_y \end{pmatrix} = \varepsilon_0 \begin{pmatrix} \varepsilon_{xx} & \varepsilon_{xy} \\ \varepsilon_{yx} & \varepsilon_{yy} \end{pmatrix} \begin{pmatrix} E_x \\ E_y \end{pmatrix}. \tag{7.13}$$

From Eq. (7.13), it can be detected that

$$\begin{cases} \varepsilon_0 \varepsilon_{xx} E_x + \varepsilon_0 \varepsilon_{xy} E_y = D_x \\ \varepsilon_0 \varepsilon_{yx} E_x + \varepsilon_0 \varepsilon_{yy} E_y = D_y \end{cases}, \tag{7.14}$$

where $\varepsilon_{xx}, \varepsilon_{xy}, \varepsilon_{yx}, \varepsilon_{yy}$ are given in (7.12). Substituting $\hat{\varepsilon}_r$ from the Drude model (Eq. (7.8)) and the lossy dielectric $\hat{\varepsilon}_\phi$ with Eq. (7.11) in the first equation of (7.14), the following was obtained:

$$\begin{aligned} &\varepsilon_0[j\omega(\omega^2 - j\omega\gamma - \omega_p^2)\cos^2\phi + (j\omega\varepsilon_\phi + \sigma)(\omega^2 - j\omega\gamma)\sin^2\phi]E_x \\ &+\varepsilon_0[j\omega(\omega^2 - j\omega\gamma - \omega_p^2) - (j\omega\varepsilon_\phi + \sigma)(\omega^2 - j\omega\gamma)]\sin\phi\cos\phi E_y \\ &= j\omega(\omega^2 - j\omega\gamma)D_x. \end{aligned} \tag{7.15}$$

Next, Eq. (7.15) was divided by the factor $j\omega$ to achieve a simpler and lower order FDTD algorithm:

$$\begin{aligned} &\varepsilon_0[(\omega^2 - j\omega\gamma - \omega_p^2)\cos^2\phi + (\varepsilon_\phi\omega^2 - j\omega(\sigma + \varepsilon_\phi\gamma) - \sigma\gamma)\sin^2\phi]E_x \\ &+\varepsilon_0[(\omega^2 - j\omega\gamma - \omega_p^2) - (\varepsilon_\phi\omega^2 - j\omega(\sigma + \varepsilon_\phi\gamma) - \sigma\gamma)]\sin\phi\cos\phi E_y \\ &= (\omega^2 - j\omega\gamma)D_x. \end{aligned} \tag{7.16}$$

The updating dispersive FDTD equation was obtained from Eq. (7.16) via the inverse Fourier transform ($j\omega \to \frac{\partial}{\partial t}$, $\omega^2 \to -\frac{\partial^2}{\partial t^2}$), giving

$$\begin{aligned} &\varepsilon_0\left[\left(\frac{\partial^2}{\partial t^2} + \gamma\frac{\partial}{\partial t} + \omega_p^2\right)\cos^2\phi + \left(\varepsilon_\phi\frac{\partial^2}{\partial t^2} + (\sigma + \varepsilon_\phi\gamma)\frac{\partial}{\partial t} + \sigma\gamma\right)\sin^2\phi\right]E_x \\ &+\varepsilon_0\left[\left(\frac{\partial^2}{\partial t^2} + \gamma\frac{\partial}{\partial t} + \omega_p^2\right) - \left(\varepsilon_\phi\frac{\partial^2}{\partial t^2} + (\sigma + \varepsilon_\phi\gamma)\frac{\partial}{\partial t} + \sigma\gamma\right)\right]\sin\phi\cos\phi E_y \\ &= \left(\frac{\partial^2}{\partial t^2} + \gamma\frac{\partial}{\partial t}\right)D_x. \end{aligned} \tag{7.17}$$

A second-order discretization procedure was applied in Eq. (7.17), where the central finite-difference operators in time ($\delta_t$ and $\delta_t^2$) and the central average operators with respect to time ($\mu_t$ and $\mu_t^2$) were used

$$\frac{\partial^2}{\partial t^2} \to \frac{\delta_t^2}{\Delta t^2}, \quad \frac{\partial}{\partial t} \to \frac{\delta_t}{\Delta t}\mu_t \quad , \omega_p^2 \to \omega_p^2\mu_t^2, \quad \sigma\gamma \to \sigma\gamma\mu_t^2, \tag{7.18}$$

where the operators $\delta_t, \delta_t^2, \mu_t, \mu_t^2$ are explained in [20] and given by

$$\delta_t \boldsymbol{F}|_{i,j,k}^n \equiv \boldsymbol{F}|_{i,j,k}^{n+\frac{1}{2}} - \boldsymbol{F}|_{i,j,k}^{n-\frac{1}{2}}, \quad \delta_t^2 \boldsymbol{F}|_{i,j,k}^n \equiv \boldsymbol{F}|_{i,j,k}^{n+1} - 2\boldsymbol{F}|_{i,j,k}^n + \boldsymbol{F}|_{i,j,k}^{n-1},$$

$$\mu_t \boldsymbol{F}|_{i,j,k}^n \equiv \frac{\boldsymbol{F}|_{i,j,k}^{n+\frac{1}{2}} + \boldsymbol{F}|_{i,j,k}^{n-\frac{1}{2}}}{2}, \quad \mu_t^2 \boldsymbol{F}|_{i,j,k}^n \equiv \frac{\boldsymbol{F}|_{i,j,k}^{n+1} + 2\boldsymbol{F}|_{i,j,k}^n + \boldsymbol{F}|_{i,j,k}^{n-1}}{4}, \tag{7.19}$$

Where $\boldsymbol{F}$ represents arbitrary field components and $(i, j, k)$ indices are the coordinates of a certain mesh point in the FDTD domain. Hence, the discretized Eq. (7.17) becomes

$$\varepsilon_0\left[\left(\frac{\delta_t^2}{\Delta t^2}+\gamma\frac{\delta_t}{\Delta t}+\omega_p^2\mu_t^2\right)\cos^2\phi+\left(\varepsilon_\phi\frac{\delta_t^2}{\Delta t^2}+(\sigma+\varepsilon_\phi\gamma)\frac{\delta_t}{\Delta t}+\sigma\gamma\mu_t^2\right)\sin^2\phi\right]E_x$$
$$+\varepsilon_0\left[\left(\frac{\delta_t^2}{\Delta t^2}+\gamma\frac{\delta_t}{\Delta t}+\omega_p^2\mu_t^2\right)-\left(\varepsilon_\phi\frac{\delta_t^2}{\Delta t^2}+(\sigma+\varepsilon_\phi\gamma)\frac{\delta_t}{\Delta t}+\sigma\gamma\mu_t^2\right)\right]\sin\phi\cos\phi E_y$$
$$=\left(\frac{\delta_t^2}{\Delta t^2}+\gamma\frac{\delta_t}{\Delta t}\right)D_x. \quad (7.20)$$

Note that $\varepsilon_\phi$ remains constant in Eq. (7.20), since it is always greater than 1, as with conventional dielectric materials. Finally, the operators (7.19) are substituted in Eq. (7.20) and the derived dispersive updating FDTD equation is

$$E_x^{n+1}=[C_1D_x^{n+1}-B_1E_y^{n+1}-C_2D_x^n+A_2E_x^n$$
$$+B_2E_y^n+C_3D_x^{n-1}-A_3E_x^{n-1}-B_3E_y^{n-1}]/A_1. \quad (7.21)$$

With exactly the same procedure, the updating FDTD equation for the $E_y$ component was derived from the second equation of (7.14) as

$$E_y^{n+1}=[C_1D_y^{n+1}-B_1E_x^{n+1}-C_2D_y^n+F_2E_y^n$$
$$+B_2E_x^n+C_3D_y^{n-1}-F_3E_y^{n-1}-B_3E_x^{n-1}]/F_1. \quad (7.22)$$

The coefficients for both Eqs. (7.21) and (7.22) are given by

$$A_1=\frac{(\cos^2\phi+\varepsilon_\phi\sin^2\phi)}{\Delta t^2}+\frac{\omega_p^2\cos^2\phi+\sigma\gamma\sin^2\phi}{4}+\frac{\gamma\cos^2\phi+(\sigma+\varepsilon_\phi\gamma)\sin^2\phi}{2\Delta t},$$

$$A_2=\frac{2(\cos^2\phi+\varepsilon_\phi\sin^2\phi)}{\Delta t^2}-\frac{\omega_p^2\cos^2\phi+\sigma\gamma\sin^2\phi}{2},$$

$$A_3=\frac{(\cos^2\phi+\varepsilon_\phi\sin^2\phi)}{\Delta t^2}+\frac{\omega_p^2\cos^2\phi+\sigma\gamma\sin^2\phi}{4}-\frac{\gamma\cos^2\phi+(\sigma+\varepsilon_\phi\gamma)\sin^2\phi}{2\Delta t},$$

$$B_1=\frac{(1-\varepsilon_\phi)\sin\phi\cos\phi}{\Delta t^2}+\frac{(\omega_p^2-\sigma\gamma)\sin\phi\cos\phi}{4}+\frac{(\gamma-\sigma-\varepsilon_\phi\gamma)\sin\phi\cos\phi}{2\Delta t},$$

$$B_2=\frac{2(1-\varepsilon_\phi)\sin\phi\cos\phi}{\Delta t^2}-\frac{(\omega_p^2-\sigma\gamma)\sin\phi\cos\phi}{2},$$

$$B_3=\frac{(1-\varepsilon_\phi)\sin\phi\cos\phi}{\Delta t^2}+\frac{(\omega_p^2-\sigma\gamma)\sin\phi\cos\phi}{4}-\frac{(\gamma-\sigma-\varepsilon_\phi\gamma)\sin\phi\cos\phi}{2\Delta t},$$

$$C_1=\frac{1}{\varepsilon_0\Delta t^2}+\frac{\gamma}{2\varepsilon_0\Delta t},C_2=\frac{2}{\varepsilon_0\Delta t^2},C_3=\frac{1}{\varepsilon_0\Delta t^2}-\frac{\gamma}{2\varepsilon_0\Delta t},$$

$$F_1 = \frac{(\sin^2\phi + \varepsilon_\phi \cos^2\phi)}{\Delta t^2} + \frac{\omega_p^2 \sin^2\phi + \sigma\gamma\cos^2\phi}{4} + \frac{\gamma\sin^2\phi + (\sigma + \varepsilon_\phi\gamma)\cos^2\phi}{2\Delta t},$$

$$F_2 = \frac{2(\sin^2\phi + \varepsilon_\phi \cos^2\phi)}{\Delta t^2} - \frac{\omega_p^2 \sin^2\phi + \sigma\gamma\cos^2\phi}{2},$$

$$F_3 = \frac{(\sin^2\phi + \varepsilon_\phi \cos^2\phi)}{\Delta t^2} + \frac{\omega_p^2 \sin^2\phi + \sigma\gamma\cos^2\phi}{4} - \frac{\gamma\sin^2\phi + (\sigma + \varepsilon_\phi\gamma)\cos^2\phi}{2\Delta t},$$

where $\Delta t$ is the temporal discretization.

However, the Eqs. (7.21) and (7.22) cannot be calculated with the FDTD algorithm. The reason is that, in the case of (7.21), the component $E_y^{n+1}$ cannot be computed at the particular time step $(n+1)$. This also applies to the $E_x^{n+1}$ component in Eq. (7.22). The solution is to substitute Eqs. (7.22) into (7.21) and the inverse. As a result, the updating FDTD equation, which computes the $E_x^{n+1}$ component, becomes

$$E_x^{n+1} = [C_1 D_x^{n+1} - a_1 \overline{D}_y^{n+1} - C_2 D_x^n + a_2 \overline{D}_y^n + b_2 E_x^n + d_1 \overline{E}_y^n + C_3 D_x^{n-1} - a_3 \overline{D}_y^{n-1} - b_3 E_x^{n-1} - d_2 \overline{E}_y^{n-1}]/b_1. \quad (7.23)$$

The updating FDTD equation for the $E_y^{n+1}$ component was found, in exactly the same way, to be

$$E_y^{n+1} = [C_1 D_y^{n+1} - e_1 \overline{D}_x^{n+1} - C_2 D_y^n + e_2 \overline{D}_x^n + f_2 E_y^n + g_1 \overline{E}_x^n + C_3 D_y^{n-1} - e_3 \overline{D}_x^{n-1} - f_3 E_y^{n-1} - g_2 \overline{E}_x^{n-1}]/f_1, \quad (7.24)$$

where the newly introduced coefficients in Eqs. (7.23) and (7.24) are

$$a_1 = \frac{B_1 C_1}{F_1}, a_2 = \frac{B_1 C_2}{F_1}, a_3 = \frac{B_1 C_3}{F_1},$$

$$b_1 = A_1 - \frac{B_1^2}{F_1}, b_2 = A_2 - \frac{B_1 B_2}{F_1}, b_3 = A_3 - \frac{B_1 B_3}{F_1},$$

$$d_1 = B_2 - \frac{B_1 F_2}{F_1}, d_2 = B_3 - \frac{B_1 F_3}{F_1},$$

$$e_1 = \frac{B_1 C_1}{A_1}, e_2 = \frac{B_1 C_2}{A_1}, e_3 = \frac{B_1 C_3}{A_1},$$

$$f_1 = F_1 - \frac{B_1^2}{A_1}, f_2 = F_2 - \frac{B_1 B_2}{A_1}, f_3 = F_3 - \frac{B_1 B_3}{A_1},$$

$$g_1 = B_2 - \frac{A_2 B_1}{A_1}, g_2 = B_3 - \frac{A_3 B_1}{A_1}.$$

For more accurate results, the overlined field components $\overline{D}_y, \overline{E}_y, \overline{D}_x, \overline{E}_x$ were calculated with a locally spatial averaging technique [29]. This method was employed because the $x$ and $y$ field components were located in different mesh points across the FDTD grid. Their averaged values were computed from [29]

$$\overline{E}_y(i,j) = \frac{E_y(i,j) + E_y(i+1,j) + E_y(i,j-1) + E_y(i+1,j-1)}{4}, \tag{7.25}$$

where $(i, j)$ are the coordinates of the mesh point.

The final step was to introduce the updating FDTD equation of the $H_z$ field component. From Eq. (7.7), the magnetic permeability $\mu_z$ component can have values both less and greater than 1. Hence, a more complicated approach was necessary to model the magnetic field $H_z$ component. When $\mu_z < 1$, the magnetic permeability was mapped with the Drude model, given by

$$\hat{\mu}_z = 1 - \frac{\omega_{pm}^2}{\omega^2 - j\omega\gamma_m}, \tag{7.26}$$

where $\omega_{pm}$ is the magnetic plasma frequency and $\gamma_m$ is the magnetic collision frequency, which measures the losses of the magnetic dispersive material. The analytical equations of $\omega_{pm}$ and $\gamma_m$ were derived in the same way as Eqs. (7.9), (7.10), and are given by

$$\omega_{pm}^2 = (1-\mu_z)\omega^2 + \mu_z\omega\gamma_m \tan\delta_m, \tag{7.27}$$

$$\gamma_m = \frac{\mu_z\omega\tan\delta_m}{(1-\mu_z)}. \tag{7.28}$$

It can be seen from Eqs. (7.27) and (7.28) that the magnetic plasma and collision frequencies are radially dependent, because they are functions of $\mu_z$, as given by Eq. (7.7).

Equation (7.26) was substituted in the constitutive equation – Eq. (7.4) – and it was discretized as in [60]. The updating FDTD equation for this case is

$$\begin{aligned} H_z^{n+1} = \Bigg\{ &\left[\frac{1}{\mu_0\Delta t^2} + \frac{\gamma_m}{2\mu_0\Delta t}\right] B_z^{n+1} - \frac{2}{\mu_0\Delta t^2} B_z^n \\ &+ \left[\frac{1}{\mu_0\Delta t^2} - \frac{\gamma_m}{2\mu_0\Delta t}\right] B_z^{n-1} + \left[\frac{2}{\Delta t^2} - \frac{\omega_{pm}^2}{2}\right] H_z^n \\ &- \left[\frac{1}{\Delta t^2} - \frac{\gamma_m}{2\Delta t} + \frac{\omega_{pm}^2}{4}\right] H_z^{n-1} \Bigg\} \Bigg/ \left[\frac{1}{\Delta t^2} + \frac{\gamma_m}{2\Delta t} + \frac{\omega_{pm}^2}{4}\right]. \end{aligned} \tag{7.29}$$

When the magnetic permeability of the cloaking material is $\mu_z \geq 1$, it was simulated with the conventional lossy magnetic model:

$$\hat{\mu}_z = \mu_z + \frac{\sigma_m}{j\omega}, \tag{7.30}$$

where the component $\mu_z$ is radially dependent and given by Eq. (7.7). The parameter $\sigma_m$ is the magnetic conductivity. The loss tangent of the lossy magnetic material is given by $\tan\delta_m = \sigma_m/\omega\mu_z$ and it is also radially dependent. The updating FDTD equation, for this type of material, is derived from the discrete equation based on the Faraday law – Eq. (7.5) – including the losses [48]. Finally, the updating FDTD

equation, between $\boldsymbol{H}$ and $\boldsymbol{E}$ field components, was related to the Ampere law – Eq. (7.6) – in free space. The currently proposed FDTD method is an extension of the one proposed in [59] and it can also simulate lossy electromagnetic cloaks. The proposed method can easily be extended in order to model three-dimensional (3-D) lossy electromagnetic cloaks.

### *7.2.2 Discussion and Stability Analysis*

Numerical approximations are inevitable, when the FDTD method is applied. Space and time are discretized, with a detrimental effect on the accuracy of the simulations. Furthermore, the permittivity and permeability are frequency dependent, described as the Drude dispersion model (7.8). Due to the presence of a discrete-time step $\Delta t$, which is inherent in the FDTD method, there will be differences between the analytical and the numerical characteristics of the cloaking material. Hence, for the proposed dispersive FDTD method, a spatial resolution of $\Delta x < \lambda/10$ is insufficient, unlike the conventional dielectric material simulations, where it is the required value [48]. From a previous analysis of left-handed metamaterials [60], it was found that spurious resonances can be found due to coarse time discretization, which leads to numerical errors and inaccuracy. It was proposed that a spatial resolution of $\Delta x < \lambda/80$ is essential for accurate simulations. The same and more dense spatial resolution restrictions have to be applied in the simulation of the cloaking structure.

The same approach as that taken in [59, 60] will be followed for the computation of the numerical values of the permittivities $\varepsilon_r, \varepsilon_\phi$, and the permeability $\mu_z$. The plane waves, described in a discrete-time form, are

$$\boldsymbol{E}^n = \boldsymbol{E}e^{jn\omega\Delta t}, \boldsymbol{D}^n = \boldsymbol{D}e^{jn\omega\Delta t}. \tag{7.31}$$

They are substituted in Eq. (7.21) and the calculated numerical permittivities $\widetilde{\varepsilon_r}, \widetilde{\varepsilon_\phi}$ are

$$\widetilde{\varepsilon_r} = \left[1 - \frac{\omega_p^2 \Delta t^2 \cos^2 \frac{\omega\Delta t}{2}}{2\sin\frac{\omega\Delta t}{2}\left(2\sin\frac{\omega\Delta t}{2} - j\gamma\Delta t\cos\frac{\omega\Delta t}{2}\right)}\right], \tag{7.32}$$

$$\widetilde{\varepsilon_\phi} = \varepsilon_\phi + \frac{\sigma\Delta t}{2j\tan\frac{\omega\Delta t}{2}}. \tag{7.33}$$

Notice that, when $\Delta t \to 0$, which leads to a very fine FDTD grid, Eqs. (7.32) and (7.33) are transformed to the Drude model (7.8) and the lossy dielectric material (7.11), respectively. Exactly the same numerical permeability $\widetilde{\mu_z}$ formulas can be produced for the dispersive magnetic model (7.26) and the conventional lossy magnetic material (7.30). The comparison between analytical and numerical material parameters is given in [59]. It is concluded that conventional spatial resolutions with values $\Delta x < \lambda/10$ are not appropriate for this kind of anisotropic material and more fine FDTD meshes, with $\Delta x < \lambda/80$, have to be applied to maintain the simulation accuracy.

Another problem, which was dominant during the FDTD modeling of cloaking structure, was numerical instability. The Courant stability criterion $\Delta t = \Delta x/\sqrt{2}c$ [48] was satisfied during the FDTD simulations, where $c$ is the speed of light in free space. The object, which was "cloaked", was chosen to be composed of a perfect electric conductor (PEC) material. Arbitrary materials can be used for the object placed inside the cloaking shell. However, for FDTD modeling, it is better to choose the PEC material, because very small field values will always be expected inside the cloaked space. This is due to the numerical approximations, which are inherent to the FDTD method. The instability was generated at two specific regions of the cloaking FDTD meshes. The first instability region was obtained at the interface between the cloaking material and the free space ($r = R_2$). The other was concentrated at the interface between the cloaking device and the "cloaked" PEC material ($r = R_1$). In both regions, the permittivities $\varepsilon_r, \varepsilon_\phi$ and the permeability $\mu_z$ are changing rapidly from finite, even 0, to infinite theoretical values. As a result, spurious cavity resonances are created, which are combined with the irregular staircase approximation of the cloaking structure's cylindrical geometry. From the discretization, with the FDTD method, of the divergence of the electric flux density $\nabla \cdot \boldsymbol{D}$, it can be concluded that the instability is present in the form of accumulated charges at these two interfaces.

In order to achieve stable FDTD simulations, a series of modifications was applied in the conventional FDTD algorithm. First, the locally spatial averaging technique (7.25) was introduced for the simulation of the constitutive equation, which is given in tensor form in Eq. (7.13). This method improved the stability and accuracy of the cloaking modeling. Fine spatial resolutions ($\Delta x < \lambda/80$) were applied, which alleviated the effect of the inevitable – for the current cylindrical geometry – staircase approximation. Ideally, an infinite spatial resolution will guarantee an accurate and stable cloaking modeling. Moreover, there are differences between the analytical and the numerical – Eq. (7.32) – material parameters, which affected the stability of the FDTD simulations in a straightforward manner. Corrected numerical electric and magnetic plasma and collision frequencies were computed. The required numerical lossy permittivity was equal to $\widetilde{\varepsilon_r} = \varepsilon_r(1 - j\tan\delta)$, where $\varepsilon_r$ was radially-dependent (7.7) and $\tan\delta$ was the loss tangent of the cloaking material. If the numerical lossy permittivity is substituted in Eq. (7.32), the resulting corrected plasma and collision frequencies were obtained as [59]

$$\widetilde{\omega}_p^2 = \frac{2\sin\frac{\omega\Delta t}{2}\left[-2(\varepsilon_r - 1)\sin\frac{\omega\Delta t}{2} + \varepsilon_r\gamma\Delta t\cos\frac{\omega\Delta t}{2}\tan\delta\right]}{\Delta t^2\cos^2\frac{\omega\Delta t}{2}}, \tag{7.34}$$

$$\widetilde{\gamma} = \frac{2\varepsilon_r\sin\frac{\omega\Delta t}{2}\tan\delta}{(1-\varepsilon_r)\Delta t\cos\frac{\omega\Delta t}{2}}. \tag{7.35}$$

For the conventional lossy dielectric/magnetic model, the only correction, for improved stability, was applied at the frequency $\omega$. The corrected frequency was easily obtained from Eq. (7.33):

$$\widetilde{\omega} = \frac{\tan\frac{\omega\Delta t}{2}}{\Delta t/2}. \tag{7.36}$$

With all the previous modifications, a stable FDTD simulation can be satisfied at the outer interface ($r = R_2$) of the cloaking structure. For the inner interface ($r = R_1$), one more modification has to be applied in the FDTD algorithm, in order to achieve stability. The correct definition of the "cloaked" perfect electric conductor (PEC) material is crucial for stable modeling of the cloak. The PEC is defined in the FDTD code as a material with infinite permittivity ($\varepsilon \to \infty$). Hence, the coefficient $\left(\frac{\Delta t}{\varepsilon}\right)$, in the discrete Ampere's Law (Eq. (7.6)), has to be set to 0 inside the PEC material, in order to achieve a correct and stable simulation. After all these modifications, which have been made to the FDTD algorithm, the resulted modeling is stable and the numerical accuracy has been improved. There are no accumulated charges at the two interfaces ($r = R_1, r = R_2$), which is evident by the FDTD simulation of the divergence of the electric flux density $\nabla \cdot \boldsymbol{D}$.

### 7.2.3 Numerical Results

A TE polarized plane-wave source was utilized to illuminate the 2-D cloaking structure. A uniform spatial discretization was used, with an FDTD cell size of $\Delta x = \Delta y = \lambda/150$, where $\lambda$ is the wavelength of the excitation signal. In this case, the operating frequency was set to be $f = 2$ GHz and the free-space wavelength was $\lambda = 15$ cm. The temporal discretization was chosen according to the Courant stability condition [48] and the time step was given by $\Delta t = \Delta x/\sqrt{2}c$, where $c$ is the speed of light in free space.

First, the lossless cloaking shell was simulated to validate the proposed FDTD method, which meant that the collision frequency in the Drude model (7.8) was set equal to 0 ($\gamma = 0$). Furthermore, the conductivity in Eq. (7.11) is also set to 0 ($\sigma = 0$). Hence, the radially-dependent plasma frequency was computed from the

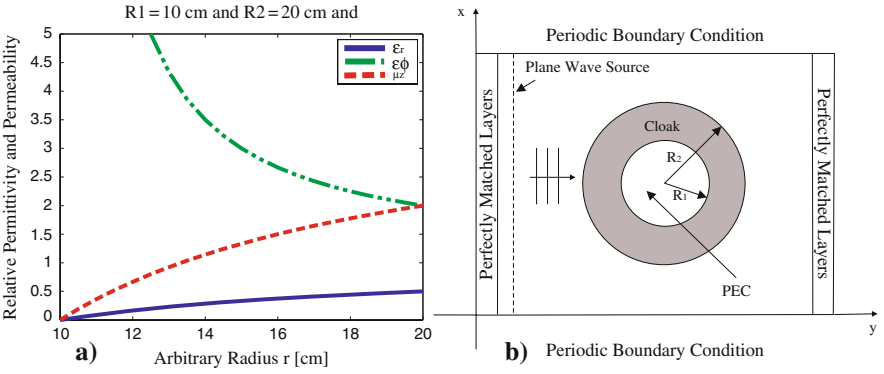


**Fig. 7.1** (**a**) The full set of cloaking material parameters used in the FDTD simulation. (**b**) 2-D FDTD computation domain of the cloaking structure for the case of plane-wave excitation.

simplified equation: $\omega_p = \omega\sqrt{1-\varepsilon_r}$, where $\varepsilon_r$ is given by Eq. (7.7). The inner and outer radius – of the cloaking device had dimensions $R_1 = 10$ cm and $R_2 = 20$ cm, respectively. The full set of the cloaking parameters (Eq. (7.7)) is changing with the cloak's radius, as shown in Fig. 7.1(a). The computational domain was terminated along the $y$-direction with the Berenger's perfectly matched layers (PMLs) [3]. The waves were fully absorbed in the PMLs, equivalent to their leaving the computation domain without introducing reflections. In the last layer of the computational domain along the $x$-direction, Bloch's periodic boundary conditions (PBCs) [48] were applied, in order to create a propagating plane wave. The FDTD computation domain for the current simulations is shown in Fig. 7.1(b). A transverse profile of the propagating field in the lossless cloaking shell is depicted in Fig. 7.2(a). The results for plane-wave excitation, when the steady state is reached, are given in Fig. 7.2(b).

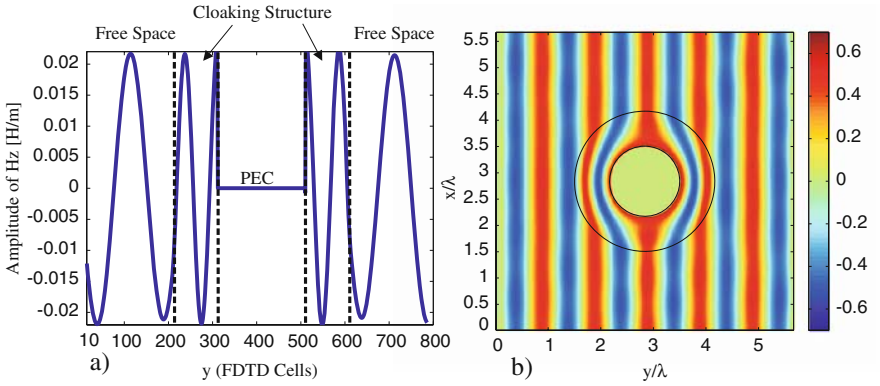


**Fig. 7.2** (**a**) Transverse profile of the magnetic field $H_z$ component propagating through the lossless cloaking device. The wave propagates from left to right undisturbed. (**b**) Normalized magnetic field distribution of the lossless cloaking device with plane-wave excitation. The wave propagates from left to right and the cloaked object is composed of PEC material.

In Fig. 7.2(b), the electromagnetic wave propagates from left to right in the FDTD computation domain. The wave bends inside the cloaking device in order to avoid the "cloaked" object, as was expected. The wave trajectory is recomposed without any disturbance behind the cloaking shell. Therefore, the object placed inside the cloaking structure appears as if it does not exist, like it is "invisible." Note that, for this type of cloaking device, there are no constraints about the size and the material type of the "hidden" object. This is in contrast to the properties of the proposed plasmonic and LHM-based cloaking devices [2, 36, 1, 14]. In Fig. 7.2(b), a small disturbance of the plane wave is visible leaving the cloak on the right-hand side. Furthermore, there is a slight scattering coming back to the source plane on the left-hand side. The reason is that the surface of the cloaking device is curved (cylindrical structure), but it is being modeled with a Cartesian FDTD mesh. As a result, a staircase approximation is inevitable, which directly reduces the simulation accuracy. This problem can be solved if a conformal

scheme [61] is utilized or a cylindrical FDTD is applied, combined with a dispersive FDTD scheme. However, the analysis of the conformal dispersive FDTD [61] technique leads to a complicated sixth-order differential equation for the simulation of the cloaking structure. This is due to the anisotropy of the cloaking material parameters.

The next step was to introduce losses in the radially-dependent and dispersive cloaking material, which is a far more practical and realistic representation of the metamaterials. The loss tangent, $\tan\delta$, was set equal to 0.1, for both the dispersive $\hat{\varepsilon}_r$ component (Eq. (7.8)) and the conventional lossy dielectric component $\hat{\varepsilon}_\phi$ (Eq. (7.11)). For the magnetic component $\hat{\mu}_z$, the magnetic loss tangent is chosen to be $\tan\delta_m = 0.1$, again for both the dispersive (Eq. (7.26)) and the conventional lossy (Eq. (7.30)) cases. The FDTD computational domain scenario used to simulate the lossy cloak is the same as in Fig. 7.1(b). The attenuation of the propagating magnetic field $H_z$ component through the lossy cloak is clearly depicted in Fig. 7.3(a). The magnetic field $H_z$ distribution, with a plane-wave excitation, is depicted in Fig. 7.3(b). It is observed that the cloaking device is working (bending of waves) properly, like the lossless case. But, due to the presence of losses in electromagnetic cloaks, there is a strong shadowing effect to the field behind the cloaking shell. For $\tan\delta = 0.01$, the magnetic field pattern is almost identical to the ideal lossless case in Fig. 7.2(b). However, the cloaking performance is impaired due to the shadow cast behind the cloaked object, for a loss tangent of $\tan\delta = 0.1$. Therefore, the proposed cloaking structure is sensitive to losses, which is a drawback toward the realization of future "invisibility" devices.

The scattering coefficients of lossless and lossy cloaks are calculated with reference to the free-space case, with no obstacles present. Equal loss values are chosen for the electric permittivities $\varepsilon_r$, $\varepsilon_\phi$ and the permeability $\mu_z$ components

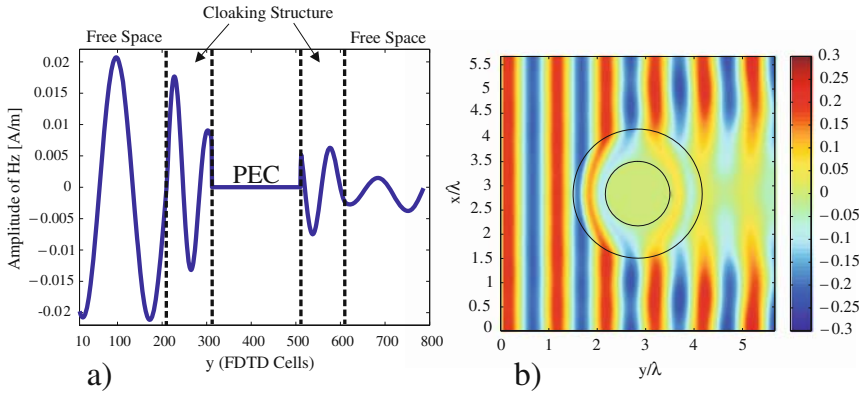


**Fig. 7.3** (**a**) Magnetic field $H_z$ component propagating through the lossy cloaking device ($\tan\delta = 0.1$). The wave propagates from left to right and it is dissipated at the right side of the cloak. (**b**) Normalized magnetic field distribution of the lossy cloaking device with plane-wave excitation. Ideal parameters are used with a loss tangent of 0.1. The wave propagates from left to right and the cloaked object is composed of PEC material.

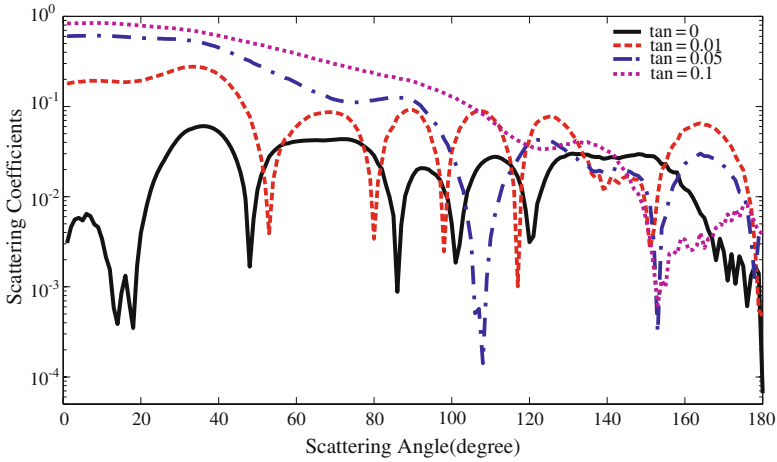


**Fig. 7.4** Scattering patterns of lossless and lossy cloaks. Equal loss tangents of the electric and magnetic parameters were chosen, which range from 0 to 0.1.

($\tan\delta = \tan\delta_m$). The scattering patterns, varying with the losses, are depicted in Fig. 7.4, where the angles of 0° and 180° are forward and backward scattering, respectively. It is interesting to compare our numerical results of Fig. 7.4 with the analytical computed far-field scattering performance of the cylindrical cloak presented in [57]. It is seen that the scattering coefficients increase with the losses; furthermore the minimum scattering is no longer at the backscattering point (angle of 180°) as the losses rise, which is in good agreement with the analytical solution of the cloak [57].

The losses directly affect the cloak's performance; moreover the cloaking material parameters are frequency dispersive. For example, it is seen in Fig. 7.5(a) how the value of $\varepsilon_r$ at the inner radius of the cloaking device ($r = R_1$) is changing with a slight deviation from the center frequency of 2 GHz. Hence, the cloak is functional only at a narrow frequency range. The FDTD method gives us the flexibility to perceive the bandwidth issues of the cloaking device, because it is a time-domain numerical technique. FDTD modeling of the lossless cloaking device will again be employed to investigate the bandwidth limitations of the cloak. The computation domain is the same as in Fig. 7.1(b) and the updating FDTD equations are given by Eqs. (7.5), (7.6), (7.23), (7.24), and (7.29). The excitation of this simulation is a wideband Gaussian pulse with a fixed bandwidth of 1 GHz (full width at half maximum – FWHM) centered at a frequency of 2 GHz.

The wideband Gaussian pulse is shown in Fig. 7.5(b) after it has propagated through the cloaking device. It is obvious that there are reflections and that the pulse trajectory is not recomposed correctly. It experiences a time delay, which is more intense close to the cloak's inner boundary, in the same way as was derived for 3-D spherical cloaks, using the Geometrical Optics [8]. However, the bending of the electromagnetic pulse inside the device is still present, same as that is seen when

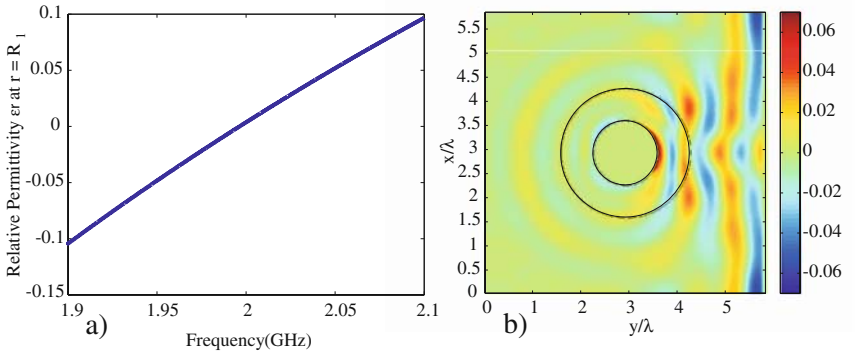


**Fig. 7.5** (**a**) Ideal cloaking material parameter $\varepsilon_r$, at the point $r = R_1$ of the cloak, varying with the frequency. Note that the values of $\varepsilon_r$ are always less than 1 and they can be negative. (**b**) A wideband Gaussian pulse propagating from the left to the right side of the cloak. The pulse has a fixed bandwidth of 1 GHz (FWHM), centered at a frequency of 2 GHz. The snapshot is taken when the pulse is recomposed at the right side of the cloak.

using the ideal cloak in Fig. 7.2(b). Finally, an interesting bandwidth study of the spherical cloak, using the analytical Mie scattering model, was published in [58].

Here, the reflection coefficient of the cloaking device was calculated, in order to measure the backscattering of the structure. The magnetic field values $H_z$ are averaged along a line parallel to the $x$-axis, close to the plane-wave source, and the excitation pulse is isolated from the reflected signal. Furthermore, the transmission coefficient was measured with the same technique of averaging the field values along a line, close to the right side PML wall. The computed reflection and transmission coefficients can be seen in Fig. 7.6(a) and (b), respectively.

To conclude, the cloak has acceptable performance over a narrow bandwidth only, with ideal behavior (no reflections and total transmission of the field) at one frequency, namely the center frequency (2 GHz). However, it is interesting that the device can operate with a tolerable percentage of reflections and a half fraction of transmitted signal in a wider frequency range.

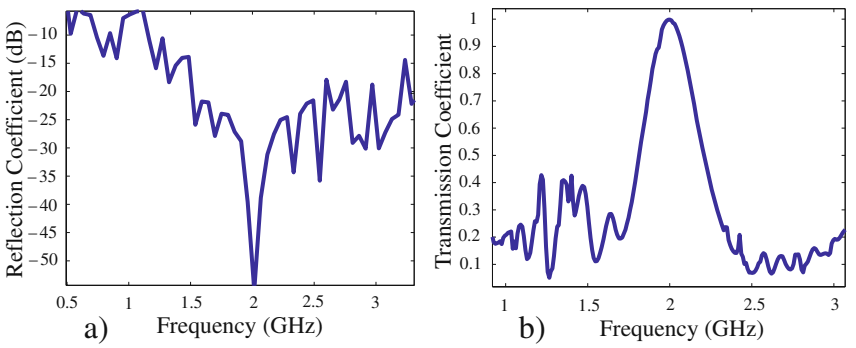


**Fig. 7.6** (**a**) Reflection coefficient of ideal cloak in dB, varying with frequency. (**b**) Transmission coefficient of ideal cloak, varying with frequency. In both cases, the device is illuminated with a wideband Gaussian pulse.

## 7.3 Parallel Dispersive FDTD Modeling of Three-Dimensional Spherical Cloaks

A complete set of material parameters of the 3-D ideal cloak in the spherical coordinate is given by [33]

$$\begin{aligned}\varepsilon_r &= \mu_r = \frac{R_2}{R_2 - R_1}\left(\frac{r - R_1}{r}\right)^2,\\ \varepsilon_\theta &= \mu_\theta = \frac{R_2}{R_2 - R_1},\\ \varepsilon_\phi &= \mu_\phi = \frac{R_2}{R_2 - R_1},\end{aligned} \tag{7.37}$$

where $R_1$ and $R_2$ are the inner and outer radii of the cloak, respectively, and $r$ is the distance from a spatial point within the cloak to the center of it. Due to its simplicity, we have chosen the ADE method [17] to model 3-D cloaks, as it was used before for the simulation of 2-D cloaks.

For the conventional Cartesian FDTD mesh, since the material parameters given in (7.37) are in the spherical coordinates, the following coordinate transformation is used [4]:

$$\begin{aligned}\begin{bmatrix}\varepsilon_{xx} & \varepsilon_{xy} & \varepsilon_{xz}\\ \varepsilon_{yx} & \varepsilon_{yy} & \varepsilon_{yz}\\ \varepsilon_{zx} & \varepsilon_{zy} & \varepsilon_{zz}\end{bmatrix} &= \begin{bmatrix}\sin\theta\cos\phi & \cos\theta\cos\phi & -\sin\phi\\ \sin\theta\sin\phi & \cos\theta\sin\phi & \cos\phi\\ \cos\theta & -\sin\theta & 0\end{bmatrix}\begin{bmatrix}\varepsilon_r & 0 & 0\\ 0 & \varepsilon_\theta & 0\\ 0 & 0 & \varepsilon_\phi\end{bmatrix}\\ &\cdot\begin{bmatrix}\sin\theta\cos\phi & \sin\theta\sin\phi & \cos\theta\\ \cos\theta\cos\phi & \cos\theta\sin\phi & -\sin\theta\\ -\sin\phi & \cos\phi & 0\end{bmatrix}.\end{aligned} \tag{7.38}$$

The tensor form of the constitutive relation is given by

$$\begin{aligned}&\varepsilon_0\begin{bmatrix}\varepsilon_{xx} & \varepsilon_{xy} & \varepsilon_{xz}\\ \varepsilon_{yx} & \varepsilon_{yy} & \varepsilon_{yz}\\ \varepsilon_{zx} & \varepsilon_{zy} & \varepsilon_{zz}\end{bmatrix}\begin{bmatrix}E_x\\ E_y\\ E_z\end{bmatrix} = \begin{bmatrix}D_x\\ D_y\\ D_z\end{bmatrix}\\ \Leftrightarrow\ &\varepsilon_0\begin{bmatrix}E_x\\ E_y\\ E_z\end{bmatrix} = \begin{bmatrix}\varepsilon_{xx} & \varepsilon_{xy} & \varepsilon_{xz}\\ \varepsilon_{yx} & \varepsilon_{yy} & \varepsilon_{yz}\\ \varepsilon_{zx} & \varepsilon_{zy} & \varepsilon_{zz}\end{bmatrix}^{-1}\begin{bmatrix}D_x\\ D_y\\ D_z\end{bmatrix},\end{aligned} \tag{7.39}$$

where

$$\begin{bmatrix}\varepsilon_{xx} & \varepsilon_{xy} & \varepsilon_{xz}\\ \varepsilon_{yx} & \varepsilon_{yy} & \varepsilon_{yz}\\ \varepsilon_{zx} & \varepsilon_{zy} & \varepsilon_{zz}\end{bmatrix}^{-1} = \begin{bmatrix}\varepsilon'_{xx} & \varepsilon'_{xy} & \varepsilon'_{xz}\\ \varepsilon'_{yx} & \varepsilon'_{yy} & \varepsilon'_{yz}\\ \varepsilon'_{zx} & \varepsilon'_{zy} & \varepsilon'_{zz}\end{bmatrix}, \tag{7.40}$$

and

$$\varepsilon'_{xx} = \frac{1}{\varepsilon_r}\sin^2\theta\cos^2\phi + \frac{1}{\varepsilon_\theta}\cos^2\theta\cos^2\phi + \frac{1}{\varepsilon_\phi}\sin^2\phi,$$

$$
\begin{aligned}
\varepsilon'_{xy} &= \frac{1}{\varepsilon_r}\sin^2\theta\sin\phi\cos\phi + \frac{1}{\varepsilon_\theta}\cos^2\theta\sin\phi\cos\phi - \frac{1}{\varepsilon_\phi}\sin\phi\cos\phi,\\
\varepsilon'_{xz} &= \frac{1}{\varepsilon_r}\sin\theta\cos\theta\cos\phi - \frac{1}{\varepsilon_\theta}\sin\theta\cos\theta\cos\phi,\\
\varepsilon'_{yx} &= \frac{1}{\varepsilon_r}\sin^2\theta\sin\phi\cos\phi + \frac{1}{\varepsilon_\theta}\cos^2\theta\sin\phi\cos\phi - \frac{1}{\varepsilon_\phi}\sin\phi\cos\phi,\\
\varepsilon'_{yy} &= \frac{1}{\varepsilon_r}\sin^2\theta\sin^2\phi + \frac{1}{\varepsilon_\theta}\cos^2\theta\sin^2\phi + \frac{1}{\varepsilon_\phi}\cos^2\phi,\\
\varepsilon'_{yz} &= \frac{1}{\varepsilon_r}\sin\theta\cos\theta\sin\phi - \frac{1}{\varepsilon_\theta}\sin\theta\cos\theta\sin\phi,\\
\varepsilon'_{zx} &= \frac{1}{\varepsilon_r}\sin\theta\cos\theta\cos\phi - \frac{1}{\varepsilon_\theta}\sin\theta\cos\theta\cos\phi,\\
\varepsilon'_{zy} &= \frac{1}{\varepsilon_r}\sin\theta\cos\theta\sin\phi - \frac{1}{\varepsilon_\theta}\sin\theta\cos\theta\sin\phi,\\
\varepsilon'_{zz} &= \frac{1}{\varepsilon_r}\cos^2\theta + \frac{1}{\varepsilon_\theta}\sin^2\theta.
\end{aligned}
\tag{7.41}
$$

Note that the inverse of the permittivity tensor matrix (7.40) exists only when $\varepsilon_r \neq 0$, $\varepsilon_\theta \neq 0$, and $\varepsilon_\phi \neq 0$. However, the inner boundary of the cloak does not satisfy the condition of $\varepsilon_r \neq 0$. Therefore, in our FDTD simulations, we place a perfect electric conductor (PEC) sphere with its radius equal to $R_1$ inside the cloak to guarantee the validity of (7.40).

Substituting (7.40) into (7.39) gives

$$
\begin{aligned}
\varepsilon_0 E_x = &\left(\frac{1}{\varepsilon_r}\sin^2\theta\cos^2\phi + \frac{1}{\varepsilon_\theta}\cos^2\theta\cos^2\phi + \frac{1}{\varepsilon_\phi}\sin^2\phi\right)D_x\\
&+\left(\frac{1}{\varepsilon_r}\sin^2\theta\sin\phi\cos\phi + \frac{1}{\varepsilon_\theta}\cos^2\theta\sin\phi\cos\phi - \frac{1}{\varepsilon_\phi}\sin\phi\cos\phi\right)D_y\\
&+\left(\frac{1}{\varepsilon_r}\sin\theta\cos\theta\cos\phi - \frac{1}{\varepsilon_\theta}\sin\theta\cos\theta\cos\phi\right)D_z,
\end{aligned}
\tag{7.42}
$$

$$
\begin{aligned}
\varepsilon_0 E_y = &\left(\frac{1}{\varepsilon_r}\sin^2\theta\sin\phi\cos\phi + \frac{1}{\varepsilon_\theta}\cos^2\theta\sin\phi\cos\phi - \frac{1}{\varepsilon_\phi}\sin\phi\cos\phi\right)D_x\\
&+\left(\frac{1}{\varepsilon_r}\sin^2\theta\sin^2\phi + \frac{1}{\varepsilon_\theta}\cos^2\theta\sin^2\phi + \frac{1}{\varepsilon_\phi}\cos^2\phi\right)D_y\\
&+\left(\frac{1}{\varepsilon_r}\sin\theta\cos\theta\sin\phi - \frac{1}{\varepsilon_\theta}\sin\theta\cos\theta\sin\phi\right)D_z,
\end{aligned}
\tag{7.43}
$$

$$
\begin{aligned}
\varepsilon_0 E_z = &\left(\frac{1}{\varepsilon_r}\sin\theta\cos\theta\cos\phi - \frac{1}{\varepsilon_\theta}\sin\theta\cos\theta\cos\phi\right)D_x\\
&+\left(\frac{1}{\varepsilon_r}\sin\theta\cos\theta\sin\phi - \frac{1}{\varepsilon_\theta}\sin\theta\cos\theta\sin\phi\right)D_y
\end{aligned}
$$

$$+\left(\frac{1}{\varepsilon_r}\cos^2\theta+\frac{1}{\varepsilon_\theta}\sin^2\theta\right)D_z. \tag{7.44}$$

Since the above equations have a similar form, in the following, the derivation of the updating equation is only given for the $E_x$ component. The updating equations for the $E_y$ and $E_z$ components can be derived following the same procedure.

Express $\varepsilon_r$ in the Drude form of (7.37), Eq. (7.42) can be written as

$$\begin{aligned}
&\varepsilon_0\left(\omega^2-j\omega\gamma-\omega_p^2\right)E_x=\left[\left(\omega^2-j\omega\gamma\right)\sin^2\theta\cos^2\phi\right.\\
&+\left(\omega^2-j\omega\gamma-\omega_p^2\right)\left.\left(\frac{\cos^2\theta\cos^2\phi}{\varepsilon_\theta}+\frac{\sin^2\phi}{\varepsilon_\phi}\right)\right]D_x\\
&+\left[\left(\omega^2-j\omega\gamma\right)\sin^2\theta\sin\phi\cos\phi+\left(\omega^2-j\omega\gamma-\omega_p^2\right)\frac{\cos^2\theta\sin\phi\cos\phi}{\varepsilon_\theta}\right.\\
&\left.-\left(\omega^2-j\omega\gamma-\omega_p^2\right)\frac{\sin\phi\cos\phi}{\varepsilon_\phi}\right]D_y+\left[\left(\omega^2-j\omega\gamma\right)\sin\theta\cos\theta\cos\phi\right.\\
&\left.-\left(\omega^2-j\omega\gamma-\omega_p^2\right)\frac{\sin\theta\cos\theta\cos\phi}{\varepsilon_\theta}\right]D_z.
\end{aligned} \tag{7.45}$$

Note that $\varepsilon_\theta$ and $\varepsilon_\phi$ remain in (7.45) since their values are always greater than 1 in the proposed cloak and, hence, there is no need to apply the Drude model in the FDTD updating equations. Applying the inverse Fourier transform and the following rules:

$$j\omega\rightarrow\frac{\partial}{\partial t},\qquad \omega^2\rightarrow-\frac{\partial^2}{\partial t^2}, \tag{7.46}$$

Equation (7.45) can be rewritten in the time domain as

$$\begin{aligned}
&\varepsilon_0\left(\frac{\partial^2}{\partial t^2}+\gamma\frac{\partial}{\partial t}+\omega_p^2\right)E_x=\left[\left(\frac{\partial^2}{\partial t^2}+\gamma\frac{\partial}{\partial t}\right)\sin^2\theta\cos^2\phi\right.\\
&+\left(\frac{\partial^2}{\partial t^2}+\gamma\frac{\partial}{\partial t}+\omega_p^2\right)\frac{\cos^2\theta\cos^2\phi}{\varepsilon_\theta}+\left.\left(\frac{\partial^2}{\partial t^2}+\gamma\frac{\partial}{\partial t}+\omega_p^2\right)\frac{\sin^2\phi}{\varepsilon_\phi}\right]D_x\\
&+\left[\left(\frac{\partial^2}{\partial t^2}+\gamma\frac{\partial}{\partial t}\right)\sin^2\theta\sin\phi\cos\phi+\left(\frac{\partial^2}{\partial t^2}+\gamma\frac{\partial}{\partial t}+\omega_p^2\right)\frac{\cos^2\theta\sin\phi\cos\phi}{\varepsilon_\theta}\right.\\
&\left.-\left(\frac{\partial^2}{\partial t^2}+\gamma\frac{\partial}{\partial t}+\omega_p^2\right)\frac{\sin\phi\cos\phi}{\varepsilon_\phi}\right]D_y+\left[\left(\frac{\partial^2}{\partial t^2}+\gamma\frac{\partial}{\partial t}\right)\sin\theta\cos\theta\cos\phi\right.\\
&\left.-\left(\frac{\partial^2}{\partial t^2}+\gamma\frac{\partial}{\partial t}+\omega_p^2\right)\frac{\sin\theta\cos\theta\cos\phi}{\varepsilon_\theta}\right]D_z.
\end{aligned} \tag{7.47}$$

The FDTD simulation domain is represented by an equally spaced 3-D grid with the periods $\Delta x$, $\Delta y$, and $\Delta z$ along the $x$-, $y$-, and $z$-directions, respectively. For the discretization of Eq. (7.47), we use the central finite-difference operators in time ($\delta_t$ and $\delta_t^2$) and the central average operator with respect to time ($\mu_t$ and $\mu_t^2$):

$$\frac{\partial^2}{\partial t^2} \to \frac{\delta_t^2}{(\Delta t)^2}, \qquad \frac{\partial}{\partial t} \to \frac{\delta_t}{\Delta t}\mu_t, \qquad 1 \to \mu_t^2,$$

where the operators $\delta_t$, $\delta_t^2$, $\mu_t$, and $\mu_t^2$ are defined as in [20]:

$$\begin{aligned}
\delta_t \boldsymbol{F}|^n_{m_x,m_y,m_z} &\equiv \boldsymbol{F}|^{n+\frac{1}{2}}_{m_x,m_y,m_z} - \boldsymbol{F}|^{n-\frac{1}{2}}_{m_x,m_y,m_z},\\
\delta_t^2 \boldsymbol{F}|^n_{m_x,m_y,m_z} &\equiv \boldsymbol{F}|^{n+1}_{m_x,m_y,m_z} - 2\boldsymbol{F}|^n_{m_x,m_y,m_z} + \boldsymbol{F}|^{n-1}_{m_x,m_y,m_z},\\
\mu_t \boldsymbol{F}|^n_{m_x,m_y,m_z} &\equiv \frac{\boldsymbol{F}|^{n+\frac{1}{2}}_{m_x,m_y,m_z} + \boldsymbol{F}|^{n-\frac{1}{2}}_{m_x,m_y,m_z}}{2},\\
\mu_t^2 \boldsymbol{F}|^n_{m_x,m_y,m_z} &\equiv \frac{\boldsymbol{F}|^{n+1}_{m_x,m_y,m_z} + 2\boldsymbol{F}|^n_{m_x,m_y,m_z} + \boldsymbol{F}|^{n-1}_{m_x,m_y,m_z}}{4},
\end{aligned} \tag{7.48}$$

where $\boldsymbol{F}$ represents field components and $m_x, m_y, m_z$ are the indices corresponding to a certain discretization point in the FDTD domain. The discretized Eq. (7.47) reads

$$\begin{aligned}
&\varepsilon_0 \left[\frac{\delta_t^2}{(\Delta t)^2} + \gamma\frac{\delta_t}{\Delta t}\mu_t + \omega_p^2\mu_t^2\right] E_x = \left\{\left[\frac{\delta_t^2}{(\Delta t)^2} + \gamma\frac{\delta_t}{\Delta t}\mu_t\right]\sin^2\theta\cos^2\phi\right.\\
&\left. + \left[\frac{\delta_t^2}{(\Delta t)^2} + \gamma\frac{\delta_t}{\Delta t}\mu_t + \omega_p^2\mu_t^2\right]\left(\frac{\cos^2\theta\cos^2\phi}{\varepsilon_\theta} + \frac{\sin^2\phi}{\varepsilon_\phi}\right)\right\} D_x\\
&+ \left\{\left[\frac{\delta_t^2}{(\Delta t)^2} + \gamma\frac{\delta_t}{\Delta t}\mu_t\right]\sin^2\theta\sin\phi\cos\phi\right.\\
&\left. + \left[\frac{\delta_t^2}{(\Delta t)^2} + \gamma\frac{\delta_t}{\Delta t}\mu_t + \omega_p^2\mu_t^2\right]\left(\frac{\cos^2\theta\sin\phi\cos\phi}{\varepsilon_\theta} - \frac{\sin\phi\cos\phi}{\varepsilon_\phi}\right)\right\} D_y\\
&+ \left\{\left[\frac{\delta_t^2}{(\Delta t)^2} + \gamma\frac{\delta_t}{\Delta t}\mu_t\right]\sin\theta\cos\theta\cos\phi\right.\\
&\left. - \left[\frac{\delta_t^2}{(\Delta t)^2} + \gamma\frac{\delta_t}{\Delta t}\mu_t + \omega_p^2\mu_t^2\right]\frac{\sin\theta\cos\theta\cos\phi}{\varepsilon_\theta}\right\} D_z.
\end{aligned} \tag{7.49}$$

Note that in (7.49), the discretization of the term $\omega_p^2$ of (7.47) is performed using the central average operator $\mu_t^2$ in order to guarantee the improved stability; the central average operator $\mu_t$ is used for the term containing $\gamma$ to preserve the second-order feature of the equation. Equation (7.49) can be written as

$$\begin{aligned}
&\varepsilon_0\left[\frac{E_x^{n+1} - 2E_x^n + E_x^{n-1}}{(\Delta t)^2} + \gamma\frac{E_x^{n+1} - E_x^{n-1}}{2\Delta t} + \omega_p^2\frac{E_x^{n+1} + 2E_x^n + E_x^{n-1}}{4}\right]\\
&= \sin^2\theta\cos^2\phi\left[\frac{D_x^{n+1} - 2D_x^n + D_x^{n-1}}{(\Delta t)^2} + \gamma\frac{D_x^{n+1} - D_x^{n-1}}{2\Delta t}\right]\\
&+ \left(\frac{\cos^2\theta\cos^2\phi}{\varepsilon_\theta} + \frac{\sin^2\phi}{\varepsilon_\phi}\right)\left[\frac{D_x^{n+1} - 2D_x^n + D_x^{n-1}}{(\Delta t)^2} + \gamma\frac{D_x^{n+1} - D_x^{n-1}}{2\Delta t}\right.
\end{aligned}$$

$$+\omega_p^2\frac{D_x^{n+1}+2D_x^n+D_x^{n-1}}{4}\Bigg]+\sin^2\theta\sin\phi\cos\phi\left[\frac{D_y^{n+1}-2D_y^n+D_y^{n-1}}{(\Delta t)^2}\right.$$
$$\left.+\gamma\frac{D_y^{n+1}-D_y^{n-1}}{2\Delta t}\right]+\left(\frac{\cos^2\theta\sin\phi\cos\phi}{\varepsilon_\theta}-\frac{\sin\phi\cos\phi}{\varepsilon_\phi}\right)$$
$$\cdot\left[\frac{D_y^{n+1}-2D_y^n+D_y^{n-1}}{(\Delta t)^2}+\gamma\frac{D_y^{n+1}-D_y^{n-1}}{2\Delta t}+\omega_p^2\frac{D_y^{n+1}+2D_y^n+D_y^{n-1}}{4}\right]$$
$$+\sin\theta\cos\theta\cos\phi\left[\frac{D_z^{n+1}-2D_z^n+D_z^{n-1}}{(\Delta t)^2}+\gamma\frac{D_z^{n+1}-D_z^{n-1}}{2\Delta t}\right]$$
$$-\frac{\sin\theta\cos\theta\cos\phi}{\varepsilon_\theta}\left[\frac{D_z^{n+1}-2D_z^n+D_z^{n-1}}{(\Delta t)^2}+\gamma\frac{D_z^{n+1}-D_z^{n-1}}{2\Delta t}\right.$$
$$\left.+\omega_p^2\frac{D_z^{n+1}+2D_z^n+D_z^{n-1}}{4}\right]. \tag{7.50}$$

After simple manipulations, the updating equation for $E_x$ can be obtained as

$$E_x^{n+1}=\Big[b_{0xx}D_x^{n+1}+b_{1xx}D_x^n+b_{2xx}D_x^{n-1}+b_{0xy}\overline{D_y}^{n+1}+b_{1xy}\overline{D_y}^{n}+b_{2xy}\overline{D_y}^{n-1}$$
$$+b_{0xz}\overline{D_z}^{n+1}+b_{1xz}\overline{D_z}^{n}+b_{2xz}\overline{D_z}^{n-1}-\left(a_{1x}E_x^n+a_{2x}E_x^{n-1}\right)\Big]/a_{0x}, \tag{7.51}$$

where the coefficients are given by

$$a_{0x}=\varepsilon_0\left[\frac{1}{(\Delta t)^2}+\frac{\gamma}{2\Delta t}+\frac{\omega_p^2}{4}\right],\quad a_{1x}=\varepsilon_0\left[-\frac{2}{(\Delta t)^2}+\frac{\omega_p^2}{2}\right],$$

$$a_{2x}=\varepsilon_0\left[\frac{1}{(\Delta t)^2}-\frac{\gamma}{2\Delta t}+\frac{\omega_p^2}{4}\right],$$

$$b_{0xx}=\sin^2\theta\cos^2\phi\left[\frac{1}{(\Delta t)^2}+\frac{\gamma}{2\Delta t}\right]+\left(\frac{\cos^2\theta\cos^2\phi}{\varepsilon_\theta}+\frac{\sin^2\phi}{\varepsilon_\phi}\right)\left[\frac{1}{(\Delta t)^2}+\frac{\gamma}{2\Delta t}+\frac{\omega_p^2}{4}\right],$$

$$b_{1xx}=-\sin^2\theta\cos^2\phi\frac{2}{(\Delta t)^2}+\left(\frac{\cos^2\theta\cos^2\phi}{\varepsilon_\theta}+\frac{\sin^2\phi}{\varepsilon_\phi}\right)\left[-\frac{2}{(\Delta t)^2}+\frac{\omega_p^2}{2}\right],$$

$$b_{2xx}=\sin^2\theta\cos^2\phi\left[\frac{1}{(\Delta t)^2}-\frac{\gamma}{2\Delta t}\right]+\left(\frac{\cos^2\theta\cos^2\phi}{\varepsilon_\theta}+\frac{\sin^2\phi}{\varepsilon_\phi}\right)\left[\frac{1}{(\Delta t)^2}-\frac{\gamma}{2\Delta t}+\frac{\omega_p^2}{4}\right],$$

$$b_{0xy}=\sin^2\theta\sin\phi\cos\phi\left[\frac{1}{(\Delta t)^2}+\frac{\gamma}{2\Delta t}\right]+\left(\frac{\cos^2\theta\sin\phi\cos\phi}{\varepsilon_\theta}-\frac{\sin\phi\cos\phi}{\varepsilon_\phi}\right)$$
$$\cdot\left[\frac{1}{(\Delta t)^2}+\frac{\gamma}{2\Delta t}+\frac{\omega_p^2}{4}\right],$$

$$b_{1xy}=-\sin^2\theta\sin\phi\cos\phi\frac{2}{(\Delta t)^2}+\left(\frac{\cos^2\theta\sin\phi\cos\phi}{\varepsilon_\theta}-\frac{\sin\phi\cos\phi}{\varepsilon_\phi}\right)\left[-\frac{2}{(\Delta t)^2}+\frac{\omega_p^2}{2}\right],$$

$$b_{2xy} = \sin^2\theta \sin\phi\cos\phi\left[\frac{1}{(\Delta t)^2} - \frac{\gamma}{2\Delta t}\right] + \left(\frac{\cos^2\theta\sin\phi\cos\phi}{\varepsilon_\theta} - \frac{\sin\phi\cos\phi}{\varepsilon_\phi}\right) \cdot \left[\frac{1}{(\Delta t)^2} - \frac{\gamma}{2\Delta t} + \frac{\omega_p^2}{4}\right],$$

$$b_{0xz} = \sin\theta\cos\theta\cos\phi\left[\frac{1}{(\Delta t)^2} + \frac{\gamma}{2\Delta t}\right] - \frac{\sin\theta\cos\theta\cos\phi}{\varepsilon_\theta}\left[\frac{1}{(\Delta t)^2} + \frac{\gamma}{2\Delta t} + \frac{\omega_p^2}{4}\right],$$

$$b_{1xz} = -\sin\theta\cos\theta\cos\phi\frac{2}{(\Delta t)^2} - \frac{\sin\theta\cos\theta\cos\phi}{\varepsilon_\theta}\left[-\frac{2}{(\Delta t)^2} + \frac{\omega_p^2}{2}\right],$$

$$b_{2xz} = \sin\theta\cos\theta\cos\phi\left[\frac{1}{(\Delta t)^2} - \frac{\gamma}{2\Delta t}\right] - \frac{\sin\theta\cos\theta\cos\phi}{\varepsilon_\theta}\left[\frac{1}{(\Delta t)^2} - \frac{\gamma}{2\Delta t} + \frac{\omega_p^2}{4}\right].$$

Following the same procedure, the updating equation for $E_y$ is

$$E_y^{n+1} = \Big[b_{0yx}\overline{D_x}^{n+1} + b_{1yx}\overline{D_x}^{n} + b_{2yx}\overline{D_x}^{n-1} + b_{0yy}D_y^{n+1} + b_{1yy}D_y^{n} + b_{2yy}D_y^{n-1} + b_{0yz}\overline{D_z}^{n+1} + b_{1yz}\overline{D_z}^{n} + b_{2yz}\overline{D_z}^{n-1} - \left(a_{1y}E_y^n + a_{2y}E_y^{n-1}\right)\Big]/a_{0y}, \quad (7.52)$$

with the coefficients given by

$$a_{0y} = \varepsilon_0\left[\frac{1}{(\Delta t)^2} + \frac{\gamma}{2\Delta t} + \frac{\omega_p^2}{4}\right], \quad a_{1y} = \varepsilon_0\left[-\frac{2}{(\Delta t)^2} + \frac{\omega_p^2}{2}\right],$$

$$a_{2y} = \varepsilon_0\left[\frac{1}{(\Delta t)^2} - \frac{\gamma}{2\Delta t} + \frac{\omega_p^2}{4}\right],$$

$$b_{0yx} = \sin^2\theta\sin\phi\cos\phi\left[\frac{1}{(\Delta t)^2} + \frac{\gamma}{2\Delta t}\right] + \left(\frac{\cos^2\theta\sin\phi\cos\phi}{\varepsilon_\theta} - \frac{\sin\phi\cos\phi}{\varepsilon_\phi}\right) \cdot \left[\frac{1}{(\Delta t)^2} + \frac{\gamma}{2\Delta t} + \frac{\omega_p^2}{4}\right],$$

$$b_{1yx} = -\sin^2\theta\sin\phi\cos\phi\frac{2}{(\Delta t)^2} + \left(\frac{\cos^2\theta\sin\phi\cos\phi}{\varepsilon_\theta} - \frac{\sin\phi\cos\phi}{\varepsilon_\phi}\right)\left[-\frac{2}{(\Delta t)^2} + \frac{\omega_p^2}{2}\right],$$

$$b_{2yx} = \sin^2\theta\sin\phi\cos\phi\left[\frac{1}{(\Delta t)^2} - \frac{\gamma}{2\Delta t}\right] + \left(\frac{\cos^2\theta\sin\phi\cos\phi}{\varepsilon_\theta} - \frac{\sin\phi\cos\phi}{\varepsilon_\phi}\right) \cdot \left[\frac{1}{(\Delta t)^2} - \frac{\gamma}{2\Delta t} + \frac{\omega_p^2}{4}\right],$$

$$b_{0yy} = \sin^2\theta\sin^2\phi\left[\frac{1}{(\Delta t)^2} + \frac{\gamma}{2\Delta t}\right] + \left(\frac{\cos^2\theta\sin^2\phi}{\varepsilon_\theta} + \frac{\cos^2\phi}{\varepsilon_\phi}\right)\left[\frac{1}{(\Delta t)^2} + \frac{\gamma}{2\Delta t} + \frac{\omega_p^2}{4}\right],$$

$$b_{1yy} = -\sin^2\theta\sin^2\phi\frac{2}{(\Delta t)^2} + \left(\frac{\cos^2\theta\sin^2\phi}{\varepsilon_\theta} + \frac{\cos^2\phi}{\varepsilon_\phi}\right)\left[-\frac{2}{(\Delta t)^2} + \frac{\omega_p^2}{2}\right],$$

$$b_{2yy} = \sin^2\theta\sin^2\phi\left[\frac{1}{(\Delta t)^2} - \frac{\gamma}{2\Delta t}\right] + \left(\frac{\cos^2\theta\sin^2\phi}{\varepsilon_\theta} + \frac{\cos^2\phi}{\varepsilon_\phi}\right)\left[\frac{1}{(\Delta t)^2} - \frac{\gamma}{2\Delta t} + \frac{\omega_p^2}{4}\right],$$

$$b_{0yz} = \sin\theta\cos\theta\sin\phi\left[\frac{1}{(\Delta t)^2} + \frac{\gamma}{2\Delta t}\right] - \frac{\sin\theta\cos\theta\sin\phi}{\varepsilon_\theta}\left[\frac{1}{(\Delta t)^2} + \frac{\gamma}{2\Delta t} + \frac{\omega_p^2}{4}\right],$$

$$b_{1yz} = -\sin\theta\cos\theta\sin\phi\frac{2}{(\Delta t)^2} - \frac{\sin\theta\cos\theta\sin\phi}{\varepsilon_\theta}\left[-\frac{2}{(\Delta t)^2} + \frac{\omega_p^2}{2}\right],$$

$$b_{2yz} = \sin\theta\cos\theta\sin\phi\left[\frac{1}{(\Delta t)^2} - \frac{\gamma}{2\Delta t}\right] - \frac{\sin\theta\cos\theta\sin\phi}{\varepsilon_\theta}\left[\frac{1}{(\Delta t)^2} - \frac{\gamma}{2\Delta t} + \frac{\omega_p^2}{4}\right].$$

And the updating equations for $E_z$ is

$$E_z^{n+1} = \Big[b_{0zx}\overline{D_x}^{n+1} + b_{1zx}\overline{D_x}^{n} + b_{2zx}\overline{D_x}^{n-1} + b_{0zy}\overline{D_y}^{n+1} + b_{1zy}\overline{D_y}^{n} + b_{2zy}\overline{D_y}^{n-1} + b_{0zz}D_z^{n+1} + b_{1zz}D_z^{n} + b_{2zz}D_z^{n-1} - \left(a_{1z}E_z^{n} + a_{2z}E_z^{n-1}\right)\Big]/a_{0z}, \tag{7.53}$$

with the coefficients given by

$$a_{0z} = \varepsilon_0\left[\frac{1}{(\Delta t)^2} + \frac{\gamma}{2\Delta t} + \frac{\omega_p^2}{4}\right], \quad a_{1z} = \varepsilon_0\left[-\frac{2}{(\Delta t)^2} + \frac{\omega_p^2}{2}\right],$$

$$a_{2z} = \varepsilon_0\left[\frac{1}{(\Delta t)^2} - \frac{\gamma}{2\Delta t} + \frac{\omega_p^2}{4}\right],$$

$$b_{0zx} = \sin\theta\cos\theta\cos\phi\left[\frac{1}{(\Delta t)^2} + \frac{\gamma}{2\Delta t}\right] - \frac{\sin\theta\cos\theta\cos\phi}{\varepsilon_\theta}\left[\frac{1}{(\Delta t)^2} + \frac{\gamma}{2\Delta t} + \frac{\omega_p^2}{4}\right],$$

$$b_{1zx} = -\sin\theta\cos\theta\cos\phi\frac{2}{(\Delta t)^2} - \frac{\sin\theta\cos\theta\cos\phi}{\varepsilon_\theta}\left[-\frac{2}{(\Delta t)^2} + \frac{\omega_p^2}{2}\right],$$

$$b_{2zx} = \sin\theta\cos\theta\cos\phi\left[\frac{1}{(\Delta t)^2} - \frac{\gamma}{2\Delta t}\right] - \frac{\sin\theta\cos\theta\cos\phi}{\varepsilon_\theta}\left[\frac{1}{(\Delta t)^2} - \frac{\gamma}{2\Delta t} + \frac{\omega_p^2}{4}\right],$$

$$b_{0zy} = \sin\theta\cos\theta\sin\phi\left[\frac{1}{(\Delta t)^2} + \frac{\gamma}{2\Delta t}\right] - \frac{\sin\theta\cos\theta\sin\phi}{\varepsilon_\theta}\left[\frac{1}{(\Delta t)^2} + \frac{\gamma}{2\Delta t} + \frac{\omega_p^2}{4}\right],$$

$$b_{1zy} = -\sin\theta\cos\theta\sin\phi\frac{2}{(\Delta t)^2} - \frac{\sin\theta\cos\theta\sin\phi}{\varepsilon_\theta}\left[-\frac{2}{(\Delta t)^2} + \frac{\omega_p^2}{2}\right],$$

$$b_{2zy} = \sin\theta\cos\theta\sin\phi\left[\frac{1}{(\Delta t)^2} - \frac{\gamma}{2\Delta t}\right] - \frac{\sin\theta\cos\theta\sin\phi}{\varepsilon_\theta}\left[\frac{1}{(\Delta t)^2} - \frac{\gamma}{2\Delta t} + \frac{\omega_p^2}{4}\right],$$

$$b_{0zz} = \cos^2\theta\left[\frac{1}{(\Delta t)^2} + \frac{\gamma}{2\Delta t}\right] + \frac{\sin^2\theta}{\varepsilon_\theta}\left[\frac{1}{(\Delta t)^2} + \frac{\gamma}{2\Delta t} + \frac{\omega_p^2}{4}\right],$$

$$b_{1zz} = -\cos^2\theta\frac{2}{(\Delta t)^2} + \frac{\sin^2\theta}{\varepsilon_\theta}\left[-\frac{2}{(\Delta t)^2} + \frac{\omega_p^2}{2}\right],$$

$$b_{2zz} = \cos^2\theta\left[\frac{1}{(\Delta t)^2} - \frac{\gamma}{2\Delta t}\right] + \frac{\sin^2\theta}{\varepsilon_\theta}\left[\frac{1}{(\Delta t)^2} - \frac{\gamma}{2\Delta t} + \frac{\omega_p^2}{4}\right].$$

Note that the field quantities $\overline{D_x}$, $\overline{D_y}$, and $\overline{D_z}$ in (7.51)–(7.53) are locally averaged values of $D_x$, $D_y$, and $D_z$, respectively, since the $x$-, $y$-, and $z$-components of the electric fields are not in the same location within each FDTD cell [29]. The averaging procedure needs to be applied to different field components corresponding to the position and orientation of material interfaces. Specifically in (7.51), the averaged $D_y$ and $D_z$ can be calculated using

$$\overline{D_y}(i,j,k) = \frac{D_y(i,j,k) + D_y(i+1,j,k) + D_y(i,j-1,k) + D_y(i+1,j-1,k)}{4},$$
$$\overline{D_z}(i,j,k) = \frac{D_z(i,j,k) + D_z(i+1,j,k) + D_z(i,j,k-1) + D_z(i+1,j,k-1)}{4},$$

where $(i,j,k)$ is the coordinate of the field component. In (7.52), the averaged $D_x$ and $D_z$ can be calculated using

$$\overline{D_x}(i,j,k) = \frac{D_x(i,j,k) + D_x(i,j+1,k) + D_x(i-1,j,k) + D_x(i-1,j+1,k)}{4},$$
$$\overline{D_z}(i,j,k) = \frac{D_z(i,j,k) + D_z(i,j+1,k) + D_z(i,j,k-1) + D_z(i,j+1,k-1)}{4}.$$

And in (7.53), the averaged $D_x$ and $D_y$ can be calculated using

$$\overline{D_x}(i,j,k) = \frac{D_x(i,j,k) + D_x(i,j,k+1) + D_x(i-1,j,k) + D_x(i-1,j,k+1)}{4},$$
$$\overline{D_y}(i,j,k) = \frac{D_y(i,j,k) + D_y(i,j,k+1) + D_y(i,j-1,k) + D_y(i,j-1,k+1)}{4}.$$

The updating equations for the magnetic fields $H_x$, $H_y$, and $H_z$ are in the same form as (7.51)–(7.53) with the same coefficients and can be obtained by replacing $\boldsymbol{E}$ with $\boldsymbol{H}$ and $\boldsymbol{D}$ with $\boldsymbol{B}$. The averaged field components can be calculated in a similar manner. Equations (7.5), (7.6), (7.51)–(7.53) and the updating equations for $\boldsymbol{H}$ from $\boldsymbol{B}$ (not given) form the updating equation set for the modeling of 3-D cloaks using the well-known leap-frog scheme [48]. If the plasma frequency in (7.8) is equal to 0, i.e., $\omega_p = 0$, and $\varepsilon_\theta = \mu_\theta = \varepsilon_\phi = \mu_\phi = 1$, the above updating equation set reduces to the updating equation set for the free space.

The numerical permittivity of $\varepsilon_r$ (due to the time discretization in FDTD) for the 3-D spherical cloak has the same form as that for the 2-D cylindrical cloak as introduced in the previous section, as, for both cases, the Drude dispersion model is used. The above averaging of field components and the correction of numerical material parameters ensure stable and accurate FDTD simulations of the 3-D cloak.

The FDTD method is a versatile numerical technique. However, similar to other numerical methods, it is computationally intensive. For large electromagnetic problems such as the modeling of 3-D cloaks, the requirement for system resources

is beyond the capability of a single personal computer (PC). One way to resolve this problem is to divide the whole computational domain into many smaller sub-domains, and each sub-domain can be handled by each machine of a PC cluster. When the PCs are linked altogether with an appropriate synchronization procedure, the original large problem can be decomposed and solved efficiently.

One of the most attractive features of the FDTD method is that it can be easily parallelized with very little modifications to the algorithm. Since it solves Maxwell equations in the time–space domain, the parallel FDTD algorithm is based on the space decomposition technique [13, 18]. The data transfer functionality between processors is provided by the message passing interface (MPI) library. Data exchange is required only for the adjacent cells at the interface among different sub-domains and is performed at each time step and, therefore, the parallel FDTD algorithm is a self-synchronized process. Figure 7.7 shows the arrangement of the field components in different sub-domains in parallel FDTD simulations. The red arrows are the transferred field components from the neighboring sub-domain during the data communication process. At the end of parallel FDTD simulations, the results calculated at each processor need to be combined to obtain the final simulation result. In comparison to conventional parallel FDTD method, the parallelization of the dispersive FDTD method introduced in this work requires additional field components to be transferred between adjacent sub-domains during the synchronization process, because of the applied field averaging scheme. The complexity of algorithm can increase further if the whole computational domain is divided along more than one direction, although the data communication load and the overall simulation time may be reduced.

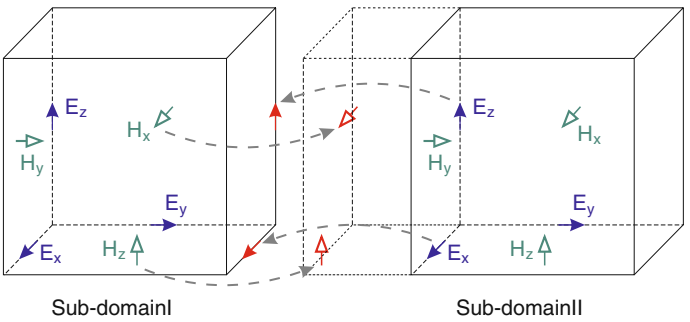


**Fig. 7.7** The arrangement of field components in different sub-domains in parallel FDTD simulations. The *red arrows* indicate the field components which are transferred from the neighboring domain during the data communication process and used to update the field components on the boundary of the current sub-domain.

The PC cluster used to simulate 3-D cloaks at Queen Mary, University of London, consists of 1 head node for monitoring purposes and 15 compute nodes for performing calculation tasks. Each node has Dual Intel Xeon E5405 (Quad Core 2.0 GHz) central processing units (CPUs) and there are 128 cores and 512 GB memory

in total. The nodes are connected by a 24-port gigabit switch. The GNU C compiler (GCC) and a free version of MPI, MPI Chameleon (MPICH), developed by Argonne National Laboratory [22], are used to compile the developed parallel dispersive FDTD code and handle the inter-core data communications, respectively.

The above developed parallel dispersive FDTD method is used to model the 3-D spherical cloaks and the simulation domain is shown in Fig. 7.8. The FDTD cell size in all simulations is $\Delta x = \Delta y = \lambda/150$, where $\lambda$ is the wavelength at the operating frequency $f = 2.0$ GHz. The time step is chosen according to the Courant stability criterion [48]. The radii of the cloak are $R_1 = 0.1$ m and $R_2 = 0.2$ m. In this work, only the ideal case (lossless) is considered with the collision frequency in (7.8) is set to be 0 ($\gamma = 0$). The radially-dependent plasma frequency can be calculated using (7.34) with a given value of $\varepsilon_r$ calculated from (7.37). The computational domain is truncated using the Berenger's perfectly matched layer (PML) [3] in $y$-direction to absorb waves leaving the computational domain without introducing reflections, and terminated with periodic boundary conditions (PBCs) in $x$- and $z$-directions for the modeling of a plane-wave source. The electric and magnetic fields of the plane wave are along the $z$- and $x$-axes, respectively, and the propagation direction is along the $y$-axis, as indicated in Fig. 7.8. For simplicity, the whole simulation domain is only divided along $y$-direction into 100 sub-domains and in total 100 processors and 220 gigabyte (GB) memory were used to run the parallel dispersive FDTD simulations. Each simulation lasts around 45 hours (13,000 time steps) before reaching the steady state.

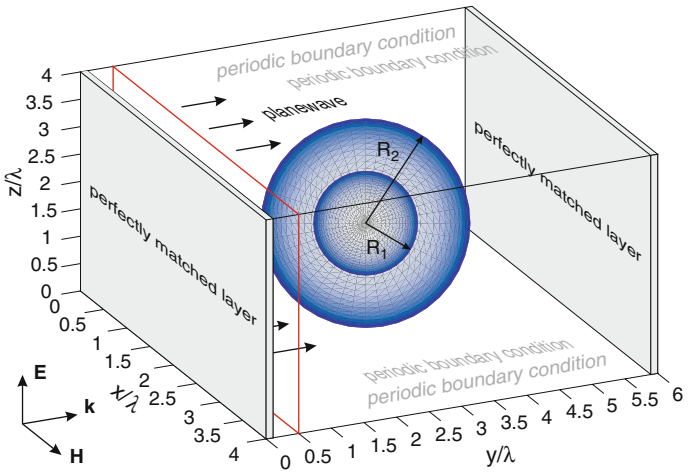


**Fig. 7.8** The 3-D parallel dispersive FDTD simulation domain for the case of plane-wave incidence on the cloak. The *red rectangle* indicates the location of the source plane.

Figures 7.9 and 7.10 show the normalized steady-state field distributions for the $E_z$ and $H_x$ components in $y$–$z$ and $x$–$y$ planes, respectively. It can be seen that the plane wave is guided by the cloak to propagate around its central region and

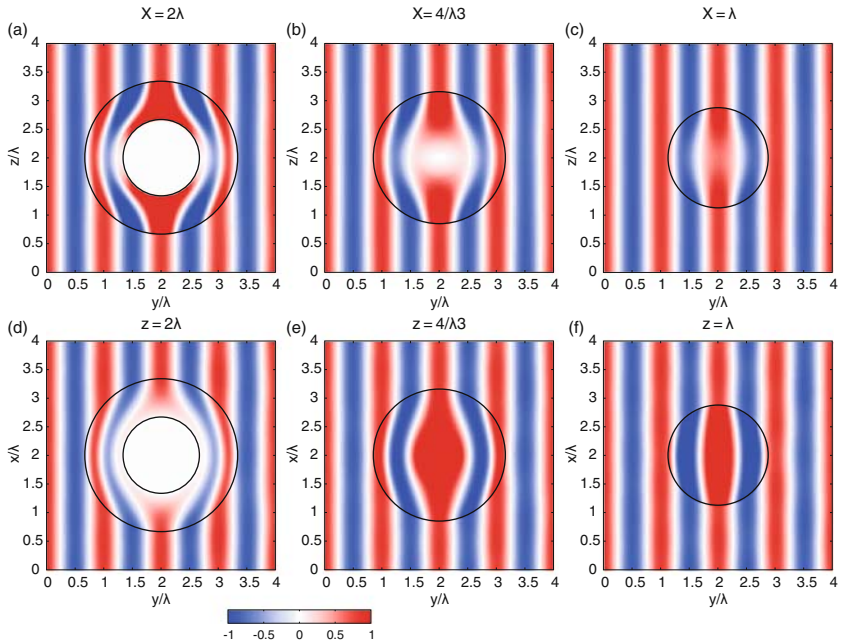


**Fig. 7.9** Normalized field distributions for the $E_z$ component in (**a**)–(**c**) $y$–$z$ plane and (**d**)–(**f**) $x$–$y$ plane in the steady state of the parallel dispersive FDTD simulations. The cutting planes are (see Fig. 7.8) (**a**) $x = 2\lambda$, (**b**) $x = 4\lambda/3$, (**c**) $x = \lambda$, (**d**) $z = 2\lambda$, (**e**) $z = 4\lambda/3$, and (**f**) $z = \lambda$. The wave propagation direction is from left to right.

re-composed after leaving the cloak. There are no visible reflections (except those minor numerical ones due to the finite spatial resolution in FDTD simulations). It is also interesting to note that the $E_z$ component in $y$–$z$ and $x$–$y$ planes in Fig. 7.9 and the $H_x$ component in $x$–$y$ and $y$–$z$ planes in Fig. 7.10 have the same distributions (with different amplitude), which is due to the fact that the ideal 3-D cloak is a rotationally symmetric structure with respect to the electric and magnetic fields. The wave behavior near the 3-D cloak can be better illustrated using the power flow diagram, as plotted in Fig. 7.11. It is shown that the Poynting vectors are diverted around the central area enclosed by the cloak. Therefore, objects placed inside the cloak do not introduce any scattering to external radiations and hence become "invisible."

The above presented results validate the developed parallel dispersive FDTD method and demonstrate the cloaking property of the structure. However, there are some numerical issues that need to be addressed in FDTD simulations. Besides the correction of numerical material parameters introduced earlier, since the cloak is a sensitive structure, for single-frequency simulations, the switching time of the sinusoidal source also has significant impact on the convergence time. Normalized field distributions from the simulations using different switching time are plotted at the time step $t = 1320\Delta t$ and shown in Fig. 7.12. It can be seen that if the source is

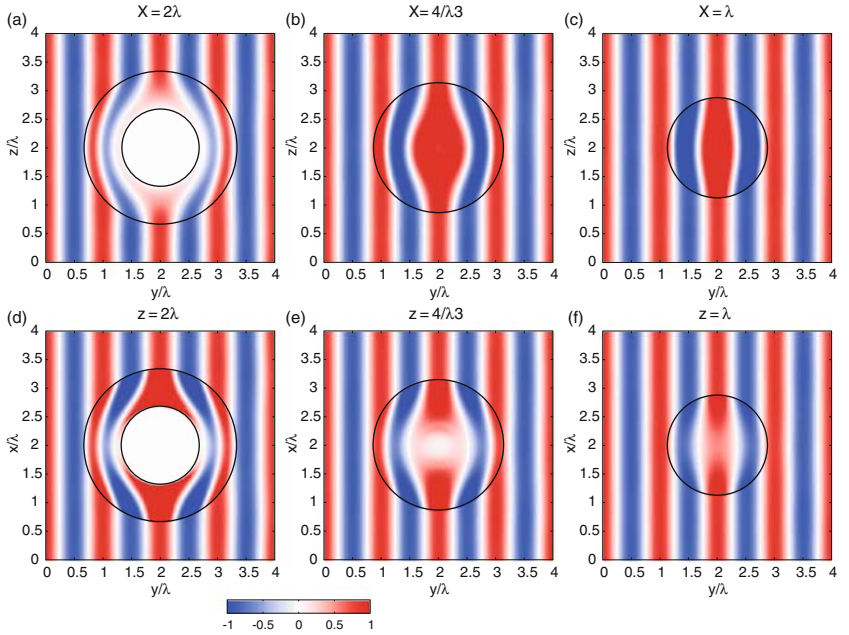


**Fig. 7.10** Normalized field distributions for the $H_x$ component in (**a**)–(**c**) $y$–$z$ plane and (**d**)–(**f**) $x$–$y$ plane in the steady state of the parallel dispersive FDTD simulations. The cutting planes are (see Fig. 7.8) (**a**) $x = 2\lambda$, (**b**) $x = 4\lambda/3$, (**c**) $x = \lambda$, (**d**) $z = 2\lambda$, (**e**) $z = 4\lambda/3$, and (**f**) $z = \lambda$. The wave propagation direction is from left to right.

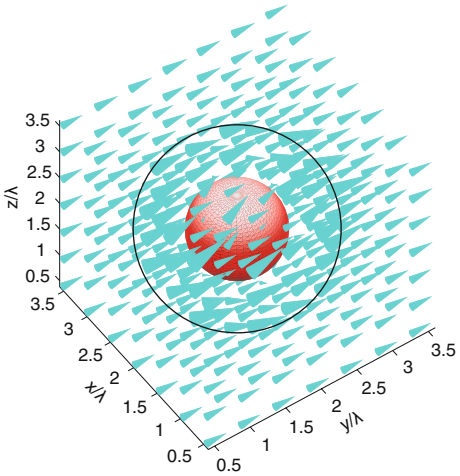


**Fig. 7.11** Power flow diagram of a plane-wave incidence on the ideal 3-D cloak calculated from parallel dispersive FDTD simulations.

switched to its maximum amplitude within a short period of time, because of the multiple frequency components excited, and the cloak is essentially a narrowband structure due to its dispersive nature, the scattering from the cloak may occur, as shown in Fig. 7.12(a). The scattered waves oscillate within the lossless cloak and hence it requires a very long time for the simulations to reach the steady state. It is also demonstrated that if the switching time is greater than $10T_0$, where $T_0$ is the period of the sinusoidal wave, the scattered waves can be significantly reduced and a much shorter convergence time in simulations can be achieved. Therefore, in the previous simulations, the switching time of $30T_0$ was used.

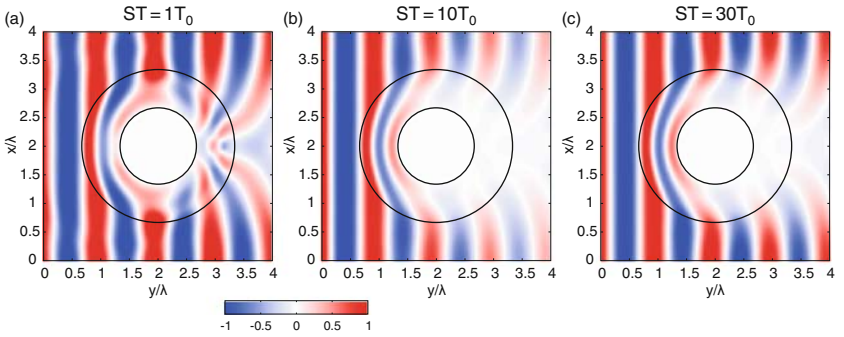


**Fig. 7.12** Comparison of the influence of different switching time (ST) of the sinusoidal source on the simulation results: (**a**) ST $= T_0$, (**b**) ST $= 10T_0$, (**c**) ST $= 30T_0$, where $T_0$ is the period of the sinusoidal wave. The wave propagation direction is from left to right and the normalized field distributions are plotted in the $x$–$y$ plane ($z = 2\lambda$, see Fig. 7.8) and at the time step $t = 1320\Delta t$.

Since the FDTD method is a time-domain technique, it is convenient to study the transient response of the 3-D cloak. The snapshots of the field distributions for the $E_z$ component at different time steps $t = 3000\Delta t$ (5.77 ns), $t = 5000\Delta t$ (9.62 ns), and $t = 8000\Delta t$ (15.40 ns) are taken and plotted in Fig. 7.13. It is shown in Fig. 7.13(a) that outside the shadow region behind the cloak ($y \sim 3.5\lambda$, $x < 0.5\lambda$, and $x > 3.5\lambda$), waves propagate at the speed of light and the wave front remains the same as the one before reaching the cloak. However, due to the fact that the waves that travel through the cloak undergo a longer path compared to the free-space one, and since the group velocity cannot exceed the speed of light, the wave front experiences a considerable delay, when the waves re-enter the free space, as it is illustrated by the field distributions at different time steps in FDTD simulations in Fig. 7.13. The convergence of simulations is rather slow and the steady state is reached in simulations only after about 13,000 time steps (25.02 ns).

In summary, a parallel dispersive FDTD method has been developed to model the ideal 3-D cloak. The radial dependent permittivity and permeability of the cloak are mapped to the Drude dispersion model and taken into account in FDTD simulations using an ADE-based method. Due to the memory restraint of a single PC, a parallel FDTD method is developed to handle the large amount of memory and simulation time required to model the 3-D cloak. FDTD simulation results are validated by

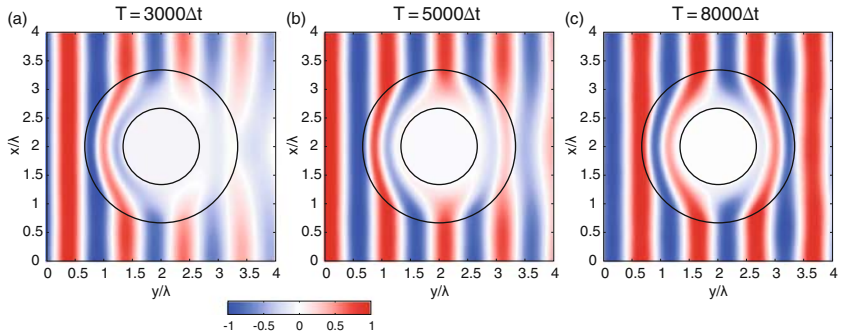


**Fig. 7.13** Snapshots of the field distributions for the $E_z$ component at different time steps in the parallel dispersive FDTD simulations: (**a**) $t = 3000\Delta t$ (5.77 ns), (**b**) $t = 5000\Delta t$ (9.62 ns), (**c**) $t = 8000\Delta t$ (15.40 ns), plotted in the $x$-$y$ plane ($z = 2\lambda$, see Fig. 7.8). The wave propagation direction is from left to right.

those obtained using analytical methods. It is demonstrated that for single-frequency simulations, the source excitation needs to be switched on slowly enough to avoid the wave scattering from the cloak, due to the sensitivity of the cloaking material. It is also shown from the transient FDTD analysis that waves passing through the cloak experience a considerable time delay comparing with the free-space propagations.

## 7.4 FDTD Modeling of the Ground-Plane Cloak

The majority of the proposed schemes for cloaking objects are based on the coordinate transformation method [38] and require materials with relative permittivity and permeability values that are anisotropic and less than unity. Although metamaterials could be eventually used widespread in constructing those cloaks, such metamaterial-based cloaks have limited implementations [44, 34], suffer from inherent losses and are not broadband due to their resonant nature [56, 49].

In an attempt to create more practical, isotropic cloaks, Li and Pendry [32] suggested the use of the coordinate transformation technique to make an object appear as a ground plane, thus rendering it invisible when the object and the cloak are placed on top of another conductive plane. Despite the fact that the whole structure needs to be embedded in a background material and that the cloak is not perfect since any magnetic permeability and anisotropy are initially ignored, only isotropic dielectric materials are required to realize the design.

Such coordinate transformations do not produce closed-form formulas for the required material parameters. Rather, they need to be extracted numerically from the non-orthogonality of the generated transformation mesh. From a simulation perspective, a non-orthogonal FDTD algorithm (NFDTD) [21] is mostly suitable for solving these scenarios, since the specified conformal grid can be directly imported to the simulation. Due to the nature of conformal FDTD, the algorithm is very efficient and a low spatial resolution (e.g., $\Delta x = \Delta y = \lambda/10$) is needed. Dispersive

NFDTD or the conventional Yee's FDTD algorithms can also be utilized, but with higher resolutions of discretization.

In this section we use a coordinate transformation to create a cloak that covers a triangular-shaped conducting object placed on a ground plane. A NFDTD algorithm that uses non-orthogonal meshes is initially utilized to test the full cloak. Subsequently, based on the principle that an impinging wave would not resolve the material features smaller than its wavelength, simple approximate cloaks are designed that consist of only a few blocks of different dielectric materials and are found through non-dispersive FDTD simulations to work almost as well as the full cloak. In addition, a ground-plane cloak embedded in free space is presented, and by further ignoring dispersive permittivity values ($\varepsilon < 1$), it is showed that a similar simplified ground-plane quasi-cloak minimizes scattering, without requiring a surrounding impedance-matched layer. The performance of the quasi-cloaks is confirmed by evaluating the spatial and spectral distributions of the scattered field energy.

The object to be concealed is a conductive triangular prism with a base $1.6\,\mu$m and height $0.2\,\mu$m, while the cloak is $3\,\mu$m long and $0.75\,\mu$m tall. Using a technique similar to the one described in [32], a 2-D near-conformal mesh is found that surrounds the domain above the object. As a result, the cells become non-orthogonal or "stretched." Given the $2 \times 2$ covariant metric $g$ for each cell, the relative permittivity of each block is found as

$$\varepsilon = \frac{\varepsilon_{ref}}{\sqrt{\det g}}. \tag{7.54}$$

Here, $\varepsilon_{ref}$ is the relative permittivity of the surrounding medium. A suitable map that reduces the anisotropy of the cloak is found by minimizing the width of the distribution of the parameter $\sqrt{\frac{g_{xy}g_{yx}}{g_{xx}g_{yy}}}$, as shown in Fig. 7.14(a), where $g_{xy}$ is a met-

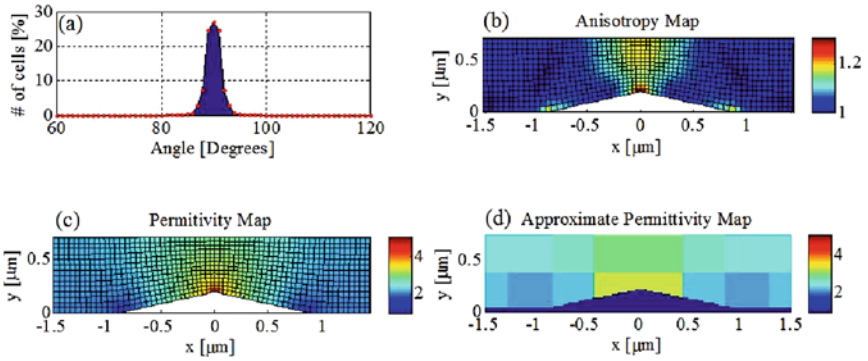


**Fig. 7.14** (**a**) The distribution of the cloaked region's cells as a function of their "stretch" or anisotropy. (**b**) The anisotropy map of the cloaked region, which is ignored in the simulations. (**c**) The relative permittivity map of the cloaked region. (**d**) An approximately constructed relative permittivity map that mimics the behavior of the material presented in (**c**).

ric tensor and $\det g$ can be calculated as $\det g = g_{xy} \cdot g_{yx} - g_{xx} \cdot g_{yy}$. For the map shown in Fig. 7.14(c), $1.79 \leq \varepsilon \leq 4.70$ and the maximum anisotropy is 1.20. The full anisotropy map is shown in Fig. 7.14(b). The latter maximum anisotropy value can be reduced more, when an object to cloak has less sharp corners, however, the proposed prism structure is preferred here because the cloak can be constructed in a simple manner using straight cuts. It should be noted that only near-orthogonal cells result in small anisotropy and thus result in a working cloak; this can be indicated by the narrow distribution of cells around 90° in Fig. 7.14(a).

Assuming that a $2.4\,\mu$m wide (FWHM) pulse at a frequency of 400 THz is launched against the object at a 45° angle, the wavelength in a material with permittivity 2.25 is $0.5\,\mu$m and thus features that are much smaller than this value are not expected to be resolved. In order to test a simpler cloak that is not as detailed as the original one in Fig. 7.14(c), we design a new "approximate" cloak by choosing only 16 evenly distributed values of permittivity in 2-D space, as shown in Fig. 7.14(d), in addition to setting their relative permeability to unity. Each of these blocks has dimensions $(dx,dy) = (0.4285\,\mu\text{m}, 0.3750\,\mu\text{m})$.

Both TE and TM waves are tested in order to demonstrate the isotropy of the structure. Figure 7.15(a) shows the scattering field distribution from the object for a TM pulse using the non-orthogonal FDTD, which has a distinct two-lobe pattern after impinging on the metallic object over the metallic ground. The spatial discretization in this case is directly derived from the mesh generated from the coordinate transformation, or $\lambda/16$, where $\lambda$ is the free-space wavelength. Figure 7.15(b) shows the scattering from the same object using conventional 2-D FDTD for a TE pulse and discretization of $\lambda/30$. The comparison confirms that both results are indeed very similar. Slight differences between the patterns in these two cases are attributed to the different positioning of the source due to the different FDTD meshes utilized.

Next, the full cloak presented in Fig. 7.14(c) is applied to the object in Fig. 7.15(a), and the result is shown in Fig. 7.15(c), using identical parameters as in Fig. 7.15(a). We observe that the scattering pattern of a pulse impinging on a flat conductive sheet is now almost fully retrieved, thus indicating the success of the cloaking structure. The object has collapsed into a ground plane, rendering it invisible since it is placed above another ground plane. The scattering pattern is not perfect due to the anisotropy that was ignored (Fig. 7.14(b)) in order to have an all-dielectric cloak.

Now we replace the full cloak with the approximate cloak that is shown in Fig. 7.14(d). For a TE impinging source pulse, the conventional FDTD result for the field distribution is shown in Fig. 7.15(d). We observe that despite the fact that the cloak consists of only 16 different pieces of simple dielectric materials, the cloaking effect is very strong and the object is effectively hidden as the scattering pattern of a flat ground plane is excellently reconstructed.

In Fig. 7.16(a)–(c) three more maps that correspond to cloaks embedded in a medium are presented. In Fig. 7.16(a) the full non-orthogonal map is shown. Next, an orthogonal grid generated by recursive division of cartesian cells is used to sample the original permittivity distribution of Fig. 7.16(a), as shown in Fig. 7.16(b). The sampled map consists of $80 \times 20$ square blocks that have dimension equal to

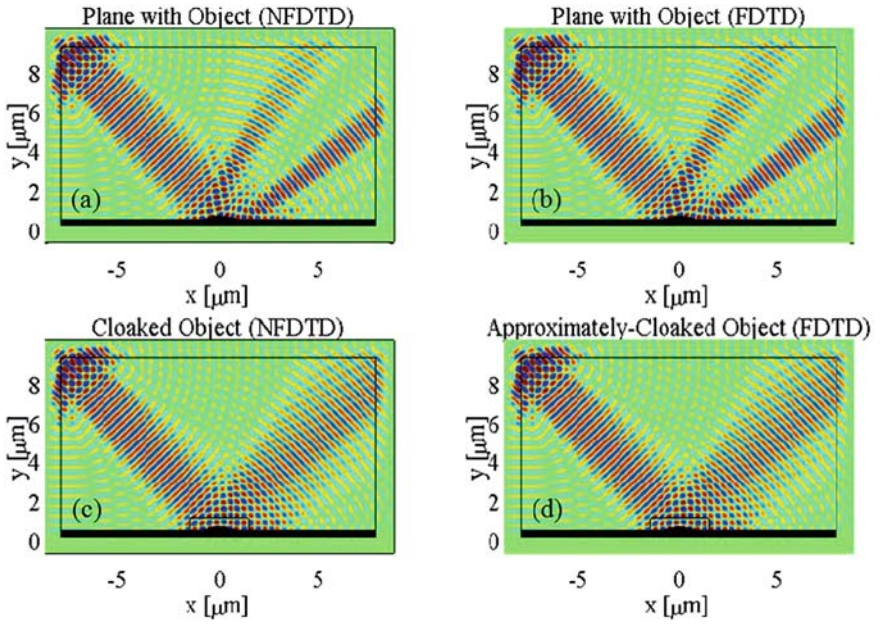


**Fig. 7.15** Comparison of field distributions between orthogonal 2-D FDTD for TE waves (right column; (**b**,**d**) ) and 2-D non-orthogonal FDTD (NFDTD) for TM waves (left column; (**a**,**c**)). A temporally long, 400 THz frequency, 2.4 $\mu$m-wide (FWHM) Gaussian pulse impinges at a 45° angle on a PEC object placed on a ground plane, with (bottom row; (**c**,**d**) ) and without (top row; (**a**,**b**)) cloaks. The cloak structure for panels (**c**) and (**d**) is given in panels 7.14(**c**) and 7.14(**d**), respectively. The excitation and the structure are embedded in a background glass material with $\varepsilon_{ref} = 2.25$. The *thin black lines* indicate the PML boundaries, while the *thick black line* is the conducting surface. The *triangular object* and the *cloak boundaries* are also shown on top of the conducting plane.

0.0375 $\mu$m. In addition, a low-resolution sampled map (quasi-cloak) is generated, consisting of $6 \times 2$ blocks that have dimensions 0.4285 $\mu$m by 0.3750 $\mu$m, as shown in Fig. 7.16(c). Again, some of the blocks are truncated to fit around the object. The latter quasi-cloak has $2.18 \leq \varepsilon \leq 3.30$. From the point of view of an impinging electromagnetic wave, these two cloaks should behave similarly if its wavelength is not much smaller than the sizes of the blocks that consist the cloaks.

Subsequently, the performance of a ground-plane cloak embedded in free space will be evaluated. A map similar to the one presented in Fig. 7.16(a) is generated, with the difference that it is surrounded by free space with $\varepsilon_{ref} = 1$. Unavoidably, the transformation generates cells near the base corners of the triangular object that correspond to permittivity values that are smaller than the background permittivity $\varepsilon_{ref}$, with a minimum value equal to $\varepsilon = 0.8$. As it will be shown in detail, since these regions are relatively small compared to the total size of the cloak and compared to the incident wavelength, they are not expected to affect the cloaking performance significantly. Thus, a high-resolution cloak is generated for free space, consisting of $80 \times 20$ blocks, and any smaller than unity values of the permittivity are set to

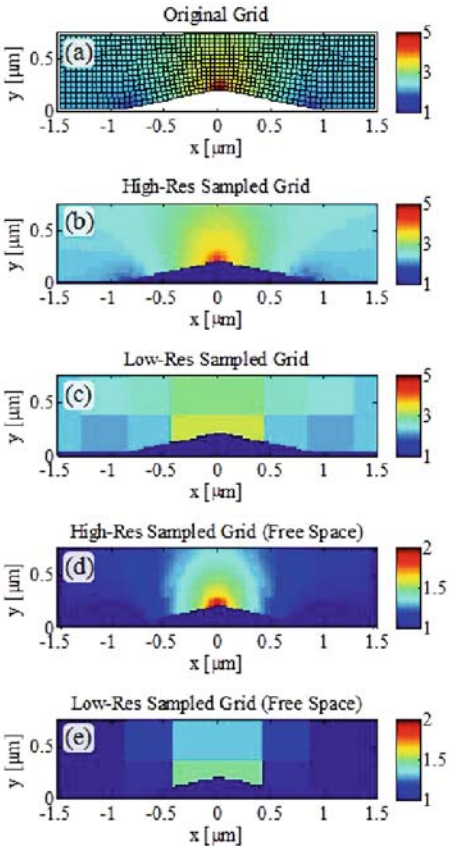


**Fig. 7.16** Relative 2-D permittivity maps for cloaking a triangular metallic object placed over a ground plane. The cloaks in (**a**)–(**c**) are embedded in glass ($\varepsilon_{ref} = 2.25$), while the cloaks in (**d**)–(**e**) are embedded in free space ($\varepsilon_{ref} = 1$). The *colored bars* indicate the relative permittivity values for each map. (**a**) Full non-orthogonal map consisting of $64 \times 15$ cells. (**b**) High-resolution sampled map consisting of $80 \times 20$ blocks. (**c**) Low-resolution sampled map consisting of $6 \times 2$ blocks. (**d**) High-resolution sampled map consisting of $80 \times 20$ blocks. (**e**) Low resolution sampled map consisting of $4 \times 2$ blocks.

one, as shown in Fig. 7.16(d). In addition, a low-resolution quasi-cloak is obtained by sampling the latter high-resolution permittivity map. This quasi-cloak is shown in Fig. 7.16(e) and consists of $4 \times 2$ blocks with the following relative permittivity values in the $x < 0$ domain (left to right, top to bottom): [1.17, 1.30, 1.02, 1.47]. The quasi-cloak is symmetric around $x = 0$.

In order to quantify the performance and also verify the broadband cloaking capabilities of the ground-plane free-space quasi-cloak of Fig. 7.16(e), a $2.4\,\mu$m wide, 4.7 fs long, TM Gaussian pulse around 600 THz is launched at 45° (in the $x < 0$ region) against the quasi-cloaked object. The total field energy crossing a semicircular curve with $4\,\mu$m radius centered at the object is recorded (in the $x > 0$ region). The pulse duration is chosen such that the frequency content of the pulse spreads over the whole visible spectrum: its FWHM is $\approx 250$ THz.

The angular distribution of the reflected energy in the $x > 0$ region is shown in Fig. 7.17(a); the angles are measured from the ground plane. When only the flat ground surface is present, the peak of the distribution is observed at a 45° angle, as expected. When the metallic object is placed on top, however, two strong lobes are observed instead, at 23° and 71°. When the quasi-cloak based on the $80 \times 20$ map

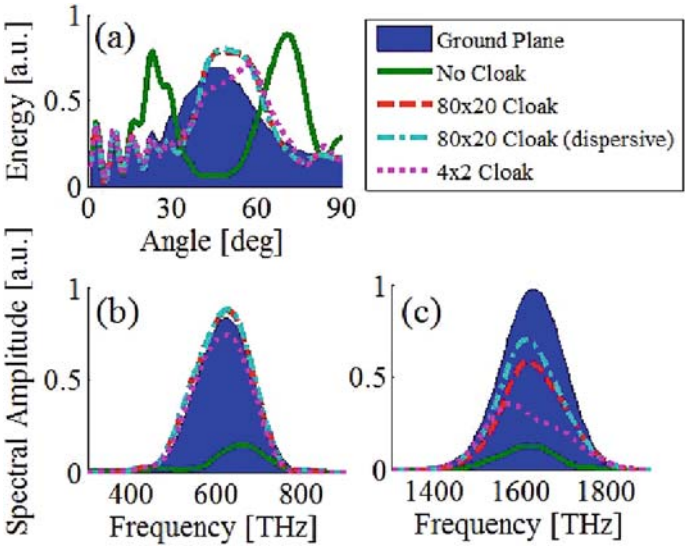


**Fig. 7.17** (**a**) Angular distribution of the scattered field energy in free space when a 4.7 fs long, 2.4 $\mu$m wide, 600 THz Gaussian pulse is incident. The patterns shown correspond to incidence on a flat plane, incidence on the metallic object placed on the plane, and incidence on the same object when covered with either the $80 \times 20$ (Fig. 7.16(d)), the $80 \times 20$ dispersive, and the $4 \times 2$ (Fig. 7.16(**e**)) quasi-cloaks. (**b**) The corresponding amplitudes of the frequency spectra of the scattered 600 THz pulse as recorded at a 45° angle. (**c**) The frequency spectra of a 1,600 THz scattered pulse in the same setup.

(Fig. 7.16(d)) is placed around the object, most of the scattered energy is now restored into a single lobe again around 49°. A similar single-lobe pattern is observed when the simplified sampled $4 \times 2$ quasi-cloak (Fig. 7.16(e)) is utilized, as shown also in Fig. 7.17(a), with only slight deterioration compared to the high-resolution cloak. The cloaking performance of simpler structures, consisting of fewer than eight blocks using this transformation map, is very limited. Note that the pattern observed for small angles (up to $\approx 20°$) in Fig. 7.17(a) is a result of the interference between the incident and reflected parts of the pulse.

In addition, the effect of the dispersive values of the original map that were ignored is analyzed. A dispersive FDTD simulation [59] with similar parameters is performed, with the difference that it includes the permittivity values $0.8 \leq \varepsilon < 1$ in the high-resolution $80 \times 20$ cloak, instead of setting that region to free space. The result of the angular distribution of the scattered energy for the dispersive cloak is also shown in Fig. 7.17(a). Indeed, it is verified that the pattern is almost identical to the pattern of the non-dispersive $80 \times 20$ cloak at that frequency.

The frequency spectra of the 600 THz scattered pulses are shown in Fig. 7.17(b), by recording the electric field amplitude as a function of time on the semi-circular curve at a 45° angle. The filled area indicates the spectrum of the reflected pulse when only the flat surface is present, which is used as a reference. We observe in Fig. 7.17(b) that the frequency spectrum of the scattered pulse, when only the bare

object is present on top of the ground plane, is severely distorted: both its amplitude and its relative distribution are different compared to the reference spectrum within the spectrum. When the quasi-cloaks are covering the object, though, the spectrum of the original pulse at 45° is almost fully recovered. Again, the dispersive sections of the cloak do not affect its performance when replaced by free space.

The strong broadband performance of the quasi-cloak is exhibited until the incident wavelength becomes much smaller than the dimensions of the cloak's block elements. This is illustrated by launching an identical 4.7 fs long pulse at 1,600 THz frequency toward the cloak, and obtaining the reflected spectra as before, which are shown in Fig. 7.17(c). It is observed that the simplified $4 \times 2$ quasi-cloak is not capable of restoring the spectrum as well as the $80 \times 20$ cloak, especially past 1,550 THz. In addition, the dispersive cloak (with its elements tuned to operate around the incident frequency) now exhibits improved performance compared to the all-dielectric one. The dispersive area is larger in terms of the incident wavelength for this higher frequency, thus introducing more error when replacing it with free space.

The results of Fig. 7.17 demonstrate that even though perfect optical cloaking is not achieved with a quasi-cloak, its cloaking performance is substantial, with the additional advantages that it is very simple to construct and it can be natively placed in free space. These two factors are obviously extremely favorable in a variety of cloaking applications, as experimental imperfections that are inevitably introduced when building more complicated structures, can be avoided. When designing a quasi-cloak, there is a tradeoff between the simplicity of the structure and the upper frequency of operation. While the broadband performance demonstrated here should be more than adequate for most applications, it can be improved when necessary by increasing the complexity of the structure.

## 7.5 Conclusion

Novel radially dependent dispersive FDTD techniques were presented to model 2-D lossy and 3-D lossless cloaking devices. The cloaking material parameters were mapped using the dispersive Drude model and the constitutive equations were discretized in space and time. The FDTD simulation results were in good agreement with similar findings from the theoretical analysis and the frequency-domain numerical modeling of the cloaking structures. From the FDTD numerical modeling, it was concluded that the cloaking structure is sensitive to losses. Moreover, it can be "invisible" only at a narrow frequency range, approximately 20% at the central frequency of 2 GHz.

The parallelization of the FDTD method is essential due to the large amount of memory and simulation time required to model the 3-D spherical cloak. It was demonstrated that for single-frequency simulations, the source excitation needs to be switched on slowly enough to avoid the wave scattering from the cloak, due to the sensitivity of the cloaking material. It was also shown from the transient FDTD analysis that waves passing through the 2-D and 3-D cloaks experience a considerable

time delay compared with the free-space propagations. These limitations are unavoidable and a direct result of the device's inherent dispersive nature.

To avoid the dispersion effects and achieve broadband invisibility devices, ground-plane cloaks were proposed and modeled with the FDTD method. It was demonstrated that ground-plane quasi-cloaks can be designed using relatively simple structures without significantly affecting their cloaking performance or bandwidth. Such quasi-cloaks designed to work in free space above a metallic surface, consisting of only a few all-dielectric blocks, can provide strong cloaking potential over the whole visible spectrum, as long as its features remain smaller than the wavelength of radiation. These designs should be straightforward to be practically implemented compared to previous ideas, e.g., by doping material blocks or by using non-resonant metamaterial cells.

## References


1. de Abajo, F.J.G., Gomez-Santos, G., Blanco, L.A., Borisov, A.G., Shabanov, S.V.: Tunneling mechanism of light transmission through metallic films. Phys. Rev. Lett. **95**, 067403 (2005)
2. Alu, A., Engheta, N.: Achieving transparency with plasmonic and metamaterial coatings. Phys. Rev. E **72**, 016623 (2005)
3. Bérenger, J.P.: A perfectly matched layer for the absorption of electromagnetic waves. J. Comp. Phys. **114**, 185–200 (1994)
4. Bower, A.F.: Applied mechanics of solids. CRC Press (2009) Boca Raton, FL, USA
5. Cai, W., Chettiar, U.K., Kildishev, A.V., Shalaev, V.M.: Optical cloaking with metamaterials. Nat. Photonics **1**, 224227 (2007)
6. Cai, W., Chettiar, U.K., Kildishev, A.V., Shalaev, V.M.: Designs for optical cloaking with high-order transformations. Opt. Express **16**(8), 5444–5452 (2008)
7. Cai, W., Chettiar, U.K., Kildishev, A.V., Shalaev, V.M., Milton, G.W.: Nonmagnetic cloak with minimized scattering. Appl. Phys. Lett. **91**, 111105 (2007)
8. Chen, H., Chan, C.: Time delays and energy transport velocities in three dimensional ideal cloaking devices. J. Appl. Phys. **104**, 033113 (2008)
9. Chen, H., Chan, C.T.: Acoustic cloaking in three dimensions using acoustic metamaterials. Appl. Phys. Lett. **91**, 183518 (2007)
10. Chen, H., Chan, C.T.: Transformation media that rotate electromagnetic fields. Appl. Phys. Lett. **90**, 241105 (2007)
11. Chen, H., Liang, Z., Yao, P., Jiang, X., Ma, H., Chan, C.T.: Extending the bandwidth of electromagnetic cloaks. Phys. Rev. B **76**, 241104 (2007)
12. Chen, H., Wu, B.I., Zhang, B., Kong, J.A.: Electromagnetic wave interactions with a metamaterial cloak. Phys. Rev. Lett. **99**, 063903 (2007)
13. Chew, K.C., Fusco, V.F.: A parallel implementation of the finite-difference time-domain algorithm. Int. J. Numerical Modeling **8**, 293–299 (1995)
14. Cory, H., Lee, Y., Hao, Y., Parini, C.: Use of conjugate dielectric and metamaterial slabs as radomes. IET Micro. Antenna Propag. **1**, 137–143 (2007)
15. Cummer, S.A., Popa, B.I., Schurig, D., Smith, D.R., Pendry, J.B.: Full-wave simulations of electromagnetic cloaking structures. Phys. Rev. E **74**, 036621 (2006)
16. Cummer, S.A., Schurig, D.: One path to acoustic cloaking. New J. Phys. **9**, 45 (2007)
17. Gandhi, O.P., Gao, B.Q., Chen, J.Y.: A frequency-dependent finite-difference time-domain formulation for general dispersive media. IEEE Trans. Micro. Theory Tech. **41**, 658665 (1993)
18. Gedney, S.: Finite-difference time-domain analysis of microwave circuit devices on high performance vector/parallel computers. IEEE Trans. Micro. Theory Tech. **43**, 2510–2514 (1995)

19. Greenleaf, A., Kurylev, Y., Lassas, M., Uhlmann, G.: Improvement of cylindrical cloaking with the SHS lining. Opt. Express **15**(20), 12717–12734 (2007)
20. Hildebrand, F.B.: Introduction to numerical analysis. New York, Mc-Graw-Hill (1956)
21. Holland, R.: Finite-difference solution of Maxwell's equations in generalized nonorthogonal coordinates. IEEE Trans. Nucl. Sci. **30**(6), 4589–4591 (1983)
22. http://wwwunix.mcs.anl.gov/mpi/mpich/
23. Huang, Y., Feng, Y., Jiang, T.: Electromagnetic cloaking by layered structure of homogeneous isotropic materials. Opt. Express **15**(18), 11133–11141 (2007)
24. Jiang, W., Cui, T., Ma, H., Yang, X., Cheng, Q.: Layered high-gain lens antennas via discrete optical transformation. Appl. Phys. Lett. **93**, 221906 (2008)
25. Kildal, P.S.: Artificially soft and hard surfaces in electromagnetics. IEEE Trans. Antennas Propagat. **38**, 1537–1544 (1990)
26. Kildal, P.S., Kishk, A., Tengs, A.: Reduction of forward scattering from cylindrical objects using hard surfaces. IEEE Trans. Antennas Propagat. **44**, 1509–1520 (1996)
27. Kong, F., Wu, B., Kong, J., Huangfu, J., Xi, S., Chen, H.: Planar focusing antenna design by using coordinate transformation technology. Appl. Phys. Lett. **91**, 253509 (2007)
28. Kwon, D.H., Werner, D.H.: Two-dimensional eccentric elliptic electromagnetic cloaks. Appl. Phys. Lett. **92**, 013505 (2008)
29. Lee, J.Y., Myung, N.H.: Locally tensor conformal FDTD method for modelling arbitrary dielectric surfaces. Microw. Opt. Tech. Lett. **23**, 245–249 (1999)
30. Leonhardt, U.: Notes on conformal invisibility devices. New J. Phys. **8**, 118 (2006)
31. Leonhardt, U.: Optical conformal mapping. Science **312**, 17771780 (2006)
32. Li, J., Pendry, J.B.: Hiding under the carpet: a new strategy for cloaking. Phys. Rev. Lett. **101**, 203901 (2008)
33. Liang, Z., Yao, P., Sun, X., Jiang, X.: The physical picture and the essential elements of the dynamical process for dispersive cloaking structures. Appl. Phys. Lett. **92**, 131118 (2008)
34. Liu, R., Ji, C., Mock, J.J., Chin, J.Y., Cui, T.J., Smith, D.R.: Broadband ground-plane cloak. Science **323**(5912), 366–369 (2009)
35. Miller, D.A.B.: On perfect cloaking. Opt. Express **14**(25), 12457–12466 (2006)
36. Milton, G.W., Nicorovici, N.P.: On the cloaking effects associated with anomalous localized resonance. Proc. R. Soc. A **462**, 3027–3059 (2006)
37. Ng, J., Chen, H., Chan, C.: Metamaterial frequency-selective superabsorber. Opt. Lett. **34**(5), 644–646 (2009)
38. Pendry, J.B., Schurig, D., Smith, D.R.: Controlling electromagnetic fields. Science **312**, 1780–1782 (2006)
39. Podolskiy, V., Narimanov, E.: Near-sighted superlens. Opt. Lett. **30**(1), 75–77 (2005)
40. Rahm, M., Cummer, S.A., Schurig, D., Pendry, J.B., Smith, D.R.: Optical design of reflectionless complex media by finite embedded coordinate transformations. Phys. Rev. Lett. **100**, 063903 (2008)
41. Rahm, M., Roberts, D., Pendry, J., Smith, D.: Transformation-optical design of adaptive beam bends and beam expanders. Opt. Express **16**(15), 11555–11567 (2008)
42. Rahm, M., Schurig, D., Roberts, D.A., Cummer, S.A., Smith, D.R., Pendry, J.B.: Design of electromagnetic cloaks and concentrators using form-invariant coordinate transformations of Maxwells equations. Phot. Nanostr. Fund. Appl. **6**, 8795 (2008)
43. Ruan, Z., Yan, M., Neff, C.W., Qiu, M.: Ideal cylindrical cloak: perfect but sensitive to tiny perturbations. Phys. Rev. Lett. **99**, 113903 (2007)
44. Schurig, D., Mock, J.J., Justice, B.J., Cummer, S.A., Pendry, J.B., Starr, A.F., Smith, D.R.: Metamaterial electromagnetic cloak at microwave frequencies. Science **314**, 977980 (2006)
45. Schurig, D., Pendry, J.B., Smith, D.R.: Calculation of material properties and ray tracing in transformation media. Opt. Express **14**(21), 9794–9804 (2006)
46. Schurig, D., Pendry, J.B., Smith, D.R.: Transformation-designed optical elements. Opt. Express **15**(22), 14772–14782 (2007)
47. Smolyaninov, I., Hung, Y., Davis, C.: Two-dimensional metamaterial structure exhibiting reduced visibility at 500 nm. Opt. Lett. **33**, 1342–1344 (2008)

48. Taflove, A., Hagness, S.C.: Computational electrodynamics: the finite-difference time domain method, 3rd edn. Artech House (2005)
49. Tretyakov, S.A., Maslovski, S.I.: Veselago materials: what is possible and impossible about the dispersion of the constitutive parameters. IEEE Antennas Propag. Magazine **49**(1), 37–43 (2007)
50. Tsang, M., Psaltis, D.: Magnifying perfect lens and superlens design by coordinate transformation. Phys. Rev. B **77**, 035122 (2008)
51. Veselago, V.G.: The electrodynamics of substances with simultaneously negative values of ? and $\mu$. Sov. Phys. Usp. **10**, 509–514 (1968)
52. Weder, R.: Rigorous analysis of high-order electromagnetic invisibility cloaks. J. Phys. A: Math. Theor. **41**, 065207 (2008)
53. Yan, M., Ruan, Z., Qiu, M.: Scattering characteristics of simplified cylindrical invisibility cloaks. Opt. Express **15**(26), 17772–17782 (2007)
54. Yan, M., Yan, W., Qiu, M.: Cylindrical superlens by a coordinate transformation. Phys. Rev. B **78**, 125113 (2008)
55. Yang, T., Chen, H., Luo, X., Ma, H.: Superscatterer: enhancement of scattering with complementary media. Opt. Express **16**(22), 18545–18550 (2008)
56. Yao, P., Liang, Z., Jiang, X.: Limitation of the electromagnetic cloak with dispersive material. Appl. Phys. Lett. **92**, 031111 (2008)
57. Zhang, B., Chen, H., Wu, B.I., Luo, Y., Ran, L., Kong, J.A.: Response of a cylindrical invisibility cloak to electromagnetic waves. Phys. Rev. B **76**, 121101R (2007)
58. Zhang, B., Wu, B., Chen, H., Kong, J.: Rainbow and blueshift effect of a dispersive spherical invisibility cloak impinged on by a nonmonochromatic plane wave. Phys. Rev. Lett. **101**, 63902 (2008)
59. Zhao, Y., Argyropoulos, C., Hao, Y.: Full-wave finite-difference time-domain simulation of electromagnetic cloaking structures. Opt. Express **16**(9), 6717–6730 (2008)
60. Zhao, Y., Belov, P., Hao, Y.: Accurate modelling of left-handed metamaterials using a finite-difference time-domain method with spatial averaging at the boundaries. J. Opt. A: Pure Appl. Opt. **9**, 468475 (2007)
61. Zhao, Y., Hao, Y.: Finite-difference time-domain study of guided modes in nano-plasmonic waveguides. IEEE Trans. Antennas Propag. **55**, 3070–3077 (2007)

# Chapter 8
# Compensated Anisotropic Metamaterials: Manipulating Sub-wavelength Images

Yijun Feng

**Abstract** In this chapter, I will discuss the image focusing, rotation, lateral shift, as well as the image magnification with sub-wavelength resolutions through differently designed structures of compensated anisotropic metamaterials. The verifications of all the proposed structures by full wave electromagnetic simulations will be demonstrated, as well as the experimental proof of imaging with sub-wavelength resolution through a compensated bilayer lens realized by TL metamaterials. Utilizing the proposed structures, planar optical image of sub-wavelength objects can be magnified to wavelength scale allowing for further optical processing of the image by conventional optics.

**Key words:** Anisotropic metamaterial, compensated anisotropic metamaterials, sub-wavelength image, anisotropic metamaterial prism, transmission line metamaterial, perfect lens, compensated bilayer lens, diffraction limit.

## 8.1 Introduction

One of the intriguing properties of the artificial left-handed metamaterials (LHMs), i.e., the composite materials possessing both negative permittivity and permeability, first introduced by Victor G. Veselago in the 1960s, is their ability to focus the electromagnetic waves from a point source by a flat slab of the material [38]. Such focusing is a straightforward consequence of the ray optics due to the negative refraction of the LHM. In 2000, John B. Pendry extended Veselago's idea of focusing by flat LHM slab and included evanescent waves in his analysis. He discovered a rather striking transmission property and predicted that the evanescent waves emitted from the source, which carry sub-wavelength structural information

Yijun Feng*
Department of Electronic Science and Engineering, Nanjing University, Nanjing, 210093, China.
*email: yjfeng@nju.edu.cn

T.J. Cui et al. (eds.), *Metamaterials*, DOI 10.1007/978-1-4419-0573-4_8,

of the object, could be amplified inside the LHM slab and reconstructed at the image plane without loss in amplitude [25]. We know that the resolution of common physical imaging devices is restricted by the so-called diffraction limit, since these devices can only work with propagating spatial harmonics emitted from the source. The conventional lens systems cannot propagate evanescent waves which carry subwavelength information, due to the exponential decay of the waves that is exhibited in natural materials. Therefore, Pendry's discovery indicated that a lossless LHM slab with $\varepsilon_r = \mu_r = -1$, where $\varepsilon_r$ is the relative dielectric permittivity and $\mu_r$ is the relative magnetic permeability, should in principle behave like a "perfect lens" to achieve super-resolution, which overcomes the diffraction limit of conventional imaging systems. Unfortunately, the promising theoretical predictions have been limited by practical difficulties in the development of LHM. The dissipation and dispersion inherent to realistic metamaterials introduce a natural limit to the achievable resolution of the "perfect lens" configuration of an LHM slab [33, 30, 41].

However, recent experimental demonstrations with different "perfect lens" structures based on metamaterials have obtained resolution better than the diffraction limit of traditional imaging systems [12, 2, 22, 23, 1, 24, 18, 13]. For example, by investigating the electromagnetic radiation focusing through a slab of artificial structured material with negative real parts of the permittivity and permeability, the well-established images of two sources separated by a distance about $1/6$ of the wavelength have been obtained experimentally, which demonstrates the ability of producing improved resolution not restricted by the diffraction limit [18]. Another attempt is to realize the LHM planar lens with a transmission line metamaterial. A. Grbic et al. have demonstrated imaging of a point source with a half-power beamwidth of 0.21 effective wavelengths, which overcomes the diffraction limit at microwave frequency [13]. The experimental images in both examples are imperfect since the image beamwidth is much wider than that of the source due to the significant degradation by the losses and deviations of the material parameters in the realistic metamaterials.

LHMs were initially characterized as an isotropic media by Veselago [38], but it is currently accepted that the artificial LHM, such as the commonly used periodic array of split-ring resonators (SRRs) and conducting wires [31, 28, 29], is better modeled by anisotropic constitutive parameters, which can be diagonalized in the coordinate system parallel with the principal axes of the metamaterial [14]. Anisotropic metamaterials (AMMs) for which some diagonal elements of the permittivity and permeability tensors have negative value have been studied theoretically and identified into four classes based on their electromagnetic wave propagation properties, which are called *cutoff*, *always-cutoff*, *never-cutoff*, and *anti-cutoff* media [32]. Analytical studies of these anisotropic media have demonstrated anomalous electromagnetic wave reflection and refraction that occurs at the interface between normal medium and the anisotropic medium. Negative refraction could be realized in such medium under some different combinations of the medium parameters [32, 40, 20], and recent experiment and simulation have confirmed the negative refraction in the AMM composed of split-ring resonators, designed to provide a permeability of – 1 along the longitudinal axis [34]. The inversion of critical angle has also been studied

when a wave propagates through an anisotropic metamaterial composed of SRR and wire array exhibiting negative permittivity and negative permeability along some specific directions [14]. Using a transmission line version of AMM, we have successfully explored and demonstrated the various salient properties of the AMM, such as the negative refraction [8, 36], partial focusing [36], anomalous Brewster effect [9], and extraordinary transmission [11]. The artificial AMMs have significantly broadened the range of electromagnetic wave propagation phenomena available.

In the rest of this chapter, we will first discuss the electromagnetic wave propagation in different kinds of AMM media, especially a bilayer of AMM that compensated with each other in Section 8.2. Such configuration is considered as an expansion of the Veselago lens structure. The compensated bilayer that employs positive and negative refracting layers of anisotropic metamaterials can accomplish near-field focusing in a similar manner to the Veselago lens system where the wave propagation in the vacuum layer is completely compensated by that in the LHM layer. The compensated bilayer AMM lens could transfer the field distribution from one side of the bilayer to the other with sub-wavelength resolution not restricted by the diffraction limit. In Section 8.3, we will analyze the imaging performance through the compensated bilayer lens theoretically and explore the effects of loss and retardation in the material parameters on the image quality, which are evitable in realistic metamaterials. The advantage to the imaging using the compensated bilayers is that they exhibit a decreased sensitivity to losses in material parameters relative to the LHM perfect lens configuration. Based on the concept of sub-wavelength imaging through compensated bilayer of AMMs, we also propose 2D prism pair structures of compensated AMMs that are capable of manipulating 2D sub-wavelength images in Section 8.4. We will demonstrate that planar image rotation with arbitrary angle, lateral image shift, as well as image magnification could be achieved with sub-wavelength resolution through properly designed compensated prism structures. In Section 8.5, we will discuss the realization of the AMM through transmission line circuit analogue and present the planar lens of anisotropic compensated bilayer through the implementation of anisotropic metamaterials by periodic transmission line circuits based on different unit cells of loaded microstrip grids. We will demonstrate by both the microwave circuit simulation and experimental measurement that compensated bilayers can produce image with sub-wavelength resolution. The experiment provides a practical result that supports the loss insensitivity of the compensated bilayer lens. Finally, in the concluding section, main ideas of this work are briefly summarized.

## 8.2 Compensated Anisotropic Metamaterial Bilayer

When LHM was first examined by Victor G. Veselago in the 1960s, it is considered as an isotropic electromagnetic medium with simultaneously negative permittivity and permeability [38]. In principle, the LHM could be isotropic in 3D but it becomes difficult when we consider the realization of the LHM. The first and

well-used LHM is the artificial composite structure of periodically arranged unit cells of split-ring resonators (SRRs) and conducting wires [31, 28, 29]. The propagation of electromagnetic (EM) wave through such composite structure is obviously dependent on the orientation of the structured metallic unit cell. For example, simultaneously negative effective permittivity and permeability are only retrieved when the electric field orientates parallel to the metal wire and the magnetic field orientates perpendicular to the plane of the SRR. This kind of structured metamaterial is better modeled by anisotropic constitutive parameters, which can be diagonalized in the coordinate system parallel with the principal axes of the metamaterial [14]. In this section, we will discuss the general wave propagation phenomena in anisotropic metamaterials.

### *8.2.1 Anisotropic Metamaterials*

In general we can define the structured composite as anisotropic metamaterial (AMM) with the following relative permittivity and permeability tensors:

$$\hat{\varepsilon} = \begin{pmatrix} \varepsilon_x & 0 & 0 \\ 0 & \varepsilon_y & 0 \\ 0 & 0 & \varepsilon_z \end{pmatrix}, \quad \hat{\mu} = \begin{pmatrix} \mu_x & 0 & 0 \\ 0 & \mu_y & 0 \\ 0 & 0 & \mu_z \end{pmatrix}. \tag{8.1}$$

The diagonal elements of the permittivity and permeability tensors could be either a positive or a negative value.

To simplify the description of EM wave propagating in an AMM medium, we only consider a TE plane wave (*S*-polarized wave) with electric field polarized along the *z*-axis as shown in Fig. 8.1 having the form of

$$\mathbf{E} = \hat{\mathbf{z}} E_0 e^{i\left(k_x x + k_y y - \omega t\right)}, \tag{8.2}$$

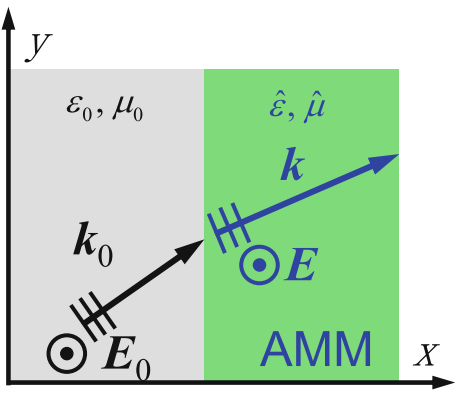


**Fig. 8.1** TE plane wave propagation through the interface between normal medium and the AMM medium.

where $\omega$ is the working frequency of the plane wave and $k_x$ or $k_y$ is the $x$- or $y$-component of the wave vector, respectively. The dispersion relation for the wave propagating in the AMM medium can be derived as

$$\frac{k_y^2}{\varepsilon_z \mu_x} + \frac{k_x^2}{\varepsilon_z \mu_y} = \frac{\omega^2}{c^2}. \tag{8.3}$$

The dispersion relation is either elliptic or hyperbolic curve in the iso-frequency plane. In the absence of losses, the plane wave solution in the anisotropic media can be either a propagating wave or an evanescent wave depending on the sign of $k_x^2$, and the media could therefore be classified into four classes based on their cutoff properties as summarized in Table 8.1, which are called the *cutoff*, *anti-cutoff*, *never-cutoff*, and *always-cutoff* media [32].

**Table 8.1** Anisotropic medium classification based on $z$-polarized (TE) wave properties.

| Medium type | Material parameters | Wave property | Cutoff condition |
|---|---|---|---|
| Cutoff media | $\varepsilon_z \mu_y > 0, \mu_y/\mu_x > 0$ | Propagating | $k_y < k_c$ |
| | | Evanescent | $k_y \geq k_c$ |
| Anti-cutoff media | $\varepsilon_z \mu_y < 0, \mu_y/\mu_x < 0$ | Evanescent | $k_y < k_c$ |
| | | Propagating | $k_y \geq k_c$ |
| Never-cutoff media | $\varepsilon_z \mu_y > 0, \mu_y/\mu_x < 0$ | Propagating | All real $k_y$ |
| Always-cutoff media | $\varepsilon_z \mu_y < 0, \mu_y/\mu_x > 0$ | Evanescent | No real $k_y$ |

Anomalous reflection and refraction phenomena have been revealed at the interface between normal media (or right-handed materials, RHMs) and *never-cutoff* or *anti-cutoff* media, which have a hyperbolic dispersion relation, such as negative refraction [14, 32, 40, 20] and partial focusing [34]. These phenomena are different from those that occur at the interface between normal media or the interface between normal media and the isotropic left-handed metamaterial.

It is also possible to consider wave propagation in the AMM with different polarization, which exhibits different classes of behavior. The TM wave analysis can be obtained similar to the TE wave through duality and the dispersion relation is just the dual case of Eq. (8.3) by interchanging permittivity and permeability everywhere.

### 8.2.2 Compensated Bilayer of AMMs

Veselago lens (or the perfect lens) can be viewed as a bilayer of vacuum and LHM, in which the LHM (with relative permittivity and permeability of $-1$) exactly compensates for the propagation effects associated with an equal length of vacuum. By combining positive and negative refracting layers of AMM media, it is possible to produce a compensated bilayer that accomplishes near-field focusing in a similar manner to the perfect lens. To describe the compensation in the AMM bilayer, we theoretically analyze the EM wave propagation through a bilayer of AMM as shown

in Fig. 8.2. Assume Region 0 and Region III are free space, while Region I and Region II are filled by AMMs with material tensor denoted as

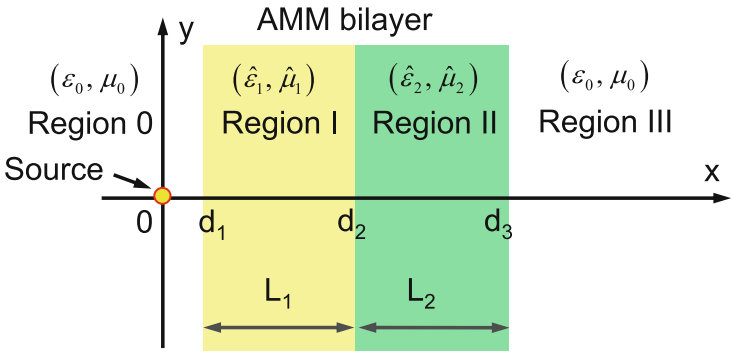


**Fig. 8.2** Two-dimensional point source propagating through a compensated AMM bilayer.

$$\hat{\varepsilon}_j = \varepsilon_0 \begin{pmatrix} \varepsilon_{jx} & 0 & 0 \\ 0 & \varepsilon_{jy} & 0 \\ 0 & 0 & \varepsilon_{jz} \end{pmatrix}, \quad \hat{\mu}_j = \mu_0 \begin{pmatrix} \mu_{jx} & 0 & 0 \\ 0 & \mu_{jy} & 0 \\ 0 & 0 & \mu_{jz} \end{pmatrix} \quad (j = 1, 2). \tag{8.4}$$

The transmission coefficient $T$ of the electric field through the bilayer can be calculated as [5]

$$\begin{aligned} T = 8[&(1+p)(1+q)(1+r)e^{-i(k_{1x}L_1+k_{2x}L_2)} \\ &+(1+p)(1-q)(1-r)e^{-i(k_{1x}L_1-k_{2x}L_2)} \\ &+(1-p)(1-q)(1+r)e^{-i(k_{1x}L_1-k_{2x}L_2)} \\ &+(1-p)(1+q)(1-r)e^{-i(k_{1x}L_1+k_{2x}L_2)}]^{-1} \end{aligned}, \tag{8.5}$$

where $L_1$ and $L_2$ are the thicknesses of the first and the second layers, respectively. The relative effective impedances $p$, $q$, and $r$ are defined as

$$p = k_{1x}/\mu_{1y}k_{0x}, \quad q = \mu_{1y}k_{2x}/\mu_{2y}k_{1x}, \quad r = \mu_{2y}k_{0x}/k_{2x} \quad . \tag{8.6}$$

$k_{0x}$, $k_{1x}$, and $k_{2x}$ are the $x$-component of the wave vector in free space, the first, and the second layer of the bilayer, respectively, which satisfy different dispersion relations

$$k_y^2 + k_{0x}^2 = k_0^2, \quad k_y^2 + k_{jx}^2\mu_{jx}/\mu_{jy} = k_0^2\varepsilon_{jz}\mu_{jx} \quad (j = 1, 2). \tag{8.7}$$

If the two AMM layers compensate with each other, a unit transmission coefficient, $T = 1$, is required for EM plane waves with any value of the transverse wave vector $k_y$. From the expression of the transmission coefficient described in Eq. (8.5), the requirement is satisfied in the following two conditions:

$$q = 1 \quad \text{and} \quad k_{1x}L_1 + k_{2x}L_2 = 0, \tag{8.8}$$

where $k_{1x}$ and $k_{2x}$ have opposite sign corresponding to propagating mode, or

$$q = -1 \quad \text{and} \quad k_{1x}L_1 - k_{2x}L_2 = 0, \tag{8.9}$$

where $k_{1x}$ and $k_{2x}$ have the same sign corresponding to evanescent mode. Under these two conditions $T$ becomes unity resulting in a compensated bilayer [14].

Obviously compensated bilayer can be composed of vacuum and anti-vacuum ($\varepsilon = -\varepsilon_0$ and $\mu = -\mu_0$) layers of same thickness, which yields the configuration of Veselago lens. Moreover, compensated bilayer can also be composed by combining positive and negative refracting layers of *never-cutoff* media (NCM) or *anti-cutoff* media (ACM). The electromagnetic field incident at the front surface of the bilayer can be restored completely in both magnitude and phase at the back surface accomplishing near-field focusing. Table 8.2 shows some examples of metamaterials with parameters' tensor element of unit magnitude and equal layer thickness that could form a compensated bilayer.

**Table 8.2** Examples of different material types for compensated bilayers.

| Bilayer type | | $\varepsilon_x$ | $\varepsilon_y$ | $\varepsilon_z$ | $\mu_x$ | $\mu_y$ | $\mu_z$ | Material |
|---|---|---|---|---|---|---|---|---|
| Veselago lens | 1st layer | 1 | 1 | 1 | 1 | 1 | 1 | Vacuum |
| | 2nd layer | −1 | −1 | −1 | −1 | −1 | −1 | LHM |
| NCM compensated bilayer | 1st layer | −1 | 1 | 1 | −1 | 1 | 1 | Positive refracting NCM |
| | 2nd layer | 1 | −1 | −1 | 1 | −1 | −1 | Negative refracting NCM |
| ACM compensated bilayer | 1st layer | 1 | −1 | −1 | −1 | 1 | 1 | Positive refracting ACM |
| | 2nd layer | −1 | −1 | 1 | 1 | −1 | −1 | Negative refracting ACM |

## 8.3 Sub-wavelength Imaging by Compensated Anisotropic Metamaterial Bilayer

### *8.3.1 Compensated AMM Bilayer Lens*

To study the sub-wavelength imaging phenomenon of the planar lens composed of AMM compensated bilayer, we assume that a 2D point source $I_0 e^{-i\omega t}$ is placed at the front interface of the bilayer with $d_1 \to 0$, as shown in Fig. 8.2. The two AMM layers in Fig. 8.2 are of the same type, which could be *cut-off* media (including isotropic RHM or LHM), NCM or ACM, but with different phase refracting property (one is positive refracting layer and the other is negative refracting layer). Following the classical electromagnetic theory, the fields radiated by the point source can be expressed as closed forms of Sommerfeld-type integrals [5]. The $e^{-i\omega t}$ time convention is assumed and suppressed throughout. We have the electric field in different regions as

$$E_z = \int_{-\infty}^{\infty} dk_y \beta \widetilde{E}_z e^{ik_y y} \quad , \tag{8.10}$$

where $\beta = -\omega\mu_0 I_0/4\pi k_{0x}$ and

$$\widetilde{E}_z = \begin{cases} e^{ik_{0x}|x|} + R_s e^{-ik_{0x}x}, & x < d_1 \\ E_1^+ e^{ik_{1x}x} + E_1^- e^{-ik_{1x}x}, & d_1 < x < d_2 \\ E_2^+ e^{ik_{2x}x} + E_2^- e^{-ik_{2x}x}, & d_2 < x < d_3 \\ Te^{-ik_{0x}(L_1+L_2)} e^{ik_{0x}x}, & x > d_3 \end{cases} . \tag{8.11}$$

According to the boundary conditions, the transmission coefficient $T$ is determined by Eq. (8.5) and the other coefficients in Eq. (8.11) can be calculated as

$$\begin{cases} R_s = \frac{1}{2}(1-p)E_1^+ e^{i(k_{1x}+k_{0x})d_1} + \frac{1}{2}(1+p)E_1^- e^{-i(k_{1x}-k_{0x})d_1} \\ E_1^+ = \frac{1}{2}(1+q)E_2^+ e^{i(k_{2x}-k_{1x})d_2} + \frac{1}{2}(1-q)E_2^- e^{-i(k_{2x}+k_{1x})d_2} \\ E_1^- = \frac{1}{2}(1-q)E_2^+ e^{i(k_{2x}+k_{1x})d_2} + \frac{1}{2}(1+q)E_2^- e^{-i(k_{2x}-k_{1x})d_2} \\ E_2^+ = \frac{1}{2}(1+r)Te^{-ik_{0x}(L_1+L_2)} e^{i(k_{0x}-k_{2x})d_3} \\ E_2^- = \frac{1}{2}(1-r)Te^{-ik_{0x}(L_1+L_2)} e^{i(k_{0x}+k_{2x})d_3} \end{cases} . \tag{8.12}$$

If the material tensors for the bilayer satisfy the compensation requirements of Eqs. (8.8) and (8.9), the bilayer will allow EM wave incident at the front surface to be restored completely in both magnitude and phase at the back surface. So the EM wave irradiated from the point source placed at the front surface will be refocused at the back surface forming a perfect image. In addition to making perfect imaging through Veselago lens that the EM wave propagation in vacuum is compensated by an equal thickness of LHM ($\varepsilon = -\varepsilon_0$ and $\mu = -\mu_0$, or called anti-vacuum), we could also build compensated bilayer lens by combining positive and negative refracting layers of NCM or ACM to perform perfect imaging.

But it should be emphasized that the mechanism of building perfect image with sub-diffraction resolution is quite different between the isotropic Veselago perfect lens and the NCM or ACM bilayer perfect lens. In the case of isotropic Veselago perfect lens, the evanescent components that carry the sub-wavelength features of the object have been recovered due to the amplification through the LHM. While in the case of NCM or ACM bilayer lens, the evanescent components from the object have been converted into propagating modes in the NCM or ACM bilayer, and then back to evanescent components at the back surface, building an image with resolution beyond the diffraction limit. The different behaviors of propagating or evanescent wave propagation in different compensated bilayers have been compared schematically in Fig. 8.3.

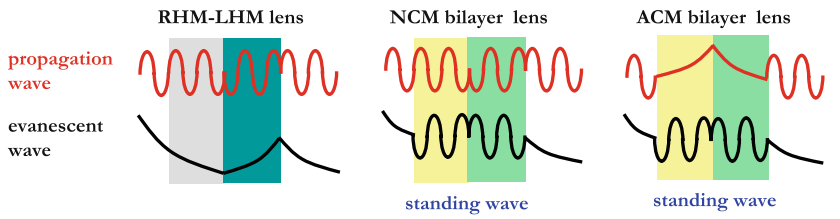


**Fig. 8.3** Comparison of propagating and evanescent waves in different compensated bilayers.

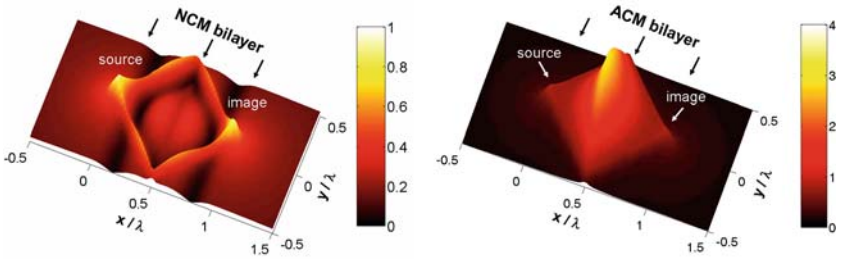


**Fig. 8.4** Electric field distribution for a 2D line source located at the left surface of (**a**) a compensated NCM bilayer and (**b**) a compensated ACM bilayer.

By analyzing the EM fields, we can examine the imaging performance of NCM or ACM bilayer lens. Figure 8.4(a) shows the amplitude distributions of the electric field for a 2D point source at the front surface ($x = 0$, $y = 0$) of an NCM compensated bilayer. We choose the material property elements as $\varepsilon_{1z} = -\varepsilon_{2z} = 1$, $\mu_{1x} = -\mu_{2x} = -1$, $\mu_{1y} = -\mu_{2y} = 1$ and the layers of equal thickness, $L_1 = L_2 = L = \lambda_0/2$, where $\lambda_0$ is the wavelength in free space. Perfect sub-wavelength image is retrieved at the back surface. The simulation result is calculated through Eqs. (8.10), (8.11), and (8.12) at work frequency of 1 GHz. Excited with the 2D point source at the front surface, a clearly focused image is observed at the back surface of the compensated bilayer. Unlike the case of an isotropic LHM planar lens, both the propagating and the evanescent components of the source incident into the NCM bilayer are converted into propagating modes, and then back to propagating and evanescent components on the back surface, building an image with resolution beyond the diffraction limit. A standing wave mode is established inside the bilayer instead of a coupled surface plasmons mode in the case of LHM planar lens [33], which is clearly reflected by the field distribution in Fig. 8.4(a).

Similar result is obtained for a compensated bilayer made of ACM. Focused image point at the back surface is well established as shown in Fig. 8.4(b). Unlike the NCM bilayer case, in the ACM bilayer the evanescent components from the source are converted into propagating waves, while the propagation components are converted into evanescent waves which grow exponentially in the positive refracting ACM layer and decay exponentially in the negative refracting ACM layer yielding a peak value along the interface between the two layers, as evident in Fig. 8.4(b).

### *8.3.2 Loss and Retardation Effects*

One of the major problems associated with the application of metamaterials is the electric or magnetic loss of the material. It has shown that loss inherent to realizable metamaterial would limit the resolution of the perfect lens [33]. Thus, we need to investigate the loss effect on sub-wavelength imaging by anisotropic compensated bilayers [4]. For simplicity, loss in anisotropic medium is characterized by an imaginary component in the constitutive tensor elements as

$$\varepsilon_{jk} = \varepsilon'_{jk} + i\varepsilon''_{jk} \quad \text{or} \quad \mu_{jk} = \mu'_{jk} + i\mu''_{jk} \qquad (j = 1,2; k = x,y,z). \tag{8.13}$$

We compare the loss effect on sub-diffraction imaging by anisotropic compensated bilayers and by isotropic LHM lens, respectively. Figure 8.5(a) shows the image profiles obtained from an isotropic LHM lens and an NCM or ACM bilayer lens, respectively. When the permeability loss tangent is about $10^{-4}$, the beamwidth of the electric field at the back interface for either the NCM bilayer or the ACM bilayer is retrieved nearly the same as that at the front interface with a beamwidth of about $\lambda_0/10$, while the beamwidth at the image plane for an isotropic LHM lens is obviously degraded to about $\lambda_0/5$. Nearly perfect sub-diffraction image is reconstructed at the back interface with either the NCM or the ACM bilayer lens when the loss tangent is less than $10^{-4}$, indicating a decreased sensitivity to losses in material parameters relative to the LHM perfect lens configuration.

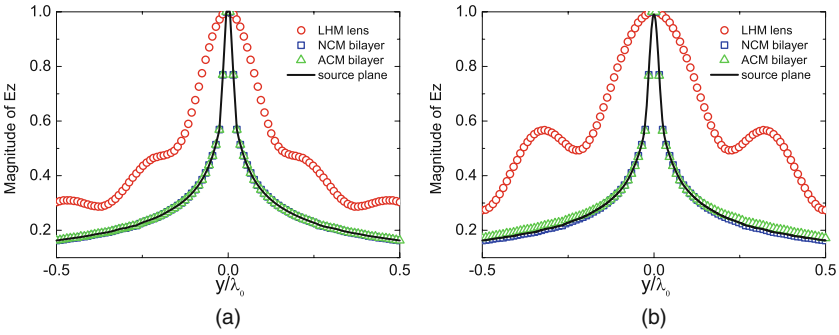


**Fig. 8.5** Comparison of the beamwidth of electric field distribution at the front and back interfaces for an LHM lens, a compensated NCM bilayer, and an ACM bilayer, with (**a**) a magnetic loss tangent of $10^{-4}$ and (**b**) a little parameter mismatch, $\delta = 10^{-3}$.

In practical cases, the bilayer could be hardly realized completely compensated and there is always retardation from the ideal case. We have also studied the retardation effect of the compensated bilayer on sub-wavelength imaging [4]. Without losing much generality, we consider mismatch in the permittivity and permeability tensors of the first layer with the form of $\varepsilon_{1z} = \varepsilon_{1z0}(1+\delta)$, $\mu_{1x} = \mu_{1x0}/(1+\delta)$, and $\mu_{1y} = \mu_{1y0}/(1+\delta)$ to keep the wave numbers in different regions constant for mathematical simplicity. We assume that $\delta$ is a small real quantity denoting the parameter retardation. It is also possible to study the more complicated cases that $\varepsilon_{1x}$, $\mu_{1y}$, and $\mu_{1z}$ have independent retardations. Here $\varepsilon_{1x0}$, $\mu_{1y0}$, and $\mu_{1z0}$ are the property tensors of region I in the completely compensated bilayer case (no retardation) as mentioned in Section 8.2.2 and material property tensors for other regions are kept unchanged (with no retardation). For comparison, in the RHM–LHM bilayer we introduce similar parameter retardation in the LHM as $\varepsilon_{2z} = \varepsilon_{2z0}(1+\delta)$, $\mu_{2x} = \mu_{2x0}/(1+\delta)$, $\mu_{2y} = \mu_{2y0}/(1+\delta)$.

Retardation effect on the resolution of sub-diffraction imaging is compared in Fig. 8.5(b) for isotropic LHM lens and NCM or ACM bilayer lens, respectively.

When $\delta = 10^{-3}$, the beamwidth of the calculated electric field at the back interface for either the NCM bilayer lens or the ACM bilayer lens is nearly the same as that at the front interface ($\sim 0.1\lambda_0$), while for isotropic LHM lens it is obviously degraded to about $0.3\lambda_0$ as shown in Fig. 8.5(b). Therefore, nearly perfect sub-diffraction image is reconstructed at the back interface with either the NCM or the ACM bilayer lens when the material retardation is less than $10^{-3}$.

Compared to the isotropic perfect lens, the compensated bilayer lens of AMM is able to produce sub-wavelength image which is less sensitive to material loss and parameter deviation. The physics behind this is that the inhomogeneous evanescent waves that are responsible for image resolution beyond the diffraction limit have been converted to propagating waves in the anisotropic bilayer. With this advantage it is believed that the compensated bilayer lens of AMM is hopeful to be realized using practically obtained or fabricated metamaterial, which inevitably approximates the ideal situation.

## 8.4 Compensated Anisotropic Metamaterial Prisms: Manipulating Sub-wavelength Images

As discussed in previous section, although compensated AMM bilayer lens provides no free space working distance, it could produce image with an enhanced resolution beyond diffraction limit that exhibits a decreased sensitivity to losses and to deviations in material parameters relative to the LHM Veselago lens configuration.

However, either the Veselago perfect lens or the AMM bilayer lens can only work for the near field [26], which makes the image difficult to be processed or brought to focus by conventional optics. To solve this problem, a new sub-diffraction-limit imaging method called "hyper-lens imaging" has been proposed [15, 27, 16] and experimentally verified [21, 35], which can resolve and magnify sub-wavelength details utilizing the unusual optical phenomenon of strongly anisotropic metamaterials. The hyper-lens can project the magnified image into the far field – where it can be further manipulated by the conventional (diffraction-limited) optics. It should be mentioned that due to the cylindrical structure, such hyperlens can only transfer image between the inner and the outer circular cylinder boundaries, which limits its optical applications. Further improvements have been reported by using the concept of coordinate transformation to design planar magnifying perfect lens [37] or hyperlens [17], but these theoretical proposals require complicated metamaterial with spatial-varying anisotropic material parameters that are difficult to realize.

In this section, by expanding the concept of sub-wavelength image through compensated bilayer of AMMs, novel 2D prism pair configurations of compensated AMM bilayer will be discussed which are capable of manipulating sub-wavelength images [39]. Utilizing the compensated AMM prisms, planar optical image of sub-wavelength objects can be magnified to wavelength scale allowing for further optical processing of the image by conventional optics.

### 8.4.1 General Compensated Bilayer Structure

As discussed in Section 8.2.2, compensated bilayer can be constructed through either isotropic RHM/LHM pair or positive refraction/negative refraction pair of AMMs. The material parameters for the two layers should satisfy the requirement of Eqs. (8.8) and (8.9), and examples of metamaterials have been listed in Table 8.2 with parameter tensor element of unit magnitude and equal layer thickness that could form a compensated bilayer. Generally, the compensated bilayer is not restricted to materials with unit tensor values and equal layer thickness. Let us consider bilayer of unequal thickness as shown in Fig. 8.6 and assuming the thickness ratio $\eta = L_2/L_1$. Compensated bilayer of NCM or ACM for both TE and TM waves requires

$$\hat{\varepsilon}_1 = \hat{\mu}_1 = \begin{bmatrix} \alpha & 0 & 0 \\ 0 & \beta & 0 \\ 0 & 0 & \gamma \end{bmatrix}, \quad \hat{\varepsilon}_2 = \hat{\mu}_2 = \begin{bmatrix} -\alpha/\eta & 0 & 0 \\ 0 & -\eta\beta & 0 \\ 0 & 0 & -\eta\gamma \end{bmatrix}, \tag{8.14}$$

where $\alpha$ , $\beta$ , and $\gamma$ are three arbitrary parameters that determine the material tensor

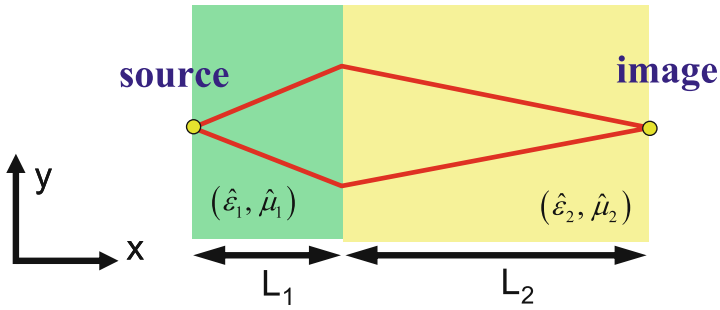


**Fig. 8.6** Schematic of a compensated bilayer of unequal thickness.

elements of the compensated bilayer. When $\beta\gamma > 0$ and $\beta/\alpha < 0$, it stands for an NCM compensated bilayer, while $\beta\gamma < 0$ and $\beta/\alpha < 0$, it stands for an ACM compensated bilayer. Sub-wavelength imaging through compensated bilayer of unequal thickness has been verified through rigorous calculation of the EM wave propagation [39]. Small electric and magnetic loss tangent of $10^{-3}$ is included to see their influences on the image quality. Excited with the two point sources that are separated about half wavelength at the front surface, two clearly focused images with sub-wavelength resolutions are observed at the back surface of the compensated bilayer as shown in Ref. [39]. Unlike the case of an Veselago planar lens, a standing wave mode is established inside the bilayer instead of a coupled surface plasmon mode in the case of Veselago lens.

## 8.4.2 Compensated AMM Prism Structures

Veselago slab lens configuration is restricted to produce identical images between parallel source and image planes. Now we could expand the compensated bilayer structure to a compensated prism pair (CPP) structure which can manipulate 2D images with sub-wavelength resolution for more comprehensive cases, for example, manipulating images between unparallel source and image planes or even producing magnified images.

### 8.4.2.1 Symmetry Compensated Prism Pair Structure

We first consider a symmetry CPP (S-CPP) configuration as shown in Fig. 8.7(a). Two prisms with a same apex angle of $\theta$ (Prism1 and Prism2) are symmetrically putting together forming a prism pair. The two prisms are composed of AMMs with one of their optical axes (the $y$-axis) aligned with the symmetry axis OO′. The material permittivity and permeability tensors satisfy the requirement of forming an equal thickness compensated AMM bilayer, which could be obtained through Eq. (8.14) with $\eta = 1$. Due to the compensation nature of the two prisms, 2D sub-wavelength objects at the left surface OA will be perfectly imaged at the right surface OB of the S-CPP structure. For example, point sources at $S_1$ and $S_2$ of the source plane will be restored at $I_1$ and $I_2$ of the image plane, respectively, with $S_1I_1$ and $S_2I_2$ perpendicular to the interface OO′ of the structure. Such an S-CPP structure acts as an optical image component that makes perfect image between unparallel source and image planes with $2\theta$ rotation in the limit of sub-wavelength resolution.

To verify the performance, full wave EM simulation based on finite element method has been carried out for the proposed S-CPP structure. Figure 8.7(b) shows the calculated electric field distribution of two point sources separated about 0.03 wavelength at the left surface of an S-CPP structure with $\theta = 30°$. The mate-

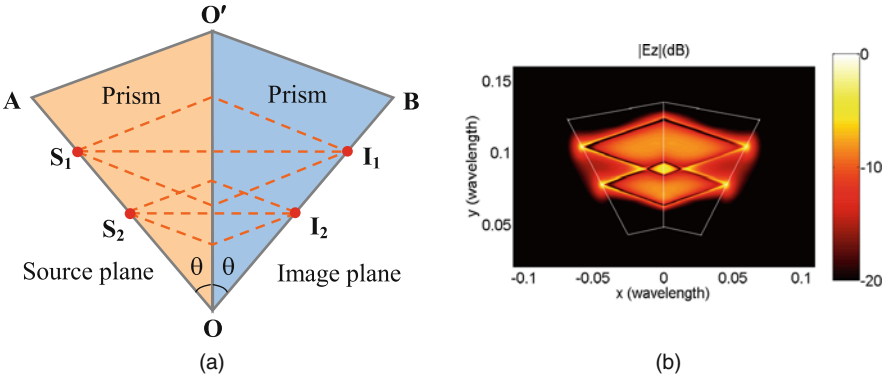


**Fig. 8.7** (**a**) Schematic of a symmetry compensated prism pair configuration. (**b**) Electric field distribution of two point sources imaged with the S-CPP structure with a loss tangent of 0.01. After Ref. [39]. Copyright ©2008 Optical Society of America, Inc.

rial tensor elements are chosen as $\mu_{1x} = -\mu_{2x} = -3$, $\mu_{1y} = -\mu_{2y} = 1/3$, and $\varepsilon_{1z} = -\varepsilon_{2z} = 1/3$, and a loss tangent of about 0.01 has been included for each tensor element. It is clearly demonstrated that at the right surface well-resolved images of the two point sources are obtained, which confirms the ability of the S-CPP structure for imaging sub-wavelength objects to an unparallel plane. It is worth noting that the sub-wavelength imaging by S-CPP is not sensitive to small material losses, similar to that of the case of a compensated bilayer lens [32]. Moreover, the boundary effect on the image quality is almost unobservable for prisms with finite sizes since most of the EM power is restricted to the rhombus area between the source and the image as indicated in Fig. 8.7(b).

The proposed S-CPP structures can be used as optical components to build more complicated imaging system. For example, it can be cascaded to make different image rotation with arbitrary angles or to produce sub-wavelength image with a lateral translation. Figure 8.8 shows that a shifted image with sub-wavelength resolution can be obtained with a lateral translation to the original object by a combination of four identical S-CPPs with apex angle of $2\theta = 45°$. Two point sources separated by 0.04 wavelength have been well imaged at the other side of the S-CPP system with a 0.15 wavelength lateral shift.

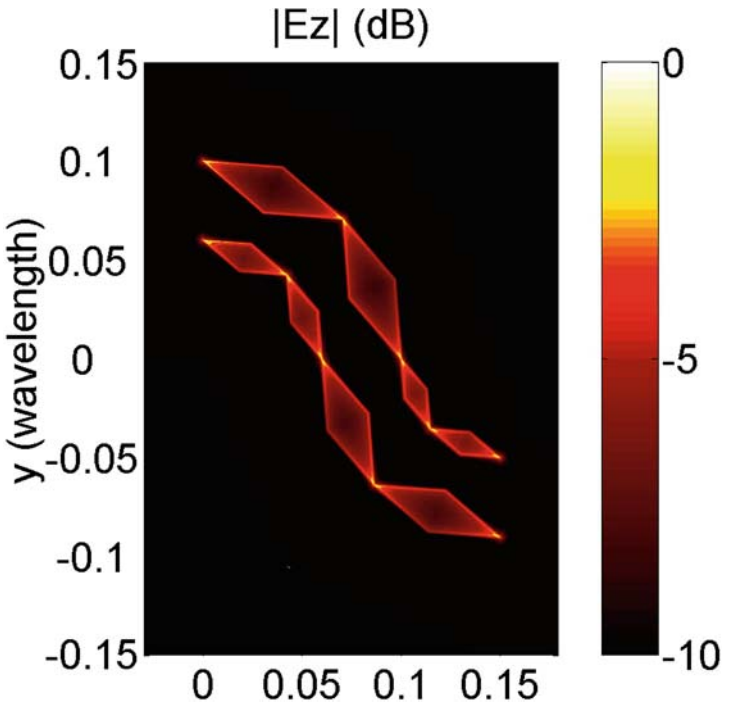


**Fig. 8.8** Electric field distribution of two point sources imaged with four identical S-CPP structures cascaded together with a loss tangent of 0.01. Such configuration could produce lateral image translation with sub-wavelength resolution. The *white lines* indicate the boundaries of the S-CPPs. After Ref. [39]. Copyright ©2008 Optical Society of America, Inc.

### 8.4.2.2 Asymmetry Compensated Prism Pair Structures

Now we consider more general case of an asymmetry CPP (AS-CPP) configuration as shown in Fig. 8.9. Two prisms with apex angles of $\alpha$ (for Prism1) and $\beta$ (for Prism2) are put together forming an asymmetry prism pair. The two prisms are composed of AMMs with one of their optical axes (the $y$-axis) aligned with the common axis OO′. The material permittivity and permeability tensors of the AMM satisfy the requirement of forming an unequal thickness compensated AMM bilayer through Eq. (8.14) with $\eta \neq 1$. Similar to the S-CPP structures, due to the compensation nature of the two prisms, sub-wavelength objects at the left surface OA will be perfectly imaged at the right surface OB of the AS-CPP structure. For example, point sources at $S_1$ and $S_2$ of the source plane will be restored at $I_1$ and $I_2$ of the image plane, respectively, with $S_1I_1$ and $S_2I_2$ perpendicular to the interface OO′ of the structure. The interesting feature of this AS-CPP structure is that the image size is unequal to that of the object with a magnification determined by

$$\tau = \frac{I_1I_2}{S_1S_2} = \frac{\cos\alpha}{\cos\beta}, \tag{8.15}$$

and the two apex angles $\alpha$ and $\beta$ are restricted by the compensation requirement of the two AMMs for the prisms, that is the thickness ratio $\eta$ in Eq. (8.14), which satisfies

$$\eta = \frac{O_1I_1}{S_1O_1} = \frac{O_2I_2}{S_2O_2} = \frac{\tan\beta}{\tan\alpha}. \tag{8.16}$$

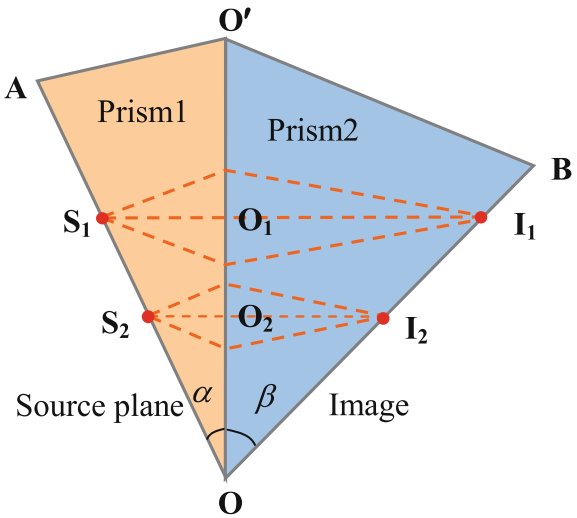


**Fig. 8.9** Schematic of an asymmetry compensated prism pair configuration. After Ref. [39]. Copyright ©2008 Optical Society of America, Inc.

Thus, from Eqs. (8.14), (8.15), and (8.16) we are able to design certain AS-CPP structure that is possible of producing magnified image of sub-wavelength objects with in principle arbitrary magnification.

As an example, we design an AS-CPP with a magnification of $\tau = 3$. For convenience we further restrict $\alpha + \beta = \pi/2$, then we yield $\eta = \tau^2 = 9$. The two apex angles of the prisms can be determined by Eqs. (8.15) or (8.16), and the material parameters can be designed through Eq. (8.14). Actually we can see that there is plenty of freedom for design such as AS-CPP. Here we choose $\varepsilon_{1x} = \mu_{1x} = -3$, $\varepsilon_{1y} = \mu_{1y} = 1/3$, $\varepsilon_{1z} = \mu_{1z} = 1/3$, $\varepsilon_{2x} = \mu_{2x} = 27$, $\varepsilon_{2y} = \mu_{2y} = -1/27$, $\varepsilon_{2z} = \mu_{2z} = -1/27$, and a loss tangent of about 0.01 has been included for each tensor element. To verify the performance, we calculated the electric field distribution (Fig. 8.10) for two 2D point sources imaged with such an AS-CPP which has been cut into a cuboid shape. The material optical axes of the two prisms are parallel or perpendicular to the interface. The two point sources placed at the left boundary with a separation of only 0.1 wavelength have been projected to the bottom boundary achieving a magnified image with sub-wavelength features of the objects. The slight intensity dimming and peak broadening at the image plane is due to the loss of the material, but the sub-wavelength features of the object have been well resolved.

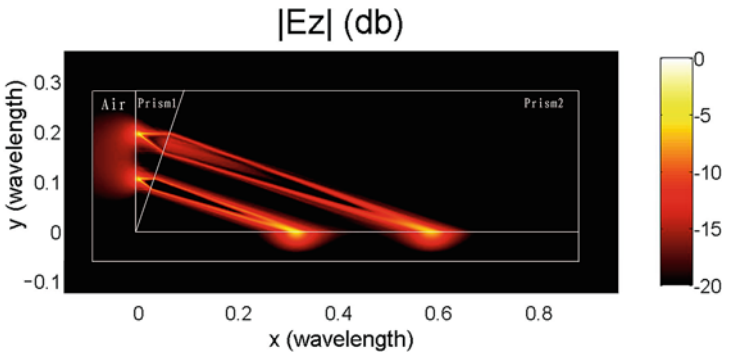


**Fig. 8.10** Electric field distribution for two point sources separated by 0.1 wavelength imaged with an AS-CPP with a designed magnification of 3. Loss tangent of 0.01 is included for each material parameter.

By cascading the AS-CPPs, we could make sub-wavelength image with larger magnification. Figure 8.11 shows the imaging of three point sources through two AS-CPPs cascaded together. The materials of the two AS-CPPs are similar to that used in the previous example, which lead to a total magnification of 9. The simulated electric field distribution is shown in Fig. 8.11(a) and line scans at the source and image planes are illustrated in Fig. 8.11(b) and (c), respectively, which indicate that the three point sources with separations within 0.1 wavelength have been well resolved and magnified to wavelength scale. The cascaded system also partially compensated the nonuniform image intensity in single AS-CPP resulting in more homogenous image intensity as shown in Fig. 8.11(c). Using the AS-CPP structure,

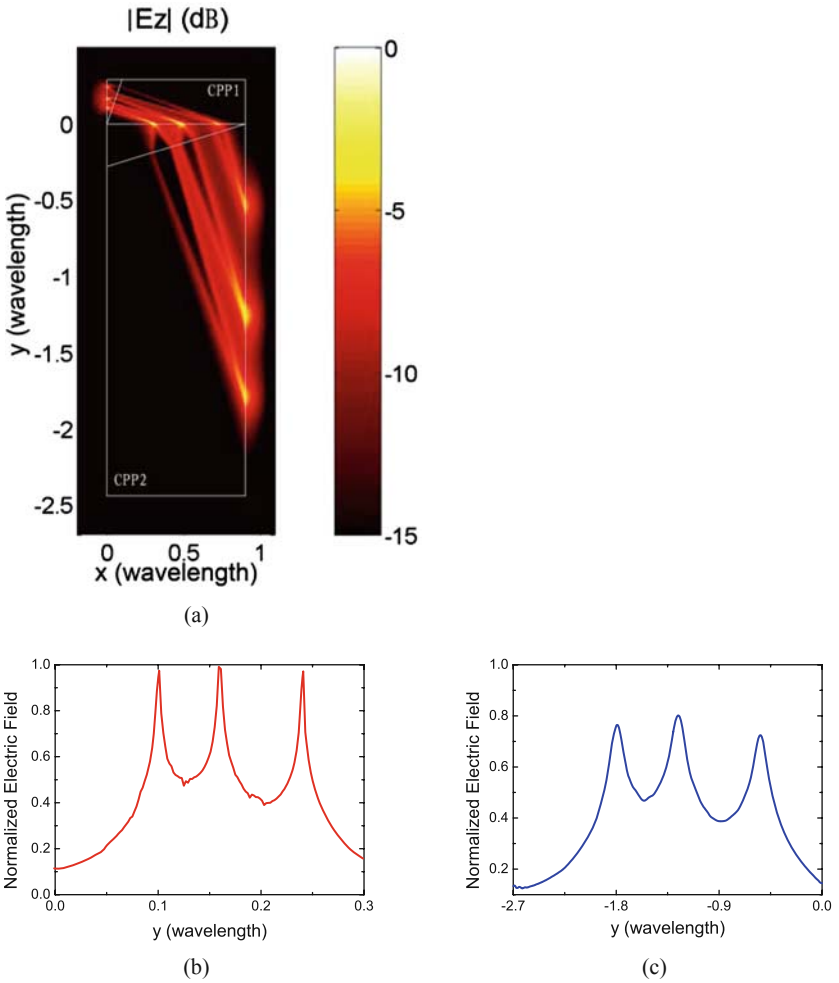


**Fig. 8.11** (**a**) Electric field distribution for three point sources imaged with two cascaded AS-CPPs with a total designed magnification of 9. Loss tangent of 0.01 is included for each material parameter. Line scans at the source (**b**) and image (**c**) planes of the electric field which have been normalized to that of the source value. After Ref. [39]. Copyright ©2008 Optical Society of America, Inc.

planar objects with deep sub-wavelength features can be projected and magnified to wavelength scale planar image. Such magnified image can be further processed by conventional optics, and the both flat object and image planes are more convenient for imaging and lithography applications.

The material requirements for building either A-CPP or AS-CPP are simply anisotropic with partial negative permittivity or permeability components and do not need any spatial variation. Thus they are more achievable compared to recent proposals of designing planar magnifying perfect lens [37] or hyperlens [17] based

on the concept of coordinate transformation. Utilizing the proposed AMM prisms, planar optical image of objects with sub-wavelength features can be magnified to wavelength scale allowing for further optical processing of the image by conventional optics. With the rapid development of the metamaterial design and fabrication techniques in optical range, we believe the proposed sub-wavelength image manipulations could be applied to optical imaging and lithography systems with sub-wavelength resolutions.

## 8.5 Realizing Compensated AMM Bilayer Lens by Transmission-Line Metamaterials

In this section, we focus on the realization and experimental study of the AMM. We will discuss the realization of both the NCM and ACM bilayers based on the recently proposed complete set of inductor (L)–capacitor (C) transmission line network representation of AMM [8, 36, 9, 11]. We will study the sub-wavelength image properties through microwave circuit simulations and experimental meas-urements. We will demonstrate that the image by compensated bilayer lens is less sensitive to material loss than that of the isotropic Veselago lens, therefore has a better resolution.

### *8.5.1 Transmission Line Models of AMMs*

Planar isotropic LHM has been synthesized by periodic structure, which is composed of unit cell of 2D transmission line (TL) grids loaded with series capacitors and shunt inductors [6, 19, 7, 3]. Such loaded TL structures have been expanded to anisotropic structure in our previous work, and a complete set of periodic L–C circuits have been proposed that could be used to represent the electromagnetic wave propagation in four different types of planar AMMs [8]. It is shown that based on the L–C circuit models different types of 2D AMMs, such as the NCM or the ACM, could be realized by L–C loaded microstrip line grids over certain operation frequency bandwidth [8, 36, 9, 11].

Assuming perpendicular electric field polarization (along $z$-axis), the unit cells of the planar TL metamaterials (extended in the $x$–$y$ plane) are schematically illustrated in Fig. 8.12. They are microstrip line grids periodically loaded by serial capacitance in $x$- or $y$-direction with (or without) shunting inductance loaded in the central node. If the TL sections in the unit cell are electrically short and the per-unit-cell phase delays are small, these TL structures can be considered as 2D effective AMMs, whose permittivity and permeability tensors are simultaneously diagonalizable, having the form of

$$\begin{aligned} \bar{\bar{\varepsilon}}_e &= \mathrm{diag}\left[\varepsilon_{xe}, \varepsilon_{ye}, \varepsilon_{ze}\right], \\ \bar{\bar{\mu}}_e &= \mathrm{diag}\left[\mu_{xe}, \mu_{ye}, \mu_{ze}\right]. \end{aligned} \tag{8.17}$$

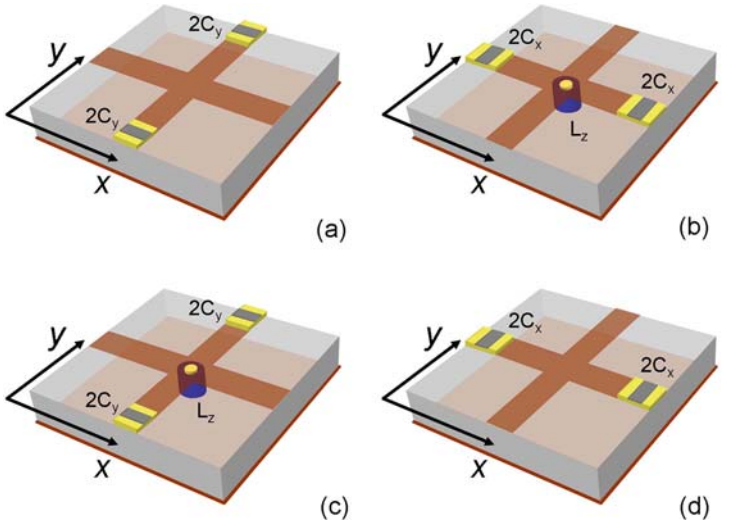


**Fig. 8.12** Unit cells of loaded microstrip TL grid circuit used to implement (**a**) positive refraction NCM, (**b**) negative refraction NCM, (**c**) positive refraction ACM, and (**d**) negative refraction ACM. Reprinted figure with permission from Ref. [10]. Copyright ©2007 by the American Physical Society.

For $z$-polarized wave (corresponding TE waves in the previous discussion), the propagation is only determined by $\varepsilon_z$, $\mu_x$, and $\mu_y$. The dispersion relations of the periodic TL metamaterials shown in Fig. 8.12 can be analyzed by rigorous periodic TL theory, which show hyperbolic dispersion curves below certain critical frequency. For example, the dispersion relation for TL circuit with unit cell of Fig. 8.12(a) is obtained as [36]

$$\begin{aligned}\cos(k_y d)+\left[1-\frac{\omega_0}{\omega}\frac{1+\cos(\beta d)}{\sin(\beta d)}\right]\cos(k_x d)\\ =\left[2-\frac{\omega_0}{\omega}\frac{1+\cos(\beta d)}{\sin(\beta d)}\right]\cos(\beta d)+\frac{\omega_0}{\omega}\sin(\beta d),\end{aligned} \tag{8.18}$$

where $\omega_0 = 1/2C_yZ_0$, $Z_0$, $\beta$, and $d$ are the characteristic impedance, the propagation constant, and the length of the TL section, respectively. Under the effective medium approximation, when $\beta d \ll 1$, $k_y d \ll 1$, $k_x d \ll 1$, Eq. (8.18) is simplified to

$$\frac{k_y^2}{2\beta^2(1-2\omega_0/\omega\beta d)}+\frac{k_x^2}{2\beta^2}=1. \tag{8.19}$$

Comparing this dispersion relation with Eq. (8.3) for TE waves in the homogenous AMMs, we obtain the equivalent effective permittivity and permeability of the loaded TL circuit as

$$\varepsilon_{ze1} = \frac{2\beta}{\omega Z_0}, \quad \mu_{ye1} = \frac{\beta Z_0}{\omega}, \quad \mu_{xe1} = \frac{\beta Z_0}{\omega}\left(1 - \frac{1}{\omega Z_0 C_y \beta d}\right). \tag{8.20}$$

Below the cutoff frequency $\omega_c$ determined by

$$1 - 1/\left(\omega Z_0 C_y \beta d\right)_{\omega=\omega_c} = 0, \tag{8.21}$$

the TL metamaterial behaves as a positive refraction NCM (P-NCM) with positive $\varepsilon_z$, $\mu_y$, and negative $\mu_x$.

Similarly, the negative refraction NCM (N-NCM) (Fig. 8.12(b)) has the following effective permittivity and permeability:

$$\varepsilon_{ze2} = \frac{2\beta}{\omega Z_0}\left(1 - \frac{Z_0}{2\omega L_z \beta d}\right), \mu_{ye2} = \frac{\beta Z_0}{\omega}\left(1 - \frac{1}{\omega Z_0 C_y \beta d}\right), \mu_{xe2} = \frac{\beta Z_0}{\omega}. \tag{8.22}$$

Below certain cutoff frequency, it has a negative $\varepsilon_z$, $\mu_y$, and a positive $\mu_x$. Similar circuit analysis also reveals that the unit cells in Fig. 8.12(c) and (d) can be used to implement the positive refraction ACM (P-ACM) and the negative refraction ACM (N-ACM) under certain operation frequency bandwidth, respectively.

### 8.5.2 *Realization of Compensated Bilayer Lens Through TL Metamaterials*

As discussed in the previous sections, compensated bilayer lens could be accomplished by anisotropic metamaterials, which enables both the propagating and the evanescent waves incident on the front surface being recovered completely at the back surface. According to Eqs. (8.8) and (8.9), for an *S*-polarization compensated bilayer, the material requirements of the two layers with equal thickness are

$$\varepsilon_{z1} = -\varepsilon_{z2}, \quad \mu_{y1} = -\mu_{y2}, \quad \mu_{x1} = -\mu_{x2}. \tag{8.23}$$

Therefore, either the two sub-classes of NCM (P-NCM and N-NCM) or the two sub-classes of ACM (P-ACM and N-ACM) could be employed to accomplish compensated bilayer lens [10].

Using the four circuit building blocks discussed in Section 8.5.1, we are able to construct 2D compensated bilayer lens composed of either P-NCM/N-NCM or P-ACM/N-ACM as described schematically in Fig. 8.13. The NCM (or ACM) bilayer is constructed by periodic TL circuit using unit cells of Fig. 8.12(a) and (b) (or Fig. 8.12(c) and (d)). To realize compensated bilayer, loaded capacitance $C_x$ or $C_y$ and inductance $L_z$ are properly chosen to satisfy the requirement of Eq. (8.23), which are designed through the effective constitutive parameters (as indicated in Eqs. (8.20), (8.21), and (8.22). This could result in

$$2C_y = 2C_x = 1/\omega Z_0 \beta d, \quad L_z = Z_0/4\omega\beta d. \tag{8.24}$$

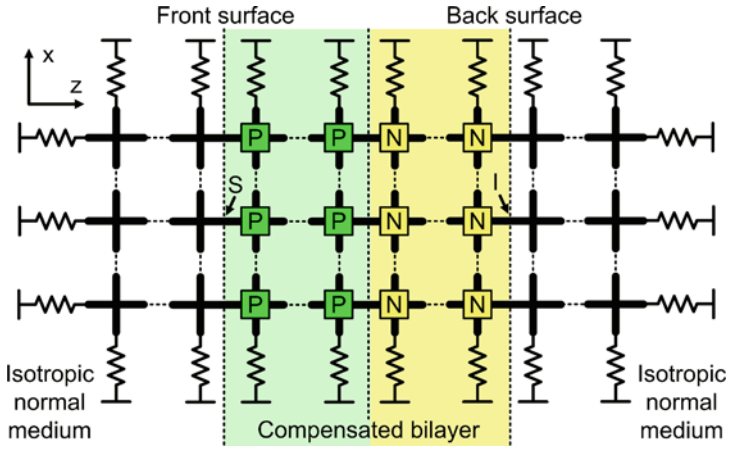


**Fig. 8.13** Compensated bilayer realized by 2D L-C loaded TL circuit sandwiched with normal medium layers realized by TL grids. Blocks denoted by P and N represent the P-NCM or P-ACM and the N-NCM or N-ACM using the corresponding unit cells in Fig. 8.12**(a)**–**(d)**, respectively. S and I indicate the source and the image positions. Reprinted figure with permission from Ref. [10]. Copyright ©2007 by the American Physical Society.

For actual implementation of the compensated bilayer lens, microstrip line structure is chosen to synthesize the 2D TL circuit in Fig. 8.13. The microstrip is designed with copper strip of 0.75 mm wide and 0.17 μm thick on a grounded microwave substrate (Rogers RO3003) with thickness of 1.52 mm and dielectric constant $\varepsilon_r = 3.0$, which could be easily fabricated by printed circuit board technique. The compensated bilayer is composed of 5×31 unit cells of P-NCM (or P-ACM) together with 5×31 unit cells of N-NCM (or N-ACM) and sandwiched between two isotropic normal medium layers realized by unloaded printed TL grids (each of 10×31 unit cells). The isotropic normal medium layer acting as the incident medium has the following effective permittivity and permeability [36, 6]:

$$\varepsilon_{RHM} = \frac{2\beta}{\omega Z_0}, \quad \mu_{RHM} = \frac{\beta Z_0}{\omega}. \tag{8.25}$$

The whole circuit network is resistively terminated to ground at the four edges with terminal impedances being matched with the corresponding Bloch impedances. In the design, we use 2.7 pF chip capacitor (ATC 500S) as the loaded capacitance $C_y$ or $C_x$ and 18 nH inductor (Toko LL1608FH) as the loaded inductance $L_z$ connecting the central node to ground through hole. Each unit cell has a dimension of $d \times d = 8.4 \times 8.4$ mm$^2$. The microstrip circuit is designed to operate at 1.0 GHz, corresponding to an effective wave number of $k = 40$ rad/m in the unloaded TL grid. The above circuit parameters are designed through Eq. (8.24), therefore from Eqs. (8.20) and (8.22) we have

$$\varepsilon_{z1} = -\varepsilon_{z2} = \frac{2\beta}{\omega Z_0}, \quad \mu_{y1} = -\mu_{y2} = \frac{\beta Z_0}{\omega}, \quad \mu_{x1} = -\mu_{x2} = -\frac{\beta Z_0}{\omega}. \tag{8.26}$$

Therefore, the effective permittivity and permeability of the AMMs relative to the incident RHM medium are

$$\varepsilon_{rz1} = -\varepsilon_{rz2} = 1, \quad \mu_{ry1} = -\mu_{ry2} = 1, \quad \mu_{rx1} = -\mu_{rx2} = -1, \tag{8.27}$$

which insure that the two layers satisfy the compensation requirement.

### *8.5.3 Simulation and Measurement of the TL Bilayer Lens*

To investigate the imaging performance of the compensated bilayer lens realized through TL metamaterials, both microwave circuit simulation and experimental measurement have been carried out. In the circuit described in Fig. 8.16, a point source is placed at the front surface and the image profile at the back surface is studied. The source is introduced by attaching a vertical monopole between columns 10 and 11 at row 16 (denoted by S at the front surface in Fig. 8.13) fed by a coaxial cable through the ground plane. The electric and magnetic wave propagation through the compensated bilayer could be appropriately mapped to the voltages and currents in the corresponding TL network, respectively.

#### 8.5.3.1 Microwave Circuit Simulations

To verify the circuit performance, we use Agilent's ADS microwave circuit simulator to calculate the node-to-ground voltages of the circuit. To include the loss effect of the TL metamaterial, both the microstrip line loss (metallic loss and the dielectric loss) and the loss associated with the chip capacitors and inductors are taken into account in the circuit simulation.

For comparison, the whole circuit is designed on the basis that it is comparable in electric size and losses to the TL circuit that represents the planar LHM lens described in [13]. The TL section as well as the losses associated with the metal strip and the substrate (with a loss tangent of 0.0016) is the same as that in the LHM lens. Both the loaded capacitors and inductors have same values and quality factors (44 for inductance and 150 for capacitance at 1 GHz) as that in the LHM lens. The electric thickness of the bilayer which equals the source to image distance is also the same (about $0.54\lambda$).

First we investigate the image focused with an NCM compensated bilayer and the nodal voltage distribution (normalized to the source voltage) of the entire structure is shown in Fig. 8.14(a) and (b). Excited with the point source at the front surface, voltage profile of a clearly focused image is observed at the back surface of the compensated bilayer. Unlike the case of an isotropic LHM planar lens, both the propagating and the evanescent components of the source incident into the NCM

bilayer are converted into propagating modes, and then back to propagating and evanescent components on the back surface, building an image with resolution beyond the diffraction limit. A standing wave mode is established inside the bilayer instead of a coupled surface plasmons mode in the case of LHM planar lens, which is clearly demonstrated by the voltage distribution in Fig. 8.14(a). The nodal voltage profiles at the source and image planes are plotted in Fig. 8.15, where the image peak is about 93% of the source peak due to the losses. We also calculate the image profile established by the isotropic LHM planar lens described in [13] using ADS simulator and plot in Fig. 8.15. It results in a half-power beamwidth of $0.215\lambda$ with good agreement with the measured data in [13], which provides that the ADS simulation on the practical TL metamaterials is reliable. As shown in Fig. 8.14(a), the NCM compensated bilayer lens produces an image profile with nearly the same beamwidth (about $0.054\lambda$) as that of the source.

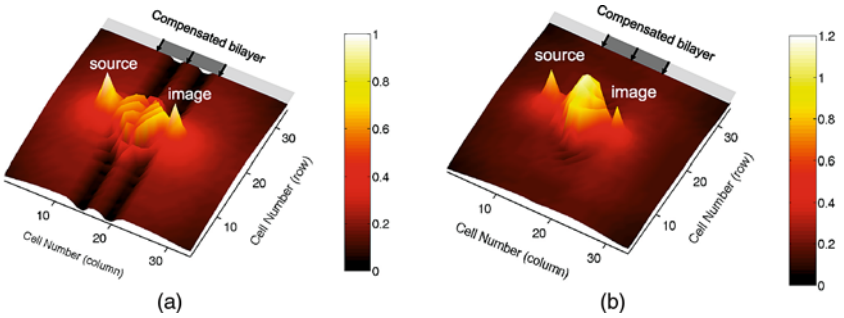


**Fig. 8.14** Nodal voltage distribution in (**a**) an NCM compensated bilayer lens and (**b**) an ACM compensated bilayer lens. The *arrows* indicate the front surface, the interface, and the back surface of the bilayer, respectively. Reprinted figure with permission from Ref. [10]. Copyright ©2007 by the American Physical Society.

For the ACM compensated bilayer, as shown in Fig. 8.14(b), focused image point at back surface is well established with peak value of about 88% of the source peak. Unlike the previous case, in the ACM layers the evanescent components from the source are converted into propagating waves, but the propagation components are converted into evanescent waves which grow exponentially in the P-ACM layer and decay exponentially in the N-ACM layer yielding a peak value along the interface between the two layers, as evident in Fig. 8.14(b). The voltage profiles at the source and image planes are also compared (not shown). It indicates that although the image peak is a little attenuated due to the losses, the beamwidth with little broadening is obtained, revealing a better sub-wavelength resolution similar to that of the NCM case.

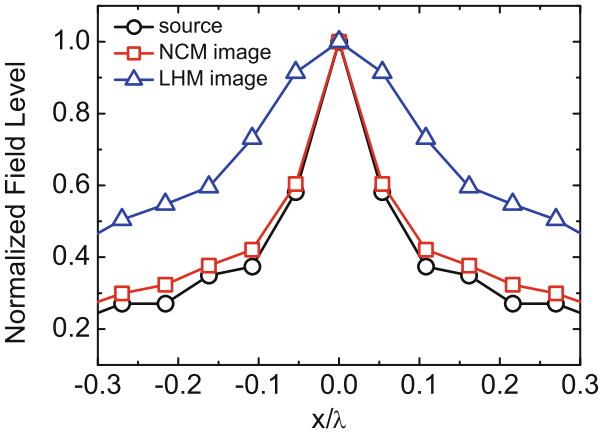


**Fig. 8.15** Voltage profiles at the source plane (*circles*) and at image plane for an NCM compensated bilayer lens (*squares*) or an isotropic LHM planar lens (*triangles*). All plots have been normalized to the source amplitude.

### 8.5.3.2 Experimental Results

To verify the above microwave circuit simulations, an NCM compensated bilayer structure has been fabricated as indicated in Fig. 8.13 by printed circuit board technique and sub-wavelength imaging through such bilayer lens has been experimentally tested. The fabricated circuit structure is shown in Fig. 8.16(a) and the circuit parameters are as that in the design shown in the previous section. The circuit has the same thickness of the NCM bilayer but a slightly smaller dimension than that of the design, which is composed of $5 \times 19$ unit cells of P-NCM together with $5 \times 19$ unit cells of N-NCM and sandwiched between two isotropic normal medium layers realized by unloaded printed microstrip line grids (each of $5 \times 19$ unit cells).

Similar to [13], using Agilent's transmission-line calculator Linecalc., we can estimate the relative medium parameters in the circuit for the two NCM layers, which are $\varepsilon_{z1} = 1.00$, $\mu_{y1} = 1.00$, $\mu_{x1} = -1.024 + 0.013i$, and $\varepsilon_{z2} = -0.981 + 0.043i$, $\mu_{y2} = -1.024 + 0.013i$, $\mu_{x2} = 1.00$. The small deviations in the real part of $\varepsilon_{z2}$, $\mu_{x1}$, and $\mu_{y2}$ come from the variation of the values of the inductor $L_z$, capacitors $C_x$ and $C_y$, since we could not obtain the chip inductor or capacitor with exactly the design value of inductance or capacitance. The loss in the TL metamaterial comes from both the microstrip line loss (metallic loss and the dielectric loss) and the loss associated with the loaded chip capacitors and inductors. We find that the loss resulted from the microstrip line is more than a magnitude less than the loss from the loaded chip capacitors and inductors; therefore, we only take into account of the capacitor and inductor loss in the above estimation. This results in an imaginary part of $\mu_{x1}$ (coming from the $C_x$), an imaginary part of $\mu_{y2}$ (coming from the $C_y$), and an imaginary part of $\varepsilon_{z2}$ (coming from the $L_z$). The imaginary part of the effective medium parameters is not remarkable.

To investigate the imaging property of the compensated bilayer lens, a point source is introduced by attaching a vertical monopole between RHM and P-NCM layers fed by a coaxial cable as indicated in Fig. 8.16(a). The vertical electric field above each node of the microstrip line circuit is detected by a high impedance coaxial probe that is scanned above the surface of the structure and measured using Agilent's E8363 network analyzer. The two ports of the network analyzer are connected to the coaxial cables that feed the exciting monopole and the detecting probe, respectively.

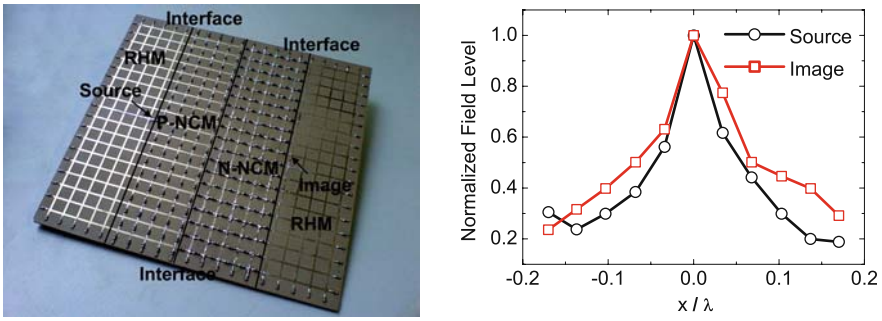


**Fig. 8.16** (**a**) The fabricated planar NCM compensated bilayer transmission line lens. (**b**) The measured vertical electric field profiles at the source (*circles*) and the image (*squares*) planes. The field peak at image plane is less than the source peak due to losses and both have been normalized to unit in the figure for comparison. Reprinted figure with permission from Ref. [10]. Copyright ©2007 by the American Physical Society.

The measured field profiles at both the source and the image planes are compared in Fig. 8.16(b). We find that the electromagnetic wave from the point source has been focused at the image plane with only slightly broadened half-power beamwidth, but the beamwidth (about $0.1\lambda$ ) is well below the diffraction limit. The small deviation of the experiment results from the simulations in Fig. 8.15 is mainly due to the variation in chip inductors and capacitors from their nominal values, as well as fabrication tolerances in the TL circuit. Comparing with the experimental results of the isotropic LHM planar lens in [13], where a beamwidth of about $0.21\lambda$ is obtained at the image plane, the NCM bilayer lens has a better sub-wavelength resolution due to its less sensitivity to material loss, since the losses in the two systems are comparable.

## 8.6 Summary

It has been demonstrated that the compensated anisotropic metamaterials, which are expansions of the Veselago perfect lens configuration, have the potential to manipu-

late sub-wavelength image information including planar focusing and imaging, arbitrary image rotation and lateral shifting, as well as image magnification through differently designed structures. The sub-wavelength imaging ability has been demonstrated experimentally by implementation of AMMs through L–C loaded TL metamaterials. The advantage to the focusing and imaging using the AMM compensated bilayer lens is that they exhibit a decreased sensitivity to losses and retardations in material parameters relative to the LHM perfect lens configuration. With the rapid development of the metamaterial design and fabrication techniques in optical range, it is believed that the proposed sub-wavelength image manipulations could be applied to optical imaging and lithography systems with sub-wavelength resolutions.

**Acknowledgments** This work is supported by the National Basic Research Program of China (2004CB719800) and the National Nature Science Foundation (nos. 60671002, 60801001).

## References

1. Belov, P.A., Simovski, C.R., Ikonen, P.: Canalization of subwavelength images by electromagnetic crystals. Phys. Rev. B **71**, 193105 (2005)
2. Belov, P.A., Hao, Y., Sudhakaran, S.: Subwavelength microwave imaging using an array of parallel conducting wires as a lens. Phys. Rev. B **73**, 033108 (2006)
3. Caloz, C., Itoh, T.: Electromagnetic metamaterials. Wiley-Interscience, New York (2006)
4. Chen, Y., Teng, X., Huang, Y., Feng, Y.: Loss and retardation effect on subwavelength imaging by compensated bilayer of anisotropic metamaterials. J. Appl. Phys. **100**, 124910 (2006)
5. Chew, W.C.: Waves and fields in inhomogenous media. Van Nostrand Reinhold, New York (1990)
6. Eleftheriades, G.V., Iyer, A.K., Kremer, P.C.: Planar negative refractive index media using periodically L-C loaded transmission lines. IEEE Trans. Micro. Theory Tech. **50**, 2702 (2002)
7. Eleftheriades, G.V., Balmain, K.G.: Negative-refraction metamaterials. Wiley-Interscience, New York (2005)
8. Feng, Y., Teng, X., Chen, Y., Jiang, T.: Electromagnetic wave propagation in anisotropic metamaterials created by a set of periodic inductor-capacitor circuit networks. Phys. Rev. B **72**, 245107 (2005)
9. Feng, Y., Teng, X., Zhao, J., Chen, Y., Jiang, T.: Anomalous reflection and refraction in anisotropic metamaterial realized by periodically loaded transmission line network. J. Appl. Phys. **100**, 114901 (2006)
10. Feng, Y., Zhao, J., Teng, X., Chen, Y., Jiang, T.: Subwavelength imaging with compensated anisotropic bilayers realized by transmission-line metamaterials. Phys. Rev. B **75**, 155107 (2007)
11. Feng, Y., Teng, X., Wang, Z., Zhao, J., Jiang, T.: Extraordinary transmission in planar waveguide loaded with anisotropic metamaterials. J. Appl. Phys. **105**, 034912 (2009)
12. Freire, M.J., Marques, R.: A planar magnetoinductive lens for three-dimensional subwavelength imaging. Appl. Phys. Lett. **86**, 182505 (2005)
13. Grbic, A., Eleftheriades, G.V.: Overcoming the diffraction limit with a planar left-handed transmission-line lens. Phys. Rev. Lett. **92**, 117403 (2004)
14. Grzegorczyk, T.M., Thomas, Z.M., Kong, J.A.: Inversion of critical angle and Brewster angle in anisotropic left-handed metamaterials. Appl. Phys. Lett. **86**, 251909 (2005)
15. Jacob, Z., Alekseyev, L.V., Narimanov, E.: Optical hyperlens: far-field imaging beyond the diffraction limit. Opt. Express **14**, 8247–8256 (2006)

16. Kildishev, A.V., Narimanov, E.E.: Impedance-matched hyperlens. Opt. Lett. **32**, 3432–3434 (2007)
17. Kildishev, A.V., Shalaev, V.M.: Engineering space for light via transformation optics. Opt. Lett. **33**, 43–45 (2008)
18. Lagarkov, A.N., Kissel, V.N.: Near-perfect imaging in a focusing system based on a lefthanded-material plate. Phys. Rev. Lett. **92**, 077401 (2004)
19. Lai, A., Caloz, C., Itoh, T.: Composite right/left-handed transmission line metamaterials. IEEE Micro. Magazine **5**, 34 (2004)
20. Lindell, V., Tretyakov, S.A., Nikoskinen, K.I., Ilvonen, S.: BW media – media with negative parameters, capable of supporting backward waves. Micro. Opt. Technol. Lett. **31**, 129 (2001)
21. Liu, Z., Lee, H., Xiong, Y., Sun, C., Zhang, X.: Far-field optical hyperlens magnifying Subdiffraction-limited objects. Science **315**, 1686–1686 (2007)
22. Maslovski, S., Tretyakov, S.: Phase conjugation and perfect lensing. J. Appl. Phys. **94**, 4241 (2003)
23. Maslovski, S., Tretyakov, S., Alitalo, P.: Near-field enhancement and imaging in double planar polariton-resonant structures. J. Appl. Phys. **96**, 1293 (2004)
24. Mesa, F., Freire, M.J., Marques, R., Baena, J.D.: Three-dimensional super-resolution in metamaterial slab lenses: experiment and theory. Phys. Rev. B **72**, 235117 (2005)
25. Pendry, J.B.: Negative refraction makes a perfect lens. Phys. Rev. Lett. **85**, 3966–3969 (2000)
26. Podolskiy, V., Narimanov, E.E.: Near-sighted superlens. Opt. Lett. **30**, 75–77 (2005)
27. Salandrino, A., Engheta, N.: Far-field subdiffraction optical microscopy using metamaterial crystals: theory and simulations. Phys. Rev. B **74**, 075103 (2006)
28. Shelby, R.A., Smith, D.R., Nemat-Nasser, S.C., Schultz, S.: Microwave transmission through a two-dimensional, isotropic left-handed metamaterial. Appl. Phys. Lett. **78**, 489 (2001)
29. Shelby, R.A., Smith, D.R., Schultz, S.: Experimental verification of a negative index of refraction. Science **292**, 77 (2001)
30. Shen, J.T., Platzman, P.M.: Near field imaging with negative dielectric constant lenses. Appl. Phys. Lett. **80**, 3286–3288 (2002)
31. Smith, D.R., Padilla, W.J., Vier, D.C., Nemat-Nasser, S.C., Schultz, S.: Composite medium with simultaneously negative permeability and permittivity. Phys. Rev. Lett. **84**, 4184 (2000)
32. Smith, D.R., Schurig, D.: Electromagnetic wave propagation in media with indefinite permittivity and permeability tensors. Phys. Rev. Lett. **90**, 077405 (2003)
33. Smith, D.R., Schurig, D., Rosenbluth, R., Schultz, S., Ramakrishna, S.A., Pendry, J.B.: Limitations on subdiffraction imaging with a negative refractive index slab. Appl. Phys. Lett. **82**, 1506–1508 (2003)
34. Smith, D.R., Schurig, D., Mock, J.J., Kolinko, P., Rye, P.: Partial focusing of radiation by a slab of indefinite media. Appl. Phys. Lett. **84**, 2244–2246 (2004)
35. Smolyaninov, I., Hung, Y., Davis, C.: Magnifying superlens in the visible frequency range. Science **315**, 1699–1701 (2007)
36. Teng, X., Zhao, J., Jiang, T., Feng, Y.: Negative refraction and partial focusing in an anisotropic metamaterial realized by a loaded transmission line network. J. Phys. D: Appl. Phys. **39**, 213–219 (2006)
37. Tsang, M., Psaltis, D.: Magnifying perfect lens and superlens design by coordinate transformation. Phys. Rev. B **77**, 035122 (2008)
38. Veselago, V.G.: The electrodynamics of substances with simultaneously negative values of $\varepsilon$ and $\mu$. Sov. Phys. Usp. **10**, 509–514 (1968)
39. Zhao, J., Feng, Y., Zhu, B., Jiang, T.: Sub-wavelength image manipulating through compensated anisotropic metamaterial prisms. Opt. Express **16**, 18057–18066 (2008)
40. Zhou, L., Chan, C.T., Sheng, P.: Anisotropy and oblique total transmission at a planar negative-index interface. Phys. Rev. B **68**, 115424 (2003)
41. Ziolkowski, R.W., Heyman, E.: Wave propagation in media having negative permittivity and permeability. Phys. Rev. E **64**, 056625 (2001)

# Chapter 9
# The Dynamical Study of the Metamaterial Systems

Xunya Jiang, Zheng Liu, Zixian Liang, Peijun Yao, Xulin Lin and Huanyang Chen

**Abstract** We investigate the dynamical characteristics of metamaterial systems, such as the temporal coherence gain of superlens, the causality limitation on the ideal cloaking systems, the relaxation process and essential elements in the dispersive cloaking systems, and extending the working frequency range of cloaking systems. The point of our study is the physical dispersive properties of meta-materials, which are well known to be intrinsically strongly dispersive. With physical dispersion, new physical pictures could be obtained for the waves propagating inside metamaterial, such as the "group retarded time" for waves inside superlens and cloak, the causality limitation on real metamaterial systems, and the essential elements for design optimization. So we believe the dynamical study of meta-materials will be an important direction for further research. All theoretical derivations and conclusions are demonstrated by powerful finite-difference time-domain simulations.

**Key words:** Dynamical study, metamaterial, left-handed material, coherence, cloaking, dispersion, group velocity, transformation optics, causality, absorption, working frequency range, pulse.

## 9.1 Introduction

Materials whose permittivity $\varepsilon$ and permeability $\mu$ are simultaneously negative are found to possess a negative refractive index $n$ with many unusual properties [50]. Negative-$n$ metallic resonating composites and 2D isotropic negative-$n$ material have been constructed [48, 46], and negative light refraction was observed [47].

Xunya Jiang*, Zheng Liu, Zixian Liang, Peijun Yao, Xulin Lin
National Key-Lab of the Functional Material, Institute of Microsystem and Information Technology, CAS, Shanghai 200050, People's Republic of China. *email: xyjiang@mail.sim.ac.cn

Huanyang Chen
Department of Physics, Hong Kong University of Science and Technology, Clear Water Bay, Kowlong, Hong Kong, China and Department of Physics, Suzhou University, Suzhou 215006, China.

T.J. Cui et al. (eds.), *Metamaterials*, DOI 10.1007/978-1-4419-0573-4_9,

The unconventional properties of such materials, such as the evanescent wave could be amplified by negative-$n$ so that the sub-wavelength resolution could be achieved [37], have drawn an increasing amount of attention in both science and engineering [33]. After negative-$n$ material, more such unconventional materials are found, so that a new concept "metamaterial" is generated, which is the effective medium both for the permittivity $\varepsilon_{eff}$ and for the effective permeability $\varepsilon_{eff}$ over a certain finite frequency band. Such physical media are composed of distinct elements (photonic atoms) which are generally constructed by metallic material, and their size and spacing are on a scale much smaller than the wavelengths in the frequency range of interest. Thus, the effective composite media could be considered homogeneous at the wavelengths under consideration. Since their abnormal properties can even go beyond the traditional physical limit and totally new optical phenomena, metamaterial becomes one of hottest topics in modern photonics. However, many of the current studies on the metamaterial are mainly concentrated on the stationary state, in which only the single-frequency properties are assumed in the study. It is understandable that the stationary state is most important because it represents the stable working state of metamaterial, and the studies of stationary state are much easier than others, i.e., the dynamical studies. But without dynamical study, many basic questions of stationary state cannot be answered, such as "How can the field gets to its stable state?" "Is there any strong scattering or oscillation in the process?" "How long is the relaxation process?" "What is the system response if the incidence is a pulse?" Furthermore, there are some physical topics that are intrinsically dynamical, for example, the temporal coherence change in propagation, the tuning of cavity frequency, and the nonlinear response. The essential point of the difference between the dynamical study and the stationary study is whether the dispersion of metamaterial is neglected. For common dielectric material, if the dispersion is very weak in the frequency range of interest, the stationary study can give us pretty clear physical picture to understand the optical properties. But we know that metamaterials are usually highly dispersive in the window of the work frequency, i.e., for the thin wire medium the permittivity can be described by the effective dielectric function $\varepsilon_{eff} = 1 - \omega_p^2/\omega^2$ with the plasma frequency $\omega_p$ related to the geometry of the wire array with typical value $\omega_p \sim 8.2\,\mathrm{GHz}$ and for the SRR medium the effective frequency-dependent permeability, usually having the form $\mu_{eff} = 1 - F\omega_0^2/(\omega^2 - \omega_0^2 - i\omega\Gamma)$. The deeper physical reason is that the strong interaction between electromagnetic field and "photonic atoms" is the origin of almost all abnormal optical properties of metamaterial, and it is the origin of the strong dispersion too. In other words, the strong dispersion and the abnormal optical property are twins with same origin. So it is not surprising that the dispersion is generally needed to explain those abnormal optical properties, such as the negative refraction of negative-$n$ material. More seriously, if the specific strong dispersion of certain metamaterial is neglected, the violation of basic physical laws is pointed out, i.e., it is deduced that there exists causality violation, such as the superluminal group velocity in cloaking systems [52] and hyper-lens systems [31]. Hence, the study with dispersion of metamaterial is not only needed but also required. Although for a linear system we can obtain the

dynamical picture theoretically if we have known the response of system at all frequency ranges, for the strongly dispersive metamaterial, it is so hard that the dynamical response needs to be studied specifically. In such dynamical studies, the numerical simulation is an important tool to obtain direct observation of the details. The well-developed finite-difference time-domain (FDTD) method is a good candidate for the dynamical simulation of metamaterials.

In this chapter, we will emphasize the dynamical picture of the metamaterial systems, such as the superlens and the electromagnetic cloak. As we have discussed, the dispersion of metamaterial is the key for whole study. From dynamical studies, we will not only reveal deeper physical pictures of metamaterial systems but also discuss the physical limitation in these systems. This chapter is organized as follows:

In the second section the image field of the negative-index superlens with the quasi-monochromatic random source is discussed, and dramatic temporal coherence gain of the image in the numerical simulation is observed, even if there is almost no-reflection and no-frequency-filtering effects. From the new physical picture, a theory is constructed to obtain the image field and demonstrate that the temporal coherence gain is from different "group" retarded time of different optical paths. Our theory agrees excellently with the numerical simulation and strict Green's function method. This study should have important consequences in the coherence studies in the related systems and the design of novel devices.

In the third section, the dynamical processes of dispersive cloak by finite-difference time-domain numerical simulation are carried out. It is found that there is a strong scattering process before achieving the stable state and its time length can be tuned by the dispersive strength. Poynting vector directions show that the stable cloaking state is constructed locally while an intensity front sweeps through the cloak. Deeper studies demonstrate that the group velocity tangent component $V_{g\theta}$ is the dominant factor in the process. This study is helpful not only for clear physical pictures but also for designing better cloaks to defend passive radars.

In the fourth section, the limitation of the electromagnetic cloak with dispersive material is investigated based on causality. The results show that perfect invisibility cannot be achieved because of the dilemma that either the group velocity $V_g$ diverges or a strong absorption is imposed on the cloaking material. It is an intrinsic conflict which originates from the demand of causality. However, the total cross section can really be reduced through the approach of coordinate transformation. A simulation of finite-difference time-domain method is performed to validate the analysis.

In the fifth section, with the "freedom trade-off" thought we introduce a new coordinate mapping from a tiny PEC cylinder to a concentric cylindrical cloaking shell so that the cloak could be accepted to be an almost perfect cloak. With such coordinate mapping, we describe how to build up a dispersive cloak in a frequency range. A constraint of the bandwidth from this method is also obtained and is called as "the invisibility uncertainty condition" which may have general meaning for cloaking design.

In the last section, we give a summary of the chapter.

## 9.2 The Temporal Coherence Gain of the Negative-Index Superlens Image

Veselago predicted that the negative-index material (NIM) has some unusual properties, such as a flat slab of the NIM could function as a lens for electromagnetic (EM) waves [50]. This research direction was further pushed by works of Pendry and others [37, 36, 18, 40, 47, 9, 15, 16, 53, 8, 54, 11, 29, 34, 30] who showed the lens with such NIM (i.e., $\varepsilon = \mu = -1 + \delta$) could be a *superlens* whose image resolution can go beyond the usual diffraction limit. After that, several beyond-limit properties of NIM systems are found, such as the sub-wavelength cavity [13] and the waveguide [45]. Some of the theoretical results are confirmed by experiments [47, 9, 16]. And these beyond-limit properties give us new physical pictures and opportunities to design devices. Recently, new numerical [40, 15] and theoretical Green's function [53] methods are used to understand the phenomena in such systems. But so far almost all studies are done with the strictly single-frequency sources, so that the coherent properties of EM waves (or photons) in the NIM systems have not been studied to the best of our knowledge. Even more seriously, there is no theory for the propagation of coherent functions in NIM systems. The importance of coherence research cannot be over-estimated since the coherence is essential in the wave interference, the imaging, the signal processing, and the telecommunication [32, 42]. Can we find new frontier to go beyond at the coherent properties in NIM systems? If so, can we develop a simple theoretical method to deal with the image coherence of superlens?

In this section, the finite-difference time-domain (FDTD) method is used in the 2D numerical experiments to study the temporal coherence of the superlens image with random quasi-monochromatic sources. We observe the dramatic temporal coherence gain of the superlens image even if the reflection and frequency-filtering effects are very weak. Based on the new physical picture of the signal (the fluctuation of random source) propagation in NIM, we construct a theory to obtain the image field and derive the equation of the temporal coherence relation between the source and its image. The new mechanism of the temporal coherence gain can be explained by the key idea that the signals on different paths have different "group" retarded time. Our theory excellently agrees with numerical results and the strict Green's function results.

*The setup* of the 2D system is shown in Fig. 9.1. The thickness of the infinite-long NIM slab is $d$. To realize the negative $\varepsilon$ and negative $\mu$, the electric polarization density $\mathbf{P}$ and the magnetic moment density $\mathbf{M}$ are phenomenologically introduced in FDTD simulation [21]. The effective permittivity and permeability of the NIM are $\varepsilon_r(\omega) = \mu_r(\omega) = 1 + \omega_P^2/(\omega_a^2 - \omega^2 - i\gamma)$. In our model, $\omega_a = 1.884 \times 10^{13}/s$, $\gamma = \omega_a/100$, $\omega_P = 10 \times \omega_a$. The quasi-monochromatic field is expressed as $E(x,t) = U(x,t)exp(-i\omega_0 t)$, where $U(x,t)$ is a slowly varying random function, $\omega_0 = \pi/20\delta_t$ is the central frequency of our random sources, and $\delta_t = 1.18 \times 10^{-15}$/s is the smallest time step in FDTD simulation. At $\omega_0$, we have $\varepsilon_r = \mu_r = -1.00 - i0.0029$. Here, we emphasize that in our FDTD simulation the smallest space step $\delta_x = \lambda_0/20$ ($\lambda_0 = 2\pi c/\omega_0$) and the distance ($d/2 = \lambda_0$) of the source from the lens are too large

to excite strong evanescent modes of NIM [40, 8, 15]. *Actually the evanescent field in our simulation can be neglected comparing with radiating field, and what we are studying is the property dominated by the radiating field.*

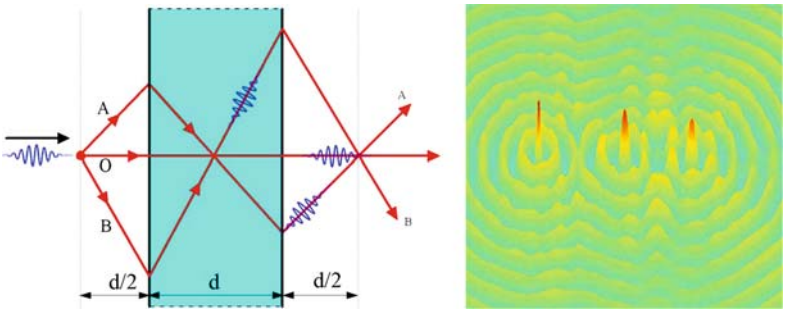


**Fig. 9.1** The schematic diagram of our model with ray paths (*left*) and the typical snapshot of electric field in our FDTD simulation (*right*).

The random source is composed of randomly generated plane wave pulses, with the average pulse length $t_p$ and the random starting phase and starting time. In the simulation, we record the field of the source and the image for a duration of $4 \times 10^5 \delta_t$ to obtain the data for analysis. For convenience, we define $E(\omega) = \lim_{T\to\infty} \int_{-T}^{T} E(t) exp(-i\omega t)$ as the *field spectrum* (FS).

*Unusual phenomena* – At first, the FS width of the random source is a little too large ($\Delta\omega_s \simeq \omega_0/20$). When we observe the image temporal coherence gain, we also find that the FS width of the image is sharper than the source ($\Delta\omega_i < \Delta\omega_s$). It is obvious that there are frequency-filtering effects because of the NIM dispersion, such as the frequency-dependent interface reflection and focal length. After increasing the pulse length $t_p$ of the source, we reduce the source FS width to $\Delta\omega_s \simeq \omega_0/100$, then the reflection and focal length difference are very small. With such source, the FS widths of source and image are almost same $\Delta\omega_i \simeq \Delta\omega_s$, as shown in Fig. 9.2a. The difference between two widths is <5%, which is our criterion of the *quasi-monochromatic* source. Even so the dramatic gain of temporal coherence is still observed. In Fig. 9.2b, the source field (up) and the image field (down) vs. time of FDTD simulation are compared. The *profiles* of them are generically similar, but the image profile is much smoother. The normalized temporal coherence function $g^{(1)}(\tau) = < E^*(t)E(t+\tau) > / < E^*(t)E(t) >$ (<> means the ensemble average) of the source (circle) and the image (asterisk) from FDTD simulation is shown in Fig. 9.3. The temporal coherence of the image field is obviously better than the source. From $g^{(1)}$, the image coherent time is obtained $T_i^{co} = \int g_i^{(1)}(\tau) d\tau = 1268\delta_t$, which is about 50% longer than the source coherent time $T_s^{co} = 860\delta_t$.

Although the gain of the spatial coherence only by propagation is well known [32], the dramatic gain of temporal coherence is generally from the high-$Q$ cavities, contrary to our case, which have strong filtering effects. To reveal the new

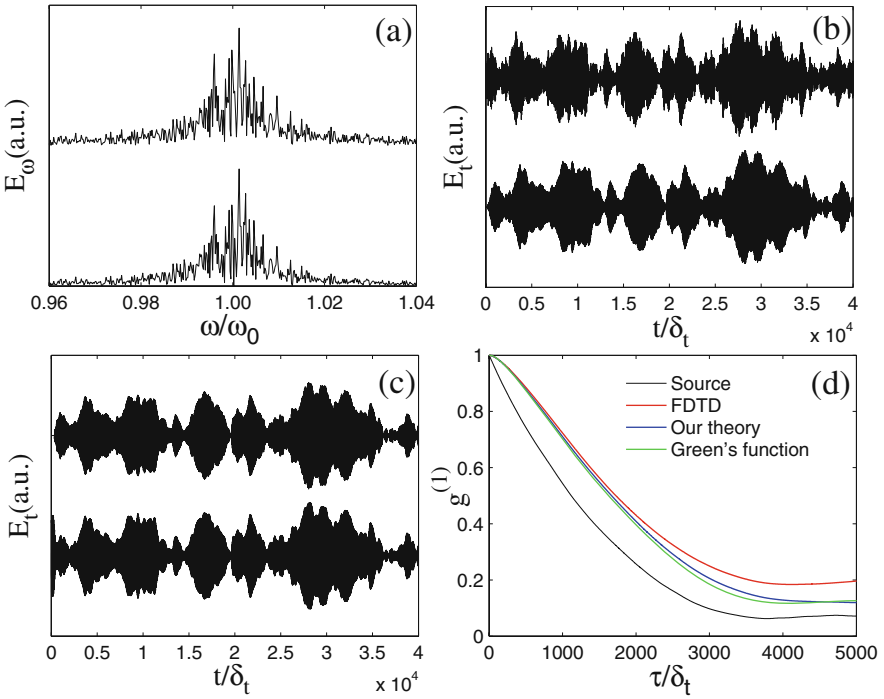


**Fig. 9.2** (**a**) The FSs of the source (*up*) and the image (*down*). (**b**) The electric field of the source (*up*) and its image (*down*) vs. time from FDTD simulation. (**c**) The image field vs. time from Eq. (9.1) (*up*), and from Green's function method (*down*).

mechanism of the temporal coherence gain in NIM systems, we also have done more numerical experiments in which *only* the ray near a certain incident angle (shown in Fig. 9.1), such as only paraxial rays ($\theta \simeq 0$), can pass through the superlens. Then the image field profile vs. time looks very like the source field and has no gain of coherence anymore. *Therefore, the gain of temporal coherence of the superlens image is not from one ray with certain incident angle, but probably from the interference between the rays with different incident angles.* Then, what is different between the rays with different incident angles? After carefully checking the field profiles of different-incident-angle cases, we find that the profiles have different retarded time. The larger the incident angle the longer the retarded time.

*Physical pictures* – To understand deeper the new mechanism of coherence gain and construct our theory, we need to make two physical pictures clear. The first one is about the optical path length (OPL) $\int nds$ which determines the wave phase and the refracted "paths" of rays in Fig. 9.1 according to Fermat's principle (or Snell's law). Based on ray optics, the superlens and traditional lenses have same focusing mechanism that all focusing rays have same OPL $\int_{paths} nds = const$ ($\int_{paths} nds = 0$ for superlens) from source to image [50]. But this picture is so well known that it suppresses the other important picture. Because the temporal coherence information is in the fluctuation signals of random field, the signal propagating picture should

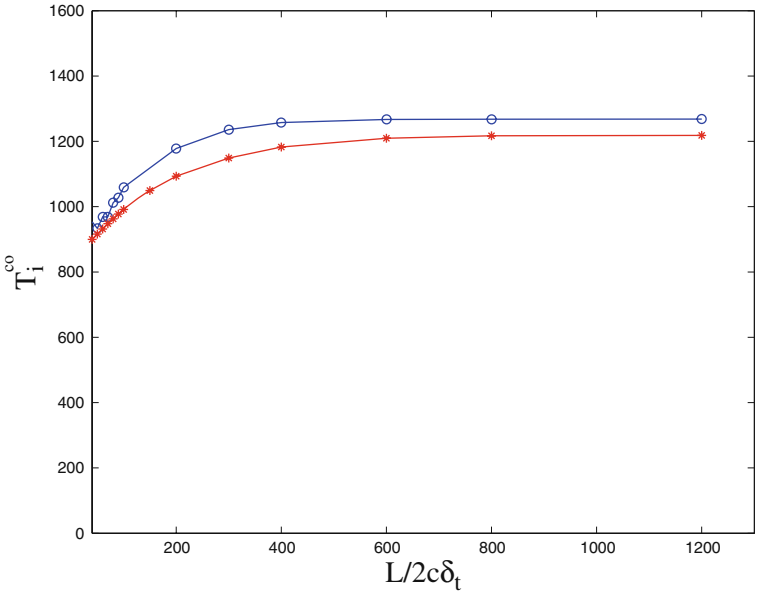


**Fig. 9.3** The coherent time vs. the superlens length $L$, from the FDTD simulation *(circle)* and from our theory (asterisk).

be essential for our study. *The optical signals propagate in the group velocity $v_g$ which is always positive*. Obviously, if the path (in Fig. 9.1) is longer (larger incident angle), the signal needs a longer propagating time, which is called *group retarded time* (GRT) in this section. Inside the NIM, the GRT of a path should be $\frac{d}{cos(\theta)v_g}$ (this is confirmed by our numerical experiments), where $\theta$ is the incident angle and $v_g = c/3.04$ is the group velocity of NIM around $\omega_0$. The total GRT from source to image is $\tau_r = \tau_0/cos(\theta)$ where $\tau_0 = d/c + d/v_g$ is the GRT of the paraxial ray. Now, the new propagating picture for a signal through superlens is that a signal, generated at $t_s$ from the source, will propagate on all focusing paths and arrive at image position at very different time $t_s + \tau_0/cos(\theta)$ from different paths (this is schematically shown in Fig. 9.1). This picture is totally different from traditional lenses, whose images do not have obvious temporal coherence gain because their focusing rays have same OPL *and similar GRT*.

*Our theory* – Based on these analysis, we suppose that *the superlens image field of the random quasi-monochromatic source is the sum of all signals from different paths with different GRT*. This is the key point of our theory, and then the image field can be obtained:

$$\begin{aligned} E_i(t) &= \frac{1}{U_0} e^{-i\omega_0 t} \sum_{paths} U_s(t - \tau_r) \\ &= \frac{1}{U_0} e^{-i\omega_0 t} \int_{-\frac{\pi}{2}}^{\frac{\pi}{2}} U_s\left(t - \frac{\tau_0}{\cos(\theta)}\right) d\theta, \end{aligned} \tag{9.1}$$

where $U_s(t)$ is the slowly varying profile function of the source and $U_0$ is the normalization factor. In Fig. 9.2c (up), we show the result of the image field based on Eq. (9.1), we can see it is in excellent agreement with the FDTD result in Fig. 9.2b (down). To show the interference effect of different paths, we assume there are only two paths (such as $A$ and $B$ in Fig. 9.1). Based on Eq. (9.1) the image field is $E_i = e^{-i\omega_0 t}(U_s(t-\tau_r^A)+U_s(t-\tau_r^B))$, then the temporal coherence of image is $G(\tau) =< E_i^*(t)E_i(t+\tau) >=< U_s^*(t-\tau_r^A)U_s(t-\tau_r^A+\tau)+U_s^*(t-\tau_r^B)U_s(t-\tau_r^B+\tau)+U_s^*(t-\tau_r^A)U_s(t-\tau_r^B+\tau)+U_s^*(t-\tau_r^B)U_s(t-\tau_r^A+\tau) >$. The first two terms are same as the source field (just a time shift) so they do not contribute to the coherence gain. The last two terms are from interference between two paths. The third (or the fourth) term could be very large at the condition $\tau \simeq \tau_r^B - \tau_r^A$ (or $\tau_r^A - \tau_r^B$). This condition can always be satisfied between any two paths since $\tau$ is a continuous variable. So the interfering terms between the paths are responsible for the image temporal coherence gain.

From Eq. (9.1), after the variable transformation $t_s = t - \tau_0/cos\theta$ and some algebra, the relation of the temporal coherence between the image and the source can be obtained:

$$\begin{aligned} G_i(\tau) &= < E_i^*(t)E_i(t+\tau) > \\ &= \frac{1}{U_0^2}\int_{-\infty}^{-\tau_0} dt_1 \int_{-\infty}^{-\tau_0+\tau} dt_2 h_i^*(t_1)h_i(t_2+\tau)G_s(t_2-t_1), \end{aligned} \tag{9.2}$$

where $h_i(t) = (\tau_0/t)^2/\sqrt{1-(\tau_0/t)^2}$ is the response function of different incident angles and $G_s(t_2-t_1) =< E_s^*(t_1)E_s(t_2) >$ is the temporal coherence function of the source. Equation (9.2) can explain the temporal coherence gain of the image too. Even if the source field is totally temporal *incoherent* $G_s(t_2-t_1) \propto \delta(t_2-t_1)$, based on Eq. (9.2) we can find that $G_i(\tau)$ is not a $\delta$-function anymore, so the image is partial temporal coherent. The product of $h_i^*(t_1)h_i(t_2+\tau)$ includes the interference between paths. According to our theory, we calculate the image coherence function $g^{(1)}$ vs. time (Fig. 9.3 circle) which agrees with our FDTD result (Fig. 9.3 asterisk) pretty well (we will discuss the deviation later).

To further confirm our theory and FDTD results, the *strict* Green's function method [53] is engaged to check our results. *We only include the radiating field (no evanescent wave) in Green's function*. The strict image field vs. time is shown in Fig. 9.2c (down), and the image temporal coherence function $g^{(1)}$ vs. time is shown in Fig. 9.2d (blue). In Fig. 9.2d, we can see that the FDTD result (red) is almost exactly same as the strict Green's function method (green). But our theory (blue) deviates from the strict result at very large $\tau > 3000\delta_t$ corresponding to very long path (or very large incident angle). This is understandable since in our theory we neglect the dispersion of NIM totally and only use $v_g(\omega_0)$. For the very large angle rays a small index difference (from the dispersion of NIM) can cause large focal-length difference. Hence the deviation is from the focus-filtering effect. When we reduce the FS width of source to an even smaller value (i.e., $\Delta\omega_s = \omega_0/500$), the deviation of our theory is smaller.

Although our theory is only a good approximation generally, owing to the picture's simplicity and clarity the theory can help us to study more complex systems qualitatively and quantitatively. The *finitely long* 2D superlens is a good example which is hard to deal by Green's function method. In Fig. 9.3, we plot the coherent time $T_i^{co}$ vs. superlens length $L$ of the FDTD simulation (circle) and of our theory (asterisk), respectively. They coincide with each other pretty well (the deviation reason has been discussed). The increase of the $T_i^{co}$ with the increase of $L$ can be explained simply according to our theory. Since the image field is $E_i(t) = \frac{1}{U_0} e^{-i\omega_0 t} \int_{\theta_{min}}^{\theta_{max}} U_s(t - \frac{\tau_0}{cos\theta}) d\theta$, the large-angle paths ($\theta > \theta_{max}$ and $\theta < \theta_{min}$) and their contribution to the temporal coherence gain are missed in the short superlens.

Obviously, Eq. (9.1) is suitable not only for random quasi-monochromatic source but also for all quasi-monochromatic fields, such as the slowly varying Gaussian pulses and slowly switching-on process mentioned in [53]. Our theory can be easily extended to 3D systems too. And owing to the fact that what we find is from the radiating field, so the temporal coherence gain is not the near-field property. Actually, the new mechanism of the temporal coherence gain is not limited for the $n \simeq -1$ superlens, also applicable to other superlenses, such as the photonic crystal superlens in [9, 30, 16]. But the specialties of $n \simeq -1$ superlens, such as almost no frequency filtering (no frequency loss) and no reflection (no energy loss), can be used to design novel optical/photonic coherence gain devices.

In summary, for the first time we have numerically and theoretically studied the temporal coherence of the superlens image with the quasi-monochromatic source. Numerically, we observe that the temporal coherence of the image can be improved considerably even almost without reflection and filtering effects. Based on new physical picture, we construct a theory to calculate the image field and temporal coherence function, which excellently agree with the FDTD results and strict Green's function results. The mechanism of the temporal coherence gain is theoretically explained by the different GRT of different paths. Although the evanescent wave is very weak in this study, the coherence of evanescent wave in NIM systems is a very interesting topic which will be discussed elsewhere [19]. Other related topics, such as the spatial coherence which is very essential for the image quality of the superlens, can also be studied through the similar methods. Although our study is within the confinement of classic optics, similar investigation can be extended to the quantum optics [32], and interesting results can be expected. Obviously, the temporal coherence gain of superlens is another evidence that the NIM phenomena are consistent with the causality [16]. We suppose that the temporal coherence gain phenomena could be observed in microwave experiments [47, 9]. Therefore, this study should have important consequences in the future studies of coherence in NIM systems. The no-reflection and no-frequency-filtering coherence gain of the superlens has some potential applications in the imaging, the coherent optical communication, and the signal processing.

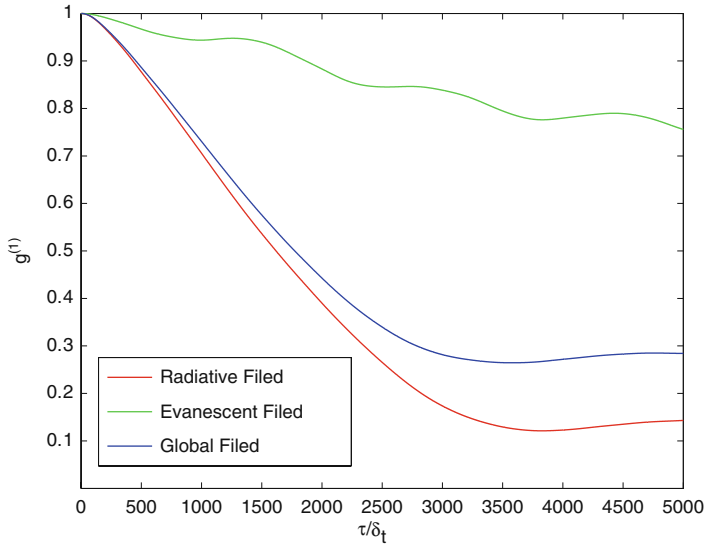


**Fig. 9.4** The normalized temporal coherence function g(1) vs. time of the source field and of the image field which obtained from the FDTD simulation, from Eq. (9.2), and from Green's function method marked with different gray level.

## 9.3 The Physical Picture and the Essential Elements of the Dynamical Process for Dispersive Cloaking Structures

Recently, the theory [25, 38] has been developed based on the geometry transformation to realize a cloaking structure (CS), in which objects become invisible from outside. Then a 2D cylindrical CS [12] and a non-magnetic optical CS [1, 2] are designed. More surprisingly, the experiment [43] demonstrates that such a 2D CS really works with a "reduced" design made of split-ring resonators. These pioneers' works are really attractive and open a new window to realize the invisibility of human dream. However, so far almost all theoretical [25, 38, 12, 1, 2, 7, 41, 26] studies of the CS are done in the frequency domain and the geometry transformation idea is supposed to work only for a single frequency, so that the effects of the dispersion have not been intensively studied. As pointed out in Ref. [38] and the quantitative study in our recent work [52], the dispersion is *required* for the cloaking material to avoid the divergent group velocity. For the dispersive CS, new topics, such as the *dynamical process*, can be introduced. Dynamical study is essential for the cloaking study since without it we cannot answer the questions, such as how can the field gets to its stable state? Is there any strong scattering or oscillation in the process? How long is the process?. More important, because the real radars generally are pulsive ones, the dynamical process is critical for the cloaking effect around the goal frequency. So the dynamical study not only gives us whole physical picture of the cloaking but also helps us to design more effective cloaks.

In this section, the dynamical process of the electromagnetic (EM) CS is investigated by finite-difference time-domain (FDTD) numerical experiments. In our simulation, the Lorentzian dispersion relations are introduced into the permittivity and the permeability models, then the *real* dynamical process can be simulated [10, 20, 51]. Based on numerical simulation, we can follow the details of the dynamical process, such as the time-dependent scattered field, the building-up process of the cloaking effect, and the final stable cloaking state. By tuning the dispersion parameters and observing their effects on the dynamical process and the scattered field, we can find the essential elements which dominate the process. Theoretical analysis of these essential elements can help us to have a deeper physical picture beyond the phenomena and to design more effective cloaks.

The *setup* of the system is shown in Fig. 9.5(a), similar as the one in Ref. [12]. $R_1$ and $R_2 = 2R_1$ are the inner and the outer cylindrical radii of the CS, respectively. A perfect electric conductor (PEC) shell is pressed against the inner surface of the CS. The CS is surrounded by the free space with $\varepsilon_0 = \mu_0 = 1$. From the left side, an incident plane wave with working frequency $\omega_0$ is scattered by the CS, the total field and the scattered field can be recorded inside and outside $B1$, respectively, by the numerical technique [49]. So the scattering cross section $\sigma$ can be calculated easily. Our study is focused on the E-polarized modes, for which only the permittivity and the permeability components $\varepsilon_z$, $\mu_r$, and $\mu_\theta$ are needed to be considered. (For H-polarized modes, considering the corresponding components $\mu_z$, $\varepsilon_r$,

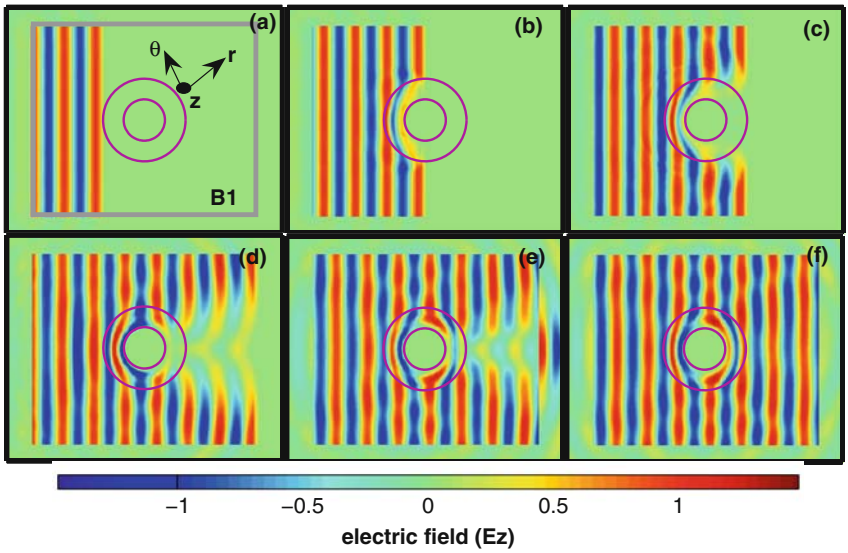


**Fig. 9.5** (Color online) (**a**) The setup of the system and the distribution of the electric field at different moments during the process. Parameters are chosen as $A_r = 0.4$, $A_\theta = 1.6$, $A_z = 0.4$ (in the position where $\varepsilon_z < 1$) or $A_z = 1.6$ (where $\varepsilon_z > 1$), and $\gamma = 0.012\omega_0$. (**a**) $t = 2.28T$; (**b**) $t = 3.60T$; (**c**) $t = 4.92T$; (**d**) $t = 7.20T$; (**e**) $t = 9.00T$; (f) stable state. $T$ is the period of the incident EM wave.

and $\varepsilon_\theta$, we can obtain the same numerical results in the dynamical process.) All of them are supposed to have the form $1+F_j(r)\times f_j(\omega)$, where subscript $j$ could be $z$, $r$, and $\theta$ for $\varepsilon_z$, $\mu_r$, and $\mu_\theta$, respectively. The filling factors $F_j(r)$ are only $r$-dependent, $\omega_p$ is the plasma frequency which sets to be a constant $\omega_p = 10\omega_0$, and $f_j(\omega) = \omega_p^2/(\omega_{aj}^2 - \omega^2 - i\omega\gamma)$ are the Lorentzian dispersive functions, where $\gamma$ is the "resonance width" or called as "dissipation factor" and $\omega_{aj}$ are the resonant frequency of "atoms" (resonant units) in metamaterials.

For the study of the dispersive CS, we suppose that the real parts of the $\varepsilon_z$, $\mu_r$, and $\mu_\theta$ always satisfy the geometry transformation of Ref. [12] at $\omega_0$:

$Re[\mu_r(r,\omega_0)] = (r-R_1)/r$, $Re[\mu_\theta(r,\omega_0)] = r/(r-R_1)$, and $Re[\varepsilon_z(r,\omega_0)] = R_2^2(r-R_1)/[(R_2-R_1)^2 r]$. Then the filling factors $F_j(r)$ at different $r$ can be obtained: $F_r(r) = \{Re[\mu_r(r,\omega_0)]-1\}/Re[f_r(\omega_0)]$, $F_\theta(r) = \{Re[\mu_\theta(r,\omega_0)]-1\}/Re[f_\theta(\omega_0)]$, and $F_z(r) = \{Re[\varepsilon_z(r,\omega_0)]-1\}/Re[f_z(\omega_0)]$.

To investigate the dispersive effect on the dynamical process, we tune the dispersion parameters $\omega_{aj}$ in our numerical experiments. We use the working frequency $\omega_0$ as the frequency unit since it is the same for all cases in this section so the ratio $A_j = \omega_{aj}/\omega_0$ represents $\omega_{aj}$. Obviously, for the Lorentzian dispersive relation, the dispersion is stronger when $\omega_0$ and $\omega_{aj}$ are closer to each other (the working frequency is near the resonant frequency), or in other words, when $A_j$ approaches 1. Since there are singular values of real part of $\varepsilon$ and $\mu$, in our numerical simulation we have done some approximations, such as we set the maximum and the minimum for $\varepsilon$ and $\mu$. Although such approximations will affect the cloaking effect of stable state [41], we find that the influence of these approximations on the dynamical process is very small and can be neglected.

First, we show an example of evolving electronic field during the dynamical process in Fig. 9.5 with concrete parameters of $A_r$, $A_\theta$, $A_z$, and $\gamma$. In Fig. 9.5(a), the plane wave arrives at the left side of the CS and is ready to enter the CS. From Fig. 9.5(b)–(e), the cloaking effect is built up step by step, at last, the field gets to the stable state shown in Fig. 9.5(f). Because of the dispersion, there is an obvious time delay in the cloaking effect and the strong scattered field is observed.

We introduce a time-dependent scattering cross section $\sigma(t)$ to quantitatively study the dynamical process, which is defined as

$$\sigma(t) = \bar{J}_{scat}(t)/\bar{S}_{inct}, \tag{9.3}$$

where $t = n\times T$, $n = 0,1,2,...$, $T$ is the period of the incident wave, $\bar{J}_{scat}(t)$ is the one-period-average energy flow of scattered field, and $\bar{S}_{inct}$ is the average energy flow density of incident field. To observe the dispersive effect on $\sigma(t)$ during the dynamical process, at the first step, we keep $A_z$ and $\gamma$ constant and change $A_r$ and $A_\theta$; the results are shown in Fig. 9.6(a). From $\sigma$ vs. $t$ curves, we can find the general properties of the dynamical process. First, there is strong scattering in the dynamical process. At the beginning, $\sigma$ increases rapidly when the wave gets to the CS, then reaches its maximum (at about ninth period). After that, $\sigma$ starts to decay until it gets to the stable value (of the stable cloaking state). Second, unlike other systems, there is no oscillation in the process. This property will be discussed later. Third,

the time length of dynamical process, called as "relaxation time" generally, can be tuned by the dispersion. From Fig. 9.6(a), we can see that the main dispersive effect is on the decaying process. From case 1 to case 5, $A_r$ and $A_\theta$ become closer to 1, so that the dispersion is stronger. We find that the stronger the dispersion, the longer the relaxation time. For comparing with the cloaking cases, we also show the $\sigma(t)$ of the naked PEC shell in case 6. From the definition of $\sigma$, we know that the area covered by these curves in Fig. 9.6(a) is proportional to the total scattered energy in the dynamical process. So the CS with *the weaker dispersion will scatter less field* (better cloaking effect) in the dynamical process. But, such a general conclusion is still not enough for us to get a clear physical picture to understand the cloaking dynamical process.

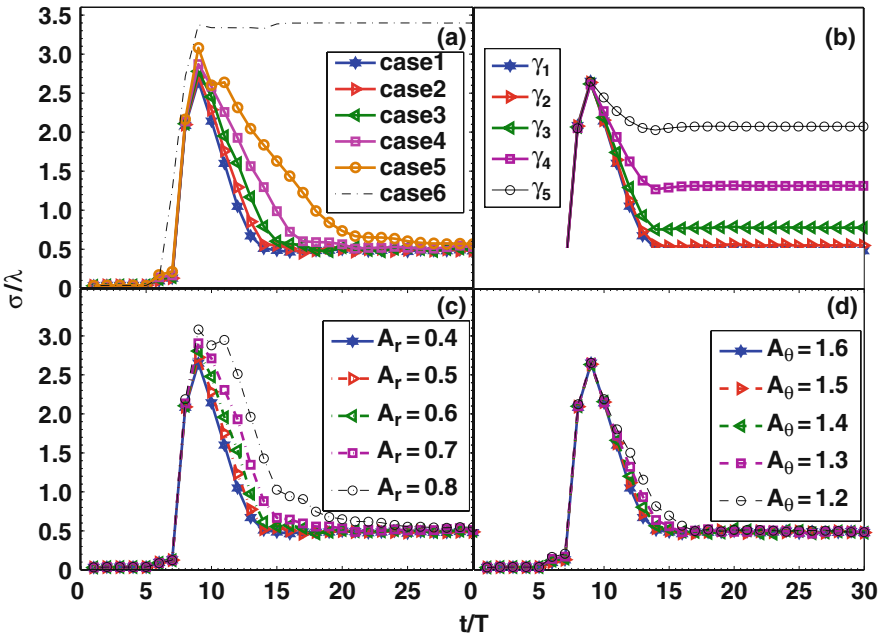


**Fig. 9.6** (Color online) The $\sigma$ vs. $t$ curves. From (**a**) to (**d**), $A_z = 0.4$ where $\varepsilon_z < 1$ or $A_z = 1.6$ where $\varepsilon_z > 1$. (**a**) Keep $\gamma = 0.012\omega_0$ unchanging, choose $A_r$ and $A_\theta$ as case 1: $A_r = 0.4$, $A_\theta = 1.6$, case 2: $A_r = 0.5$, $A_\theta = 1.5$, case 3: $A_r = 0.6$, $A_\theta = 1.4$, case 4: $A_r = 0.7$, $A_\theta = 1.3$, case 5: $A_r = 0.8$, $A_\theta = 1.2$, and case 6: only PEC shell without CS. (**b**) Keep $A_r = 0.4$, $A_\theta = 1.6$ unchanging, choose $\gamma_1 = 0.012\omega_0$, $\gamma_2 = 0.024\omega_0$, $\gamma_3 = 0.048\omega_0$, $\gamma_4 = 0.096\omega_0$, and $\gamma_5 = 0.192\omega_0$. (**c**) Keep $A_\theta = 1.6$ and $\gamma = 0.012\omega_0$ unvaried, and change $A_r$. (**d**) Keep $A_r = 0.4$ and $\gamma = 0.012\omega_0$ unvaried, and change $A_\theta$.

Next, we check whether the absorption of the CS is important in the process. The absorption is determined by the imaginary part of $\varepsilon$ and $\mu$. To study this effect, we hold $A_r$, $A_\theta$, and $A_z$ constant but modify the dispassion factor $\gamma$. We modify the filling factors $F_j$ simultaneously, so that the real parts of $\varepsilon$ and $\mu$ are kept unchanged at $\omega_0$. In such way, we can keep the dispersion strength almost unchanged, but with

the imaginary parts of $\varepsilon$ and $\mu$ changed. Results in Fig. 9.6(b) show that the stronger absorption only leads to larger stable value of $\sigma$, leaving the relaxation time nearly unchanged. Thus, we can exclude the absorption from the relevant parameter list, since it only influences the $\sigma(t)$ of stable state considerably.

To obtain deeper insight of the dynamical process, we need to study the dynamical process more carefully. From Fig. 9.5(b)–(e), we can see that the "field intensity" (shown by different colors in the figures) propagates slower inside the CS than that in the outside vacuum. And when the inside field intensity "catches up" the outside one [in Fig. 9.5(f)], the field in the CS gets to the stable state and the cloaking effect is built up. In fact, this catching-up process of the field intensity can be shown more clearly by the direction of Poynting vectors during the dynamical process. From Fig. 9.7(a)–(d), we show the direction of Poynting vectors in moments of Fig. 9.5(c)–(f), respectively. In Fig. 9.7, we see that there is the "intensity front" (shown by red dashed curve) which separates two regions of the CS. At the right side of the front, the field intensity in the CS is much weaker than the outside and the Poynting vector directions are not regular (especially near the front). But at the left-side region which is swept by the intensity front, the Poynting vectors are very regular and nearly along the "cloaking rays" which was predicted at the coordinate transformation [38]. Since the cloaking effect can be interpreted by the mimic picture that the light runs around the cloaking area through these curved cloaking rays, it is not surprising to find that the stable cloaking state is achieved when the intensity front sweeps through the whole CS and these optical rays are well constructed. The

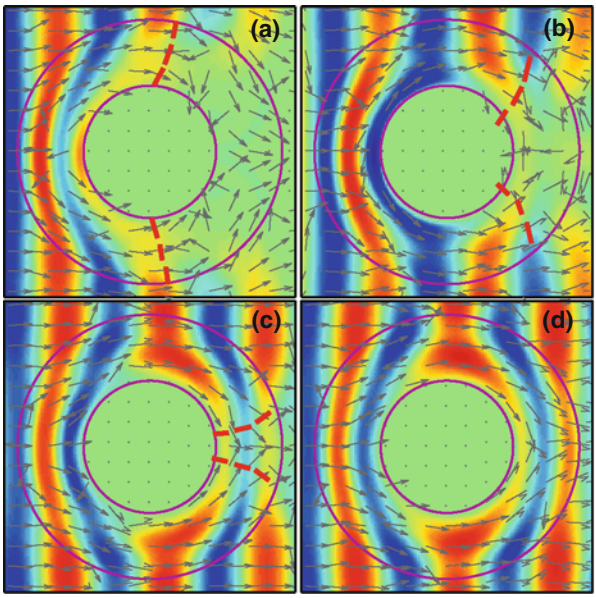


**Fig. 9.7** (Color online) Direction of Poynting vectors and the intensity front (shown by *gray dashed curves*) at moments during the dynamical process. Parameters are chosen as that of Fig. 9.5: (**a**) $t = 4.92$ T; (**b**) $t = 7.20$ T; (**c**) $t = 9.00$ T; and (**d**) stable state.

surprising thing is that *the stable cloaking state seems to be constructed locally.* We believe this property is related to the original cloaking recipe [38], which makes the cloaking material is almost impedance matched layer by layer. This also explains why there is no oscillation in the cloaking dynamical process generally. This picture can also interpret the strong scattered field in the dynamical process, since these "irregular rays" at the right-side region of the intensity front must be scattered strongly. Further, we can use this picture to analyze the dynamical process of other incident waves, such as the Gaussian beams, which are composed of different plane wave components.

With this understanding, now we are ready to find the correlation between the relaxation time and the CS dispersion. It is well known that the field intensity (or energy) propagates at the group velocity $V_g$, which is controlled by the material dispersion. So the intensity front, which determines the dynamical process, should move in $V_g$. Thus, we can explain the results in Fig. 9.6, since our modification of the dispersive parameters can cause the $V_g$ changed. But because the cloaking material is the strong anisotropic material, the $V_g$ at different directions could be very different. Can we predict more precisely which component dominates the relaxation time? The answer is "yes." In Fig. 9.7(d), we can see that the stable energy flow in the CS is nearly along the $\theta$ direction at most regions of the CS. Then it is reasonable for us to argue that it is the component along the $\theta$ direction $V_{g\theta}$, not the component along the $r$ direction $V_{gr}$, that dominates the relaxation time and the total scattered energy in the dynamical process.

For the anisotropic cloaking material, the $V_{g\theta}$ and $V_{gr}$ can be expressed as follows:

$$V_{g\theta} = [\nabla_{\mathbf{k}}\omega(\mathbf{k})]_\theta = \left(\frac{2c}{\sqrt{\varepsilon_z\mu_r}}\right) / \left(2 + \frac{\omega}{\varepsilon_z}\frac{d\varepsilon_z}{d\omega} + \frac{\omega}{\mu_r}\frac{d\mu_r}{d\omega}\right)$$

and

$$V_{gr} = [\nabla_{\mathbf{k}}\omega(\mathbf{k})]_r = \left(\frac{2c}{\sqrt{\varepsilon_z\mu_\theta}}\right) / \left(2 + \frac{\omega}{\varepsilon_z}\frac{d\varepsilon_z}{d\omega} + \frac{\omega}{\mu_\theta}\frac{d\mu_\theta}{d\omega}\right),$$

where $c$ is the velocity of light in vacuum.

In order to illustrate our prediction, $\sigma(t)$ under different $V_{g\theta}$ and $V_{gr}$ are investigated, respectively. First, we keep the $V_{gr}$ unvaried by holding $A_\theta$, $A_z$, and $\gamma$ constant (keep $d\varepsilon_z/d\omega$ and $d\mu_\theta/d\omega$ unchanged), and only modify $A_r$ to change the $V_{g\theta}$. The results are shown in Fig. 9.6(c), when $A_r$ is closer to 1, $V_{g\theta}$ becomes smaller (with larger $d\mu_r/d\omega$), the relaxation time is longer, and more energy scattered in the dynamical process. So the larger $V_{g\theta}$ means the better cloaking effect in the dynamical process. On the other hand, when we keep the $V_{g\theta}$ unvaried and change $V_{gr}$ by holding $A_r$, $A_z$, and $\gamma$ constant and modifying $A_\theta$, the results are shown in Fig. 9.6(d). We find that the relaxation time is almost unchanged with the change of $V_{gr}$. Obviously, $V_{g\theta}$ is the dominant element in the dynamical process. This conclusion can help us to design a better CS to defend the pulsive radars. In the expression of $V_{g\theta}$, it is also shown how to tune $V_{g\theta}$ by modifying dispersion parameters.

It seems that the larger $V_{g\theta}$, the better cloaking effect in the dynamical process. However, since the $V_g$ (and its components) cannot exceed $c$ generally, there is a minimum limit for the relaxation time of the cloaking dynamical process. We can estimate it through dividing the mean length of the propagation rays by $V_{g\theta}$. In our model, the mean length is $\pi(R_2+R_1)/2$, about three wavelengths. So the relaxation time cannot be shorter than three periods. Figure 9.6 shows that our estimation is coincident with our simulation results. Actually, here we are facing a very basic conflict to make a "better" CS, which is more discussed in our other works [52, 6]. The conflict is from the fact that the *pretty strong* dispersion is required to realize a good *stable* cloaking effect at a certain frequency [38, 52], but at this research we show that the *weaker* dispersion can realize a better cloaking effect in the *dynamical* process. At real design of the CS, there should be an optimized trade-off.

Based on causality, the limitation of the electromagnetic cloak with dispersive material is investigated in this section The results show that perfect invisibility cannot be achieved because of the dilemma that either the group velocity $V_g$ diverges or a strong absorption is imposed on the cloaking material. It is an intrinsic conflict which originates from the demand of causality. However, the total cross section can really be reduced through the approach of coordinate transformation. A simulation of finite-difference time-domain method is performed to validate our analysis.

## 9.4 Limitation of the Electromagnetic Cloak with Dispersive Material

Through the ages, people have dreamed to have a magic cloak whose owner cannot be seen by others. For this fantastic dream, plenty of work has been done by scientists all over the world. For example, the researchers diminished the scattering or the reflection from objects by absorbing screens [14] and small, non-absorbing, compound ellipsoids [22]. More recently, based on the coordinate transformation, J.B. Pendry et al. theoretically proposed a general recipe for designing an electromagnetic cloak to hide an object from the electromagnetic (EM) wave [38]. An arbitrary object may be hidden because it remains untouched by external radiation. Meanwhile, Ulf Leonhardt described a similar method where the Helmholtz equation is transformed to produce similar effects in the geometric limit [25, 26]. Soon, Steven A. Cummer et al. simulated numerically (COMSOL) the cylindrical version of this cloak structure using ideal and non-ideal (but physically realizable) electromagnetic parameters [12]. Especially, Schurig et al. experimentally demonstrated such a cloak by split-ring resonators [43]. In addition, Wenshan Cai et al. proposed an electromagnetic cloak using high-order transformation to create smooth moduli at the outer interface and presented a design of a non-magnetic cloak operating at optical frequencies [1, 2]. According to the general recipe, the electromagnetic cloak is supposed to be perfect or "fully functioned" at certain frequency as long as we can get very close to the ideal design although there is a singularity in the distribution, which has been elucidated further in several literatures [7, 41]. However, in all these

pioneering works, the interests are mainly focused on single-frequency EM waves, so that the effects of the dispersion, which is related to very basic physical laws, are not well studied. If the dispersion is introduced into the study, can we have a deeper insight into the cloaking physics?

In this section we will show the ideal cloaking cannot be achieved because of another more basic physical limitation – the causality limitation (based on the same limitation, Chen et al. obtained a constraint of the bandwidth that limits the design of an invisibility cloak [5]). Starting from dispersion relation and combining with the demand of causality, we will demonstrate that the ideal cloaking will lead to the dilemma that either the group velocity $V_g$ diverges or a strong absorption is imposed on the cloaking material. Our derivation and numerical experiments based on the finite-difference time-domain (FDTD) methods will show that the absorption cross section will be pretty large and dominate the total cross section for a dispersive cloak, even with very small imaginary parts of permittivity and permeability.

Let us consider a more general coordinate transformation on an initial homogeneous medium with $\varepsilon_i = \mu_i$ in $r$ space: $r' = f(r)$, $\theta' = \theta$, $\varphi' = \varphi$, following the approach in Ref. [44] and [27], we get the following radius-dependent, anisotropic relative permittivity and permeability:

$$\varepsilon_{r'} = \mu_{r'} = \varepsilon_i \left(\frac{r}{f(r)}\right)^2 \frac{df(r)}{dr}, \varepsilon_{\theta'} = \mu_{\theta'} = \varepsilon_i / \frac{df(r)}{dr}, \text{and } \varepsilon_{\varphi'} = \mu_{\varphi'} = \varepsilon_i / \frac{df(r)}{dr}.$$

We emphasize that since the transformation is directly acted on the Maxwell equations, the above equations are also suited for the imaginary parts of constitutive parameters, and all physical properties of wave propagation in $r$ space should be inherited in $r'$ space, such as the absorption. This is very important for us to have consistent physical pictures in both spaces. At working frequency $\omega_0$, for a propagating mode with $k$-vector as $\{k_{r'}, k_{\theta'}, k_{\varphi'}\}$ inside the cloak, we have the dispersion relation of the anisotropic material [44] as $k_{r'}^2/n_{r'}^2 + k_{t'}^2/n_{t'}^2 = \omega^2/c^2$, where $k_{t'}^2 = k_{\theta'}^2 + k_{\varphi'}^2$, $n_{r'} = \sqrt{\varepsilon_{\varphi'}\mu_{\theta'}} = n_i / \frac{df(r)}{dr}$, $n_{t'} = n_{\theta'} = n_{\varphi'} = \sqrt{\varepsilon_{r'}\mu_{\theta'}} = n_i r/f(r)$, and $n_i = \sqrt{\varepsilon_i \mu_i}$. Then we can define $k_{r'} = \frac{\omega}{c} n_{r'} cos\alpha$ and $k_{t'} = \frac{\omega}{c} n_{t'} sin\alpha$, the group velocity can be obtained as

$$V_g = c\sqrt{\frac{(cos\alpha)^2}{n_{r'}^2} + \frac{(sin\alpha)^2}{n_{t'}^2}} \Big/ \left((cos\alpha)^2 \frac{m_{r'}}{n_{r'}} + (sin\alpha)^2 \frac{m_{t'}}{n_{t'}}\right), \tag{9.4}$$

where $m_{r'} = n_{r'} + \omega \frac{dn_{r'}}{d\omega}$ and $m_{t'} = n_{t'} + \omega \frac{dn_{t'}}{d\omega}$.

If the transformation has the following characteristics $f(r=0) = R_1$, $f(r=R_2) = R_2$, then when $r' \to R_1$ (or $r \to 0$), $n_{t'}$ will tend to zero, and the group velocity is approximated as

$$V_g \approx \frac{c}{|sin\alpha|\omega \frac{dn_{t'}}{d\omega}}. \tag{9.5}$$

We will discuss Eq. (9.5) in two cases. The first case is with the finite $\frac{dn_{t'}}{d\omega}$. Obviously, $V_g$ will diverge when $sin\alpha \to 0$ for any finite $\frac{dn_{t'}}{d\omega}$. Such divergence is shown in Fig. 9.8 for a concrete example, in which the transformation is $r' = f(r) = (R_2 - R_1)r/R_2 + R_1$ as Ref. [38], $R_2 = 2R_1$, thus $n_{r'} = 2$ and $n_{t'} = 2 - 4/(r/R_1 + 2)$. The dispersion parameters are set as $m_{r'} = 2.5$, $\omega\frac{dn_{t'}}{d\omega} = 4$ at working frequency. In Fig. 9.8, the curves of $V_g$ vs. $\alpha$ are plotted for different $R_1/r$ values. We can see that, for large $R_1/r (r \to 0)$, the group velocity (more precisely, the tangential component of $V_g$) will diverge at both peaks around $\alpha = 0$.

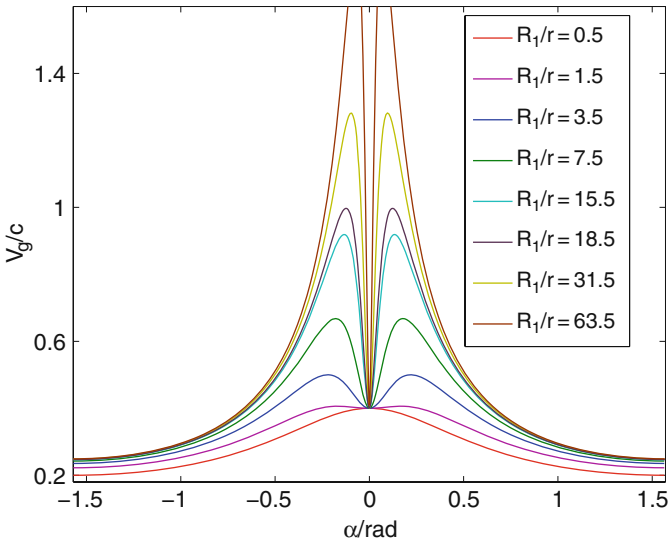


**Fig. 9.8** The group velocity $V_g$ vs. $\alpha$ for different $R_1/r$ values.

Because of the causality limitation, it is well known that the group velocity cannot exceed $c$ except in the "strong dispersion" frequency range (or called "resonant range"). But if the working frequency is in the "strong-dispersion" range of the cloaking material, the absorption must be very strong and it will destroy the ideal cloaking obviously. So perfect invisibility cannot be achieved for the finite $\frac{dn_{t'}}{d\omega}$ because it will lead to superluminal velocity or strong absorption.

In addition, the curves with the criterion condition $V_g = c$ on the plane $[R_1/r, \alpha]$ are plotted for different $\omega\frac{dn_{t'}}{d\omega}$ in Fig. 9.9. The region to the left of curves is corresponding to $V_g < c$ and the region to the right is corresponding to $V_g > c$. There exists a maximum $max\{R_1/r\}$ for each curve in order that $V_g \leq c$ can be hold for all $\alpha$. Especially, for the no-dispersion case $\omega\frac{dn_{t'}}{d\omega} = 0$, we can see that $V_g > c$ at all $R_1/r$ for large $\alpha$ values, which means the whole cloak is not physical if there is no dispersion. This "dispersion-is-required" conclusion can be generally derived from Eq. (9.4), and it is consistent with the analysis in Ref. [38]. From Fig. 9.9, we know

that the larger $\omega\frac{dn_{t'}}{d\omega}$, the larger $max\{R_1/r\}$. But anyway, for arbitrarily finite $\omega\frac{dn_{t'}}{d\omega}$, $max\{R_1/r\}$ cannot be infinite, so that the superluminal range always exists.

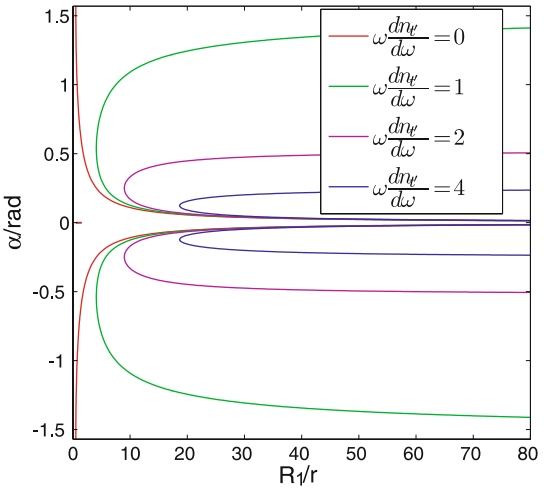


**Fig. 9.9** The relation between $R_1/r$ and $\alpha$ when $V_g = c$ for different $\omega\frac{dn_{t'}}{d\omega}$.

The second case of Eq. (9.5) is with divergent $\frac{dn_{t'}}{d\omega}$. From the previous discussion, we know that if the ideal cloak exists, the cloak must be dispersive and $\frac{dn_{t'}}{d\omega}$ must be divergent when $r \to 0$. Actually, when $r \to 0$, since $\sqrt{\varepsilon_{r'}} \propto r$, $\frac{dn_{t'}}{d\omega} \propto \frac{d\varepsilon_{t'}}{d\omega}/\sqrt{\varepsilon_{r'}}$ is really divergent for non-zero $\frac{d\varepsilon_{t'}}{d\omega}$. From Eq. (9.5), we can see that now $V_g \to 0$ for a finite $\frac{d\varepsilon_{t'}}{d\omega}$ (generally true) at all $\alpha$ values except $\alpha = 0$ (or $\pi$), so that the group velocity difficulty seems to be overcome. But, since the causality limitation, the non-zero $\frac{d\varepsilon_{t'}}{d\omega}$ means non-zero imaginary part of permittivity (non-zero dissipation). The non-zero dissipation and the almost-zero group velocity will result in very strong absorption. This means that the energy of rays near the inner cloaking radius $R_1$ is almost totally absorbed by the cloaking material. As we pointed out at the beginning that the absorption in $r'$ space should also appear in $r$ space, because of the consistence between two spaces. The strong absorption in $r$ space can be interpreted in the following way. From the transformation (which is also suited for imaginary part), we can find that when $r \to 0$, the finite imaginary part in $r'$ space corresponds to the infinite imaginary part in $r$ space, which also means very strong absorption in the initial homogeneous medium. So the perfect cloaking is still impossible because of the strong absorption which is enforced by the causality limitation.

For a 2D coordinate transformation: $r' = f(r)$, $\theta' = \theta$, $z' = z$, the same conclusions of the causality limitation can be obtained through the similar analysis, although the coordinate transformation and the singularities are different from the 3D case.

Next, we will discuss the physical meaning of the dilemma that either the group velocity $V_g$ diverges or a strong absorption is imposed on the cloaking material. First, it is an intrinsic conflict which cannot be solved by the methods, for example, "the system is imbedded in a medium" [38]. We believe that the ideal cloaking is impossible because of the causality limitation and this conclusion is consistent with the statement of previous studies [27] that the perfect invisibility is unachievable because of the wave nature of light. Second, we have to face the question, "Why the causality is violated for ideal cloaking which is based on the simple coordinate transformation?" Our answer is that the causality is only guaranteed by the Lorentz co-variant transformation, but the coordinate transformation for ideal cloaking is not Lorentz co-variant. Such violation is obvious if we suppose the initial medium in the $r$ space is not dispersive, such as the vacuum, but as we have pointed out (also mentioned in Ref. [38]), the cloaking material (in $r'$ space) must be dispersive to avoid the group velocity over $c$. Such Lorentz co-variant violation is generally true for "transformation optics" since material parameters are non-relativistic, so the causality limitation should be checked widely. Third, from Eq. (9.4), we can find that not only the inner layers of the cloak ($r' \to R_1$) but also the other layers ($r' > R_1$) must be dispersive. For every layer, a certain dispersive strength is needed to avoid $V_g > c$.

In the following, we will validate that the total cross section can be reduced drastically, and that the perfect cloaking cannot be achieved because of strong absorption by FDTD numerical experiments. Compared with other frequency-domain simulation methods, such as the finite element methods or the transfer-matrix methods, the FDTD simulation can better reflect the real physical process of cloaking. For example, we note that the FDTD calculation will be numerically unstable when the dispersion is not included in the cloak's material. For simplicity, the simulation is limited to 2D cloak [12]. Without loss of generality, only TE modes are investigated in this study (TE modes have the electric field perpendicular to the 2D plane of our model). Thus the constitutive parameters involved here are $\varepsilon_{z'}, \mu_{r'}, \mu_{\theta'}$. The dispersion is introduced into our FDTD by standard Lorentz model:

$$\begin{aligned}
\tilde{\varepsilon}_{z'}(r',\omega)| &= 1 + F_{z'}(r')\omega_{pz'}^2/(\omega_{az'}(r')^2 - \omega^2 - i\omega\gamma_{z'}),\\
\tilde{\mu}_{r'}(r',\omega) &= 1 + F_{r'}(r')\omega_{pr'}^2/(\omega_{ar'}(r')^2 - \omega^2 - i\omega\gamma_{r'}),\\
\tilde{\mu}_{\theta'}(r',\omega) &= 1 + F_{\theta'}(r')\omega_{p\theta'}^2/(\omega_{a\theta'}(r')^2 - \omega^2 - i\omega\gamma_{\theta'}),
\end{aligned} \tag{9.6}$$

$$r' = \frac{R_2(\theta) - R_1(\theta)}{R_2(\theta)} r + R_1(\theta), \tag{9.7}$$

$$\theta' = \theta, \tag{9.8}$$

where $\omega_{pz'}$, $\omega_{pr'}$, $\omega_{p\theta'}$ are plasma frequencies, $\omega_{az'}$, $\omega_{ar'}$, $\omega_{a\theta'}$ are atom resonated frequencies, $\gamma_{z'}$, $\gamma_{r'}$, $\gamma_{\theta'}$ are damping factors, and $F_{pz'}$, $F_{pr'}$, $F_{p\theta'}$ are filling factors. In our simulation, an $E$-polarized time-harmonic uniform plane wave whose wavelength $\lambda_0$ in vacuum is 3.75 cm is incident from left to right. The real parts of the

constitutive parameters at $\omega_0 = 2\pi c/\lambda_0$ satisfy the cloaking coordinate transformation [12], and they are

$$\mu_{r'} = \frac{r' - R_1}{r'}, \mu_{\theta'} = \frac{1}{\mu_{r'}}, \varepsilon_{z'} = \left(\frac{R_2}{R_2 - R_1}\right)^2 \frac{r' - R_1}{r'},$$

where $R_1$ is $0.665\lambda_0$, $R_2$ is $1.33\lambda_0$. And the dispersive parameters are set as follows: if $\varepsilon_{z'} > 1$ then $\omega_{az'} = 1.4\omega_0$, else $\omega_{az'} = 0.6\omega_0$, $\omega_{ar'} = 0.6\omega_0$, $\omega_{a\theta'} = 1.4\omega_0$, $\gamma_{z'} = \gamma_{r'} = \gamma_{\theta'} = \omega_0/100$. $\omega_{pz'} = \omega_{pr'} = \omega_{p\theta'} = 4\omega_0$,

$$F_{z'}(r) = (\varepsilon_{z'} - 1)\frac{(\omega_{az'}^2 - \omega_0^2)^2 + \omega_0^2\gamma_{z'}^2}{(\omega_{az'}^2 - \omega_0^2)\omega_{pz'}^2}, F_{r'}(r) = (\mu_{r'} - 1)\frac{(\omega_{ar'}^2 - \omega_0^2)^2 + \omega_0^2\gamma_{r'}^2}{(\omega_{ar'}^2 - \omega_0^2)\omega_{pr'}^2},$$

$$F_{\theta'}(r) = (\mu_{\theta'} - 1)\frac{(\omega_{a\theta'}^2 - \omega_0^2)^2 + \omega_0^2\gamma_{\theta'}^2}{(\omega_{a\theta'}^2 - \omega_0^2)\omega_{p\theta'}^2}.$$

In fact, these parameters have many possible choices. The different groups of parameters correspond to different dynamic processes which we will discuss in another section [28].

Figure 9.10 shows the snapshots of the electric field distribution in two cases: the cloak with the perfect electric conductor (PEC) at radius $R_1$(left) and the naked PEC with radius $R_1$(right). Obviously, the cloak is very effective. Quantitatively, we calculate the absorption cross section and the scattering cross section of the cloak at the stable state, and they are $0.67\lambda_0$ and $0.24\lambda_0$, respectively, while the scattering cross section of the naked PEC is $3.14\lambda_0$. So, with dispersive cloak, the total cross section is three times smaller and the absorption cross section dominates as we predicted. To emphasize the huge absorption of the cloak, we use a common homogeneous isotropic media, with $\varepsilon = \mu = 1.1$ but all other parameters are the same as the cloak, to replace the cloaking material. Then we find the absorption cross section is only $0.089\lambda_0$ which is about one order smaller. The reason of strong absorption has been discussed before.

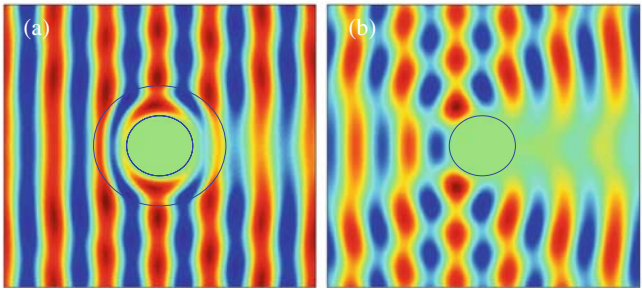


**Fig. 9.10** The snapshots of the electric field distribution in the vicinity of PEC: (**a**) the cloaking structure with a PEC at radius $R_1$ and (**b**) the naked PEC with radius $R_1$.

Now we can have a full view of cloaking recipe based on the coordinate transformation. First, the cloaking material must be dispersive, and the strong absorption can not be avoided because of the causality limitation. Thus it is not perfectly invisible. Second, the scattering cross section of the dispersive cloak could be small, so that the scattered field is weak. Although the ideal invisibility is impossible, the cloaking recipe still has a main advantage. The "strong-absorption and weak-scattering" property means that the cloak almost cannot be observed except from the forward direction. so that such cloak can well defend the "passive radars" which detect the perturbation of the original field. It is well known that at the Rayleigh scattering case, where the radius of the scatterer is much smaller than the wavelength, the absorption cross section could be larger than the scattering cross section because of the diffraction. The cloaking can be thought as giant Rayleigh scattering case, where the light rays are forced to "diffract" around the cloaked area.

In conclusion, the properties of the dispersive cloak are investigated and the limitation of causality is revealed. Our study shows that the superluminal velocity or a strong absorption cannot be overcome since the intrinsic conflict between the coordinate transformation to obtain the cloaking and the causality limitation. In addition, we validate the results using a numerical simulation which is performed in FDTD algorithm with physical parameters. The numerical experiments show that the absorption cross section is dominant and the scattering cross section can be reduced significantly. The study gives us a full view of the cloaking recipe based on the coordinate transformation and will have further profound influence on the related topics.

## 9.5 Expanding the Working Frequency Range of Cloak[1]

The recent cloaking has become a very fantastic topic in optics [38, 43, 1] and other wave systems [35, 12]. Other kinds of interesting devices were also designed based on the transformation method, such as the concentrator [43], rotation coating [4], and electromagnetic wormhole [17]. However, all kinds of the transformation media were designed to work at a single frequency. For example, the electromagnetic cloak at microwave frequencies was designed to work at 8.5 GHz [43], the optical cloaking can only work at the $\lambda = 632.8$ nm [1]. As pointed out by Pendry et al. in the original work [38], since the propagating path length inside the cloaking structure is longer than outside and the group velocity of cloaking material cannot be larger than the vacuum light speed $c$, so that ideal cloaking is supposed to be only realizable for single frequency. But, in the later experimental research [43], a "reduced" cloaking version is shown, which gives us a clue to the new window for the realizable dispersive cloaking. Obviously, an usable cloaking, which fulfills the human dream for 1000 years, must be a dispersive one, so the importance of the dispersion study on this research direction cannot be over emphasized.

[1] This work is cooperated with the following co-workers Hongru Ma, and C. T. Chan.

Based on the same geometry transformation idea, we suggest a general "freedom trade-off" method from which a dispersive cloaking in a frequency range could be realized. The study of the dispersive cloaking also presents a deeper understanding of the difficulties of the dispersive cloaking, such as where is the causality conflicting from and why we have to use a "reduced design" in the real experiments (the real material is always dispersive). Furthermore, we obtain a dispersive cloaking limitation rule, which although from a special freedom trade-off method may have general meaning and could be very essential for further dispersive cloaking studies. At last, our numerical experiments also confirm our design which can broaden the cloaking frequency range.

Our research is from one basic thought that if we can have two frequency points which satisfy the cloaking effect, then we can have a frequency range, instead of a frequency point, which can almost be cloaked. But we will show that it is impossible generally because of the causality reason. Then if we really hope to get the almost ideal cloaking in a frequency range, we must need physical freedom(s) which can be used to trade off the frequency range. This goal guide us to the fundamental thought of the cloaking mechanism, which is the geometry transformation of ideal cloaking in Ref. [12] on the radius. The ideal transformation is from the range $[0,\ b]$ to the range $[a,\ b]$ $(b > a)$. If we use the radius geometry transformation from $[r_0,\ b]$ to $[a,\ b]$ instead of original ideal one, it means that the largest scattering effect is determined by $r_0$. Also because of the causality, in the real experiment in which the material is always dispersive, we have to reduce the ideal design for a real reduced design at certain level and the cross section of a reduced cloaking cannot be zero actually. It is well known that, if radius $r_0$ of a scatterer is much smaller than the wavelength, the scattering effect should be weak, hence $[r_0, b]$ the transformation should be acceptable generally. The tolerance of geometry transformation of $r_0$ gives us a new "freedom" which is possible to trade off. Obviously, instead of the most straightforward freedom of $r_0$, there could be "other freedoms" to trade off generally, such as the functional freedom in the geometry transformation, which means that we can replace all $r$ in the geometry transformation of Pendry's original one into $f(r)$. Clearly, our method is a very general one based on the "freedom trade-off" in the geometry transformation and can be developed in many ways depending on certain goal and material requirement. We will give some comments on these other trade-off methods at the end of this section.

With this "freedom trade-off" thought, next work of us is to construct a way to transfer the freedom of radius with the frequency range of cloaking effects and demonstrate that such a way is physically achievable without violating any physics law. The original 2D ideal cloak should follow the requirements for anisotropic permittivity and permeability in the cloaking shell [12]:

$$\mu = \frac{r-a}{r},\ \mu_\theta = \frac{r}{r-a},\ \varepsilon_z = \left(\frac{b}{b-a}\right)^2 \frac{r-a}{r}. \tag{9.9}$$

This cloak is generated by compressing a cylindrical region $r < b$ into a concentric cylindrical shell $a < r < b$. The mapping is $r' = a + r\frac{b-a}{b}$. The cloaking is equivalent to the free space.

Suppose we have a PEC (perfect electrical conductor) cylinder with its radius $r = r_0$ in the free space. If the wavelength of the incident wave is much larger than $r_0$, the system approximates the free space. We compress the concentric cylindrical shell region into another shell $a < r < b$ with the coordinate transformation $r' = b - \frac{b-a}{b-r_0}(b-r)$. The requirements for anisotropic permittivity and permeability in the cloaking shell $(a < r < b)$ is obtained [3, 52]:

$$\mu = \frac{r-a'}{r},\ \mu_\theta = \frac{r}{r-a},\ \varepsilon_z = \left(\frac{b-r_0}{b-a}\right)^2 \frac{r-a'}{r}, \tag{9.10}$$

where $a' = b\frac{a-r_0}{b-r_0}$, if $r_0 = 0$, Eq. (9.10) reduces to Eq. (9.9).

Next is the essential step to construct the relation between the $r_0$ freedom and the frequency range. Suppose that, in a dispersive shell (the dispersion relation is known), we can find such a frequency range $[\omega_a - \omega_b]$, at $\omega_a$ the cloaking with $\varepsilon_z(\omega_a)$, $\mu_r(\omega_a)$, and $\mu_\theta(\omega_a)$ satisfies the ideal case corresponding to $r_0 = 0$ (same as the Pendry case), but at $\omega_b$ the cloaking with $\{\varepsilon_z(\omega_a), \mu_r(\omega_a)$ and $\mu_\theta(\omega_a)\}$ satisfies Eq. (9.10) with $r_0 \neq 0$ but still a small value. In this frequency range, generally a small range (the dispersion is a single-value function), we can suppose there is a mapping function between every $\omega$ value and every $r_0$ value. In other words, we can define $r_0$ as the function of $\omega$, say $r_0 = r_0(\varepsilon_z(\omega),\ \mu_r(\omega),\ \mu_\theta(\omega)) \equiv r_0(\omega)$ (see Fig. 9.2c), if the dispersion of the material is known. Now, the relation between the frequency range (also dispersion of material) with the geometry transformation freedom is constructed.

For a real material (except gain media) with causality confinement, it is well known that the slope of the dispersion curve of both $\varepsilon(\omega)$ and $\mu(\omega)$ should be positive if we are away from the resonant range (in which the absorption is very large so that it cannot be used on cloaking). Suppose when the frequency increases, $r_0$ increases, then $\mu_r$ increases but $\mu_\theta$ decreases. That is the slope of $\mu_r(\omega)$ is positive but the one of $\mu_\theta$ is negative. A good method to avoid this is to use similar reduction of the experiments [43]:

$$\mu = \frac{r-a'}{r},\ \mu_\theta = 1,\ \varepsilon_z = \left(\frac{b-r_0}{b-a}\right)^2. \tag{9.11}$$

A further reduction should be followed due to the different signs of the slope of $\mu_r(\omega)$ and $\varepsilon_z(\omega)$. We will show that the difference of the signs comes from the dissatisfaction of the causality for this version of cloak.

We define the principal refractive indexes for Eqs. (9.10) and (9.11) as

$$n_r = \sqrt{\varepsilon_z \mu_\theta} = \frac{b-r_0}{b-a}, \tag{9.12}$$

$$n_\theta = \sqrt{\varepsilon_z \mu_r} = \frac{b-r_0}{b-a}\frac{r-a'}{r} = \frac{r(b-r_0) - b(a-r_0)}{r(b-a)}. \tag{9.13}$$

From the general derivation of propagation vector from Eq. (9.10) or Eq. (9.11) [44, 6], we can have the dispersion relation

$$\frac{k_r^2}{n_r^2}+\frac{k_\theta^2}{n_\theta^2}=\frac{\omega^2}{c^2}, \tag{9.14}$$

where $k_r^2$ and $k_\theta^2$ are the components in polar coordinate, that is $\mathbf{k}=k_r\hat{r}+k_\theta\hat{\theta}$. The magnitude of the group velocity is then derived as [20, 3]

$$v_g=\frac{\omega\sqrt{\frac{k_r^2}{n_r^4}+\frac{k_\theta^2}{n_\theta^4}}}{\frac{k_r^2}{n_r^2}\frac{n_r+\omega\frac{dn_r}{d\omega}}{n_r}+\frac{k_\theta^2}{n_\theta^2}\frac{n_\theta+\omega\frac{dn_\theta}{d\omega}}{n_\theta}}. \tag{9.15}$$

From the limit of the causality, the group velocity at any direction should be less than the velocity of light in free space. The case $r_0=0$ for not the one $r_0\neq 0$, Eq. (9.15), requires that both conditions satisfied $v_g=\frac{c}{n_\theta+\omega\frac{dn_\theta}{d\omega}}<c$ when $k_\theta=\frac{\omega}{c}n_\theta(k_r=0)$ and $v_g=\frac{c}{n_r+\omega\frac{dn_r}{d\omega}}<c$ when $k_r=\frac{\omega}{c}n_r(k_\theta=0)$. *However we find that these two conditions conflict with each other at any frequency point from the causality confinement of the material dispersion relation.* From such dispersion, it is easy to demonstrate from Eq. (9.10) or Eq. (9.11) that two conditions conflict with each other (cannot be less than simultaneously) [3]. This is also why we have to make a further modification from Eq. (9.11) to produce a potential dispersive cloak.

Then we just modify Eq. (9.11) into

$$\mu_r=\left(\frac{r-a'}{r}\right)^2,\ \mu_\theta=1,\varepsilon_z=\left(\frac{b-\bar{r}}{b-a}\right)^2, \tag{9.16}$$

where $\bar{r}$ is a constant without dependency of frequency anymore, so that $\varepsilon_z$ and $\mu_\theta$ is not a function of frequency or in real world they have positive slopes but the slopes are almost zero. If the frequency increases, $r_0$ increases, then $\mu_r(\omega)$ has a positive slope. After this kind of modification, we can produce a potential dispersive cloak. But at least, it still has the causality constraint.

After modification $n_r$ is not a function of frequency but $n_\theta$ still is. The causality confinement of Eq. (9.15) can give us important information. From Eq. (9.16), we can obtain a constraint

$$\left(\frac{n_\theta^2}{n_r^2}cos^2\tau+sin^2\tau\right)<\left(n_\theta cos^2\tau+\left(n_\theta+\omega\frac{dn_\theta}{d\omega}\right)sin^2\tau\right)^2 \tag{9.17}$$

when we introduce an auxiliary angle such as $k_r=\frac{\omega}{c}n_r cos\tau$ and $k_\theta=\frac{\omega}{c}n_\theta sin\tau$. Notice that this condition should be satisfied in every place and any direction in the cloak. So at least $n_\theta$ should not be zero, otherwise the constraint would be broken. To avoid this, we break the cloak into many shells (we describe in detail in the

following section). Another method is to keep $r_0 \neq 0$. To extract some important intrinsic physical information we only consider the direction $k_r = 0$, then we have

$$n_\theta + \omega \frac{dn_\theta}{d\omega} = \frac{b-\bar{r}}{b-a}\left(\frac{r(b-r_0)-b(a-r_0)}{r(b-r_0)} + \frac{b(b-a)}{r(b-r_0)^2}\omega\frac{dr_0}{d\omega}\right) > 1 \tag{9.18}$$

or

$$\omega\frac{dr_0}{d\omega} > \left(\frac{b-a}{b-\bar{r}} - \frac{r(b-r_0)-b(a-r_0)}{r(b-r_0)}\right)\frac{r(b-r_0)^2}{b(b-a)}. \tag{9.19}$$

Since the maximum of

$$\left(\frac{b-a}{b-\bar{r}} - \frac{r(b-r_0)-b(a-r_0)}{r(b-r_0)}\right)\frac{r(b-r_0)^2}{b(b-a)} \text{ is } \frac{b}{b-\bar{r}}a,$$

Eq. (9.19) can be rewritten as

$$\omega\frac{dr_0}{d\omega} > \frac{b}{b-\bar{r}}a. \tag{9.20}$$

Since $\bar{r}$ is much smaller than $b$, at last we have a clean and meaningful inequality:

$$\omega\frac{dr_0}{d\omega} > a \text{ or } \frac{\Delta\omega}{\omega} < \frac{\Delta r_0}{a}, \tag{9.21}$$

which we call "the invisibility uncertainty condition." The physical meaning of this condition is very clear. If we hope to have to be invisible in a larger frequency range for the cloaking based on the geometry transformation, we must have more tolerance of $r_0$ (the cross section is larger and easier to be observed). Actually, the $r_0$ could be larger than the wavelength if we really deadly need a wide frequency range for cloaking and can bear a little larger scattering effect.

Here, we present a dispersive cloak design working at a microwave frequency range with metamaterial of SRR (split-ring resonator). With the known dispersion relation, for different frequencies the different values of $r_0$ are tested. Two frequency points at the ends of frequency range are chosen at 8.5 and 8.75 GHz, to follow the invisibility uncertainty condition we chose $r_0 = 0$ and 4 mm, respectively. The curve of $r_0(f = \omega/2\pi)$ at whole range is shown in Fig 9.13c. With $r_0(f)$, we can obtain $\mu_r(r, f)$ from Eq. (9.16), then the cloak is designed in the frequency range. Following the reported microwave experimental technique, we also break the continuous cloaking material into 10 shells at radial direction. For the most inner shell we have $\mu_r(a + \frac{b-a}{20}, 8.5 \text{ GHz}) = 0.003 \neq 0$, this is the minimum of $\mu_r(r, f)$ to avoid $n_\theta = 0$. Here we set $\bar{r} = 2$ mm or $\varepsilon_z = (\frac{b-2\text{mm}}{b-a})^2 = 3.2$. Since we know $\mu_r$ for each shell at 8.5 GHz with $r_0$ [43] and also at 8.75 GHz with $r_0 = 4$ mm, following Eq. (9.16), we can fit out for each shell. The dispersion of the LC model of SRR [48, 37] is

$$\mu = 1 - \frac{Ff^2}{f^2 - f_0^2 + if\gamma}. \tag{9.22}$$

After choosing $\gamma = 0.01\,\text{GHz}$, we can fit $F$ and $f_0$ out for each shell of resonators. Table 9.1 shows the fitting result for each shell of SRR.

Table 9.1 The permeability of each shell at different frequencies and the fitting parameters of it for the LC model of SRR and the Lorentz model.

| Cyl | $\mu_r$(8.5 GHz) | $\mu_r$(8.75 GHz) | $F$ | $f_0$(GHz) | $\mu_r$(8.625 GHz) | $f_a$(GHz) |
|---|---|---|---|---|---|---|
| 1 | 0.003 | 0.0186 | 0.777566 | 3.98772 | 0.0110 | 7.49527 |
| 2 | 0.023 | 0.0495 | 0.653523 | 4.89096 | 0.0367 | 6.87147 |
| 3 | 0.052 | 0.0859 | 0.571633 | 5.35577 | 0.0696 | 6.42655 |
| 4 | 0.085 | 0.1238 | 0.512269 | 5.63920 | 0.1052 | 6.08370 |
| 5 | 0.120 | 0.1614 | 0.468967 | 5.80921 | 0.1416 | 5.82090 |
| 6 | 0.154 | 0.1975 | 0.431116 | 5.95249 | 0.1768 | 5.58105 |
| 7 | 0.188 | 0.2318 | 0.403528 | 6.02870 | 0.2110 | 5.39953 |
| 8 | 0.220 | 0.2640 | 0.378390 | 6.09923 | 0.2431 | 5.22864 |
| 9 | 0.250 | 0.2941 | 0.355596 | 6.16397 | 0.2732 | 5.06871 |
| 10 | 0.279 | 0.3224 | 0.337370 | 6.20024 | 0.3018 | 4.93710 |

After fitting the formula out, we can also obtain $\mu_r$ for other frequencies in 8.5–8.75 GHz. For example, in Table 9.1 we show $\mu_r$ for each shell for frequency 8.625 GHz. Notice that the parameter chosen here has been tested and ensure the original constraint (9.17). All the designs should strictly satisfy Eq. (9.17).

First, comparing Fig. 9.11a with 9.11b, we see that the setting $\varepsilon_z = 3.2$ is reasonable for the similar pattern with each other. Noted at frequency 8.625 GHz do not follow Eq. (9.16) strictly but extracted from the SRR model; however, Fig. 9.1(d) shows the accepted cloaking result of it. From Fig. 9.11b, c, d we can see that the cloak designed here works pretty well at the frequency range (with the central frequency 8.625 GHz and a bandwidth of 3%). As the imaginary parts are smaller than 0.002 due to the small $\gamma$ we omit the absorption here.

Next, we will show the advantage of this dispersive cloak to the original single-frequency cloak [43], since the original one is designed for single frequency 8.5 GHz. We use the Lorentz model [23]:

$$\mu = 1 - \frac{f_a^2}{f^2 - f_0^2 + if\gamma}. \tag{9.23}$$

With $f_0$ and $\gamma$ same to the LC model of SRR but $f_a = \sqrt{F}8.5$ GHz so that it will satisfy Eq. (9.16) with $r_0 = 0$ at frequency 8.5 GHz only, we use $\varepsilon_z = 3.43$ for it. The values of $f_a$ in each shell are shown in Table 9.1 as well.

Figure 9.12 shows the relative scattering cross section at different frequencies for different kinds of cloaks to the bare PEC cylinder with the radius 27.1 mm. We find that the dispersive cloak with $\varepsilon_z = 3.2$ works in a broader frequency range (from 8.45 to 8.75 GHz) than the original one (from 8.45 to 8.55 GHz). We also try some different $\varepsilon_z$ as it is chosen arbitrarily, and we find that different $\varepsilon_z$ have similar

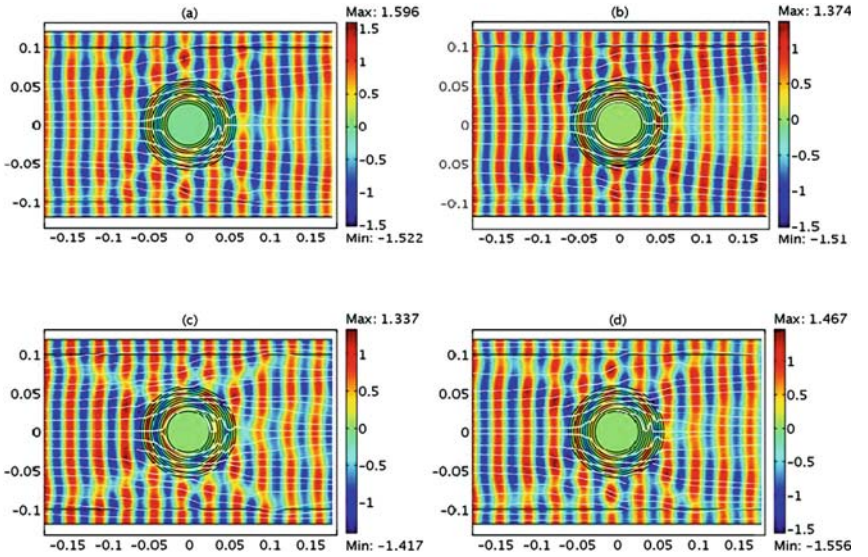


**Fig. 9.11** (Color online) (**a**) The electric field distribution in the vicinity of the original cloak. Power-flow lines (in *white*) show the smooth deviation of EM power. (**b**) Same as (**a**) but for the dispersive cloak at 8.5 GHz. (**c**) Same as (**a**) but for the dispersive cloak at 8.75 GHz. (**d**) Same as (**a**) but for the dispersive cloak at 8.625 GHz.

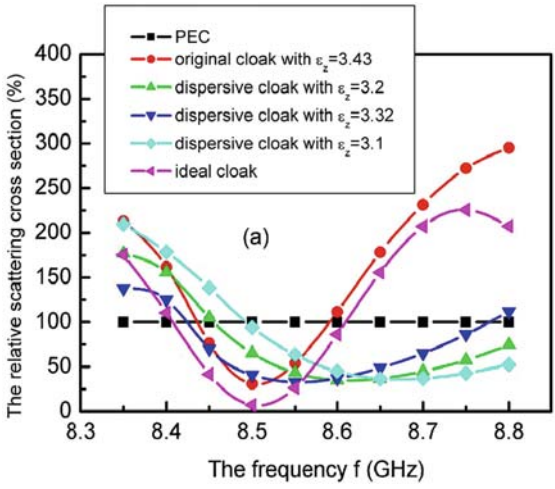


**Fig. 9.12** The relative scattering cross sections depend on different frequencies. The *square symbols* are for the PEC cylinder, the *circle symbols* are for the original cloak with $\varepsilon_z = 3.43$ , the *up triangle symbols* are for the dispersive cloak with $\varepsilon_z = 3.2$, the *down triangle symbols* are for the dispersive cloak with $\varepsilon_z = 3.2$, the *diamond symbols* are for the dispersive cloak with $\varepsilon_z = 3.1$, and the *left triangle symbols* are for the ideal cloak.

bandwidths but different central frequencies. For example, the dispersive cloak with $\varepsilon_z = 3.32(\bar{r} = 1)$ mm works in (8.4–8.7 GHz) and the cloak with $\varepsilon_z = 3.31(\bar{r} = 3)$ mm works in (8.5–8.8 GHz). Compared to the PEC case, we find that the dispersive cloaks can reduce the scattering cross section to about 50% of it as well as the original one. They all have strong scattering far away from 8.5 GHz because they are scatterers with larger radius than the PEC cylinder. An ideal cloak is also designed to work near 8.5 GHz, which we use the Drude model for simplicity with $\gamma = 0.01$ GHz in

$$\mu = 1 - \frac{f_a^2}{f(f + if\gamma)}. \tag{9.24}$$

Notice that designing a cloak works near a single frequency, the scattering cross section will show similar dispersive properties for different models.

To show the frequency dependence of $r_0$, we use the above dispersive cloak with $\varepsilon_z = 3.2$, for instance. First, we know that for 8.5 GHz, $r_0 = 0$ and for 8.75 GHz, $r_0 = 4$ mm. However, at $\mu_r$ frequencies between 8.5 and 8.75 GHz do not follow Eq. (9.16) strictly but extracted from the SRR model. For a specific frequency, we can obtain the scattering cross section, after that we scan $r_0$ in Eq. (9.16) to see whether it will bring the same total scattering cross section, mapping it to the frequency. Figure 9.13b shows the scattering cross section from SRR model and from different $r_0$ scanned to produce the same scattering at different frequencies. Figure 9.13c shows the frequency dependence of $r_0$. One can tune the permeability to follow Eq. (9.16) at two preconcerted frequencies each for different $r_0$, so that the cloak can be designed to work between these two frequencies dispersively based on the invisibility uncertainty condition.

In conclusion, with the "freedom trade-off" thought we introduce a new coordinate mapping from a tiny PEC cylinder to a concentric cylindrical cloaking shell so

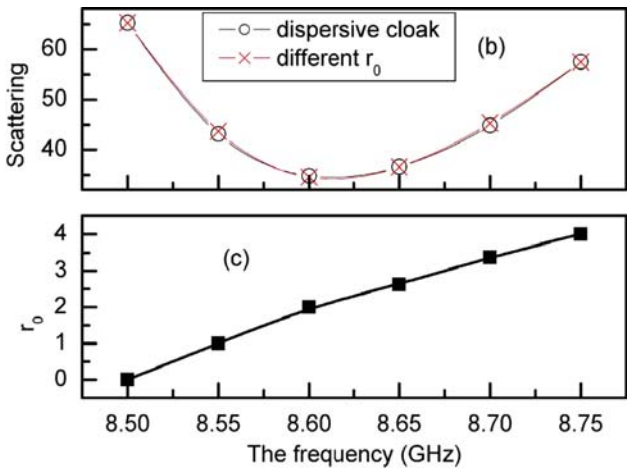


**Fig. 9.13** (**a**) The scattering cross section from SRR model and from different scanned to produce the same scattering at different frequencies of $r_0$. (**b**) The frequency dependence of $r_0$.

that the cloak could be accepted to be an almost perfect cloak. With such coordinate mapping, we describe how to build up a dispersive cloak in a frequency range. A constraint of the bandwidth from this method is also obtained and is called as "the invisibility uncertainty condition" which may have general meaning for cloaking design.

## 9.6 Summary

In summary in this chapter we have investigated the dynamical properties of the metamaterial by taking dispersion into account. Deeper physical pictures involved with metamaterial systems have been revealed. For example, the temporal coherence gain of the image formed by negative-index superlens with the quasi-monochromatic random source, the dynamical process of the dispersive cloak before achieving the stable state and the essential element to determine relaxation time and scattered energy, the limitation to the perfect invisibility of the electromagnetic cloak due to the material's dispersion and the physical causality limit, the method to expanding the cloaking frequency range. Very recently, we have done another work on the dynamical process on the interface between hyperbolic material and common dielectric material and find a new mechanism to stop (slow) light which will be published elsewhere. Actually, we believe that only with the well-constructed dynamical picture, the deeper understanding of the abnormal optical/photonic properties of metamaterials is possible. All these research works show that the dynamical study of metamaterials can lead us to many new interesting topics, which are still waiting for further research.

## References

1. Cai, W., Chettiar, U.K., Kildishev, A.V., Shalaev, V.M.: Optical cloaking with metamaterials. Nat. Photonics **1**, 224 (2007)
2. Cai, W., Chettiar, U.K., Kildishev, A.V., Shalaev, V.M.: Nonmagnetic cloak with minimized scattering. Appl. Phys. Lett. **91**, 111105 (2007)
3. Chen, H., Chan, C.T.: The brief report for the detail of the causality constraint.
4. Chen, H., Chan, C.T.: Transformation media that rotate electromagnetic fields. Appl. Phys. Lett. **90**, 241105 (2007)
5. Chen, H., Jiang, X., Chan, C.T.: Extending the bandwidth of electromagnetic cloaks. Phys. Rev. B **76**, 241104 (2007)
6. Chen, H., Liang, Z., Yao, P., Jiang, X., Ma, H., Chan, C.T.: Extending the bandwidth of electromagnetic cloaks. Phys. Rev. B **76**, 241104 (2007)
7. Chen, H., Wu, B.-I., Zhang, B., Kong, J.A.: Electromagnetic wave interactions with a metamaterial cloak. Phys. Rev. Lett. **99**, 063903 (2007)
8. Chen, L., He, S., Shen, L.: Finite-size effects of a left-handed material slab on the image quality. Phys. Rev. Lett. **92**, 107404 (2004)
9. Cubukcu, E., Aydin, K., Ozbay, E., Foteinopoulou, S., Soukoulis, C.M.: Subwavelength resolution in a two-dimensional photonic-crystal-based superlens. Phys. Rev. Lett. **91**, 207401

(2003); Cubukcu, E., Aydin, K., Ozbay, E., Foteinopoulou, S., Soukoulis, C.M.: Electromagnetic waves: Negative refraction by photonic crystals. Nature **423**, 604 (2003)
10. Cummer, S.A.: Dynamics of causal beam refraction in negative refractive index materials. Appl. Phys. Lett. **82**, 2008 (2003)
11. Cummer, S.A.: Simulated causal subwavelength focusing by a negative refractive index slab. Appl. Phys. Lett. **82**, 1503 (2003)
12. Cummer, S.A., Popa, B.-I., Schurig, D., Smith, D.R.: Full-wave simulations of electromagnetic cloaking structures. Phys. Rev. E **74**, 036621 (2006)
13. Engheta, N.: An idea for thin subwavelength cavity resonators using metamaterials with negative permittivity and permeability. IEEE Antenn. Wireless Propag. Lett. **1**, 10, (2002)
14. Fante, R.L., McCormack, M.T.: Reflection properties of the Salisbury screen. IEEE Trans. Antenn. Propag. **36**, 1443 (1988)
15. Feise, M.W., Kivshar, Y.S.: Sub-wavelength imaging with a left-handed material flat lens. Phys. Lett. A **334**, 326 (2005)
16. Foteinopoulou, S., Economou, E.N., Soukoulis, C.M.: Refraction in media with a negative refractive index. Phys. Rev. Lett. **90**, 107402 (2003); Pendry, J.B., Smith, D.R.: Comment on "Wave refraction in negative-index media: Always positive and very inhomogeneous". Phys. Rev. Lett. **90**, 029703 (2003)
17. Greenleaf, A., Kurylev, Y., Lassas, M., Uhlmann, G.: Electromagnetic wormholes and virtual magnetic monopoles from metamaterials. Phys. Rev. Lett. **99**, 183901 (2007)
18. Gomez-Santos, G.: Universal features of the time evolution of evanescent modes in a left-handed perfect lens. Phys. Rev. Lett. **90**, 077401 (2003)
19. Jiang, X., et al.: unpublished.
20. Jiang, X., Han, W., Yao, P., Li, W.: Temporal-coherence gain of superlens image with quasi-monochromatic source. Appl. Phys. Lett. **89**, 221102 (2006)
21. Jiang, X., Soukoulis, C.M.: Time dependent theory for random lasers. Phys. Rev. Lett. **85**, 70 (2000)
22. Kerker, M.: Invisible bodies. J. Opt. Soc. Am. **65**, 376 (1975)
23. Koschny, T., Kafesaki, M., Economou, E.N., Soukoulis, C.M.: Effective medium theory of left-handed materials. Phys. Rev. Lett. **93**, 107402 (2004)
24. Landau, L.D., Lifshitz, E.M.: Electrodynamics of Continuous Media. Pergamon Press, Oxford, Ch. 11, pp. 315–321 (1975)
25. Leonhardt, U.: Optical conformal mapping. Science **312**, 1777 (2006)
26. Leonhardt, U.: Notes on conformal invisibility devices. New J. Phys. **8**, 118 (2006)
27. Leonhardt, U., Philbin, T.G.: General relativity in electrical engineering. New J. Phys. **8**, 247 (2006)
28. Liang, Z., Yao, P., Jiang, X., Sun, X.: unpublished.
29. Loschialpo, P.F., Smith, D.L., Forester, D.W., Rachford, F.J., Schelleng, J.: Electromagnetic waves focused by a negative-index planar lens. Phys. Rev. E **67**, 025602(R) (2003)
30. Luo, C., Johnson, S.G., Joannopoulos, J.D., Pendry, J.B.: Subwavelength imaging in photonic crystals. Phys. Rev. B **68**, 045115 (2003)
31. Luo, H., Hu, W., Shu, W., Li, F., Ren, Z.: Superluminal group velocity in an anisotropic metamaterial. Europhys. Lett. **74** 1081 (2006)
32. Mandel, L., Wolf, E.: Optical Coherence and Quantum Optics. Cambridge University, Cambridge (1995); Scully, M.O., Zubairy, M.S.: Quantum Optics. Cambridge University Press, Cambridge (1997)
33. Markos, P., Soukoulis, C.M.: Transmission studies of left-handed materials. Phys. Rev. B **65**, 033401 (2001); Markos, P., Soukoulis, C.M.: Numerical studies of left-handed materials and arrays of split ring resonators. Phys. Rev. E **65**, 036622 (2002)
34. Merlin, R.: Analytical solution of the almost-perfect-lens problem. Appl. Phys. Lett. **84**, 1290 (2004)
35. Milton, G.W., Briane, M., Willis, J.R.: On cloaking for elasticity and physical equations with a transformation invariant form. New J. Phys. **8**, 248 (2006)

36. Pendry, J.B.: Comment on "Left-handed materials do not make a perfect lens". Phys. Rev. Lett. **91**, 099701 (2003); Smith, D.R., Schurig, D., Rosenbluth, M., Schultz, S., Ramakrishna, S.A., Pendry, J.B.: Limitations on subdiffraction imaging with a negative refractive index slab. Appl. Phys. Lett. **82**, 1506 (2003)
37. Pendry, J.B., Holden, A.J., Robbins, D.J., Stewart, W.J.: Magnetism from conductors and enhanced nonlinear phenomena. IEEE Trans. Micro. Theo Tech. **47**, 2075 (1999); Pendry, J.B.: Negative refraction makes a perfect lens. Phys. Rev. Lett. **85**, 3966 (2000)
38. Pendry, J.B., Schurig, D., Smith, D.R.: Controlling electromagnetic fields. Science **312**, 1780 (2006)
39. Pendry, J.B., Smith, D.R.: Comment on "Wave Refraction in Negative-Index Media: Always Positive and Very Inhomogeneous" Phys. Rev. Lett. **90**, 029703 (2003)
40. Rao, X.S., Ong, C.K.: Amplification of evanescent waves in a lossy left-handed material slab. Phys. Rev. B **68**, 113103 (2003); Rao, X.S., Ong, C.K.: Subwavelength imaging by a left-handed material superlens. Phys. Rev. E **68**, 067601 (2003)
41. Ruan, Z., Yan, M., Neff, C.W., Qiu, M.: Ideal cylindrical cloak: perfect but sensitive to tiny perturbations. Phys. Rev. Lett. **99**, 113903 (2007)
42. Saleh, B.E.A., Teich, M.C.: Fundamentals of Photonics. John Wiley & Sons, New York (1991)
43. Schurig, D., Mock, J.J., Justice, B.J., Cummer, S.A., Pendry, J.B., Starr, A.F., Smith, D.R.: Metamaterial electromagnetic cloak at microwave frequencies. Science **314**, 977 (2006)
44. Schurig, D., Pendry, J.B., Smith, D.R.: Calculation of material properties and ray tracing in transformation media. Opt. Express **14**, 9794 (2006)
45. Shadrivov, I.V., Sukhorukov, A.A., Kivshar, Y.S.: Guided modes in negative-refractive-index waveguides. Phys. Rev. E **67**, 057602 (2003); Peacock, A.C., Broderick, N.G.R.: Guided modes in channel waveguides with a negative index of refraction. Opt. Express **11**, 2502 (2003)
46. Shelby, R.A., Smith, D.R., Nemat-Nasser, S.C., Schultz, S.: Microwave transmission through a two-dimensional, isotropic left-handed metamaterial. Appl. Phys. Lett. **78**, 489 (2001)
47. Shelby, R.A., Smith, D.R., Schultz, S.: Experimental verification of a negative index of refraction. Science **292**, 77 (2001)
48. Smith, D.R., Padilla, W.J., Vier, D.C., Nemat-Nasser, S.C., Schultz, S.: Composite medium with simultaneously negative permeability and permittivity. Phys. Rev. Lett. **84**, 4184 (2000)
49. Taflove, A., Hagness, S.C.: Computational Electrodynamics: The Finite-Difference Time-Domain Method, 2nd ed. Artech House, Boston (2000)
50. Veselago, V.G.: The electrodynamics of substances with simultaneously negative values of φ and μ. Sov. Phys. Usp. **10**, 509 (1968)
51. Yao, P., Li, W., Feng, S., Jiang, X.: The temporal coherence improvement of the twodimensional negative-index slab image. Opt. Express **14**, 12295 (2006)
52. Yao, P., Liang, Z., Jiang, X.: Limitation of the electromagnetic cloak with dispersive material. Appl. Phys. Lett. **92**, 031111 (2008)
53. Zhou, L., Chan, C.T.: Vortex-like surface wave and its role in the transient phenomena of metamaterial focusing. Appl. Phys. Lett. **86**, 101104 (2005); Zhang, Y., Grzegorczyk, T.M., Kong, J.A.: Propagation of electromagnetic waves in a slab with negative permittivity and negative permeability. PIER **35**, 271 (2002)
54. Ziolkowski, R.W., Heyman, E.: Wave propagation in media having negative permittivity and permeability. Phys. Rev. E **64**, 056625 (2001)

# Chapter 10
# Photonic Metamaterials Based on Fractal Geometry

Xueqin Huang, Shiyi Xiao, Lei Zhou, Weijia Wen, C. T. Chan and Ping Sheng

**Abstract** We review our effort in understanding the rich electric, magnetic, and plasmonic properties of photonic metamaterials based on a planar fractal geometry. We employed both experiments and finite-difference time-domain simulations to study the electromagnetic properties of such systems and established effective medium models to characterize these complex structures. These fractal photonic metamaterials are shown to exhibit subwavelength and multiband functionalities with many interesting potential applications.

**Key words:** Fractal, electric metamaterials, magnetic metamaterials, plasmonic metamaterials, subwavelength functionality, multiband functionality, extraordinary transmission, surface plasmon polariton, super imaging, perfect tunneling, light polarizations.

## 10.1 Introduction

In 1968 Veselago proposed that a medium with simultaneously negative permittivity and permeability can exhibit a negative refractive index, with many attendant unusual electromagnetic (EM) properties [47]. However, this proposal did not draw immediate attention since it is well accepted that natural materials possess no magnetism at high frequencies [18]. The negative index of refraction idea was revived in the late 1990s when Pendry proposed two structures, metallic wires [28] and split ring resonators [27], that can exhibit negative electric and magnetic responses

Xueqin Huang, Shiyi Xiao, and Lei Zhou*
Surface Physics Laboratory (State Key Laboratory) and Physics Department, Fudan University, Shanghai 200433, P. R. China. *email: phzhou@fudan.edu.cn

Weijia Wen, C. T. Chan and Ping Sheng
Physics Department, Hong Kong University of Science and Technology, Clear Water Bay, Hong Kong, China.

T.J. Cui et al. (eds.), *Metamaterials*, DOI 10.1007/978-1-4419-0573-4_10,

at pre-designed frequencies. In 2001, Shelby *et al*. successfully fabricated the first negative index material by combining these two structures and experimentally verified the negative refraction phenomenon [40]. The term "metamaterial" was proposed to denote a man-made composite composed of subwavelength EM resonant structures that possess arbitrary values of permittivity $\varepsilon$ and/or permeability $\mu$ dictated by the local resonance(s). In addition to negative refraction, many other unusual EM phenomena were predicted or demonstrated based on metamaterials, such as super focusing [26, 10], invisibility cloaking [20, 30, 38], unusual photonic bandgap effects [22, 39, 44], unusual nonlinear effects [17, 53, 23]. In general, metamaterials offer novel EM characteristics complementing those observed in natural substances or photonic crystals. The challenge so far comes from the designs and fabrications of good-quality metamaterial samples with desired (frequency-dependent) $\varepsilon$ and $\mu$. During the last decade, there has been an explosion of activities searching for unit cell elements to realize metamaterials with either new or better characteristics. These structures include the S-ring [6], $\Omega$-ring [43], metallic rod pair [7, 31], metallic cross [36].

Concurrent with the above developments there has also been the effort to utilize fractal geometries to realize electromagnetic characteristics that may be denoted today as belonging to the "metamaterials" category. Since a fractal structure possesses self-similar properties, scaling law indicates that such structures naturally exhibit multiband EM responses covering an ultra-broad frequency regime. Many interesting EM wave properties were investigated in various fractal structures. It was shown that a multiband antenna can be designed based on a Sierpinski gasket pattern [33], and a metallic Sierpinski carpet (gasket) possesses rich diffraction properties [19]. Recently, it was shown that a three-dimensional Menger Sponge fractal cavity could localize microwaves [46] and terahertz waves [24], and finite-difference time-domain (FDTD) simulations were performed to calculate the eigenmode properties in such a cavity [37]. More recently, surface plasmon-induced extraordinary optical transmissions (EOT) were found in a metallic film perforated with air holes arranged in a Sierpinski-carpet pattern [1]. Research was also carried out on the reflection and transmission properties of Cantor bar fractal multilayers [45, 4].

In this chapter, we review our effort in employing fractal structures to construct photonic metamaterials. We found that a specific type of planar fractal (sometimes called a space-filling curve) is particularly suitable to achieve this goal. As shown in Fig. 10.1, this fractal pattern was generated from a line of length $a$, defined as the master line, or the first level of the structure, placed parallel to the $y$ axis in the $xy$ plane. The $(k + 1)$th level structure contains $2^k$ lines, with the midpoint of each perpendicularly connected to the ends of the $k$th level lines. The length of the $(k + 1)$th level lines was scaled from that of the $k$th level line by a factor of 2(1) if $k$ is an even (odd) number. The number of levels ($N$) and the initial line length ($a$), together with the line width and thickness, collectively define the fractal structure. Simply described, the fractal has an H-shaped generator, a geometrical scaling factor of 2, with no self-intersections. As $N$ tends to infinity, the structure eventually becomes a space-filling curve that tiles a $2a \times 2a$ square. We depict in Fig. 10.1 a 6-level fractal pattern as an illustration. Distinct from other fractal

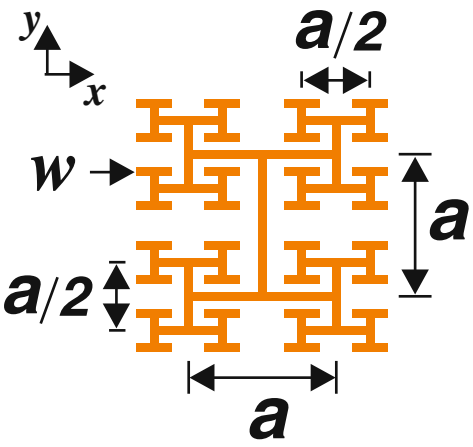


**Fig. 10.1** Geometry of a 6-level H-shaped fractal pattern.

patterns [33, 19, 46, 24, 37, 1, 45, 4], all lines in this fractal structure are connected. This important character offers our fractal an important characteristic – the structure can be very subwavelength in size at resonance. The multiband functionality and subwavelength effect are the two most important features of this H-shaped fractal. In the following, we describe how to exploit such features to design photonic metamaterials with a variety of EM characteristics. In particular, we show that based on this fractal pattern, one can construct electric metamaterials [50, 55, 56], magnetic metamaterials [57, 13], and plasmonic metamaterials [15, 51, 49, 48] with desirable photonic properties.

In what follows, we show in Section 10.2 that a single layer of metallic fractal pattern is an electric metamaterial possessing a series of self-similar electric resonances. We review our effort to experimentally characterize this electric metamaterial and to establish an effective medium model to describe such a metamaterial [50, 55]. An important application of such a system [56] is also introduced. In Section 10.3, we demonstrate that a magnetic metamaterial can be made by combining a metallic planar fractal and a metallic sheet. We show that such a composite material can reflect EM wave in-phase at a series of frequencies, with some of the corresponding wavelengths much longer than the reflector's own size [57]. We found the physics to be governed by a series of intrinsic magnetic resonances and the system can be well described by a double-layer effective medium model [57, 13]. Section 10.4 is devoted to the surface plasmon polariton (SPP) properties of a plasmonic metamaterial based on fractal geometry [15, 51, 49, 48]. We show that a metallic plate drilled with periodic fractal-shaped slits is a plasmonic metamaterial to support SPPs in both transverse-magnetic (TM) and transverse-electric (TE) polarizations [15, 51]. Therefore, such fractal plates support SPP-induced EOT [49, 48] and work as a super lens to focus near field sources with subwavelength resolutions [15, 51]. In Section 10.5, we introduce two additional applications of these fractal photonic metamaterials. We first show that EM waves can transmit perfectly through a slab of negative permittivity media sandwiched between two identical

fractal electric metamaterial slabs, although each single slab is nearly opaque [58]. We next show that a fractal magnetic metamaterial can be employed to manipulate the polarization states of EM waves efficiently [14]. Finally, we summarize our results in the last section.

## 10.2 Electric Metamaterials Based on Fractal Geometry

### *10.2.1 Characterization and Modeling of a Metallic Fractal Plate*

We first study the EM properties of a single layer of metallic fractal plate [50]. Figure 10.2a shows part of a 15-level fractal sample, with the first-line length $a$ = 144.78 mm. The real sample is made by the shadow-masking/etching technique on a 30 cm×30 cm×1 mm dielectric plate (with $\varepsilon = 5.3$). Both the line width and thickness of the copper lines are 0.1 mm. Figure 10.2(b, c) show the measured normal transmission and reflection of the fractal plate. A HP83711B generator was connected to a double-ridged waveguide horn antenna (HP11966E) to generate the microwave. Another identical receiver horn was placed at a distance of 100 cm from the source, connected to a power meter (Agilent E4418B). The fractal plate was placed on a stage, 15 cm from the receiver horn, which can be rotated about the $z$ axis (defined as $\theta = \phi = 0^\circ$) by an angle $\theta$(**E** perpendicular to the plane of incidence) and $\phi$(**E** parallel to the plane of incidence). Reflection measurements were carried out by putting both the source and the receiver horns on one side, separated by a small angle of 8°. The open circles in Fig. 10.2(b, c) denote the measured transmission and reflection, respectively, when the normally incident **E** field was polarized along the $y$ axis. The measured transmission [Fig. 10.2(b)] shows three stop bands, at which Fig. 10.2(c) shows strong reflections. Between any stop bands there is a pass band where the maximum transmission can be close to 100%. This is intriguing at first sight, since the metallic lines are connected and cover the entire plate. The relevant wavelength is also much larger than the spaces between the metallic lines.

To understand the observed phenomena, we performed FDTD simulations [60] on the realistic structure. As limited by our computational power, it is difficult to directly study the 15-level fractal plate adopted in the experiment, since the number of mesh points required is prohibitively large for an accurate simulation. Fortunately, calculations reveal that certain frequencies would excite only particular subdomains of the fractal. With increasing frequency, the relevant characteristics are governed by localized currents in higher level sub-structures. Therefore, we first applied a coarse discretization to calculate the response of the whole fractal (periodically replicated), yielding the low-frequency characteristics involving long current paths in the fractal structure. But the results are inaccurate for the high frequencies. To determine the accurate higher frequency characteristics, we focused only on the higher level substructures (also periodically replicated), but with finer discretization. With this approach, converged results for the experimentally adopted 15-level fractal plate were

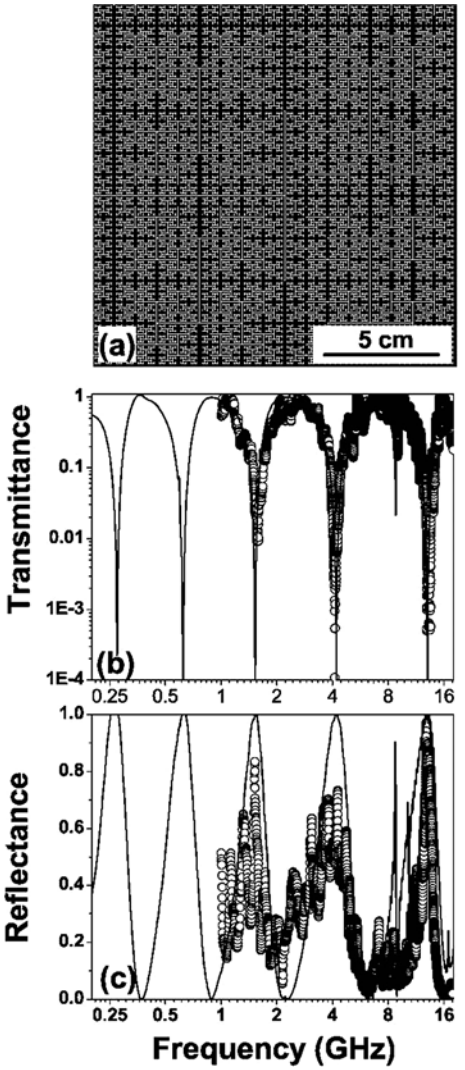


**Fig. 10.2** (**a**) A computer-generated image of part of a fractal structure. The white lines correspond to copper in the sample. Measured (*circles*) and calculated (*lines*) transmittance (**b**) and reflectance (**c**) of a 15-level fractal pattern for EM waves polarized with **E** along the *y* axis. Reproduced from Ref. [50] with the permission of American Physical Society.

obtained. These are shown as solid lines in Fig. 10.2(b)–(c). The low (0.1–0.9 GHz), mid (0.9–2.2 GHz), and high frequency (2.2–18 GHz) results were calculated (for the *y*-polarization) from periodic replica of 11-, 9-, and 7-level substructures of the 15-level fractal, respectively. There is exactly the same number of resonances as the number of levels in a fractal. Hence, there are more resonances at lower and higher frequencies than those shown in Fig. 10.2. For *x*-polarized normally incident wave, the results (not shown here) are similar like Fig. 10.2. The simulations reproduced all the salient features of the experiments. We see that the calculated and measured spectra have quasi-log periodicity. This is a manifestation of the fractal's geometric self-similarity. The log-periodicity of the spectra is not exact for the present fractal

structure with a finite number of levels, but the spectra will approach log-period behavior as the number of levels increases. Log-periodicity also implies that the resonance frequencies cover an ultra-broad range, in contrast to the conventional photonic crystal (PC) slabs and frequency-selective surfaces which typically have one single dominant response, and high harmonics typically cover a linear scale in the frequency spectrum.

An analysis of the simulation results offers us a picture of the underlying physics [55]. The phase changes for transmitted and reflected waves are depicted in Fig. 10.3(c) as open circles, compared with the FDTD simulated transmission and reflection spectra re-plotted in Fig. 10.3(a) and (b) as open circles. We found through FDTD simulations that the EM field excites currents in the sub-structure of the metallic lines of the fractal, with the current amplitude reaching a maximum at those frequencies where the fractal is strongly reflecting. As shown in Fig. 10.3, the relative phase of the current with respect to the input wave undergoes a $\pi$ jump whenever the frequency is varied across each maximum reflection point, indicating a resonance behavior. Each resonance has currents excited mainly along the metal lines of one specific level, flowing toward the higher level structures. As an illustration, the amplitude of the surface current density distribution (calculated by $\mathbf{J} = \mathbf{n} \times \mathbf{H}$) is shown in Fig. 10.4(a, b) for the resonance at 4.2, and 13.1 GHz. The current amplitude is seen to peak at the 11th level lines for resonance frequency 4.2 GHz and to peak at the 13th level lines for the 13.1 GHz resonance, each flowing to higher level lines on both sides. It is known that the dielectric constant of a dispersive medium with localized resonances takes a general form $\varepsilon(f) = a + \sum_{j=1}^{N} b_j/(f_j^2 - f^2)$, where $f_j$ is the $j$th resonance frequency, $f$ is

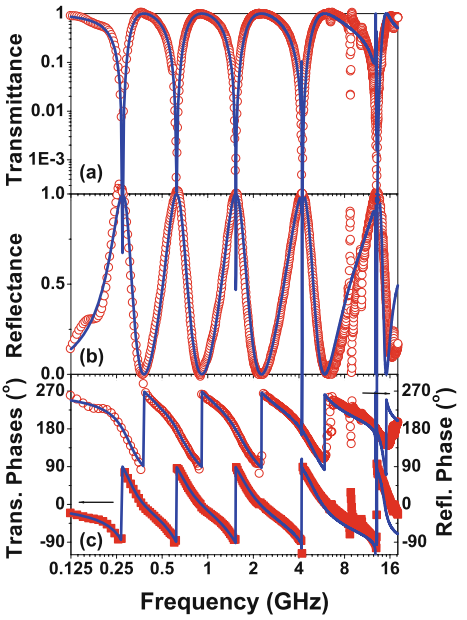


**Fig. 10.3** Transmittance (**a**), reflectance (**b**), transmission phase change and reflection phase change (**c**) for a 15-level fractal plate with respect to an $y$-polarized normally incident wave. Symbols denote FDTD simulation results; solid lines the effective medium model. Reproduced from Ref. [55] with the permission of Institute of Physics.

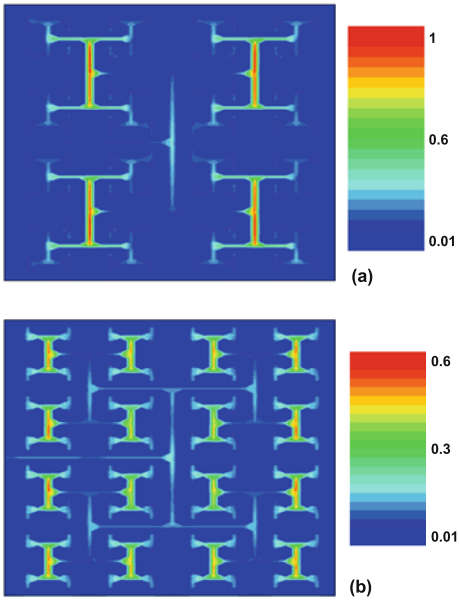


**Fig. 10.4** Surface current density (in A mm$^{-1}$) distribution on the fractal surface under an incident EM wave with frequency 4.2 GHz (**a**) and 13.1 GHz (**b**). Reproduced from Ref. [55] with the permission of Institute of Physics.

the frequency, and $a, b_j$ are some model parameters [16]. Adjusting parameters $a, b_j$ to fit our calculation results, we find that the fractal response at normal incidence can be accurately modeled by a thin homogeneous plate (of the same thickness of the real plate 1.1 mm) with an effective dielectric constant of the form

$$\begin{aligned}\varepsilon_{xx}(f) &= 11 + \frac{15}{0.477^2 - f^2} + \frac{48}{1.07^2 - f^2} + \frac{130}{2.66^2 - f^2} + \frac{470}{7.55^2 - f^2} \\ \varepsilon_{yy}(f) &= 11 + \frac{10}{0.274^2 - f^2} + \frac{23}{0.623^2 - f^2} + \frac{60}{1.53^2 - f^2} + \frac{190}{4.19^2 - f^2} + \frac{500}{13.06^2 - f^2},\end{aligned} \tag{10.1}$$

where $f$ denotes the frequency measured in GHz. Solid lines in Fig. 10.3 are the results calculated based on such an effective medium. Excellent agreement with the FDTD results is noted for not only the amplitudes but also the phases of the transmission/reflection coefficients. The effective medium model also offers us an explanation for the total transmissions, which appeared at first sight to be particularly intriguing since the metallic lines in the fractal pattern are finely separated (much smaller than the relevant wavelength). In between any two total reflection frequencies, there is a frequency at which the currents induced on two adjacent resonance structures are roughly of the same magnitude but 180° out of phase, leading to a cancellation of their radiations in far-field. A metallic structure with induced currents effectively canceling each other (seen in far-field) is then transparent to the incident EM wave.

The above discussions show that a metallic fractal plate is an ideal electric metamaterial with well-defined effective permittivity. In the next two subsections, we continue to explore other important EM wave properties of this fractal electric metamaterial.

### *10.2.2 Mimicking Photonic Bandgap Materials*

Since the fractal metamaterial exhibits multiple stop bands for EM waves, it is natural to ask if such a system can mimic a 3D PC in terms of stop band properties. However, we note that such a stop band is polarization dependent. By stacking two identical fractal patterns, one rotated by 90° relative to the other to form a rotationally invariant structure, we demonstrate that this double stack structure can indeed mimic a 3D PC and exhibits a polarization and incidence angle-independent stop band [50]. Figure 10.5 shows the transmission of such a double stack when it was rotated and tilted, so as to change the angle of incidence. We found the transmissions to be nearly identical for different angles of incidence; hence the spectral gap frequencies are stable with respect to a large range of incidence angles. In addition, the transmission is independent of polarization since the double stack is rotationally invariant.

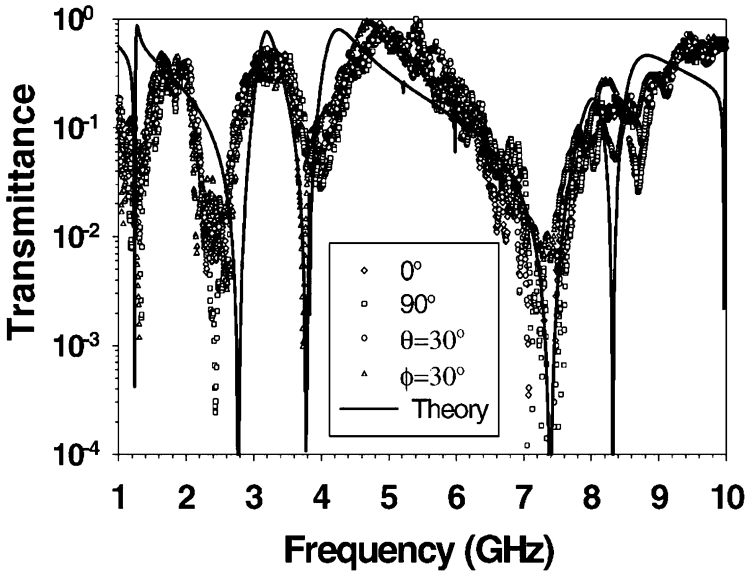


**Fig. 10.5** Transmission through two stacked identical fractal plates with a 90° rotation with respect to each other. The diamonds and squares denote measured normal transmission, with **E** polarized along the $x$ and $y$-axes, respectively. The lines are calculated results for normal incidence (identical for both polarizations). The circles and triangles are transmissions measured with the plates rotated ($\theta$) and tilted ($\phi$) by 30°, respectively, from the normal. Reproduced from Ref. [50] with the permission of American Physical Society.

Another point about our metamaterial is that the size of the stop bands, measured by the dimensionless parameter $\Delta f/f_0$(gap/midgap ratio, ~5% for a single fractal) can be significantly enhanced by stacking identical fractals together [50], in contrast to conventional 3D PC's, where increasing the slab thickness sharpens the band edges. The effect of stacking up to five fractals is shown in Fig. 10.6 for

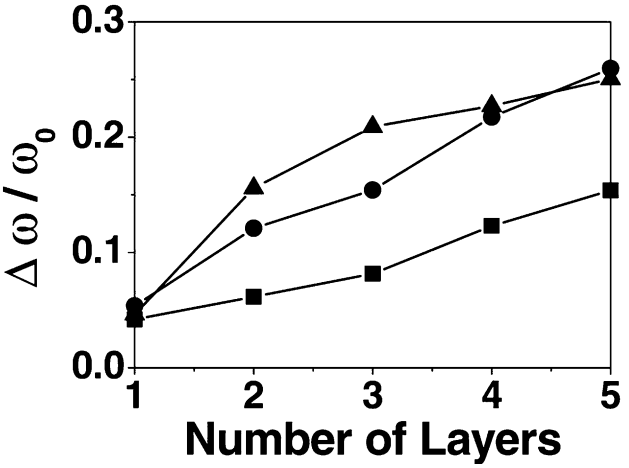


**Fig. 10.6** The calculated gap/midgap ratio as a function of the number of stacking layers for three spectral gaps at 1.6 (*square*), 4.4 (*circle*), and 13 (*triangle*) GHz. The dielectric substrates are 1 mm thick, separated by an air gap of 1 mm. Reproduced from Ref. [50] with the permission of American Physical Society.

three resonance frequencies (1.6, 4.4, and 13 GHz). The $\Delta f/f_0$ ratio is seen to increase rather significantly according to the FDTD simulation. A stack of several fractals, plus the corresponding 90° rotated counterparts, is still negligible in thickness compared to the relevant wavelengths. The stop bands can also be expanded by increasing the width of metal lines in the fractal.

### *10.2.3 Subwavelength Reflectivity*

Another important characteristic of our fractal metamaterial is the subwavelength property, that is, the total size of the system is much smaller than the wavelength along all directions at resonance. This unique property indicates that our fractal plates can act as very compact reflectors [56], which we demonstrate below. Figure 10.7 schematically illustrates the experimental setup and a 6-level fractal structure deposited on a 1.6 mm thick dielectric substrate studied both theoretically and experimentally. Such a fractal plate was perpendicularly put on a $60 \times 60$ mm metallic ground plane, and a monopole antenna was fed from a 50 $\Omega$ coaxial line (see Fig. 10.7). The radiation patterns for both the H-plane and the E-plane were calculated by FDTD simulations [60]. We find that the fractal plate can effectively reflect EM waves at four frequency ranges centered at 2.25, 3.85, 7.0, and 10.5 GHz. For comparison, we have also calculated the radiation patterns with the fractal plate replaced by a perfect metallic plate of exactly the same size, under the same conditions.

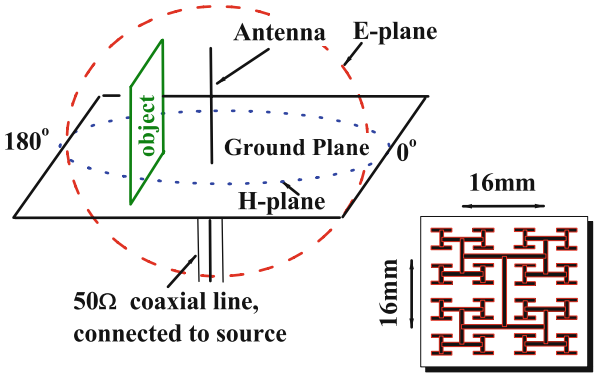


**Fig. 10.7** Schematic picture of the experimental setup. Inset shows the 6-level fractal structure: First-level line length 16 mm, line width = 1 mm, and thickness = 0.5 mm. The plate measures $28 \times 29$ mm. Reproduced from Ref. [56] with the permission of American Institute of Physics.

In our experiments, the monopole antenna was excited by a function generator (HP83711B). The radiation power was measured by a receiver horn (HP11966E) placed 20–25 cm from the antenna, connected to a power meter (Agilent E4418B). In Fig. 10.8, the solid and dotted lines denote the calculated H-plane radiation patterns for the case of fractal plate and the metal (copper) plate, respectively. Open (fractal) and solid (metal) symbols denote the experiment. Good agreement between theory and experiment is noted. It is clear from Fig. 10.8(a, b) that the metallic plate cannot block EM waves at 2.25 and 3.85 GHz. At these frequencies, the correspond-

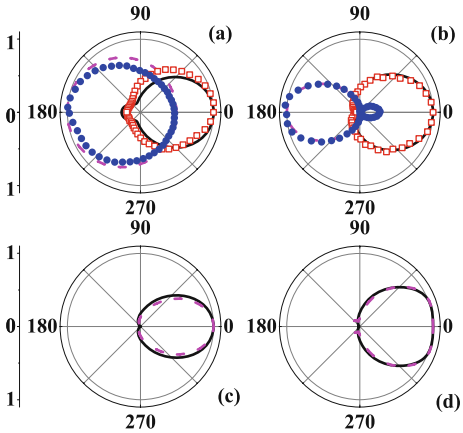


**Fig. 10.8** FDTD calculated and experimentally measured H-plane radiation patterns for a monopole antenna of length $L$ under an operation frequency $f$, with a fractal plate ( FDTD: *solid lines*; experimental: *open squares*) or a metal plate (FDTD: *dashed lines*; experimental: *solid circles*) placed at a distance $d$ from the antenna. (**a**) $f$ = 2.25 GHz, $L$ = 24 mm, and $d$ = 15 mm; (**b**) $f$ = 3.85 GHz, $L$ = 24 mm, and $d$ = 9 mm; (**c**) $f$ = 7.0 GHz, $L$ = 8 mm, and $d$ = 9 mm, and (d) $f$ = 10.5 GHz, $L$ = 8 mm, and $d$ = 9 mm. Reproduced from Ref. [56] with the permission of American Institute of Physics.

ing half-wavelengths (∼67 and ∼39 mm) are larger than the lateral dimension of the plate (∼29 mm). In contrast, the fractal plate can effectively reflect at these two frequencies (the reflectivity is a bit worse for the lower-frequency case). At the two higher frequencies [Figs. 10.8(c, d)], where half-wavelengths are smaller than the plate size, both the fractal and the metallic plates reflect the EM waves effectively, with similar radiation patterns. The calculated E-plane radiation patterns (not shown here) are similar with the H-plane case [56].

## 10.3 Magnetic Metamaterials Based on Fractal Geometry

In this section, we utilize the fractal pattern to construct metamaterials with magnetic responses and study their EM wave properties [57, 13]. Similar to last section, we also establish an effective medium model to describe such a system and present a typical application of this metamaterial.

### *10.3.1 Characterizations and Modeling of the Fractal Magnetic Metamaterial*

The most crucial characteristic of a magnetic metamaterial is that it reflects EM waves in-phase at resonance. In contrast, an electric metamaterial reflects EM waves with a phase reversal as shown in Fig. 10.3(c). Here, we show that, by combining a metallic fractal with a metal sheet [57], a magnetic metamaterial can be made which can reflect EM waves in-phase at a series of frequencies [57]. While a mushroom structure [42] also reflects EM wave in-phase at a particular frequency, our structure has the advantages of multiband and subwavelength functionalities.

Figure 10.9 shows schematically the structure of our composite and the experimental setup. A 12-level copper fractal pattern was deposited on a 0.8 mm thick dielectric substrate ($\varepsilon = 4$). We calculated the transmission/reflection properties of the composite through FDTD simulations. No transmission is found through the composite in our simulations, since there is a flat metal plate on the back. The reflection phase as a function of frequency is shown in Fig. 10.10 (a), (b) for the normally incident $x$-polarized wave (**E** perpendicular to the first level of the fractal) and in Fig. 10.11(a, b) for the $y$-polarized one, respectively. While the reflected wave has a $\pi$ phase change in most frequency regimes like the case of metal, we find multiple frequency regimes where the reflection phase varies continuously from $180^\circ$ to $-180^\circ$, indicating that the reflection becomes in-phase at some specific frequencies.

In our experiments, we put a center-fed dipole antenna directly on the top surface of the composite and measured the forward radiation power as a function of frequency. We also measured the radiation spectra for the free antenna and that on a metal sheet of the same size for comparison. We used a longer antenna (12 mm)

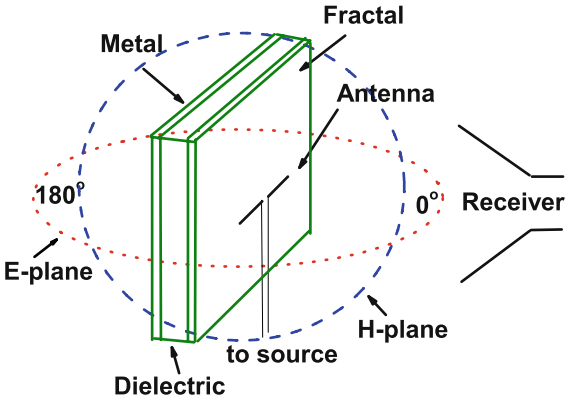


**Fig. 10.9** A schematic picture of the composite structure and the experimental setup. Fractal details: 12 levels, first level line length 128 mm, line width 1 mm, and film thickness 0.1 mm. Metal sheet size: 25 × 25 cm and thickness 0.1 mm. Reproduced from Ref. [57] with the permission of American Institute of Physics.

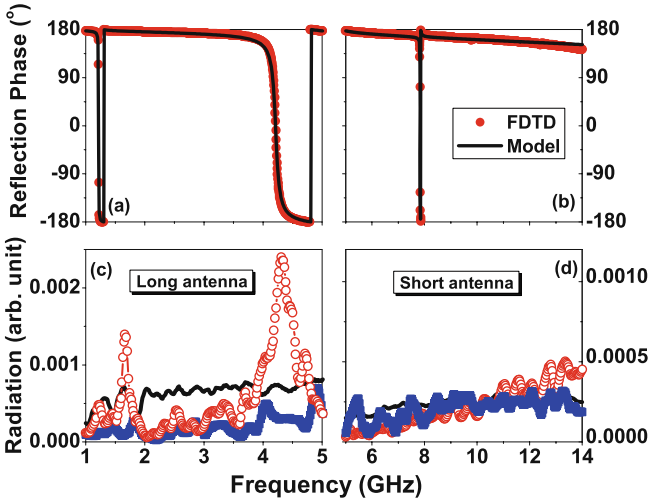


**Fig. 10.10** (**a**), (**b**) Reflection phase change on the surface of our composite, calculated by FDTD simulation (*solid symbols*) and an effective medium model (*solid lines*), for *x*-polarized incident wave. (**c**), (**d**) Measured forward radiation spectra for free antennas (*solid line*), antennas on the surface of a metal sheet (*solid squares*), and on the surface of the composite (*open circles*). The fractal's first-level line is perpendicular to the antennas' wires. Reproduced from Ref. [57] with the permission of American Institute of Physics.

for 1–5 GHz and a shorter antenna (6 mm) for 5–14 GHz. The measured results are shown in Figs. 10.10(c, d) and 10.11(c, d) for two different polarizations. As shown in the figures, under a constant input power, radiations from the free antennas are increasing functions of frequency before reaching their quarter-wavelength maxima. When put on the surface of a metal sheet, forward radiations are significantly lower

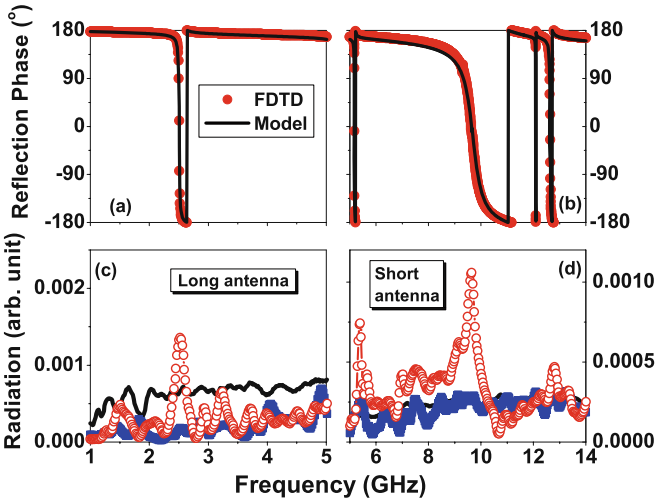


**Fig. 10.11** Theoretical (**a**), (**b**) and experimental results (**c**), (**d**) for the *y*-polarization case. Other details are the same as those described in the caption of Fig. 10.10. Reproduced from Ref. [57] with the permission of American Institute of Physics.

than free antenna because of destructive interference between reflected and source waves. Replacing the metal sheet by our composite, we find the antenna's forward radiations are strongly enhanced at frequency regimes centered at 1.6 and 4.3 GHz for the *x*-polarization case, and at 2.6, 5.4, 9.8, and 12.8 GHz for the *y*-polarization, implying the interference between reflected and source waves to be constructive at these frequencies. Out of these frequency bands, we find the forward radiations to be clearly lower than those of a free antenna, similar to the metal case. The peaks in the radiation spectra coincide well with the in-phase reflection frequencies found from the simulation. However, our experiments failed to detect two narrow in-phase reflection bands centered at 7.83 GHz for *x* polarization and 12.1 GHz for *y* polarization, which were found by the FDTD simulations. These two bands are too narrow so that the integrated resonance strength is too weak to be detectable by our experiment where noises are always present.

The composite system can be homogenetized as a magnetic metamaterial [57]. As we have shown in last section, a single metallic fractal possesses multiple local resonances which response to the **E** field of the incoming wave. When a metal sheet is placed on the back, each resonance couples to the metal sheet to generate a resonance that corresponds to the **H** field response. According to Farady's law $\nabla \times \mathbf{E} = -\dot{\mathbf{B}}/c$, surface currents of opposite signs on the metal and on the fractal will be induced in response to the time-varying **B** field sandwiched between the fractal and the metal. FDTD simulations revealed that such induced currents had typical resonance responses at a series of frequencies, characterized by the current amplitude reaching a maximum while its phase undergoing a $\pi$ jump across the resonance frequency. For example, at one resonance frequency of 4.21 GHz, FDTD simulation showed that the currents were mainly excited on the 10th levels of the fractal and flow to higher level structures. At the same time, currents with almost

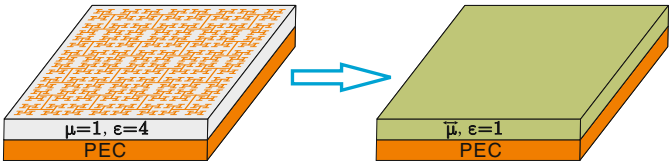


**Fig. 10.12** Geometry of our double-layer effective medium model for the fractal magnetic metamaterial.

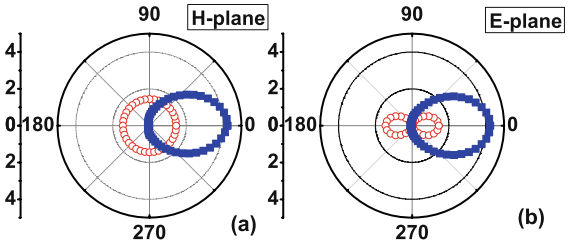


**Fig. 10.13** (**a**) H-plane and E-plane radiation patterns of a 24 mm long central-fed dipole antenna on our magnetic reflector (*solid squares*) and of the same bare antenna (*open circles*) at $f$ = 3.73 GHz. The magnetic reflector includes a 7-level fractal (first level length = 16 mm, line width = 1 mm, thickness = 0.2 mm, and total size 30×29×0.2 mm) and a 0.2-mm thick metal sheet separated by a 1.6-mm-thick dielectric substrate ($\varepsilon = 4$), and the dipole antenna is orientated perpendicular to the fractal's first-level line. The patterns are normalized such that the total radiated powers are the same in the two cases. Reproduced from Ref. [57] with the permission of American Institute of Physics.

the same amplitude but opposite signs were induced on the surface of the metallic sheet. In fact, we can model this composite by a double-layer system consisting of a 0.9 mm-thick (thickness of the fractal plus the dielectric layer) homogeneous magnetic material with permeability tensor $\overleftrightarrow{\mu}$ and a perfect metal layer, as schematically shown in Fig. 10.12. The solid lines in Figs. 10.10(a–b) and 10.11(a–b) are the result calculated by such a model with elements given by

$$\begin{aligned}\mu_{yy}(f) &= 1 + \frac{0.2}{1.22^2 - f^2} + \frac{4.8}{4.21^2 - f^2} + \frac{0.3}{7.83^2 - f^2} \\ \mu_{xx}(f) &= 1 + \frac{0.8}{2.51^2 - f^2} + \frac{0.5}{5.17^2 - f^2} + \frac{28}{9.66^2 - f^2} + \frac{0.2}{12.08^2 - f^2} + \frac{1.2}{12.63^2 - f^2}. \\ \mu_{zz}(f) &= 1\end{aligned} \tag{10.2}$$

Excellent agreement is noted between the model and the FDTD results. Such a model permeability exhibits resonant frequencies at which $\mu$ diverges, which in turn gives a very large impedance ($Z$) and a very large effective index ($n$). A large $Z$ gives in-phase reflectance and a large $n$ ensures that the effect manifests itself in a thin layer with thickness much smaller than the free-space wavelength.

In fact, the established double-layer model works for all high-impedance surfaces with different microstructures. As shown in Ref. [13], such a model cannot only perfectly describe the propagating wave properties of high-impedance structures but also describe well the surface wave characteristics of such complex structures.

### *10.3.2 A Typical Application of the Fractal Magnetic Metamaterial*

The fractal magnetic metamaterial could find many applications in practice. Besides the multiband functionality, this structure has an additional characteristic that it can reflect in-phase at wavelengths that are much longer than the reflector's lateral dimension [57]. Figure 10.13 shows the FDTD-calculated radiation patterns (see Fig. 10.9 for the definitions of H-plane and E-plane) of a dipole antenna put on a small piece of the fractal magnetic reflector. The working frequency is 3.73 GHz, coinciding with one of the resonance frequencies of the magnetic reflector. We note that 3.73 GHz corresponds to a wavelength of ∼80 mm, while the reflector's size is only ∼30 mm. In contrast to the free antenna patterns, we find that the reflector shields the antenna's radiation (in the backward direction) while at the same time increases the forward radiation power. The combined system thus serves as a subwavelength directional antenna. It is noted that a metal sheet of the same size cannot reflect at this frequency, because the corresponding half wavelength is longer than the metal plate's own size. Although the stand-alone fractal pattern can serve as a subwavelength reflector as we demonstrated in last section, the antenna does not radiate efficiently when it is too close to the reflector. Therefore, this fractal magnetic metamaterial is an ideal candidate to serve as a compact and multiband antenna ground plane.

## 10.4 Plasmonic Metamaterials Based on Fractal Geometry

We now study another type of metamaterial – plasmonic metamaterial. We design a plasmonic metamaterial based on fractal geometry and then investigate its SPP characteristics as well as transmission properties. Finally, we illustrate one important application of such a fractal plasmonic metamaterial [15, 51, 49, 48].

### *10.4.1 SPP Band Structures of Fractal Plasmonic Metamaterials*

Surface plasmon polaritons (SPPs) are elementary EM excitations bounded at metal/dielectric interfaces and attracted considerable attention recently [2]. For a natural material, its plasmon frequency ($\omega_p$) is fixed by the electron density, so that many SPP-based applications only work at a single frequency. Although $\omega_p$ can be modified via using semiconductors [35] or metal/dielectric composites [5], such tunability is limited and cannot cover the entire frequency range. Recently, people showed that Bragg scatterings can modulate the SPPs significantly and found the SPP-induced EOT in a silver film drilled with periodic holes [8, 32, 21]. However, the Bragg mechanism can only fold the SPP bands into the first Brillouin zone, but cannot change the plasmon frequency of a material. Although metamaterials [40, 52] can in principle possess any desired EM wave properties at arbitrary

frequencies, the fabrications of high-quality metamaterials are still challenging. In 2004, Pendry *et al*. demonstrated that a metallic plate with periodic square holes can mimic a plasmonic metamaterial in terms of SPP properties, with effective $\omega_p$ being the waveguide cut-off frequency of the hole [12, 29]. This opens up a way to design artificial plasmonic metamaterials at any desired frequencies. However, to make the idea work, one has to fill the holes with high-index materials to make the cut-off wavelength much longer than the periodicity [12, 29]. The high-index material is not easy to find in practice, particularly at higher frequencies. Very recently, Shin *et al*. [41] showed that high-index insertion is not necessary if the square holes are replaced by narrow rectangle holes with cross sections $b_x \times b_y$ ($b_x \ll b_y$). Indeed, such a hole has a cut-off wavelength $\lambda = 2b_y$ much longer than the periodicity along $x$ direction [41]. However, since such holes are subwavelength only along one direction, we will show that the generated SPPs on such structures only possess TM polarization traveling along one ($x$) direction. This limitation restricts the applications of such structures to many cases.

In this subsection, we demonstrate that a metallic plate drilled with fractal-shaped slit patterns exhibits SPPs in both TM and TE polarizations, with $\omega_p$ dictated by the fractal geometry. Figure 10.14 schematically shows our structure – a 0.5-μm-thick silver film caved with 4-level fractal slits arranged periodically with a lattice constant $a = 1\mu$m. We performed FDTD simulations [11] with dispersive $\varepsilon_{Ag}$ given by [9] to calculate the SPP band structure of the designed system. Since this system shows no $x-y$ symmetry, we depicted in Fig. 10.15(a) and (b) the SPP bands along $\Gamma \to X$ and $\Gamma \to X'$ directions, respectively, with $X = [\pi/a, 0, 0]$, $X' = [0, \pi/a, 0]$. In each panel, we found two SPP bands well below the light lines (pink line), which bend drastically at two frequencies ($f_{P1} = 41$ THz, $f_{P2} = 78.7$ THz). In fact, the two plamon frequencies $f_{P1}$ and $f_{P2}$ correspond to two independent lateral resonances of an individual fractal pattern, induced by incident fields with $\mathbf{E}||\hat{x}$ and $\mathbf{E}||\hat{y}$, respec-

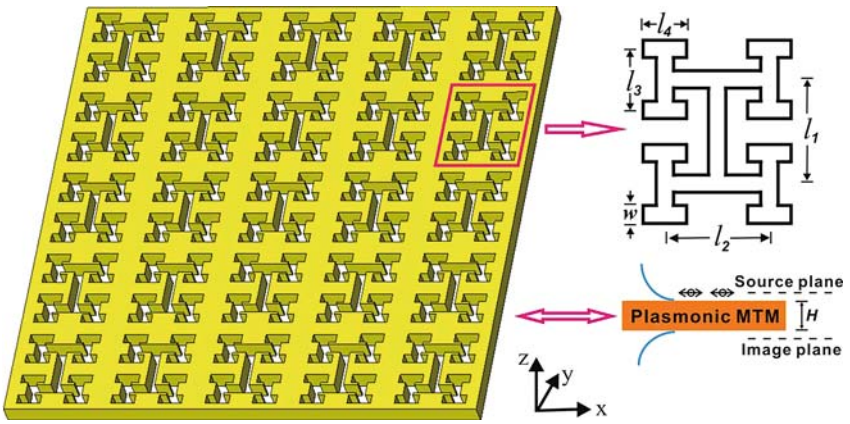


**Fig. 10.14** Geometry of the fractal plasmonic metamaterial (MTM). Unit cell strcuture $l_1 = l_2 = 0.5\ \mu$m, $l_3 = l_4 = 0.25\ \mu$m, $w = 0.06\ \mu$m, and $H = 0.5\mu$m. Ref. [15].

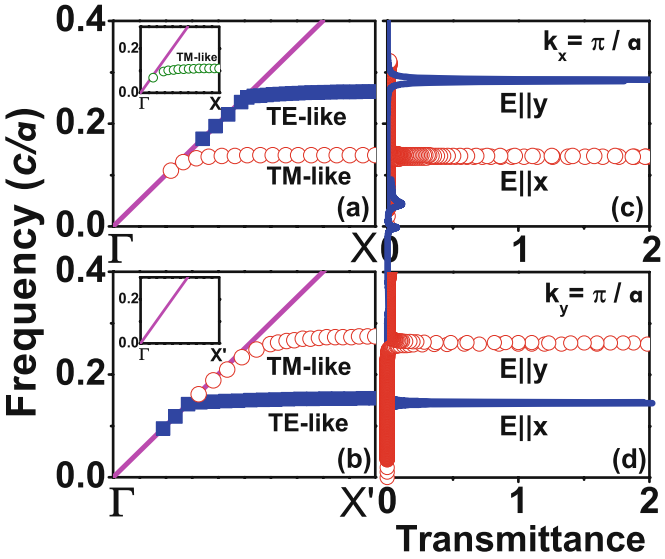


**Fig. 10.15** SPP band structures of the fractal plate calculated by FDTD simulations for (**a**) $\Gamma \rightarrow X$ and (b) $\Gamma \rightarrow X'$ directions; Under the conditions of (**c**) $k_x = \pi/a$ and (d) $k_y = \pi/a$, FDTD-calculated transmission spectra under incident plane evanescent waves with different polarizations. Insets: SPP band structures of rectangle-hole plate calculated by FDTD simulations, with structural details $d = 1\mu\text{m}$, $s = 4.2d, a = 0.3d, L = 0.5d$ (see Ref. [41]). Ref. [15].

tively. The coupling between such localized resonances leads to the running SPP modes on the structure surface.

We employed the attenuated total reflection technique to identify the polarization characteristics of those SPP bands. With $k_x$ fixed as $\pi/a$, we shine plane evanescent waves with different polarizations on the structure and depicted in Fig. 10.15(c) the transmission spectra for $\mathbf{E}||\hat{x}$ (red circles) and $\mathbf{E}||\hat{y}$ (blue line) polarizations. By comparing Fig. 10.15(a) with 10.15(c), we found that the lower SPP band in Fig. 10.15(a) is apparently TM like, since a TM-polarized evanescent wave can excite this mode but a TE one cannot. Similarly, we can identify the polarization properties of all SPP bands and then label them correspondingly on the figure. This is intriguing at first sight, since a complex structure at resonance usually exhibits very complicated local field distribution, making it difficult to separate the TE and TM polarizations for its eigenmodes. However, thanks to the high symmetry of the fractal geometry, here a SPP eigenmode can only couple to one particularly polarized evanescent wave, so that we can successfully identify its polarization. One can also understand this point in the spirit of metamaterial. Since the probing field wavelength is much longer than the inhomogenity feature size of the complex structure, we can homogenize the entire system by performing field average over a unit cell. The eigenwaves obtained upon field averaging show well-defined polarizations as illustrated in Fig. 10.15.

The crucial advantage of our fractal structure is thus clear. Whereas a flat Ag film supports only TM-polarized SPP [34], our system supports simultaneously TM- and TE-polarized SPPs related to each resonance. We also studied a metal plate with narrow rectangular holes [41] and depicted its SPP dispersions in the insets to Fig. 10.15(a)–(b). Indeed, this structure exhibits a SPP band even without high-index insertions. However, in sharp contrast to our case, such a system supports only a single TM-like SPP band traveling along $x$ direction (Fig. 10.15(a)). This is because the rectangle shape is subwavelength along only one ($x$) direction, and therefore, the SPP band along $y$ direction cannot be formed since the subwavelength condition is not satisfied [12, 29]. In contrast, our fractal pattern is subwavelength along all directions and possesses multiple resonances, so that for each resonance, SPP bands along both $x$ and $y$ directions can be formed (see Fig. 10.15). The plasmon frequencies of our fractal plasmonic metamaterial can be changed via adjusting the fractal geometry and scaling the unit cell size. Therefore, one can in principle design a plasmonic metamaterial with any desired SPP properties at an arbitrary frequency. We note that the plasmon frequencies are solely determined by the lateral fractal structure, independent of the sample thickness.

### *10.4.2 Extraordinary Optical Transmissions Through Fractal Plasmonic Metamaterials*

We performed experiments and FDTD simulations to study the optical transmissions through such fractal plasmonic metamaterials, in both microwave [49] and infrared (IR) [48] frequency regimes. The fabricated microwave and IR samples are shown in Fig. 10.16.

Figures 10.17(a, b) show the transmission spectra through the microwave samples [49] with different thicknesses, where (a) and (b) are for $\mathbf{E}||\hat{y}$ and $\mathbf{E}||\hat{x}$ polarizations, respectively. We found EOT bands centered at 4.1 and 17.2 GHz for $\mathbf{E}||\hat{y}$ and at 2.4 and 9.0 GHz for $\mathbf{E}||\hat{x}$, with peak frequencies almost independent of the sample thickness. It should be noted that at the lowest peak frequency, the incident wavelength (12.5 cm) is 12.5 times the longest slit (1 cm) on the metal plate. Hence the cross section of a fractal aperture is subwavelength in both dimensions. The transmission characteristics of the microwave fractal samples were investigated by FDTD simulations shown as solid lines in Fig. 10.17(a, b). Except for the two thick samples, the agreement is seen to be excellent ($<1\%$ difference). It is interesting to observe that for a reference sample consisting of an array of square holes ($18\times18$ mm opening), the transmission is considerably lower, as shown in Fig. 10.17(c). Thus by removing metal, the sample becomes less transparent. The periodicity and incident angle dependencies were also investigated, with experimental results shown in Fig. 10.18. It is seen that neither the periodicity of the array nor the incident angle of the EM wave has any noticeable effect on the positions of the EOT peaks.

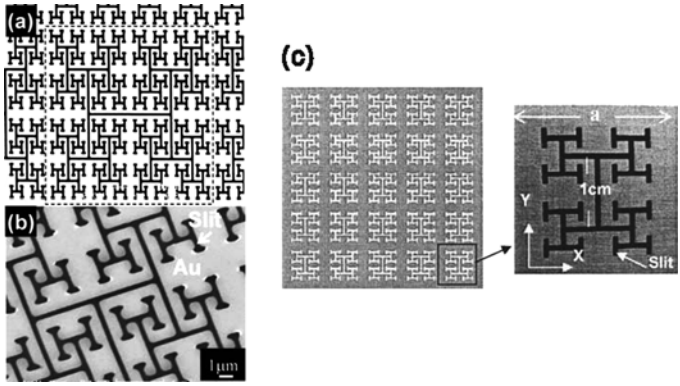


**Fig. 10.16** Pictures of fractal plasmonic metamaterial samples in IR frequency regime (**a**–**b**) and microwave frequency regime (**c**). Geometrical parameters: (**a**–**b**) The dimension of the whole sample is $15\times15$ mm$^2$, which is composed of periodically replicated fractal units ($55.6 \times 55.6\,\mu$m$^2$ with nine fractal levels). The slits are 0.5 μm wide and the longest line measuring 27.8 μm. (**c**) A total of 25 fractal slit units were made on a $12 \times 12$ cm$^2$ steel plate. The unit cell of the array consists of a 5-level fractal, the width of each slit is 0.8 mm, and the longest slit is 1 cm. (**a**–**b**) Reproduced from Ref. [48] with the permission of American Institute of Physics. (**c**) Reproduced from Ref. [49] with the permission of American Physical Society.

Similar EOT phenomena were observed with the IR samples [48]. Figure 10.19(a) shows the transmission (curve a), reflection (curve b), and relative emission (curve c) of the sample at normal incidence. For each IR fractal sample, the emission spectra were taken from a gray body (reflectivity <5%) $E_B$, the sample $E_S$, and a gold film (reflectivity = 98%) $E_G$, all heated to 150°C. The relative emission of the sample was then determined by $(E_S - E_G)/(E_B - E_G)$. For the transmission spectrum, there are two EOT bands entered at 7.5 and 11.5 μm, respectively, with a maximum transmission of about 36%, with $\mathbf{E}||\hat{x}$ polarization. Since the bare silicon substrate was measured to have 40% transmission, the transmission of the fractal slit pattern alone could be significantly higher than 36%. Moreover, as shown in Fig. 10.19(b), there is almost no shift for the EOT center positions as the incident angle was varied from 0° to 45°, while maintaining the electric field to be perpendicular to the plane of incidence.

We note that the EOT phenomena reported here are quite different from those on a silver film with periodic subwavelength hole array [8]. In the latter case, the EOT peak frequencies strongly depend on the incident angles of the input waves, and the periodicity of the hole array, since the EOT is induced by couplings of incident wave with SPPs modulated by Bragg scatterings [8]. Here, the wavelength of the EOT band is much longer than periodicity owing to the subwavelength properties of a fractal shape [49, 48], and therefore, the conventional Bragg mechanism does not work. Initially, such EOT phenomena were successfully explained by the couplings of the incident propagating wave with the cut-off waveguide mode of the fractal-shaped hole [49, 48]. After considering the fractal plate as a plasmonic metamaterial with SPP properties depicted in Figs. 10.15(a, b),

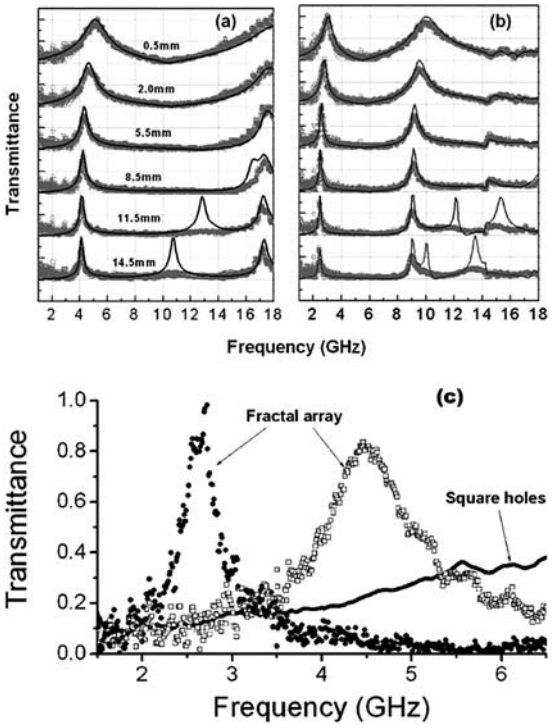


**Fig. 10.17** Microwave transmittance through the 5 × 5 fractal arrays of various thicknesses for (**a**) $\mathbf{E}||\hat{y}$ polarization and (**b**) $\mathbf{E}||\hat{x}$ polarization; the *dark gray* symbols and *dark solid lines* are the measured and simulated results, respectively. (**c**) Comparison of measured transmittances (of the two polarizations ) for the fractal array (symbols) with the square-hole array (*solid dark line*) on a 3-mm-thick metallic plate with the same periodicity. Reproduced from Ref. [49] with the permission of American Physical Society.

we found an additional mechanism to re-interpret these unusual EOT phenomena. We believe that such unusual EOT bands were not only induced by the waveguide cut-off resonance of a single fractal hole but also induced by the SPPs on the fractal plasmonic metamaterial [51]. The Bragg scatterings fold the SPP bands shown in Fig. 10.15 back to propagation-wave regime so that a plane incident wave can couple to such SPPs. Since the SPP bands are very flat, varying incidence angle has very little effect on the EOT frequency. On the other hand, since the plasmon frequency is essentially determined by a single fractal structure, varying the periodicity of the fractal array does not change the SPP characteristics of the plasmonic metamaterial so that the EOT frequency does not change either [51].

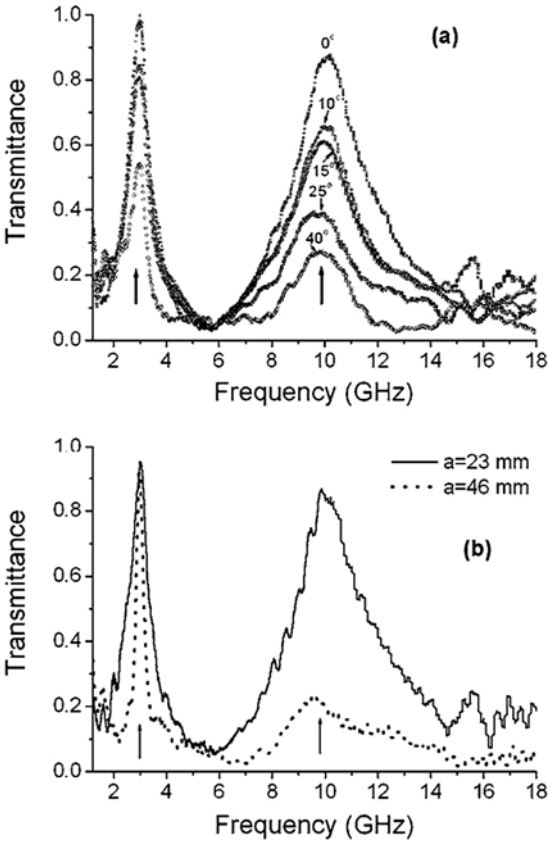


**Fig. 10.18** Variation of the measured transmission spectra as a function of (**a**) the incident angle $\theta$ and (**b**) periodicity $a$ with $\mathbf{E}||\hat{x}$ polarization. The calculated peak frequencies are shown as arrows. Reproduced from Ref. [49] with the permission of American Physical Society.

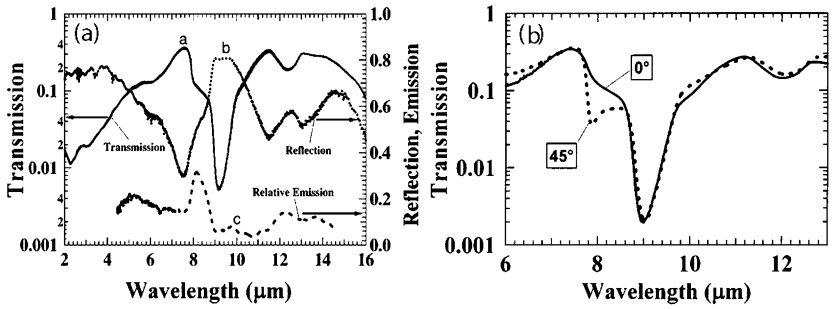


**Fig. 10.19** (**a**) Curves a, b, and c show the infrared transmission, reflection, and emission of the fractal sample with 0.5 μm slits on the gold film with $\mathbf{E}||\hat{x}$ polarization. (**b**) Transmission spectra measured with two different incident angles. Reproduced from Ref. [48] with the permission of American Institute of Physics.

### *10.4.3 Super Imaging with a Fractal Plasmonic Metamaterial as a Lens*

In this subsection, we introduce an important application for our fractal plasmonic metamaterials. It was shown both theoretically [26] and experimentally [10] that a silver film works as a lens to focus near-field light sources with subwavelength resolution. However, such a super lens does not function at a frequency other than silver's natural SPP frequency, and since silver only supports TM-polarized SPPs, the source has to be carefully designed to emit *p* waves only [10]. In what follows, we show that our structure can collect both *s* and *p* waves emitted from a source to form an all-dimensional subwavelength image and can work at any frequency with appropriate design [61].

We first performed microwave experiments to demonstrate this idea. We designed a plasmonic metamaterial [picture given in Fig. 10.20(a)] with unit cell shown schematically in the right panel of Fig. 10.20(a). The structure slightly differs from an ideal fractal after optimizations. We then fabricated a series of samples with different thicknesses $H$. In our imaging experiments, we put a dipole antenna on the source plane 1 mm above the lenses and place a receiver dipole antenna on an image plane 1 mm below the lenses to measure the field distributions of the images [59]. Both antennas are polarized along the *y* direction, connected to a vector network analyzer (Agilent 8722ES), and working at $f = 2.52$ GHz coinciding with the plasmon frequency of the designed lenses for *y* polarization [61]. When the source antenna is put at the unit-cell center, the images formed by two lenses with thicknesses $H$ =

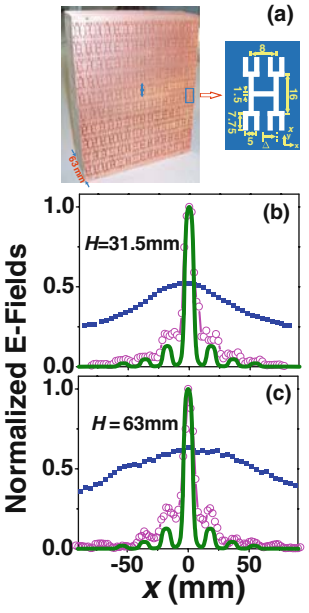


**Fig. 10.20** (**a**) Picture of a 63-mm-thick fractal plasmonic metamaterial and its unit cell structure (all lengths are measured in mm). Here the periodicity is 18 mm (32 mm) in *x*(*y*) direction. (**b**)–(**c**) Electric field distributions along the line perpendicular to the antenna on the image plane obtained by experiments (*open circles*) and FDTD simulations (*solid lines*) for different lens thickness, referenced by the experimental results measured without any lens (*solid squares*). Here, the maximum electric field is normalized to 1 in the presence of a lens. Ref. [15].

31.5 mm and $H = 63$ mm are depicted in Fig. 10.20(b) and (c) as open circles, which are in excellent agreements with the corresponding FDTD simulations (solid lines). Both measurements and FDTD results show that the images focused by our lenses are only $\sim$8 mm wide, which are $\sim \lambda/15$ recalling $\lambda \approx 119$ mm. Apparently, such a subwavelength resolution is obtainable only in presence of our lenses, since the images formed without lenses (solid squares) do not show any subwavelength resolutions at all. In addition, the field strength is enhanced when a lens is added. The subwavelength resolution and enhanced field strength are two important characteristics of the SPP [2]. In contrast to a flat silver-slab lens [26, 10], our lens is not laterally homogeneous, and thus we need to test the position dependence of the imaging quality. A detailed analysis based on microwave experiments and FDTD simulations [51] show that the overall resolution of our lens is bounded by the periodicity $a$ of the fractal array, which is $\sim\lambda/7$ in the present case.

Similar effects can be realized at IR frequencies using the fractal structure as shown in Fig. 10.14. As a comparison, we also adopted the rectangle-hole structure (same as that for Fig. 10.15) as a lens to focus light sources. We considered two types of source, i.e., two $x$-polarized dipoles working at 41 THz separated by 1μm either in $x$ direction (case 1) or in $y$ direction (case 2). For these two cases, we show the FDTD-calculated images formed without any lenses in Fig. 10.21(a) and (d), those with a 0.5-μm-thick rectangle-hole structure lens in Fig. 10.21(b) and (e), and those with our fractal structure lens in Fig. 10.21(c) and (f), correspondingly. Here, the source (image) plane is 0.1μm above (below) the lens [see the right panel in Fig. 10.14]. Since the sources are located within a subwavelength region (separation $1\mu\text{m} \ll \lambda = 7.3\,\mu\text{m}$), the two sources cannot be clearly distinguished without the lens [Fig. 10.21(a) and (d)]. With the rectangle-hole structure lens, case 1 can be distinguished [Fig. 10.21(b)] but the resolution along $y$ direction is not subwavelength. More seriously, this lens cannot distinguish case 2 at all [Fig. 10.21(e)]. These are all caused by the fact that this structure does not support TE-polarized SPPs (see Fig. 10.15). With our lens, however, two sources are clearly distinguishable in both cases, and the formed images are subwavelength along all directions, with much enhanced field strength (see the $E$-field scales in Fig. 10.21).

We now explore the underlying physics of the super lensing effect. Assume that the point source takes the simplest form $\mathbf{J}(\mathbf{r},t) = \hat{x}P_0\delta(\mathbf{r})e^{-i\omega t}$, we employ a standard Green's function method [54] to calculate the EM field distribution. We find the fields on the image plane as

$$E_x(x,y) = -\frac{i\mu_0 P_0}{8\pi^2}\int \frac{e^{ik_{||}(x\cos\phi+y\sin\phi)}e^{-ik_z d}}{k_z}[T^{TE}(k_{||})\sin^2\phi, + \frac{k_z^2}{k_0^2}T^{TM}(k_{||})\cos^2\phi]k_{||}dk_{||}d\phi \tag{10.3}$$

where $k_z = \sqrt{k_0^2 - k_{||}^2}$ with $k_0 = \omega/c$, $d$ is the source–image distance, and $T^{TE}(k_{||})$ and $T^{TM}(k_{||})$ are the transmission coefficients for TE and TM waves with $\mathbf{k} = k_z\hat{z} + \mathbf{k}_{||}$. To get an all-dimensional subwavelength resolution, we need to collect the evanescent components (with $k_{||} > k_0$) radiated from the point source with both TE and TM polarizations. When there is no lens, these evanescent components will

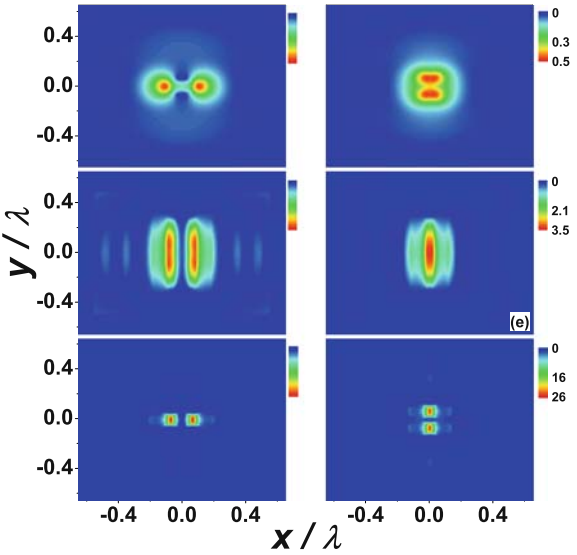


**Fig. 10.21** FDTD-calculated $E$-field patterns on the image planes obtained without a lens (**a**)+(**d**), with a rectangle-hole structure lens (**b**)+(**e**), and with our fractal structure lens (**c**)+(**f**). Here, the two $x$-polarized dipole sources are separated by 1μm in $x$ direction for (**a**), (**b**), and (**c**), and in $y$ direction for (**d**), (**e**), and (**f**). Both the rectangle-hole structure and the fractal structure are the same as those in Fig. 10.15. Ref. [15].

decay in amplitude and no subwavelength image can be formed on the image plane. However, in the presence of our lens, since the system possesses flat SPP bands right at this frequency [see Fig. 10.15(a) and (b)] for both TE and TM polarizations, those evanescent components with $k_0 < k_{||} < G$ can be transmitted across the lens, aided by the SPPs. The maximum $k$ vector of the SPP band sets a natural resolution limit, so that the highest resolution obtained by our plasmonic lens is $a$, which is much less than the working wavelength $\lambda_p$, a property unique to the fractal geometry.

Our mechanism is different from many others [25, 3]. In the mechanisms described in Refs. [25] and [3], the operation frequencies were dictated by the lens thickness, since the resonance frequency is determined by the rod length in [25] and Fabry–Perot (FP) resonances were employed to reduce reflections in [3]. In contrast, our working frequency is independent of the lens thickness, demonstrated both experimentally and theoretically in Fig. 10.20. Such a unique property makes our structure a good candidate for far-field imaging, since we can in principle make the image–source distance much larger than the working wavelength.

## 10.5 Other Applications of Fractal Photonic Metamaterials

In this section, we illustrate two additional applications of the photonic metamaterials constructed based on fractal geometry [58, 14].

### 10.5.1 Perfect EM Wave Tunneling Through Negative Permittivity Medium

It is well known that a slab of negative-$\varepsilon$ media (denoted as "B" layer) is opaque for EM waves, since the wave inside the medium is evanescent. However, if we attach two identical slabs with positive $\varepsilon$ (denoted as "A" layer) to the B layer to form a symmetrical ABA structure, we found that the entire system is perfectly transparent when certain conditions are met. Denote the permittivity of A layer as $\varepsilon_1$ and that of B layer as $\varepsilon_2$ and assume the two layers to have the same thickness $d$. Figure 10.22(a) shows the values of $\varepsilon_1$ yielding perfect transmission ($T = 1$) through the ABA structure, as a function of $d$ by setting $\varepsilon_2 = -2,000$. We find the existence of two solutions up to a critical thickness at which the solutions merge together and disappear abruptly. The first solution recovers the effective medium theory (EMT) value (i.e., satisfying $\bar{\varepsilon} = (2\varepsilon_1 + \varepsilon_2)/3 = 1$) in the limit of $k_0 d \to 0$. A $\varepsilon_2 \sim d$ phase diagram is shown in Fig. 10.22(b) for this EMT-derived solution $\varepsilon_1$, scaled by its corresponding EMT value. A phase boundary is found to separate the lower left region which supports the $T = 1$ solutions from the upper right one which dose not. The solution is closer to the EMT value in regions closer to the lower left corner where EMT is better applicable. However, $T = 1$ solutions survive when EMT is apparently no longer valid.

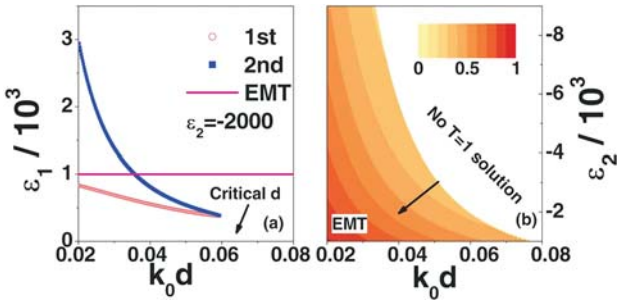


**Fig. 10.22** (**a**) $\varepsilon_1$ satisfying equation obtained by rigorous calculation for perfect transmission as functions of $d$. Horizontal (*magenta online*) line denotes the EMT solution $\varepsilon_{EMT} = 3/2 - \varepsilon_2/2$. (b) $\varepsilon_2 \sim d$ phase diagram depicting the value of $\varepsilon_1/\varepsilon_{EMT}$ for the EMT-derived perfect transmission solution. Reproduced from Ref. [58] with the permission of American Physical Society.

We performed microwave experiments to verify these theoretical predictions. We designed and fabricated two slabs of fractal electric metamaterials to model "A" layer and a 0.1-mm-thick metallic mesh to model "B" layer. The measured transmission spectra within 1–10 GHz for both A and B layers were shown in Fig. 10.23(a, b), which were in perfect agreement with the FDTD results. From the FDTD results, we found that the "B" layer can be modeled as a homogeneous slab with $\varepsilon_2 = 6.5 - 62^2/f^2$, while the "A" layer can be modeled as a homogenous slab with $\varepsilon_1 = 4.0 + 200/(4.59^2 - f^2)$. We found that a single "B" layer possesses

a large negative permittivity, while a single "A" layer possesses arbitrarily positive permittivity near resonance.

Figure 10.23(c–e) shows the transmission spectra of the ABA structure with different air gaps between layers A and B. When the gap is very small, FDTD simulations [lines in Fig. 10.23(c)] show two perfect transmission peaks at about 3.15 and 3.83 GHz. We note that neither layer A nor B is transparent within 3–4 GHz (see Fig. 10.23(a–b)), yet the combination of these opaque layers can lead to perfect transparency. At other frequencies, there exist strong reflections. When the gap becomes larger, the two peaks persist until a critical thickness (a little bit larger than 2 mm) is reached when they merge together [Fig. 10.23(d)]. If the gap is bigger than the critical thickness, no perfect transmission exists and the maximum transmittance is less than unity [Fig. 10.23(e)]. Experimental results were shown in the same figure as open circles. The overall agreement between experiments and theory is quite good for all three cases. In particular, near the critical thickness, experiments do show ∼100% transmissions at the frequency predicted by the theory. However, for the case of very small gap, the experimental peak is much broader than theoretical predictions and there is only one main peak instead of two, probably due to finite size effects and absorptions. We note that this type of transparency is accompanied by high magnetic fields and is robust against incidence angles, which is quite different from the SPP-aided EOT phenomenon [8].

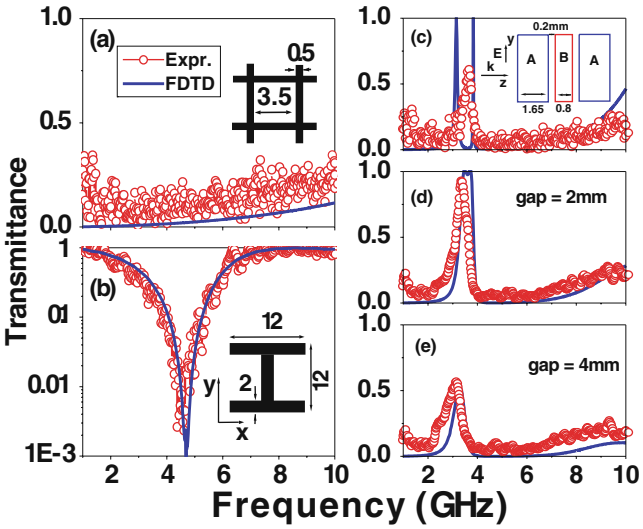


**Fig. 10.23** Measured (*circles*) and calculated (*lines*) transmission spectra through a single "B" layer (**a**) and a single "A" layer (**b**). The unit cell structures of "B" and "A" layers are shown in the insets with all lengths measured in mm, and please refer to Ref. [58] for more details of the structure. (c-e) Measured (*circles*) and calculated (*lines*) transmission spectra of the ABA structure with different air gaps between layers A and B. Reproduced from Ref. [58] with the permission of American Physical Society.

### 10.5.2 Manipulating Light Polarizations with Anisotropic Magnetic Metamaterials

We now describe another interesting application of our fractal metamaterials. In Section 10.3, we have demonstrated that the fractal magnetic metamaterial can be perfectly described as a double-layer system with the top layer being an anisotropic magnetic layer with a permeability tensor $\vec{\vec{\mu}}$. We then developed a theoretical approach to study the scatterings of light by such a double-layer reflector in a general situation as depicted in Fig. 10.24(a)) [14]. The theoretical calculations showed that the polarization state of the incident wave can be efficiently manipulated by such a double-layer reflector. In particular, a linearly polarized light could convert its polarization completely to the cross direction after reflection under certain conditions [14].

Again, we designed and fabricated appropriate fractal magnetic metamaterial (with structure shown in Fig. 10.24(b)) and performed microwave experiments (with experimental setup schematically depicted in Fig. 10.24(c)) to verify these theoretical conjectures. Let us define a polarization conversion ratio (PCR), which measures

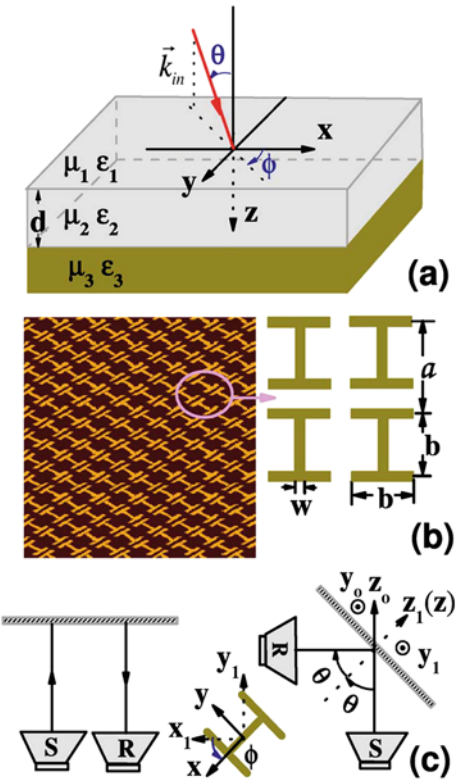


**Fig. 10.24** (**a**) Geometry of the model system studied here. (**b**) Image of part of the experimental sample. (**c**) A schematic picture of the experimental setup. Starting from the laboratory coordinate system $\{\hat{x}_0, \hat{y}_0, \hat{z}_0\}$, we first rotate the sample for an angle of $\theta$ with respect to the $\hat{y}_0 (= \hat{y}_1)$ axis , then for an angle of $\phi$ with respect to the $\hat{z}_0 (= \hat{z})$ axis, and finally arrive at the local coordinate system $\{\hat{x}, \hat{y}, \hat{z}\}$ attached to the sample. Reproduced from Ref. [14] with the permission of American Physical Society.

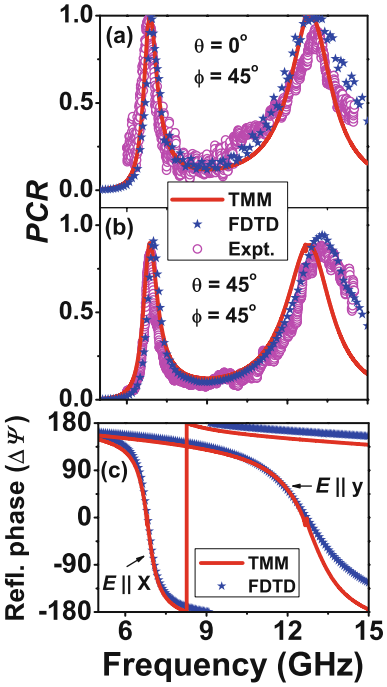


**Fig. 10.25** PCR as the functions of frequency, obtained by transfer matrix method (TMM) calculations on the model system (*solid lines*), FDTD simulations on realistic structures (*solid stars*), and experimental measurements (*open circles*). The incident direction is (**a**) $\theta = 0°, \phi = 45°$, and (**b**) $\theta = \phi = 45°$. (**c**) Frequency dependences of the reflection phase changes $\Delta\psi_{y(x)}$ on the metamaterial reflector surface for normally incident waves with polarizations $\mathbf{E}||\hat{x}$ and $\mathbf{E}||\hat{y}$, calculated by TMM on model system (solids lines) and FDTD simulations on realistic structures (solid stars). Reproduced from Ref. [14] with the permission of American Physical Society.

the energy portion transformed from the original polarization, assumed as the *s* polarization for definiteness, to the other polarization (*p* polarization) after reflection. The measured PCR spectra are shown as open circles in Fig. 10.25(a) for a normal incidence case with $\phi = 45°$ and in Fig. 10.25(b) for an oblique incidence case with $\theta = \phi = 45°$, which are in excellent agreements with both FDTD results in realistic structures (solid stars) and numerical calculations based on the double-layer model (solid lines) with effective medium and geometrical parameters $\mu_{xx} = 1 + \frac{70}{12.71^2 - f^2}, \mu_{yy} = 1 + \frac{22}{6.80^2 - f^2}, \mu_{zz} = 1, \varepsilon_2 = 1, d = 1.3$ mm. We find the PCR to be strongly enhanced around two frequencies, ∼12.7 and ∼6.8 GHz, corresponding precisely to the two magnetic resonances of the fractal magnetic metamaterial. In particular, for the normal incidence case studied in Fig. 10.25(a), both experiments and theory show that PCR ∼ 100% at the two resonance frequencies, indicating that a linearly polarized light converts its polarization to cross direction completely after the reflection.

The underlying physics lies on the anisotropic properties of the fractal magnetic metamaterial. Suppose the incident wave is described by $\mathbf{E}^i = (E_x\hat{x} + E_y\hat{y})e^{i(-\omega z/c + \omega t)}$, then after reflection by our system, the reflected wave is $\mathbf{E}^r = E_0(r_x\hat{x} + r_y\hat{y})e^{i(\omega z/c + \omega t)}$, where $r_x, and r_y$ are the reflection coefficients of the reflector for two linear polarizations. Our structure is always totally reflecting, i.e., $r_x = r_y \equiv 1$, since there is a metal plate on the back. However, the phase $\Delta\Psi$ of the reflection coefficient, defined as $r_{x(y)} = e^{i\Delta\psi_{x(y)}}$, strongly depends on the metamaterial parameters. The

calculated reflection phases ($\Delta\Psi_x, \Delta\Psi_y$) for the model system have been depicted in Fig. 10.25(c) as functions of frequency. Near each magnetic resonance, we found that one of $\mu_{xx}, \mu_{yy}$ becomes very large while another close to 1, and thus there must be a frequency where $\Delta\psi_x - \Delta\psi_y = \pm 180^\circ$ [see Fig. 10.25(c)] and thus $r_x/r_y = -1$. For the configuration studied in Fig. 10.25(a) with $E_x = E_y$, when the condition $r_x/r_y = -1$ is realized, the polarization direction of the reflected wave would be $-\hat{x} + \hat{y}$, which is perpendicular to that of the original wave. A complete polarization conversion is thus realized. It is easily expected that if we add more levels to the fractal structure, we will have more frequency bands inside which the light polarizations can be efficiently manipulated.

## 10.6 Conclusions

In summary, we have reviewed in this chapter our recent effort in utilizing a planar fractal geometry to design photonic metamaterials with rich EM properties and employing such metamaterials to realize many applications in practice. Specifically, we described how to design electric, magnetic, and plasmonic metamaterials employing the fractal concept and presented effective medium models for such metamaterials. In addition, we proposed several applications of these photonic metamaterials, which were all successfully verified by experiments and FDTD simulations. We believe that more physics and applications are to be explored for these fractal photonic metamaterials.

## References

1. Bao, Y., Zhang, B., Wu, Z., Si, J., Wang, M., Peng, R., Lu, X., Shao, J., Li, Z., Hao, X., Ming, N.: Surface-plasmon-enhanced transmission through metallic film perforated with fractal-featured aperture array. Appl. Phys. Lett. **90**, 251914 (2007)
2. Barnes, W.L., Dereux, A., Ebbesen, T.W.: Surface plasmon subwavelength optics. Nature **424**, 824–830 (2003)
3. Belov, P.A., Hao, Y., Sudhakaran, S.: Subwavelength microwave imaging using an array of parallel conducting wires as a lens. Phys. Rev. B **73**, 033108 (2006)
4. Bertolotti, M., Masciulli, P., Sibilia, C.: Spectral transmission properties of a self-similar optical Fabry-Perot resonator. Opt. Lett. **19**, 777–779 (1994)
5. Cai, W., Genov, D.A., Shalaev, V.M.: Superlens based on metal-dielectric composites. Phys. Rev. B **72**, 193101 (2005)
6. Chen, H., Ran, L., Huangfu, J., Zhang, X., Chen, K., Grzegorczyk, T.M., Kong, J.A.: Left-handed materials composed of only S-shaped resonators. Phys. Rev. E **70**, 057605 (2004)
7. Dolling, G., Enkrich, C., Wegener, M., Zhou, J.F., Soukoulis, C.M., Linden, S.: Cut-wire pairs and plate pairs as magnetic atoms for optical metamaterials. Opt. Lett. **30**, 3198–3200 (2005)
8. Ebbesen, T.W., Lezec, H.J., Ghaemi, H.F., Thio, T., Wolff, P.A.: Extraordinary optical transmission through sub-wavelength hole arrays. Nature **391**, 667–669 (1998)
9. El-Kady, I., Sigalas, M.M., Biswas, R., Ho, K.M., Soukoulis, C.M.: Metallic photonic crystals at optical wavelengths. Phys. Rev. B **62**, 15299–15302 (2000)

10. Fang, N., Lee, H., Sun, C., Zhang, X.: Sub-diffraction-limited optical imaging with a silver superlens. Science **308**, 534–537 (2005)
11. Farjadpour, A., Roundy, D., Rodriguez, A., Ibanescu, M., Bermel, P., Joannopoulos, J.D., Johnson, S.G., Burr, G.W.: Improving accuracy by subpixel smoothing in the finite-difference time domain. Opt. Lett. **31**, 2972–2974 (2006)
12. Garcia-Vidal, F.J., Martin-Moreno, L., Pendry, J.B.: Surfaces with holes in them: new plasmonic metamaterials. J. Opt. A: Pure Appl. Opt. **7**, S97–S101 (2005)
13. Hao, J.M., Zhou, L., Chan, C.T.: An effective-medium model for high-impedance surfaces. Appl. Phys. A **87**, 281–284 (2007)
14. Hao, J., Yuan, Y., Ran, L., Jiang, T., Kong, J.A., Chan, C.T., Zhou, L.: Manipulating electromagnetic wave polarizations by anisotropic metamaterials. Phys. Rev. Lett. **99**, 063908 (2007)
15. Huang, X., Ye, D., Xiao, S., Huangfu, J., Wang, Z., Ran, L., Zhou, L.: Fractal plasmonic metamaterials for subwavelength imaging. arXiv:0908.0201
16. Jackson, J.D.: Classical Electrodynamics. Wiley, New York (1975)
17. Klein, M.W., Enkrich, C., Wegener, M., Linden, S.: Second-harmonic generation from magnetic metamaterials. Science **313**, 502–504 (2006)
18. Landau, L.D., Lifshitz, E.M.: Electrodynamics of Continuous Media. Elsevier, New York (1984)
19. Lehman, M.: Fractal diffraction gratings built through rectangular domains. Opt. Commun. **195**, 11–26 (2001)
20. Leonhardt, U.: Optical conformal mapping. Science **312**, 1777–1780 (2006)
21. Lezec, H.J., Degiron, A., Devaux, E., Linke, R.A., Martin-Moreno, L., Garcia-Vidal, F.J., Ebbesen, T.W.: Beaming light from a subwavelength aperture. Science **297**, 820–822 (2002)
22. Li, J., Zhou, L., Chan, C.T., Sheng, P.: Photonic band gap from a stack of positive and negative index materials. Phys. Rev. Lett. **90**, 083901 (2003)
23. Liu, Y., Bartal, G., Genov, D.A., Zhang, X.: Subwavelength discrete solitons in nonlinear metamaterials. Phys. Rev. Lett. **99**, 153901 (2007)
24. Miyamoto, Y., Kanaoka, H., Kirihara, S.: Terahertz wave localization at a three-dimensional ceramic fractal cavity in photonic crystals. J. Appl. Phys. **103**, 103106 (2008)
25. Ono, A., Kato, J., Kawata, S.: Subwavelength optical imaging through a metallic nanorod array. Phys. Rev. Lett. **95**, 267407 (2005).
26. Pendry, J.B.: Negative refraction makes a perfect lens. Phys. Rev. Lett. **85**, 3966–3969 (2000)
27. Pendry, J.B., Holden, A.J., Robbins, D.J., Stewart, W.J.: Magnetism from conductors and enhanced nonlinear phenomena. IEEE Trans. Microw. Theory Tech. **47**, 2075–2084 (1999)
28. Pendry, J.B., Holden, A.J., Stewart, W.J., Youngs, I.: Extremely low frequency plasmons in metallic mesostructures. Phys. Rev. Lett. **76**, 4773–4776 (1996)
29. Pendry, J.B., Martin-Moreno, L., Garcia-Vidal, F.J.: Mimicking surface plasmons with structured surfaces. Science **305**, 847–848 (2004)
30. Pendry, J.B., Schurig, D., Smith, D.R.: Controlling electromagnetic fields. Science **312**, 1780–1782 (2006)
31. Podolskiy, V.A., Sarychev, A.K., Shalaev, V.M.: Plasmon modes and negative refraction in metal nanowire composites. Opt. Express **11**, 735–745 (2003)
32. Porto, J.A., Garcia-Vidal, F.J., Pendry, J.B.: Transmission resonances on metallic gratings with very narrow slits. Phys. Rev. Lett. **83**, 2845–2848 (1999)
33. Puente-Baliarda, C., Romeu, J., Pous, R., Cardama, A.: On the behavior of the Sierpinski multiband fractal antenna. IEEE Trans. Antenn. Propagat. **46**, 517–524 (1998)
34. Raether, H.: Surface Plasmons (ed. G. Hohler). Springer, Berlin (1988)
35. Rivas, J.G., Schotsch, C., Bolivar, P.H., Kurz, H.: Enhanced transmission of THz radiation through subwavelength holes. Phys. Rev. B **68**, 201306 (2003)
36. Rogacheva, A.V., Fedotov, V.A., Schwanecke, A.S., Zheludev, N.I.: Giant gyrotropy due to electromagnetic-field coupling in a bilayered chiral structure. Phys. Rev. Lett. **97**, 177401 (2006)
37. Sakoda, K.: Electromagnetic eigenmodes of a three-dimensional photonic fractal. Phys. Rev. B **72**, 184201 (2005)

38. Schurig, D., Mock, J.J., Justice, B.J., Cummer, S.A., Pendry, J.B., Starr, A.F., Smith, D.R.: Metamaterial electromagnetic cloak at microwave frequencies. Science **314**, 977–980 (2006)
39. Shadrivov, I.V., Sukhorukov, A.A., Kivshar, Y.S.: Complete band gaps in one-dimensional left-handed periodic structures. Phys. Rev. Lett. **95**, 193903 (2005)
40. Shelby, R.A., Smith, D.R., Schultz, S.: Experimental verification of a negative index of refraction. Science **292**, 77–79 (2001)
41. Shin, Y., So, J., Jang, K., Won, J., Srivastava, A., Park, G.: Evanescent tunneling of an effective surface plasmon excited by convection electrons. Phys. Rev. Lett. **99**, 147402 (2007)
42. Sievenpiper, D., Zhang, L., Broas, R.F.J., Alexopolous, N.G., Yablonovitch, E.: High-impedance electromagnetic surfaces with a forbidden frequency band. IEEE Trans. Microw. Theory Tech. **47**, 2059–2074 (1999)
43. Simovski, C.R., He, S.: Frequency range and explicit expressions for negative permittivity and permeability for an isotropic medium formed by a lattice of perfectly conducting $\Omega$ particles. Phys. Lett. A **311**, 254–263 (2003)
44. Sun, S., Huang, X., Zhou, L.: Two-dimensional complete photonic gaps from layered periodic structures containing anisotropic left-handed metamaterials. Phys. Rev. E **75**, 066602 (2007)
45. Sun, X., Jaggard, D.L.: Wave interactions with generalized Cantor bar fractal multilayers. J. Appl. Phys. **70**, 2500–2507 (1991)
46. Takeda, M.W., Kirihara, S., Miyamoto, Y., Sakoda, K., Honda, K.: Localization of electromagnetic waves in three-dimensional fractal cavities. Phys. Rev. Lett. **92**, 093902 (2004)
47. Veselago, V.G.: The electrodynamics of substances with simultaneously negative values of $\varepsilon$ and $\mu$. Sov. Phys. Usp. **10**, 509–514 (1968)
48. Wen, W., Yang, Z., Xu, G., Chen, Y., Zhou, L., Ge, W., Chan, C.T., Sheng, P.: Infrared pass-bands from fractal slit patterns on a metal plate. Appl. Phys. Lett. **83**, 2106–2108 (2003)
49. Wen, W., Zhou, L., Hou, B., Chan, C.T., Sheng, P.: Resonant transmission of microwaves through subwavelength fractal slits in a metallic plate. Phys. Rev. B **72**, 153406 (2005)
50. Wen, W., Zhou, L., Li, J., Ge, W., Chan, C.T., Sheng, P.: Subwavelength photonic band gaps from planar fractals. Phys. Rev. Lett. **89**, 223901 (2002)
51. Xiao, S., Huang, X., Zhou, L., unpublished.
52. Yen, T.J., Padilla, W.J., Fang, N., Vier, D.C., Smith, D.R., Pendry, J.B., Basov, D.N., Zhang, X.: Terahertz magnetic response from artificial materials. Science **303**, 1494–1496 (2004)
53. Zharov, A.A., Shadrivov, I.V., Kivshar, Y.S.: Nonlinear properties of left-handed metamaterials. Phys. Rev. Lett. **91**, 037401 (2003)
54. Zhou, L., Chan, C.T.: Relaxation mechanisms in three-dimensional metamaterial lens focusing. Opt. Lett. **30**, 1812–1814 (2005)
55. Zhou, L., Chan, C.T., Sheng, P.: Theoretical studies on the transmission and reflection properties of metallic planar fractals. J. Phys. D: Appl. Phys. **37**, 368–373 (2004)
56. Zhou, L., Wen, W., Chan, C.T., Sheng, P.: Reflectivity of planar metallic fractal patterns. Appl. Phys. Lett. **82**, 1012–1014 (2003)
57. Zhou, L., Wen,W., Chan, C.T., Sheng, P.: Multiband subwavelength magnetic reflectors based on fractals. Appl. Phys. Lett. **83**, 3257–3259 (2003)
58. Zhou, L., Wen, W., Chan, C.T., Sheng, P.: Electromagnetic-wave tunneling through negative-permittivity media with high magnetic fields. Phys. Rev. Lett. **94**, 243905 (2005)
59. In our experiments, we only measured the one-dimensional field distributions along the line perpendicular to the antenna on the image planes.
60. Simulations were performed using the software package CONCERTO, developed by Vector Fields Limited, England, 2001.
61. We note that the imaging functionality of the present lens depends on the electric polarization of the source.

# Chapter 11
# Magnetic Plasmon Modes Introduced by the Coupling Effect in Metamaterials

H. Liu, Y. M. Liu, T. Li, S. M. Wang, S. N. Zhu and X. Zhang

**Abstract** Magnetic metamaterials consist of magnetic resonators smaller in size than their excitation wavelengths. Their unique electromagnetic properties were characterized by the effective media theory at the early stage. However, the effective media model does not take into account the interactions between magnetic elements; thus, the effective properties of bulk metamaterials are the result of the "averaged effect" of many uncoupled resonators. In recent years, it has been shown that the interaction between magnetic resonators could lead to some novel phenomena and interesting applications that do not exist in conventional uncoupled metamaterials. In this chapter, we will give a review of recent developments in magnetic plasmonics arising from the coupling effect in metamaterials. For the system composed of several identical magnetic resonators, the coupling between these units produces multiple discrete resonance modes due to hybridization. In the case of a system comprising an infinite number of magnetic elements, these multiple discrete resonances can be extended to form a continuous frequency band by strong coupling. This kind of broadband and tunable magnetic metamaterial may have interesting applications. Many novel metamaterials and nanophotonic devices could be developed from coupled resonator systems in the future.

**Key words:** Metamaterial, magnetic plasmon, polariton, magneto-inductive wave, subwavelength waveguide, stereometamaterial, hybridization effect, average effect, coupling effect, optical activity, split-ring resonator, fishnet, slit-hole resonator.

H. Liu[1*], Y. M. Liu[2], T. Li[1], S. M. Wang[1], S. N. Zhu[1] and X. Zhang[2,3]
[1]Department of Physics, Nanjing University, Nanjing 210093, People's Republic of China.
[2]Nanoscale Science and Engineering Center, University of California, 5130 Etcheverry Hall, Berkeley, California 94720-1740, USA.
[3]Materials Sciences Division, Lawrence Berkeley National Laboratory, 1 Cycletron Road, Berkeley, CA 94720, USA.
*e-mail: liuhui@nju.edu.cn
*URL: http://dsl.nju.edu.cn/dslweb/images/plasmonics-MPP.htm

T.J. Cui et al. (eds.), *Metamaterials*, DOI 10.1007/978-1-4419-0573-4_11,

## 11.1 Introduction

All classical electromagnetic (EM) phenomena in various media are determined by the well-known Maxwell's equations. To describe the EM properties of a material, two important parameters are introduced, that is, electric permittivity $\varepsilon$ and magnetic permeability $\mu$. In principle, if the $\varepsilon$ and $\mu$ of materials are known, then the propagation of EM waves inside materials or the EM phenomena at the surface between two materials can be well predicted. For example, the refraction of an EM wave at the interface is described by Snell's law, $\sin\theta_i/\sin\theta_r = n_r/n_i$, which states that the relation between the incident angle ($\theta_i$) and the refracted angle ($\theta_r$) is determined by the refractive index, $n = \sqrt{\varepsilon\mu}$, of the two media involved.

Clearly, if we can modify $\varepsilon$ and $\mu$ artificially, then the propagation behavior of EM waves in the material can be manipulated as well. For instance, in 1967 when Veselago first theoretically studied the EM properties of a material with a negative refractive index (simultaneously negative $\varepsilon$ and $\mu$), he found that light will be refracted negatively at the interface between such a material and a normal positive index material [66]. This so-called negative refraction phenomenon does not violate the laws of physics, yet it challenges our physical perception and intuition. In such negative index media (NIM), a number of other surprising phenomena were also predicted, such as the reversed Doppler shift and Cerenkov radiation. However, Veselago's work was ignored for a long time because no such double negative materials (i.e., where both $\varepsilon < 0$ and $\mu < 0$) are obtainable in nature, making negative refraction seemingly impossible. Indeed, we are limited by the natural material properties. Most dielectrics only have positive permittivities. For most metals, $\varepsilon < 0$ can be met at optical range, and the plasma frequency can be moved downward into microwave range by replacing the bulk metal with a rodded medium [4, 45, 39], yet permeability is always positive. Negative $\mu$ is accessible in some ferromagnetic materials in the microwave region, but they are difficult to find above terahertz frequencies in the natural world.

In recent years, to achieve designable EM properties, especially negative $\mu$ at high frequencies, people have invented novel artificial materials known as metamaterials. The basic idea of a metamaterial is to design artificial elements that possess electric or magnetic responses to EM waves. Many such elements can work as artificial "atoms" to constitute a metamaterial "crystal." The geometric size of these atoms and the distances between them are much smaller than the wavelength of EM waves. Then, for an EM wave, the underlying metamaterial can be regarded as a continuous "effective medium." Correspondingly, the property of a metamaterial can be described by two effective parameters: effective permittivity $\varepsilon_{eff}$ and permeability $\mu_{eff}$. In 1999, Pendry first designed a metallic magnetic resonance element: a split-ring resonator (SRR) [38]. When an SRR is illuminated by light, the magnetic component of the EM wave induces the faradic current in this structure, giving rise to a magnetic dipole. Using SRRs as structure elements, Pendry constructed a new kind of magnetic metamaterial. The effective permeability, $\mu_{eff}$, of this metamaterial has the form

$$\mu_{eff} = 1 - \frac{F\omega^2}{\omega^2 - \omega_{mp}^2 + i\gamma\omega}, \tag{11.1}$$

where $F$ is the fractional volume of the cell occupied by the SRR. Equation (11.1) suggests that $\mu_{eff}$ follows a Drude–Lorentz resonance and $\mu_{eff}$ can be negative around the frequency $\omega_{mp}$ if the damping term $\gamma$ is not so large. Such plasmon resonance in SRR is caused by a magnetic field, so the corresponding resonance frequency, $\omega_{mp}$, here is called the magnetic plasmon (MP) frequency. Motivated by Pendry's work, D.R. Smith combined SRR and metallic wires to construct a metamaterial with simultaneously negative $\varepsilon_{eff}$ and $\mu_{eff}$ [55]. The negative refraction proposed by Veselago was finally experimentally verified in the microwave region [52].

One of the most important applications of NIMs is a superlens, which allows imaging resolution beyond the diffraction limit [7, 22, 35, 73, 74, 77]. Considering its significant applications in the visible region, increasing the MP frequency $\omega_{mp}$, to obtain negative refraction for visible light is a very valuable and challenging task. Given that $\omega_{mp}$ arises from an inductor–capacitor circuit (LC) resonance in SRRs and is determined by the geometric size of this structure, it can be increased by shrinking the size of the SRRs. In 2004, X. Zhang and colleagues fabricated a planar structure composed of SRRs. The size of the SRR was just a few micrometers and $\omega_{mp}$ was around 1 THz [75]. Immediately after X. Zhang's work, Soukoulis and colleagues fabricated an SRR sample with a unit cell of several hundred nanometers and $\omega_{mp}$ was raised to 100 THz [21]. Another result is obtained around 1.5 μm, which is the telecommunication wavelength in the infrared range [6]. As the structure of an SRR is so complex, it is very difficult to decrease its geometric size any further with the existing nanofabrication technique. To obtain MP resonance at higher frequencies, people began to seek other simple MP structures. In fact, inductive coupled rod pairs are very simple structures that Zheludev and colleagues proposed as constituting chiral metamaterials [57]. Shalaev and colleagues found that such nanorod pairs could also be used to produce MP resonance and negative refraction at the optical communication wavelength of 1.5 μm [41, 50]. Almost at the same time, S. Zhang et al. proposed a double-fishnet structure to obtain negative refraction at about 2 μm [76]. Although Shalaev and S. Zhang verified that their structures possessed a negative refraction index by measuring the phase difference of the transmitted waves, they could not directly observe the negative refraction in their monolayer metamaterial structures. Until quite recently, direct negative refraction was observed by X. Zhang and colleagues in the three-dimensional bulk metamaterials of nanowires [68] and fishnet structures [65] in the optical region. Besides the aforementioned important works on negative refraction, many other studies from recent years provide a good introduction to the rapid progress that has taken place in this field [36, 37, 49, 56, 67]. In addition to negative refractions, MP resonance has also been applied to another metamaterial that has attracted considerable attention, namely cloaking materials [40, 47, 28].

Although the invention of the metamaterial has stimulated the interest of many researchers and its various applications have been widely discussed, the basic design

idea is very simple: composing effective media from many small structured elements and controlling its artificial EM properties. According to the effective media model, the coupling interactions between the elements in metamaterials are somewhat ignored; therefore, the effective properties of metamaterials can be viewed as the "averaged effect" of the resonance property of the individual elements. However, the coupling interaction between elements should always exist when they are arranged into metamaterials. Sometimes, especially when the elements are very close, this coupling effect is not negligible and will have a substantial effect on the metamaterial's properties. Under such circumstances, the uncoupling model is no longer valid, and the effective properties of the metamaterial cannot be regarded as the outcome of the averaged effect of a single element (see Fig. 11.1). Many new questions arise: How do we model the coupling in metamaterials? What new phenomena will be introduced by this coupling effect? Can we find any new interesting applications in these coupled systems?

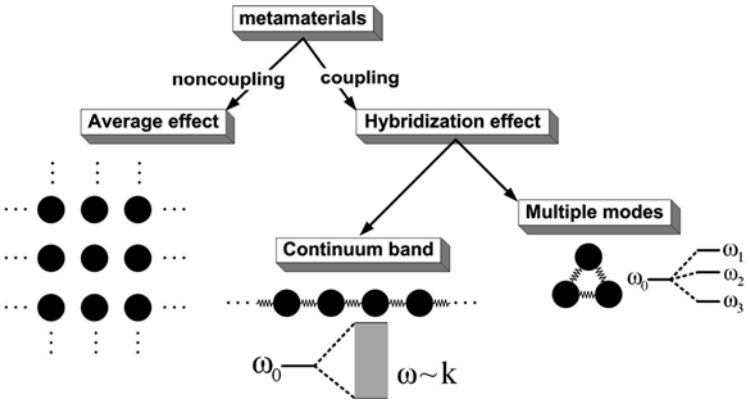


**Fig. 11.1** "Average effect" and "hybridization effect" in metamaterials.

Magnetic metamaterials consisting of resonance elements with a strong coupling interaction have already developed into an important branch of metamaterial research. The "hybridization effect" caused by these coupling interactions between magnetic resonators in metamaterials is attracting increased interest. Some multiple hybrid modes or continuum collective MP modes were found in magnetic metamaterials after including this hybridization effect (see Fig. 11.1). Quite a number of papers have already reported this new kind of coupled MP resonance modes. Various novel phenomena and properties have been explored and these have led to many new interesting applications that do not exist in uncoupled metamaterials. In this chapter, we will give an overall introduction to these recent developments in MP modes that were introduced by the coupling effect in metamaterials. First, the hybridization effect of MP resonance in two coupled magnetic resonators is presented in Section 11.2. Second, we will describe the MP propagation waves in a one-dimensional chain of magnetic resonators in Section 11.3. Then, the excitation

of MP in a two-dimensional coupled system will be discussed in Section 11.4. In the last section, an outlook will be presented to predict possible future developments of coupled MP modes in metamaterials.

## 11.2 Hybrid Magnetic Plasmon Modes in Two Coupled Magnetic Resonators

In 2003 [43], Halas and colleagues introduced a hybridization model to describe the plasmon response of complex nanostructures. It was shown that the resonance modes of a complex metallic nanosized system could be understood as the interaction or hybridization result of the elementary geometries. The hybridization principle provides a simple conceptual approach to designing nanostructures with desired plasmon resonances. In their following work, this method was successfully used to describe the plasmon resonance in a nanoshell [42], nanoparticle dimers [32], nanoshell dimers [2, 34], and nanoparticles near metallic surfaces [33].

In fact, the hybridization model could also be applied to deal with the EM wave response of metamaterials that comprise many resonance elements. SRR is the best-known magnetic "atom" of metamaterials. Therefore, the investigation of how SRRs interact with each other is both a fundamental and typical study. Apparently, a magnetic dimer (MD) made of two SRRs is the simplest system with which to study the coupling effect [22, 20]. In Fig. 11.2, we present the general configuration of an MD, composed of two identical SRRs separated by a finite distance, $D$. To study the magnetic response of this MD, an MP hybridization model was established. In our approach, we use the Lagrangian formalism, first calculating the magnetic energy of a single SRR and later expanding the theory for a system of two coupled SRRs. For simplicity, in the analysis we consider each SRR an ideal LC circuit composed of a magnetic loop (the metal ring) with inductance $L$ and a capacitor with capacitance

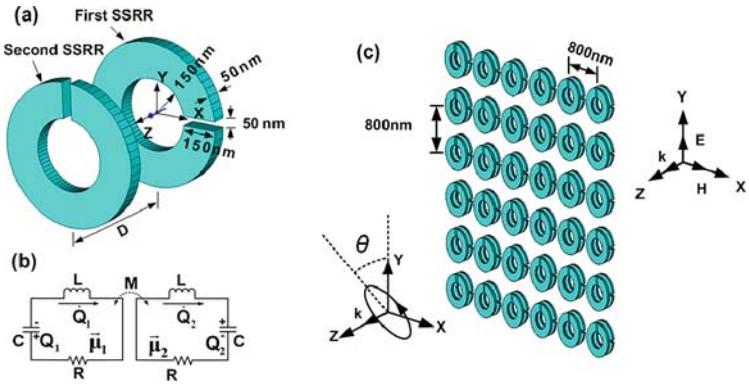


**Fig. 11.2** (**a**) Structure of a magnetic dimer; (**b**) equivalent LC circuit; and (**c**) metamaterial made of identical dimer elements. Reprinted with permission from [22].

$C$ (corresponding to the gap). The resonance frequency of the structure is given by $\omega_0 = 1/\sqrt{LC}$ and the magnetic moment of the SRR originates from the oscillatory behavior of the currents induced in the resonator. If we define the total charge, $Q$, accumulated in the slit as a generalized coordinate, the Lagrangian corresponding to a single SRR is written as $\Im = L\dot{Q}^2/2 - Q^2/(2C)$, where $\dot{Q}$ is the induced current, $L\dot{Q}^2/2$ relates to the kinetic energy of the oscillations, and $Q^2/(2C) = L\omega_0^2 Q^2/2$ is the electrostatic energy stored in the SRR's gap. Similarly, the Lagrangian that describes the MD is a sum of the individual SRR contributions with an additional interaction term

$$\Im = \frac{L}{2}(\dot{Q}_1^2 - \omega_0^2 Q_1^2) + \frac{L}{2}(\dot{Q}_2^2 - \omega_0^2 Q_2^2) + M\dot{Q}_1\dot{Q}_2, \tag{11.2}$$

where $Q_i$ $(i = 1,\ 2)$ are the oscillatory charges and $M$ is the mutual inductance. By substituting $\Im$ in the Euler–Lagrange equations

$$\frac{d}{dt}\left(\frac{\partial \Im}{\partial \dot{Q}_i}\right) - \frac{\partial \Im}{\partial Q_i} = 0 \quad (i = 1,\ 2), \tag{11.3}$$

it is straightforward to obtain the magnetic plasmon eigenfrequencies, $\omega_{+/-} = \omega_0/\sqrt{1 \mp \kappa}$, where $\kappa = M/L$ is a coupling coefficient. The high energy or antibonding mode, $|\omega_+\rangle$, is characterized by antisymmetric charge distribution $(Q_1 = -Q_2)$, while the opposite is true for the bonding or low energy $|\omega_-\rangle$ magnetic resonance $(Q_1 = Q_2)$. Naturally, the frequency split $\Delta\omega = \omega_+ - \omega_- \approx \kappa\omega_0$ is proportional to the coupling strength.

The Lagrangian (hybridization) formalism provides a phenomenological picture of the electromagnetic response of the system. To study quantitatively the resonance behavior, and check the model, we rely on FDTD numerical simulations using a commercial software package, CST Microwave Studio (Computer Simulation Technology GmbH, Darmstadt, Germany). In the calculations, the metal permittivity is given by the Drude model: $\varepsilon(\omega) = 1 - \omega_p^2/(\omega^2 + i\omega_\tau\omega)$, where $\omega_p$ is the bulk plasma frequency and $\omega_\tau$ is the relaxation rate. For gold, the characteristic frequencies, fitted to experimental data, are $\omega_p = 1.37 \times 10^4$ THz and $\omega_\tau = 40.84$ THz.

For excitation of the magnetic dimer (MD) we use a plane wave, with $\vec{E}$ field polarized in the $y$-direction and $\vec{H}$ field in the $x$-direction, as shown in Fig. 11.2(a). For a normal incidence, the magnetic field vector is in the plane of the SRRs and direct magnetic response is unattainable. However, the electric component of the incident field excites an electric response in the slit and thus a magnetic field could be indirectly induced [21]. To study the local magnetic field we position probes at the center of the first SRR and vary the incident frequency. The recorded magnetic response is shown in Fig. 11.2 where the distance between the resonators is set at $D = 250$ nm. As expected, two distinctive resonances with eigenfrequencies $\omega_-$= 61.6 THz and $\omega_+$= 73.3 THz are recorded. The magnetic response of the constituent SRR is also depicted, showing a fundamental resonance at $\omega_0$= 66.7 THz.

The hybridization of the magnetic response in the case of a dimer is mainly due to inductive coupling between the SRRs. If each SRR is regarded as a quasi-atom,

then the MD can be viewed as a hydrogen-like quasi-molecule with energy levels, $\omega_-$ and $\omega_+$, originating from the hybridization of the original (decoupled) state $\omega_0$. The strength of the inductive coupling depends strongly on the distance between the quasi-atoms and for the considered geometry is estimated as $\kappa \approx 0.17$. The specific nature of the MP eigenmodes is studied in Fig. 11.2 where the local magnetic field distributions are depicted for the low energy $\omega_-$ and high energy $\omega_+$ states, respectively. In accordance to the prediction based on the Lagrangian approach the SRRs oscillates in-phase for the bonding mode $|\omega_-\rangle$ and out of phase for the antibonding mode $|\omega_+\rangle$.

Since the mutual inductance $M$ decreases dramatically with distance, one should expect a strong change in the resonance frequencies $\omega_\pm$. This phenomenon is demonstrated in Fig. 11.3, where MP eigenfrequncies $\omega_\pm$ and the frequency change $\Delta\omega = \omega_+ - \omega_-$ are calculated. With decreasing separation between the SRR an increase in the frequency gap $\Delta\omega$ is observed. The opposite effect takes place at large distances where the magnetic response is decoupled. The specific profile of the frequency gap could be explained by estimating the self- and mutual inductance of the SRRs: $\Delta\omega \approx \omega_0\kappa = \omega_0 M/L \propto \int_0^\infty dk \cdot e^{-kD} J_1^2(kR)$ where $R$ is the SRR's radius [13]. For $D > 2R$, we can expand the integral in series and write $\Delta\omega \propto (R/D)^3 - 3(R/D)^5 + 9.38(R/D)^7$. As evident from Fig. 11.3(d), this approximated relationship, based on the hybridization method, fits the numerical data quite well.

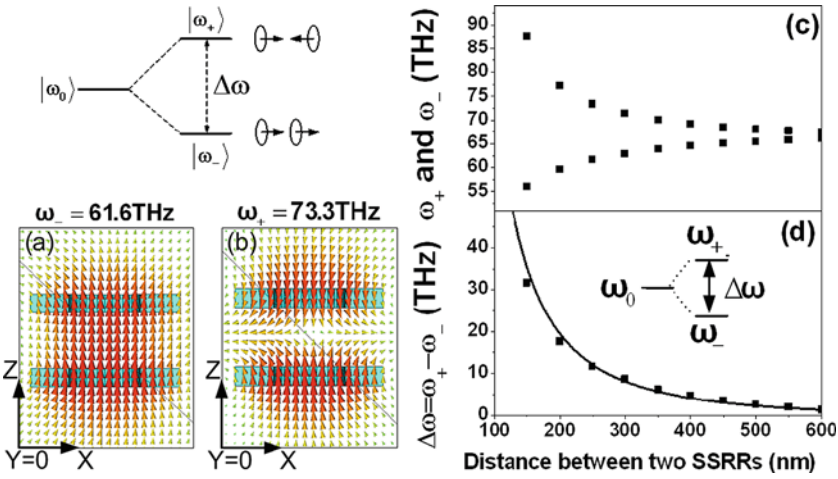


**Fig. 11.3** The local magnetic field profiles for the (**a**) bonding and (**b**) antibonding MP modes; The dependence of the resonance frequencies (**c**) and the frequency gap (**d**) on the distance between two SRRs. Reprinted with permission from [22].

It is important to mention that the SRR's size and shape, considered here, have been chosen in order to optimize the magnetic response and allow for a successful

nanofabrication. There are several ways to tune the MP properties of the structure, with geometrical modifications having the most significant effect on the MP resonances. For instance, scaling down the size of the resonator $R$ increases the resonance frequency $\omega_0 = 1/\sqrt{LC} \sim 1/R$, due to a linear increase of the inductance $L \sim R$ and capacitance $C \sim R$. However, the kinetic energy of the electrons in the metal is no longer negligible in the infrared range and results in saturation of the magnetic resonance frequency at about 400 THz for noble metals [79]. Another way to tune the resonance is to use different materials, both metals and insulators. For instance, encapsulating the MDs with high index materials causes red-shift of the magnetic resonances (for $D = 250$ nm and $\varepsilon = 2$, $\omega_- = 43.3$ THz and $\omega_+ = 51.5$ THz). However, our studies show that optimal magnetic dipole moment is achieved for silver–air or gold–air systems (due to the relatively low intrinsic loss) and a circular-shaped SRR.

Having determined the fundamental response of the proposed MD, next, we study the propagation property of EM wave in such a metamaterial composed of periodically arranged magnetic dimers (see Fig. 11.2(c)). Although the incident light is linearly polarized ($\vec{E} = E_y\hat{y}$), the transmission wave is found to acquire both $x$ and $y$ electric field components in the resonance frequency range and some phase difference between the two orthogonal components. This change in polarization and phase delay origins from the specific three-dimensional chiral arrangement of two SRRs (see Fig. 11.2(a)): one SRR is shifted a distance from the other and rotates 90°. The electric field in the slit of the first SRR is aligned along the $y$-axis, and thus a $y$ polarized incident wave is electrically coupled into the system. At resonance, strong magnetic interaction between the SRRs helps to transfer the energy from the front resonator to the back SRR. Since the electric field in the slit gap of the second SRR is along $\hat{x}$, the electric dipole radiation carries the same polarization. Thus the transmitted wave, detected in far field, is a superposition of $x$ and $y$ polarized light. According to the classic model developed by Born and Kuhn, two spatially separated coupled oscillators, with a chiral symmetry, will induce optical activity for an impinging EM wave. In our system, the hybridization of the MP states constitutes a new mechanism for achieving optical activity in the near-infrared range, thus opening new opportunities for designing novel type of chiral metamaterials.

This theoretical result was experimentally proven in the microwave range [20]. The propagation property of microwave through chiral metamaterial based on a magnetic dimer was studied experimentally. As predicted by the above theoretical model, two resonance peaks were obtained in the transmission spectrum, and they originated from the hybridization effect of magnetic resonance modes in this system. An optical activity was also observed in the transmission wave. Various elliptical polarization states appeared in the transmission, and the polarization state changed dramatically around the magnetic resonance frequency: the transmitted wave becomes elliptically polarized with the major polarization axis almost perpendicular to that of the linear incident wave, and the ellipse is very compressed though it is not exactly the linear polarization. This coupled magnetic dimer system provides doable method of the designing of the tunable optically active medium and devices.

Recently, the coupling mechanism between two stacked SRRs was found not only to be determined by the distance between the two elements but also to depend on the relative twist angle, $\varphi$ [26]. The Lagrangian of such a twisted structure is a combination of two individual SRRs with the additional electric and magnetic interaction terms

$$\Im = \frac{L}{2}(\dot{Q}_1^2 - \omega_0^2 Q_1^2) + \frac{L}{2}(\dot{Q}_2^2 - \omega_0^2 Q_2^2) + M_H \dot{Q}_1 \dot{Q}_2 - M_E \omega_0^2 Q_1 Q_2 \cdot \left(\cos\phi - \alpha \cdot \cos^2\phi + \beta \cdot \cos^4\phi\right). \tag{11.4}$$

In fact, magnetic and electric coupling coexist in the system when $\varphi \neq 90°,\ 270°$. When $\varphi$ is changed, although magnetic coupling maintains the same value, electric coupling will change significantly (see Fig. 11.4). Magnetic and electric interactions contribute oppositely and positively for $\varphi = 0°$ and 180° twisted structures, respectively. By solving the Euler–Lagrange equations, the eigenfrequencies of these coupled systems can be obtained as

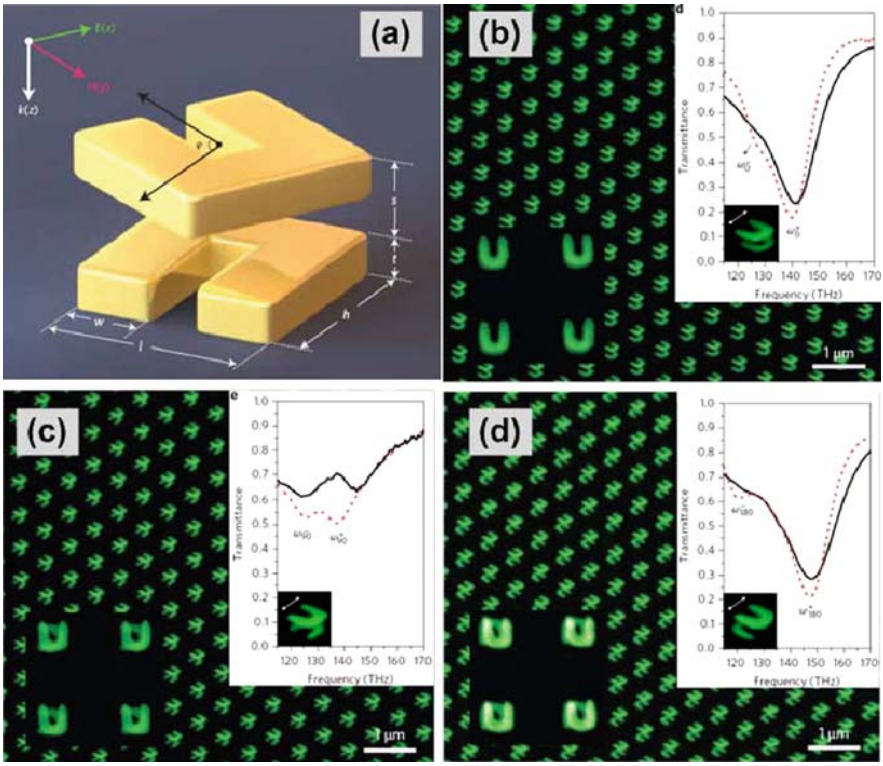


**Fig. 11.4** (**a**) Schematic of the stereo-SRR dimer metamaterials twist angle; experimental transmittance spectra for the 0° (**b**), 90° (**c**), and 180° (**d**) twisted SRR dimer metamaterials. The *black* and *dotted curves* represent the experimental and simulated results, respectively. Reprinted with permission from [26].

$$\omega_{\pm} = \omega_0 \cdot \sqrt{\frac{1 \mp \kappa_E \cdot \left(\cos\phi - \alpha \cdot \cos^2\phi + \beta \cdot \cos^4\phi\right)}{1 \mp \kappa_H}}, \tag{11.5}$$

where $\kappa_E = M_E/L$ and $\kappa_H = M_H/L$ are the coefficients of the overall electric and magnetic interactions, respectively.

These results lead to an exciting new concept of plasmonic structures: stereometamaterials. The new concept of stereometamaterials adds a significant degree of freedom through the interplay of electric and magnetic interactions, and tremendously enhances the versatility of nanophotonic structures. Stereometamaterials allow us to use higher order electric multipolar as well as magnetic interactions, which can be nearly as large as the electric dipolar interaction. This is completely different from molecules, where electric dipolar interaction is the essential contribution determining optical properties. It will also be interesting to study the geometry and distance dependence of the different coupling effects. Our concept can be extended to more complex artificial molecules, such as stereotrimers, stereoquadrumers. The tunability of the resonant behavior of these new artificial materials by altering the spatial arrangement of their constituents offers great flexibility for exploring useful metamaterial applications, such as chiral structures with negative refraction, invisibility cloaks, and magneto-optically active materials. Stereometamaterials open up the potential for optical polarization control, which so far has been dominated by stereoisomers and liquid crystals. Stereometamaterials might also serve as artificial nanosystems for emulating the optical properties of complex biomolecules, such as double-helix DNA chiral proteins and drug enzymes, which have profound application potentials in biophotonics, pharmacology, as well as diagnostics.

In another work by Giessen and colleagues, the hybridization effect of an MP was also observed in four stacked SRRs [25]. In addition to identical resonators, hybrid MP modes were found in coupled structures composed of different resonators, including SRR pairs [11], cut-wire pairs [27], tri-rods [69], and nanosandwiches in defective photonic crystals [29]. These hybrid MP modes could lead to some new interesting and useful properties, such as optical activity [22, 20] and omni-directional broadband negative refraction [69].

## 11.3 Magnetic Plasmon Modes in One-Dimensional Chain of Resonators

In the above section, we presented the hybridization effect of MP modes among several coupled magnetic resonators. In this section, we will generalize the theoretical model to one-dimensional infinite chains of coupled magnetic resonators. We will show that the collective excitation of infinite magnetic atoms in metamaterials can induce a new kind of wave, namely an MP wave.

Linear chains of closely spaced metal nanoparticles have been intensely studied in recent years. Due to the strong near-field coupling interaction among these

nanoparticles, a coupled electric plasmon (EP) propagation mode can be established in this chain and can be used to transport EM energy in a transverse dimension that is considerably smaller than the corresponding wavelength of illumination [3, 15, 30, 44, 53, 72]. As this system can overcome the diffractive limit, it can function as a novel kind of integrated subwavelength waveguide.

According to the classic electrodynamics theory, the radiation loss of a magnetic dipole is substantially lower than the radiation of an electric dipole of a similar size [13]. Thus, using MP to guide EM energy over long distances has great potential for direct application in novel subdiffraction-limited transmission lines without significant radiation losses.

Indeed, MP resonance has been already applied to a one-dimensional subwavelength waveguide in the microwave range [10, 51, 61]. Shamonina et al. proposed a propagation of waves supported by capacitively loaded loops using a circuit model in which each loop is coupled magnetically to a number of other loops [51]. Since the coupling is due to induced voltages, the waves are referred to as magneto-inductive waves (MI). The one-dimensional axial structure of the designed capacitively loaded loops is shown in Fig. 11.5(a) and the calculated dispersion curves for the wave vector $k$ and attenuation coefficient $\alpha$ are given in Fig. 11.5(b–c). MI waves propagating on such one-dimensional lines may exhibit both forward and backward waves depending on whether the loops are arranged in an axial or planar configuration. Moreover, the band broadening could be obtained due to the excitation of

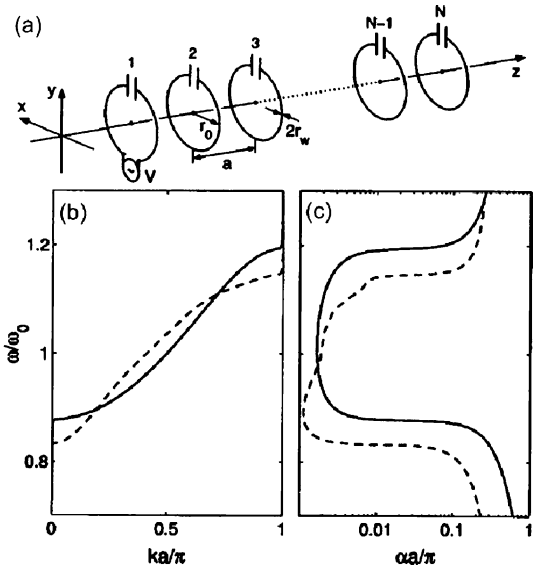


**Fig. 11.5** (**a**) One-dimensional axial structure of capacitively loaded loops. (**b**) Dispersion curves for the one-dimensional axial structure: nearest-neighbor interactions only (*solid line*), interactions between five neighbors (*dashed line*). Reprinted with permission from [51].

MI waves, and the bandwidth changes dramatically as we vary the coupling coefficient between the resonators [48]. A kind of polariton mode could be formed by the interaction between the electromagnetic and MI waves, resulting in a tenability of the range where $\mu$ becomes negative [61]. In a biperiodic chain of magnetic resonators, the dispersion of the MI wave will be split into two branches analogous to acoustic waves in solids, and this can be used to obtain specified dispersion properties [60, 58]. In addition to this kind of MI wave, electro-inductive (EI) waves were also reported in the microwave range [1]. Further, the coupling may be either of the magnetic or electric type, depending on the relative orientation of the resonators. This causes the coupling constant between resonators to become complex and leads to even more complicated dispersion [12]. Up to now, a series of microwave devices based on MI waves have been proposed, such as magneto-inductive waveguides [63], broadband phase shifters [31], parametric amplifiers [64], and pixel-to-pixel subwavelength imagers [9, 59].

However, in the optical range, the ohmic loss inside metallic structures is much higher than in the microwave range. The MI coupling between the elements is not strong enough to transfer the energy efficiently. In order to improve the properties of the guided MP wave, the exchange current interaction between two connected SRRs is proposed [23], which is much stronger than the corresponding MI coupling.

Figure 11.6(b) shows one infinite chain of SRRs constructed by connecting the unit elements (see Figure 11.6(a)) one by one. The magnetic dipole model can be applied to investigate this structure. If a magnetic dipole, $\mu_m$, is assigned to each resonator and only nearest-neighbor interactions are considered, then the Lagrangian and the dissipation function of the system can be written as

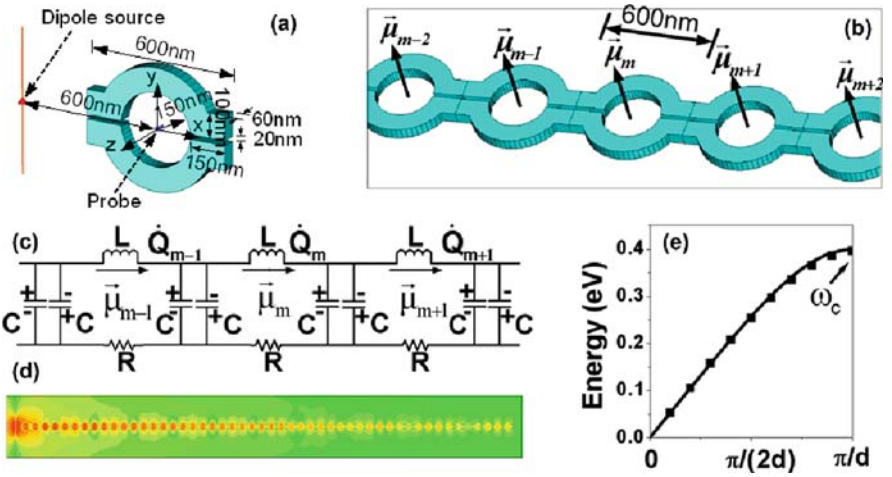


**Fig. 11.6** (**a**) Structure of a single SRR; (**b**) one-dimensional chain of SRRs; (**c**) equivalent circuit of the chain; (**d**) FDTD simulation of MP wave propagation along the chain; and (**e**) dispersion curve of the MP wave. Reprinted with permission from [23].

$$\begin{aligned}\Im &= \sum_m \left( \frac{1}{2} L \dot{q}_m^2 - \frac{1}{4C} (q_m - q_{m+1})^2 + M \dot{q}_m \dot{q}_{m+1} \right), \\ \Re &= \sum_m \frac{1}{2} \gamma \dot{q}_m^2.\end{aligned} \tag{11.6}$$

Substitution of (11.6) into the Euler–Lagrangian equations yields the equations of motion for the magnetic dipoles

$$\ddot{\mu}_m + \omega_0^2 \mu_m + \Gamma \dot{\mu}_m = \frac{1}{2} \kappa_1 \omega_0^2 (\mu_{m-1} + 2\mu_m + \mu_{m+1}) - \kappa_2 (\ddot{\mu}_{m-1} + \ddot{\mu}_{m+1}), \tag{11.7}$$

where $\kappa_1$ and $\kappa_2$ are the coefficients of the exchange current and MI interactions, respectively. The general solution of (11.7) corresponds to an attenuated MP wave: $\mu_m = \mu_0 \exp(-m\alpha d) \exp(\mathrm{i}\omega t - \mathrm{i}mkd)$, where $\omega$ and $k$ are the angular frequency and wave vector, respectively, $\alpha$ is the attenuation per unit length, and $d$ is the size of the SRR. By substituting $\mu_m(t)$ into (11.7) and working in a small damping approximation ($\alpha d \ll 1$), simplified relationships for the MP dispersion and attenuation are obtained:

$$\omega^2(k) = \omega_0^2 \frac{1 - \kappa_1 [1 + \cos(kd)]}{1 + 2\kappa_2 \cos(kd)}. \tag{11.8}$$

In Fig. 11.6(e), numerically and analytically estimated MP dispersion properties are depicted as dots and solid curves, respectively. In contrast to the electric plasmon polariton in a linear chain of nanosized metal particles [3, 15, 30, 44, 53, 72], where both transverse and longitudinal modes could exist, the magnetic plasmon is exclusively a transversal wave. It is manifested by a single dispersion curve (black solid line in Fig. 11.6(e)) which covers a broad frequency range $\omega \in (0,\ \omega_c)$, with a cut-off frequency $\hbar\omega_c \approx 0.4$ eV. On the other hand, if the SRRs interact only through the magneto-inductive force, the propagating band shrinks to a very narrow range of frequencies $\Delta\omega \cong 2\omega_0\kappa_2$ centered around $\omega_0$. Such relatively short bandwidths are characteristic for the electric plasmon and follows from the rapid fall of the magneto-inductive force with the distance.

Strong wave dissipation has been one of the major obstacles for utilization of surface plasmons in optical devices. The subdiffraction-sized MP transmission line, proposed in this work, promises a considerable improvement in the wave transmission as shown in Fig. 11.6(d). For most of the propagation band, $\alpha(\omega)$ stays constant and have relatively low value. For instance, at an incident frequency $\hbar\omega = 0.3$ eV, the MP attenuation coefficient is $\alpha = 0.65 \times 10^5$ m$^{-1}$ (signal attenuation 0.57 dB/μm), which gives a field decay length of 15.4 μm (3.7 free space wavelengths) or 25.7 unit cells. For comparison, the gold nanoparticle system presented in [30] manifests at $\omega = 2.4$ eV a field decay length of about 410 nm (signal attenuation 21.4 dB/μm) which also corresponds to 5.4 unit cells or 0.8 free space wavelengths. Thus, the proposed MP transmission line performs better compared to the EP not only in terms of the absolute value of the propagation length but also in its relation to the operation free space wavelength and the size of each individual resonator. The reason behind this improvement in MPs transmission is easily

understood by looking at the expected attenuation when one of the coupling mechanisms is artificially impeded. Clearly, MPs excited entirely by inductive coupling, similar to the EPs, exhibit strong attenuation, while introduction of direct physical link between the resonators improves transmission. This effect is also manifested in the MP group velocity $v_g = \partial\omega/\partial k$, which reaches values up to 0.25 $c$ at the center of the propagation band, and is a factor of 4 faster than the result reported for EP [30]. Thus, compared to the EP an MP pulse could travel at higher speeds and propagates greater distances.

Finally, it is important to mention that the MP properties can be tuned by changing the material used and the size and shape of the individual SRRs. For instance, at $\omega$=0.3 eV, utilization of silver instead of gold results in longer MP's field decay length of about 16.6 μm. However, silver is easily oxidized, which make MP transmission lines based on this metal less versatile and difficult to integrate with the current CMOS technology. From our simulations, not presented here, it is also clear that system size manipulation such as downscaling or change of the capacitor gap width has strong effect on the magnetic response. Generally, the MP resonance frequency increases linearly with the decrease of the overall SRR size. Unfortunately, for high frequencies ($\hbar\omega > 1.2$ eV), this scaling tends to saturates as shown in [79]. An alternative way is to employ more complicated shapes of magnetic resonators or to change the dielectric constant of the surrounding media. All those prospective solutions and their effect on the MP propagation require further studies. Excitation of MP in one-dimensional system could be a promising candidate for the development of a wide range of optical devices, including in-plane, CMOS-compatible subwavelength optical waveguides, fast optoelectronic switches, and transducers.

Besides SRR, another new kind of magnetic resonators, slit-hole resonators (SHR) were proposed to construct one-dimensional diatomic chain [24]. For a monoatomic chain, SRRs is proposed by Ref. [23]. However, its dispersion relation curve lies below the light line. At a given photon energy, the wave vector is not conserved when the photon is transformed into the MP mode. Such MP mode could not be excited by a far-field incident wave, and the EM energy could not be radiated out from the chain either. However, for a diatomic chain, the dispersion of MP mode includes two branches due to the strong exchange current interaction: acoustic branch at lower frequency and optical branch at higher frequency. The dispersion curve is divided into two parts by the blue light line. The part above the blue line is the bright MP mode, which can couple to the far-zone optical field. Apparent extraordinary optical transmission (EOT) peaks induced by the MP mode were observed in our measured spectra at infrared frequencies. The strongest EOT peak was obtained at 1.07 eV with an incident angle of 20°. The measured dependence of EOT peaks on the incident angle coincided with the theoretical results quite well. This proposed MP propagation mode in SHR structure has good potential applications in multi-frequency nonlinear optical processes. Aside from the EOT reported, the bright MP mode could also be used to produce efficient nanolasers, which has recently aroused intense interest. Meanwhile, the rest part below the blue line corresponds to the dark MP mode, which cannot be excited by the far-field wave and whose energy does not radiate outward. Without radiation loss, the dark MP mode

can be greatly amplified by the stimulated emission from an active medium (e.g., quantum dots and the like) similarly as SPASER achieved in dark SPP mode. This could provide a good nanoscale optical source for numerous potential applications in nonlinear optical processes, such as single-molecule detection and fluorescence imaging.

The nanorod [68] and, nanosandwich [71] are good alternatives to make sub-wavelength waveguides because of their simple structures and high working-frequency regime. Figure 11.7(a) presents the geometry of a single nanosandwich, composed of two equal-sized gold nanodiscs and a dielectric middle layer. Such a magnetic atom can also be used to construct a linear magnetic chain (Fig. 11.7(b)). Due to the near-field electric and magnetic coupling interactions, the MP propagation mode is established in this one-dimensional system. When excited by an EM wave, a strong local magnetic field is obtained in the middle layer at a specific frequency (Fig. 11.7(c)). For this magnetic plasmon resonance mode, the corresponding electric fields are given in Fig. 11.7(d). Through a Fourier transform method, the wave vectors of this MP wave at different EM wave frequencies are calculated. Then, the MP wave's dispersion property is obtained (shown as a white line in Fig. 11.7(e)). The light line in free space is also given as the black dotted line in the figure. The MP curve is divided into two parts by the light line. The part above the light line corresponds to bright MP modes whose energy can be radiated out from the chain, while the part below the light line corresponds to dark MP modes whose energy can be well confined within the chain. It is easy to see that the bright MP modes are much weaker than the dark MP modes for their leaky property. Therefore, only those EM waves in the frequency range of the dark MP modes can be transferred efficiently without radiation loss. The above results for a mono-periodic chain of nanosandwiches have been generalized to graded structures [70]. Some new inter-

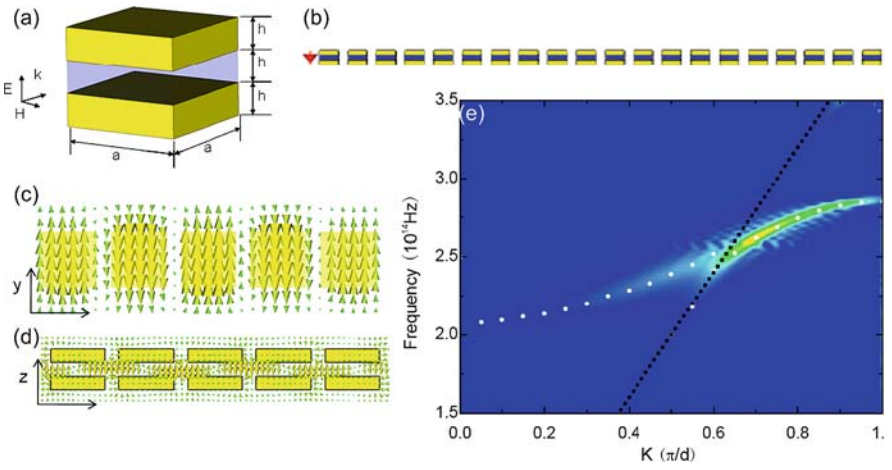


**Fig. 11.7** (**a**) Structure of a single nanosandwich; (**b**) one-dimensional chain of nanosandwich; (**c**) electric field and (**d**) magnetic field of the MP wave propagation along the chain; and (**e**) dispersion curve of the MP wave. Reprinted with permission from [71].

esting properties, such as slow group velocity and band folding of MP waves, are found in these more complex structures.

## 11.4 Magnetic Plasmon Modes in Two-Dimensional Metamaterials

In addition to the above-mentioned one-dimensional structures, the MP mode introduced by the coupling effect in two-dimensional systems is also an interesting topic. For two-dimensional metamaterials, the most important applications are negative refraction, focusing, and superlensing. How do the coupling interactions between elements affect the above processes? They cannot be handled by the conventional effective medium theory.

In the microwave range, MI wave theory has been proposed to deal with the coupling effect in the two-dimensional system. An MI superlens was proposed based on employing the coupling between resonators [9, 59], which eliminates the weakness of Wiltshire's first Swiss-roll superlens [73, 74] and has potential for MRI applications. The focusing of indefinite media, originally treated by Smith [54], has been investigated by Kozyrev with the aid of MI wave theory. It was found that partial focusing and multiple transmitted beams can be formed by the excitation of MI waves [16]. A further comparison between effective medium theory and MI wave theory was also given by Shadrivov [48], in which the reflection and refraction of MI waves on the boundary of two different effective media were studied. It was shown that both positive and negative refractions may occur under some configurations of the elements [62]. Another interesting finding is that spatial resonances could be formed by the propagation of MI waves on a two-dimensional array of magnetic resonators [80]. Different boundary conditions will produce different current and magnetic field distributions. For example, Fig. 11.8(a–c) gives the current distributions for circular boundary conditions at various frequencies.

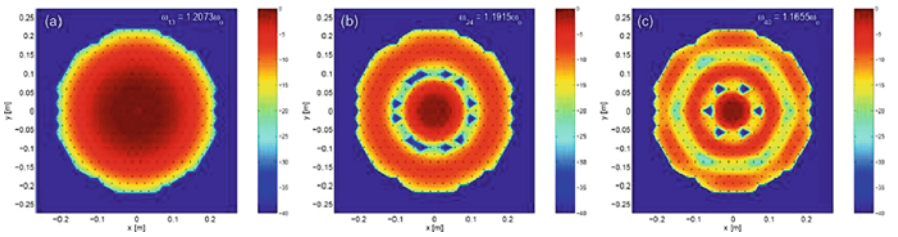


**Fig. 11.8** Current distributions for circular boundary conditions at various frequencies (**a**–**c**). Reprinted with permission from [80].

In the optical frequency range, fishnet structures are well-known magnetic metamaterials [76], constructed by a metal/insulator/metal (MIM) sandwich with perforated periodic nanohole arrays. The fundamental physics to realize the neg-

ative permeability in this structure is based on the artificial magnetic atoms that consist of the magnetically excited LC resonance between the two coupled metallic layer segments. In fishnet structures, all of these resonance elements are connected together, and strong exchange current interactions exist between them. Due to this strong coupling effect, MP waves with strong dispersion can be excited in the two-dimensional plane (double-fishnet) or three-dimensional bulk (multilayer-fishnet) structures.

For the one-dimensional system discussed in the last section, the MP waves are confined within the chain of SRRs and have only one possible propagation direction. However, for the planar double-fishnet structures, MP waves can propagate in any direction on this plane. Therefore, the excitation MP waves in these two-dimensional systems are much more complex compared with the one-dimensional system. Analogous to the polariton modes in MI waves [61], when the MP wave inside the fishnet structure is coupled with the incident electromagnetic waves, a new kind of polariton can be formed: a magnetic plasmon polariton (MPP).

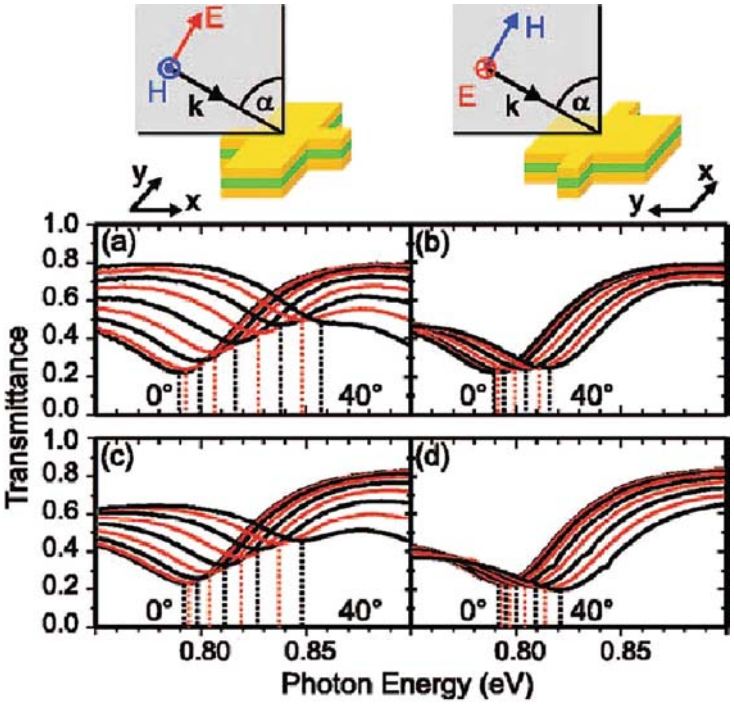


**Fig. 11.9** (**a**) and (**b**) Measured oblique-incidence transmittance spectra for different incident angles with respect to the surface normal, from 0 to 40 in steps of 5 (for clarity, the color alternates between *black* and *grey*). The geometry is indicated on the *top*. (**c**) and (**d**) Calculated spectra corresponding to (**a**) and (**b**), respectively. Reprinted with permission from [5].

In 2006, G. Dolling et al. observed the transmission dip induced by the excitation of an MPP in such a double-fishnet structure [5]. By measuring and calculating the oblique-incidence transmittance spectra of this system, the authors inferred the in-plane dispersion relation of the magnetization wave (see Fig. 11.9). From the geometry and the dispersion shape, the authors conclude that coupling is predominantly via magnetic dipoles for waves propagating along the magnetic dipole direction. These magnetization waves are the classical analogue of magnon excitations of quantum-mechanical spins.

What they observed is essentially only the lowest mode of the MPP. In the following, multiple MPP modes related to the reciprocal vectors of the array lattice were convincingly demonstrated [17]. Figure 11.10(a–b) shows the magnetic field distributions of two mentioned MPP modes associated with the reciprocal vectors of $G(0,\ 1)$ and $G(1,\ 1)$. Figure 11.10(c) is a calculated transmission map with the $SiO_2$ layer thickness ranging from 25 to 55 nm, where two MPP modes and SPP modes are clearly exhibited. A clear physics picture could be presented to interpret these results. When a light is normally incident on a perforated metal film, optical field is enhanced at proper wavelengths due to the excitation of the SPPs (or other surface waves). These EM energies will reradiate through the holes array leading to a strong broad transmission band if only one metal layer is presented. However, the trilayer structure composes many magnetic resonators by LC circuits, which will absorb the EM energies around their resonant frequency with relative narrow linewidth. If this mode is rightly located inside or near the transmission band, it will appear as a dip or a step in spectrum correspondingly. Notably, these magnetic responses are actually modulated by the periodic structure via the lateral coupling, thus multi-MPP modes are excited as different reciprocal vectors $G_{m,n}$ are involved, which behave in a similar manner of the $G_{m,n}$ associated SPP excitations.

Afterward, we also studied the dispersion properties of the MPP modes in the fishnet structure with rectangular hole arrays [19]. By careful investigation of

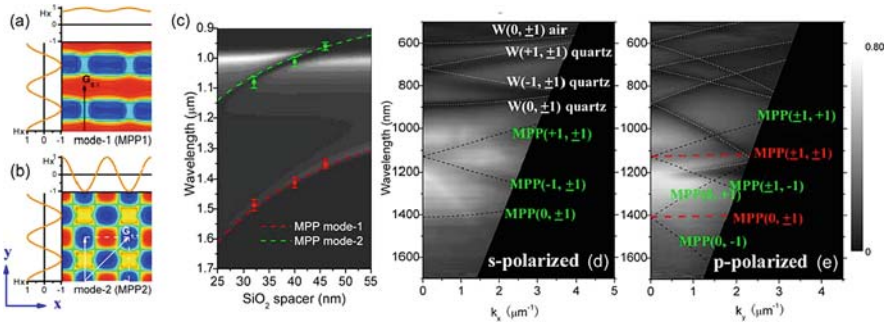


**Fig. 11.10** Results of fishnet with square hole: (**a**) Simulated magnetic field distribution for mode 1 (**a**) and for mode 2 (**b**) in the middle $SiO_2$ layer of fishnet; (**c**) calculated transmittance map of fishnet as middle layer thickness ranging from 25 to 55 nm; results of fishnet with rectangular hole: measured transmission maps on an intuitive gray scale versus wavelength and wave vectors for (**d**) *s*-polarization and (**e**) *p*-polarization. Reprinted with permission from [17] and [19].

the transmission property on the oblique incidence for the *s*- and *p*-polarization cases, we found a polarization-dependent dispersion property of the concerned MPP modes, which was indicated in the transmission maps for these two polarizations, as shown in Fig. 11.10(d–e). From this, we can see that the MPP(1, 1) mode in the *s*-polarization actually exhibits much larger dispersions than the lowest mode, resulting in two split modes MPP(+1, 1) and MPP(−1, 1) that break the degeneration. This is very similar to the property of SPP in plasmonic crystals. As for the anisotropic properties, we can attribute them to different coupling intensities among the artificial magnetic atoms in different directions. In brief, the MPP excitations in the fishnet are not the behavior of a single isolated element. Instead, they come from the coupling effect between the artificial magnetic atoms, which are the delocalized mode in the fishnet structures [18]. This MPP offers another way to tailor the optical property in addition to the SPP-enhanced extraordinary transmissions.

## 11.5 Outlook

Although metamaterials composed of uncoupled magnetic resonance elements have been successfully applied to produce intriguing effects such as negative refraction, cloaking, and superlensing, all of these were devised within a very narrow frequency range around a specific resonance frequency. This disadvantage restricts the practical applications of metamaterials.

In addition to the above-mentioned applications of the linear optical effect, due to the great enhancement of the local field inside magnetic resonators, magnetic metamaterials have also been proposed for use in nonlinear optical processes, such as SERS [38], SHG [8, 14], nanolasers [46], and SPASER [78]. However, the nonlinear optical processes that occur between waves of several different frequencies typically require a broad frequency bandwidth. The narrow single resonance property of conventional metamaterials is a considerable disadvantage for their potential nonlinear optical applications.

The MP modes introduced by the coupling effect in metamaterials may provide a possible way to overcome the above-mentioned obstacle. As described in this chapter, hybrid MP resonance modes could be attained in a system with several coupled resonators. This hybridization effect results in multiple discrete resonance frequencies of magnetic metamaterials. When all the resonance elements in metamaterials are coupled together through a particular method, the multiple resonance levels will be extended to a continuous frequency band. Therefore, the excitation of MP modes in such metamaterials can be continually tuned within a rather wide range. Compared with conventional metamaterials made from uncoupled elements, this kind of broadband tunable magnetic metamaterial based on the coupling effect will have much more interesting and prospective applications, especially on the nonlinear optical effect. Based on this discussion, we anticipate that many novel metamaterials and nanophotonic devices will be developed from coupled resonator systems.

## References


1. Beruete, M., Falcone, F., Freire, M.J., Marques, R., Baena, J.D.: Electroinductive waves in chains of complementary metamaterial elements. Appl. Phys. Lett. **88**, 083503 (2006)
2. Brandl, D.W., Oubre, C., Nordlander, P.: Plasmon hybridization in nanoshell dimers. J. Chem. Phys. **123**, 024701 (2005)
3. Brongersma, M.L., Hartman, J.W., Atwater, H.A.: Electromagnetic energy transfer and switching in nanoparticle chain arrays below the diffraction limit. Phys. Rev. B **62**, 16356 (2000)
4. Brown, J.: Artificial dielectrics having refractive indices less than unity. Proc. IEE **100**, 51 (1953)
5. Dolling, G., Wegener, M., Schadle, A., Burger, S., Linden, S.: Observation of magnetization waves in negative-index photonic metamaterials. Appl. Phys. Lett. **89**, 231118 (2006)
6. Enkrich, C., Wegener, M., Linden, S., Burger, S., Zschiedrich, L., Schmidt, F., Zhou, J.F., Koschny, T., Soukoulis, C.M.: Magnetic metamaterials at telecommunication and visible frequencies. Phys. Rev. Lett. **95**, 203901 (2005)
7. Fang, N., Lee, H., Sun, C., Zhang, X.: Sub-diffraction-limited optical imaging with a silver superlens. Science **308**, 534 (2005)
8. Feth, N., Linden, S., Klein, M.W., Decker, M., Niesler, F.B.P., Zeng, Y., Hoyer, W., Liu, J., Koch, S.W., Moloney, J.V., Wegener, M.: Second-harmonic generation from complementary split-ring resonators. Opt. Lett. **33**, 1975 (2008)
9. Freire, M.J., Marques, R.: Planar magnetoinductive lens for three-dimensional subwavelength imaging. Appl. Phys. Lett. **86**, 182505 (2005)
10. Freire, M.J., Marques, R., Medina, F., Laso, M.A.G., Martin, F.: Planar magnetoinductive wave transducers: theory and applications. Appl. Phys. Lett. **85**, 4439 (2004)
11. Guo, H.C., Liu, N., Fu, L.W., Meyrath, T.P., Zentgraf, T., Schweizer, H., Giessen, H.: Resonance hybridization in double split-ring resonator metamaterials. Opt. Express **15**, 12095 (2007)
12. Hesmer, F., Tatartschuk, E., Zhuromskyy, O., Radkovskaya, A.A., Shamonin, M., Hao, T., Stevens, C.J., Faulkner, G., Edwards, D.J., Shamonina, E.: Coupling mechanisms for split ring resonators: theory and experiment. Phys. Stat. Sol. B **244**, 1170 (2007)
13. Jackson, J.D.: Classical Electrodynamics. Wiley, NY (1999)
14. Klein, M.W., Enkrich, C., Wegener, M., Linden, S.: Second-harmonic generation from magnetic metamaterials. Science **313**, 502 (2006)
15. Koenderink, A.F., Polman, A.: Complex response and polariton-like dispersion splitting in periodic metal nanoparticle chains. Phys. Rev. B **74**, 033402 (2006)
16. Kozyrev, A.B., Qin, C., Shadrivov, I.V., Kivshar, Y.S., Chuang, I.L., Weide, D.W.V.D.:Wave scattering and splitting by magnetic metamaterials. Opt. Express **15**, 11714 (2007)
17. Li, T., Li, J.Q., Wang, F.M., Wang, Q.J., Liu, H., Zhu, S.N., Zhu, Y.Y.: Exploring magnetic plasmon polaritons in optical transmission through hole arrays perforated in trilayer structures. Appl. Phys. Lett. **90**, 251112 (2007)
18. Li, T., Liu, H., Wang, F.M., Li, J.Q., Zhu, Y.Y., Zhu, S.N.: Surface-plasmon-induced optical magnetic response in perforated trilayer metamaterial. Phys. Rev. E **76**, 016606 (2007)
19. Li, T., Wang, S.M., Liu, H., Li, J.Q., Wang, F.M., Zhu, S.N., Zhang, X.: Dispersion of magnetic plasmon polaritons in perforated trilayer metamaterials. J. Appl. Phys. **103**, 023104 (2008)
20. Li, T.Q., Liu, H., Li, T., Wang, S.M., Wang, F.M., Wu, R.X., Chen, P., Zhu, S.N., Zhang, X.: Magnetic resonance hybridization and optical activity of microwaves in a chiral metamaterial. Appl. Phys. Lett. **92**, 131111 (2008)
21. Linden, S., Enkrich, C., Wegener, M., Zhou, J.F., Koschny, T., Soukoulis, C.M.: Magnetic response of metamaterials at 100 terahertz. Science **306**, 1351 (2004)
22. Liu, H., Genov, D.A.,Wu, D.M., Liu, Y.M., Liu, Z.W., Sun, C., Zhu, N., Zhang, X.: Magnetic plasmon hybridization and optical activity at optical frequencies in metallic nanostructures. Phys. Rev. B **76**, 073101 (2007)

23. Liu, H., Genov, D.A.,Wu, D.M., Liu, Y.M., Steele, J.M., Sun, C., Zhu, S.N., Zhang, X.: Magnetic plasmon propagation along a chain of connected subwavelength resonators at infrared frequencies. Phys. Rev. Lett. **97**, 243902 (2006)
24. Liu, H., Li, T., Wang, Q.J., Zhu, Z.H., Wang, S.M., Li, J.Q., Zhu, S., Zhu, Y.Y., Zhang, X.: Extraordinary optical transmission induced by excitation of a magnetic plasmon propagation mode in a diatomic chain of slit-hole resonators. Phys. Rev. B **79**, 024304 (2009)
25. Liu, N., Guo, H.C., Fu, L.W., Kaiser, S., Schweizer, H., Giessen, H.: Three-dimensional photonic metamaterials at optical frequencies. Nat. Mat. **7**, 31 (2008)
26. Liu, N., Liu, H., Zhu, S.N., Giessen, H.: Stereometamaterials. Nat. Phot. **3**, 157 (2009)
27. Liu, N., Guo, H.C., Fu, L.W., Kaiser, S., Schweizer, H., Giessen, H.: Plasmon hybridization in stacked cut-wire metamaterials. Adv. Mat. **19**, 3628 (2007)
28. Liu, R., Ji, C., Mock, J.J., Chin, J.Y., Cui, T.J., Smith, D.R.: Broadband ground-plane cloak. Science **323**, 366 (2009)
29. Lu, D.Y., Liu, H., Li, T.,Wang, S.M.,Wang, F.M., Zhu, S.N., Zhang, X.: Creation of a magnetic plasmon polariton through strong coupling between an artificial magnetic atom and the defect state in a defective multilayer microcavity. Phys. Rev. B **77**, 214302 (2008)
30. Maier, S.A., Kik, P.G., Atwater, H.A.: Optical pulse propagation in metal nanoparticle chain waveguides. Phys. Rev. B **67**, 205402 (2003)
31. Nefedov, I.S., Tretyakov, S.A.: On potential applications of metamaterials for the design of broadband phase shifters. Micro. Opt. Tech. Lett. **45**, 98 (2005)
32. Nordlander, P., Oubre, C., Prodan, E., Li, K., Stockman, M.I.: Plasmon hybridization in nanoparticle dimers. Nano. Lett. **4**, 899 (2004)
33. Nordlander, P., Prodan, E.: Plasmon hybridization in nanoparticles near metallic surfaces. Nano. Lett. **4**, 2209 (2004)
34. Oubre, C., Nordlander, P.: Finite-difference time-domain studies of the optical properties of nanoshell dimers. J. Chem. Phys. B **109**, 10042 (2005)
35. Pendry, J.B.: Negative refraction makes a perfect lens. Phys. Rev. Lett. **85**, 3966 (2000)
36. Pendry, J.B.: Negative refraction. Cont. Phys. **45**, 191 (2004)
37. Pendry, J.B.: Photonics: Metamaterials in the sunshine. Nat. Mat. **5**, 599 (2006)
38. Pendry, J.B., Holden, A.J., Robbins, D.J., Stewart, W.J.: Magnetism from conductors and enhanced nonlinear phenomena. IEEE Trans. Micro. Theo. Tech. **47**, 2075 (1999)
39. Pendry, J.B., Holden, A.J., Stewart, W.J., Youngs, I.: Extremely low frequency plasmons in metallic mesostructures. Phys. Rev. Lett. **76**, 4773 (1996)
40. Pendry, J.B., Schurig, D., Smith, D.R.: Controlling electromagnetic fields. Science **312**, 1780 (2006)
41. Podolskiy, V.A., Sarychev, A.K., Shalaev, V.M.: Plasmon modes in metal nanowires and left-handed materials. J Nonl. Opt. Phys. Mater. **11**, 65 (2002)
42. Prodan, E., Nordlander, P.: Plasmon hybridization in spherical nanoparticles. J. Chem. Phys. **120**, 5444 (2004)
43. Prodan, E., Radloff, C., Halas, N.J., Nordlander, P.: A hybridization model for the plasmon response of complex nanostructures. Science **302**, 419 (2003)
44. Quinten, M., Leitner, A., Krenn, J.R., Aussenegg, F.R.: Electromagnetic energy transport via linear chains of silver nanoparticles. Opt. Lett. **23**, 1331 (1998)
45. Rotman, W.: Plasma simulation by artificial dielectrics and parallel-plate media. IRE Trans. Ant. Prop. **10**, 82 (1962)
46. Sarychev, A.K., Tartakovsky, G.: Magnetic plasmonic metamaterials in actively pumped host medium and plasmonic nanolaser. Phys. Rev. B **75**, 085436 (2007)
47. Schurig, D., Mock, J.J., Justice, B.J., Cummer, S.A., Pendry, J.B., Starr, A.F., Smith, D.R.: Metamaterial electromagnetic cloak at microwave frequencies. Science **314**, 977 (2006)
48. Shadrivov, I.V., Reznik, A.N., Kivshar, Y.S.: Magnetoinductive waves in arrays of split-ring resonators. Physica B **394**, 180 (2007)
49. Shalaev, V.M.: Optical negative-index metamaterials. Nat. Phot. **1**, 41 (2007)
50. Shalaev, V.M., Cai, W.S., Chettiar, U.K., Yuan, H.K., Sarychev, A.K., Drachev, V.P., Kildishev, A.V.: Negative index of refraction in optical metamaterials. Opt. Lett. **30**, 3356 (2005)

51. Shamonina, E., Kalinin, V., Ringhofer, K.H., Solymar, L.: Magnetoinductive waves in one, two, and three dimensions. J. Appl. Phys. **92**, 6252 (2002)
52. Shelby, R.A., Smith, D.R., Schultz, S.: Experimental verification of a negative index of refraction. Science **292**, 77 (2001)
53. Simovski, C.R., Viitanen, A.J., Tretyakov, S.A.: Resonator mode in chains of silver spheres and its possible application. Phys. Rev. E **72**, 066606 (2005)
54. Smith, D.R., Kolinko, P., Schurig, D.: Negative refraction in indefinite media. J. Opt. Soc. Am. B **21**, 1032 (2004)
55. Smith, D.R., Padilla, W.J., Vier, D.C., Nemat-Nasser, S.C., Schultz, S.: Composite medium with simultaneously negative permeability and permittivity. Phys. Rev. Lett. **84**, 4184 (2000)
56. Soukoulis, C.M., Linden, S., Wegener, M.: Negative refractive index at optical wavelengths. Science **315**, 47 (2007)
57. Svirko, Y., Zheludev, N., Osipov, M.: Layered chiral metallic microstructures with inductive coupling. Appl. Phys. Lett. **78**, 498 (2001)
58. Sydoruk, O., Radkovskaya, A., Zhuromskyy, O., Shamonina, E., Shamonin, M., Stevens, C.J., Faulkner, G., Edwards, D.J., Solymar, L.: Tailoring the near-field guiding properties of magnetic metamaterials with two resonant elements per unit cell. Phys. Rev. B **73**, 224406 (2006)
59. Sydoruk, O., Shamonin, M., Radkovskaya, A., Zhuromskyy, O., Shamonina, E., Trautner, R., Stevens, C.J., Faulkner, G., Edwards, D.J., Solymar, L.: Mechanism of subwavelength imaging with bilayered magnetic metamaterials: theory and experiment. J. Appl. Phys. **101**, 073903 (2007)
60. Sydoruk, O., Zhuromskyy, O., Shamonina, E., Solymar, L.: Phonon-like dispersion curves of magnetoinductive waves. Appl. Phys. Lett. **87**, 072501 (2005)
61. Syms, R.R.A., Shamonina, E., Kalinin, V., Solymar, L.: A theory of metamaterials based on periodically loaded transmission lines: interaction between magnetoinductive and electromagnetic waves. J. Appl. Phys. **97**, 064909 (2005)
62. Syms, R.R.A., Shamonina, E., Solymar, L.: Positive and negative refraction of magnetoinductive waves in two dimensions. Eur. Phys. J. B **46**, 301 (2005)
63. Syms, R.R.A., Shamonina, E., Solymar, L.: Magneto-inductive waveguide devices. IEE Proc. Micro. Ant. Prop. **153**, 111 (2006)
64. Syms, R.R.A., Solymar, L., Young, I.R.: Three-frequency parametric amplification in magneto-inductive ring resonators. Metamaterials **2**, 122 (2008)
65. Valentine, J., Zhang, S., Zentgraf, T., Ulin-Avila, E., Genov, D.A., Bartal, G., Zhang, X.: Three dimensional optical metamaterial exhibiting negative refractive index. Nature **455**, 376 (2008)
66. Veselago, V.G.: The electrodynamics of substances with simultaneously negative values of φ and μ. Sov. Phys. Usp. **10**, 509 (1968)
67. Veselago, V.G., Narimanov, E.E.: The left hand of brightness: past, present and future of negative index materials. Nat. Mate. **5**, 759 (2006)
68. Wang, F.M., Liu, H., Li, T., Wang, S.M., Zhu, S.N., Zhu, J., Cao, W.W.: Highly confined energy propagation in a gap waveguide composed of two coupled nanorod chains. Appl. Phys. Lett. **91**, 133107 (2008)
69. Wang, F.M., Liu, H., Li, T., Zhu, S.N., Zhang, X.: Omnidirectional negative refraction with wide bandwidth introduced by magnetic coupling in a tri-rod structure. Phys. Rev. B **76**, 075110 (2007)
70. Wang, S.M., Li, T., Liu, H.,Wang, F.M., Zhu, S.N., Zhang, X.: Selective switch made from a graded nanosandwich chain. Appl. Phys. Lett. **93**, 233102 (2008)
71. Wang, S.M., Li, T., Liu, H., Wang, F.M., Zhu, S.N., Zhang, X.: Magnetic plasmon modes in periodic chains of nanosandwiches. Opt. Express **16**, 3560 (2008)
72. Weber, W.H., Ford, G.W.: Propagation of optical excitations by dipolar interactions in metal nanoparticle chains. Phys. Rev. B **70**, 125429 (2004)
73. Wiltshire, M.C.K., Hajnal, J.V., Pendry, J.B., Edwards, D.J., Stevens, C.J.: Metamaterial endoscope for magnetic field transfer: near field imaging with magnetic wires. Opt. Express **11**, 709 (2003)

74. Wiltshire, M.C.K., Pendry, J.B., Young, I.R., Larkman, D.J., Gilderdale, D.J., Hajnal, J.V.: Microstructured magnetic materials for RF flux guides in magnetic resonance imaging. Science **291**, 849 (2001)
75. Yen, T.J., Padilla, W.J., Fang, N., Vier, D.C., Smith, D.R., Pendry, J.B., Basov, D.N., Zhang, X.: Terahertz magnetic response from artificial materials. Science **303**, 1494 (2004)
76. Zhang, S., Fan, W.J., Panoiu, N.C., Malloy, K.J., Osgood, R.M., Brueck, S.R.J.: Experimental demonstration of near-infrared negative-index metamaterials. Phys. Rev. Lett. **95**, 137404 (2005)
77. Zhang, X., Liu, Z.W.: Superlenses to overcome the diffraction limit. Nat. Mat. **7**, 435 (2008)
78. Zheludev, N.I., Prosvirnin, S.L., Papasimakis, N., Fedotov, V.A.: Lasing spaser. Nat. Phot. **2**, 351 (2008)
79. Zhou, J., Koschny, T., Kafesaki, M., Economou, E.N., Pendry, J.B., Soukoulis, C.M.: Saturation of the magnetic response of split-ring resonators at optical frequencies. Phys. Rev. Lett. **95**, 223902 (2005)
80. Zhuromskyy, O., Shamonina, E., Solymar, L.: 2D metamaterials with hexagonal structure: spatial resonances and near field imaging. Opt. Express **13**, 9299 (2005)

# Chapter 12
# Enhancing Light Coupling with Plasmonic Optical Antennas

Jun Xu, Anil Kumar, Pratik Chaturvedi, Keng H. Hsu and Nicholas X. Fang

**Abstract** We describe in this chapter development of plasmonic optical antennas for light concentration and near-field enhancement. A set of bow tie nanoantennas are fabricated and characterized with optical and electron excitation methods. Optical spectroscopy of these subwavelength antennas displays pronounced extinction peaks at resonant wavelength, showing total extinction cross sections as much as 10 times of their physical dimensions. On the other hand, coherent excitation of the bow tie antennas allows tuning the peak wavelength of the scattered light by changing the periodicity. Under dark-field microscopy, we observed the scattered waves from arrays of different bow tie antennas in complete visible spectrum. The local resonant modes of the bow tie antennas are also probed by focused electrons. Such cathodoluminescence spectroscopy reveals the fine details of enhanced field on the optical nanoantennas at resolution down to 20 nm. Finally, we show examples of surface-enhanced Raman spectroscopy on the nanoantennas. Effective designs based on local enhancement and radiation engineering of the plasmonic optical antennas would promise revolutionary changes in highly compact and integrated photonics for photon energy conversion, adaptive sensing, and image processing.

**Key words:** plasmonic structures, optical antenna, solar spectrum, dipole radia tion, nanofabrication, e-beam lithography, solid-state superionic stamping, surface-enhanced Raman spectroscopy, extinction cross section, cathodoluminescence, localized plasmon, dark-field microscopy

## 12.1 Introduction

The continuous miniaturization of integrated photonic elements will soon offer designers a continuum of electromagnetic spectrum from RF to optical without

Jun Xu[1], Anil Kumar[2], Pratik Chaturvedi[1], Keng H. Hsu[1] and Nicholas X. Fang[1*]
[1]Department of Mechanical Science and Engineering, [2]Department of Electrical and Computer Engineering, University of Illinois at Urbana-Champaign, Urbana, IL, USA.
*e-mail: nicfang@illinois.edu

T.J. Cui et al. (eds.), *Metamaterials*, DOI 10.1007/978-1-4419-0573-4_12,

gaps. Such optimism is supported by the recent demonstration of resonant deep sub-wavelength optical nanoantennas [27]. The link of propagating radiation and confined/enhanced microwave fields now finds its counterpart in the optical domain. Likewise, surface plasmon and other traditional optical phenomena are now designed and realized in microwave metamaterials and devices [34]. The convergence of RF and optical device designs will bring revolutionary changes in highly compact and integrated photonics for adaptive sensing and image processing. Similar to the microwave antenna, the resonance condition for optical antenna is a function of its geometry and surrounding medium [9, 6], whereas this relationship is far more complex [29] for optical antennas due to the inherent losses in metals at optical wavelengths.

Current research on optical antennas is largely focusing on concentrating the optical field intensity at a certain point using plasmonic nanostructures. Comparing to the linear antenna in microwave domain, optical antennas with a characteristic cross section much smaller than the dimension along the axis were explored [27, 34, 10], and the resonant wavelength was found to be around half of the free space wavelength $\lambda_0$. However, due to the plasmonic effects in optical domain, the analogy for microwave antennas to optical antennas can be sometimes challenging. Counterintuitively, later theoretical efforts suggest the effective wavelength was actually close to $\lambda_0$ [6], after considering the guided wavelength determined by the geometries and material properties. A plethora of possible geometries were proposed such as planar wedge [34], spherical particle or particle pairs, chains, and groups [6, 21], crescent-shaped plasmonic particles [33]. In Fig. 12.1, we show some possible designs of optical antennas with different geometries currently being explored by our group.

Different applications using optical antennas have been reported, for example, in single molecule fluorescence, emission, and microscopy area [33, 13]; enhancing the photodetector performance [13, 35]; surface-enhanced Raman scattering (SERS) [29, 21, 35]. Besides the plasmonic materials, antenna effects in optical range were also observed and discussed on carbon nanotubes [36, 25].

One of the potential applications of optical antenna is to couple more energy in solar cell. Figure 12.2 shows the typical solar radiation spectrum at sea level. Photon capture and energy transfer to the photovoltaic devices would largely benefit from optical nanoantennas that act as a light harvester to reduce reflection loss and increase the effective cross section for absorption. Reducing device areas in photovoltaic devices gains the advantages of reduced transit time in the depletion layer and also a lower material cost per power output. However, under a constant input of solar radiation flux, having smaller active area implies smaller throughput. To overcome this trade-off between speed and sensitivity, the incident light should be efficiently guided, confined, and slowed down. The specially designed optical antenna can play important role in achieving the goals.

Therefore, there are mainly two important criteria for designing optical nanostructures: (i) to enhance optical near field in a small volume and (ii) to provide proper coupling with incident photons over a large area. In the first case, the so-called hotspots are generated by using dimer antenna structures [29, 20], of which a bow tie-shaped dimer of triangular structure has proven to be very effective [31, 15]. Except for certain cases, a qualitative description of the phenomena observed by any

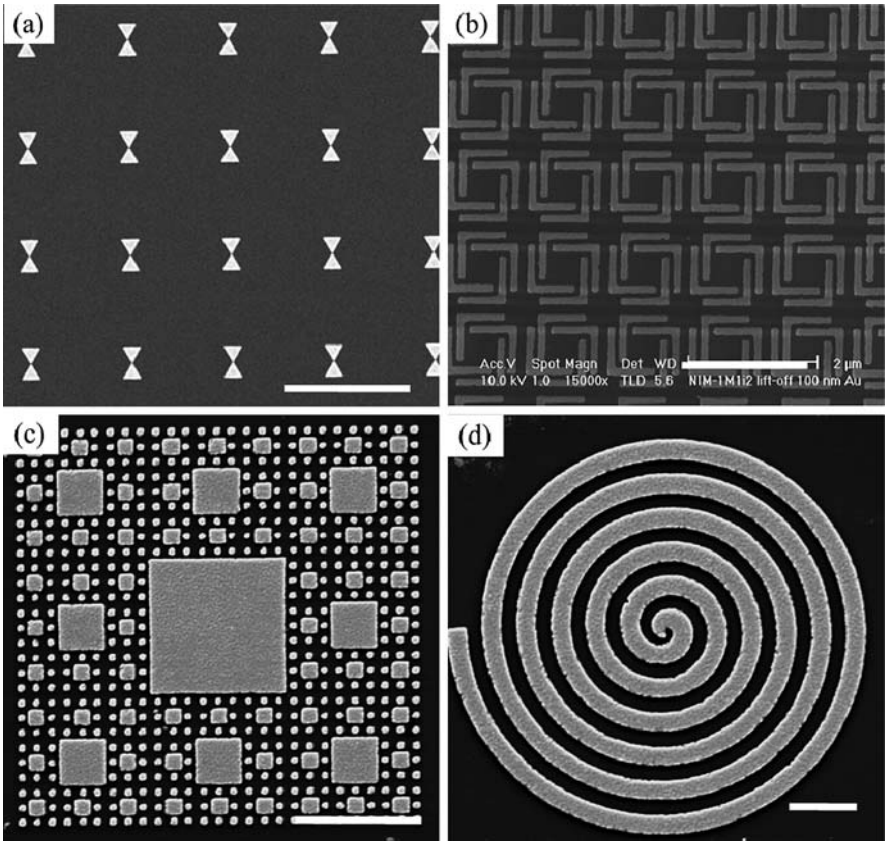


**Fig. 12.1** Scanning electron micrograph of (**a**) bow tie structure; (**b**) L-shaped resonators; (**c**) fractal structure; and (**d**) spiral structure. Scale bars are all 2 µm.

geometry may be generalized to a wide range of optical antennas [36]. In this chapter, we will focus on the properties of bow tie structure, including the fabrication techniques, optical measurements, and applications.

Optical nanoantennas share the basic principles of electromagnetic antennas. Taking an elementary dipole antenna as an example, charge oscillations on a dipole result in field generation at the antenna surface, transferring signal and power to the surrounding medium. Such a mechanism of charge oscillation in an electrical antenna is shown in Fig. 12.3, where the dipole center is fed with an alternating current. At the beginning of the cycle, at $t = 0$, charges accelerate away from the center of the dipole. Electric field lines start from the positive charge and end at negative charge. As the charges move further away from this point, total amount of acceleration reduces and charges accumulate at the ends. At this stage, at $t = T/4$, the AC input will reach its maximum value; charges will start accelerating in opposite directions and the field lines will start to bend forming semicircles, which will eventually lead to closed loops of electric field. As the AC polarity changes the charge

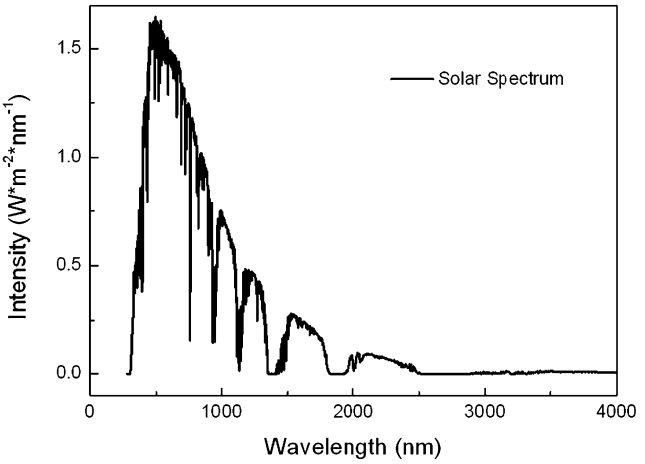


**Fig. 12.2** Solar spectral irradiance at sea level. Note that most of the energy is concentrated in the visible and near-IR region. The dips are due to absorption by atmospheric gases, especially water vapor which absorbs in the near-visible spectrum. This missing energy demands a careful control of resonance frequency which has to be matched with the spectral peaks preferably in high-intensity regions.

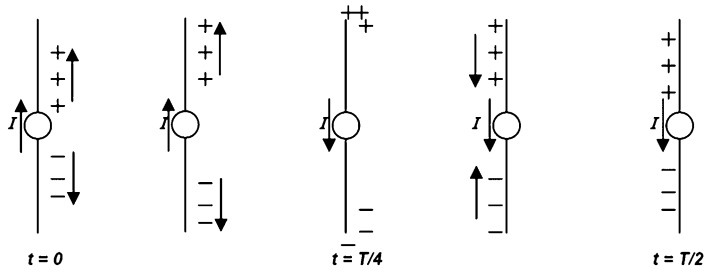


**Fig. 12.3** Charge oscillations on a dipole as a function of time. For an electric dipole the alternating current is supplied externally into the circuit. For nanostructures in our work, the oscillations are generated by an electric field.

polarity will be switched at the feed point, the electrical lines will form a complete loop in order to accommodate for the reversal in direction of the magnetic field. This process will now repeat on opposite arms of the dipole. One complete cycle results in one wavelength of field that is being radiated from the antenna surface.

As Maxwell's equations are scalable in all frequency domains, antenna theory should generally apply to optical frequencies as it does for microwaves, however,

- material constants change significantly as we move from radio frequencies to optical frequencies;
- metals are no longer perfect conductors in optical frequencies and suffer significant losses;

- additional features unique to optical frequencies like collective surface resonance of electrons, i.e., surface plasmon, allow dramatic modification in the interaction of field with nanostructures and can be utilized to counter the losses.

The simple model of charge oscillation shown above can be applied to nanostructures where the field and electrons now couple on the nanostructure surface. This coupling has a maximum at the resonant wavelength and can be tailored by varying the different parameters. This charge interaction at the surface can be enhanced using several parameters. Variations in field intensity due to modifications in radius of curvature and tip angle have been reported [9]. A sharper tip or smaller angle leads to higher charge density at the tip leading to an enhanced field. If two such structures are brought closer to each other, the enhancement can be dramatically improved. Other parameters can be optimized to improve the field enhancements and values $>10^3$ have been reported in Ref. [9].

On the other hand, circuit theory in the microwave domain can provide important guidelines for efficient design of antenna devices. Adopting the concept in the microwave range, a circuit theory for these optical structures has been explored recently [2, 12, 1]. Three basic circuit elements, nanoresistors, nanocapacitors, and nanoinductors, are discussed in small nanostructures with different material properties. Such coupled nanoscale circuits in IR and visible range have been proposed [15]. By using the proper "loading" techniques of nanocircuits, the optical response of nanoantenna can be tuned [2].

## 12.2 Fabrication Methods

The size of optical antenna is typically in the order of 100 nm to several microns, comparable to the wavelength of interest. Fabricating such structures requires techniques with nanoscale spatial resolution. In this section, we will introduce electron beam lithography used in prototyping these nanoantennas and a novel technique developed in our laboratory with potential of manufacturing the devices over large arrays, namely solid-state superionic stamping (S4).

### *12.2.1 Electron Beam Lithography*

One of the common methods used in fabricating nanoscale device is electron beam lithography, which is suitable for bow tie-shaped silver/gold nanostructures. Samples were prepared on substrates of indium tin oxide (ITO) on glass or Si. Since charge dissipation is required for electron beam, only conducting substrates can be used. The procedure used for preparing the samples with electron beam lithography is shown in Fig. 12.4(a).

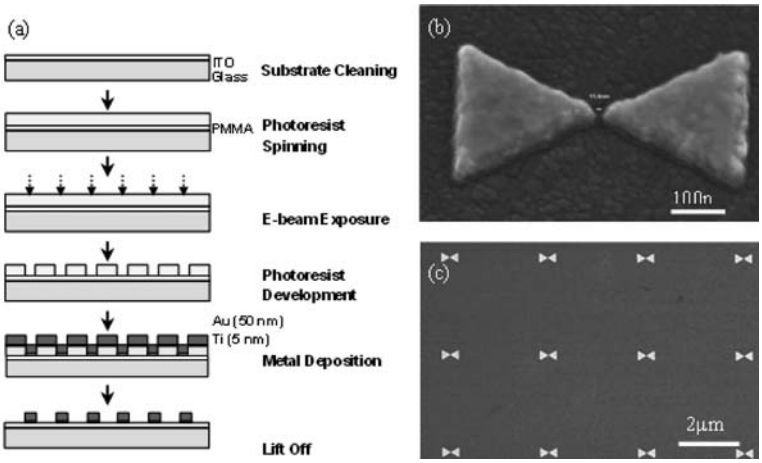


**Fig. 12.4** (**a**) Process flowchart for nanofabrication using electron beam lithography. (**b**) Bow tie antenna array prepared on ITO glass using electron beam lithography. Each bow tie consists of equilateral triangles with height of 240 nm and base 280 nm. The tip-to-tip distance between two triangles is around 20 nm. (**c**) The bow tie array is in square lattice with lattice constant 3 μm.

Prior to fabrication, the samples were cleaned in ultrasonic bath of acetone for 5 min. PMMA (950K in 2% anisole) was then spun at 2,000 RPM for 60 s followed by a soft baking for 2 min (at 200°C). A dose of 1,000 C/sq. μm and a 20 pA current were used on a JEOL 6000FS Electron Beam Nanowriter. After exposure the sample was developed with MIBK (1:3) for 3 min. During metal deposition, a Ti layer of 5 nm was first deposited for adhesion underneath a 50 nm layer of Au. The PMMA was then dissolved in acetone for at least 12 h for complete lift-off of metal and the sample was finally cleaned with IPA & DI water. In Fig. 12.4(b), we show one of the bow tie structures fabricated with triangle height 240 nm and edge 280 nm. The triangles are separated by 20 nm and each bow tie is separated by 3 μm in *x*- and *y*-directions on a square array of side 0.5 mm.

### *12.2.2 Solid-State Superionic Stamping*

As a parallel approach to electro-beam lithography, a novel technique, solid-state superionic stamping (S4) [22, 32], has been developed at the University of Illinois to fabricate optical antennas with nanoscale features. In this technique, we directly print high-resolution metallic nanopatterns in a single step. Unlike traditional imprint lithography [7, 8], S4 is a direct metal patterning process by electrochemical etching of metal films. This process can fabricate nanoscale features over large areas with very low mechanical force and external voltages.

In our process a solid-state mixed conductor, silver sulfide ($Ag_2S$), is used for solid-state oxidation at the interface between a silver film and a silver sulfide stamp.

Patterning of the stamp (shown in Fig. 12.5(b)) is accomplished by focused ion beam (FIB) milling (FEI Dual-Beam DB-235) with a 50-pA aperture at a milling rate of about 50 nm/min. The electrochemical process, similar to an electrolytic cell, is unique in the sense that it utilizes a solid-state conductor for the high pattern transfer fidelity and resolution. Figure 12.5(a) shows the process schematic at different stages. The best feature size achieved so far is close to 30 nm as in Fig. 12.5(c).

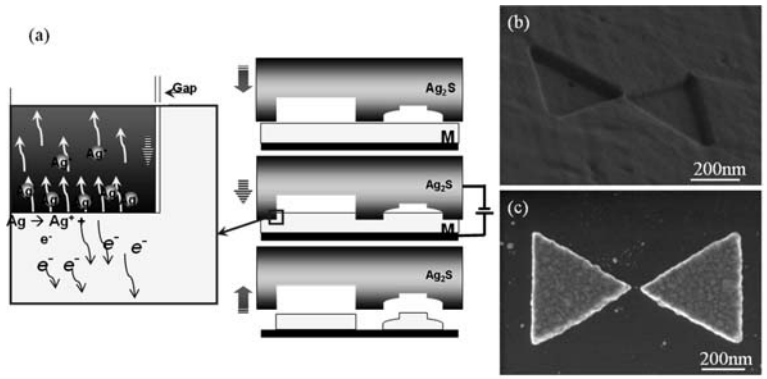


**Fig. 12.5** (**a**) Schematic showing the process of solid-state superionic stamping. First, a pre-patterned silver sulfide stamp is brought closer to a silver film that is to be patterned. Due to potential gradient $Ag^+$ ions are removed from the interface through the solid-state conductor and electrons are removed through silver. A replica of the stamp is then patterned on the silver film until complete removal of the ions shows no more current flow in the circuit. (**b**) A stamp made of silver sulfide and patterned using FIB with a bow tie structure in square lattice. (**c**) The results of superionic stamping on silver film.

Comparing to electron beam lithography, S4 technique holds promise for a fast and cost-effective fabrication of large area patterns. However, the highest resolution is still a little bit lower by using FIB to fabricate the mold that brings the limitation of tip-to-tip distance in bow tie structure. Recently, the stamp made by embossing an electron beam lithography fabricated mold can achieve the resolution close to 15 nm.

## 12.3 Measurement and Analysis

Bow tie optical antenna has been fabricated by nanofabrication techniques. In the fabrication procedure, the size and spacing of bow tie structures can be accurately controlled, which afford the opportunity to research the optical characteristics of single bow tie structure and bow tie array. In this part, we will measure the optical spectrum by using bright-field and dark-field illumination to exhibit novel optical properties. Furthermore, cathodoluminescence spectroscopy will be used to reveal the interaction between the electron and photon in such optical antenna.

Furthermore, computer simulation by discrete dipole approximation (DDA) method [11] has been used to calculate the extinction spectrum and field distribution at resonant frequency of designed bow tie structure. The results will be shown in the measurement section to compare with the experimental data.

## *12.3.1 Optical Scattering by Nanoantennas*

### 12.3.1.1 Bright-Field Spectra (Extinction Cross Section)

Transmission spectra were measured on the periodic array (square lattice) sample fabricated by electron beam lithography method using a Varian Cary 5 G spectrometer system with a wavelength range of 175–3,300 nm. The sketch of the measurement setup is shown in Fig. 12.6. In this configuration, the optical antenna array sample was mounted on a metallic plate with aperture diameter of 0.5–2 mm and illuminated uniformly by halogen lamp from the glass side.

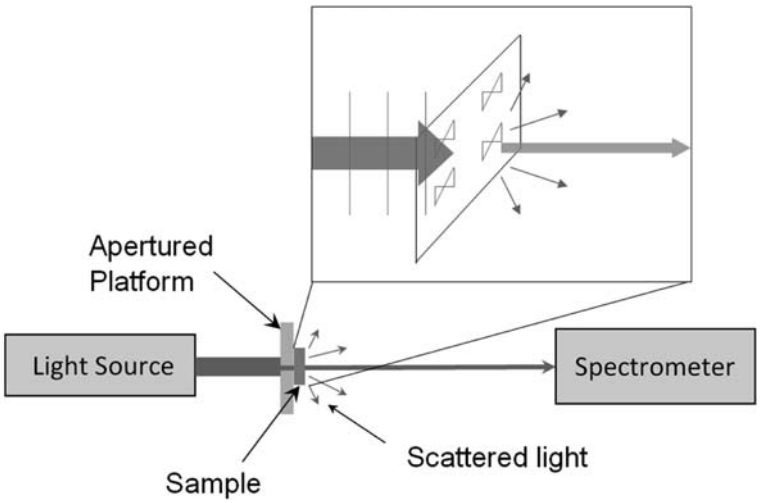


**Fig. 12.6** The sketch of the far-field measurement using Varian Cary 5G spectrometer system.

The transmission spectrum is shown in Fig. 12.7, using illumination with three different circular apertures (0.5, 1, and 2 mm in diameter). From the transmission spectrum, we can clearly observe several characteristic dips, corresponding to the resonant wavelength of the bow tie antenna. It is noted that the kinks at 800 and 1,200 nm are artifacts of the instrument when different photodetectors are switched.

These transmission dips that are related to the decreasing of the power received by spectrometer are due to the increased scattering and absorption of bow tie

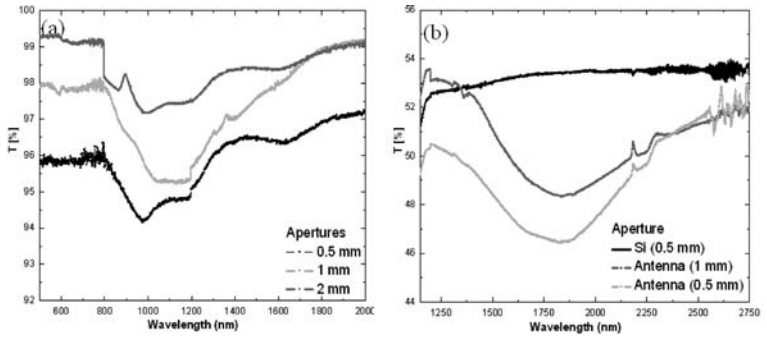


**Fig. 12.7** Transmission measurements showing a strong resonance at particular wavelength: (**a**) close to 960 nm for an ITO/glass substrate ($n_{ITO} \sim 1.95$) and (**b**) close to 1.8 $\mu$m for a Si substrate ($n_{\mathrm{Si}} \sim 3.47$).

optical antenna at resonant wavelength. The scattering of electric and magnetic fields is produced by the radiation of the antennas, and the absorption is due to ohmic losses in the metal antenna increasing with the stronger current flow on resonance, that reduces the transmitted intensity measured by spectrometer. So the transmitted intensity $I$ at the spectrometer is the function of the incident beam power, absorption, and scattering in the antenna at each wavelength that can be expressed by [5]

$$I(\lambda) = I_{inc}(\lambda) - I_{abs}(\lambda) - I_s(\lambda),$$

where $I_{inc}$ is the intensity of incident beam (the intensity measured without samples), $I_{abs}$ is the intensity loss due to the absorption of antenna, and $I_s$ is the intensity loss due to the scattering including all directions. Also, the transmitted intensity can be written as [9]

$$I(\lambda) = I_{inc}(\lambda) - C_{ext} \times S_{inc},$$

where $S_{inc}$ is the power density at the sample and $C_{ext}$ is the extinction cross section of the optical antenna (in unit of area). $C_{ext}$ can also be regarded as the area of the "geometric shadow" of the antenna, since the rate at which energy would impinge upon this area equals to the actual rate of energy removal from the incident beam due to the scattering and absorption by the antenna.

Figure 12.8 shows one measurement of extinction cross section for samples on ITO/glass substrate. Extinction cross section $C_{ext}$ and extinction efficiency $Q_{ext}$ – the ratio of the extinction cross section to geometrical cross section – are presented by black and red curves, respectively. In this sample, each equilateral triangle in the bow tie has a height of 240 nm and side of 280 nm, the gap between adjacent tips is 20 nm and sample thickness is 50 nm; the total geometrical area of the bow tie is 0.0672 $\mu$m$^2$. The bow tie structures are arranged at square lattice with spacing 3 µm, which is relatively large compared to the size of bow tie. Therefore the interaction between the bow tie structures can be neglected. At the peak of the extinction curve in Fig. 12.8, the value of $Q_{ext}$ is larger than 10, indicating the optical antenna appears 10 times larger than its original geometrical size at

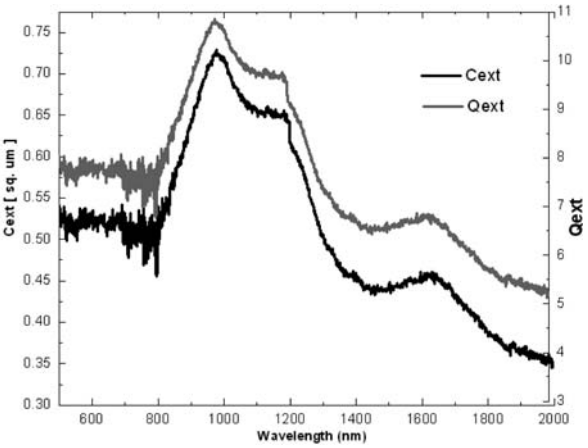


**Fig. 12.8** Extinction cross section of bow tie structures prepared on ITO/glass substrate. The actual geometric cross section is 0.0672 $\mu m^2$, while a value 10 times geometric cross section is observed by the detector.

this wavelength. To our knowledge, this is the best extinction efficiency reported experimentally.

Furthermore, bow tie structures of different sizes are prepared by electron beam lithography. The thickness and gap between nearest tips are maintained as 50 and 20 nm, respectively. The sides of the equilateral triangles vary from 100 to 350 nm. Similar transmission spectra have been measured for different samples and the resonant wavelengths for different sized bow tie structures are plotted in Fig. 12.9. From

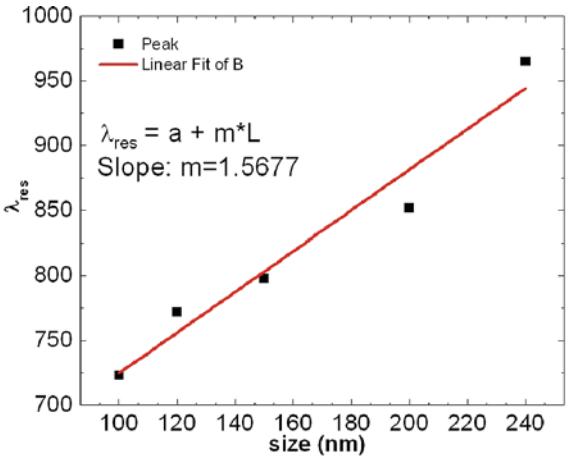


**Fig. 12.9** The resonant wavelength vs. the size of the bow tie. The resonant wavelengths are obtained from the peaks transmission spectra, which are plotted by *dots*, and the *line* is the linear fitting. The fitting parameters are shown in the inset table.

the figure, a nearly linear relationship between the size and resonant wavelength could be found for this range of resonant structure [9, 6].

From the transmission spectrum of bow tie structure, several peaks are evident, indicating different resonance modes related to different polarizations. When the polarization direction of incident light is parallel to the bow tie structure, due to a capacitive coupling between two triangles, the resonant wavelength red-shifts compared to the perpendicular polarization. We rotated the polarization of the incident light from parallel to perpendicular to the bow tie structure and measured the corresponding transmitted spectra, as shown in Fig. 12.10(b). Here, we choose extinction efficiency at 772 nm, the resonant wavelength for parallel polarization, and at 672 nm for perpendicular polarization. As revealed in the polar plot (Fig. 12.10(c)), a dipole-like extinction cross section is observed at both cases, suggesting dominant dipolar radiation modes of these bow tie structures. We also find the dipole strength along the long axis of bow tie structure is much stronger than that along the perpendicular direction.

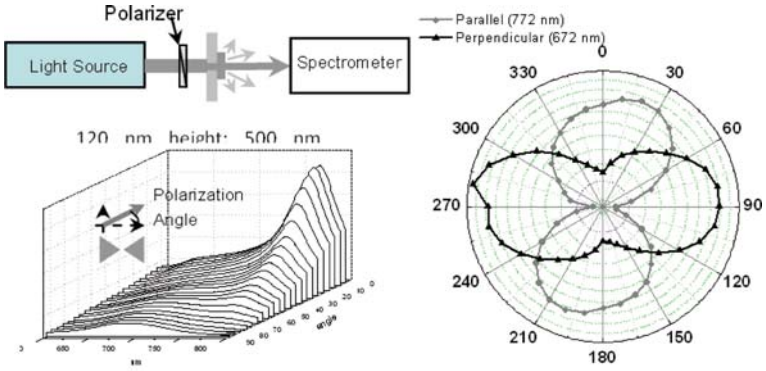


**Fig. 12.10** (**a**) Sketch of optical path in polarization-dependent transmission measurement. (**b**) Transmission spectrum measured by different polarization illumination. In the case, gold bow tie structure is made on ITO/glass substrate by electron beam lithography, the size of the triangle is 120 nm in height, pitch is 500 nm, gap between tip to tip is 20 nm, and thickness 50 nm. (**c**) The extinction intensity for different polarizations of incident light at resonant wavelength that are chosen at 772 nm (*grey*) and 672 nm (*black*) corresponding to parallel and perpendicular illumination, respectively. For clear observation, the scale of *black curve* is five times larger than *grey curve*.

We also conducted computer simulation by discrete dipole approximation (DDA) method to calculate the extinction spectrum of these designed bow tie structures. Figure 12.11 shows the extinction spectrum for 120 nm-sized triangles with tip-to-tip gap of 20 nm bow tie sample. Parallel (red) and perpendicular (blue) illumination was considered and single triangle sample (black) was also calculated for comparison. The simulation results are generally in good agreement with the experimental data.

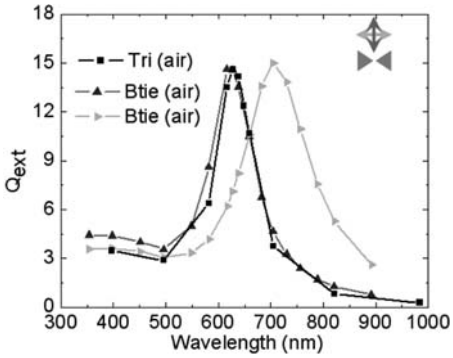


**Fig. 12.11** Simulated extinction spectrum by DDA method. *Light grey* and *dark grey curves* are the sample illuminated by parallel and perpendicular polarization incident light, respectively. Single triangle case plotted in *black curve* has been calculated for comparison.

### 12.3.1.2 Dark-Field Spectra

To enhance contrast of the scattered field, we also performed spectra measurement using dark-field illumination techniques. The principle of dark-field illumination is that the direct transmission of the illuminated light of a large solid angle is rejected by a finite aperture in the objective lens, so that only the scattered light from the sample at a relatively smaller solid angle will be detected with a dark background. Figure 12.12 shows the diagram of the illumination light path on a dark-field microscope. In such dark-field illumination, a metal-coated window with annular ring opening blocks the central beams from the light source, only leaving an outer ring of illumination. The condenser lens then focuses the light to the sample on the platform. Hence the illumination light on the sample is with a large incident angle. Most of the light is directly transmitted through the sample, while some is scattered. One selected objective lens with small NA, that collection angle is smaller than the illumination one, is used to collect the scattered light only. The directly transmitted light will miss the objective lens. Therefore, the image is produced by the scattered light from the sample. In our experiment, dark-field spectrum is measured using Micro-Spectroscopy/Light Microscopy Workstation (Zeiss Axio Observer D1 inverted microscope equipped with two incident-light halogen lamp illuminators, a 100-W Hg lamp, and a Zeiss AxioCam MRC color CCD camera).

In the above configuration, dark-field microscopy can effectively remove directly transmitted light and collect the scattered waves from the patterned optical nanoantenna samples, enhancing signal-to-noise ratio of resonantly scattered waves in the optical antenna system. In our experiment, gold bow tie structures (side length 120 nm, gap between tip to tip 20 nm, and thickness 50 nm) with different periodicities from 500 nm to 3 μm arranged in square lattice are fabricated by electron beam lithography. The total sample size is $50 \times 50 \mu m^2$. In the experimental setup, the incident angle of illumination light is around 53°, and 20× objective lens with NA = 0.45 is used to collect the scattered light. Figure 12.13(a) shows the optical

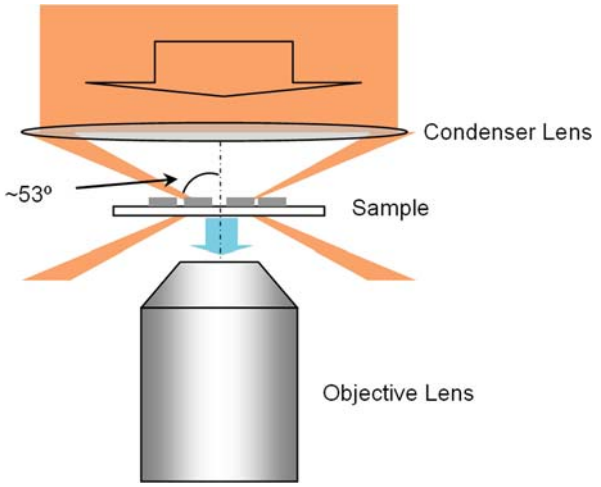


**Fig. 12.12** The sketch of optical path in dark-field measurement.

image taken in the dark-field microscope. The color of the dark-field image changes from blue to red and some of them are resonant in infrared range with increased spacing of these bow tie structures. The scattered spectra in visible range are measured using three different lattice constants and shown in Fig. 12.13(b). From the spectrum, the peaks scattered light are located at 530, 588, and 691 nm for lattice constants 750, 850, and 1,000 nm, respectively.

To understand the above result, we first assume that the color of the dark-field image is due to the diffraction from the square lattice of bow tie array under angular illumination. For simplification, the emitted light from each bow tie structure can be treated as the dipole radiation. This approximation is confirmed by measurement of polarization-dependent extinction spectrum of the bow tie nanoantennas under bright-field illumination. The dipole radiation from each bow tie has different initial phase due to the difference in position. By calculating the far-field interference of such arrays of dipoles, the scattered spectrum can be synthesized. Figure 12.14 shows the simulated spectrum for a dipole array arranged in square lattice with periodicity of 750, 850, and 1,000 nm, respectively. Because the substrate is not considered in the simple model, the peak position of simulated results displays a red shift. Nevertheless, the colors observed in the captured dark-field images are well explained by this simple model effectively. In the far field, the strongest scattered light is dominated by the dipole–dipole interaction due to the lattice.

### *12.3.2 Cathodoluminescence Spectroscopy*

In this study of optical nanoantennas, we also probe the plasmon modes of silver (Ag) bow tie structures using focused electron beam excitation of cathodoluminescence (CL) imaging and spectroscopy. Exploiting local electromagnetic field

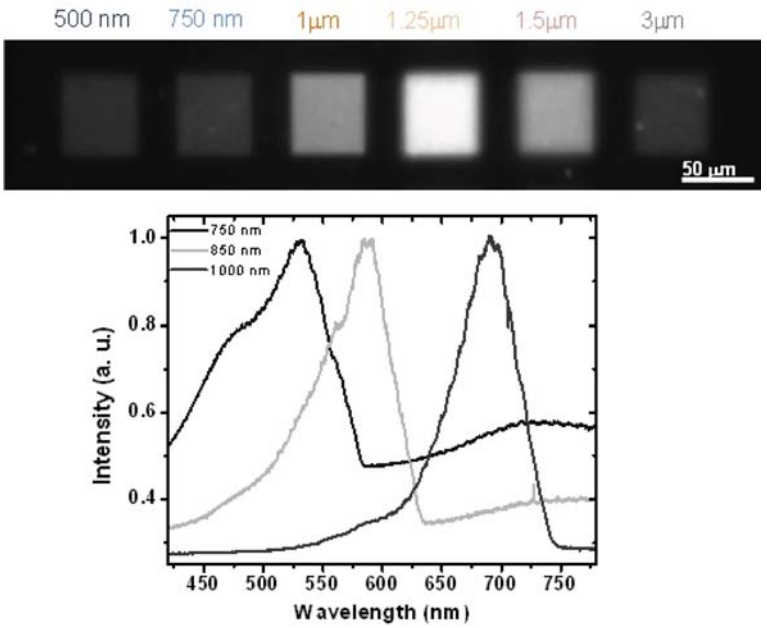


**Fig. 12.13** (**a**) Optical image captured in dark-field microscope. The periodicities of bow tie square arrays are 500 nm, 750 nm, 1 μm, 1.25 μm, 1.5 μm, and 3 μm, respectively. The size of each sample is $50 \times 50\ \mu m^2$. (**b**) The scattered light spectrum in visible range for periodicity is 750 nm (*black*), 850 nm (*light grey*), and 1,000 nm (*dark grey*), respectively.

enhancement associated with these plasmonic nanoantenna structures has led to several interesting applications such as enhanced fluorescence [4], enhanced photocarrier generation [23], and other nonlinear effects [26]. Often the field is confined

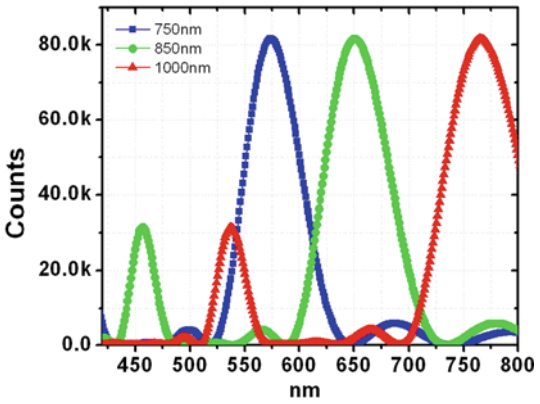


**Fig. 12.14** Simulated spectrum for dipole array arranged in square lattice with periodicity 750 nm (*black*), 850 nm (*light grey*), and 1,000 nm (*dark grey*), respectively.

spatially on length scales on the order of 10–50 nm and varies strongly with particle shape, size, and material composition [19]. Unfortunately, diffraction-limited optical imaging techniques do not have enough spatial resolution to image these plasmon modes or precisely locate the "hot-spots" responsible for producing enormous enhancement. Due to the diffraction limit, optical techniques are limited in their resolution capability to image the plasmon eigenmodes. Near-field scanning optical microscopy (NSOM) has been used to investigate these plasmon modes; however, the resolution is limited by the tip size ($\sim$ 50–100 nm). On the other hand, electron excitation can couple to these plasmon modes of large momentum mismatch with vacuum light. Recently electron excitation technique has been described to directly reveal the local density of plasmon states [17]. It is potentially capable of resolving details below tens of nanometers. Resolving surface plasmon modes and understanding the underlying physics are crucial to design better plasmonic devices tailored to specific applications.

In SEM-based CL imaging, an electron beam scans over a desired area of the sample. Luminescence induced by the electron beam is collected by a paraboloidal mirror and sent to the detector through an optical fiber (shown in Fig. 12.15(a)). The luminescence (photon emission) map is constructed based on the photocounts rate and the position of the electron beam. In spectroscopy mode, the emitted light is

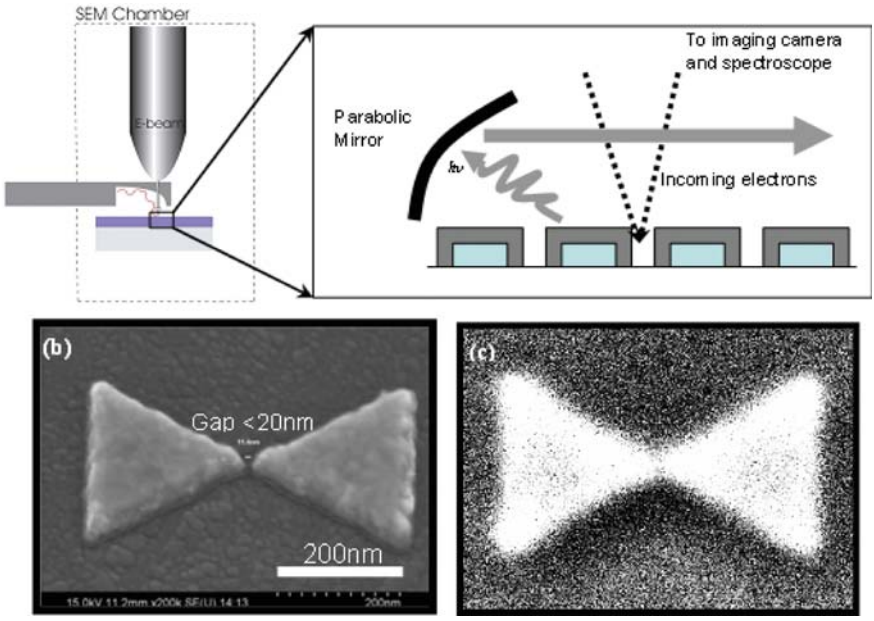


**Fig. 12.15** (**a**) The sketch of SEM-based cathodoluminescence system. The electron beam passes through an aperture in the paraboloidal mirror to the sample surface. The sample is placed at the focus of the mirror. Light emitted by the sample is collected by the mirror and directed to the detectors through a light guide. (**b**) Scanning electron micrograph of bow tie structure. (**c**) Panchromatic CL image of the same.

collected through a spectrometer which separates out different wavelength components. In panchromatic mode of imaging, only the sum of emitted light is recorded in the photodetector. Our measurements are performed using a 15 kV electron beam and a photomultiplier tube (PMT) detector with sensitivity encompassing near-ultraviolet (UV) and visible wavelengths (250–850 nm). Mechanism of photon emission or luminescence induced by an electron beam on its interaction with a metal particle has been well studied [16].

In the CL measurement, an array of Ag bow tie structure is fabricated by electron beam lithography. The size of each triangle is around 200 nm with thickness of 40 nm and the gap between adjacent tips is smaller than 20 nm. Silicon is chosen as the substrate material, to suppress background cathodoluminescence in the wavelength range of interest (near-UV and visible).

Figure 12.15(b) shows the secondary electron image (SEI) of one bow tie structure which gives the topographic information about the specimen. Figure 12.15(c) is a panchromatic CL image (PanCL). In such panchromatic mode all of the emitted light is collected by the detector and hence the intensity at each pixel represents the integrated photon counts in the sensitivity range of the detector. PanCL image clearly depicts plasmon-induced luminescence in such Ag bow tie. This luminescence arises due to induced electromagnetic field on the nanostructure caused by the impinging focused electrons. By raster scanning the focused electron beam and collecting emitted photons rather than secondary electrons, a complete luminescence image is acquired on the bow tie nanoantenna.

Collecting the emitted light through a grating monochromator allows resolving spectral features as shown in Fig. 12.16. The grey curve was obtained on a flat

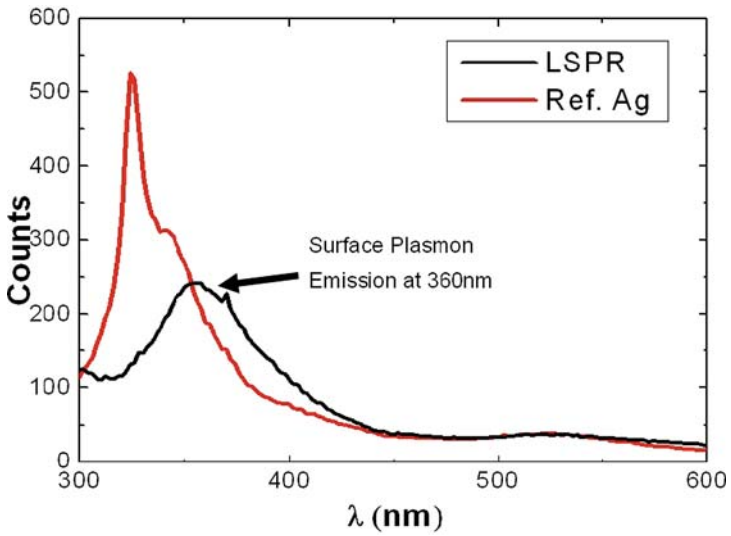


**Fig. 12.16** The emission spectrum of Ag triangular array structure (*black*) and bulk Ag film (*grey*) using electron excitation in spectroscopy mode.

silver film with no surface features (except the native roughness of the film, RMS ∼ 1–2 nm). We can clearly observe a sharp emission peak at 325 nm, corresponding to the bulk plasmon mode of silver, accompanied by a surface plasmon mode at 340 nm. The location of these resonant peaks matches with the material permittivity data of silver [30] within ±5 nm. In contrast, from the emission spectra of Ag bow tie structure (the black curve), we see a dominant peak around 360 nm, indicating strong contribution of localized surface plasmon from the nanostructures. From the PanCL image, we can observe that the high plasmon density modes of resonance are concentrated at the corner and edge of the bow tie structure.

In summary, we experimented direct electron excitation and photoemission of decoupled surface plasmon modes with CL spectroscopy on bow tie optical antenna. In panchromatic mode photon maps, we are able to observe the locally resonant plasmon mode with fine resolution (down to 20 nm).

## 12.4 Application

### *12.4.1 Surface-Enhanced Raman Spectroscopy*

Surface-enhanced Raman scattering (SERS) is a surface-sensitive excitation process that results in the enhancement of Raman scattering of molecules near metal surfaces. The potential of this phenomenon in a variety of applications such as biochemical sensing, semiconductor characterization, and energy science has stimulated great interest in understanding and quantifying such processes using plasmonic nanostructures. One of the possible mechanisms behind this enhancement is based on electromagnetic effects [24] wherein the increased intensity of the Raman signal is a result of the enhanced electric field on the metal surface due to localized surface plasmon excitation. The field enhancement is greatest when the plasmon frequency is in resonance with the radiation.

SERS substrates have conventionally relied on electrochemical roughening of noble metal surfaces such as Ag, Cu, Pt [14]. These processes lack flexibility in assigning enhancements to specific locations. More recently, the surfaces are often prepared by using a set of metal nanoparticles on the surfaces [28]. The shape and size of the metal nanoparticles, acting as nanoantennas, strongly affect the strength of the enhancement since the factors influence the ration of absorption and scattering events [3]. In this section, we will explore the experimental efforts of using array of bow ties as the SERS substrate.

In this study, silver bow tie structures are fabricated by solid-state superionic stamping (S4). The size of the triangle varies from 120 to 500 nm and the gap between nearest tips changes from 0 to 20 nm. SEM image of a single bow tie structure is shown in Fig. 12.17(a). The thickness of bow tie structure is maintained at 50 nm and they are aligned in square lattice with periodicity of 3 μm. $Al_2O_3$ (2 nm) was deposited by atomic layer deposition (ALD) on the top of the surface to minimize charge-transfer effect from the absorbent molecules to the metal particles [18].

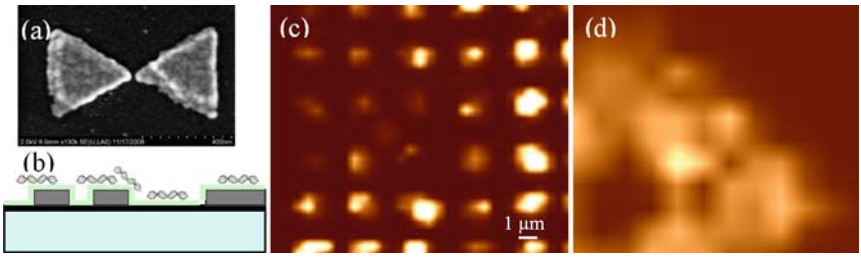


**Fig. 12.17** (**a**) SEM image of one bow tie structure with triangle size 350 nm and gap between tip to tip 30 nm; (**b**) sketch of cross section; (**c**) Raman map of bow tie array with 1 M 2′,2-cyanine; and (**d**) Raman map of Cr thin film with 1 mM 2,2′-cyanine.

2,2′-Cyanine solution of 1 mM and 1 μM was used to examine the effect of concentration on Raman scattering as well as EM-field enhancement of the gold bow tie structures. The substrates were treated with the 2, 2′-cyanine solutions of different concentrations by incubating the patterned area in the solutions for 30 min to promote adsorption of the molecules to the alumina surface and rinsed with deionized water and dried with a flow of compressed air. With this approach, the 2, 2′-cyanine molecules were spaced from the surface of the silver features and the effect of EM-field enhancement could be examined. The sketch of cross section of the sample is shown in Fig. 12.17(b).

Raman spectra were taken on the Jobin Yvon LabRam HR 800 micro-Raman spectrometer with a 532 nm laser source and a 100× objective. For EM-field enhancement spatial effect, Raman mapping was used to collect the Raman spectra of the entire bow tie pattern. The excitation laser intensity was tuned to 148 μW for all mapping, and the step size and integration time at each step were set at 0.5 $\mu$m and 0.5 s, respectively. The accumulated Raman intensity over the entire map was then plotted for analysis. Figure 12.17(c) and (d) shows the comparison of the Raman map of the bow tie array and reference Cr surface. The concentration of 2, 2′-cyanine solutions for these two samples are 1 μM and 1 mM, respectively. The Raman spectrum for bow tie structure, silver thin film, and Cr thin film have been shown in Fig. 12.18. It should be mentioned that the concentration of 2, 2′-cyanine solution for bow tie structure is 1 μM, while it is 1 mM for Ag and Cr thin film.

To calculate enhancement factor, $EF$, we are comparing the measured intensity on the bow ties against a reference substrate. Since a uniform $Al_2O_3$ coating is applied on both bow ties and reference surfaces, we assume the surface coverage is nearly the same, so the enhancement factor can be defined as follows:

$$EF = \frac{I_{SERS}/I_{ext} \times A_{SERS} \times t_{SERS}^{int} \times C_{SERS}}{I_{ref}/I_{ext} \times A_{ref} \times t_{ref}^{int} \times C_{ref}},$$

where $I_{SERS}$ is the Raman peak intensity from nanopatterned area, $I_{ref}$ is the Raman signal intensity obtained from reference area, $I_{ext}$ is the excitation intensity, $t$s are the integration time for either cases, and $C$s are the concentrations of the solution used

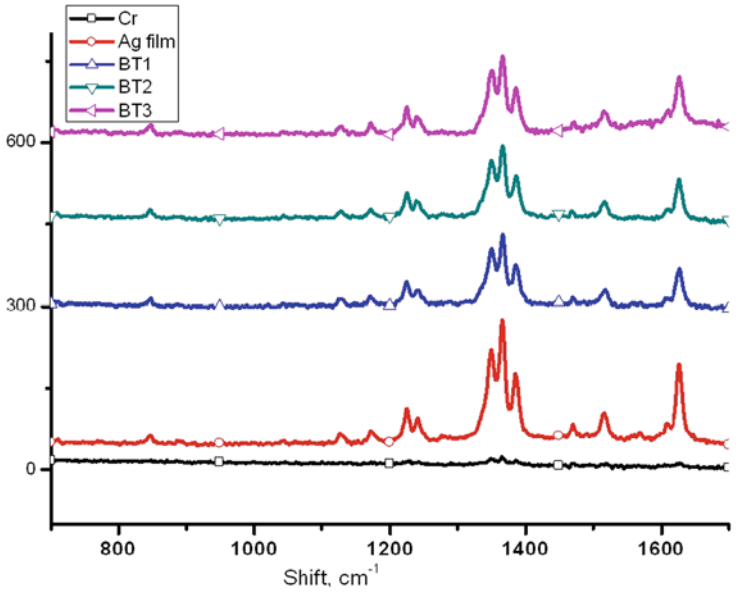


**Fig. 12.18** Raman spectrum of the 1 M 2,2′-cyanine enhanced by the localized surface plasmon resonance of the bow tie structure, comparing with the Ag/Cr substrate treated with 1 mM 2,2′-cyanine solutions.

to treat the nanopatterned region and that of the solution treating the reference. The *EF*s for different parameters of bow tie structure have been plotted in Fig. 12.19, which shows enhancement of $10^6$–$10^7$ in Raman signal.

This short example outlines the use of the optical antenna – bow tie array as SERS substrate to study the effect on Raman scattering intensity of 2,2′-cyanine molecules situated on these structures. Our study suggests that Raman scattering process can indeed be tuned by the geometry and loading of the bow tie antennas, which shows good potential of optical antenna used as SERS substrate.

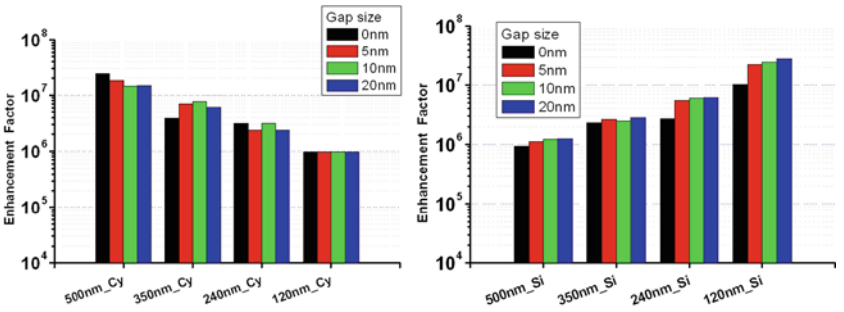


**Fig. 12.19** The enhancement factor of different-sized bow ties fabricated on different substrates.

## 12.5 Summary

Harvesting and confining light using plasmonic nanoantennas represent an interesting frontier of metamaterial research. The convergence of RF and optical device designs will bring revolutionary changes in highly compact and integrated photonics for photon energy conversion, adaptive sensing, and image processing. We expect many inspirations from RF metamaterial research to be transformed on the study of optical antennas and this could bring a profound impact to the field of nanophotonics.

**Acknowledgments** The authors are grateful for the financial supports from the Defense Advanced Research Projects Agency (grant HR0011-05-3-0002), Office of Naval Research (grant N00173-07-G013), and National Science Foundation (grant CMMI-0709023). Cathodoluminescence experiments were carried out in the Frederick Seitz Materials Research Laboratory Central Facilities, University of Illinois, which are partially supported by the U.S. Department of Energy under grants DE-FG02-07ER46453 and DE-FG02-07ER46471.

## References

1. Alu, A., and Engheta, N.: Tuning the scattering response of optical nanoantennas with nanocircuit loads. Nat. Photon. **2**, 307–310 (2008)
2. Alu, A., and Engheta, N.: Input impedance, nanocircuit loading and radiation tuning of optical nanoantennas. Phys. Rev. Lett. **101**, 043901–043904 (2008)
3. Aroca, R.: Surface-enhanced Vibrational Spectroscopy. UK John Wiley & Sons Ltd, Chichester (2006)
4. Bharadwaj, P., and Novotny, L.: Spectral dependence of single molecule fluorescence enhancement. Opt. Express **15**, 14266–14274 (2007)
5. Bohren, C.F., and Huffman, D.R.: Absorption and Scattering of Light by Small Particles. Wiley, New York (1998)
6. Bryant, G.W., Abajo, F.J.G., and Aizpurua, J.: Mapping the plasmon resonances of metallic nanoantennas. Nano Lett. **8**, 631–636 (2008)
7. Chou, S. Y., Krauss, P. R., and Renstrom, P. J.: Nanoimprint lithography. J. Vac. Sci. Technol. B **14**, 4129–4133 (1996)
8. Chou, S. Y., Krauss, P. R., Zhang, W., Guo, L., and Zhuang, L.: Sub-10 nm imprint lithography and applications. J. Vac. Sci. Technol. B **15**, 2897–2904 (1997)
9. Crozier, K.B., Sundaramurthy, A., Kino, G.S., and Quate, C.F.: Optical antennas: resonators for local field enhancement. J. Appl. Phys. **94**, 4632–4642 (2003)
10. Cubukcu, E., Kort, E.A., Crozier, K.B., and Cappaso, F.: Plasmonic laser antenna. Appl. Phys. Lett. **89**, 093120–093123 (2006)
11. Draine, B.T., and Flatau, P.J.: User guide for the Discrete Dipole Approximation Code DDSCAT 7.0. http://arxiv.org/abs/0809.0337
12. Engheta, N., Salandrino, A., and Alu, A.: Circuit elements at optical frequencies: Nanoinductors, nanocapacitors and nanoresistors. Phys. Rev. Lett. **95**, 095504.4 (2005)
13. Farahani, J.N., Eisler, H.J., Pohl, D.W., Pavius, M., Fluckiger, P., Gasser, P., and Hecht, B.: Bow-tie optical antenna probes for single-emitter scanning near-field optical microscopy. Nanotechnology **18**, 125506 (2007)
14. Fleischmann, M., Hendra, P.J., and McQuillan, A.J.: Raman spectra of pyridine ad-sorbed at a silver electrode. Chem. Phys. Lett. **26**, 163–166 (1974)

15. Fromm, D.P., Sundaramurthy, A., Schuck, P.J., Kino, G., and Moerner, W.E.: Gap-dependent optical coupling of single bowtie nanoantennas resonant in the visible. Nano Lett. **4**, 957–961 (2005)
16. Garcia de Abajo, F.J., and Howie, A.: Relativistic electron energy loss and electron-induced photon emission in inhomogeneous dielectrics. Phys. Rev. Lett. **80**, 5180 (1998)
17. Garcia de Abajo, F.J., and Kociak, M.: Probing the photonic local density of states with electron energy loss spectroscopy. Phys. Rev. Lett. **100**, 106804.4 (2008)
18. Grant, A.M., and Creighton, J.A.: Anomalously intense Raman spectra of pyridine at a silver electrode. J. Am. Chem. Soc. **99**, 5215–5219 (1977)
19. Haes, A.J., Haynes, C.L., McFarland, A.D., Schatz, G.C., Van Duyne, R.R., and Zou, S.L.: Plasmonic materials for surface-enhanced sensing and spectroscopy. MRS Bull. **30**, 368–375 (2005)
20. Hao, E., and Schatz, G.C.: Electromagnetic fields around silver nanoparticles and dimers. J. Chem. Phys. **120**, 357–366 (2004)
21. Hewageegana, P., and Stockman, M.I.: Plasmonic enhancing nanoantennas for photodetection. Infrared Phys. Tech. **50**, 177–181 (2007)
22. Hsu, K.H., Schultz, P.L., Ferreira, P.M., and Fang, N.X.: Electrochemical nanoim-printing with solid-state superionic stamps. Nano Lett. **7**, 446–451 (2007)
23. Ishi, T., Fujikata, J., Makita, K., Baba, T., and Ohashi, K.: Si nano-photodiode with a surface plasmon antenna. Japan. J. Appl. Phys. **44**, L364–L366 (2005)
24. Jeanmaire, D.L., and Van Duyne, R.P.: Surface Raman electrochemistry part I. Heterocyclic, aromatic and aliphatic amines adsorbed on the anodized silver electrode. J. Electro Anal. Chem. **84**, 1–20 (1977)
25. Kempa, K., Rybczynski, J., Huang, Z., Gregorczyk, K., Vidan, A., Kimball, B., Carl-son, J., Benham, G., Wang, Y., Herczynski, A., and Ren, Z.: Carbon nanotubes as optical antennae. Adv. Mater. **19**, 421–426 (2007)
26. Kim, S., Jin, J.H., Kim, Y.J., Park, I.Y., Kim, Y., and Kim, S.W.: High-harmonic gen-eration by resonant plasmon field enhancement. Nature **453**, 757–760 (2008)
27. Mühlschlegel, P., Eisler, H.-J., Martin, O.J.F., Hecht, B., and Pohl, D.W.: Resonant optical antennas. Science **308**, 1607–1609 (2005)
28. Mock, J.J.: Shape effects in plasmon resonance of individual colloidal silver nanopar-ticles. J. Chem. Phys. **116**, 6755 (2002)
29. Novotny, L.: Effective wavelength scaling for optical antennas. Phys. Rev. Lett. **98**, 266802–266804 (2007)
30. Palik, E.D.: Handbook of Optical Constants of Solids. Academic Press, Orlando, FL (1984)
31. Schuck, P.J., Fromm, D.P., Sundaramurthy, A., Kino, G.S., and Moerner, W.E.: Im-proving the mismatch between light and nanoscale objects with gold bowtie nanoantennas. Phys. Rev. Lett. **94**, 017402–017404 (2005)
32. Schultz, P.L., Hsu, K.H., Fang, N.X., and Ferreira, P.M.: Solid-state electrochemical nanoim-printing of copper. J. Vac. Sci. Technol. B **25**, 2419–2424 (2007)
33. Shumaker-Parry, J.S., Rochholz, H., and Kreiter, M.: Fabrication of crescent-shaped optical antennas. Adv. Mater. **17**, 2131–2134 (2005)
34. Sivenpiper, D. et al.: High-impedance EM surfaces with a forbidden frequency band. IEEE Trans. Micro. Theo. Tech. **47**, 2059 (1999)
35. Tang, L., and Miller, D.A.B.: C-shaped nanoaperture-enhanced Germanium photodetector. Opt. Lett. **31**, 1519–1521 (2006)
36. Wang, Y., Kempa, K., Kimball, B., Carlson J.B., Benham, G., Li, W.Z., Kempa, T., Rybczynski, J., Herczynski, A., and Ren, Z. F.: Receiving and transmitting light-like ra-diowaves: antenna effect in arrays of aligned carbon nanotubes. Appl. Phys. Lett. **85**, 2607–2609 (2004)

# Chapter 13
# Wideband and Low-Loss Metamaterials for Microwave and RF Applications: Fast Algorithm and Antenna Design

Le-Wei Li, Ya-Nan Li and Li Hu

**Abstract** In this chapter, a fast solver, i.e., adaptive integral method (AIM) which is based on hybrid volume–surface integral equation, is utilized in the numerical simulation of electromagnetic scattering from composite left-handed materials (LHM) such as split-ring resonators (SRR) with rods/wires. The volume electric field integral equation (EFIE) is applied to the dielectric region of this LHM, and the surface EFIE is applied on the conducting surface. The method of moments (MoM) is used to discretize the integral equation into a matrix solution and AIM is employed to reduce the memory requirement and CPU time for the matrix solution. Numerical results and computational complexity analysis have shown that the AIM solver can significantly reduce the computational cost while maintaining a good accuracy. Inspired by the periodicity of SRR, the ASED-AIM, a new adaptive integral approach based on accurate sub-entire-domain method, has been proposed to solve the electromagnetic scattering by large-scale finite periodic arrays, especially the LHM structures like SRR. Several results are shown to demonstrate the efficiency of the method in solving periodic structures. Additionally, further computational time saving scheme for calculating the near-zone interaction matrix has been proposed. Both 2-D and 3-D periodic structures can be solved by this fast solver with impressive efficiency and accuracy. In the last section of this chapter, a novel rectangular patch antenna was specifically designed using planar-patterned LHM concepts. This new antenna has demonstrated to have left-handed characteristics. It is shown to have great impact on the antenna performance enhancement in terms of the bandwidth significantly broadened and also in terms of high efficiency, low loss, and low VSWR. A good agreement is achieved between the simulation and measured results. This new antenna designed has strong radiation in the horizontal direction within the entire working band, which is desirable for some special applications.

Joshua Le-Wei Li*, Ya-Nan Li and Li Hu
Department of Electrical and Computer Engineering, National University of Singapore, 10 Kent Ridge Crescent, Singapore 119260. *e-mail: lwli@nus.edu.sg

T.J. Cui et al. (eds.), *Metamaterials*, DOI 10.1007/978-1-4419-0573-4_13,

**Key words:** Method of moments, split-ring resonator, adaptive integral method, electric field integral equations, hybrid volume surface integral equations, ASED-AIM, finite periodical structure, scattering, RCS, LHM antenna, wideband, high gain, horizontal radiation, planar LHM, RF application.

## 13.1 Adaptive Integral Method (AIM) for Left-Handed Material (LHM) Simulation

Left-handed material (LHM) [43], which is also known as negative index material (NIM), represents a material of simultaneous negative permeability and permittivity. Typical LHMs, such as split-ring resonator (SRR) structure [41], are composed of a large array of periodical elements of dielectric body and conducting patches which usually require considerable computational costs during numerical simulation. Previous researchers have often used the method of moments (MoM) [18] to carry out numerical simulations and have proven its reliability and accuracy. Among several fast solvers which are developed based on MoM, the adaptive integral method (AIM) [3, 23, 13] is one of the very efficient solvers which can tremendously reduce the memory requirement for LHM structures like SRR and accelerate the matrix-vector multiplications in the iterative solution procedure.

### *13.1.1 Hybrid Volume–Surface Integral Equation (VSIE) and MoM for SRRs*

For SRR structures, both the dielectric substrate and the metal layer have induced currents and therefore contribute to scattered field to the total electromagnetic (EM) field. So, we need to adopt hybrid volume–surface integral equations (VSIE) to characterize the field.

In the dielectric region $V$, by taking the scattered field from both the surface current and the volume current into consideration, the total electric field becomes

$$\boldsymbol{E}(\boldsymbol{r}) = \boldsymbol{E}^i(\boldsymbol{r}) + \boldsymbol{E}^s_V(\boldsymbol{r}) + \boldsymbol{E}^s_S(\boldsymbol{r}), \quad \boldsymbol{r} \in V, \tag{13.1}$$

where $\boldsymbol{E}(\boldsymbol{r})$ represents the total field in region $V$, $\boldsymbol{E}^i(\boldsymbol{r})$ denotes the incident field, while $\boldsymbol{E}^s_V(\boldsymbol{r})$ and $\boldsymbol{E}^s_S(\boldsymbol{r})$ stand for the electric fields scattered by volume elements and surface elements in region $V$, respectively.

Since the SRR structure consists of a very thin metal layer and dielectric body where the thickness of the metal layer can be considered to be almost 0, the tangential components of total electric field vanishes on conducting surface:

$$\hat{\boldsymbol{n}} \times \boldsymbol{E}^i(\boldsymbol{r}) = -\hat{\boldsymbol{n}} \times \boldsymbol{E}^s_V(\boldsymbol{r}) - \hat{\boldsymbol{n}} \times \boldsymbol{E}^s_S(\boldsymbol{r}). \tag{13.2}$$

Equations (13.1) and (13.2) are known as the electric field integral equations (EFIE) as they involve only electric field. The EFIE is suitable for structures with open conducting surface. Inside the dielectric region $V$ and on the surface $S$ of conducting body, the incident wave induces a volume current $\boldsymbol{J}_V$ and a surface current $\boldsymbol{J}_S$. The induced volume and surface currents can generate scattered electromagnetic field as follows:

$$\boldsymbol{E}^s_\Omega(\boldsymbol{r}) = -jk_0\eta_0\boldsymbol{A}_\Omega(\boldsymbol{r}) - \nabla\Phi_\Omega(\boldsymbol{r}), \qquad \Omega = S \text{ or } V, \tag{13.3}$$

where the magnetic vector potential is defined as

$$\boldsymbol{A}_\Omega(\boldsymbol{r}) = \int_\Omega \boldsymbol{J}_\Omega(\boldsymbol{r},\boldsymbol{r}')g(\boldsymbol{r},\boldsymbol{r}')d\boldsymbol{r}', \qquad \Omega = S \text{ or } V, \tag{13.4}$$

while the electric scalar potential is defined as

$$\Phi_\Omega(\boldsymbol{r}) = -\frac{\eta_0}{jk_0}\int_\Omega \nabla'\cdot\boldsymbol{J}_\Omega(\boldsymbol{r},\boldsymbol{r}')g(\boldsymbol{r},\boldsymbol{r}')d\boldsymbol{r}', \qquad \Omega = S \text{ or } V, \tag{13.5}$$

where $g(\boldsymbol{r},\boldsymbol{r}') = \dfrac{e^{-jk_0|\boldsymbol{r}-\boldsymbol{r}'|}}{4\pi|\boldsymbol{r}-\boldsymbol{r}'|}$, $\eta_0 = \sqrt{\frac{\mu_0}{\varepsilon_0}}$, and $k_0$ denotes the wave number of background medium (free space in this SRR investigation).

The volume of dielectric material and surface of conducting body of SRR are meshed into tetrahedral elements and triangular patches, respectively. These basis function elements are used because of their flexibility to model arbitrarily shaped 3-D objects. The volume and surface currents are expanded using different vector basis functions. For surface elements, it is convenient to use the planar triangular basis functions or the Rao–Wilton–Glisson (RWG) basis functions [37] to expand the equivalent surface electric current. As for volume elements, similarly, we can apply the Schaubert–Wilton–Glisson (SWG) basis functions [39] to expand the equivalent volume electric current, that is,

$$\boldsymbol{J}_S = \sum_{n=1}^{N_S} I_n^S \boldsymbol{f}_n^S, \tag{13.6a}$$

$$\boldsymbol{J}_V = j\omega\sum_{n=1}^{N_V}\frac{\tilde{\varepsilon}(\boldsymbol{r})-\varepsilon_0}{\tilde{\varepsilon}(\boldsymbol{r})}I_n^V\boldsymbol{f}_n^V = j\omega\sum_{n=1}^{N_V}\kappa(\boldsymbol{r})I_n^V\boldsymbol{f}_n^V, \tag{13.6b}$$

where $\kappa(\boldsymbol{r}) = \dfrac{\tilde{\varepsilon}(\boldsymbol{r})-\varepsilon_0}{\tilde{\varepsilon}(\boldsymbol{r})}$ denotes the contrast ratio and $\tilde{\varepsilon}(\boldsymbol{r})$ represents the permeability of a tetrahedron element.

After substituting above equations into the EFIE, we apply the Galerkin's MoM testing procedure. Then, the integral equations are converted into a linear equation system written as

$$\begin{bmatrix} \boldsymbol{Z}^{\bar{V}V} & \boldsymbol{Z}^{\bar{V}S} \\ \bar{\boldsymbol{Z}}^{SV} & \bar{\boldsymbol{Z}}^{SS} \end{bmatrix}\begin{bmatrix} \boldsymbol{I}^V \\ \boldsymbol{I}^S \end{bmatrix} = \begin{bmatrix} \boldsymbol{E}^V \\ \boldsymbol{E}^S \end{bmatrix}, \tag{13.7}$$

where the vectors $\boldsymbol{I}^V$ and $\boldsymbol{I}^S$ represent the expansion coefficients of volume currents and surface currents, respectively. The excitation vector can be computed using

$$\boldsymbol{E}_m^V = \int_{V_m} \boldsymbol{f}_m^V \cdot \boldsymbol{E}^i(\boldsymbol{r}')d\boldsymbol{r}', \tag{13.8a}$$

$$\boldsymbol{E}_m^S = \int_{S_m} \boldsymbol{f}_m^S \cdot \boldsymbol{E}^i(\boldsymbol{r}')d\boldsymbol{r}'. \tag{13.8b}$$

The elements of the block matrices in Eq. (13.7) can be computed using the formulas shown below:

$$Z_{mn}^{VV} = \int_{V_m} \frac{\boldsymbol{f}_m^V \boldsymbol{f}_n^V}{\tilde{\varepsilon}} d\boldsymbol{r} - \omega k_b \eta_b \int_{V_m} \boldsymbol{f}_m^V \left[ \int_{V_n} \kappa \boldsymbol{f}_n^V g(\boldsymbol{r},\boldsymbol{r}')d\boldsymbol{r}' + \frac{\nabla}{k_b^2} \int_{V_n} \nabla' \cdot \left(\kappa \boldsymbol{f}_n^V\right) g(\boldsymbol{r},\boldsymbol{r}') \right] d\boldsymbol{r}, \tag{13.9a}$$

$$Z_{mn}^{VS} = jk_b \eta_b \int_{V_m} \boldsymbol{f}_m^V \cdot \left[ \int_{S_n} \boldsymbol{f}_n^s g(\boldsymbol{r},\boldsymbol{r}')d\boldsymbol{r}' + \frac{\nabla}{k_b^2} \int_{S_n} \nabla' \cdot \boldsymbol{f}_n^S g(\boldsymbol{r},\boldsymbol{r}')d\boldsymbol{r}' \right] d\boldsymbol{r}, \tag{13.9b}$$

$$Z_{mn}^{SV} = -\omega k_b \eta_b \int_{S_m} \boldsymbol{f}_m^S \cdot \left[ \int_{V_n} \kappa \boldsymbol{f}_n^V g(\boldsymbol{r},\boldsymbol{r}')d\boldsymbol{r}' + \frac{\nabla}{k_b^2} \int_{V_n} \nabla' \cdot \left(\kappa \boldsymbol{f}_n^V\right) g(\boldsymbol{r},\boldsymbol{r}')d\boldsymbol{r}' \right] d\boldsymbol{r}, \tag{13.9c}$$

$$Z_{mn}^{SS} = jk_b \eta_b \int_{S_m} \boldsymbol{f}_m^S \cdot \left[ \int_{S_n} \boldsymbol{f}_n^S g(\boldsymbol{r},\boldsymbol{r}')d\boldsymbol{r}' + \frac{\nabla}{k_b^2} \int_{S_n} \nabla' \cdot \boldsymbol{f}_n^S g(\boldsymbol{r},\boldsymbol{r}')d\boldsymbol{r}' \right] d\boldsymbol{r}, \tag{13.9d}$$

where $\kappa$ denotes a constant value within the tetrahedron and can be taken out from the integration:

$$\nabla \cdot \left(\kappa \boldsymbol{f}_n^V\right) = \kappa \nabla \cdot \boldsymbol{f}_n^V + \nabla \kappa \cdot \boldsymbol{f}_n^V. \tag{13.10}$$

The second term given by the above equation in (13.10) is

$$\nabla \kappa \cdot \boldsymbol{f}_n^V = \begin{cases} I_n^V(\kappa_n^+ - \kappa_n^-), & \text{on the common face } t; \\ 0, & \text{elsewhere.} \end{cases} \tag{13.11}$$

### *13.1.2 Formulations for AIM*

The matrix-vector multiplication implemented inside the AIM solution procedure can be summarized using the following four steps [14]:

- to project the sources distributed on the basis functions onto the regular grid by matching their vector and scalar potentials at some given test points to guarantee the approximate equality of their far fields;
- to evaluate the potentials at other grid locations produced by these grid-projected sources by a 3-D convolution;
- to interpolate the grid point potentials onto the testing functions; the projection and interpolation operators are represented by sparse matrices, and the

convolution can be carried out rapidly using discrete fast Fourier transforms (FFTs); and
- to compute the near-field interactions directly and remove the errors introduced by the far-field operators.

To employ the AIM, the object is enclosed in a rectangular grid and then recursively subdivided into small rectangular grids. In order to use the FFT to approximate the far-zone interaction, we need to transfer the SWG and RWG basis functions into the Cartesian grids. It is noted that by using vector identity and divergence theorem, the $\nabla$ operator in Eq. (13.9a) can be shifted and operated on the testing functions [37, 39]. Hence, we can denote $\gamma_n$ to represent any one of the components $\{\boldsymbol{f}^S, \kappa\boldsymbol{f}^V, \nabla\cdot(\kappa\boldsymbol{f}_V)\}$ and express all the matrix elements in Eq. (13.9a) in the following unified form:

$$Z_{mn} = \int_{\alpha_m}\int_{\alpha_n} \gamma_m(\boldsymbol{r}) g(\boldsymbol{r},\boldsymbol{r}')\gamma_n(\boldsymbol{r}')d\boldsymbol{r}'d\boldsymbol{r}. \tag{13.12}$$

The transformation function $\gamma_n(\boldsymbol{r})$ can be approximated as a linear combination of Dirac delta functions, i.e.,

$$\gamma_n(\boldsymbol{r}) \approx \hat{\gamma}(\boldsymbol{r}) = \sum_{u=1}^{(m+1)^3} \Lambda_{nu}\delta(\boldsymbol{r}-\boldsymbol{r}'), \tag{13.13}$$

where $m$ represents the expansion order, while $\Lambda_{nu}$ denotes the expansion coefficients of $\gamma_n(\boldsymbol{r})$ and it can be determined using the multipole expansion or far-field approximation [23]. The multipole expansion method is applied based on the criterion that the coefficients $\Lambda_{nu}$ produce the same multipole moments of the original basis function for $0 \le \{m_1, m_2, m_3\} \le M$:

$$\begin{aligned}\int_{\alpha_n} \gamma_n(\boldsymbol{r})(x-x_0)^{m_1}(y-y_0)^{m_2}(z-z_0)^{m_3}d\boldsymbol{r} \\ = \sum_{u=1}^{(m+1)^3} (x_{nu}-x_0)^{m_1}(y_{nu}-y_0)^{m_2}(z_{nu}-z_0)^{m_3}\Lambda_{nu},\end{aligned} \tag{13.14}$$

where the reference point $\boldsymbol{r}_0 = (x_0, y_0, z_0)$ is chosen as the center of the basis function. The far-field approximation method matches the far fields produced by $\gamma_n(\boldsymbol{r})$ and $\hat{\gamma}_n(\boldsymbol{r})$ on a unit sphere, and it thus obtains the expansion coefficients. Once the transformation function has been determined, the matrix elements can be approximated as

$$Z_{mn} = \sum_{v=1}^{(m+1)^3}\sum_{u=1}^{(m+1)^3} \Lambda_{mv} g(\boldsymbol{r}_v, \boldsymbol{r}'_u)\Lambda_{nu}. \tag{13.15}$$

By using the transformation function, now we are able to compute the two components in the matrix-vector multiplications in Eq. (13.7) with

$$\overline{\boldsymbol{Z}}^{\text{far}} = \overline{\boldsymbol{\Lambda}}\overline{\boldsymbol{g}}\overline{\boldsymbol{\Lambda}}^{T}, \tag{13.16a}$$

$$\overline{\boldsymbol{Z}}^{\text{near}} = \overline{\boldsymbol{Z}}_{nz}^{\text{MoM}} - \overline{\boldsymbol{Z}}^{\text{far}}, \tag{13.16b}$$

where $\overline{\boldsymbol{Z}}^{\text{near}}$ denotes the matrix containing only the direct interaction of neighbor elements and $\overline{\boldsymbol{\Lambda}}$ represents the basis transformation matrix of the elements. The matrix $\overline{\boldsymbol{g}}$ is Toeplitz and this enables the use of FFT to compute the 3-D convolution efficiently. Hence we can represent the matrix-vector multiplication as

$$\overline{\boldsymbol{Z}}\boldsymbol{I} = \overline{\boldsymbol{Z}}^{\text{near}}\boldsymbol{I} + \overline{\boldsymbol{Z}}^{\text{far}}\boldsymbol{I} = \overline{\boldsymbol{Z}}^{\text{near}}\boldsymbol{I} + \overline{\boldsymbol{\Lambda}}\Im^{-1}\left\{\Im\{\overline{\boldsymbol{g}}\}\cdot\Im\{\overline{\boldsymbol{\Lambda}}^{T}\boldsymbol{I}\}\right\}, \tag{13.17}$$

where $\Im\{\bullet\}$ and $\Im^{-1}\{\bullet\}$ stand for the FFT and its inverse FFT, respectively.

### *13.1.3 Numerical Results of AIM Simulation*

First, we work with a row of SRR structures (three inclusions placed side by side along the *y*-direction). The geometry and dimensions of this kind of inclusions are shown in Fig. 13.1. The width of all metal strips is 0.25 mm, the thickness of dielectric is 0.254 mm, and the dimension of each side of the square is 3.3 mm. The relative permittivity of dielectric material is set to be $\varepsilon_r = 1.05$ in the simulation. We characterize the scattering cross section (SCS) [45] of one row of three elements and plot it versus frequency in Fig. 13.2. It can be seen that the resonant frequency of this SRR design is 15.80 GHz.

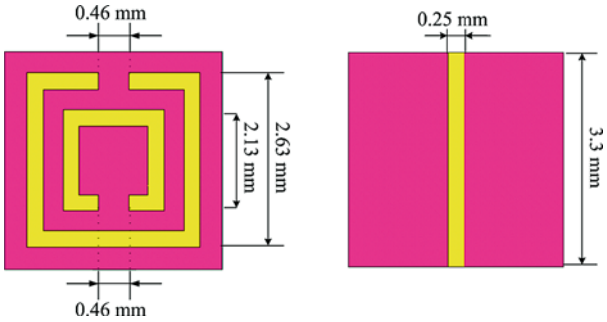


**Fig. 13.1** The front-side and back-side views of SRR unit cell inclusion.

Then, at this resonant frequency, the propagation characteristics of electromagnetic wave in a LHM sample placed in the free space are analyzed. It is a LHM slab composed of many rows of inclusions shown in Fig. 13.1. The 3-D view of this slab is depicted in Fig. 13.3. The space distances of the inclusions denoted, respectively, by $d_x$, $d_y$, and $d_z$ in the *x*-, *y*-, and *z*-directions, are all 3.3 mm. In total, 54 SRR elements are aligned into 18 rows along the *x*-direction and 3 columns along the

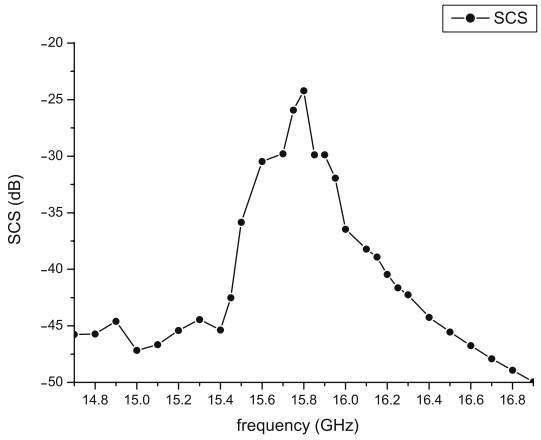


**Fig. 13.2** Scattering cross section versus frequency for a row of three SRR inclusions.

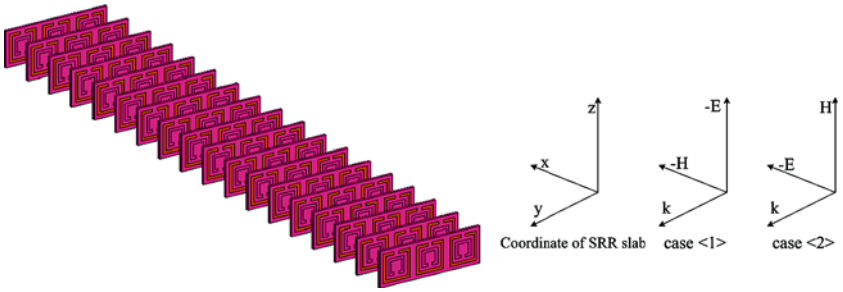


**Fig. 13.3** LHM slab composed of SRRs and wires with two different incidences of waves in the reference frame.

*y*-direction. In order to show that our AIM algorithm is suitable for this structure, the slab is illuminated by two different plane waves propagating in the *y*-direction, as shown in Fig. 13.3. Then, the RCS of this SRR slab in each case is checked. Actually, SRR requires the incident electric field $\boldsymbol{E}^i$ in parallel with the plane of the ring (the *y*–*z* plane) to lead to the maximum magnetic resonance. In other words, the rings are not supposed to be placed on the $\boldsymbol{H}$-$\boldsymbol{k}$ plane [21]. That is to say, if $\boldsymbol{E}^i$ is perpendicular to the plane of rings (incident is Case $< 2 >$ in Fig. 13.3), the RCS must be very small and the whole structure becomes an ordinary scatterer which does not acquire negative refractive index. Figures 13.4 and 13.5 show the $\boldsymbol{E}_z$ and RCS values when the incident waves are of polarizations in Case $< 1 >$ and Case $< 2 >$, respectively.

It can be seen from Figs. 13.4 and 13.5 that when the electric field is parallel in polarization with the plane of the ring the incident power can be transmitted to the other side of the LHM slab, which satisfies the property of LHM. When the electric field is perpendicular to the ring plane, however, there is neither magnetic resonance nor negative refractive index.

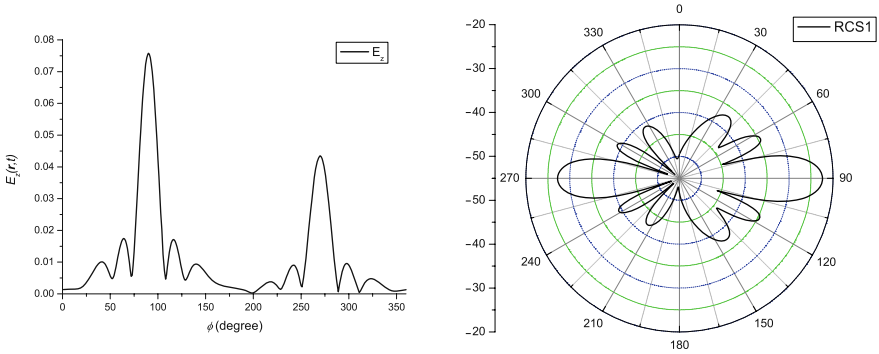


**Fig. 13.4** $E_z(\boldsymbol{r},t)$ and RCS values due to the slab when the incident wave of Case $<1>$ in Fig. 13.3 at 15.8 GHz is considered.

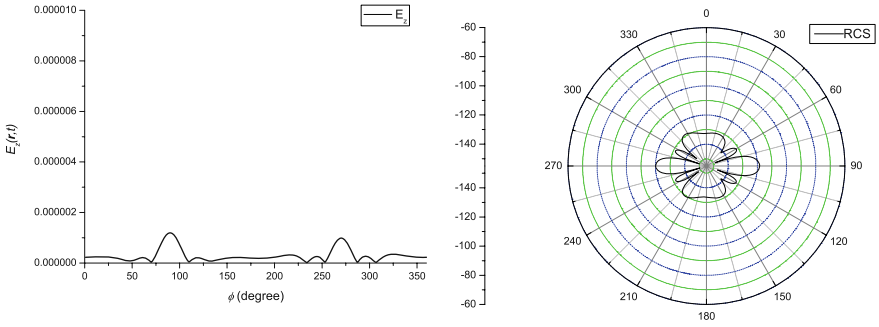


**Fig. 13.5** $E_z(\boldsymbol{r},t)$ and RCS values due to the slab when the incident wave of Case $<2>$ in Fig. 13.3 at 15.8 GHz is considered.

By using the fast solver, the adaptive integral method, we can significantly reduce the simulation time and hardware requirements: a direct solver of the MoM requires $O(N^3)$ operations to solve the equation and an iterative solver requires $O(N^2)$ operations in each iteration, while solvers require $O(N^2)$ memory to store the matrix elements. However, the computational complexity for the AIM is only $O(N^{1.5}\log N)$ and $O(N\log N)$ for surface and volume scatterer objects, respectively.

## 13.2 ASED-AIM for LHM Numerical Simulations

In the previous section, we have applied the AIM for numerical characterization of split-ring resonators (SRRs). It is noticed that for these structures, the inclusions are usually arranged periodically. Besides the typical LHM (such as SRR), many other designs like frequency selective surfaces and photonic crystals also have periodicity. Thus, a new adaptive integral approach based on an accurate sub-entire-domain method can be used in the electromagnetic simulation of large-scale finite periodic

array. It is a further acceleration procedure as compared with the existing AIM. This approach, referred to as the ASED-AIM, is also developed based on volume–surface integral equations and is able to solve problems associated with composite metallic and dielectric materials in a much faster and more efficient way of desirable accuracy.

### 13.2.1 Formulations for Hybrid VSIE and ASED-AIM

The VSIE equations involved here are formulated as follows:

$$\boldsymbol{E}^i(\boldsymbol{r}) = \boldsymbol{E}(\boldsymbol{r}) - \boldsymbol{E}^s(\boldsymbol{r}), \quad \boldsymbol{r} \in V, \tag{13.18a}$$

$$\boldsymbol{E}^i(\boldsymbol{r})\big|_{\tan} = -\boldsymbol{E}^s(\boldsymbol{r})\big|_{\tan}, \quad \boldsymbol{r} \in S. \tag{13.18b}$$

Volume equivalent electric current $\boldsymbol{J}_V(\boldsymbol{r})$ and surface equivalent electric current $\boldsymbol{J}_S(\boldsymbol{r})$ are related to total electric field $\boldsymbol{E}(\boldsymbol{r})$ and scattered electric field $\boldsymbol{E}^s(\boldsymbol{r})$ via

$$\boldsymbol{J}_V(\boldsymbol{r}) = j\omega\kappa\boldsymbol{D}(\boldsymbol{r}) = j\omega(\varepsilon - \varepsilon_0)\boldsymbol{E}(\boldsymbol{r}), \quad \boldsymbol{r} \in V, \tag{13.19a}$$

$$\begin{aligned}\boldsymbol{E}^s(\boldsymbol{r}) = &-j\omega\mu_0 \int_V g(\boldsymbol{r},\boldsymbol{r}')\boldsymbol{J}_V(\boldsymbol{r}')dV' - j\omega\mu_0 \int_S g(\boldsymbol{r},\boldsymbol{r}')\boldsymbol{J}_S(\boldsymbol{r}')dS' \\ &+ \frac{\nabla}{j\omega\varepsilon_0}\int_V g(\boldsymbol{r},\boldsymbol{r}')\nabla'\cdot\boldsymbol{J}_V(\boldsymbol{r}')dV' + \frac{\nabla}{j\omega\varepsilon_0}\int_S g(\boldsymbol{r},\boldsymbol{r}')\nabla'\cdot\boldsymbol{J}_S(\boldsymbol{r}')dS',\end{aligned} \tag{13.19b}$$

where $g(\boldsymbol{r},\boldsymbol{r}') = \dfrac{e^{-jk|\boldsymbol{r}-\boldsymbol{r}'|}}{4\pi|\boldsymbol{r}-\boldsymbol{r}'|}$ denotes the free space Green's function, $\mu_0$ and $\varepsilon_0$ are free space permeability and permittivity, respectively, $\varepsilon$ stands for the permittivity in the dielectric object, and $\kappa = \dfrac{\varepsilon - \varepsilon_0}{\varepsilon}$ represents the contrast ratio.

For simplicity, herein we consider 2-D large-scale periodic structures. The 3-D periodic problem can be analyzed in the same fashion. Based on the ASED method, we can first solve a small problem with nine cells for 2-D periodic structures. Then, the resultant solution is used to construct the basis function for each cell for solving the whole problem in the next stage. If there are $M$ unknowns for each cell and $N_0 = N_x N_y$ cells, the total number of unknowns will be $MN_0$. But the number of unknowns has been greatly reduced to $N_0$ via the ASED. For the $p$th cell, in order to ensure the normal continuity of surface current in the metallic surface, surface currents can be expanded as

$$\boldsymbol{J}_p^S = \sum_{m=1}^{N_S} I_{pm}^S \boldsymbol{f}_{pm}^S. \tag{13.20}$$

In order to ensure the normal continuity of electric flux density inside the dielectric objects, $\boldsymbol{D}$ can be expanded as

$$\boldsymbol{D}_p = \frac{1}{j\omega}\sum_{m=1}^{N_V} I_{p_m}^V \boldsymbol{f}_{p_m}^V. \tag{13.21}$$

Thus, volume currents can be expanded as

$$\boldsymbol{J}_p^V = \sum_{m=1}^{N_V} I_{p_m}^V \kappa \boldsymbol{f}_{p_m}^V, \tag{13.22}$$

where $\boldsymbol{f}_{p_m}^S$ and $\boldsymbol{f}_{p_m}^V$ denote RWG and SWG basis functions associated with the $m$th surface and volume basis functions of the $p$th cell, respectively. $N_S$ is the number of the RWG basis function and $N_V$ is the number of SWG basis function. $I_{p_m}^S$ and $I_{p_m}^V$ are the coefficients to be solved. Thus, electric current for the $p$th cell can be written as

$$\boldsymbol{J}_p = \boldsymbol{J}_p^S + \boldsymbol{J}_p^V. \tag{13.23}$$

The total current for the nine-cell problem can be written as the sum of

$$\boldsymbol{J} = \sum_{p=1}^{9} \boldsymbol{J}_p. \tag{13.24}$$

Then, the Galerkin MoM procedure is used to test the VSIE and to obtain the following matrix equation:

$$[Z_{p_m q_n}][I_{q_n}] = [V_{p_m}], \tag{13.25}$$

where $p_m$ denotes the $m$th testing function in the $p$th cell and $q_n$ stands for the $n$th basis function in the $q$th cell. After solving the nine-cell problem, we can obtain the nine types of cell basis functions and use them to solve the entire problem. Now, the current can be rewritten as

$$\boldsymbol{J} = \sum_{p=1}^{N_0} j_p \boldsymbol{J}_p, \tag{13.26}$$

where $j_p$ denotes unknown coefficients to be solved for. The cell impedance matrix elements can be written as

$$Z_{pq}^C = \sum_{m=1}^{M}\sum_{n=1}^{M} I_{p_m} Z_{p_m q_n} I_{q_n}. \tag{13.27}$$

Although there are $N_0$ cells for the whole domain, there are only nine types of basis functions. The nine types of basis functions can be mapped to the whole domain, as shown in Fig. 13.6. When $N_0$ is large, we can use the AIM to accelerate the solution process. We should combine the ASED with the AIM to solve large-scale periodic structures. The basic idea of AIM is to calculate the far-zone interaction via projecting the basis functions to, and interpolating potentials from, grid space associated with each basis function while the near-zone interactions are directly calculated. Since the free space Green's function is translational invariant and the

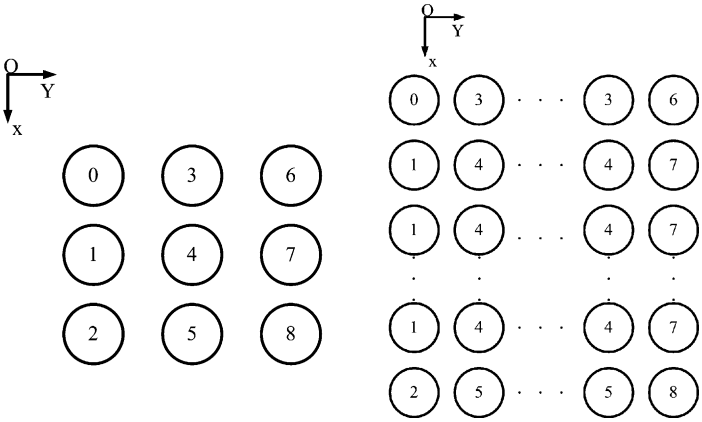


**Fig. 13.6** Mapping of ASED basis functions. (**a**) Nine-cell problem and (**b**) the entire problem.

calculation is made based on grid space, so the FFT can be used and it can greatly reduce the memory requirement and computational time. Using the conventional AIM, the matrix-vector multiplication is written as

$$\overline{\boldsymbol{Z}} \cdot \boldsymbol{I} = \overline{\boldsymbol{V}} \cdot \overline{\boldsymbol{H}} \cdot \overline{\boldsymbol{P}} \cdot \boldsymbol{I} + \overline{\boldsymbol{Z}}^{\text{near}} \cdot \boldsymbol{I}, \tag{13.28}$$

where $\overline{\boldsymbol{V}}$ stands for the interpolation matrix, $\overline{\boldsymbol{H}}$ denotes the Green's function matrix, and $\overline{\boldsymbol{P}}$ represents the projection matrix. It follows the four steps in the conventional AIM, which were described in the previous section and are shown in Fig. 13.7.

For the far-zone interaction, the impedance matrix elements can be approximated as

$$Z_{p_m q_n} \approx \tilde{Z}_{p_m q_n} = \sum_s \sum_t V_{m_s} H_{m_s n_t} P_{n_t}, \tag{13.29}$$

where $\sum$ denotes summation of all the contributions from the grids associated with the basis functions. Thus, for cell interaction in the far zone, we have

$$\begin{aligned} \left[\overline{\boldsymbol{Z}}^C\right]_{pq} &= \sum_m \sum_n I_{p_m} Z_{p_m q_n} I_{q_n} \\ &\approx \sum_m \sum_s \sum_n \sum_t I_{p_m} V_{m_s} H_{m_s n_t} I_{q_n} P_{n_t} \\ &= \left[\overline{\boldsymbol{V}}^C\right]_p \cdot \left[\overline{\boldsymbol{H}}\right]_{pq} \cdot \left[\overline{\boldsymbol{P}}^C\right]_q, \end{aligned} \tag{13.30}$$

where $\overline{\boldsymbol{V}}^C$ and $\overline{\boldsymbol{P}}^C$ denote the interpolation and projection matrices for cell basis functions and they can be written as

$$\left[\overline{\boldsymbol{V}}^C\right]_p = \sum_m \sum_s I_{p_m} V_{m_s}, \tag{13.31a}$$

$$\left[\overline{\boldsymbol{P}}^C\right]_q = \sum_n \sum_t I_{q_n} P_{n_t}. \tag{13.31b}$$

By using the ASED-AIM, the matrix-vector multiplication can be written as

$$\overline{\boldsymbol{Z}}^{C} \cdot \boldsymbol{I}^{C} = \overline{\boldsymbol{V}}^{C} \cdot \overline{\boldsymbol{H}} \cdot \overline{\boldsymbol{P}}^{C} \cdot \boldsymbol{I}^{C} + \overline{\boldsymbol{Z}}^{C,\text{near}} \cdot \boldsymbol{I}^{C}, \tag{13.32}$$

which takes the four steps as follows:

- Summing up all the projections from every basis function within each cell
- Evaluating the potentials at other grid locations produced by these grid-projected sources using a 3-D convolution
- Interpolating the grid point potentials onto each cell rather than individual testing functions and
- Computing the near-field interactions directly from at most nine near neighbors.

These four steps for the ASED-AIM are shown in Fig. 13.7.

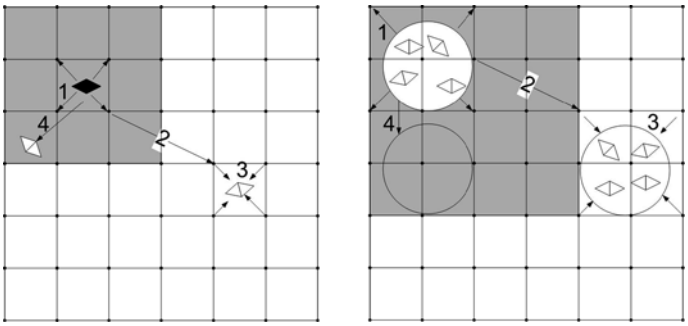


**Fig. 13.7** Graphic representation of AIM. (**a**) Conventional AIM. (**b**) The ASED-AIM.

### *13.2.2 Computational Complexity and Memory Requirement for the ASED-AIM*

In the first step of the ASED-AIM, the conventional AIM is carried out to solve a problem with $9M$ unknowns. Thus, the memory requirement and computational time are $O(M)$ and $O(M\log(M))$, respectively. It should be noted that in [27], the authors focused on metallic structures; thus, the number $M$ is usually small for a cell, for example, $M = 65$. Thus, the memory requirement and computational time are not large. In the present case, the method of moments can be employed to solve the nine-cell problem. But it is not the case when composite metallic and dielectric objects are within a cell since $M$ is large, for example, $M = 1,000$. Thus, this portion of memory and computational time should be taken into consideration as can be shown in the numerical results to be discussed subsequently.

In the second step of the ASED-AIM, since there are only nine types of cell basis functions, the memory requirement for interpolation and projection matrix is a constant $C$ and the computational time is $O(N_0)$ where $N_0$ is the number of cells in the whole domain. For the FFT operation, since the grid number $N_g$ is directly

proportional to the total number of cells $N_0$, the memory requirement is $O(N_0)$ and computational time is $O(N_0 \log N_0)$. In [27], disaggregation (equivalent to interpolation in the AIM), aggregation (equivalent to projection in the AIM), and translation (equivalent to FFT in AIM) have to be carried out for each $k$ direction (which is of the order $M$), respectively, per iteration. Interpolation and projection only, however, need FFT process once and twice per iteration in the AIM, respectively. Thus, the computational time can be reduced greatly. For the near-field interaction, the computational time will be quite large if we calculate directly using

$$Z_{pq}^{C,\text{near}} = Z_{pq}^{C} - \tilde{Z}_{pq}^{C} = \sum_{m=1}^{M} \sum_{n=1}^{M} I_{p_m} \left( Z_{p_m q_n} - \tilde{Z}_{p_m q_n} \right) I_{q_n}. \tag{13.33}$$

This operation takes $O(M^2)$ multiplications and additions. In fact, we can utilize the near-zone interaction matrix $Z^{\text{near}}$ in the first step. We know that $Z^{\text{near}}$ is a sparse $9M \times 9M$ matrix, which is made up of $9 \times 9$ sub-matrices with each matrix $M \times M$ elements, each element is $\left( Z_{p_m q_n} - \tilde{Z}_{p_m q_n} \right)$. Consider the fifth row of the sub-matrices which are calculated when the cell $p$ is surrounded by nine most near neighboring cells $q$, as shown in Fig. 13.6(a) where $p = 4$ and $q = 0, \ldots, 8$. The sub-matrices are all sparse, since

$$Z_{p_m q_n} - \tilde{Z}_{p_m q_n} = 0, \quad d_{p_m q_n} > d_{\text{near}}, \tag{13.34}$$

where $d_{\text{near}}$ is the near-zone threshold. Thus, $O(M^2)$ multiplications and additions can be greatly reduced using sparse matrix-vector multiplication.

For the near-zone interactions, there are at most nine near neighbors for each cell. That is to say, the memory requirement and computational time are both $O(N_0)$. So the total memory requirement is

$$O(M) + C + O(N_0) + O(N_0) = O(M) + O(N_0) \tag{13.35}$$

and the total computational (CPU) time is

$$O(M \log M) + O(N_0) + O\left[N_0 \log(N_0)\right] + O(N_0) = O(M \log M) + O\left[N_0 \log(N_0)\right]. \tag{13.36}$$

### *13.2.3 Numerical Results of the ASED-AIM*

In this part, several examples will be given to demonstrate the validity and efficiency of our code to characterize electromagnetic scattering by large-scale periodic structures consisting of composite metallic and dielectric objects. The generalized minimum residual (GMRES) solver is adopted as the iterative solver and it terminates when the normalized residue falls below $10^{-3}$.

First, we consider a 2-D periodic structure shown in Fig. 13.8. Geometry of a unit cell is shown in Fig. 13.8, which comprises of a dielectric cube with length 0.2 m and a metallic square patch with length 0.2 m above the cube. The unit cell is discretized with 467 tetrahedrons and 36 triangles resulting in $M = 1,087$ unknowns. The gap

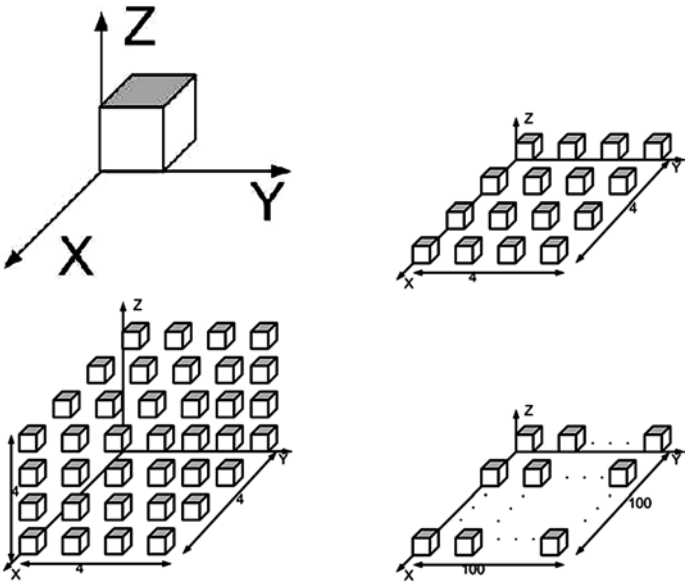


**Fig. 13.8** Examples of arrays calculated in the numerical results. (**a**) The structure of a unit cell, where $d = 0.2$ m. Shaded area represents a metallic patch, and the cube is a dielectric object with $\varepsilon_r = 2.2$. (**b**) The $4 \times 4$ array. (**c**) The $4 \times 4 \times 4$ array. (**d**) The $100 \times 100$ array.

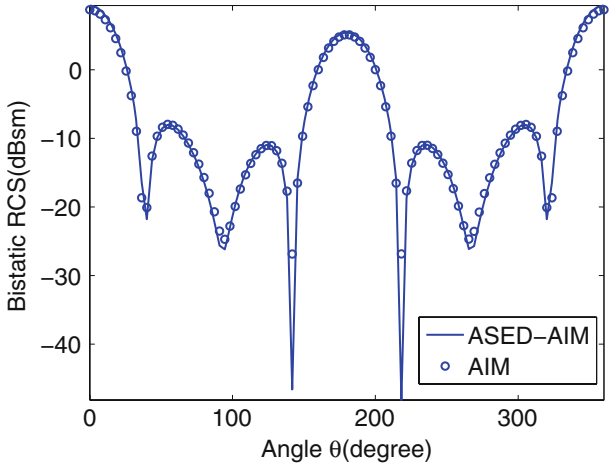


**Fig. 13.9** Bistatic RCS results of the $4 \times 4$ array with each cell shown in Fig. 13.8 at an incidence of $\theta_i = 0^o$ and $\phi_i = 0^o$ with electric field $\theta$-polarized, the gap is 0.2 m in both $x$- and $y$-directions. The results are computed by the AIM (*circle line*) and the ASED-AIM (*solid line*).

distances between two neighboring cells in both $x$- and $y$-directions are 0.2 m. The $4 \times 4$ array is illuminated at normal incidence ($\theta_i = 0^o$ and $\phi_i = 0^o$) by a plane wave with a frequency of 300 MHz, whose electric field is $\theta$-polarized. Far-

field radar cross section (RCS) results and near-field results calculated by using the conventional AIM and the ASED-AIM have been shown in Figs. 13.9 and 13.10, respectively. The electric field in the plane $z = 1$ m is calculated. It is clear that the results obtained using the two methods are almost the same, which demonstrates the good accuracy of the ASED-AIM.

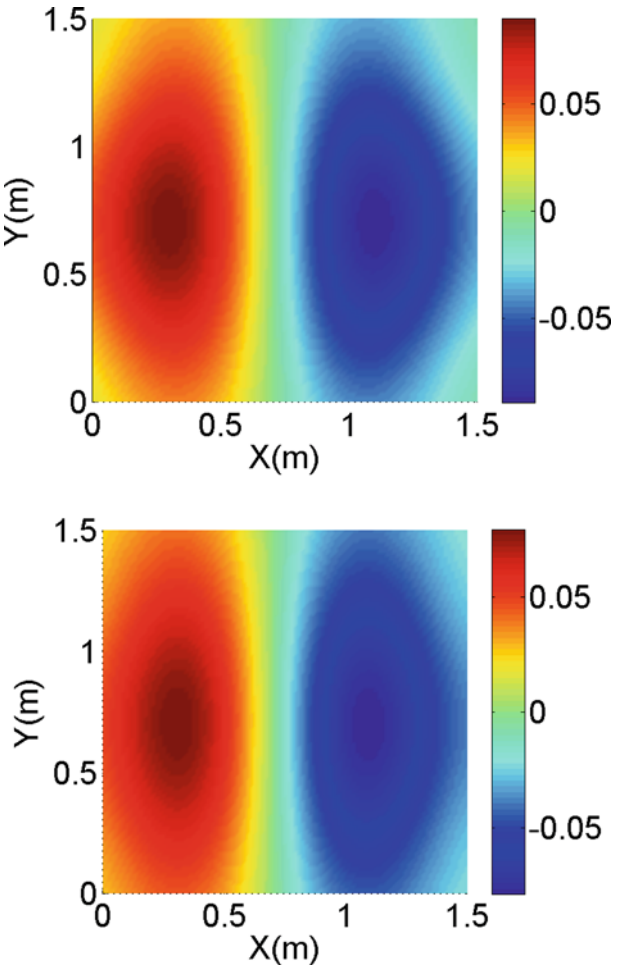


**Fig. 13.10** (Color online) Electric field density in the $z = 1$ m plane by the $4 \times 4$ array with each cell shown in Fig. 13.8 at the normal incidence of $\theta_i = 0^o$ and $\phi_i = 0^o$ with electric field $\theta$-polarized, the gap is 0.2 m in both $x$- and $y$-directions.

Now, we investigate the computational complexity and memory requirement of ASED-AIM and compare them with conventional AIM. Figure 13.11 shows the relationship between the computational time and the number of unknowns using the ASED-AIM and the AIM. Figure 13.12 shows the relationship between the mem-

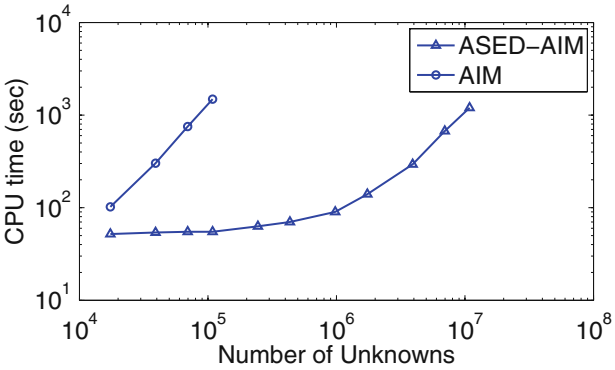


**Fig. 13.11** Relationship between computational time and number of unknowns consumed inside the ASED-AIM (*triangle line*) and the AIM (*circle line*).

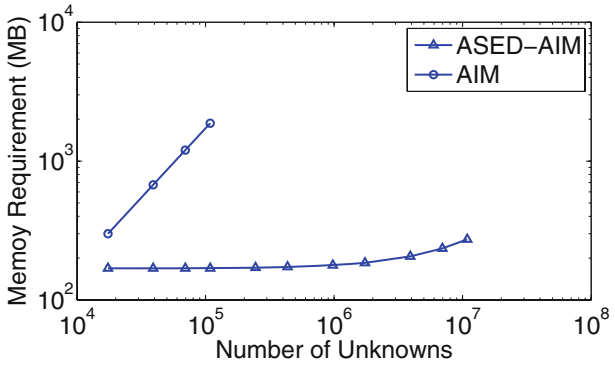


**Fig. 13.12** Relationship between memory requirement and number of unknowns consumed inside the ASED-AIM (*triangle line*) and the AIM (*circle line*).

ory usage and the number of unknowns using the ASED-AIM and the AIM. From these figures, we can see that using the AIM, the computational time and memory requirement are proportional to the number of unknowns. When $N$ reaches $10^5$, the memory requirement is above $10^3$ MB and CPU time is above $10^3$ s. When using the ASED-AIM, the computational time and memory requirement are much less than the conventional AIM; even when $N$ reaches 10 million, the memory requirement is still below $10^3$ MB and CPU time is about $10^3$ s. Especially, they are nearly the same when the number of unknowns is below $10^6$. When the number of unknowns goes up beyond $10^6$, the memory requirement and CPU time start to show its proportion to the number of unknowns. This observation agrees well with the previous complexity analysis. The memory requirement is $O(M)+O(N_0)$ while the computational time is $O(M\log M)+O(N_0\log N_0)$. When $N_0$ is small as compared to $M$, $M$ determines the memory requirement and computational time. This means

most of the time and memory have been spent on the first stage of the ASED-AIM. From our present results, 168 MB memory and 50 s have been consumed in the first stage. When $N$ is smaller than $10^6$, only several MB and seconds have been spent in the seconds stage. When $N$ is larger than $10^6$, $N_0$ becomes dominant in the cost consumption. The memory requirement and CPU time both go up linearly with $N_0$.

The method described above can also be extended to characterize 3-D finite periodic structures. In this case, a small domain with 27 cells is solved first. Then the whole domain with 27 types of cell basis functions is considered and its problem is solved by extending the above algorithm. In Fig. 13.13, the RCS values due to a $4 \times 4 \times 4$ array shown in Fig. 13.8 are calculated using the ASED-AIM and the AIM and then compared; the distances between each cell in $x$-, $y$-, and $z$-directions are all 0.2 m. The array is illuminated by a plane wave at normal incidence with electric field $\theta$-polarized. From Fig. 13.13 it is apparent that RCS results obtained using the ASED-AIM and the AIM are in good agreement. The number of unknowns for the $4 \times 4 \times 4$ array problem is 68,992, and its solution requires 507 MB memory and 178 s computational time using the ASED-AIM while it needs 1,200 MB memory and 753 s using the AIM. Then we considered a $10 \times 10 \times 10$ array problem whose number of unknowns is over 1 million. It takes the ASED-AIM 516 MB memory and 229 s to calculate the RCS result. Compared with $4 \times 4 \times 4$ array problem, the memory requirement and CPU time increase only very slightly, from 507 to 516 MB and from 178 s to 229 s, respectively, but the number of unknowns has increased from 68,992 to over a million. The 3-D situation is similar to a 2-D situation, which demonstrates that the ASED-AIM is also very efficient to characterize 3-D periodic structures.

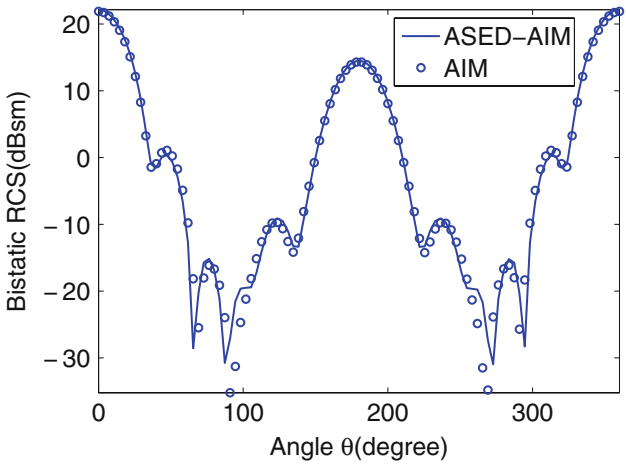


**Fig. 13.13** Bistatic RCS of the $4 \times 4 \times 4$ array with each cell shown in Fig. 13.8 when illuminated by a plane wave at normal incidence of $\theta_i = 0^o$ and $\phi_i = 0^o$ with electric field $\theta$-polarized. The gap distances are all 0.2 m in $x$-, $y$-, and $z$-directions. The results are computed using the AIM (*circle line*) and the ASED-AIM (*solid line*).

Finally, a very large finite periodic structure with $100 \times 100$ array elements shown in Fig. 13.8 is considered. The total number of unknowns is now 10.87 million. The structure is illuminated by a plane wave at an incident angle of $\theta = 0^{\circ}$ and $\phi = 0^{\circ}$, and its electric field is $\theta$-polarized. The calculated RCS values are shown in Fig. 13.14. For such a large structure with over 10 million unknowns, the ASED-AIM requires only 273 MB memory and 1,200 s in CPU time, which demonstrates the high efficiency of the new method in solving large-scale periodic structure problems.

From the above results, we can see that this new AIM approach is very efficient, developed based on the ASED basis functions to characterize electromagnetic scattering by large-scale finite periodic arrays. In the formulation, the volume–surface integral equation (VSIE) is utilized, thus the method can be used to analyze arrays with metallic and dielectric materials, especially the split-ring resonators and many other types of planar LHM designs. Generally, two steps are most important when this ASED-AIM is applied to solve the array problems. First, a small problem with nine cells is solved for a 2-D array and with 27 cells for a 3-D array. The objective is to obtain the ASED basis function. Second, the ASED basis function for each cell should be used to solve the entire problem. The AIM has been modified to incorporate the ASED basis function which reduces greatly the memory requirement and computational time in solving the array problems. The accuracy of the ASED-AIM is comparable to that of the conventional AIM, in solving the large-scaled finite array problems which involve a very large number of unknowns. Complexity analysis reveals that the memory requirement is $O(M) + O(N_0)$ and computational time is $O(M \log M) + O(N_0 \log N_0)$ (where $M$ denotes the number of unknowns in each cell and $N_0$ represents the number of cells of the entire array).

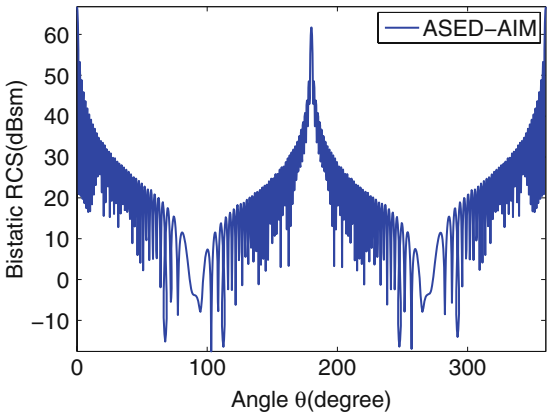


**Fig. 13.14** Bistatic RCS of the $100 \times 100$ array with each cell shown in Fig. 13.8 at the normal incidence of $\theta_i = 0^{\circ}$ and $\phi_i = 0^{\circ}$ with electric field $\theta$-polarized. The gap distances are all 0.2 m in $x$-, $y$-, and $z$-directions. The result is computed using the ASED-AIM.

## 13.3 A Novel Design of Wideband LHM Antenna for Microwave/RF Applications

### *13.3.1 Microstrip Patch Antenna and LHM Applications*

A microstrip patch antenna [1] represents one kind of the most commonly utilized printed antennas in practice. It enjoys its advantages of low profile, simple structure, low cost, and omnidirectional radiation patterns [2]. A narrow bandwidth is, however, the main drawback of the microstrip patch antennas. Some approaches have been therefore developed for bandwidth enhancement [6, 12]. Among those common ones, one is to increase the height of the dielectric substrate while another is to decrease the substrate dielectric constant. Certainly, the latter will induce the matching circuits to be impractical due to excessively wide lines designed.

Since the artificial left-handed materials (LHMs) were proposed, theoretically characterized, and experimentally realized [43, 32, 41, 36, 16], scientists and engineers have tried various ways to bring these special material into practical applications. LHMs have even been successfully applied in optical frequency band, for example, optical imaging [33, 17]. Although it is easier to realize LHM in microwave frequency region for negative refractions, there was still little progress toward practical applications [40]. At microwave frequencies, potential applications include primarily (a) substrate materials for antenna and microwave component designs and fabrications and (b) absorbing materials for engineering and radar applications. For example, split-ring resonators (SRRs) [41, 45, 19] and some other planar structures [38] were applied in some antenna fabrications to minimize the size and enhance the radiation. Also in some other designs, artificial magnetic materials [41, 44] with stacks of SRRs under patch antenna were proposed and it was found that the resonant frequency of the ordinary patch antenna can be significantly reduced. There are, however, still primarily fundamental issues at microwave frequencies: narrow bandwidth (when both negative permittivity and negative permeability occur in the same band) and high loss (due to the ohmic loss and radiation loss of inclusion elements), and this drawback becomes especially serious when the SRR and other inclusion types of LHM are used as the patch antenna's substrate.

We want to enhance, in a completely different approach, the bandwidth and gain of a conventional patch antenna by applying the planar LH-patterned structures directly on the upper patch and the bottom ground of the dielectric substrate, so that the patch antenna can have an excellent performance. The new idea therefore opens a new window for LHM applications at microwave frequencies.

### *13.3.2 A Novel Design of Wideband LH Antenna*

A conventional microstrip patch antenna is usually mounted on a substrate and backed by a conducting ground plane. In the present investigation, as shown in Fig. 13.15, a planar left-handed material pattern on the rectangular patch antenna

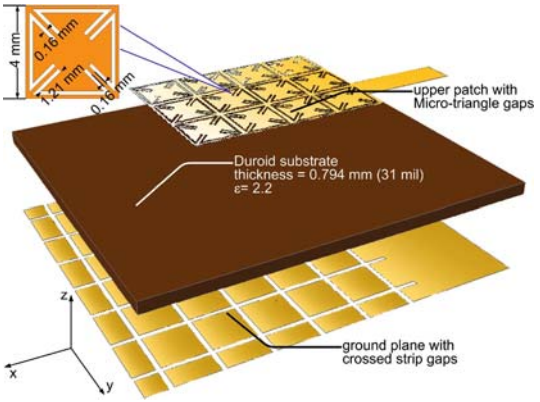


**Fig. 13.15** (Color online) Three-dimensional view of layered configuration of the proposed patch antenna and 2-D view of one front element.

mounted on the substrate is designed to enhance its horizontal radiation as well as to broaden its working bandwidth via its coupling with the conducting ground backed to the substrate and patterned in a different way. On the upper patch, the periodic gaps are designed in the form of isolated micro-triangles. It is similar to the Babinet metamaterials [16, 7]. On the bottom ground plane, periodically distributed cross strip-line gaps are designed. To maintain the transmission consistency of input energy, the metal in and around the feed-line area is, however, not etched. The prototype and the dimension of the two patterned planes of the proposed antenna are shown in Figs. 13.15 and 13.16. The left-handed characteristics of these patterns were already demonstrated in [30] and thus will not be further discussed here. We have also optimized the original patterns slightly to achieve a better performance of the antenna. Physically, the upper patch and bottom plane are coupled to form a C–L (capacitor–inductor) equivalent circuit and thus can induce backward wave

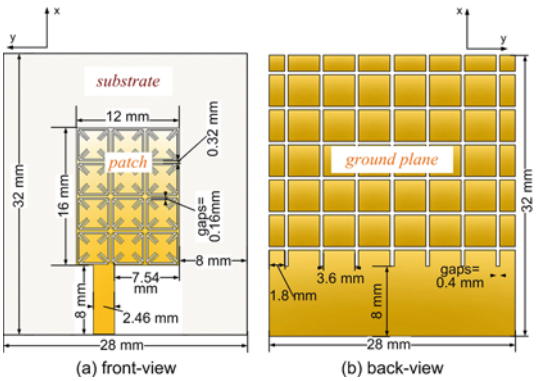


**Fig. 13.16** (Color online) Two-dimensional view of proposed patch antenna with size denoted: (**a**) front view and (**b**) back view.

which travels along the plane of patch. In this connection, the radiation along the patch direction is significantly enhanced.

An ordinary rectangular patch antenna of the same size is used as a reference for comparison and both the conventional patch and the proposed new patch antenna are fed by an off-centered microstrip line. The substrate used here is Duroid with a relative permittivity of $\varepsilon_r = 2.2$, and its thickness is 31 mil. The area of the upper patch mounted is $12 \times 16$ mm$^2$. Two different widths $g$ of the gaps (i.e., 0.3 and 0.4 mm) on the ground plane are assumed. Therefore, different inductance components of the LHM characteristics can be obtained so as to control the resonance frequency and also the working bandwidth of the designed antenna.

### *13.3.3 Simulation and Measurement Results*

The LHM patch antenna was numerically simulated, physically fabricated, practically measured, and comparatively studied with theoretical results. To optimize it for various parameters, a full wave finite element method simulator was used. The computed $S_{11}$ values of the proposed antenna and the original reference patch antenna are obtained and shown in Fig. 13.17. Here the $-10$ dB bandwidth is used, which corresponds to about 10% of the incident power being reflected. It is the normally accepted scientific and industry standard. As seen from Fig. 13.17, the – 10 dB bandwidth of the conventional patch antenna is between 7.1 and 7.3 GHz (which is relatively narrow). The proposed new antenna is designed to have the 0.4 mm gap at the bottom, and the $-10$ dB bandwidth falls within 5.3 and 8.5 GHz, which is rather wide. When the gap at the bottom becomes 0.3 mm, the $-10$ dB bandwidth turns within 5.7 and 8.6 GHz.

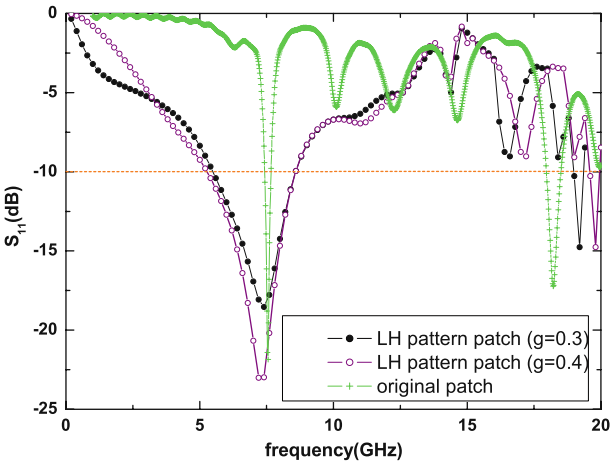


**Fig. 13.17** (Color online) Computed $S_{11}$ values of the proposed antenna and reference patch antenna.

To verify the accuracy of designs, two proposed antennas with different gap widths (one of which is shown in Fig. 13.18) are then fabricated and measured. Experimental results are compared with numerically predicted results in Fig. 13.19, and a good agreement between them is found.

(a) Front view of fabricated antenna
(b) Back view of fabricated antenna

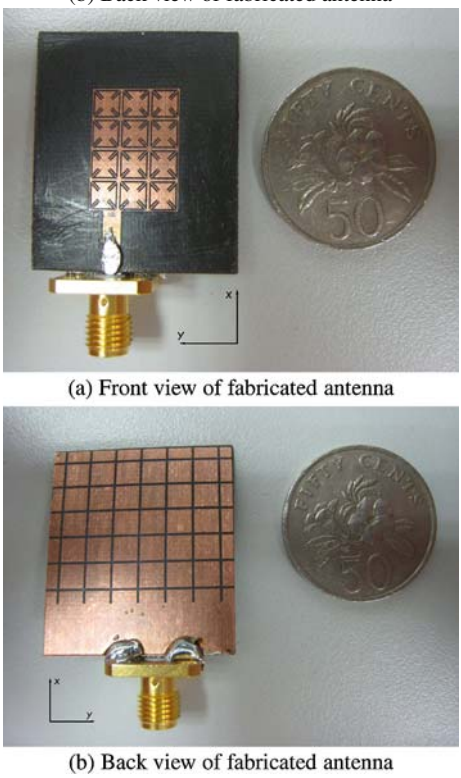


**Fig. 13.18** (Color online) Front and back views of a fabricated patch antenna.

Measurements of antenna gain are made within the entire frequency band as shown in Fig. 13.20. The gain is generally above 4 dB with the peak of 7.2 dB. Also, the simulated voltage standing wave ratio (VSWR) is well below 2 within the frequency band as shown in Fig. 13.21, which satisfies the requirement of antenna design. Due to the left-handed transmission characteristics, the wave propagation along the patch induces the strongest radiation in horizontal direction instead of the vertical direction of the conventional patch antenna. To further confirm this, two frequencies, i.e., 6.66 and 7.77 GHz both in the working bandwidth, are randomly chosen to characterize radiation of the antenna. According to the computed results, the 3-D radiation patterns at these two frequencies are shown in Fig. 13.22. It is apparent that the radiations are more directed to the horizontal directions. To further

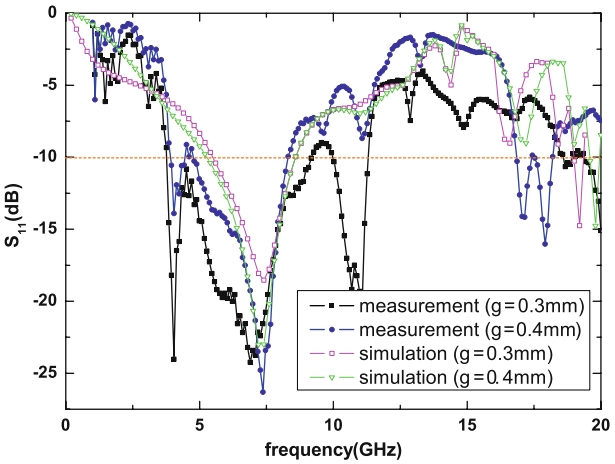


**Fig. 13.19** (Color online) Computed and measured $S_{11}$ values of the proposed antenna with different gap widths.

verify the results, the measured co-polarization and cross-polarization radiation patterns are plotted in 2-D in Figs. 13.23 and 13.24, respectively. The gain is found to be able to reach as high as 7.14 dB, which is quite desirable for a single patch and it would never happen if an ordinary patch antenna of this size is used. Also seen from the 2-D patterns at both of these randomly picked frequencies, the radiated energy is mainly focused in the $x$-direction in the case of the co-polarization. In the case of the cross-polarization, the radiation level is well suppressed except at around 210° of the $\theta$-direction in the $x$–$y$ plane. So we may also take a good advantage of this special characteristic for beam control.

From the above, we can see that this novel broad bandwidth patch antenna is designed and fabricated using the LHM concept via the pattern-etched upper patch

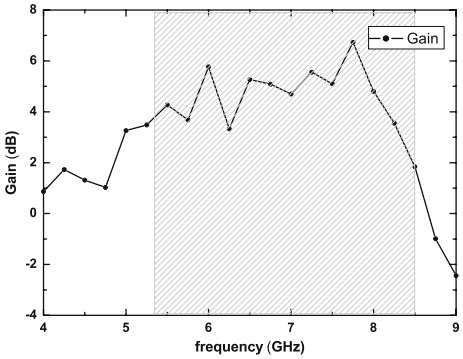


**Fig. 13.20** Measured antenna gain of proposed antenna (when gap = 0.4 mm). Shaded area shows the working band.

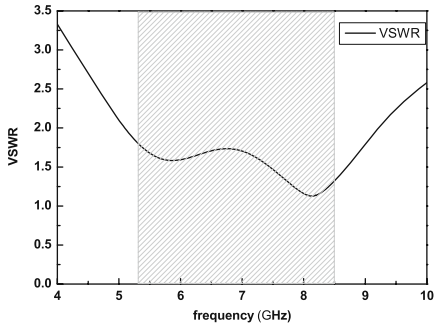


**Fig. 13.21** Simulated VSWR of proposed antenna (when gap = 0.4 mm). Shaded area depicts the working band.

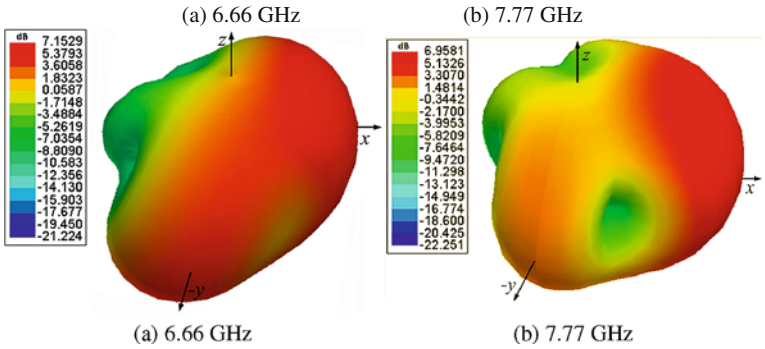


**Fig. 13.22** (Color online) Computed 3-D radiation patterns at (**a**) 6.66 GHz and (**b**) 7.77 GHz, respectively.

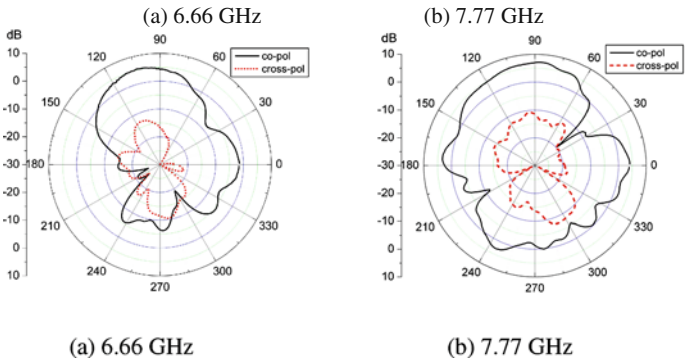


**Fig. 13.23** Measured radiation patterns of co-polarization (*solid line*) and cross-polarization (*dotted line*) in the *x*–*y* plane at (**a**) 6.66 GHz and (**b**) 7.77 GHz, respectively.

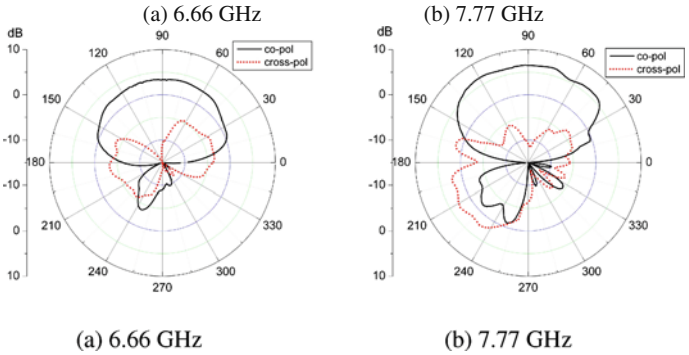


**Fig. 13.24** Measured radiation patterns of co-polarization (*solid line*) and cross-polarization (*dotted line*) in the *x*–*z* plane at (**a**) 6.66 GHz and (**b**) 7.77 GHz, respectively.

and bottom ground plane which form a C–L equivalent circuit of negative index for enhancing the antenna performance. Both simulated and measured results are obtained and the working frequency bandwidth of the rectangular patch antenna is significantly broadened (from about 200 MHz to 3 GHz).

In fact, this new patch antenna designed using the LHM concept has very high efficiency of above 98% according to simulation results, very low loss (or high gain according to measurements) and low VSWR. Practical experiments demonstrate a general agreement in trends between simulation and measurement results of the S-parameters and the antenna patterns. Most interesting thing is that this new antenna could radiate toward the horizontal directions within the entire working frequency band, while the vertical radiation is well suppressed – which is a completely different feature from the traditional patch antennas and can lead to many practical applications in wireless communication subsystems.

**Acknowledgments** The authors are grateful for their useful discussions with Dr. Cheng-Wei Qiu in the Dept of Electrical and Computer Engineering at the National University of Singapore, Kent Ridge, Singapore; Dr. Wei-Bin Ewe in the Dept of Computational Electronics and Plasmonics at the Institute of High Performance Computing, Science Park, Singapore; and Dr. Hai-Ying Yao in Temasek Laboratories at the National University of Singapore, Kent Ridge, Singapore. This work has been partially supported by the AFOSR/AOARD Projects: AOARD-06-4031, AOARD-07-4024, and AOARD-09-4069.

## References

1. Balanis, C.A.: Antenna Theory: Analysis and Design, John Wiley & Sons. (1982)
2. Bancroft, R.: Microstrip and Printed Antenna Design, 1st edn. Noble Publishing, Atlanta (2004)
3. Bleszynski, E., Bleszynski, M., and Jaroszewicz, T.: A fast integral-equation solver for electromagnetic scattering problems. AP-S. Digest **1**, 416 (1994)

4. Bleszynski, E., Bleszynski, M., and Jaroszewicz, T.: AIM: Adaptive integral method for solving large-scale electromagnetic scattering and radiation problems. Radio Sci. **31**, 1225 (1996)
5. Catedra, M.F., Cuevas, J.G., and Nuno, L.: A scheme to analyze conducting plates of resonant size using the conjugate-gradient method and the fast Fourier transform. IEEE Trans. Ant. Prop. **36**, 1744 (1988)
6. Chang, Y., and Harrington, R.F.: A surface formulation for characteristic modes of material bodies. IEEE Trans. Ant. Prop. **25**, 789 (1977)
7. Chen, H.-T., O'Hara, J.F., Taylor, A.J., Averitt, R.D., Highstrete, C.H., Lee, M., and Padilla, W. J.: Complementary planar terahertz metamaterials. Opt. Express **15**, 1084 (2007)
8. Coifman, R., Rokhlin, V., and Wandzuraz, S.: The fast multipole method for the wave equation: a pedestrian prescription. IEEE Ant. Prop. Magaz. **35**, 7 (1993)
9. Cui, T.J., and Chew, W.C.: Fast algorithm for electromagnetic scattering by buried 3-D dielectric objects of large size. IEEE Trans. Geosci. Remote Sensing **37**, 2597 (1999)
10. Cui, T.J., Chew, W.C., Chen, G., and Song, J.M.: Efficient MLFMA, RPFMA, and FAFFA algorithms for EM scattering by very large structures. IEEE Trans. Ant. Prop. **52**, 759 (2004)
11. Engheta, N., Murphy, W.D., Rokhlin, V., and Vassiliou, M.S.: The fast multipole method (FMM) for electromagnetic scattering problems. IEEE Trans. Ant. Prop. **40**, 634 (1992)
12. Enoch, S., Tayeb, G., Sabouroux, P., Guérin, N., and Vincent, P.: A metamaterial for directive emission. Phys. Rev. Lett. **89**, 213902 (2002)
13. Ewe, W.-B., Li, L.-W., and Leong, M.-S.: Fast solution of mixed dielectric/conducting scattering problem using volume-surface adaptive Integral method. IEEE Trans. Ant. Prop. **52**, 3071 (2004)
14. Ewe, W.-B., Li, L.-W., and Leong, M.-S.: Preconditioners for adaptive integral method implementation. IEEE Trans. Ant. Prop. **53**, 2346 (2005)
15. Ewe, W.-B., Li, E.-P., Chu, H.-S., and Li, L.-W.: AIM Analysis of electromagnetic scattering by arbitrarily shaped magnetodielectric object. IEEE Trans. Ant. Prop. **55**, 2073 (2007)
16. Falcone, F., Lopetegi, T., Laso, M.A.G., Baena, J.D., Bonache, J., Beruete, M., Marqués, R., Martín, F., and Sorolla, M.: Babinet principle applied to the design of metasurfaces and metamaterials. Phys. Rev. Lett. **93**, 197401 (2004)
17. García de Abajo, F.J., and Sáenz, J.J.: Electromagnetic surface modes in structured perfect conductor surfaces. Phys. Rev. Lett. **95**, 233901 (2005)
18. Harrington, R.F.: Field Computation by Moment Methods, 1st edn. Wiley-IEEE Press (1993)
19. Gay-Balmaz, P., and Martin, O.J.: Efficient isotropic magnetic resonators. Appl. Phys. Lett. **81**, 939 (2002)
20. Joannopoulos, J.D., Meade, R.D., and Winn, J.N.: Photonic, Crystal. Princeton University Press, Princeton (1995)
21. Katsarakis, N., Koschny, T., and Kafesaki, M.: Electric coupling to the magnetic resonance of split ring resonators. Appl. Phys. Lett. **84**, 2943 (2004)
22. Ling, F., Wang, C.F., and Jin, J. M.: Application of adaptive integral method to scattering and radiation analysis of arbitrarily shaped planar structures. AP-S.Digest **3**, 1778–1781 (1998)
23. Ling, F., Wang, C. F., and Jin, J.M.: An efficient algorithm for analyzing large-scale microstrip structures using adaptive integral method combined with discrete complex-image method. IEEE Trans. Micro. Theo. Tech. **48**, 832 (2000)
24. Lu, C.C., and Chew, W.C.: Fast algorithm for solving hybrid integral equations [EM wave scattering]. IEE Proc.-H **140**, 455–460 (1993)
25. Lu, W.B., Cui, T.J., Qian, Z.G., Yin, X.X., and Hong, W.: Accurate analysis of large-scale periodic structures using an efficient sub-entire-domain basis function method. IEEE Trans. Ant. Prop. **52**, 3078 (2004)
26. Lu, W.B., Cui, T.J., Yin, X.X., Qian, Z.G., and Hong, W.: Fast algorithms for large-scale periodic structures using subentire domain basis functions. IEEE Trans. Ant. Prop. **53**, 1154 (2005)
27. Lu, W.B., Cui, T.J., and Zhao, H.: Acceleration of fast multipole method for large-scale periodic structures with finite sizes using sub-entire-domain basis functions. IEEE Trans. Ant. Prop.. **55**, 414 (2007)

28. Maaskant, R., Mittra, R., and Tijhuis, A.: Fast analysis of large antenna arrays using the characteristic basis function method and the adaptive cross approximation algorithm. IEEE Trans. Ant. Prop. **56**, 3440 (2008)
29. Matekovits, L., Laza, V., and Vecchi, G.: Analysis of large complex structures with the synthetic-functions approach. IEEE Trans. Ant. Prop. **55**, 2509 (2007)
30. Matsunaga, N., Sanada, A., and Kubo, H.: Novel two-dimensional planar negative refractive index structure. IEICE Trans. Electron. **E89-C**, 1276 (2006)
31. Munk, B.A.: Frequency Selective Surfaces, Theory and Design, 1st edn. John. Wiley and Sons, New York (2000)
32. Pendry, J.B.: Negative refraction makes a perfect lens. Phys. Rev. Lett. **85**, 3966 (2000)
33. Pendry, J.B., Schurig, D., and Smith, D.R.: Controlling electromagnetic fields. Science **312**, 1780 (2006)
34. Peters, T.J., and Volakis, J.L.: Application of a conjugate gradient FFT method to scattering from thin planar material plates. IEEE Trans. Ant. Prop. **36**, 518 (1998)
35. Prakash, V.V.S., and Mittra, R.: Characteristic basis function method: A new technique for efficient solution of method of moments matrix equations. Micro. Opt. Technol. Lett. **36**, 95 (2003)
36. Qiu, C.W., Yao, H.Y., Li, L.-W., Zouhdi, S., and Yeo, T.-S.: Backward waves in magneto-electrically chiral media: Propagation, impedance, and negative refraction. Phys. Rev. B **75**, 155120 (2007)
37. Rao, S.M., Wilton, D.R., and Glisson, A.W.: Electromagnetic scattering by surfaces of arbitrary shape. IEEE Trans. Ant. Prop. **30**, 409 (1982)
38. Sanada, A., Caloz, C., and Itoh, T.: Planar distributed structures with negative refractive index. IEEE Trans. Micro. Theo. Tech. **52**, 1252 (2004)
39. Schaubert, D.H., Wilton, D.R., and Glisson, A.W.: A tetrahedral modeling method for electromagnetic scattering by arbitrarily shaped inhomogeneous dielectric bodies. IEEE Trans. Ant. Prop. **32**, 77 (1984)
40. Schurig, D., Mock, J.J., Justice, B.J., Cummer, S.A., Pendry, J.B., Starr, A.F., and Smith, D.R.: Metamaterial electromagnetic cloak at microwave frequencies. Science **314**, 977 (2006)
41. Smith, D.R., Padilla, W.J., Vier, D.C., Nemat-Nasser, S.C., and Schultz, S.: Composite medium with simultaneously negative permeability and permittivity. Phys. Rev. Lett. **84**, 4184 (2000)
42. Suter, E., and Mosig, J.: A subdomain multilevel approach for the efficient MoM analysis of large planar antennas. Micro. Opt. Technol. Lett. **26**, 270 (2000)
43. Veselag, V.G.: The electrodynamics of materials with simultaneously negative values of ? and μ. Sov. Phys. Usp. **10**, 509 (1968)
44. Yao, H.-Y., Li, L.-W., Wu, Q., and Kong, J.A.: Macroscopic performance analysis of metamaterials synthesized from microscopic 2-D isotropic cross split-ring resonator array. Prog. Electromagnet. Res. **51**, 197 (2005)
45. Yao, H.-Y., Xu, W., Li, L.-W., Wu, Q., and Yeo, T.-S.: Propagation property analysis of metamaterial constructed by conductive SRRs and wires using the MGS-based algorithm. IEEE Trans. Micro. Theo. Tech. **53**, 1469 (2005)
46. Yeo, J., Prakash, V.V.S., and Mittra, R.: Efficient analysis of a class of microstrip antennas using the characteristic basis function method (CBFM). Micro. Opt. Technol. Lett. **39**, 456 (2003)
47. Zwamborn, P., and van den Berg, P.M.: The three dimensional weak form of the conjugate gradient FFT method for solving scattering problems. IEEE Trans. Micro. Theo. Tech. **40**, 1757 (1992)

# Chapter 14
# Experiments and Applications of Metamaterials in Microwave Regime

Qiang Cheng, X. M. Yang, H. F. Ma, J. Y. Chin, T. J. Cui, R. Liu and D. R. Smith

**Abstract** In this chapter some experiments and applications of metamaterials in the microwave regime have been presented. Although metamaterials are composed of structures with finite periodicity, they can still be regarded as effective medium when the periodicity is far smaller than the wavelength. We discuss some interesting experiments such as the tunneling structure and the partial focusing phenomenon and investigate several applications like gradient index circuit and the Luneberg lens antenna. The simulation and experimental results show that metamaterials may have great potentials in the design of microwave devices and antennas.

**Key words:** Anisotropic metamaterial, zero index metamaterial, broadband metamaterial, complementary metamaterial, tunneling effect, Luneberg lens antenna, partial focusing, microwave retarder, polarizer, beam steering.

## 14.1 Introduction

As introduced in the previous chapters, the metamaterials are actually artificial composites, which are composed of periodic arrays of electric or magnetic resonators. These basic units have offered us a powerful way to adjust the electromagnetic characteristics (i.e., the permittivity and the permittivity) of the materials freely by changing the unit patterns or dimensions. Therefore we can design various kinds of inhomogeneous media in order to meet the requirements of specific devices like the lens antennas or tunneling bends which will be discussed below.

Qiang Cheng, Xinmi Yang, Hui Feng Ma, Jessie Y. Chin and Tie Jun Cui*
State Key Laboratory of Millimeter Waves, Department of Radio Engineering, Southeast University, Nanjing 210096, P. R. China. *e-mail: tjcui@seu.edu.cn.
Ruopeng Liu and David R. Smith+
Department of Electrical and Computer Engineering, Duke University, Box 90291, Durham, North Carolina 27708, USA. +e-mail: drsmith@ee.duke.edu.

T.J. Cui et al. (eds.), *Metamaterials*, DOI 10.1007/978-1-4419-0573-4_14,

In practice metamaterials are often used in the design of narrow-band devices due to the high $Q$-value of the resonant units. Furthermore, the loss of the artificial materials may be another obstacle for the realistic application. In some typical experiments or applications for metamaterials, such as negative refraction lens or the invisible cloak, the bandwidth and the material loss have severely affected the performance of the related devices. Recently, more and more attentions have been focused on the applications based on the broadband, low-loss metamaterials, like the carpet cloak, where the I-shaped units have been used.

In the following sections, six interesting experiments or applications will be introduced. The results show that metamaterials are good candidates to replace the traditional devices in some cases, which is very important for the development of the area in the future.

## 14.2 Gradient Index Circuit by Waveguided Metamaterials

In this section, the metamaterial-based gradient index (GRIN) lens are proposed and demonstrated as an example of inhomogeneous effective medium realized by metamaterials in microwave region [18]. Two distinct designs of GRIN lenses, beam-steering and focusing lens, have been described in this section. Both designs are restricted to 2D cases.

The beam-steering lens characterizes a constant gradient index along one direction. It can deflect incident wave toward the side with relatively large index. From geometrical optics, the deflection angle of a normally incident beam by a beam-steering lens whose index grades perpendicular to the incident radiation is given by the formula [37]

$$\sin(\theta) = t \cdot dn/dx, \tag{14.1}$$

where $\theta$ is the beam-steering angle, $t$ is the thickness of the lens along $z$-axis, and $n$ is its refraction index relative to free space which grades along $x$-axis. The external beam is incident from $z$-axis.

Equation (14.1) assumes that the index of beam-steering lens varies continuously while in practice metamaterials are composed of periodic structures whose refraction index varies discretely in space. Therefore, in order to design GRIN lens based on metamaterials, Eq. (14.1) should be modified to the difference form

$$\sin(\theta) = N_z a_z \Delta n / a_x, \tag{14.2}$$

where $a_z$ and $a_x$ are metamaterial unit cell separations along $z$- and $x$-axes, respectively. $N_z$ is the number of unit cells along $z$-axis and $\Delta n$ is the linear difference of relative refraction index between two neighboring unit cells along $x$-axis. In this design, the unit cell dimensions are chosen to be $N_z = 6$, $a_z = 3.5\,\text{mm}$, and $a_x = 3.45\,\text{mm}$. Given the wave deflection angle (10° here) and the refraction index of the first metamaterial unit cell, all refraction indexes along the $x$-direction can be determined using Eq. (14.2). In the design, the index range is from 1.3537 to 2.1929

with $\Delta n = 0.029$, which indicates that there are totally 30 metamaterial unit cells along the $x$-direction. Note that all metamaterial unit cells are the same along the $z$-direction but linearly distributed in the $x$-direction.

The gradient index focusing lens is also a kind of lens whose refractive index has a gradual variation, which is in the direction perpendicular to the optical axis. Unlike the traditional curve-shaped lens, the GRIN focusing lens has planar optical surfaces, causing the light rays to bend continuously within the lens until finally they are focussed on a spot. Now GRIN focusing lenses are commonly used in the optical region, like photocopiers and scanners, in which a lot of very small lenses are needed to be mounted together. To design the focusing slab, again the gradient index optics is applied to the distribution of refractive index along the $x$-axis, which is expressed as

$$\Delta n_i = \frac{\sqrt{(i \cdot a_x)^2 + f^2} - f}{N_z \cdot a_z}, \tag{14.3}$$

In the above formula, $i$ is the sequence number of unit cell starting from the middle of the slab along the $x$-axis and the middle unit cell holds the first sequence number 0. Besides, $f$ gives the focal distance and $\Delta n_i$ represents the index difference between the $i$th unit cell and the middle unit cell. The incident beam propagates along $z$-axis. In the design, a six-layer ($N_z = 6$) focusing slab with 29 unit cells along the $x$-direction is constructed. The refraction index varies from 1.7589 in the middle to 1.3537 on two ends, resulting in a 42 mm focal distance in simulation at 9.5 GHz. Note that the theoretical calculation from Eq. (14.3) gives the focal distant of 90 mm. However, due to the abberation and boundary effect of gradient index lens, the simulated focal distant deviates from the theoretical value.

Various kinds of electrical small resonant particles could be used as the metamaterial unit cells to construct GRIN lenses designed above. In the literature, split-ring resonators (SRRs) array was chosen to form bulk inhomogeneous GRIN metamaterial [6, 9, 37]. Here, a configuration of waveguided metamaterial by array of complementary split-ring resonators (CSRRs) [8] is introduced and utilized. In this configuration (shown in Fig. 14.1), CSRR array is integrated into a planar waveguide. The planar waveguide height is $h = 1$ mm. CSRR array pattern is milled out in the lower metal plate attaching to an FR4 substrate with the thickness of 0.2026 mm.

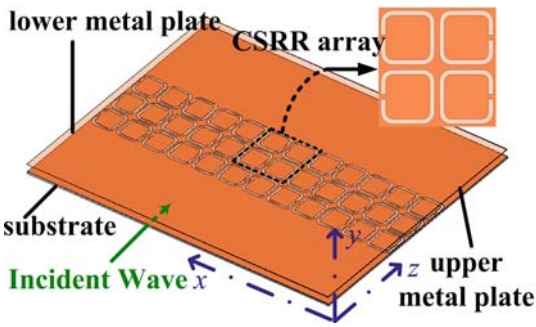


**Fig. 14.1** Configuration of the waveguided metamaterials composed of split-ring resonators array.

The substrate is cut by 0.1 mm due to the milling-machine fabrication. The relative permittivity and dielectric loss tangent of FR4 are 4.4 and 0.02, respectively. Similar to bulk metamaterials, the milling out CSRR structure can form equivalent electromagnetic medium by providing proper response inside the planar waveguide.

Retrieval process can be applied in the planar waveguide to extract the electromagnetic parameters of the waveguided metamaterial. The detailed approach can be found in Ref. [17]. Typically, as mentioned in Ref. [17], in the planar waveguide configuration CSRR behaves as an electric resonator, responding to the electric field penetrating across the milling-out complementary structure. Note that only TEM modes in the planar waveguide is supported if the height of waveguide is less than half wavelength. Figure 14.2 illustrates the CSRR structure and retrieved permittivity and permeability in the planar waveguide using the commercial software Ansoft HFSS 10.0. The permittivity and permeability responses shown in Fig. 14.2 exhibit electric resonate property with frequency dispersion and spatial dispersion [16]. It indicates that such type of waveguided metamaterials behave just like volumetric metamaterials.

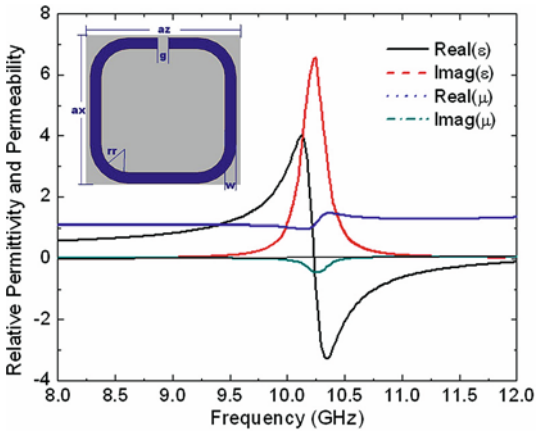


**Fig. 14.2** Retrieval results for CSRR structure with dimensions: $rr = 0.6$ mm, $w = 0.25$ mm, $g = 0.25$ mm, $l = 3.2$ mm, $a_x = 3.45$ mm, and $a_z = 3.5$ mm. The CSRR structure is shown in the inset. Copyright ©2009 American Institute of Physics.

Therefore, by use of the proposed 2D planar waveguided metamaterials, various designs based on the electromagnetic theory or gradient index optics can be implemented conveniently in planar circuits or waveguide systems. The effective permittivity can be flexibly achieved through the careful design of CSRRs. As an example, the effective wave impedance and refraction index of CSRR at 9.5 GHz (before resonance) in terms of CSRR's corner radius, *rr*, are illustrated in Fig. 14.3. The corresponding fitted curves are also shown in Fig. 14.3. Although other geometrical dimension of the unit cell structure can also tune electromagnetic response, it is found in simulation that the change of *rr* can achieve large index variation. Moreover, usage of the frequency region right before the resonance can result in good impedance matching condition ($Z = 1$).

Note that results in Fig. 14.3 correspond to CSRR unit cells with the same size as the earlier description, that is, $a_z = 3.5$ mm and $a_x = 3.45$ mm. According to

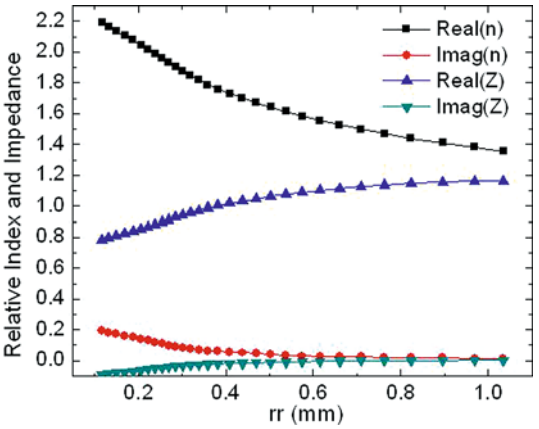


**Fig. 14.3** Relationship between the dimension *rr* of CSRR and its effective index and impedance. Copyright ©2009 American Institute of Physics.

the dependence of refraction index on the corner radius *rr*, each CSRR unit cell's detailed dimension (*rr*) can be implemented to meet all unit cell index requirements determined from Eqs. (14.2) and (14.3). The design frequency is 9.5 GHz.

Then the CSRR array-based GRIN lens samples are fabricated and their near-field distributions are measured using a 2D near-field microwave scanning apparatus (2D mapper), which has been described in detail in Ref. [14]. Figure 14.4(a) depicts the configuration of waveguided metamaterials measurement, in which the upper metal plate of 2D mapper is not closed. Figure 14.4(b) shows the fabricated

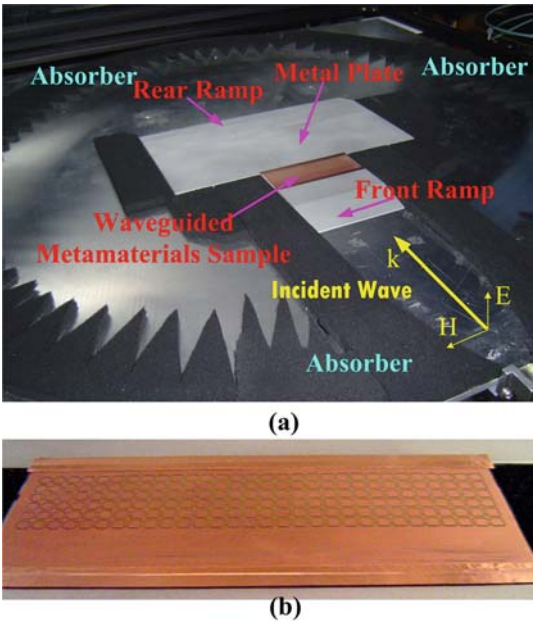


**Fig. 14.4** (**a**) Measurement configuration and (**b**) the fabricated beam-steering lens sample.

beam-steering lens sample. To achieve a strong signal from source and avoid large reflection, we additionally place two metal ramps before and after the sample. The height between the sample and upper metal plate of 2D mapper is controlled to be 1 mm.

Figure 14.5(a) shows the mapping result of beam-steering sample at 9.5 GHz, in which the deflection angle is observed around 12°, agreeing with the theoretical design very well. Due to the careful control on impedance, the return loss is relatively lower than that of the traditional lenses. The differences in deflection angles are due to the inaccuracy of fabrication, the height-control error, and the PCB substrate

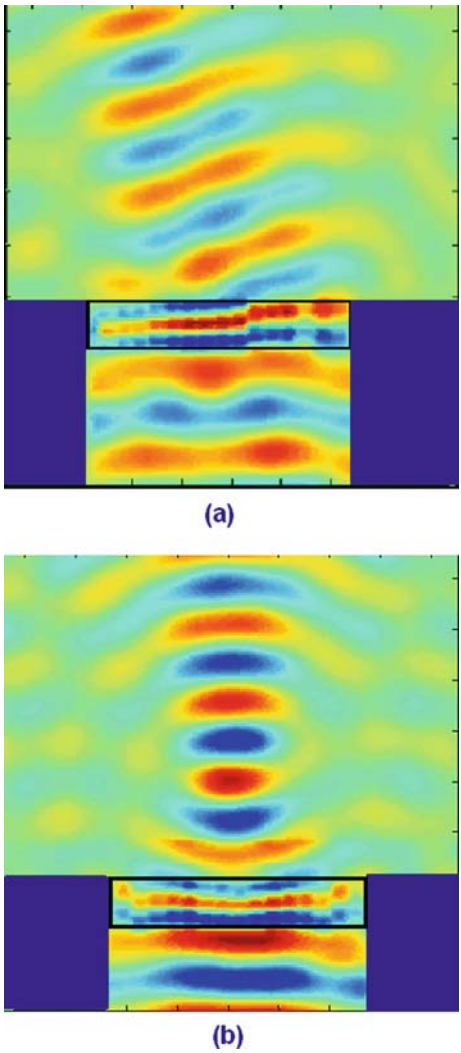


**Fig. 14.5** (**a**) The mapping result of the near-field distribution of the beam-steering sample at 9.6 GHz and (**b**) the mapping result of the near-field distribution of the beam focusing sample at 9.6 GHz. Copyright ©2009 American Institute of Physics.

variation. Figure 14.5(b) illustrates the near-field mapping result of the focusing lens. The focal distance is 40 mm, which is very close to the design.

## 14.3 Experimental Demonstration of Electromagnetic Tunneling Through an Epsilon-Near-Zero Metamaterial at Microwave Frequencies

In this section, we will analyze the tunneling phenomenon based on the metamaterial with the permittivity close to zero [17]. It shows that this property could be widely applied in the design of microwave components such as filters and transmission lines.

In the family of artificial metamaterials, the materials with the electric permittivity $\varepsilon$ or the magnetic permeability $\mu$ less than unity have attracted the attentions of many scientists due to their unusual electromagnetic properties. Although metamaterials usually have more loss near the resonant frequencies, they can still be used to develop some useful devices. Recently more and more attentions have been focused on the zero index metamaterials: either the permittivity $\varepsilon$ or the permeability $\mu$ approaches zero, or both are near zero simultaneously. The wavelength in these materials are extremely large compared to that in free space; however, the physical dimensions of the unit cells for metamaterials are still small.

It has been reported that the zero index metamaterials could be used to design some interesting devices like highly directive antennas [7] and compact resonators [15]. The tunneling of electromagnetic waves through an arbitrarily shaped epsilon-near-zero (ENZ) channel has also been proved, which is a good solution for wave transmission around the junctions with great impedance mismatch.

In this experiment, we use the planar complementary split-ring resonators (CSRRs) to replace the volumetric metamaterials made of the wire medium. The CSRR structure was first investigated by Falcone et al. based on the Babinet principle [8]. It usually has an electric response under the excitation of the external electric field normal to the CSRR surface. Therefore a waveguide with CSRR patterns at the bottom is equivalent to a hollow waveguide filled with the metamaterials.

The experiment was performed in a planar waveguide apparatus [14]. Three waveguide sections have been set up by adjusting the height $h$ of bottom plate, as shown in Fig. 14.6, where the left and right regions are planar waveguides with $h = 11$ mm and the middle region is a narrow waveguide with $h = 1$ mm. The planar waveguide is bounded by absorbing material on each side to reduce the wave reflection. And the main mode for this waveguide is nearly TEM waves as has been measured through experiment [14]. Note that the difference of the height for the three regions may cause severe impedance mismatch which prevents waves transmitting from left waveguide to the right, except that the resonance condition exists related to the channel length and the effective wavelength. The tunneling principle could be simply described as

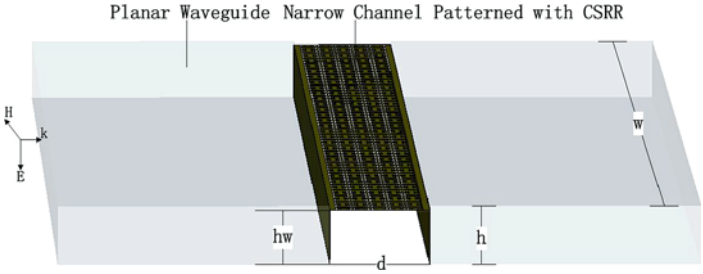


**Fig. 14.6** Experimental setup with a planar waveguide, in which $h = 11$ mm, $hw = 10$ mm, $d = 18.6$ mm (16.6 mm for CSRR Regime), $w = 200$ mm.

$$R = \frac{R_{12}(1 - e^{i2k_{2z}d})}{1 - R_{12}^2 e^{i2k_{2z}d}}, \tag{14.4}$$

in which $R_{12} = (Z_2 - Z_1)/(Z_2 + Z_1)$. $R_{12}$ is the reflection coefficient between the planar waveguide and the channel, $d$ is the effective length of the channel, and $k_{2z}$ is the wave vector inside the channel. $Z_1$ and $Z_2$ are the effective wave impedance at the transition outside narrow channel and the one inside narrow channel. It is clear that the reflection coefficient vanishes when $\varepsilon$ and $\mu$ are simultaneously approaching zero, since $1 - e^{i2k_{2z}d} \approx 0$ while $1 - R_{12}^2 e^{i2k_{2z}d} \neq 0$. In the current configuration, however, since $Z_1 \gg Z_2$ (extremely small channel area), the only approach to reach impedance match through manipulating the medium property inside the channel is to increase the wave impedance inside the channel for the sake of $R_{12} = 0$, that is, according to $Z_2 = \sqrt{\mu_0/\varepsilon_{eff}}$, to make effective permittivity very small – near zero, which is actually another type of tunneling effect. It is easy to establish the equivalence between the ENZ metamaterial and the CSRR structure through the retrieval procedure depicted in Fig. 14.7. In order to obtain the effective permittivity of the CSRR unit, the commercial electromagnetic software Ansoft HFSS has been used to simulate the corresponding $S$-parameters. The simulation configuration is shown in Fig. 14.7(b), which is different from the common setup for the volumetric metamaterial unit. The polarization of the incident state could be determined by the PEC and PMC boundaries on the sides of the computational domain. The height for the waveguide is 1 mm and the gap between the upper and lower PEC plates is 11 mm. The radiation boundaries have been assigned at the surfaces below the two ports. Note that the ports are placed far enough to avoid the coupling between the structure and the ports. The de-embedding algorithm has been used to remove the phase shift of the waveguide regions without the CSRR patterns. Figure 14.7(a) shows the retrieval result for the CSRR unit and Fig. 14.7(c) shows the simulation setup for the whole tunneling structure. The permittivity of the CSRR structure $\varepsilon$ is near zero at approximately 8.8 GHz, where tunneling through the channel can be expected to occur.

We have roughly estimated $Z_1 = 11Z_0$ and $Z_2 = Z_0/\sqrt{\varepsilon_{eff,r}}$ in order to use a simplified model for direct calculation of transmission and reflection from Eq. (14.4). Here we choose the effective length $d$ to be 13 mm considering the influence of

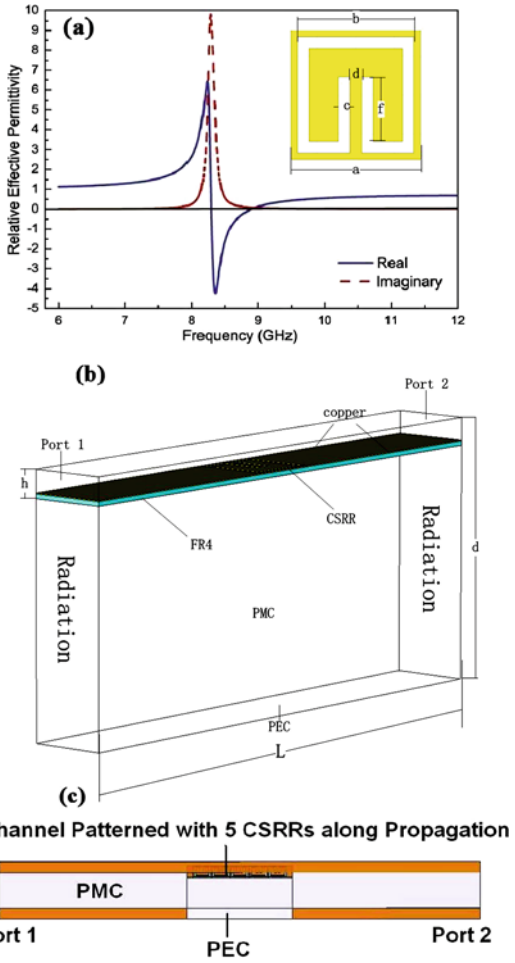


**Fig. 14.7** Retrieval results, dimensions of CSRRs, and simulation setup. (**a**) Extracted permittivity and CSRRs' dimensions, in which, $a = 3.333$ mm, $b = 3$ mm, $c = d = 0.3$ mm, and $f = 1.667$ mm. (**b**) Simulation configuration for CSRR unit cell: $d = 11$ mm, $h = 1$ mm, and $L = 23.333$ mm. (**c**) Configuration of tunneling effect simulation.

high-order modes at transition. It is clear that $\varepsilon_{eff,r}$ is required to be $1/121$ in terms of impedance match. The result for the simplified model has been compared with the simulation result in Fig. 14.9, where we can see that the two curves matche very well. In Fig. 14.8(a), the poynting vector distribution has been given along the whole structure at 8.8 GHz, where we can see that the waves are squeezing to the narrow channel while high-order modes emerge at transition point, which changes the effective wave impedance of planar waveguide. To validate the ENZ properties of the CSRR region, a channel patterned with CSRRs was fabricated and its scattering was compared to an unpatterned control channel. Both the CSRR and control channels were fabricated upon a copper-clad FR4 circuit board with the thickness 0.4 mm. The array of CSRR elements (shown in Fig. 14.7) was patterned on the circuit board using standard photolithography. Altogether 200 CSRRs (5 in the propagation direction, 40 in the transverse direction) were fabricated on the FR4

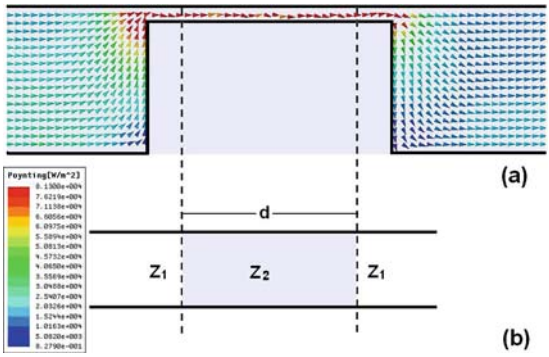


**Fig. 14.8** (**a**) Simulated poynting vector distribution in the planar waveguide. (**b**) The simplified medium model for theoretical prediction. Copyright ©2008 The American Physical Society.

board. The CSRR/control substrates were then placed on a styrofoam support, with dimensions $18.6 \times 10 \times 200(\text{mm}^3)$. Copper tape was used to cover the sides of the styrofoam to ensure the good electrical contact between the copper-clad substrates and the bottom plate of the waveguide. X-band waveguide-to-coaxial adapters were used to connect the waveguide to a vector network analyzer.

At first the control sample was placed in the 2D planar waveguide and the corresponding transmission coefficient was measured. The results are shown in Fig. 14.9 and compared with those from the simplified model calculation and the numerical simulation based on HFSS. The passband of the control slab has shifted to 7 GHz compared to that in the simulation. The frequency shift may be caused by the differences between the experimental environment and the simulation model (for example, finite slab width and fluctuation of channel height). The simulation curve and the measurement curve agree very well if the frequency scale is uniformly shifted (note the two scales indicated on the top and bottom axes). When the control slab is replaced by the CSRR channel, the measured transmitted power (shown in Fig. 14.9) reveals a passband near 7.9 GHz (8.8 GHz from the simulation) which is identical with retrieval prediction. In the control case the passband vanishes, which shows that

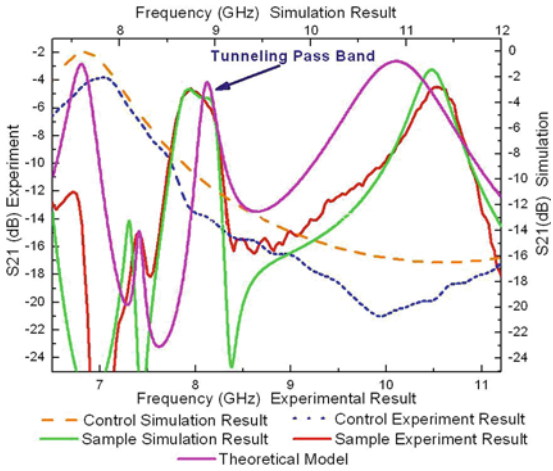


**Fig. 14.9** Experimental, theoretical, and simulated transmissions for the tunneling and control samples. Copyright ©2008 The American Physical Society.

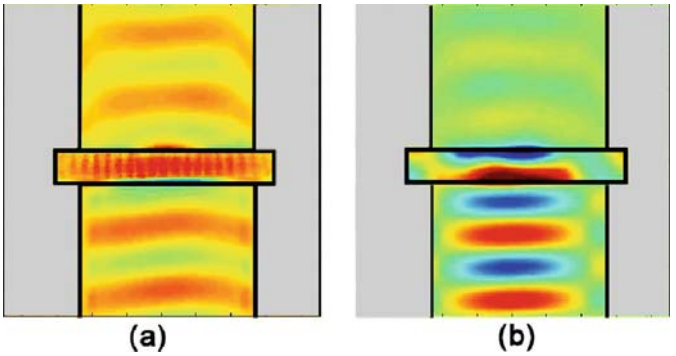


**Fig. 14.10** Two-dimensional mapper results at 8.04 GHz: (**a**) field distribution of tunneling sample and (**b**) field distribution of control. Copyright ©2008 The American Physical Society.

electromagnetic tunneling takes place at approximately the frequency where the effective permittivity of the ENZ region approaches zero. To further demonstrate that the emergence of the passband is due to the tunneling phenomenon with $\varepsilon \approx 0$, phase-sensitive maps of the spatial electric field distribution throughout the channel region were constructed [15]. The electric field magnitude was mapped inside a $180 \times 180$ ($mm^2$) square region for both the copper control and CSRR channels. In Fig. 14.10, the mapped fields for both cases have been plotted at $f = 8.04$ GHz, where the effective permittivity approaches zero. Note that the color scale is different since the field is normalized by the average field strength. It is obvious that electromagnetic waves are allowed to transmit through the CSRR region. However, little energy could propagate through the control slab. Note the uniform phase variation across the channel at the tunneling frequency, $f = 8.04$ GHz.

The phase distribution gives a further demonstration on the tunneling effect through the ENZ channel instead of the Fabry–Perot-like resonant scattering, as shown in Fig. 14.11. This mechanism of transmission has been investigated in detail by Hibbins et al. [11]. Strong phase variation exists across the control channel at $f =$

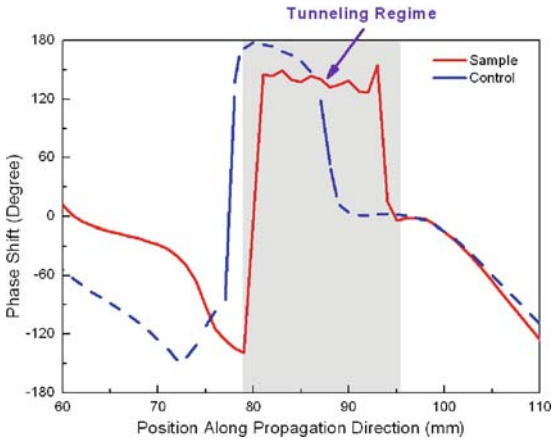


**Fig. 14.11** Phase shift for 5 unit cell tunneling sample at 8.04 GHz and control at 7 GHz. Copyright ©2008 The American Physical Society.

7 GHz, as shown in Fig. 14.11, which corresponds to the passband in Fig. 14.9. The phase advance within the channel implies that the propagation constant is non-zero. The large transmittance results from a resonance condition related to the length of the channel. By contrast, the spatial phase variation for the CSRR channel is shown in Fig. 14.11 for $f$ = 8.04 GHz (the passband of the CSRR loaded channel), where we can see that the phase advance across the channel at this frequency is negligible. The phase variation is near zero, which shows that $\varepsilon_{eff}$ for the CSRR slab is very close to zero. Although the CSRR structures are not volumetric metamaterials, we can see that the waveguide with CSRR patterns etched at the bottom plate can still be treated as a planar waveguide filled with ENZ medium. The ENZ medium could be used as highly efficient couplers in microwave and THz devices. Also it can be used in the visible frequency band where the ENZ medium could be realized by metals like silver or gold.

## 14.4 Partial Focusing by Indefinite Complementary Metamaterials

In this section, a partial focusing experiment by indefinite waveguided metamaterial in microwave region is demonstrated. Indefinite metamaterials refer to metamaterials whose effective permittivity or permeability take the form of tensors [33, 34, 36]. Similar to the isotropic metamaterials, indefinite metamaterials are also composed of electric or magnetic resonant units. These materials may find exotic characteristics due to their complex dispersion relations [36]. Therefore they have aroused many interest within the scientific community. Some interesting applications have been proposed based on these artificial materials, such as invisible cloaks and energy localization devices [29, 2].

The partial focusing phenomenon has ever been investigated in Ref. [35] using the 3D split-ring resonators. The focusing phenomena in the indefinite metamaterials have also been investigated by other groups with different techniques [13, 21, 28, 38]. Here, a waveguided resonant structure is utilized to construct indefinite metamaterials for partial focusing [3]. The proposed waveguided metamaterials, unlike bulk metamaterials, are made up of 2D periodic units and usually complementary to normal bulk metamaterial units. These complementary structures, which were first investigated by Falcone et al. in 2003 [8], can still be regarded as metamaterial units when their dimensions are much smaller than the wavelength of the TEM mode in planar waveguide [17, 18].

Note that there is another kind of 2D indefinite metamaterials (TIM) previously investigated in [1], where inductor–capacitor grids act as TIM units. However, in such configuration, waves or signals can only be guided along the circuit components, and they cannot penetrate the areas within the grids. Therefore this kind of TIM is actually only valid from the circuit point of view.

In the present TIM configuration, CELC structure has been selected as the basic metamaterial unit, as illustrated in Fig. 14.12. The CELC structure refers to the

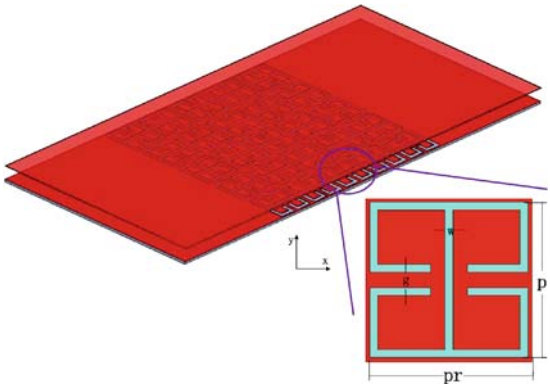


**Fig. 14.12** Waveguided metamaterial composed of CELC structure is chosen to realize the indefinite medium for partial focusing.

planar-waveguide unit with the ELC pattern etched at the bottom metallic plate. When the working frequency is selected to be lower than the cutoff frequency for the second-order mode (TE mode) of the planar waveguide, only the dominant TEM mode could be supported. The corresponding electric field is just parallel to the axis of the CELC unit in the $z$-direction and the magnetic response will be produced under the excitation of the dominant mode. Note that the components of the permeability tensor in the $x$- and $y$-directions are different since the shape of the CELC unit is not identical in these two directions. Therefore the effective medium composed of the CELC particles is actually indefinite, which is suitable for realization of the partial focusing phenomenon as will be discussed later.

The principle of partial focusing by indefinite medium was discussed in Ref. [35]. The dispersion relation for the TM to $z$-wave in the indefinite medium, whose permittivity tensor is $\bar{\bar{\varepsilon}} = \hat{x}\hat{x}\varepsilon_x + \hat{y}\hat{y}\varepsilon_y + \hat{z}\hat{z}\varepsilon_z$ and the permeability tensor is $\bar{\bar{\mu}} = \hat{x}\hat{x}\mu_x + \hat{y}\hat{y}\mu_y + \hat{z}\hat{z}\mu_z$, is expressed as [36]

$$\frac{k_x^2}{\mu_y} + \frac{k_y^2}{\mu_x} = \left(\frac{\omega}{c}\right)^2 \varepsilon_z. \tag{14.5}$$

It is obvious that when $\mu_y < 0$, $\mu_z > 0$, and $\varepsilon_x > 0$, the dispersion curve for Eq. (14.5) is a hyperbola. In such a case, the phase velocity of the incident TM to $z$-waves will undergo a positive refraction, while the group (or energy) velocity will undergo a negative refraction at the boundary between air and the indefinite medium, which will help to refocus the incident waves inside or outside the slab [35]. In Ref. [35], ray-tracing diagram has been given to describe the propagation of the waves emitted from a source in front of the indefinite slab, showing the occurrence of negative refraction at the interface between air and the indefinite medium, and also the existence of partial focusing for incident waves.

Figure 14.13 roughly shows the configuration of our waveguided metamaterials-based partial focusing experiment. In the configuration, the planar waveguide is divided into three regions. The middle region is covered by an indefinite slab mentioned above, the left and the right regions are occupied by air, with the

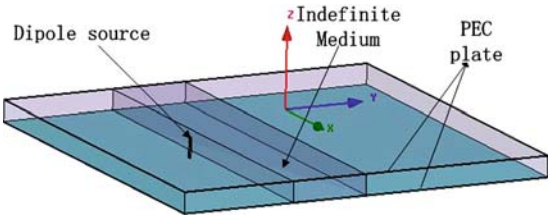


**Fig. 14.13** (Color online) Theoretical model for partial focusing in a planar waveguide. An indefinite metamaterial slab is inserted into the waveguide, with a dipole source excitation.

permittivity $\varepsilon_0$ and the permeability $\mu_0$. An electric dipole is placed before the anisotropic slab, whose ends are connected with the top and bottom perfectly electric conducting plates, respectively, yielding TM to $z$-waves within the planar waveguide.

In Fig. 14.12, the CELC region can be regarded as the effective indefinite slab in the model shown in Fig. 14.13. In order to get the effective permittivity and permeability of the CELC unit for partial focusing slab design, full-wave numerical simulations have been made to obtain the $S$-parameters for the whole structure. Then, the standard retrieval procedure is performed to get the effective medium parameters [32]. The detailed description for the simulation setup could be found in Ref. [17]. Note that in order to retrieve the effective medium parameters, it is not sufficient to simulate only one CELC unit due to the strong mutual coupling between adjacent CELC structures. Therefore, the advanced parameter retrieval method has been adopted, which is quite efficient for the resonant structures with strong coupling among the neighbors [12]. Two different simulations with orthogonal wave incident directions are needed to get the components of the permittivity and permeability tensors when the magnetic field of the TEM mode is along $x$- and $y$-directions, respectively, as shown in Fig. 14.14. Both simulation setups have been shown in Figs. 14.14(a) and (b). Two sets of effective permittivity and permeability curves for these two simulation setups are shown in Figs. 14.15 and 14.16, respectively. The effective $\varepsilon_z$ and $\mu_x$ from Fig. 14.14(a) are plotted in

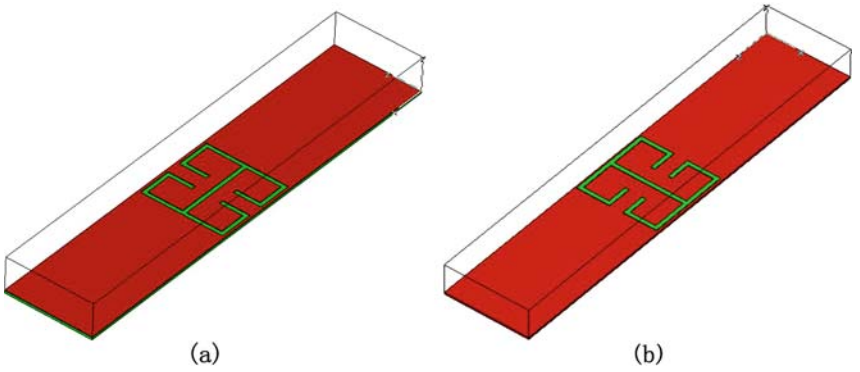


**Fig. 14.14** Simulation setups for the anisotropic CELC unit cell where the plane waves are incident from two orthogonal directions.

Fig. 14.15, while the effective $\varepsilon_z$ and $\mu_y$ from Fig. 14.14(b) are demonstrated in Fig. 14.16.

From Figs. 14.15 and 14.16, it is clear that the effective $\varepsilon_z$ varies a lot in the observation band in the two cases due to the particle response and the coupling between adjacent units. However, at the design frequency, $f = 11.5$ GHz, both $\varepsilon_z$ are quite close to each other. In Fig. 14.15(a), $\varepsilon_z = 1.085 - i0.1123$ and in Fig. 14.16(a), $\varepsilon_z = 1.047 - i0.1338$. Hence it can be assumed that at 11.5 GHz the effective permittivity in the $z$-direction does not change for waves incident from $x$- and $y$-directions. From Figs. 14.15 and 14.16, it can also be observed that $\mu_x = 2.489 + i0.193$ and $\mu_y = -0.970 + i0.122$ at 11.5 GHz. The extracted effective constitutive parameters have already met the requirements for the anisotropic slab to realize the partial focusing.

The fabricated partial focusing sample is shown in Fig. 14.17(b), where the CELC patterns are etched from copper-clad FR4 circuit board with the thickness of 0.2 mm. Standard photolithography has been used in the fabrication. The dimen-

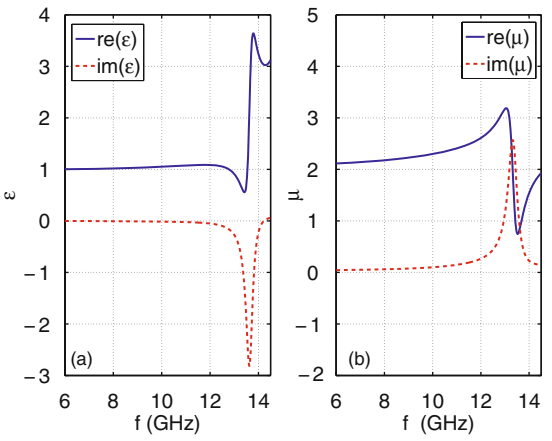


**Fig. 14.15** The effective permittivity and permeability curves for the simulation setup in Fig. 14.14(**a**). (**a**) $\varepsilon_z$. (**b**) $\mu_x$. Copyright ©2008 The American Physical Society.

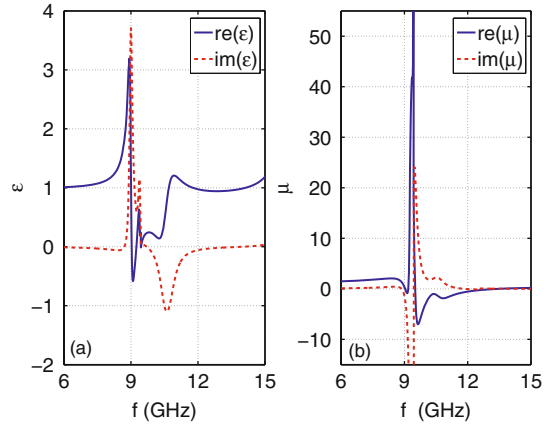


**Fig. 14.16** The effective permittivity and permeability curves for the simulation setup in Fig. 14.14(b). (**a**) $\varepsilon_z$. (**b**) $\mu_y$. Copyright ©2008 The American Physical Society.

sions for the CELC unit shown in Fig. 14.12 are selected as $pr = 3.333$ mm, $p = 3$ mm, and $w = g = 0.3$ mm, and the thickness of the copper layer is 0.018 mm. There are altogether 12 units in the longitudinal direction and 60 units in the transverse direction and the sample is placed upon a cubic styrofoam.

A 2D near-field microwave scanning apparatus (2D mapper) is used for observation of the field distributions in the planar waveguide and within the CELC region in the subsequent experiment. The 2D mapper is a parallel-plate waveguide apparatus in the X-band frequencies [14], as shown in Fig. 14.17(a). There is a probe in the upper plate of the waveguide, which can measure the electric field at different positions with the network analyzer. The gap between the top and bottom plates is 11 mm. In the experiment, the gap between the patterned planar CELC sample structure and the top metal plate of the waveguide is kept as 1 mm. There is a hole below the CELC patterns, as shown in Fig. 14.17(b), where the excitation antenna could

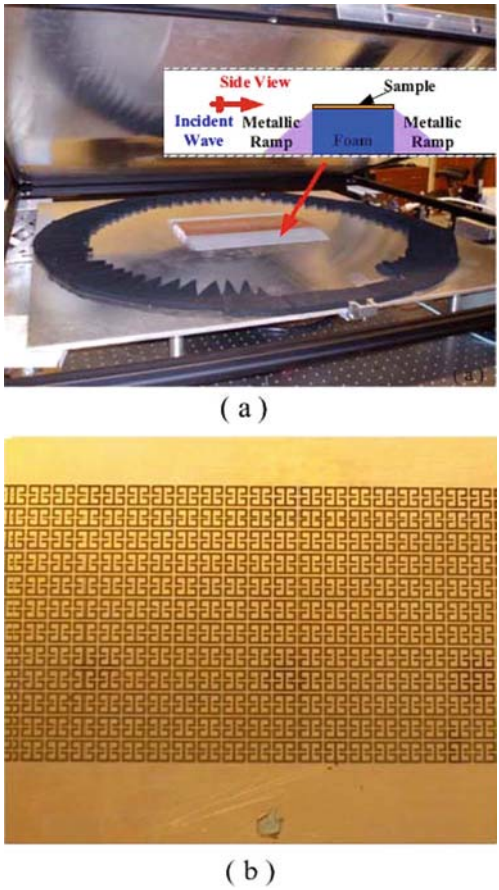


**Fig. 14.17** (**a**) The experimental setup for the partial focusing. (inset) Side view of the experimental setup. (**b**) Details of the fabricated CELC sample. Copyright ©2008 The American Physical Society.

protrude into the waveguide after penetrating the styrofoam. Two metallic ramps are placed on each side of the sample to avoid the severe impedance mismatch due to huge difference between the height of the 2D mapper and the gap in the CELC region (see the inset in Fig. 14.17(a)). There are two copper regions beside the CELC patterns on the circuit board, which forms a planar waveguide together with the top PEC plate. Thus the experimental configurations are consistent with the theoretical model described in Fig. 14.17. To reduce the reflection of electromagnetic waves at the edge of plates, a ring of microwave absorber with saw-toothed pattern has been placed near the boundary of the 2D mapper.

The experimental result for the distribution of the real part of the electric field in the internal and external regions of the CELC array at 11.5 GHz is shown in Fig. 14.18, where the sign "X" indicates the location of the excitation antenna, and the region between the two dashed lines are covered with the CELC structures. From Fig. 14.18 it is obvious that there exist several foci inside and outside the indefinite slab. The waves continue to propagate radially behind the focus above the slab, just like the cylindrical waves radiated from a 2D point source. The corresponding numerical simulation has also been made using the software package HFSS at $f =$ 11.5 GHz, which is based on the extracted permittivity and permeability mentioned above. The distribution of the real part of the electric field is illustrated in Fig. 14.19. It can be seen that the experimental result and the numerical simulation has excellent agreement and the partial focusing phenomenon is quite obvious. Note that the field amplitudes in the two figures are not consistent since the excitation current in the simulation is not the same as that in the experiment.

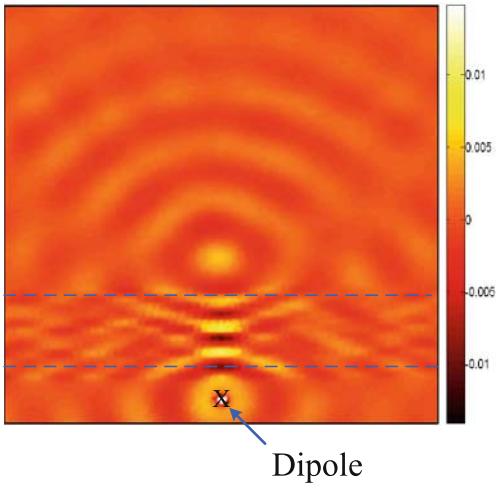


**Fig. 14.18** The experimental result for the electric field distributions inside the 2D mapper at 11.5 GHz. Copyright ©2008 The American Physical Society.

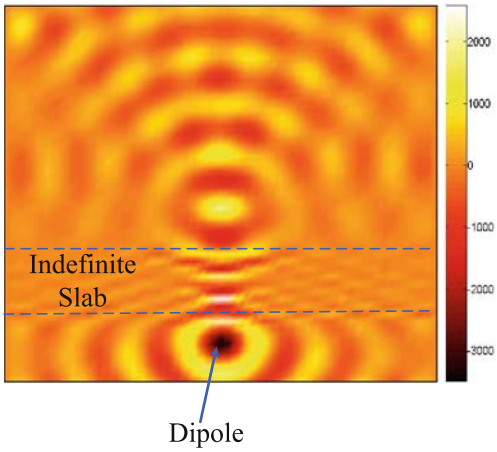


**Fig. 14.19** The distribution of simulated electric fields in a section of the planar waveguide at 11.5 GHz. Copyright ©2008 The American Physical Society.

## 14.5 A Metamaterial Luneberg Lens Antenna

In this section, we will show how the Luneberg lens antenna is constructed by the artificial metamaterials [24]. It has been shown that metamaterials may find a lot of potential applications [26, 27, 31, 29, 37] based on their novel physical properties. The most significant characteristics of metamaterials is that it can be designed to achieve any permittivity and permeability in principle, which is very important for the microwave device composed of the materials with varying refraction index. The Luneberg lens [22] antennas have been used widely as a kind of mature technology at the microwave frequency, which is spherically symmetrical. The refractive index of the Luneberg lens varies from 1 to $\sqrt{2}$ and satisfies $n = \sqrt{2-(r/R)^2}$, where $R$ is the radius of the lens and $0 \leq r \leq R$. Usually the lens is made up of some homogeneous dielectric concentrically layered media with different permittivities. Luneberg lens can transform the cylindrical/spherical waves from a point source on the surface $r = R$ into plane waves on the diametrically opposite side of the lens, which also can focus parallel beams of waves from any different direction at the other surface of the sphere. One application of the Luneberg lens is mobile satellite communications based on its high degree of symmetry. However, the Luneberg lens in practical is expensive and bulky limited by the existing materials and fabricating technology.

Here we have designed and realized a 2D metamaterial Luneberg lens antenna. The metamaterial units are carefully designed based on the non-resonant artificial structures [19], whose relative refractive index can be varied from 1.1 to 1.414 exactly. So the novel metamaterial Luneberg antenna can be achieved with metamaterials which is made up of the non-resonant structures. The near-field distributions of the 2D metamaterial Luneberg lens antenna are measured using 2D near-field microwave scanning apparatus (2D mapper) [14] and the radiation pattern is obtained

using near–far-field transformation technology [23]. Both the near-field distributions and the radiation pattern of the experiment all have good agreements with the simulations, which show the exact directivity and high gain performance. Compared to the traditional Luneberg lens, the metamaterials whose refractive indexes vary from 1 to 1.414 can be easily realized with the non-resonant artificial structures, so the novel metamaterial Luneberg lens is easier to fabricate at a lower price with the lighter weight.

It is well known that the 2D Luneberg lens has the circular symmetry with the refractive index varying as $n = \sqrt{2 - (r/R)^2}$, where the $R$ is the radius of the Luneberg lens and $0 \leq r \leq R$. Here, a metamaterial Luneberg lens is designed at the frequency $f = 8$ GHz with the radius $R = 49.4$ mm (Fig. 14.20). A series of rectangular grids with different lengths are applied to approach a circle (whose radius is $R = 49.4$ mm) in order to realize the refractive index $n$ of the Luneberg lens, as shown in Fig. 14.21(a). The width of each rectangular grid is $\Delta y = 3.8$ mm. The refractive index distributions for discrete Luneberg lens is shown in Fig. 14.21(b). Therefore the refractive index in each rectangular grid, which has the gradient distributions along the $x$-axis as shown in Fig. 14.21(b), should be exactly designed

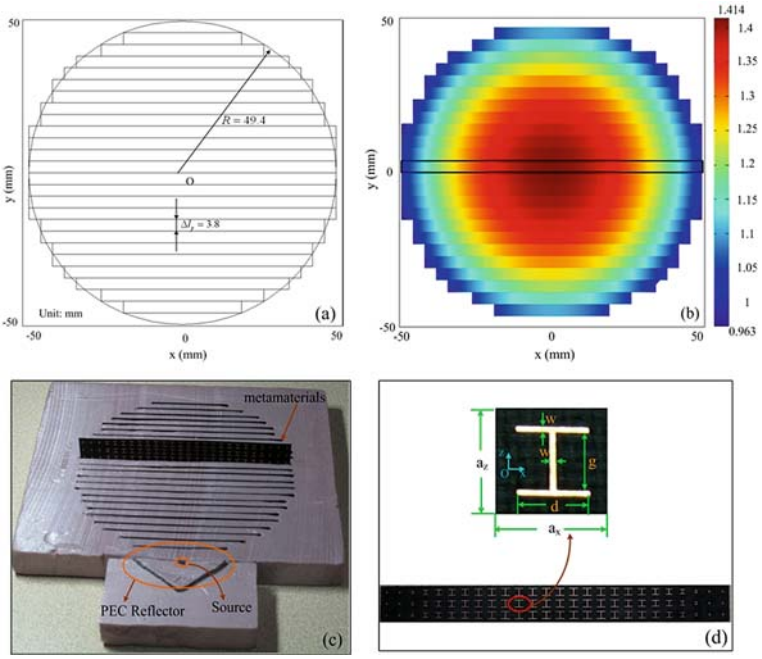


**Fig. 14.20** The design of metamaterial Luneberg lens antenna: (**a**) the discrete rectangular grid approaching to a circular Luneberg lens; (**b**) the relative refractive index distributions; (**c**) the experimental sample of the lens; and (**d**) the details of the metamaterials in (**c**).

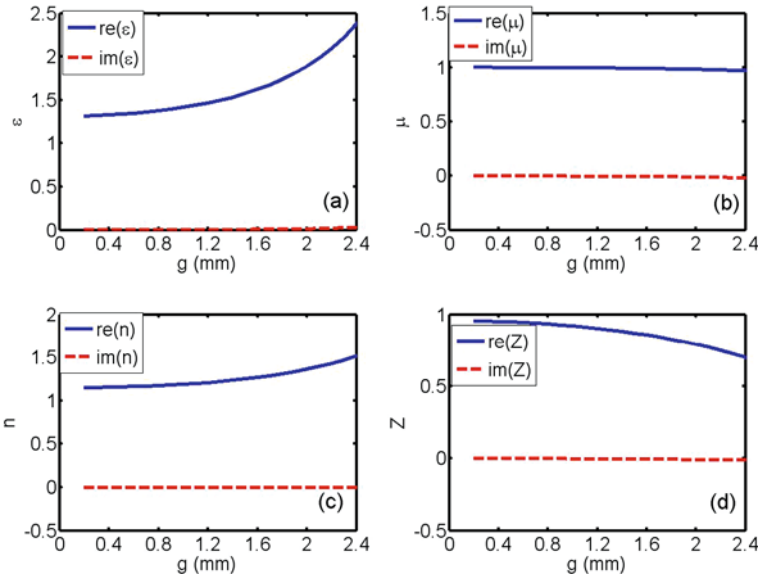


**Fig. 14.21** The relationship between the geometry of the I-shaped and the effective parameters.

by using the metamaterials. The non-resonant structures (I-shaped) are chosen to realize the required metamaterials as illustrated in Fig. 14.21(c) and (d). To support the pieces of printed circuit boards, the foam with relative permittivity $\varepsilon_f = 1.2$ is chosen and the electromagnetic responses of the I-shaped structure are shown in Fig. 14.21 by changing the length of $g$, where $a_x = a_z = 3.8$ mm, $w = 0.2$ mm, and $d = g + 2w$. In this experiment the PCB is chosen to be the copper-clad F4B with thickness 0.25 mm and the thickness of the copper layer is 0.018 mm. When $g$ varies from 0.2 to 2.4 mm, the corresponding relative permittivity $\varepsilon_r$ increases gradually from 1.31 to 2.38 and the relative permeability $\mu_r$ decreases gradually from 1 to 0.97, as shown in Fig. 14.21. Therefore the relative refractive index of the I-shaped structures varies from 1.15 to 1.52 and the characteristic impedance varies from 0.96 to 0.7.

According to the parameters listed above, the metamaterials can meet the requirement for the refractive index distributions of the Luneberg lens and the impedance matching can also be achieved. Note that the minimum $n$ achieved with the design is 1.15, so the relative refractive indexes of the discrete Luneberg lens as shown in Fig. 14.21(b), where $n$ is smaller than 1.15, are all designed to 1.15. In the equipment of the metamaterial Luneberg lens antennas in Fig. 14.21(c), there are 24 boards with different lengths embedded in the foam to realize the required relative refractive indexes and 1548 unit cells are involved in our design. A conducting reflector is used to restrain the back radiation excited by the source to improve the directivity of lens antenna.

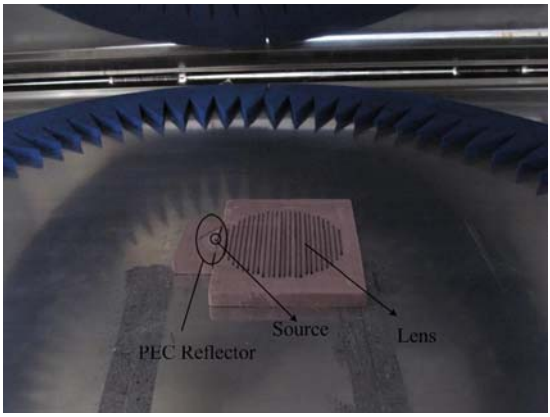


**Fig. 14.22** The sample of metamaterial Luneberg lens antenna located in the 2D mapper.

In order to observe the electric field distributions of the metamaterial Luneberg lens antenna, the 2D near-field microwave scanning apparatus (2D mapper) is used in this experiment. The 2D mapper is a parallel waveguide as shown in Fig. 14.22, the distance between two metal plates is 13 mm, and a probe drilled through the bottom layer serves as the 2D point source. The height of the sample is 12 mm and the sample is located at the bottom metal plate, so the probe actually serves as the source of the lens as shown in Fig. 14.22. The radius of the lens is $R = 49.4$ mm and the designed frequency $f = 8$ GHz. The measured result has a good agreement with the simulation, as illustrated in Fig. 14.23(a) and (b). Figure 14.23(a) shows the simulation result, where the relative refractive index distribution of the Luneberg lens is $n = \sqrt{2-(r/49.4)^2}$ and $0 \le r \le 49.4$. The amplitude of the current source is $I = 0.001e^{j\pi/2}$. It is clear that the Luneberg lens has transformed the waves from point source into the plane wave on the diametrically opposite point source. Figure 14.23(b) shows the experimental result measured by 2D mapper. By comparing Fig. 14.23(b) with (a), the experimental result has a good agreement with the simulation. The lens antenna has a wide bandwidth since the unit cells of the metamaterials are non-resonant structures whose permittivity and permeability varies slowly in a wide frequency range. Figure 14.23(c) and (d) has given the electric field distributions of lens antenna at 7 and 8.5 GHz, showing that the metamaterial lens antenna can work very well in broadband frequencies.

## 14.6 Metamaterial Polarizers by Electric-Field-Coupled Resonators

In this section a transmission polarizer has been realized by an anisotropic slab, where the function and the transmission efficiency of the polarizer can be designably controlled. As is well known, polarization devices have wide applications like liquid

crystal display, radio frequency antenna radiation, satellite communication, and optical instrumentation. Conventionally, polarizers can get a single polarization state by reflecting the unwanted state or by splitting mixed-polarization waves into two wave beams with perpendicular polarizations. Usually the transmission polarizer has favorable advantages of little absorption and small reflections. Compared to the reflector polarizer [10], the incoming and outgoing waves are naturally well separated, and therefore do not interfere with each other.

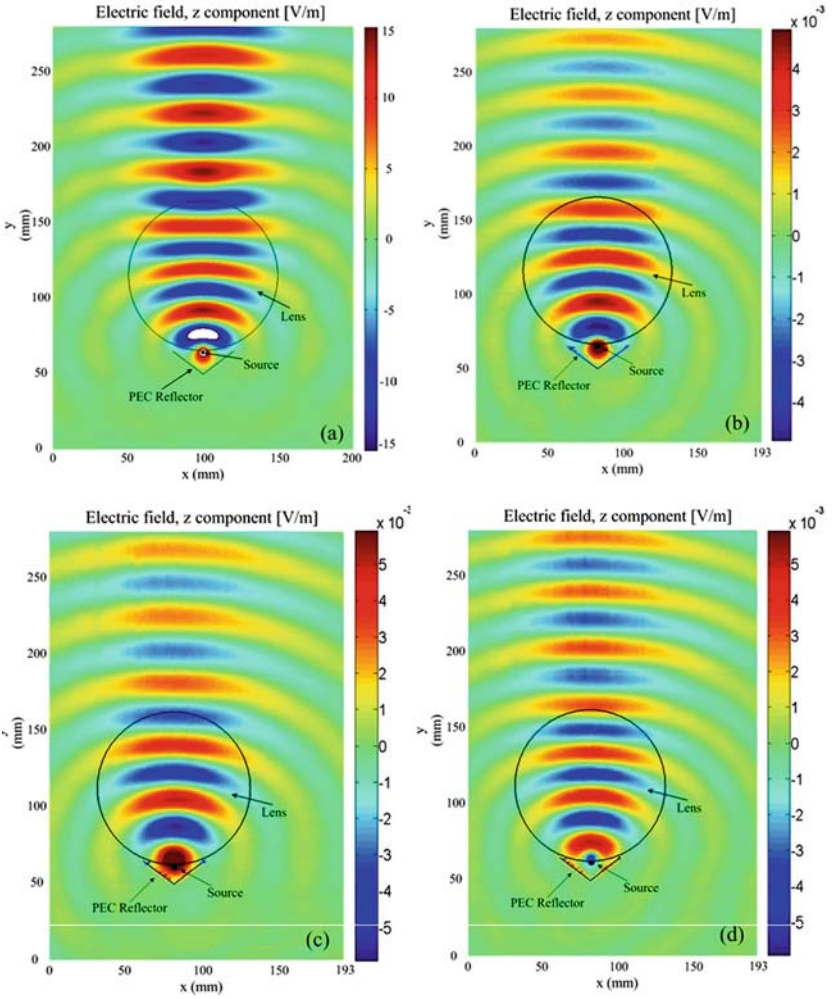


**Fig. 14.23** The electric field distributions of the metamaterial Luneberg lens antenna: (**a**) the simulated result at 8 GHz; (**b**) the measured result at 8 GHz; (**c**) the measured result at 7 GHz; and (**d**) the measured result at 8.5 GHz.

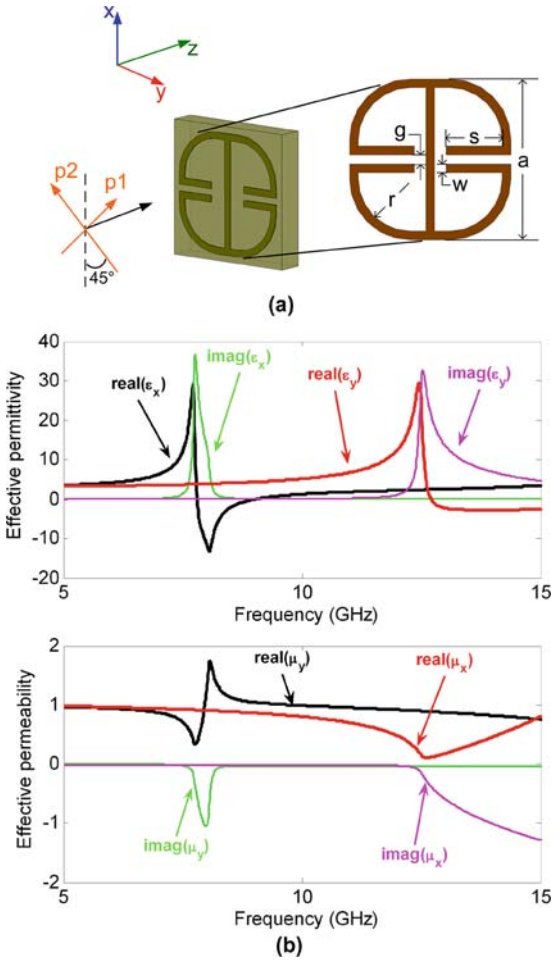


**Fig. 14.24** (**a**) The ELC unit for polarization design: $a = 3.6\,\text{mm}$, $w = 0.2\,\text{mm}$, $g = 0.2\,\text{mm}$, $s$ and $r$ are variables. The copper thickness is 0.035 mm and the substrate thickness is 0.75 mm. (**b**) The retrieved permittivity and permeability for the optimized ELC from 5 to 15 GHz. Copyright ©2008 American Institute of Physics.

Here the designed polarizer is based on the electric-LC resonator (ELC) particle which has a strong electric response under the excitation of the external field [30, 25]. In Ref. [25], different types of ELC particles have been investigated, where the ELC with two pairs of arms shown in Fig. 14.24(a) is finally chosen for its anisotropic material response and merit of being electrically small.

According to the classical electromagnetic theory, the propagating waves inside an anisotropic metamaterial slab along the $z$-axis can be decomposed into two modes with the electric fields along the $x$-axis and $y$-axis, respectively. The transmission coefficients $T^x$ and $T^y$ for the two modes could be expressed as

$$T^{x,y} = \frac{\exp(ik_{x,y}d) - r_{x,y}^2 \exp(ik_{x,y}d)}{1 - r_{x,y}^2 \exp(2ik_{x,y}d)}, \tag{14.6}$$

where $d$ is the thickness of the metamaterial slab, $k_{x,y}$ is the wave number for the two wave modes, and $r_{x,y}$ is the reflection coefficient at the interface between air and metamaterials

$$r_{x,y} = \frac{\eta_0 - \eta_{x,y}}{\eta_0 + \eta_{x,y}}, \tag{14.7}$$

in which $\eta_0$ is the wave impedance of air and $\eta_{x,y}$ is the wave impedance for the two wave modes inside the metamaterials.

Suppose that the electric field for an incident TEM wave could be written as $\overline{E} = \hat{x}E_x + \hat{y}E_y$. The condition for linear outgoing waves is derived as

$$|E_x| \cdot |T^x| = p\left|E_y\right| \cdot |T^y|, \tag{14.8}$$

$$[\arg(E_x) + \arg(T^x)] - [\arg(E_y) + \arg(T^y)] = k\pi, \tag{14.9}$$

where $k = 0, \pm 1, \pm 2, \pm 3, \ldots$, and $p$ decides the orientation of the electric field ($0 \leq p \leq 1$). The condition for elliptical outgoing waves is

$$|E_x| \cdot |T^x| = q\left|E_y\right| \cdot |T^y|, \tag{14.10}$$

$$[\arg(E_x) + \arg(T^x)] - [\arg(E_y) + \arg(T^y)] = \tfrac{k\pi}{2}, \tag{14.11}$$

where $q$ is the minor to major ratio of the polarization ellipse. When $q = 1$, the circular polarization could be obtained for the outgoing wave. Note that $T^x$ and $T^y$ could be controlled by adjusting the material properties of the metamaterial slab. By controlling the orientation of the slab with respect to the polarization of the incident waves, we are able to adjust $|E_x|/\left|E_y\right|$. If $T^x$ and $T^y$ are tuned close to unity, the linear polarization can be efficiently rotated by an arbitrary angle and waves can be switched between any elliptical polarizations or circular polarizations with little loss of energy.

The instances of converting the linear polarization to circular polarization and to its cross-polarization have been considered in this section. For the linearly polarized incident waves, $|E_x| = \left|E_y\right|$ and $\arg(E_x) = \arg(E_y)$ while $T^x$ and $T^y$ have the following relation:

$$|T^x| = |T^y|, \tag{14.12}$$

$$\arg(T^x) - \arg(T^y) = -\tfrac{3\pi}{2}. \tag{14.13}$$

Equations (14.10) and (14.11) will be satisfied with $q = 1$ and the outgoing waves will be circularly polarized. If $|T^x|$ and $|T^y|$ are designed to be close to 0 dB, little electromagnetic waves would be reflected at the polarizer surface. For four layers of the same ELC structures, we therefore have $|T^x| = |T^y|$ and $\arg(T^x) - \arg(T^y) = -3\pi$, which means with the same linear incident waves, the metamaterial slab will polarize the wave to its cross-linear polarization.

A 4 mm × 4 mm × 4 mm ELC particle shown in Fig. 14.24(a) has been simulated using the commercial software HFSS, where the substrate has been chosen to be F4B with a relative permittivity of $3.0 + i0.01$. First the $S$-parameters of ELC with electric boundary condition along the $x$-axis and magnetic boundary condition along

the $y$-axis have been simulated in order to get the effective permittivity $\varepsilon_x$ and permeability $\mu_y$. From Eq. (14.6), $T^x$ could be calculated for ELC metamaterial slab with different thicknesses. Likewise, $\varepsilon_y$, $\mu_x$, and $T^y$ can be calculated from simulated S-parameters with electric boundary condition along the $y$-axis and magnetic boundary condition along the $x$-axis. By changing the geometry parameters $s$ and $r$, all the available values of $T^x$ and $T^y$ at 9.5 GHz have been searched for one up to three layers of ELC, and eventually the optimal $T^x$ and $T^y$ have been obtained to match the relations of Eqs. (14.12) and (14.13) in the case of two-layer ELC. The optimized geometry parameters are $s = 0.99\,\text{mm}$ and $r = 1.18\,\text{mm}$ while $T^x$ and $T^y$ are kept to be greater than $-1\,\text{dB}$. Retrieved anisotropic permittivity and permeability are plotted in Fig. 14.24 (b). For the linear-to-circular polarizer, two pieces of $20\,\text{cm} \times 20\,\text{cm}$ substrate patterned with periodic ELC structures were fabricated and fixed with 3.25 mm spacing. The reflection and transmission waves were measured using a pair of X-band lens antennas connected to the vector network an-

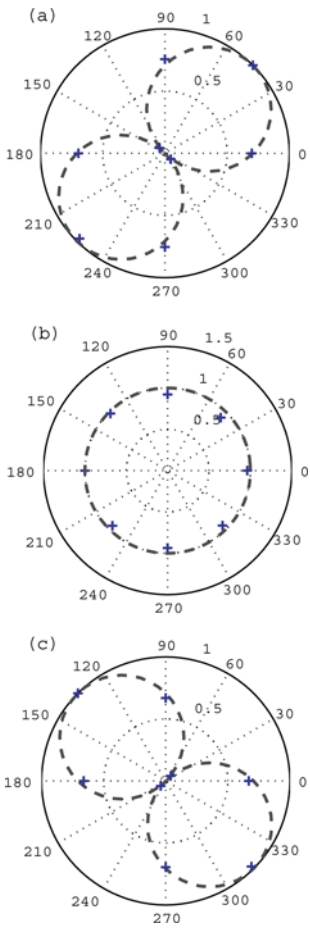


**Fig. 14.25** The theoretical polarization patterns (*dotted lines*) and the measured polarization patterns (*plus signs*) of the (**a**) incident waves, (**b**) transmitted waves through the two-layer ELC sample, and (**c**) transmitted waves through the four-layer ELC sample. Copyright ©2008 American Institute of Physics.

alyzer (Rohde and Schwarz ZVA40). Note that there are $48 \times 48$ ELC unit cells on each substrate. The electric field of the transmitting antenna is polarized along the direction $p1$, as seen in Fig. 14.24(a), with a 45° angle with respect to the vertical direction so that the electric fields of the two modes for incident waves are related by $|E_x| = |E_y|$ and $arg(E_x) = arg(E_y)$. A calibration was conducted by removing the sample and having the receiving antenna aligned at the same direction with the transmitting antenna, which is marked as 45°. The receiving antenna has been rotated from 0° to 315° by a step of 45° in order to achieve the polarization pattern of the incident waves. The comparison of polarization patterns from the measurement and theoretical prediction is shown in Fig. 14.25(a) for the incident wave at the frequency of 10 GHz.

Then the sample is placed between the two antennas and the polarization pattern of the transmitted waves has been measured. The comparison of the patterns for the measurement and theoretical prediction is shown in Fig. 14.25(b). For circular polarization, the amplitude of electric field is supposed to be invariant (see the gray dotted line) and the variation is less than 1 dB in the measurement. Besides, the phase distribution changes linearly along the circle as expected. The simulated and measured transmissions have been compared in Fig. 14.26 from the incident polarization ($p_1$) to the same polarization direction ($p_1$) and to its cross-polarization ($p_2$). Here, $p_1$ and $p_2$ are defined in Fig. 14.24(a). Over the frequency range around 10 GHz, the field intensity in the two polarization directions is roughly equal to each other at about $-3$ dB, indicating a full conversion to circular polarization. The frequency dispersion of the polarizer agrees well with the simulation despite the fabrication factor and random error in measurements.

Similarly a linear-to-linear polarizer with four pieces of the structures of the same ELC pattern has been measured, where the polarization pattern is illustrated in Fig. 14.25(c). The direction of the electric field has been rotated by 90° as expected. Figure 14.27 compares the simulated and measured transmissions from $p_1$ to $p_1$ and from $p_1$ to $p_2$. It is obvious that the field intensity of the cross-polarization is close to 0 dB over the frequency range around 10 GHz and that of the original polarization is less than $-20$ dB, which shows the small loss and little reflections of the polarizer. Note that both measurement results are reciprocal.

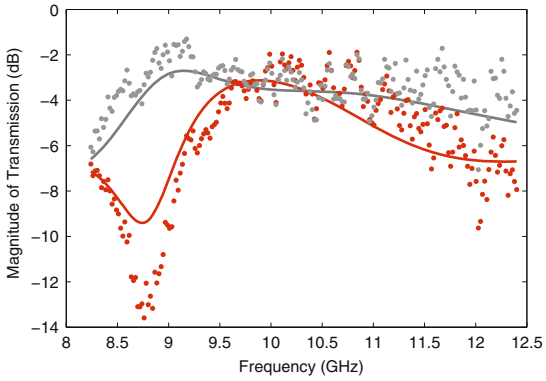


**Fig. 14.26** The simulated (*solid lines*) and measured (*dots*) transmission of electric field from one polarization to another: $p_1$ to $p_1$ (*upper lines and dots*) and $p_1$ to $p_2$ (*lower lines and dots*). Copyright ©2008 American Institute of Physics.

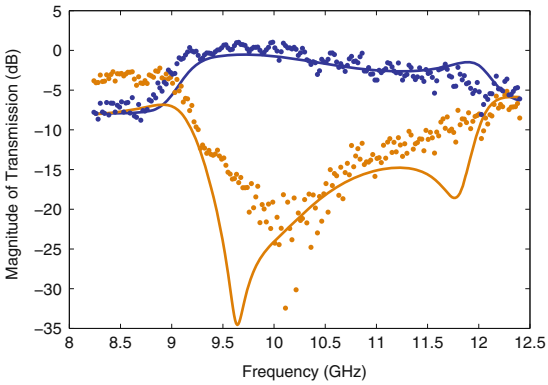


**Fig. 14.27** The simulated (*solid lines*) and measured (*dots*) transmission of electric field from one polarization to another: $p_1$ to $p_1$ (*lower lines and dots*) and $p_1$ to $p_2$ (*upper lines and dots*). Copyright ©2008 American Institute of Physics.

## 14.7 An Efficient Broadband Metamaterial Wave Retarder

In this section, the non-resonant metamaterial particle has been adopted to design a highly efficient broadband wave retarder, which has been introduced in Ref. [19]. The loss of the retarder is quite small since the metamaterials we use has little absorption at the non-resonant frequency. The impedance matched layers (IMLs) [20, 19] are also applied so that the wave retarder has a gradient impedance distribution which minimizes the reflection of the incident and exiting waves. A half-wave retarder has been designed and fabricated to demonstrate excellent performance in agreement with simulations.

As is well known, an anisotropic metamaterial slab is capable of controlling the polarization state of transmitted electromagnetic waves [4, 5]. The polarization conversion theory has successfully been verified by the experimental results. According to the requirement for the refraction index and the wave impedance, the electric inductance–capacitance resonators (ELCs) have been used to realize the anisotropic transmission coefficients.

Here a metamaterial wave retarder is designed to operate on TEM (transverse electric–magnetic) waves. The propagation wave number $k$ is assumed to lie along the $z$-axis, and the TEM waves incident with arbitrary polarization can be divided into two modes with the electric fields along the $x$- and $y$-axes, respectively. Suppose that the principal axes of the anisotropic metamaterial lie along the $x$- and $y$-axes. A multi-layered metamaterial slab (see Fig. 14.28(a)) with a smoothly gradient impedance variation is virtually reflectionless. By shifting the phase between the two wave modes traveling through the slab, the polarization state could be manipulated. In order to convert the linear polarization $p_1$, which makes a 45° angle with the $x$-axis, to its cross-polarization $p_2$ ($p_1$ and $p_2$ are depicted in Fig. 14.28(a)) in the same fashion as demonstrated in Ref. [5], phase advances of the two modes need to satisfy the condition that

$$\sum_i \theta_x^{(i)} - \sum_i \theta_y^{(i)} = p\pi, \tag{14.14}$$

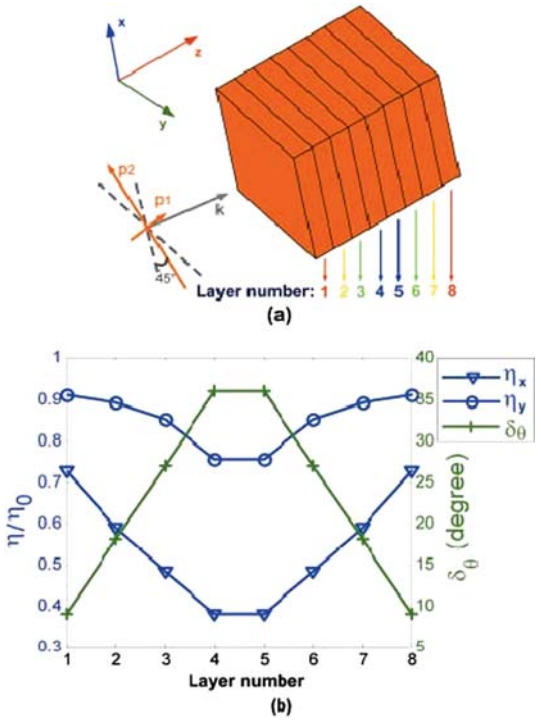


**Fig. 14.28** (**a**) A multi-layer half-wave retarder. (**b**) The distribution of wave impedances and the phase difference between the two modes inside the metamaterial layers; $\eta_x$ and $\eta_y$ are the wave impedance of the mode with electric field directed along $x$-axis and $y$-axis, respectively; $\delta_\theta$ is the phase difference between the two modes. Copyright ©2009 Optical Society of America.

where $p = \pm 1, \pm 3, \pm 5, ..., i = 1, 2, ..., m$ indexes the different layers and $\theta_x^{(i)}$ and $\theta_y^{(i)}$ are phase advances over the layer numbered $i$ for the two modes with electric field along $x$- and $y$-axes, respectively. $m$ is the total number of the metamaterial layers.

Here the I-shaped metamaterial element shown in Fig. 14.29(a) is chosen to be the basic particle of the retarder in order to reduce the absorption and broaden its bandwidth. The resonant frequencies of the copper I-shapes are relatively high; therefore their electric responses to the excitation of an external dynamic electric field along the $x$-axis vary quite slowly at the lower frequency band. At the mean time, there are little electric response in the other two directions. The nearly non-dispersive responses to the electric fields in different directions lead to a constant anisotropic effective permittivity. Also an anisotropic refractive index $n$ and an anisotropic wave impedance $\eta$ could be obtained from I-shaped metamaterial over a broad bandwidth. The phase advances of the two different wave modes through the slab with the thickness $d$ are $n_x k_0 d$ and $n_y k_0 d$, where $k_0 = 2\pi\sqrt{\mu_0 \varepsilon_0} f$ is the wave number in free space. Hence, the difference between the two $\theta_x - \theta_y = n_x k_0 d - n_y k_0 d$ changes linearly with the frequency and the dispersion is predictably small. To make this broadband wave retarder reflectionless, a series of I-shaped metamaterial geometry elements have been selected such that the wave impedances of the two wave modes vary smoothly from that of the air $\eta_0$ to a smaller value. At the same time,

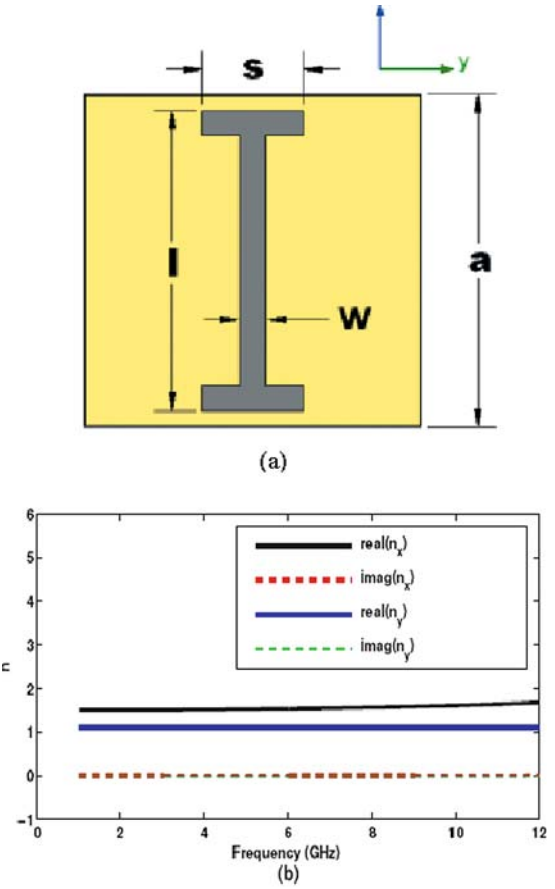


**Fig. 14.29** (**a**) The structure of an I-shaped metamaterial particle and (**b**) simulated refractive indices of the two wave modes when $s = 1\,\text{mm}$. Copyright ©2009 Optical Society of America.

the refractive indices vary over the layers while satisfying the relation indicated in Eq. (14.14).

In order to get the effective parameters of the metamaterial elements, the commercial software package CST Microwave Studio has been used in the numerical simulation. The basic I-shaped element is shown in Fig. 14.29(a), where the substrate is chosen to be FR4 with the thickness 0.2026 mm and the relative permittivity of $3.84 + i0.01$. The family of I-shaped elements is constructed from the initial design shown in Fig. 14.29(a) for which $a = 3.333\,\text{mm}$, $l = 3.0833\,\text{mm}$, $w = 0.25\,\text{mm}$, $s = 1\,\text{mm}$.

From the standard retrieval procedure [32], multiple simulations with different boundary conditions were conducted [5] to achieve the simulated effective constitutive parameters. As shown in Fig. 14.29(b), the effective refractive indices of the two wave modes $n_x$ and $n_y$ are almost non-dispersive from 0 to 12 GHz and the difference between the two remains approximately constant. The imaginary parts of $n_x$ and $n_y$ are so small that it could be neglected in the design of the retarder. Simulation

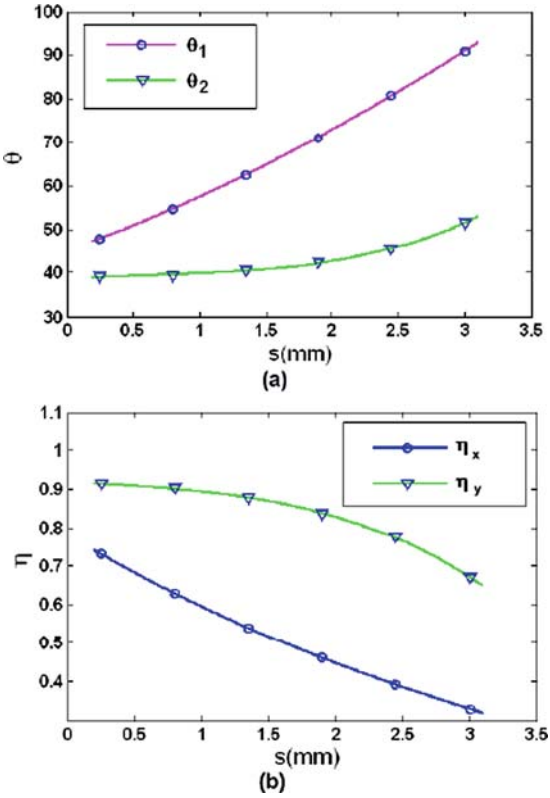


**Fig. 14.30** Variation of phase advances (**a**) and wave impedances (**b**) of the two modes with geometry parameter $s$. Copyright ©2009 Optical Society of America.

results for the variation of wave impedances and the anisotropic phase advances with the geometry variable $s$ which is swept from 0.2 to 3.0 mm at 8.94 GHz are shown in Fig. 14.30(a) and (b). It is clear that as the value of $s$ increases, the wave impedance of one mode, $\eta_x$, changes from $0.91\eta_0$ to $0.67\eta_0$ while that of the other $\eta_y$ changes from $0.74\eta_0$ to $0.32\eta_0$. At the mean time, the difference between the phase advances of the two modes increases from 8.61 to 41.14°.

In the experiment an eight-layered half-wave retarder has been chosen to realize the polarization conversion. The parameter $s$ has been optimized (the other geometry parameters are fixed) for the gradient difference between the phase advances of the two modes $\delta_\theta$ to be $\delta_\theta = -9°$, $-18°$, $-27°$, $-36°$, $-36°$, $-27°$, $-18°$, and $-9°$ for the eight layers, which add to the required 180° phase shift. The corresponding values of $s$ are $s = 0.26$ mm, $s = 1.03$ mm, $s = 1.735$ mm, $s = 2.56$ mm, $s = 2.56$ mm, $s = 1.735$ mm, $s = 1.03$ mm, and $s = 0.26$ mm. The distribution of the wave impedance for one mode is $0.9124\eta_0$, $0.8914\eta_0$, $0.8520\eta_0$, $0.7547\eta_0$, $0.7547\eta_0$, $0.8520\eta_0$, $0.8914\eta_0$, and $0.9124\eta_0$, and that of the other mode is $0.7278\eta_0$ to $0.5896\eta_0$, $0.4834\eta_0$, $0.3785\eta_0$, $0.3785\eta_0$, $0.4834\eta_0$, $0.5896\eta_0$, and $0.7278\eta_0$ (see Fig. 14.28(b)).

The entire half-wave retarder with the eight layers of I-shape has been simulated, and the polarization properties of the outgoing waves have also been analyzed. In Fig. 14.31, the simulated conversion factor from the original polarization $p_1$ to its cross-polarization $p2$ is shown together with the polarization isolation over the frequency span from 6 to 12 GHz. From the simulation result, it is obvious that the outgoing waves are converted to the cross-polarization state of the incoming wave around 8.8 GHz, and the polarization isolation of the linearly polarized waves is smaller than $-20$ dB over the frequency band from 8.04 to 9.56 GHz. The corresponding bandwidth of the half-wave retarder is therefore 1.52 GHz and the relative bandwidth is 17%.

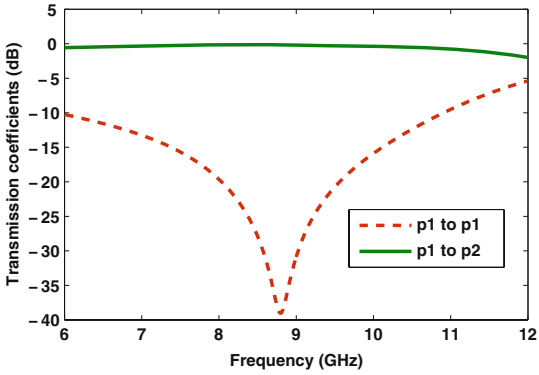


**Fig. 14.31** Transmission coefficients (*Simulation*) from incident waves polarized along $p_1$ to outgoing waves polarized along $p_1$ (*dashed line*) and $p_2$ (*solid line*). Copyright ©2009 Optical Society of America.

Based on the structures designed above, eight sheets of $43 \times 43$ I-shaped patterns have been fabricated on FR4 board. A styrofoam with the thickness of 3 mm was placed between adjacent layers as a spacer. The total thickness of the half-wave retarder is 26.67 mm, nearly $4/5$ of the wavelength around the designed frequency.

At first two horn antennas with a distance of 2 m which are connected to a network analyzer have been utilized to measure the polarization property. The designed half-wave retarder was placed between the antennas. The incident electric field of the transmitting horn antenna is directed along $p_1$ and $E_x = E_y$. The receiving antenna was attached to a gimbal which could rotate 360° to measure the polarization pattern. The measured polarization patterns at 8.0, 8.5, and 9 GHz have been shown in Figs. 14.32(a)–(c), respectively. In comparison to Fig. 14.32(d) it is clear that the polarization direction of the incident electric field is rotated by 90°.

Next the dispersion property and the transmission coefficient of the half-wave retarder will be measured in the experiment, where two X-band lens antennas with collimated beam connected to a network analyzer were set 1.3 m apart. The transmission coefficient of the half-wave retarder for the two wave modes have been measured separately, with different electric field orientations along $x$- and $y$-axes. As shown in Fig. 14.33(a), transmission coefficients of the two modes are identical from 6 to 10 GHz, with the overall loss smaller than 2.5 dB, which verifies the as-

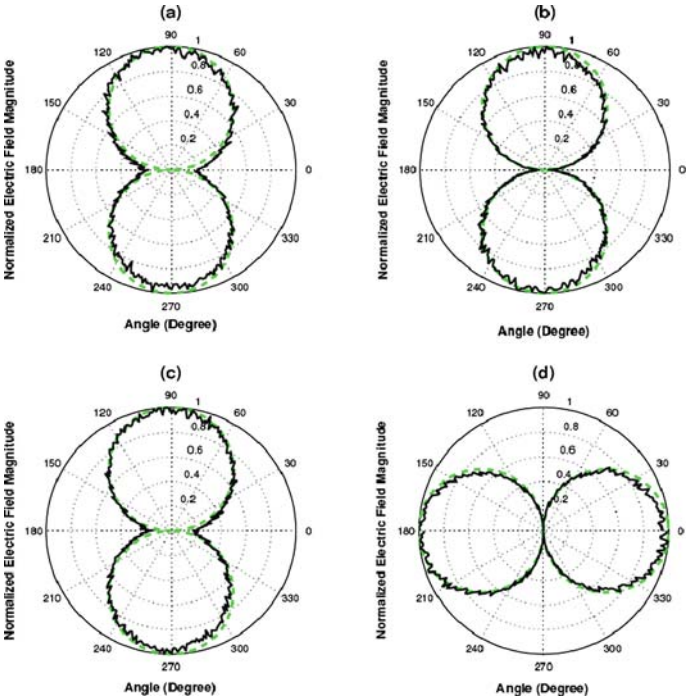


**Fig. 14.32** Measured polarization patterns (*solid line*) and ideal polarization patterns (*dashed line*) of the transmitted waves at 8.0 GHz (**a**), 8.5 GHz (**b**) and 9.0 GHz (**c**) compared with measured polarization pattern of the incident waves at 9.0 GHz (**d**). Copyright © 2009 Optical Society of America.

sumption of negligible reflection and absorption. The existence of oscillation is due to multi-reflection between the lens antennas.

The conversion efficiency and polarization isolation were also measured with the same antennas, where the polarization direction of the transmitter antenna is set to be $p_1$ and that of the receiver antenna is set to be $p_1$ and $p_2$, respectively. The measured transmission coefficients (see Fig. 14.33(b)) prove a 90° rotation of the incident electric field around 8.56 GHz and that over the frequency band from 7.935 to 8.94 GHz the polarization isolation is less than −20 dB, which is consistent with the simulation. Therefore, the measured relative bandwidth is about 12%.

Note that horn antennas have a better linear polarization but a divergent beam. Therefore they were adopted in the first set of measurements concentrating on the polarization patterns. Lens antennas with collimated beams were used in cases when transmission coefficients were measured and convergence of the beam did not adversely affect the measurement results. In the mean time, the experimental data in Fig. 14.33(b) are slightly different from the simulation result in Fig. 14.31 presumably since the radiation of the lens antenna is not of perfect linear polarization.

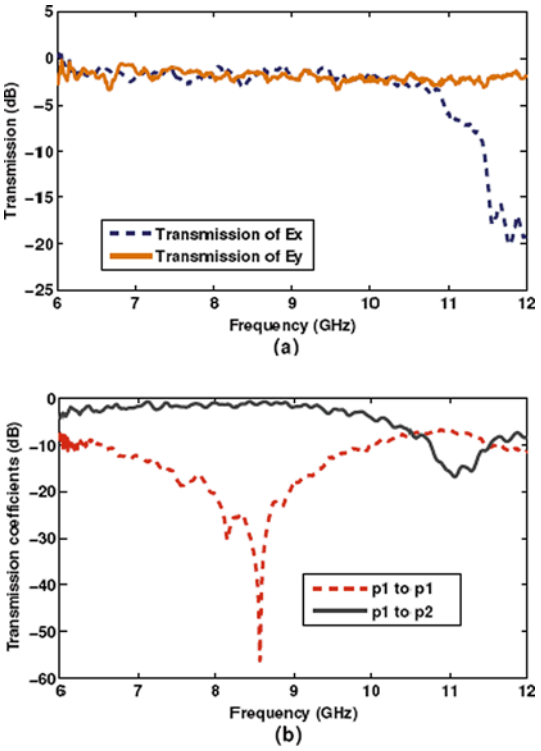


**Fig. 14.33** (**a**) Measured transmission coefficients of Ex (*dashed blue line*) and Ey (*solid yellow line*); (**b**) measured transmission coefficients from $p_1$ (*dashed line*) to $p_1$ and from $p_1$ to $p_2$ (*solid line*). Copyright © 2009 Optical Society of America.

**Acknowledgments** This work was supported in part by a major project of the National Science Foundation of China under Grant Nos. 60990320 and 60990324, the Natural Science Foundation of Jiangsu Province under Grant No. BK2008031, the National Basic Research Program (973) of China under Grant No. 2004CB719802, the National Science Foundation of China under Grant Nos. 60871016, 60671015, 60901011, and 60621002, and in part by the 111 Project under Grant No. 111-2-05.

## References

1. Balmain, K.G., Lüttgen, A.A.E., Kremer, P.C.: Power flow for resonance cone phenomena in planar anisotropic metamaterials. IEEE Trans. Ant. Prop. **51**, 2612–2618 (2003)
2. Cheng, Q., Cui, T.J.: Energy localization using anisotropic metamaterials. Phys. Lett. A. **367**, 259–262 (2007)
3. Cheng, Q., Liu, R., Mock, J.J., Cui, T.J., Smith, D.R.: Partial focusing by indefinite complementary metamaterials. Phys. Rev. B **78**, 121102(R) (2008)
4. Chin, J.Y., Lu, M., Cui, T.J.: A Transmission Polarizer by Anisotropic Metamaterials. Proceedings of the IEEE-AP/S International Symposium & URSI Radio Science Meeting, (2008).
5. Chin, J.Y., Lu, M., Cui, T.J.: Metamaterial polarizers by electric-field-coupled resonators. Appl. Phys. Lett. **93**, 251903 (2008)

6. Driscoll, T., Basov, D.N., Starr, A.F., Rye, P.M., Nemat-Nasser, S., Schurig, D., Smith, D.R.: Free-space microwave focusing by a negative-index gradient lens. Appl. Phys. Lett. **88**, 081101 (2006).
7. Enoch, S., Tayeb, G., Sabouroux, P., Guérin, N., Vincent, P.: A metamaterial for directive emission. Phys. Rev. Lett. **89**, 213902 (2002)
8. Falcone, F., Lopetegi, T., Laso, M.A.G., Baena, J.D., Bonache, J., Beruete, M.: Babinet principle applied to the design of metasurfaces and metamaterials. Phys. Rev. Lett. **93**, 197401 (2004).
9. Greegor, R.B., Parazzoli, C.G., Nielsen, J.A., Thompson, M.A., Tanielian, M.H., Smith, D.R.: Simulation and testing of a graded negative index of refraction lens. Appl. Phys. Lett. **87**, 091114 (2005)
10. Hao, J., Yuan, Y., Ran, L., Jiang, T., Kong, J.A., Chan, C.T., Zhou, L.: Manipulating electromagnetic wave polarizations through anisotropic meta-materials. Phys. Rev. Lett. **99**, 063908 (2007)
11. Hibbins, A.P., Lockyear, M.J., Sambles, J.R.: The resonant electromagnetic fields of an array of metallic slits acting as Fabry-Perot cavities. J. Appl. Phys. **99**, 124903 (2006)
12. Hou, L.L., Chin, J.Y., Yang, X.M., Lin, X.Q., Liu, R., Xu, F.Y., Cui, T.J.: Advanced parameter retrievals for metamaterial slabs using an inhomogeneous model. J. Appl. Phys. **103**, 064904 (2008)
13. Jacob, Z., Alekseyev, L.V., Narimanov, E.: Optical hyperlens: Far-field imaging beyond the diffraction limit. Opt. Express **14**, 8247–8256 (2006)
14. Justice, B.J., Mock, J.J., Guo, L., Degiron, A., Schurig, D., Smith, D.R.: Spatial mapping of the internal and external electromagnetic fields of negative index metamaterials. Opt. Express **14**, 8694–8705 (2006)
15. Lai, A., Caloz, C., Itoh, T.: Composite right left-handed transmission line metamaterials. Micro. Mag. **5**, 34–50 (2004)
16. Liu, R., Cui, T.J., Huang, D., Zhao, B., Smith, D.R.: Description and explanation of electromagnetic behaviors in artificial metamaterials based on effective medium theory. Phys. Rev. E **76**, 026606 (2007)
17. Liu, R., Cheng, Q., Hand, T., Mock, J.J., Cui, T.J., Cummer, S.A., Smith, D.R.: Experimental demonstration of electromagnetic tunneling through an epsilon-near-zero metamaterial at microwave frequencies. Phys. Rev. Lett. **100**, 023903 (2008)
18. Liu, R., Yang, X.M., Gollub, J.G., Cui, T.J., Smith, D.R.: Gradient index circuit by waveguided metamaterials. Appl. Phys. Lett. **94**, 073506 (2009)
19. Liu, R., Ji, C., Mock, J.J., Chin, J.Y., Cui, T.J., Smith, D.R.: Broadband ground-plane cloak. Science **323**, 366–369 (2009)
20. Liu, R., Cheng, Q., Chin, J.Y., Mock, J.J., Cui, T.J., Smith, D.R.: Broadband Gradient Index Optics Based on Non-Resonant Metamaterials. (Unpublished)
21. Liu, Z., Lee, H., Xiong, Y., Sun, C., Zhang, X.: Far-field optical hyperlens magnifying sub-diffraction-limited objects. Science **315**, 1686 (2007)
22. Luneberg, R.K.: Mathematical Theory of Optics. Brown University Press, Providence, Rhode Island (1944)
23. Ma, H.F., Cui, T.J., Yang, X.M., Jiang, W.X., Cheng, Q.: Far-field predictions of metamaterials from two-dimensional near-field measurement system. unpublished
24. Ma, H.F., Chen, X., Yang, X.M., Xu, H.S., Cheng, Q., Cui, T.J.: A broadband metamaterial cylindrical lens antenna. unpublished
25. Padilla, W.J., Aronsson, M.T., Highstrete, C., Lee, M., Taylor, A.J., Averitt, R.D.: Electrically resonant terahertz metamaterials: Theoretical and experimental investigations. Phys. Rev. B **75**, 041102(R) (2007)
26. Pendry, J.B.: Negative refraction makes a perfect lens. Phys. Rev. Lett. **85**, 3966–3969 (2000)
27. Pendry, J.B., Schurig, D., Smith, D.R.: Controlling electromagnetic fields. Science **312**, 1780–1782 (2006)
28. Salandrino, A., Engheta, N.: Far-field subdiffraction optical microscopy using metamaterial crystals: Theory and simulations. Phys. Rev. B **74**, 075103 (2006)

29. Schurig, D., Mock, J.J., Justice, B.J., Cummer, S.A., Pendry, J.B., Starr, A.F., Smith, D.R.: Metamaterial electromagnetic cloak at microwave frequencies. Science **314**, 977–980 (2006)
30. Schurig, D., Mock, J.J., Smith, D.R.: Electric-field-coupled resonators for negative permittivity metamaterials. Appl. Phys. Lett. **88**, 041109 (2006)
31. Shelby, R.A., Smith, D.R., Schultz, S.: Experimental Verification of a negative index of refraction. Science **292**, 77–79 (2001)
32. Smith, D.R., Schultz, S., Markos, P., Soukoulis, C.M.: Determination of effective permittivity and permeability of metamaterials from reflection and transmission coefficients. Phys. Rev. B **65**, 195104 (2002)
33. Smith, D.R., Schurig, D.: Electromagnetic wave propagation in media with indefinite permittivity and permeability tensors. Phys. Rev. Lett. **90**, 077405 (2003)
34. Smith, D.R., Rye, P., Vier, D.C., Starr, A.F., Mock, J.J., Perram, T.: Design and measurement of anisotropic metamaterials that exhibit negative refraction. IEICE Trans. Electron. **E87-C**, 359 (2004)
35. Smith, D.R., Schurig, D., Mock, J.J., Kolinko, P., Rye, P.: Partial focusing of radiation by a slab of indefinite media. Appl. Phys. Lett. **84**, 2244 (2004)
36. Smith, D.R., Kolinko, P., Schurig, D.: Negative refraction in indefinite media. J. Opt. Soc. Am. B **21**, 1032 (2004)
37. Smith, D.R., Mock, J.J., Starr, A.F., Schurig, D.: Gradient index metamaterials. Phys. Rev. E. **71**, 036609 (2005)
38. Smolyaninov, I.I., Huang, Y.J., Davis, C.C.: Magnifying superlens in the visible frequency range. Science **315**, 1699–1701 (2007)

# Chapter 15
# Left-handed Transmission Line of Low Pass and Its Applications

Xin Hu and Sailing He

**Abstract** We introduce a novel left-handed (LH) transmission line (TL), which is based on a structure of identical symmetrical lattice type. While all the LH-TLs reported previously are of high pass, the present LH-TL has a wide left-handed low-pass band. Compared with a conventional right-handed transmission line, this LH-TL has a phase shift difference of 180° independent of the frequency. We also analyze the effect of a non-ideal component in a practical case, i.e., when the inductance of the shorted line in the lattice section cannot be neglected. The dispersion relations between the practical case and the ideal case are given and compared. It is shown that the introduction of the inductance of the shorted line will not change the left-handedness and low-pass property of the LH-TL, but make the phase response vary slightly. In the application example of broadband 180° hybrid ring, the constant-phase-shift property of the proposed LH-TL is utilized. The broadband hybrid ring is shown to have a very high isolation and about 42% bandwidth ratio.

**Key words:** metamaterial, left handed, transmission line, broadband, hybrid ring

## 15.1 Introduction

An artificial dielectric medium that exhibits simultaneously negative electric permittivity and magnetic permeability, known as a left-handed (LH) material [with a negative refractive index (NRI)], was first predicted theoretically by Veselago [1]. A planar NRI transmission line was later realized by periodically loading a conventional transmission line (TL) with lumped elements of series capacitors and shunt inductors [2, 3]. Positive refractive index (PRI) material is equivalent to a TL with

Xin Hu
Center for Optical and Electromagnetic Research, Zhejiang University, Hangzhou, 310058, China Sailing He*
Division of Electromagnetic Engineering, School of Electrical Engineering, Royal Institute of Technology, S-100 44 Stockholm, Sweden; Center for Optical and Electromagnetic Research, Zhejiang University, Hangzhou, 310058, China, *email: sailing@kth.se

T.J. Cui et al. (eds.), *Metamaterials*, DOI 10.1007/978-1-4419-0573-4_15,

$L = \mu(H/m)$ and $C = \varepsilon(F/m)$ (in a distributed sense), where $L$ and $C$ are positive per-unit-length series inductance and parallel capacitance of the distributed TL, respectively. To obtain an equivalent material of negative material parameters, the authors of [2] proposed a high-pass transmission line of NRI with distributed series capacitance and parallel inductance. These left-handed transmission lines are of high pass, while a conventional right-handed transmission line is of low pass.

Here we introduce a different model of left-handed transmission line, which has a low-pass property as a conventional right-handed transmission line, but a 180°-phase shift difference for all the frequencies. As an application example, a broadband 180° hybrid ring based on this LH transmission line is studied.

## 15.2 Theory

To obtain a left-handed transmission line of low pass, we utilize a lattice section in the unit cell of the proposed LH-TL shown in Fig. 15.1(a). The section is a four-terminal network of balanced symmetry [4]. The impedance between terminals 1 and 2 when terminals 3 and 4 are open or shorted is denoted by open circuit impedance $Z_{OC}$ or short circuit impedance $Z_{SC}$. The unit cell can be transformed into its equivalent unbalanced circuit of T-section shown in Fig. 15.1(b), as the open/short circuit impedances have the same values for these two configurations:

$$Z_{OC} = Z_{ser} + \frac{1}{Y_{par}}, \tag{15.1a}$$

$$Z_{SC} = Z_{ser} + \frac{Z_{ser}}{Z_{ser}Y_{par} + 1}, \tag{15.1b}$$

where the series impedance $Z_{ser}$ and parallel admittance $Y_{par}$ are given by

$$Z_{ser} = j\omega\left(2L - \frac{1}{\omega^2 C}\right), \tag{15.2a}$$

$$Y_{par} = -2j\omega C. \tag{15.2b}$$

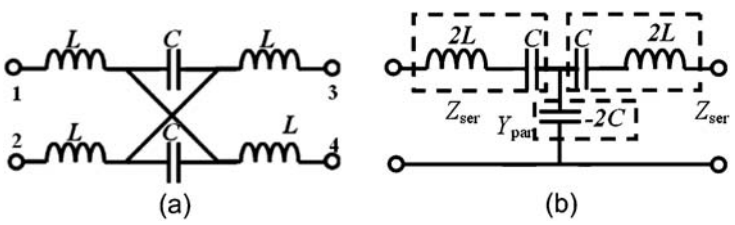


**Fig. 15.1** (**a**) The unit cell of LH-TL and (**b**) its equivalent circuit.

From the equivalent circuit we can derive the following transmission matrix of the unit cell:

$$\begin{bmatrix} A & B \\ C & D \end{bmatrix} = \begin{bmatrix} 1+Z_{ser}Y_{par} & Z_{ser}(2+Z_{ser}Y_{par}) \\ Y_{par} & 1+Z_{ser}Y_{par}. \end{bmatrix}. \tag{15.3}$$

Consequently, the dispersion relationship for such an infinitely periodic structure is

$$\begin{aligned} \cosh rd &= \frac{A+D}{2} \\ &= 1+Z_{ser}Y_{par} \\ &= 4\omega^2 LC - 1, \end{aligned} \tag{15.4}$$

where $\gamma = \alpha + j\beta$ is the propagation constant for the periodic structure.

From the transmission line theory, a conventional (right-handed) transmission line (C-TL) can be equivalent to an LC circuit. The unit cell of C-TL with balanced symmetry or four terminals [coplanar strip line (CPS), for example] is shown in Fig. 15.2(a), whose equivalent circuit is presented in Fig. 15.2(b). The dispersion relation of the C-TL can be written as

$$\begin{aligned} \cosh rd &= 1+Z_{ser}Y_{par} \\ &= 1-4\omega^2 LC. \end{aligned} \tag{15.5}$$

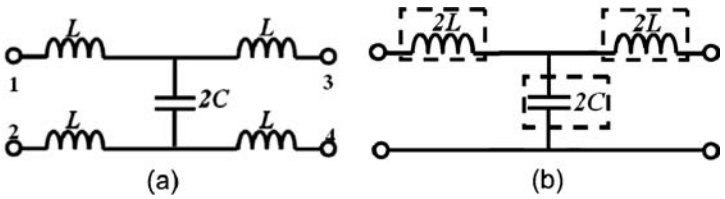


**Fig. 15.2** (**a**) The unit cell of C-TL and (**b**) its equivalent circuit.

Comparing the dispersion relations of LH-TL and C-TL, we can find that they look the same except the different sign, which means that a 180° phase difference exists between them. The dispersion relations (15.4) and (15.5) are plotted in Fig. 15.3 while $L$ and $C$ are equal to 1 nH and 0.2 pF, respectively. The LH-TL (solid curve) dispersion curve gives the same magnitude response as the C-TL (dashed curve), i.e., a low-pass property (a left-handed passband between 0 and cutoff frequency $\omega_C$), where

$$\omega_C = \frac{1}{\sqrt{2LC}}. \tag{15.6}$$

In the passband of LH-TL, energy propagation takes place by backward waves for which the phase velocity (i.e., the slope of the line from the origin to a point on the dispersion curve) is opposite to the energy velocity (or group velocity, the slope of the tangent to the dispersion curve), implying that the LH-TL supports backward

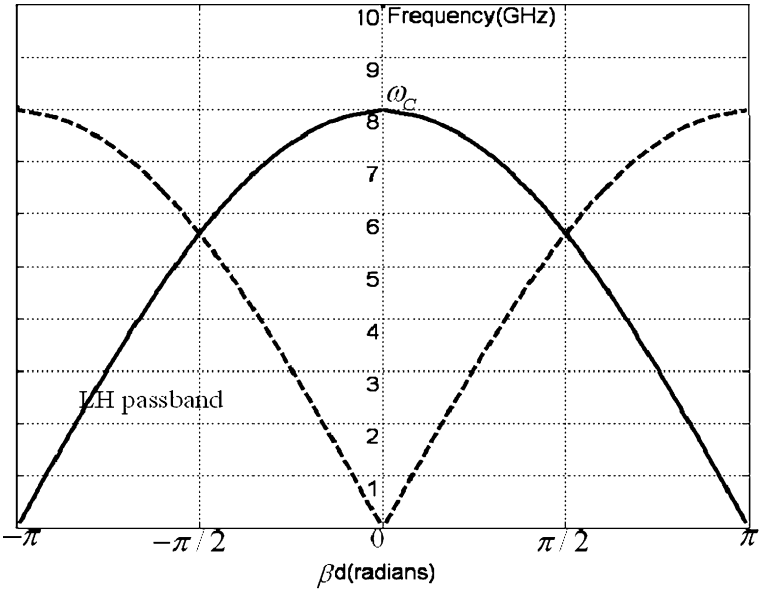


**Fig. 15.3** Dispersion relations of LH-TL (*solid curve*) and C-TL (*dashed curve*).

waves and the passband exhibits left-handedness. The phase shift difference between the LH-TL and C-TL keeps a constant of 180° over the entire passband.

To avoid the reflection at the end of the structure and achieve a perfect match to the LC network of the proposed structure, we should consider the ratio of voltages and currents in the network (with the unit cell of Fig. 15.1(a)). As the network is periodic, the ratio is constant at any $n$th point of the structure. This constant is called the Bloch impedance $Z_B$, which can be obtained from the following expression (for the positively traveling waves):

$$\begin{aligned} Z_B &= \frac{B}{\sqrt{A^2-1}} \\ &= \frac{\sqrt{(Z_{ser}Y_{par})^2 + 2Z_{ser}Y_{par}}}{Y_{par}} \\ &= \sqrt{\frac{L}{C}\left(1-(4\omega^2 LC-1)\right)} \\ &= \sqrt{\frac{L}{C}(1-\cosh rd)}. \end{aligned} \tag{15.7}$$

Since the characteristic impedance $Z_B$ is frequency dependent, broadband matching is complicated. However, if the frequency of interest lies in the range where $\cosh rd \ll 1$ (this is valid in our analysis below), the characteristic impedance can be simplified as $Z_B \approx \sqrt{L/C}$, which is almost a constant and can be matched to

the characteristic impedance of the homogeneous TL (shown in Fig. 15.2(a)) in the homogeneity limit.

For a practical case, we should take into consideration the unwanted parasitic effect, i.e., the inductance of the shorted line in the unit cell shown in Fig. 15.1(a). The unit cell can be modified into the one shown in Fig. 15.4, where the inductance $L_S$ of the shorted line is introduced in the lattice section of the unit cell.

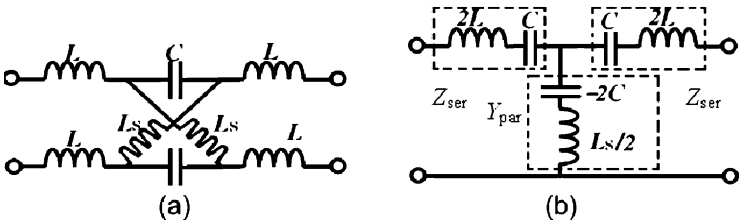


**Fig. 15.4** (**a**) The modified unit cell with the inductance of the shorted line and (**b**) its equivalent circuit.

Using the same approach in the above discussion, we can derive the equivalent circuit of the modified unit cell as shown in Fig. 15.4(b), and its dispersion relation is given by

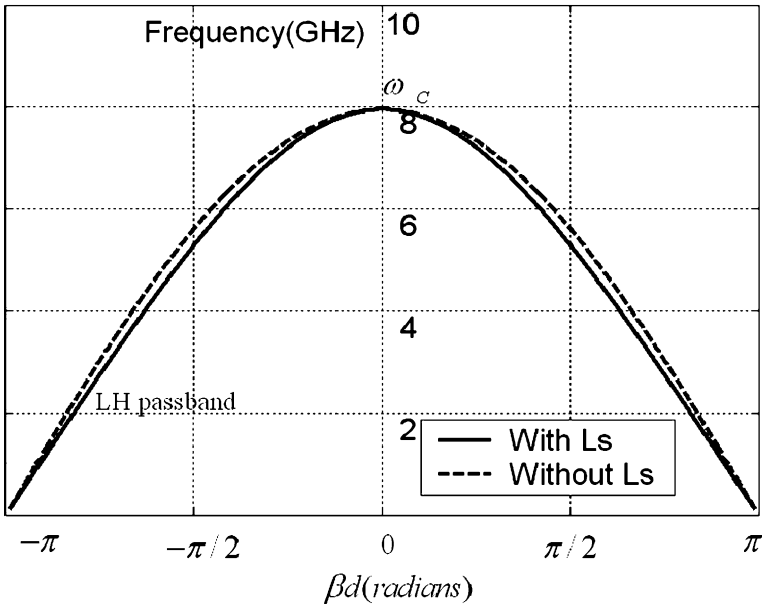


**Fig. 15.5** Dispersion relations of LH-TL in the practical case (*solid curve*) and in an ideal case (*dashed curve*).

$$\begin{aligned}\cosh rd &= 1 + Z_{ser}Y_{par} \\ &= \frac{\omega^2 C(4L + L_S) - 1}{\omega^2 C L_S + 1},\end{aligned} \tag{15.8}$$

where

$$Z_{ser} = (-2\omega^2 LC + 1)/j\omega C, \tag{15.9a}$$

$$Y_{par} = -2j\omega C/(\omega^2 L_S C + 1). \tag{15.9b}$$

When $L_S$ approaches to zero, Eq. (15.8) will reduce to Eq. (15.4) as expected. Dispersion relations (15.4) and (15.8) are plotted in Fig. 15.5 while $L$, $C$, and $L_S$ are chosen to 1 nH, 0.2 pF, and 0.5 nH, respectively. From the dispersion relation, we can see that the modified unit cell still possesses the low-pass property and the left-handedness in the passband between 0 and cutoff frequency $\omega_C$ defined by Eq. (15.6). The introduction of the inductance of the shorted line in the unit cell will only make the phase response vary slightly from that of the ideal case shown in Fig. 15.1, as long as $L_S$ is much smaller than $L$ in the unit cell.

## 15.3 Application: A 180° Hybrid Ring (Rat-Race)

A band-broadened hybrid ring of rat-race type is shown in Fig. 15.6 as an application of the present LH-TL of low pass. It consists of three C-TL sections and one LH-TL section with normalized impedance of 70.7 ohm ($\sqrt{L/C}$ for LH-TL and $\sqrt{2L/C}$ for C-TL). The values of inductances and capacitors are 1 nH and 0.4 pF in the C-TL sections, and 1 nH and 0.2 pF in the LH-TL section. The characteristic impedances of four ports are all 50 ohm in our simulation.

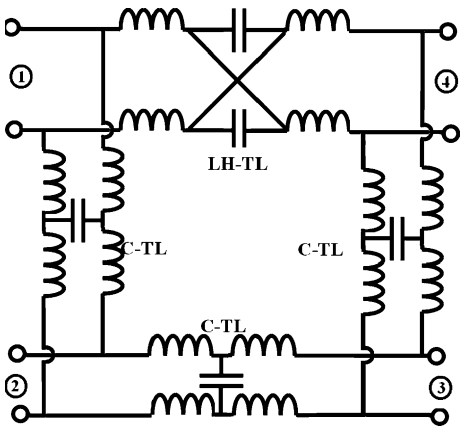


**Fig. 15.6** A band-broadened hybrid ring.

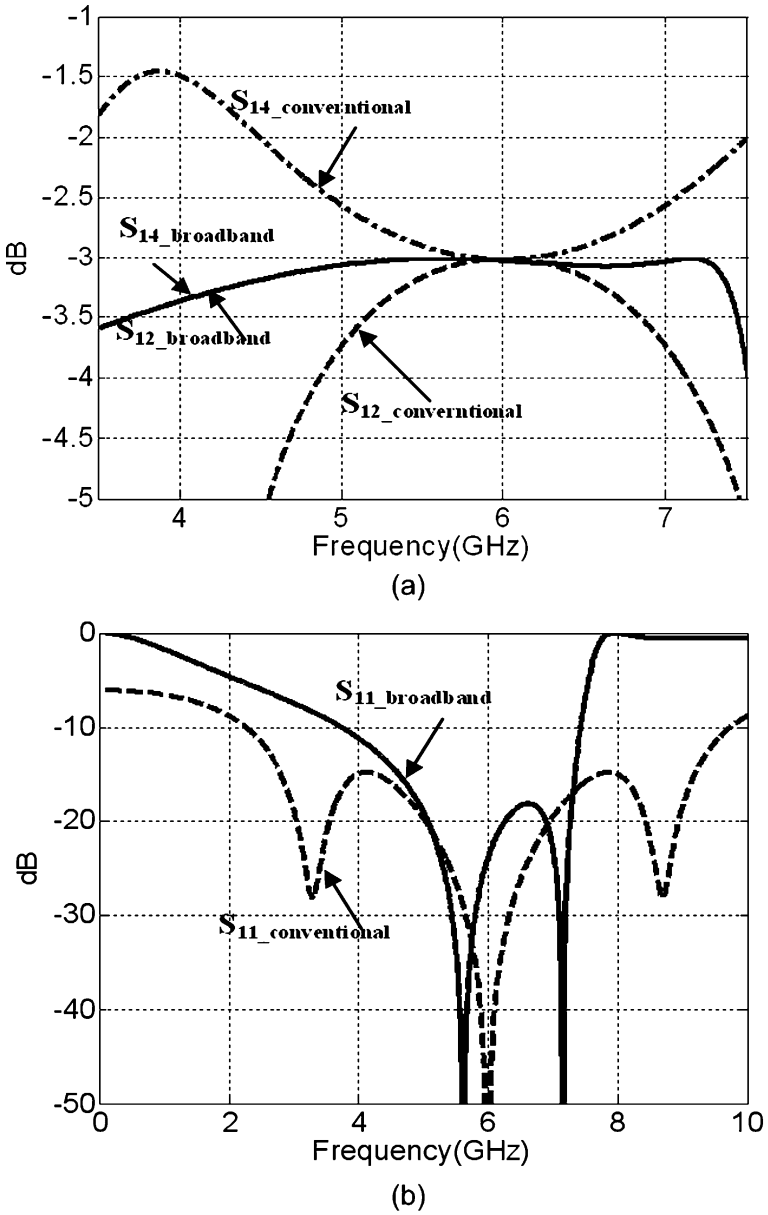


**Fig. 15.7** Comparison of the band-broadened hybrid ring and a conventional hybrid ring [5]: (**a**) Coupling coefficients $S_{12}$ and $S_{14}$ and (**b**) reflection coefficient $S_{11}$.

Figure 15.7 shows the simulated frequency characteristics of the scattering parameters for the proposed hybrid ring and a conventional hybrid ring (consisting of four sections of C-TL with electrical length of $\lambda/4$ and characteristic impedance of 70.7 ohm). Due to the frequency-independent 180° phase shift between the C-TL

section and the present LH-TL section, the isolations between port 1 and port 3 (i.e., $S_{13}$), port 2 and port 4 (i.e., $S_{24}$) are much less than $-100$ dB over the whole frequency band and thus are not shown in this figure. This property does not exist in a conventional hybrid ring [5] or any other hybrid ring. From Fig. 15.6(a) we can see that the powers distributed to port 2 and port 4 are the same and vary slowly with the frequency. From 4.8 to 7.3 GHz, $S_{12}$ and $S_{14}$ are in the range of ($-3.1$ dB, $-3$ dB), exhibiting a 42% bandwidth (with respect to the central frequency of 6 GHz), which is much larger than that of a conventional hybrid ring (typically only 15%). Reflection coefficient $S_{11}$ is shown in Fig. 15.7(b).

## 15.4 Conclusion

We have demonstrated a novel realization of left-handed transmission line by utilizing a lattice circuit in the unit cell. The proposed LH-TL is shown to have the same low-pass property as a C-TL, but with a 180° phase shift difference from a C-TL over the whole passband. Based on the latter property, a hybrid ring with an extremely broad band has been successfully designed as an application of the present LH-TL. It has high isolation and equal power distribution over a large band. The proposed LH-TL can have many other potential applications such as filters and lead/leg shifters.

**Acknowledgments** This work was supported by the National Basic Research Program (973) of China (no. 2004CB719802) and the Swedish Research Council (VR) under project no. 2006-4048.

## References

1. Veselago, V.G.: The electrodynamics of materials with simultaneously negative values of $\underline{\varepsilon}$ and $\mu$. Sov. Phys. Usp **10**, 509–514 (1968)
2. Eleftheriades, G.V., Iyer, A.K., Kremer, P.C.: Planar negative refractive index media using periodically L-C loaded transmission lines. IEEE Trans. Micro. Theory Tech. **50**, 2702–2712 (2002)
3. Iyer, A.K., Eleftheriades, G.V.: Negative refractive index metamaterials supporting 2-D waves. Proc. IEEE Int. Symp. Micro. Theory Tech. **2**, 1067–1070 (2002)
4. Scott, R.E., Essigman, M.W.: Linear circuits, part 1, time-domain analysis. Addison Wesley, Reading, MA, Chapter **5** (1960)
5. Collin, R.E.: Foundations of microwave engineering, 2nd edn. McGraw Hill, 435–444 (1992)

# Index



T.J. Cui et al. (eds.), *Metamaterials*, DOI 10.1007/978-1-4419-0573-4,